Molecular Tuning of Electrocatalysts for Generation of Commodity Chemicals

Thesis by
Gavin P. Heim

In Partial Fulfillment of the Requirements for the Degree of
Doctor of Philosophy in Chemistry

CALIFORNIA INSTITUTE OF TECHNOLOGY
Division of Chemistry and Chemical Engineering
Pasadena, California
2024
(Defended March 11th, 2024)

Gavin P. Heim
ORCID: 0000-0002-9244-6565

"*Do not pray for easy lives; pray to be stronger men! Do not pray for tasks equal to your powers; pray for powers equal to your tasks! Then the doing of your work shall be no miracle.*" —Phillips Brooks

ACKNOWLEDGEMENTS

I have had the opportunity to be a PhD student in chemistry, one of the most tremendous intellectual experiences. My time at the California Institute of Technology was rife with joyous high points and unfortunate lows, both of which allowed me to build character that is necessary for success and learning beyond the laboratory or classroom. Despite the PhD student's requirement to make novel, individual contributions to their field, this journey would not have been accomplished without the crucial help of many individuals.

I would first like to thank my PhD advisor, Theo Agapie for his unmatched engagement and mentorship, which were crucial for my development as a scientist. His excitement for science was obvious upon visiting Caltech, before even starting grad school! I am beyond appreciative of Theo's support and constructively critical perspectives on my projects, writing, presentations, and approach to teaching. I most enjoyed dropping by his office for impromptu discussions. We had some truly engaging conversations which tremendously facilitated my learning and scientific development.

I would also like to thank Jonas Peters for being the chair of my thesis committee and advising the heterogeneous CO_2 reduction project. I received great high-level feedback on my projects during candidacy which really sharpened my scientific inquiry skills. The feedback I received after my proposal exam was especially useful in coming up with intellectually novel proposals and how to make them well-written.

My other two committee members, Brian Stoltz and Karthish Manthiram were also instrumental in my development as a scientist. Brian taught me the importance of engaging a broad audience of scientists when presenting research/novel ideas. Karthish inspired me to

really push myself in gaining expertise in subjects that I wasn't immediately familiar with to help gain new insights into my ongoing scientific pursuits.

I am grateful to the following individuals for teaching tremendously stimulating coursework that I had the opportunity to be enrolled in: Theo, Jonas, Harry Gray, Kim See, and Mike Takase.

I would also like to acknowledge the collaborations I had with other PIs both at Caltech and other institutions, including John Gregoire, Bill Goddard, Walter Drisdell (LBL), Cliff Kubiak (also my undergraduate advisor, UCSD), Smaranda Marinescu (USC), Graham de Ruiter (Technion), Alexis T. Bell (LBL), Frances Houle (LBL), Adam Weber (LBL), and Shane Ardo (UCI). I am grateful for the work of researchers in these collaborations, including Ty Lai, Matthias Richter, Charles Musgrave III, Laura Paradis-Fortin (LBL), Thomas Chan (UCSD), David Velazquez (USC), Alex King (LBL), Doug Kushner (LBL), and Jen Urbine (UCI).

I am grateful to countless individuals who were my colleagues and friends over the years. I received great mentorship in the lab when I first arrived at Caltech in the summer of 2018. I am indebted to my original postdoc mentor, Arnaud Thevenon for his tireless engagement and mentorship in the numerous laboratory techniques in which I lacked basic experience. His teachings in molecular chemistry as well as electrochemistry really gave me the confidence to tackle any interdisciplinary scientific question. He also helped me think beyond the day-to-day of the lab minutiae and think critically about the bigger picture of all my projects and new ideas. I am also grateful to other former and current postdocs and staff scientists from whom I received invaluable teachings: Alonso Rosas-Hernández, Masa

Hirahara, Manar Shoshani, Gwen Bailey, Weixuan Nie, Ian Sullivan, Yueshen Wu, Hai Dong, Priyo Ghana, and Paramita Saha.

I would not have been able to make accomplishments in the lab were it not for the wisdom of many former/current graduate student friends/colleagues. I would like to thank Marcus Low, HB Lee, Chris Reed, Nate Hirscher, Charlie Arnett, Ryan Ribson, and Jessica Sampson for setting a high-level, rigorous example of carrying out scientific research and molecular synthesis techniques in the Agapie group. I had the pleasure of working nearly five years with several students older than myself including Meaghan Bruening, Anna Scott, Sam Xiong, and Angela Shiau. I am grateful to each of them for the stimulating conversations, outside-of-lab hangouts, and invaluable advice. I am especially grateful to Meaghan for her industrious synthetic efforts on our most recent CO_2 reduction project.

I would like to acknowledge the companionship and camaraderie of other individuals in the Agapie and Peters labs. Nick Watkins and I had to build up a lot of systems and protocols in the beginning of the LiSA era. I am grateful for him as a co-worker and a friend. I am glad we got to share interests in heavy metal, soccer, and our nascent forays into married life! Many thanks to other grad student members, past and present, of the LiSA project: Madeline Hicks, Matthew Salazar, and Max Zhelyabovskiy. I am grateful to these individuals for their critical feedback on my work. Despite my responsibility in mentoring Matthew and Max, they each taught me a lot about electrochemistry, basic engineering principles, and solid-state NMR! I am grateful to all current members of the Agapie group not yet mentioned: Matt Espinosa, Linh Le, Mike He, Fernando Guerrero, and Adjeoda Tekpor. I tirelessly thank all members of the Agapie group, past and present, with whom I have interacted for enhancing my development as a scientist.

I would like to thank the following individuals for giving me a chance to provide mentorship in the laboratory setting: Vidhya Dev, David Dumas, and Matthew Salazar. Thank you, all, for working with me and teaching me about my strong suits and limitations. I will watch your careers closely and look forward to your scientific achievements.

I would like to thank other scientists for helping me with instrumentation and maintaining the facilities that make Caltech a one-of-a-kind research institution. Dave Vander Velde (liquid NMR), Sonjong Hwang (solid state NMR), Mona Shahgholi (mass spectrometry), Mike Takase (X-ray crystallography), and Larry Henling.

I am grateful to other staff in CCE, including Alison Ross for organizing prospectives visits, teaching assignments, and overall maintaining a great research program. Margarita Davis, Tiffani Walker, Tomomi Kano, Martha Hepworth, Joyce Wu, and Julianne Just are thanked for helping me organize various LiSA and committee meetings. I am grateful to Nathan Hart for fixing and preparing many glassware items for the lab. I am also grateful to the efforts of Joe Drew (facilities) and Nate Siladke (Environmental Health and Safety).

My genesis as a scientist would not have been remotely possible without the dedication and mentorship of several individuals at my undergraduate institution, University of California, San Diego. I am grateful to Cliff Kubiak for taking me on as a second-year student in the spring of 2016 making me greatly interested in working in the lab chasing novel scientific phenomena. I would like to thank Tyler Porter, my grad student mentor for his immense dedication to my learning and encouraging me to work hard in the lab to achieve rigorous results. I am also grateful to the following individuals for stimulating career and science discussions: Felix Brunner, Chris Miller, Andy Ostericher, Alissa Sasayama, Melissa

Helm, Steven Chabolla, Kate Waldie, Alma Zhanaidarova, Gwen Lee, Po Ling Cheung, John Goeltz, and Eric Benson.

I would especially like to point out the tremendous assistance with job searching and obtaining interviews from the following: Steven Chabolla, Po Ling Cheung, John Goeltz, Jacob Kanady, Tanvi Ratani, Eric Benson, Hai Dong, Javier Fajardo Jr., Nina Gu, Alejo Lifschitz, Slobodan Mitrovic, Ryan DeBlock, Alex Welch, and John Gregoire. After an arduous job search, I am excited to embark on the next stage of my career at Intel!

On a more personal note, I am grateful for the continuous, indefatigable support of friends and family, without which I would not have survived my PhD studies. I am grateful to my parents, Peter and Therese, for their love, support, and curiosity about my career interests throughout all of my schooling. I must also thank my brother, Colin. The lessons he taught me in soccer and life from a young age made it possible for me to develop the drive to work hard towards achieving anything. Thank you, Colin, for pushing me in every way possible to become the best in any endeavor that I undertook. I miss you very much, and I hope we can reconnect someday. I am also thankful for the encouragement from my cousins, aunts, uncles, and grandparents from the Heim and Dufault families.

I am grateful for the support and encouragement of my wife's family, Louriane and Ron. Thank you for the immense curiosity about my work and support for my career choices.

Thank you, Noah Kim, Massoud Maher, and Matt Williams, for being great friends since undergrad. Thank you for standing by my side at the altar at the wedding. I hope someday to reciprocate and be a groomsman at each of your weddings!

Thank you, Ruben Mirzoyan, Roman Korol, and Alex Buser, for being great roommates and friends when we were all just starting our PhDs. I reminisce over the great

times we had hanging out in the apartment, going to the gym, and visiting Old Town Pasadena. I wish all of you the best of luck in life and your careers.

Finally, I have the ultimate joy of thanking my wife, Bonnie for being my other half and sticking by my side. Bonnie, thank you, from the bottom of my heart for being a tremendously loving and empathetic wife. Thank you for your patience and relentless support. You have taught me the importance of family and life outside of the lab; nothing we do in our work matters if we cannot maintain what we have at home. Thank you for making me a better person; I have learned more from you than many experiments I performed! You are and incredibly creative and resilient individual who doesn't back down from hardship. I look forward to an amazing future together.

ABSTRACT

Improving our understanding of electrocatalytic transformations is envisioned to facilitate society's implementation of technologies that achieve a net zero carbon footprint. Carbon dioxide is one of the most emitted greenhouse gases, and improvement in CO_2 capture technologies along with decreasing costs of renewable energy provide an opportunity to convert this species to value-added chemicals using electrochemical processes. Tuning homogeneous and heterogeneous electrocatalyst performance with well-defined molecular species can render systems more selective and active while also allowing us to readily predict variables crucial in achieving these transformations. This thesis investigates 1) molecular and polymeric species as electrode coatings for enhanced generation of carbon-coupled products and 2) discrete electrocatalyst active sites for formation CO_2 reduction products at low overpotentials; generation of highly reduced liquid fuels is observed with molecular electrocatalysts supported on electrodes.

Chapter I provides context and background to the contents of this thesis.

Chapter II discusses novel, polyaromatic molecular additives utilized for low pH CO_2 reduction on Cu electrodes. *N*-phenyl isoquinolinium triflate film facilitates high selectivity for C_{2+} products in 0.1 M H_3PO_4/KH_2PO_4, suggesting enhancement in CO_2 mass transport rather than limiting proton carrier diffusion. Improvement in long-term stability and tolerance to lower pH compared to previous films is observed.

Chapter III reports on a series of polystyrene-based ionomers to probe the effect of local $[K^+]$ in the Cu electrode microenvironment on CO_2R performance. Partial current density towards C_{2+} products ($|j_{C2+}|$) increases monotonically with $[K^+]$ in ionomer, up to 225 mA cm^{-2}. Replacing K^+ with $[Me_4N]^+$ lowers performance to the level of bare Cu,

highlighting the crucial role of K^+ in improving C_{2+} product selectivity. Molecular dynamics simulations and partial pressure CO_2 electrolysis experiments are consistent with enhanced CO_2 mass transport due to K^+ in the film.

Chapter IV discusses variation of ionomer/polymer structures to maximize CO_2R performance. Incorporation of neutral comonomers bearing cross-linking units rich in biphenyl and terphenyl motifs result in high current densities (~270 mA cm^{-2}) towards C_{2+} products with 82% Faradaic efficiency. The analogous neutral variants (i.e., those lacking the charged comonomer) show comparable $|j_{C2+}|$ to the K^+-containing polymers, suggesting a non-innocent role of the aryl-rich polymers in boosting performance.

Chapter V presents novel four-coordinate, dicationic Co complexes supported on carbon nanotubes capable of generating MeOH from CO_2. Electrolysis with CO also leads to formation of MeOH, suggesting a CO-bound complex to be a crucial intermediate in CO_2R to MeOH. This work highlights rare examples of molecular systems facilitating multi-electron electrochemical transformations to highly demanded commodity chemicals.

Chapter VI presents work on molecular electrocatalysts bearing novel polyaromatic ligands that lower the electrocatalytic potential (E_{cat}) of CO_2R by ~310 mV compared to state-of-the-art complexes as determined via cyclic voltammetry. The extended π system motif is more proximal to the metal center relative to previously reported nanographene-containing electrocatalysts. Well-defined characterization was obtained via single-crystal X-ray diffraction in addition to solution-state techniques. Density functional theory calculations reveal significant ligand contributions in the frontier orbitals of relevant CO_2R intermediates.

Chapter VII highlights a polycyclic aromatic hydrocarbon (PAH) bearing twelve edge nitrogen atoms. Spectroscopy, electrochemistry, and computational results suggest a

significant narrowing of the HOMO-LUMO gap compared to the N-free analogue owing to the electron-deficient extended π system imposed by the nitrogen dopants. Changes to absorption and emission spectra from titration of the PAH with metal salts suggest that coordination chemistry provides an additional degree of freedom towards tuning electronic structure. Dramatic changes from addition of trifluoromethanesulfonic acid suggest this material to be a possible pH sensor. This approach in judiciously tuning the band gap of bulk graphene materials via saturation of the nanographene edge sites with nitrogen atoms gives rise to a novel comound with intriguing electronic properties

Appendix A describes systematic attempts in demonstrating cascade electrocatalysis between molecular CO_2-to-CO complexes and pyridinium film-modified Cu towards enhanced rates of C_{2+} products formation.

Appendix B provides results coupling electrodeposited imidazolium-derived films with pyridinium towards enhanced CO_2R to C_{2+} on Cu. While promising performance is achieved, the difficulty in characterizing the films limits the tractability of these systems with respect to their impacts on the microenvironment.

Appendix C discusses developing coordination complexes of heteroatom containing polyaromatic hydrocarbons. Several examples characterized via X-ray crystallography are reported.

Appendix D shows CO_2R data on K^+ ionomer-coated Au. Elevation in $|j_{CO}|$ is demonstrated as a function of potassium content in the electrode-electrolyte interface provided by the film.

Appendix E discusses attempts to determine and CO_2 uptake by K^+ ionomers via solid state NMR spectroscopy.

PUBLISHED CONTENT AND CONTRIBUTIONS

Chapter II:

1. Nie, W.; **Heim, G.P.**; Watkins, N.B.; Agapie, T.; Peters, J.C. Organic Additive-derived Films on Cu Electrodes Promote Electrochemical CO_2 Reduction to C_{2+} Products Under Strongly Acidic Conditions. *Angew. Chem. Int. Ed.* **2023**. *135*. e202216102. DOI: 10.1002/anie.202216102

W.N. designed and carried out most electrochemistry experiments. G.P.H. performed some electrochemistry and synthesis. N.B.W. aided in experimental design. T.A. and J.C.P. supervised the project. All authors analyzed data and prepared the manuscript.

2. **Heim, G.P.**; Nie, W.; Peters, J.C.; Agapie, T. *Manuscript in preparation.*

G.P.H. performed all electrochemistry experiments. W.N. aided in data analysis. T.A. and J.C.P. oversaw the project. All authors analyzed data and prepared the manuscript.

Chapter III:

3. **Heim, G.P.**[†]; Bruening, M.A.[†]; Musgrave III, C.B.; Goddard III, W.A. Peters, J.C.; Agapie, T. *Joule.* **2024**. *Accepted article.*

G.P.H. designed and carried out electrochemistry experiments. M.A.B. synthesized all polymers. C.B.M performed computations. T.A., J.C.P., and W.A.G. supervised the project. All authors analyzed data and prepared the manuscript.

Chapter VI:

4. **Heim, G.P.**; Dev, V.M.; Agapie, T. *Manuscript submitted.*

G.P.H. performed all experiments. V.M.D. aided in performing computations. T.A. supervised the project. All authors analyzed data and prepared the manuscript

Chapter VII:

5. **Heim, G.P.**; Hirahara, M.; Dev, V.M.; Agapie, T. *Manuscript submitted.*

G.P.H. performed spectroscopy experiments, optimized the synthesis, and performed computations. M.H. and V.M.D. initially investigated the synthesis of the titular compound. T.A. supervised the project. All authors analyzed data and prepared the manuscript

Other publications:

6. Lai, Y.; Watkins, N.B., Rosas-Hernández, A.; Thevenon, A.; **Heim, G.P**.; Zhou, L.; Wu, Y.; Peters, J.C.; Gregoire, J.; Agapie, T. Breaking Scaling Relationships in CO_2 Reduction on Copper Alloys with Organic Additives. *ACS Central Science.* **2021,** *7*, 1756-1762. DOI: 10.1021/acscentsci.1c00860

Y.L. carried out experiments. N.B.W., A.R.H., A.T., and G.P.H. aided in data analysis. L.Z. performed materials characterization. J.C.P., J.G., and T.A. supervised project. All authors prepared manuscript.

TABLE OF CONTENTS

CHAPTER I

GENERAL INTRODUCTION

Towards a net-zero carbon emissions landscape. Converting CO_2 to value-added chemicals electrochemically using renewable energy is a potential avenue toward achieving a net-zero carbon economy.[1,2] CO_2 is envisioned to be an inexpensive source of carbon as a result of developing sequestration technologies.[3] Electrocatalysts are well-suited for facilitating CO_2 conversion to value-added chemicals in order to close the anthropogenic carbon cycle.[4] Electrocatalysts offer much tractability over performance metrics including selectivity, efficiency, activity, and durability.[5] Moreover, these systems provide an opportunity to drive commodity chemical production via renewable energy.

Table 1. Commodity chemicals production and market size

	Ethylene	Ethanol	Sulfuric acid	Sodium hydroxide	Propylene	Nitrogen
Total production 2022 (Mt)	214	45	260	70	85	117
Market size (billions of USD)	170	75	10	29	96	31

Electrochemical CO_2 reduction (CO_2R) to commodity chemicals is an attractive pursuit as there remains several pressing scientific questions related to fundamental aspects of electrochemistry and reactivity involving molecular and materials-based electrocatalysts. In addition, several engineering challenges exist related to scalability.[6] In order to render electrolyzers as attractive technologies, it is necessary to convert CO_2 to globally demanded commodity chemicals at high activities to minimize energy input costs.[7] Ethylene and ethanol are highly produced and demanded carbon-containing products (Table 1), serving as a precursor to plastics and additive in gasoline, respectively.[8–10] Generation of commodity

chemicals with high selectively and activity using appropriate electrocatalyst platforms remains a leading challenge in the CO_2R field.

Tuning metallic electrocatalyst performance. Heterogeneous electrocatalysts can enact electrochemical transformations at high activities with exceptional durability.[11–19] Product separation is more feasible compared to homogeneous systems.[13,15,20] Cu is the only metallic electrode where value-added multi-carbon (C_{2+}) products, including ethylene, ethanol, and 1-propanol, and acetic acid are produced from electrochemical CO_2R (Scheme 1).[21] However, Cu alone suffers from poor selectivity towards C_{2+} products owing to the significant generation of C_1 products and hydrogen.[21–23]

Scheme 1. Products detected from CO_2R on Cu electrodes

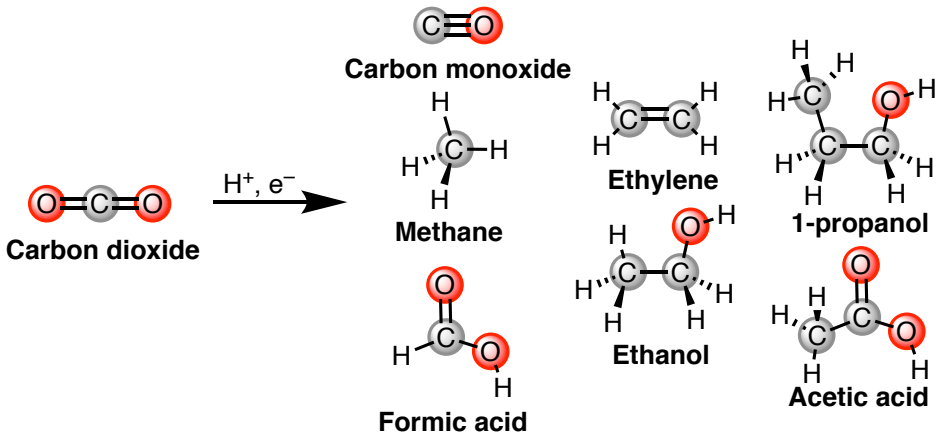

Other metallic electrodes (Ag, Au) are selective for generation of CO.[24] There is much interest in boosting CO_2R performance on Cu towards C_{2+} products such that these products are generated with greater Faradaic efficiencies (selectivity) and current density magnitudes (activity). Aspects that have been investigated to impact performance of Cu include mass transport,[25] hydrodynamics,[26] local electric field,[27,28] and bulk electrode properties.[29–31] Films have also emerged species that tune electrocatalyst performance. Organic coatings derived from molecular precursors such as pyridinium,[32–36] ionic liquids,[37–39] amines,[40,41] and aryl

diazonium and iodonium species[42] have shown promise. *In situ* electrodeposition of water-soluble aryl pyridnium compounds to generate water-insoluble films boosted Faradaic efficiency for C_{2+} products (FE_{C2+}) while attenuating FE_{H2}; the partial current for H_2 ($|j_{H2}|$) decreased by 13-fold.[35] $|j_{C2+}|$ was found to decrease by a factor of 1.5. Additional studies were performed to uncover the films' impacts on proton carrier mass transport,[32] alteration of Cu morphology,[33] and the stability of CO_2R intermediates.[34] Recent work has demonstrated dramatic hydrogen evolution reaction (HER) suppression in low pH electrolyte;[36] follow-up work is presented in Chapter II.

While a complete understanding of the pyridinium-derived films' impacts on CO_2R performance remains elusive, proton mass transport is evidently the most consequential phenomenon with respect to pyridinium's impact on the microenvironment.[32] Moreover, current results suggest difficulty in judiciously designing films to obtain desired results. Several additional factors impacting performance exist that are not readily predicted by most film strategies; these include alkali cation effect, local CO_2 concentration/mass transport, hydrophobicity, and local electric field.[23,43–46] Polymers bearing charges (i.e., ionomers) have recently been implemented to boost CO_2R performance on Cu attempting to control some of these aspects.[47–49] It is of interest to study systems amenable to development of systematic structure-function relationships to more generally address the role factors governing CO_2R performance.[48]

Electrocatalysis with well-defined molecular complexes. Molecular electrocatalysis is advantageous for allowing precise electronic or steric modulation of active species to provide desired impacts on performance;[12,50–64] such studies have provided insight into catalytic mechanisms facilitated by *in situ* spectroscopy.[65] Molecular

CO_2R electrocatalysts typically yield CO, a component of synthesis gas utilized in Fisher-Tropsch chemistry.[66–68] State of the art molecular systems perform CO_2R at high turnover frequencies and low overpotentials (Figure 1).[69]

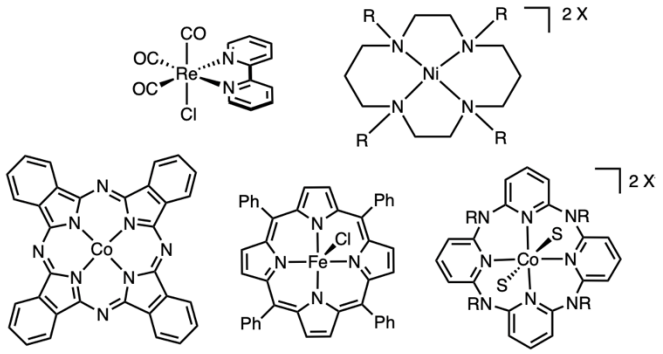

Figure 1. Examples of molecular CO_2R electrocatalysts.

Previous work in electrocatalysis has utilized single-atom catalysts (SACs) demonstrating high selectivity at low overpotentials for CO_2R, where the proposed active metal site is embedded in a heteroatom-doped graphene.[70–74] Recent work has investigated well-defined nanographene molecules as model systems for SACs able to demonstrate high electrocatalytic performance.[75–78] Modifications to the 2,2-bipyridine ligand in Lehn complexes with a polycyclic aromatic hydrocarbon (PAH) have been reported and are able to lower the potential for CO_2R by up to 800 mV relative to the parent system (Figure 2).[75,77,78] However, there are few reports of discrete molecular systems where the polyaromatic moiety is proximal to the metal center, a way to further enhance communication between the ligand and the substrate binding site. Studies discussing this strategy have observed poor CO_2R performance attributed to aggregation of the molecular complex.[77] Incorporation of different heteroatoms in extended π system ligands for

electrocatalysis has been less explored but could provide an additional degree of freedom for tuning electrocatalytic performance.

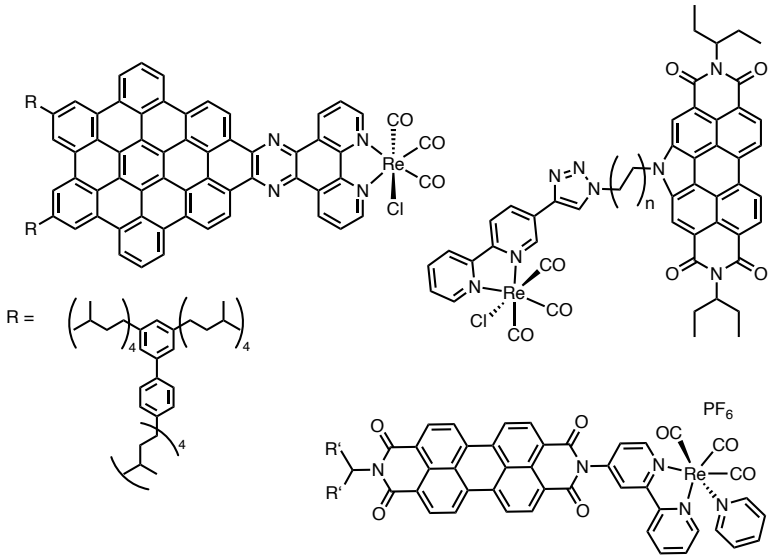

Figure 2. Extended π system ligands supporting Re for electrochemical CO_2R.

Metal phthalocyanine (Pc) complexes were studied as proposed model complexes for SACs.[79] **CoPc** immobilized onto carbon nanotubes has demonstrated high CO_2R current density for generating CO, comparable to metallic Ag and Au electrocatalysts.[80,81] Recent work demonstrated high Faradaic efficiency to MeOH; CO_2R products generated from more than two electrons are not typically observed from molecular electrocatalysis.[82] **CoPc** is to date the only reported molecular complex that has facilitated electrochemical CO_2 conversion to MeOH. Investigating additional examples with ligand environments bearing greater modularity can inform on electronic properties necessary for optimal reactivity in generating MeOH.

Heteroatom-containing polyaromatic hydrocarbons for novel electronic properties. Polycyclic aromatic hydrocarbons (PAHs) have attracted substantial interest in

the development of charge-carrying materials owing to their unique optical and electronic properties.[83–88]

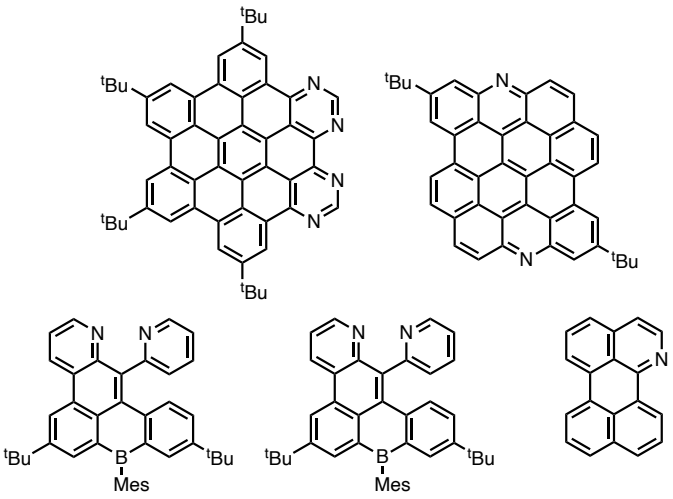

Figure 3. Examples of N- and N, B-containing polyaromatic hydrocarbons.

Preparation from molecular precursors affords discrete nanographenes that are amenable to well-defined characterization via solution-state spectroscopy and X-ray crystallography.[86,89] Hexabenzocoronenes (HBCs) have received much attention due to high thermal stability and modular preparations.[83,84,90,91] Facile tunability of electronic structure is of interest to ascertain the ability of nanographene molecules as candidate materials for organic electronics;[85] strategies include incorporation of heteroatom dopants,[92,93] functionalization with electron-withdrawing/donating substituents,[86,94,95] and coordination to metal centers.[75,96,97] Moreover, nitrogen-containing polyaromatics have displayed novel photophysical properties;[88,92,96–98] maximization of nitrogen content could provide enhancement with respect to band gap tunability.[71,88,99] Incorporation of nitrogen atoms allowed utilization of coordination chemistry to affect electronic structure.[88,96,97] However, generation of these complexes on preparative scales with well-defined characterization has been elusive.[92]

REFERENCES

(1) Nitopi, S.; Bertheussen, E.; Scott, S. B.; Liu, X.; Engstfeld, A. K.; Horch, S.; Seger, B.; Stephens, I. E. L.; Chan, K.; Hahn, C.; et al. Progress and Perspectives of Electrochemical CO2 Reduction on Copper in Aqueous Electrolyte. *Chem. Rev.* **2019**, *119* (12), 7610–7672.

(2) Chu, S.; Majumdar, A. Opportunities and Challenges for a Sustainable Energy Future. *Nature* **2012**, *488* (7411), 294–303.

(3) Jiang, Y.; Mathias, P. M.; Zheng, R. F.; Freeman, C. J.; Barpaga, D.; Malhotra, D.; Koech, P. K.; Zwoster, A.; Heldebrant, D. J. Energy-Effective and Low-Cost Carbon Capture from Point-Sources Enabled by Water-Lean Solvents. *J. Clean. Prod.* **2023**, *388*, 135696.

(4) Lewis, N. S.; Nocera, D. G. Powering the Planet: Chemical Challenges in Solar Energy Utilization. *Proc. Natl. Acad. Sci.* **2006**, *103* (43), 15729–15735.

(5) Seh, Z. W.; Kibsgaard, J.; Dickens, C. F.; Chorkendorff, I.; Nørskov, J. K.; Jaramillo, T. F. Combining Theory and Experiment in Electrocatalysis: Insights into Materials Design. *Science (80-.).* **2017**, *355* (6321), eaad4998.

(6) Sun, J. W.; Fu, H. Q.; Liu, P. F.; Chen, A.; Liu, P.; Yang, H. G.; Zhao, H. Advances and Challenges in Scalable Carbon Dioxide Electrolysis. *EES Catal.* **2023**, *1* (6), 934–949.

(7) Moore, T.; Oyarzun, D. I.; Li, W.; Lin, T. Y.; Goldman, M.; Wong, A. A.; Jaffer, S. A.; Sarkar, A.; Baker, S. E.; Duoss, E. B.; et al. Electrolyzer Energy Dominates Separation Costs in State-of-the-Art CO2 Electrolyzers: Implications for Single-Pass CO2 Utilization. *Joule* **2023**, *7* (4), 782–796.

(8) The Search for Greener Ethylene. *Chemical and Engineering News*. 2023.

(9) 5 Most Common Industrial Chemicals. *Noah Chemicals*.

(10) Global Ethylene Industry Outlook to 2028. *GlobalData*.

(11) Zhanaidarova, A.; Jones, S. C.; Despagnet-Ayoub, E.; Pimentel, B. R.; Kubiak, C. P. Re(TBu-Bpy)(CO)3Cl Supported on Multi-Walled Carbon Nanotubes Selectively Reduces CO2 in Water. *J. Am. Chem. Soc.* **2019**, *141* (43), 17270–17277.

(12) Grammatico, D.; Bagnall, A. J.; Riccardi, L.; Fontecave, M.; Su, B.-L.; Billon, L. Heterogenised Molecular Catalysts for Sustainable Electrochemical CO2 Reduction. *Angew. Chemie Int. Ed.* **2022**, *61* (38), e202206399.

(13) Willkomm, J.; Bertin, E.; Atwa, M.; Lin, J.-B.; Birss, V.; Piers, W. E. Grafting of a Molecular Rhenium CO2 Reduction Catalyst onto Colloid-Imprinted Carbon. *ACS Appl. Energy Mater.* **2019**, *2* (4), 2414–2418.

(14) Wu, Y.; Liang, Y.; Wang, H. Heterogeneous Molecular Catalysts of Metal Phthalocyanines for Electrochemical CO2 Reduction Reactions. *Acc. Chem. Res.* **2021**, *54* (16), 3149–3159.

(15) Bullock, R. M.; Das, A. K.; Appel, A. M. Surface Immobilization of Molecular Electrocatalysts for Energy Conversion. *Chem. – A Eur. J.* **2017**, *23* (32), 7626–7641.

(16) Schild, J.; Reuillard, B.; Morozan, A.; Chenevier, P.; Gravel, E.; Doris, E.; Artero, V. Approaching Industrially Relevant Current Densities for Hydrogen Oxidation with a Bioinspired Molecular Catalytic Material. *J. Am. Chem. Soc.* **2021**, *143* (43), 18150–18158.

(17) Ghedjatti, A.; Coutard, N.; Calvillo, L.; Granozzi, G.; Reuillard, B.; Artero, V.; Guetaz, L.; Lyonnard, S.; Okuno, H.; Chenevier, P. How Do H2 Oxidation Molecular Catalysts Assemble onto Carbon Nanotube Electrodes? A Crosstalk between Electrochemical and Multi-Physical Characterization Techniques. *Chem. Sci.* **2021**, *12* (48), 15916–15927.

(18) Serna, P.; Gates, B. C. Molecular Metal Catalysts on Supports: Organometallic Chemistry Meets Surface Science. *Acc. Chem. Res.* **2014**, *47* (8), 2612–2620.

(19) Sun, C.; Gobetto, R.; Nervi, C. Recent Advances in Catalytic CO2 Reduction by Organometal Complexes Anchored on Modified Electrodes. *New J. Chem.* **2016**, *40* (7), 5656–5661.

(20) Oh, S.; Gallagher, J. R.; Miller, J. T.; Surendranath, Y. Graphite-Conjugated Rhenium Catalysts for Carbon Dioxide Reduction. *J. Am. Chem. Soc.* **2016**, *138* (6), 1820–1823.

(21) Hori, Y.; Kikuchi, K.; Suzuki, S. Production of CO and CH_4 in Electrochemical Reduction of CO_2 at Metal Electrodes in Aqueous Hydrogencarbonate Solution. *Chem. Lett.* **1985**, *14* (11), 1695–1698.

(22) Kuhl, K. P.; Cave, E. R.; Abram, D. N.; Jaramillo, T. F. New Insights into the Electrochemical Reduction of Carbon Dioxide on Metallic Copper Surfaces. *Energy Environ. Sci.* **2012**, *5* (5), 7050–7059.

(23) Murata, A.; Hori, Y. Product Selectivity Affected by Cationic Species in Electrochemical Reduction of CO2 and CO at a Cu Electrode. *Bull. Chem. Soc. Jpn.* **1991**, *64* (1), 123–127.

(24) Sassenburg, M.; de Rooij, R.; Nesbitt, N. T.; Kas, R.; Chandrashekar, S.; Firet, N. J.; Yang, K.; Liu, K.; Blommaert, M. A.; Kolen, M.; et al. Characterizing CO2 Reduction Catalysts on Gas Diffusion Electrodes: Comparing Activity, Selectivity, and Stability of Transition Metal Catalysts. *ACS Appl. Energy Mater.* **2022**, *5* (5), 5983–5994.

(25) Richard, D.; Tom, M.; Jang, J.; Yun, S.; Christofides, P. D.; Morales-Guio, C. G. Quantifying Transport and Electrocatalytic Reaction Processes in a Gastight Rotating Cylinder Electrode Reactor via Integration of Computational Fluid Dynamics Modeling and Experiments. *Electrochim. Acta* **2023**, *440*, 141698.

(26) Watkins, N. B.; Schiffer, Z. J.; Lai, Y.; Musgrave, C. B. I. I. I.; Atwater, H. A.; Goddard, W. A. I. I. I.; Agapie, T.; Peters, J. C.; Gregoire, J. M. Hydrodynamics Change Tafel Slopes in Electrochemical CO2 Reduction on Copper. *ACS Energy Lett.* **2023**, *8* (5), 2185–2192.

(27) Erick, H. J.; Fengwang, L.; Adnan, O.; Armin, S. R.; Pelayo, G. de A. F.; Shijie, L.; Shuzhen, Z.; Mingchuan, L.; Xue, W.; Yanwei, L.; et al. CO2 Electrolysis to Multicarbon Products in Strong Acid. *Science (80-.).* **2021**, *372* (6546), 1074–1078.

(28) Gu, J.; Liu, S.; Ni, W.; Ren, W.; Haussener, S.; Hu, X. Modulating Electric Field Distribution by Alkali Cations for CO2 Electroreduction in Strongly Acidic Medium. *Nat. Catal.* **2022**, *5* (4), 268–276.

(29) Liu, K.; Smith, W. A.; Burdyny, T. Introductory Guide to Assembling and Operating Gas Diffusion Electrodes for Electrochemical CO2 Reduction. *ACS Energy Lett.* **2019**, *4* (3), 639–643.

(30) Nguyen, T. N.; Dinh, C.-T. Gas Diffusion Electrode Design for Electrochemical Carbon Dioxide Reduction. *Chem. Soc. Rev.* **2020**, *49* (21), 7488–7504.

(31) Lees, E. W.; Mowbray, B. A. W.; Parlane, F. G. L.; Berlinguette, C. P. Gas Diffusion Electrodes and Membranes for CO2 Reduction Electrolysers. *Nat. Rev. Mater.* **2021**.

(32) Thevenon, A.; Rosas-Hernández, A.; Fontani Herreros, A. M.; Agapie, T.; Peters, J. C. Dramatic HER Suppression on Ag Electrodes via Molecular Films for Highly Selective CO2 to CO Reduction. *ACS Catal.* **2021**, *11* (8), 4530–4537.

(33) Thevenon, A.; Rosas-Hernández, A.; Peters, J. C.; Agapie, T. In-Situ Nanostructuring and Stabilization of Polycrystalline Copper by an Organic Salt Additive Promotes Electrocatalytic CO2 Reduction to Ethylene. *Angew. Chemie Int. Ed.* **2019**, *58* (47), 16952–16958.

(34) Li, F.; Thevenon, A.; Rosas-Hernández, A.; Wang, Z.; Li, Y.; Gabardo, C. M.; Ozden, A.; Dinh, C. T.; Li, J.; Wang, Y.; et al. Molecular Tuning of CO2-to-Ethylene Conversion. *Nature* **2020**, *577* (7791), 509–513.

(35) Han, Z.; Kortlever, R.; Chen, H.-Y.; Peters, J. C.; Agapie, T. CO2 Reduction Selective for C≥2 Products on Polycrystalline Copper with N-Substituted Pyridinium Additives. *ACS Cent. Sci.* **2017**, *3* (8), 853–859.

(36) Nie, W.; Heim, G. P.; Watkins, N. B.; Agapie, T.; Peters, J. Organic Additive-Derived Films on Cu Electrodes Promote Electrochemical CO2 Reduction to C2+ Products Under Strongly Acidic Conditions. *Angew. Chemie Int. Ed.* **2023**, *n/a* (n/a).

(37) Cheng, B.; Du, J.; Yuan, H.; Tao, Y.; Chen, Y.; Lei, J.; Han, Z. Selective CO2 Reduction to Ethylene Using Imidazolium-Functionalized Copper. *ACS Appl. Mater. Interfaces* **2022**, *14* (24), 27823–27832.

(38) Buckley, A. K.; Cheng, T.; Oh, M. H.; Su, G. M.; Garrison, J.; Utan, S. W.; Zhu, C.; Toste, F. D.; Goddard, W. A. I. I. I.; Toma, F. M. Approaching 100% Selectivity at Low Potential on Ag for Electrochemical CO2 Reduction to CO Using a Surface Additive. *ACS Catal.* **2021**, *11* (15), 9034–9042.

(39) Rosen, B. A.; Salehi-Khojin, A.; Thorson, M. R.; Zhu, W.; Whipple, D. T.; Kenis, P. J. A.; Masel, R. I. Ionic Liquid–Mediated Selective Conversion of CO2 to CO at Low Overpotentials. *Science (80-.).* **2011**, *334* (6056), 643–644.

(40) Chen, X.; Chen, J.; Alghoraibi, N. M.; Henckel, D. A.; Zhang, R.; Nwabara, U. O.; Madsen, K. E.; Kenis, P. J. A.; Zimmerman, S. C.; Gewirth, A. A. Electrochemical CO2-to-Ethylene Conversion on Polyamine-Incorporated Cu Electrodes. *Nat. Catal.* **2021**, *4* (1), 20–27.

(41) Wei, X.; Yin, Z.; Lyu, K.; Li, Z.; Gong, J.; Wang, G.; Xiao, L.; Lu, J.; Zhuang, L. Highly Selective Reduction of CO2 to C2+ Hydrocarbons at Copper/Polyaniline Interfaces. *ACS Catal.* **2020**, *10* (7), 4103–4111.

(42) Watkins, N. B.; Wu, Y.; Nie, W.; Peters, J. C.; Agapie, T. In Situ Deposited Polyaromatic Layer Generates Robust Copper Catalyst for Selective Electrochemical CO2 Reduction at Variable PH. *ACS Energy Lett.* **2023**, *8* (1), 189–195.

(43) Qin, H.-G.; Li, F.-Z.; Du, Y.-F.; Yang, L.-F.; Wang, H.; Bai, Y.-Y.; Lin, M.; Gu, J. Quantitative Understanding of Cation Effects on the Electrochemical Reduction of CO2 and H+ in Acidic Solution. *ACS Catal.* **2023**, *13* (2), 916–926.

(44) Ringe, S.; Clark, E. L.; Resasco, J.; Walton, A.; Seger, B.; Bell, A. T.; Chan, K. Understanding Cation Effects in Electrochemical CO2 Reduction. *Energy Environ. Sci.* **2019**, *12* (10), 3001–3014.

(45) Zhao, Y.; Hao, L.; Ozden, A.; Liu, S.; Miao, R. K.; Ou, P.; Alkayyali, T.; Zhang, S.; Ning, J.; Liang, Y.; et al. Conversion of CO2 to Multicarbon Products in Strong Acid by Controlling the Catalyst Microenvironment. *Nat. Synth.* **2023**, *2* (5), 403–412.

(46) Monteiro, M. C. O.; Dattila, F.; Hagedoorn, B.; García-Muelas, R.; López, N.; Koper, M. T. M. Absence of CO2 Electroreduction on Copper, Gold and Silver Electrodes without Metal Cations in Solution. *Nat. Catal.* **2021**, *4* (8), 654–662.

(47) Kim, C.; Bui, J. C.; Luo, X.; Cooper, J. K.; Kusoglu, A.; Weber, A. Z.; Bell, A. T. Tailored Catalyst Microenvironments for CO2 Electroreduction to Multicarbon Products on Copper Using Bilayer Ionomer Coatings. *Nat. Energy* **2021**, *6* (11), 1026–1034.

(48) Wang, J.; Cheng, T.; Fenwick, A. Q.; Baroud, T. N.; Rosas-Hernández, A.; Ko, J. H.; Gan, Q.; Goddard III, W. A.; Grubbs, R. H. Selective CO2 Electrochemical Reduction Enabled by a Tricomponent Copolymer Modifier on a Copper Surface. *J. Am. Chem. Soc.* **2021**, *143* (7), 2857–2865.

(49) Pelayo, G. de A. F.; Cao-Thang, D.; Adnan, O.; Joshua, W.; Christopher, M.; R., K. A.; Dae-Hyun, N.; Christine, G.; Ali, S.; Xue, W.; et al. CO2 Electrolysis to Multicarbon Products at Activities Greater than 1 A Cm−2. *Science (80-.).* **2020**, *367* (6478), 661–666.

(50) Boutin, E.; Merakeb, L.; Ma, B.; Boudy, B.; Wang, M.; Bonin, J.; Anxolabéhère-Mallart, E.; Robert, M. Molecular Catalysis of CO2 Reduction: Recent Advances and Perspectives in Electrochemical and Light-Driven Processes with Selected Fe, Ni and Co Aza Macrocyclic and Polypyridine Complexes. *Chem. Soc. Rev.* **2020**, *49* (16), 5772–5809.

(51) Wang, J.-W.; Yamauchi, K.; Huang, H.-H.; Sun, J.-K.; Luo, Z.-M.; Zhong, D.-C.; Lu, T.-B.; Sakai, K. A Molecular Cobalt Hydrogen Evolution Catalyst Showing High Activity and Outstanding Tolerance to CO and O2. *Angew. Chemie Int. Ed.* **2019**, *58* (32), 10923–10927.

(52) Jacques, P.-A.; Artero, V.; Pécaut, J.; Fontecave, M. Cobalt and Nickel Diimine-Dioxime Complexes as Molecular Electrocatalysts for Hydrogen Evolution with Low Overvoltages. *Proc. Natl. Acad. Sci.* **2009**, *106* (49), 20627–20632.

(53) Seo, S.; Lee, K.; Min, M.; Cho, Y.; Kim, M.; Lee, H. A Molecular Approach to an Electrocatalytic Hydrogen Evolution Reaction on Single-Layer Graphene. *Nanoscale* **2017**, *9* (11), 3969–3979.

(54) O'Hagan, M.; Ho, M.-H.; Yang, J. Y.; Appel, A. M.; DuBois, M. R.; Raugei, S.; Shaw, W. J.; DuBois, D. L.; Bullock, R. M. Proton Delivery and Removal in [Ni(PR2NR′2)2]2+ Hydrogen Production and Oxidation Catalysts. *J. Am. Chem. Soc.* **2012**, *134* (47), 19409–19424.

(55) McCrory, C. C. L.; Szymczak, N. K.; Peters, J. C. Evaluating Activity for Hydrogen-Evolving Cobalt and Nickel Complexes at Elevated Pressures of Hydrogen and Carbon Monoxide. *Electrocatalysis* **2016**, *7* (1), 87–96.

(56) McCrory, C. C. L.; Uyeda, C.; Peters, J. C. Electrocatalytic Hydrogen Evolution in Acidic Water with Molecular Cobalt Tetraazamacrocycles. *J. Am. Chem. Soc.* **2012**, *134* (6), 3164–3170.

(57) Barrett, J. A.; Miller, C. J.; Kubiak, C. P. Electrochemical Reduction of CO2 Using Group VII Metal Catalysts. *Trends Chem.* **2021**, *3* (3), 176–187.

(58) Clark, M. L.; Cheung, P. L.; Lessio, M.; Carter, E. A.; Kubiak, C. P. Kinetic and Mechanistic Effects of Bipyridine (Bpy) Substituent, Labile Ligand, and Brønsted Acid on Electrocatalytic CO2 Reduction by Re(Bpy) Complexes. *ACS Catal.* **2018**, *8* (3), 2021–2029.

(59) Pegis, M. L.; Wise, C. F.; Martin, D. J.; Mayer, J. M. Oxygen Reduction by Homogeneous Molecular Catalysts and Electrocatalysts. *Chem. Rev.* **2018**, *118* (5), 2340–2391.

(60) Baran, J. D.; Grönbeck, H.; Hellman, A. Analysis of Porphyrines as Catalysts for Electrochemical Reduction of O2 and Oxidation of H2O. *J. Am. Chem. Soc.* **2014**, *136* (4), 1320–1326.

(61) Carver, C. T.; Matson, B. D.; Mayer, J. M. Electrocatalytic Oxygen Reduction by Iron Tetra-Arylporphyrins Bearing Pendant Proton Relays. *J. Am. Chem. Soc.* **2012**, *134* (12), 5444–5447.

(62) Dey, S.; Mondal, B.; Chatterjee, S.; Rana, A.; Amanullah, S.; Dey, A. Molecular Electrocatalysts for the Oxygen Reduction Reaction. *Nat. Rev. Chem.* **2017**, *1* (12), 98.

(63) Ostericher, A. L.; Waldie, K. M.; Kubiak, C. P. Utilization of Thermodynamic Scaling Relationships in Hydricity To Develop Nickel Hydrogen Evolution Reaction Electrocatalysts with Weak Acids and Low Overpotentials. *ACS Catal.* **2018**, *8* (10), 9596–9603.

(64) Brunner, F. M.; Neville, M. L.; Kubiak, C. P. Investigation of Immobilization Effects on Ni(P2N2)2 Electrocatalysts. *Inorg. Chem.* **2020**, *59* (23), 16872–16881.

(65) Machan, C. W.; Sampson, M. D.; Chabolla, S. A.; Dang, T.; Kubiak, C. P. Developing a Mechanistic Understanding of Molecular Electrocatalysts for CO2 Reduction Using Infrared Spectroelectrochemistry. *Organometallics* **2014**, *33* (18), 4550–4559.

(66) Sapountzi, F. M.; Gracia, J. M.; Weststrate, C. J. (Kees-J.; Fredriksson, H. O. A.; Niemantsverdriet, J. W. (Hans). Electrocatalysts for the Generation of Hydrogen, Oxygen and Synthesis Gas. *Prog. Energy Combust. Sci.* **2017**, *58*, 1–35.

(67) Ail, S. S.; Dasappa, S. Biomass to Liquid Transportation Fuel via Fischer Tropsch Synthesis – Technology Review and Current Scenario. *Renew. Sustain. Energy Rev.* **2016**, *58*, 267–286.

(68) Lu, S.; Shi, Y.; Meng, N.; Lu, S.; Yu, Y.; Zhang, B. Electrosynthesis of Syngas via the Co-Reduction of CO2 and H2O. *Cell Reports Phys. Sci.* **2020**, *1* (11), 100237.

(69) Francke, R.; Schille, B.; Roemelt, M. Homogeneously Catalyzed Electroreduction of Carbon Dioxide—Methods, Mechanisms, and Catalysts. *Chem. Rev.* **2018**, *118* (9), 4631–4701.

(70) Nguyen, T. N.; Salehi, M.; Le, Q. Van; Seifitokaldani, A.; Dinh, C. T. Fundamentals of Electrochemical CO2 Reduction on Single-Metal-Atom Catalysts. *ACS Catal.* **2020**, *10* (17), 10068–10095.

(71) Guo, D.; Shibuya, R.; Akiba, C.; Saji, S.; Kondo, T.; Nakamura, J. Active Sites of Nitrogen-Doped Carbon Materials for Oxygen Reduction Reaction Clarified Using Model Catalysts. *Science (80-.).* **2016**, *351* (6271), 361 LP – 365.

(72) Jiang, K.; Siahrostami, S.; Zheng, T.; Hu, Y.; Hwang, S.; Stavitski, E.; Peng, Y.; Dynes, J.; Gangisetty, M.; Su, D.; et al. Isolated Ni Single Atoms in Graphene Nanosheets for High-Performance CO2 Reduction. *Energy Environ. Sci.* **2018**, *11* (4), 893–903.

(73) Liu, K.; Fu, J.; Lin, Y.; Luo, T.; Ni, G.; Li, H.; Lin, Z.; Liu, M. Insights into the Activity of Single-Atom Fe-N-C Catalysts for Oxygen Reduction Reaction. *Nat. Commun.* **2022**, *13* (1), 2075.

(74) Liu, J.; Zhang, G.; Ye, K.; Xu, K.; Sheng, Y.; Yu, C.; Zhang, H.; Li, Q.; Liang, Z.; Jiang, K. Top-down Manufacturing of Efficient CO2 Reduction Catalysts from the Gasification Residue Carbon. *Chem. Commun.* **2023**, *59* (5), 611–614.

(75) Qiao, X.; Li, Q.; Schaugaard, R. N.; Noffke, B. W.; Liu, Y.; Li, D.; Liu, L.; Raghavachari, K.; Li, L. Well-Defined Nanographene–Rhenium Complex as an Efficient Electrocatalyst and Photocatalyst for Selective CO2 Reduction. *J. Am. Chem. Soc.* **2017**, *139* (11), 3934–3937.

(76) Li, Q.; Noffke, B. W.; Wang, Y.; Menezes, B.; Peters, D. G.; Raghavachari, K.; Li, L. Electrocatalytic Oxygen Activation by Carbanion Intermediates of Nitrogen-Doped Graphitic Carbon. *J. Am. Chem. Soc.* **2014**, *136* (9), 3358–3361.

(77) Koenig, J. D. B.; Dubrawski, Z. S.; Rao, K. R.; Willkomm, J.; Gelfand, B. S.; Risko, C.; Piers, W. E.; Welch, G. C. Lowering Electrocatalytic CO2 Reduction Overpotential Using N-Annulated Perylene Diimide Rhenium Bipyridine Dyads with Variable Tether Length. *J. Am. Chem. Soc.* **2021**, *143* (40), 16849–16864.

(78) Schaugaard, R. N.; Raghavachari, K.; Li, L. Redox "Innocence" of Re(I) in Electrochemical CO2 Reduction Catalyzed by Nanographene–Re Complexes. *Inorg. Chem.* **2018**, *57* (17), 10548–10556.

(79) Chang, Q.; Liu, Y.; Lee, J.-H.; Ologunagba, D.; Hwang, S.; Xie, Z.; Kattel, S.; Lee, J. H.; Chen, J. G. Metal-Coordinated Phthalocyanines as Platform Molecules for Understanding Isolated Metal Sites in the Electrochemical Reduction of CO2. *J. Am. Chem. Soc.* **2022**, *144* (35), 16131–16138.

(80) Zhang, X.; Wu, Z.; Zhang, X.; Li, L.; Li, Y.; Xu, H.; Li, X.; Yu, X.; Zhang, Z.; Liang, Y.; et al. Highly Selective and Active CO2 Reduction Electrocatalysts Based on Cobalt Phthalocyanine/Carbon Nanotube Hybrid Structures. *Nat. Commun.* **2017**, *8* (1), 14675.

(81) Boutin, E.; Wang, M.; Lin, J. C.; Mesnage, M.; Mendoza, D.; Lassalle-Kaiser, B.; Hahn, C.; Jaramillo, T. F.; Robert, M. Aqueous Electrochemical Reduction of Carbon Dioxide and Carbon Monoxide into Methanol with Cobalt Phthalocyanine. *Angew. Chemie Int. Ed.* **2019**, *58* (45), 16172–16176.

(82) Benson, E. E.; Kubiak, C. P.; Sathrum, A. J.; Smieja, J. M. Electrocatalytic and Homogeneous Approaches to Conversion of CO2 to Liquid Fuels. *Chem. Soc. Rev.* **2009**, *38* (1), 89–99.

(83) Narita, A.; Verzhbitskiy, I. A.; Frederickx, W.; Mali, K. S.; Jensen, S. A.; Hansen, M. R.; Bonn, M.; De Feyter, S.; Casiraghi, C.; Feng, X.; et al. Bottom-Up Synthesis of Liquid-Phase-Processable Graphene Nanoribbons with Near-Infrared Absorption. *ACS Nano* **2014**, *8* (11), 11622–11630.

(84) Wu, J.; Pisula, W.; Müllen, K. Graphenes as Potential Material for Electronics. *Chem. Rev.* **2007**, *107* (3), 718–747.

(85) Narita, A.; Wang, X.-Y.; Feng, X.; Müllen, K. New Advances in Nanographene Chemistry. *Chem. Soc. Rev.* **2015**, *44* (18), 6616–6643.

(86) Liu, Y.-M.; Hou, H.; Zhou, Y.-Z.; Zhao, X.-J.; Tang, C.; Tan, Y.-Z.; Müllen, K. Nanographenes as Electron-Deficient Cores of Donor-Acceptor Systems. *Nat. Commun.* **2018**, *9* (1), 1901.

(87) Fantuzzi, P.; Candini, A.; Chen, Q.; Yao, X.; Dumslaff, T.; Mishra, N.; Coletti, C.; Müllen, K.; Narita, A.; Affronte, M. Color Sensitive Response of Graphene/Graphene Quantum Dot Phototransistors. *J. Phys. Chem. C* **2019**, *123* (43), 26490–26497.

(88) Jin, E.; Yang, Q.; Ju, C.-W.; Chen, Q.; Landfester, K.; Bonn, M.; Müllen, K.; Liu, X.; Narita, A. A Highly Luminescent Nitrogen-Doped Nanographene as an Acid- and Metal-Sensitive Fluorophore for Optical Imaging. *J. Am. Chem. Soc.* **2021**, *143* (27), 10403–10412.

(89) Luo, H.; Liu, J. Facile Synthesis of Nitrogen-Doped Nanographenes with Joined Nonhexagons via a Ring Expansion Strategy. *Angew. Chemie Int. Ed.* **2023**, *62* (21), e202302761.

(90) Watson, M. D.; Fechtenkötter, A.; Müllen, K. Big Is Beautiful−"Aromaticity" Revisited from the Viewpoint of Macromolecular and Supramolecular Benzene Chemistry. *Chem. Rev.* **2001**, *101* (5), 1267–1300.

(91) Clar, E.; Ironside, C. T.; Zander, M. 28. The Electronic Interaction between Benzenoid Rings in Condensed Aromatic Hydrocarbons. 1 : 12-2 : 3-4 : 5-6 : 7-8 : 9-10 : 11-Hexabenzocoronene, 1 : 2-3 : 4-5 : 6-10 : 11-Tetrabenzoanthanthrene, and 4 : 5-6 : 7-11 : 12-13 : 14-Tetrabenzoperopyrene. *J. Chem. Soc.* **1959**, No. 0, 142–147.

(92) Hertz, V. M.; Massoth, J. G.; Bolte, M.; Lerner, H.-W.; Wagner, M. En Route to Stimuli-Responsive Boron-, Nitrogen-, and Sulfur-Doped Polycyclic Aromatic Hydrocarbons. *Chem. – A Eur. J.* **2016**, *22* (37), 13181–13188.

(93) Hertz, V. M.; Bolte, M.; Lerner, H.-W.; Wagner, M. Boron-Containing Polycyclic Aromatic Hydrocarbons: Facile Synthesis of Stable, Redox-Active Luminophores. *Angew. Chemie Int. Ed.* **2015**, *54* (30), 8800–8804.

(94) Yamaguchi, R.; Ito, S.; Lee, B. S.; Hiroto, S.; Kim, D.; Shinokubo, H. Functionalization of Hexa-Peri-Hexabenzocoronenes: Investigation of the Substituent Effects on a Superbenzene. *Chem. – An Asian J.* **2013**, *8* (1), 178–190.

(95) Yamaguchi, R.; Hiroto, S.; Shinokubo, H. Synthesis of Oxygen-Substituted Hexa-Peri-Hexabenzocoronenes through Ir-Catalyzed Direct Borylation. *Org. Lett.* **2012**, *14* (10), 2472–2475.

(96) Draper, S. M.; Gregg, D. J.; Madathil, R. Heterosuperbenzenes: A New Family of Nitrogen-Functionalized, Graphitic Molecules. *J. Am. Chem. Soc.* **2002**, *124* (14), 3486–3487.

(97) Draper, S. M.; Gregg, D. J.; Schofield, E. R.; Browne, W. R.; Duati, M.; Vos, J. G.; Passaniti, P. Complexed Nitrogen Heterosuperbenzene: The Coordinating Properties of a Remarkable Ligand. *J. Am. Chem. Soc.* **2004**, *126* (28), 8694–8701.

(98) Krzeszewski, M.; Dobrzycki, Ł.; Sobolewski, A. L.; Cyrański, M. K.; Gryko, D. T. Bowl-Shaped Pentagon- and Heptagon-Embedded Nanographene Containing a Central Pyrrolo[3,2-b]Pyrrole Core. *Angew. Chemie Int. Ed.* **2021**, *60* (27), 14998–15005.

(99) Gryko, D. T.; Piechowska, J.; Gałęzowski, M. Strongly Emitting Fluorophores Based on 1-Azaperylene Scaffold. *J. Org. Chem.* **2010**, *75* (4), 1297–1300.

CHAPTER II

POLYAROMATIC, PYRIDINIUM-DERIVED MOLECULAR FILMS FACILITATE HIGH SELECTIVITY TOWARDS C_{2+} PRODUCTS FROM CO_2 REDUCTION ON Cu ELECTRODES

Some text and figures for this chapter possess material from:

Nie, W.; **Heim, G.P.**; Watkins, N.B.; Agapie, T.; Peters, J.C. *Angew. Chem. Int. Ed.* **2023**. *135*. e202216102.

Heim, G.P.; Nie, W.; Peters, J.C.; Agapie, T. *Manuscript in preparation.*

ABSTRACT: The film generated *in situ* from **PyTolyl** facilitates CO_2R on metallic electrodes via suppression of the hydrogen evolution reaction (HER) and C_1 product formation at neutral pH. A systematic increase in the partial current density, j, towards C_{2+} product formation is observed as the π system on the aryl group is more extended (from **PyPh** to **PyAnthr**) in 0.1 M $KHCO_{3(aq)}$. The ability of these materials to suppress HER renders them as organic coatings that can facilitate CO_2R on Cu in pH = 2 electrolyte. *N*-phenyl isoquinolinium (**IsqPh**) film facilitates high selectivity for C_{2+} products (FE_{C2+} = 69%) in 0.1 M $H_3PO_4/KH_2PO_{4(aq)}$, suggesting enhancement in CO_2 mass transport rather than attenuation in proton carrier diffusion. Improvement in long-term stability and tolerance to lower pH compared to previous films is observed. FE_{C2+} = 64% is obtained when j = -100 mA cm^{-2} on Cu gas diffusion electrodes. These results highlight the ability to tune electrocatalyst performance via molecular films at low pH, leading to improved C_{2+} product selectivity and attenuated hydrogen evolution.

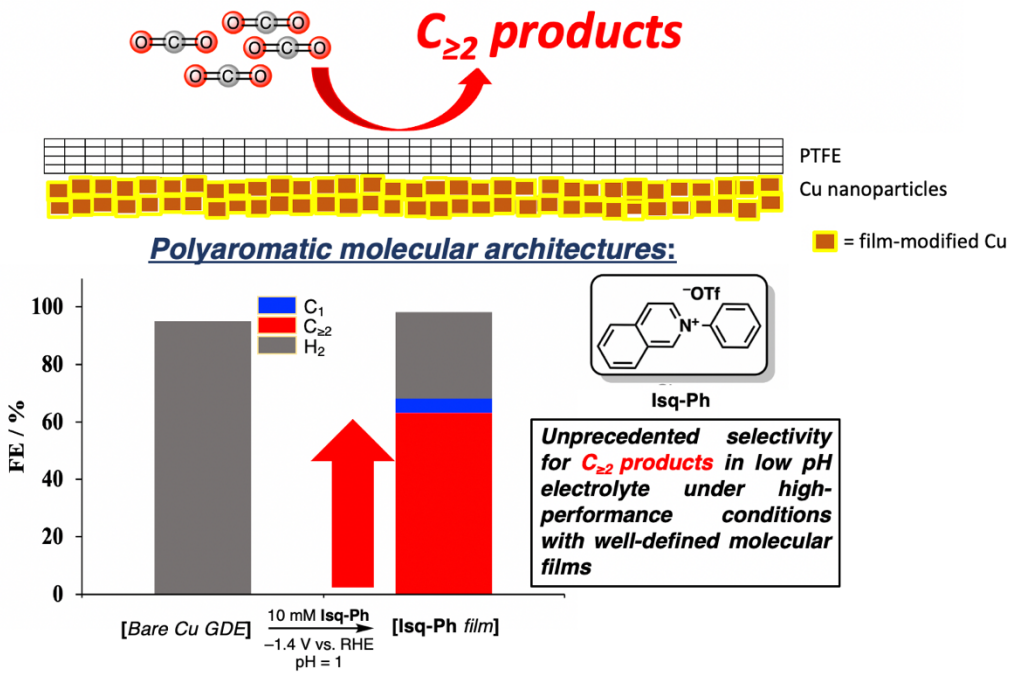

ACKNOWLEDGMENTS

I am grateful for the mentorship of Dr. Weixuan Nie. This material is based on work performed by the Liquid Sunlight Alliance, which is supported by the U.S. Department of Energy, Office of Science, Office of Basic Energy Sciences, Fuels from Sunlight Hub under Award DE-SC0021266. The Resnick Sustainability Institute at Caltech is acknowledged for support of the laboratory facilities in which this research was conducted.

INTRODUCTION

Electrocatalytic carbon dioxide reduction (CO_2R) with Cu electrodes is a potential avenue towards preparation of multi-carbon (C_{2+}) products with renewable energy towards creating a net-zero carbon economy.[1–3] While substantial progress has been achieved in boosting the selectivity towards C_{2+} products in neutral and basic electrolytes,[4–12] low CO_2 utilization is encountered due to carbonate formation in high local pH microenvironment.[13–16] Carbonate formation can be mitigated by performing CO_2R in a low pH electrolyte.[17]

CO_2R in 1.0 M $H_3PO_{4(aq)}$ on Cu gas diffusion electrodes (GDEs) was reported by Sinton, Sargent, and co-workers utilizing high potassium concentration ($[K^+]$ = 3 M) on ionomer-coated Cu, obtaining C_{2+} product Faradaic efficiency (FE_{C2+}) of 48%.[15] Koper and co-workers achieved ~99% FE for CO on roughened Au foil in pH = 3.[18,19] Hu and co-workers reported electrochemical CO_2R to C_{2+} products (~36% FE_{C2+}) on Cu GDE in 0.1 M $H_2SO_{4(aq)}$.[20]

We recently reported CO_2R at low pH with **PyTolyl**, where the FE_{C2+} exceeds 70% in pH = 2 H_3PO_4 ($[K^+]$ = 0.1 M, 15 mM **PyTolyl**).[21] Rotating disk electrochemistry (RDE) experiments revealed proton carrier mass transport limitation facilitated hydrogen evolution reaction (HER) suppression and boosted selectivity for C_{2+} products. High FE_{C2+} was achieved at low current densities ($|j| < 2$ mA cm^{-2}) and low cation concentration (0.1 M K^+).[15] Optimization in CO_2R performance as a function of molecular film structure was sought after in low pH electrolyte by preparing a series of polyaromatic, N-heterocycle molecular additives.

Herein is reported high selectivity on Cu electrodes imparted by **IsqPh** in acidic electrolyte, yielding FE_{CO2R} = 87% and FE_{C2+} = 69%. RDE and variable partial pressure CO_2 studies suggest more facile CO_2 mass transport rather than limited proton carrier diffusion as previously observed with **PyTolyl**. The **IsqPh**-modified Cu (**Cu/IsqPh**) is more tolerant in pH = 1 electrolyte and possesses greater stability over a 12-h electrolysis as measured by FE_{C2H4} over time. Electrolysis on Cu GDEs reveals an apparent record-level selectivity for low pH CO_2R on Cu with **IsqPh** (FE_{C2+} = 64%) at a current density (*j*) of –100 mA cm^{-2} at pH = 1. Our results highlight screening of molecular film precursors to optimize performance and selectivity in CO_2R at low pH.[22] Moreover, these organic film-modified electrodes can steer CO_2R selectivity towards C_{2+} at high current densities independent of alkali metal cation concentration.[15,23]

RESULTS AND DISCUSSION

i) Examining effects of extended π system in 0.1 M $KHCO_{3(aq)}$ (pH = 6.8)

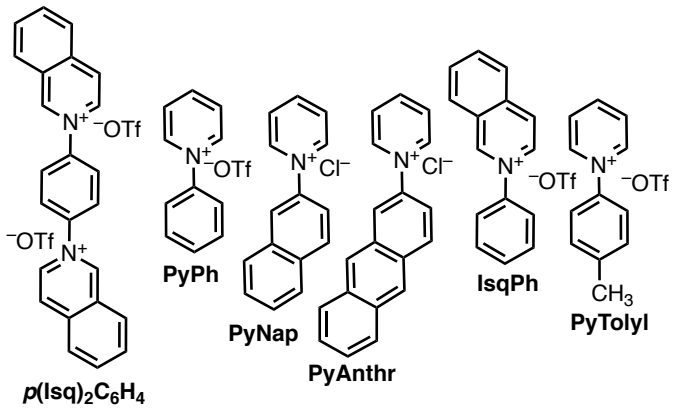

Figure 1. Molecular additives bearing napthyl, anthracenyl, and isoquinolinium motifs alongside previously reported *N*-phenyl pyridinium triflate and *N*-(*p*-tolyl) pyridinium triflate.

Seeking to investigate systematic modifications to molecular additive/film structure to ascertain effects on electrochemical CO_2R performance, a novel series of molecular additives were prepared bearing extended π systems on each the aryl and pyridinium side of the film precursors (Figure 1).

The hypothesis is that more extended π systems relative to previously reported films would impart more robust coverage of the electrode, thereby limiting HER and enhancing CO_2 reduction performance to C_{2+} products.[24] In addition, prior work had suggested that bulky substituents on pyridinium (i.e., *tert*-butyl) relative to the interaction with Cu surface attenuate CO_2R performance (Figure 2). *N*-(4-*tert*-butylphenyl)pyridinium chloride provided worse selectivity for C_{2+} products (34%) relative to *N*-(4-methylphenyl)pyridinium chloride (80%).[22]

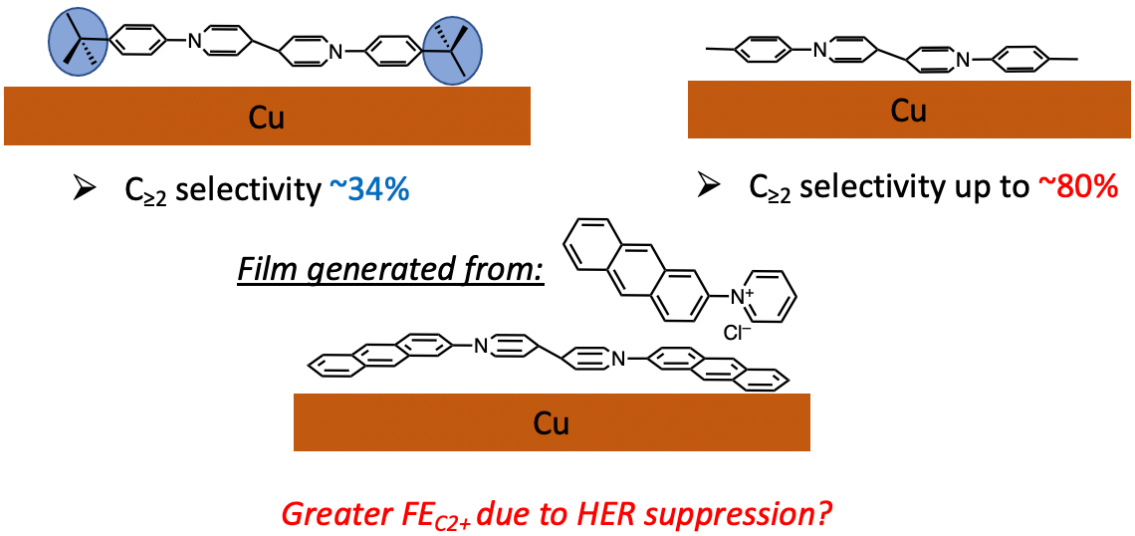

Figure 2. Representation of flatter versus more bulky molecular films generated from *in situ* electrodeposition.

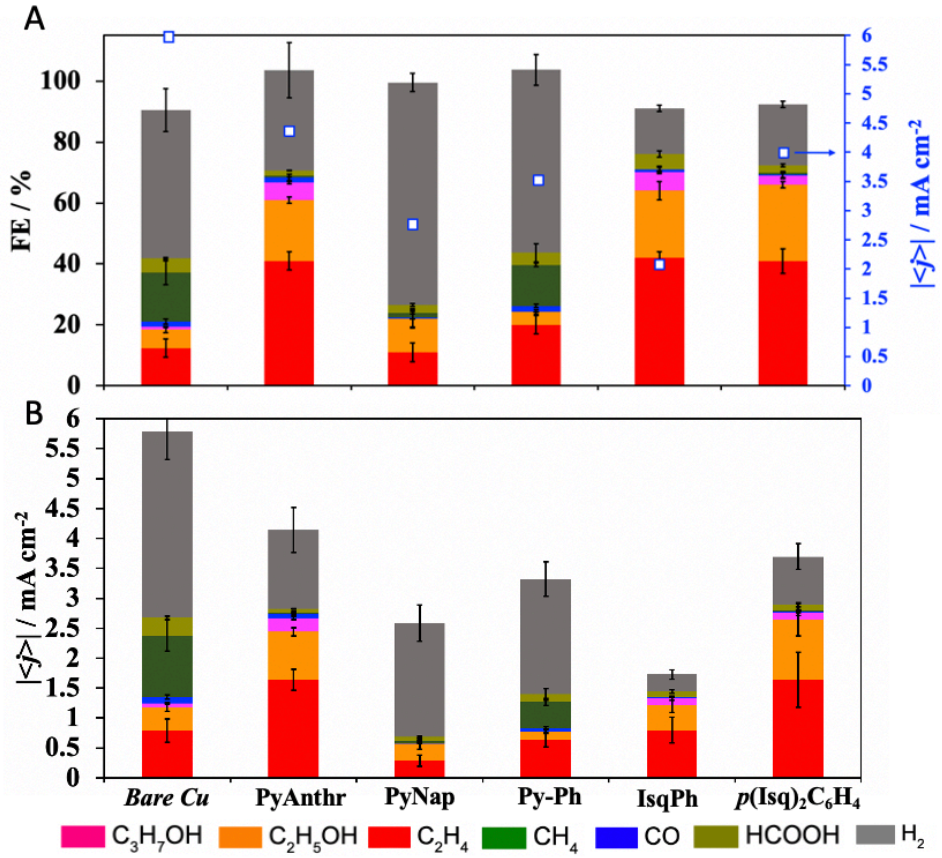

Figure 3. A. Faradaic efficiencies (FEs, columns) and current densities (white squares) from CO_2R on Cu foil in the presence of *N*-heterocycle molecular additives (10 mM dissolved in 0.1 M $KHCO_{3(aq)}$, pH = 6.8). Electrolysis was performed with 10 sccm $CO_{2(g)}$ via chronoamperometry; $E_{applied}$ = –1.1 V vs. RHE). B. Partial current densities (columns) of each product.

CO_2R was carried out in a divided H-cell in 0.1 M $KHCO_{3(aq)}$ (pH = 6.8) with polycrystalling Cu foil serving as the working electrode.[22,25] A 10 mM solution of each additive was dissolved in the cathode electrolyte prior to electrolysis. At constant potential ($E_{applied}$ = –1.1 V vs. RHE), a systematic increase in magnitude of partial current for C_{2+} products ($|j_{C2+}|$) is observed via increasing the length of the acene substituent, with **PyAnthr** displaying the largest $|j_{C2+}|$ (Figure 3). Notably, this material increases $|j_{C2+}|$

relative to bare Cu, a rare observation for pyridinium-derived films.[11,26] Faradaic efficiency for C_{2+} products (FE_{C2+}) is improved relative to bare Cu. Characterization of the film is achieved via dissolution in CD_2Cl_2 and submission for ^1H NMR spectroscopy, suggesting coupling at the *para* position of the pyridinium to be the dominant pathway.[22,26]

Notably, **PyNap** and **IsqPh** each elevate CO_2R performance relative to **PyPh** while suppressing HER, suggesting that preparation of fused polyaromatics is a beneficial strategy. Given the success in suppressing HER in near-neutral pH electrolyte,[11,22,26,27] we hypothesized that these film precursors would serve as good candidates for CO_2R at low pH.[15,21,28]

ii) Investigating films in low pH electrolyte

Scheme 1. *In-situ* electrodeposition of phenyl isoquinolinium triflate (**Isq-Ph**).

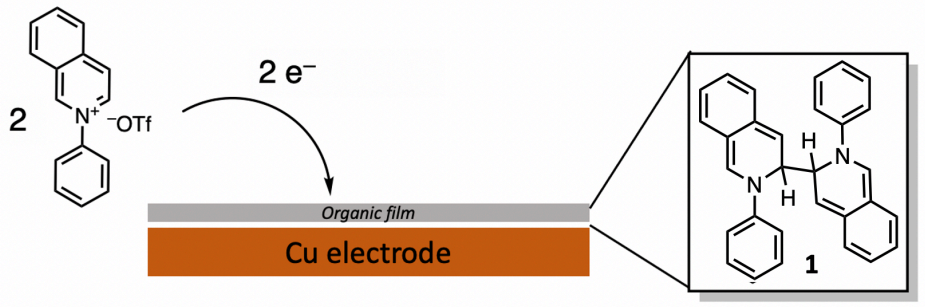

The scope of additives was expanded for low pH CO_2R with compounds synthesized using methodologies reported in our previous work.[22,26] Each additive was dissolved in CO_2-saturated 0.1 M KH_2PO_4/H_3PO_4 to prepare a 10 mM solution in the catholyte. Electrolysis was performed with a polycrystalline Cu foil working electrode at constant potential $E_{applied}$ = –1.4 V vs. RHE for 35 minutes flowing 10 standard cubic centimeters per minute (sccm) $CO_{2(g)}$ (Figure 4). **IsqPh** provided the highest FEs for all

CO_2R products, enabling FE_{CO2R} = 87% and FE_{C2+} = 69%, among the best CO_2R selectivity reported in low pH electrolyte on Cu.[15,17,20,21,29,30] HER is suppressed 65-fold ($|j_{H2}|$ = 0.28 mA cm^{-2}) relative to bare Cu ($|j_{H2}|$ = 18 mA cm^{-2}). **Cu/IsqPh** was submitted for electrolysis in catholyte with 0 mM **IsqPh**. The selectivity profile was unchanged while yielding a modestly larger $|\langle j \rangle|$ (3.0 vs. 1.9 mA cm^{-2}), demonstrating that the electrodeposited film is crucial for the generation of CO_2R products at low pH (Table 3). *In situ* electrodeposition of each molecular additive yields a corresponding film and increased FE_{CO2R} relative to bare Cu, highlighting an excellent strategy in boosting CO_2R at low pH.

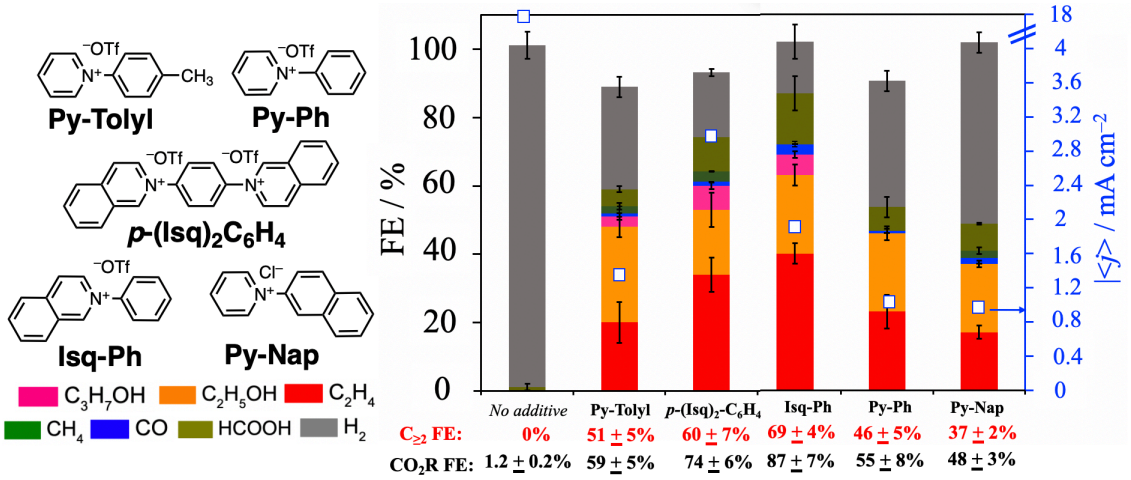

Figure 4. Faradaic efficiencies (FEs, columns) and current densities (white squares) from CO_2R on Cu foil in the presence of *N*-heterocycle molecular additives (10 mM dissolved in 0.1 M KH_2PO_4/H_3PO_4, pH = 2). Electrolysis was performed with 10 sccm $CO_{2(g)}$ via chronoamperometry; $E_{applied}$ = –1.4 V vs. RHE).

Cu/IsqPh is rinsed with CD_2Cl_2 to dissolve the film and obtain an ^1H NMR spectrum illustrating resonances between 6.0 and 7.5 ppm (Figure 5). The spectrum is reproduced from reduction of **IsqPh** with 1 equivalent of cobaltocene in CH_2Cl_2.[22] A major

species is obtained after precipitation of the crude mixture in 1,2-dimethoxyethane and extraction into benzene. Assignment of the NMR as the dimer **1** (Scheme 1) coupled at the 3 position is consistent with previous ^{1}H NMR spectra revealing exclusively *ortho* coupling for *N*-aryl pyridinium additives bearing *para* substituents.[26]

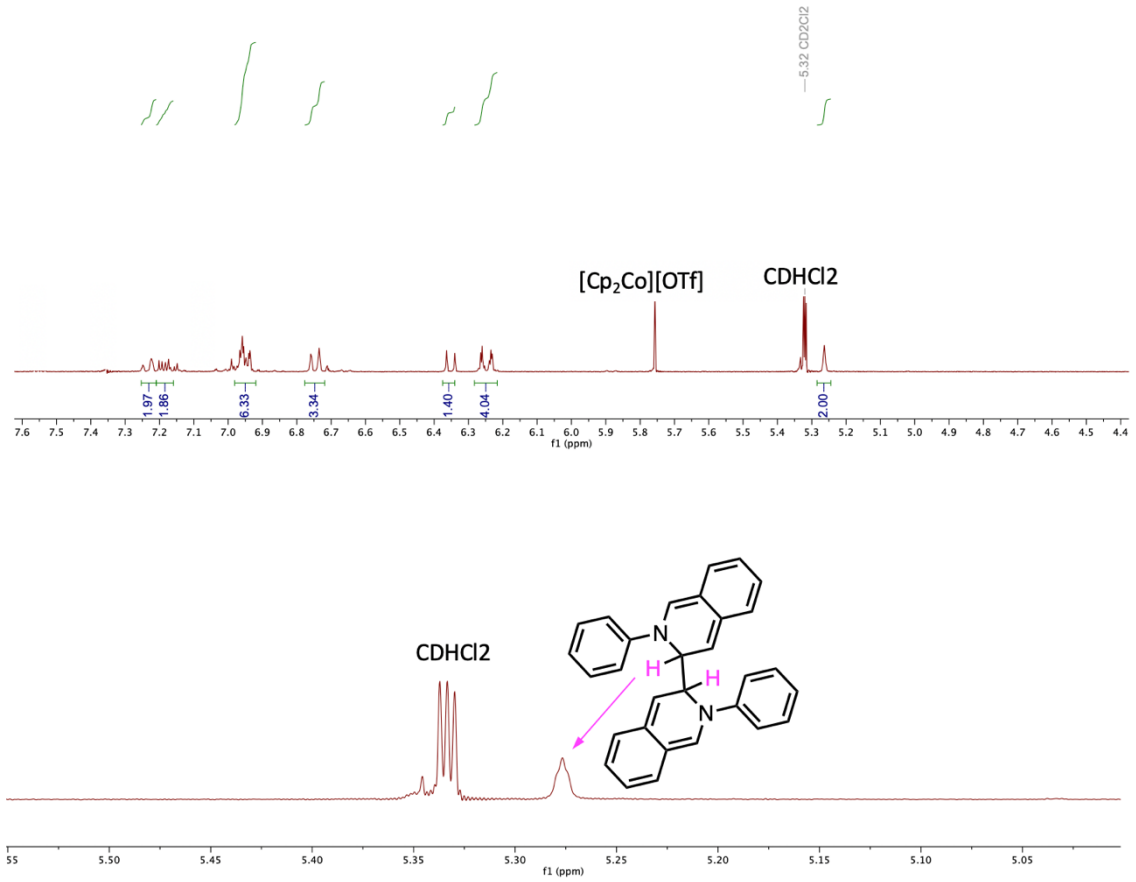

Figure 5. ^{1}H NMR spectra (400 MHz, CD_2Cl_2) of (top) **1** from 4.8-7.6 ppm and (bottom) from 5.0-5.5 ppm

The peak at 5.27 ppm is assigned as the aliphatic alpha proton to the nitrogen and correlates with a multiplet at 7.0 ppm (Figure 20).[11,26] **PyPh** and **PyNap** films are each assigned as *para*-coupled dimers based on ^{1}H NMR analysis in CD_2Cl_2 (Figure 21),[22,26] while the film of

***p*-(Isq)$_2$-C$_6$H$_4$** yields an intractable mixture likely containing an oligomer similarly observed with the pyridinium analogue.[26]

Further bulk electrolysis experiments were undertaken to assess the stability of the **IsqPh** film. Improved stability over a 12-h electrolysis was obtained compared to **PyTolyl** (Figure 6A). FE_{H2} surpasses FE_{C2H4} after 100 minutes with **PyTolyl**; the selectivity for H_2 is never greater than for C_2H_4 at any point in time in the case of **IsqPh**. To examine the tolerance of the **IsqPh** film in more acidic environment, a 10 mM solution was prepared in 1.0 M H_3PO_4 (pH = 1), where $[K^+]$ = 0.1 M and submitted for electrolysis in which $E_{applied}$ = –1.45 V vs. RHE. CO_2R products were observed (FE_{CO2R} = 41%, FE_{C2+} = 18%), while under the same conditions for **Py-Tolyl** FE_{CO2R} = 15% (Figure 7) with poor selectivity owing to the lack of film formation. The performance of **IsqPh** is further augmented in 1 M $H_3PO_{4(aq)}$ with greater $[K^+]$ in the electrolyte; j_{C2+} is increased by a factor of 2.5 with a 10-fold increase in $[K^+]$ (Figure 2B).

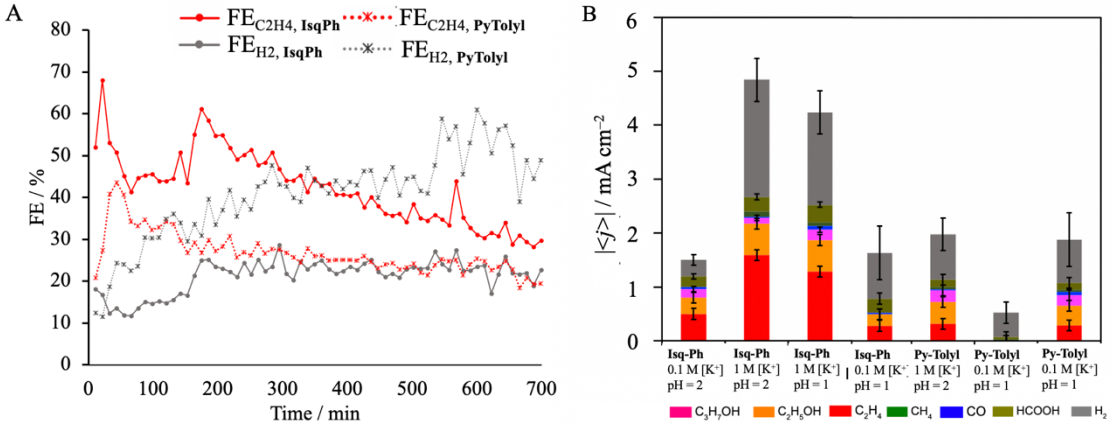

Figure 6. A) Faradaic efficiency for C_2H_4 (red) and Faradaic efficiency for H_2 (grey) over 12-h CO_2 electrolysis in 0.1 M KH_2PO_4/H_3PO_4 for 10 mM **Isq-Ph** (solid lines) and 10 mM **Py-Tolyl** (dotted lines). B) Partial current densities from selectivity profiles in electrolytes of various pH values and $[K^+]$.

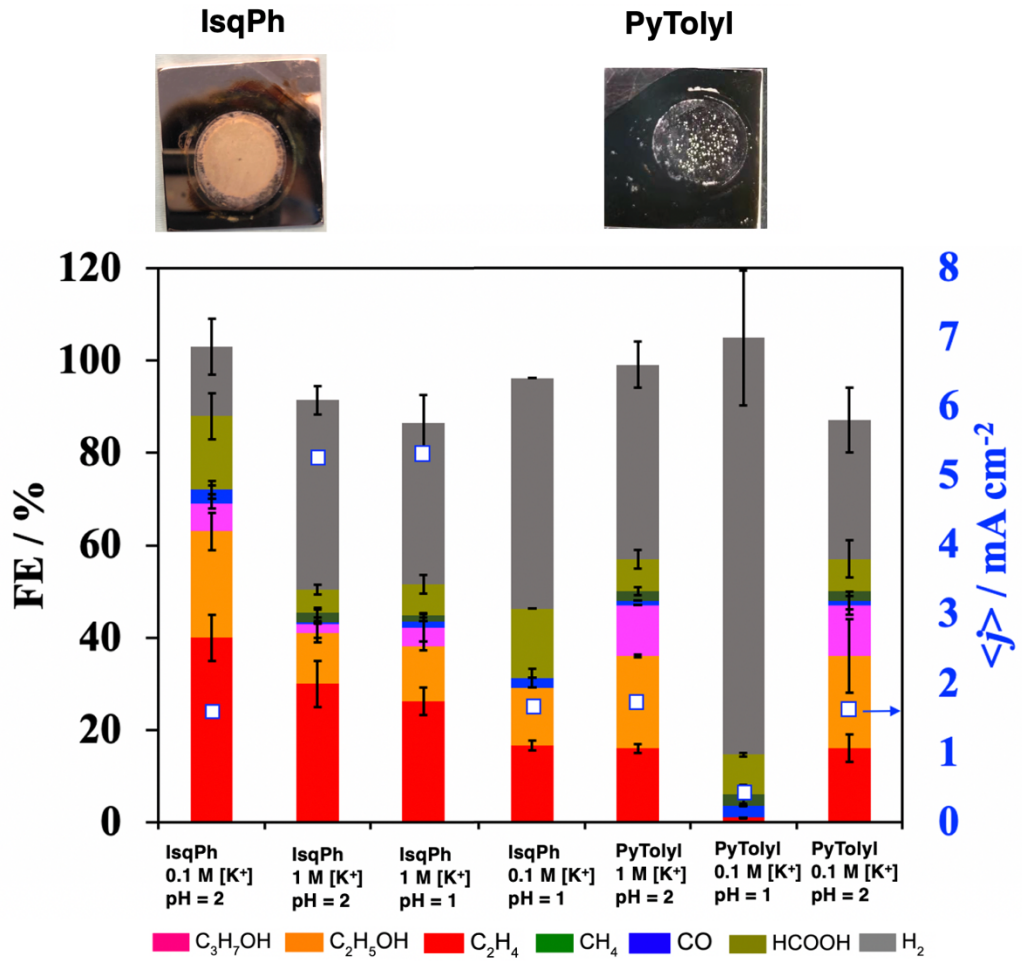

Figure 7. (top) Cu foil post-electrolysis with (left) 10 mM **IsqPh** and (right) 10 mM **PyTolyl**. 35-minute chronoamperometry where $E_{applied}$ = –1.45 V vs. RHE in 0.1 M $KCl_{(aq)}$/1 M $H_3PO_{4(aq)}$. (bottom) Faradaic efficiencies and total current densities (white squares) from CA in various CO_2-saturated electrolytes. All values represent means, and error bars represent standard deviations from three independent measurements. "pH = 2" electrolyte is KCl/0.1 M $H_3PO_{4(aq)}$; $E_{applied}$ = –1.4 V vs. RHE. "pH = 1" electrolyte is KCl/1 M $H_3PO_{4(aq)}$; $E_{applied}$ = –1.45 V vs. RHE.

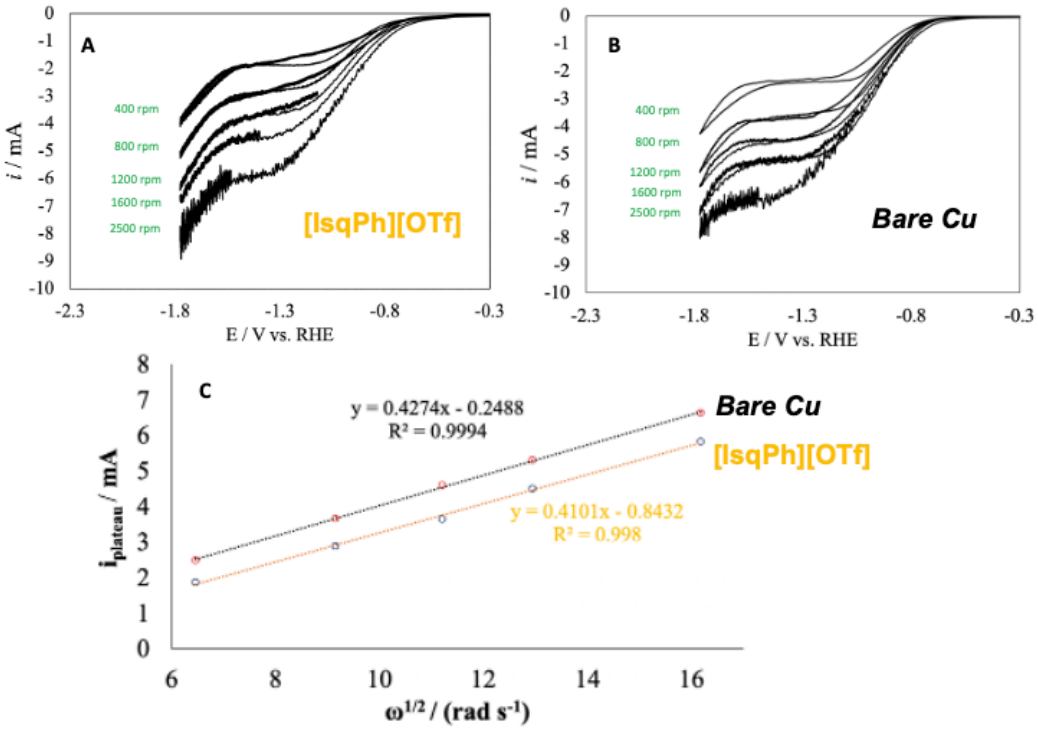

Figure 8. CVs of the Cu RDE with (A) **IsqPh** film and (B) the bare Cu in N_2-saturated 0.1 M $KClO_4$ (pH ~ 2.1) with different rotating rates, scan rate: 50 mV/s; (C) Linear fitting of plateau currents vs. square root of rotating rates for the bare Cu RDE (black) and the Cu RDE with deposited film (orange) based on Levich equation.

RDE experiments were undertaken to understand the effect of the **IsqPh** film on proton carrier mass transport.[21,27] Proton carrier diffusion coefficients (D_{H+}) were obtained from the Levich equation revealed by plotting plateau current ($i_{plateau}$) vs. square root of rotation rate ($\omega^{1/2}$) for each bare Cu and **Cu/IsqPh.** D_{H+} was not significantly lower in the presence of the film ($D_{H+,\textbf{Cu-IsqPh}}/D_{H+,Cu}$ = 0.93), suggesting that proton carrier mass transport limitation does not facilitate HER suppression and thereby CO_2R (Figure 8).[31] We previously showed that **PyTolyl** film attenuated the mass transport of proton carrier ($D_{H+,\textbf{Cu-PyTolyl}}/D_{H+,Cu}$ = 0.77).[21]

Partial pressure CO_2 (pCO_2) studies were carried out with **Cu/IsqPh** to shed further light on the film's role in enhancing CO_2R at low pH. Decreasing pCO_2 to 0.2 atm increases FE_{H2} (15% vs. 75%) and does not significantly change $\langle j \rangle$ (Figure 9). With **Cu/Py-Tolyl**, FE_{C2+} is sustained while $|\langle j \rangle|$ decreases as a function of pCO_2 (Figure 24, 1.4 vs. 0.6 mA cm^{-2}).[21]

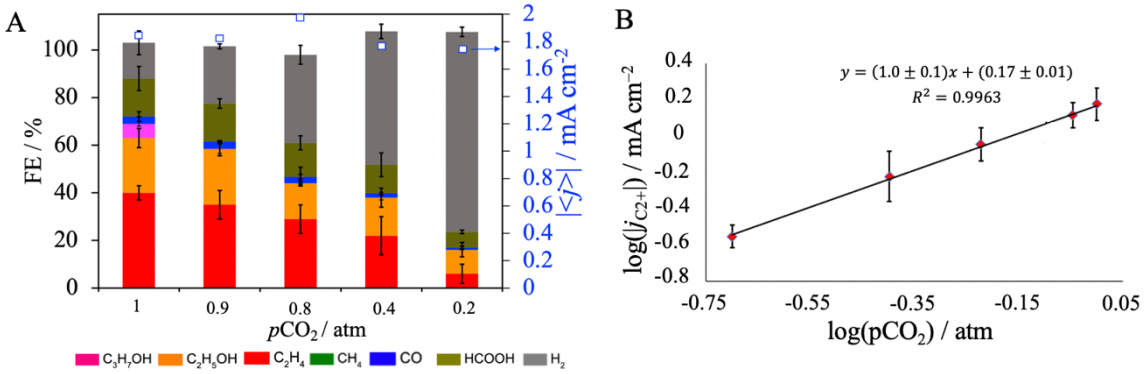

Figure 9. A) FEs and total current densities with varying CO_2 partial pressure. B) Log-log plot of $|j_{C2+}|$ vs. pCO_2.

Cu/PyTolyl can uphold high CO_2R selectivity owing to the **PyTolyl** film's ability in limiting proton mass transport while possibly maintaining a locally high CO_2/H_2O.[21] Since the **IsqPh** film does not substantially limit proton carrier mass transport, HER is the dominant reaction due to the lower local CO_2 concentration at lower pCO_2. However, **Cu/IsqPh** performs CO_2R at higher $|\langle j \rangle|$ at 1 atm (1.9 vs. 1.4 mA cm^{-2}), and j_{C2+} increases with pCO_2 following a first-order relationship (Figure 9). These phenomena suggest that the film enhances CO_2 mass transport.[20,27]

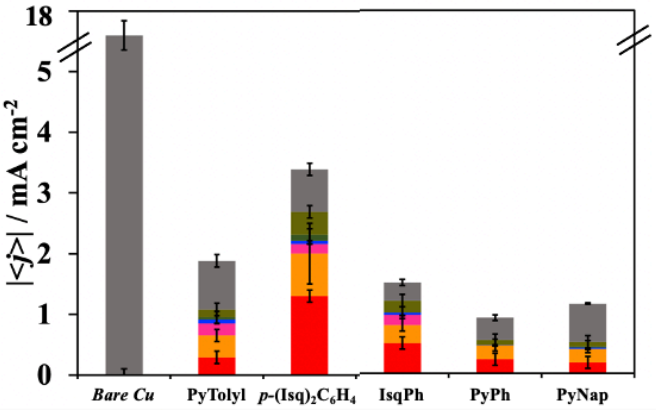

Figure 10. Absolute values of partial current densities for the additives presented in Figure 4 (main text). Error bars represent standard deviations from three independent measurements.

Low current densities (Figure 10, $|j_{C2+}| < 2$ mA cm^{-2}) can limit scalability of CO_2R.[9,32] Electrolysis on GDEs bearing high surface area Cu can lead to higher current densities.[9,33,34] We previously reported CO_2R on GDEs with electrodeposited pyridinium-derived films in 1 M $KHCO_{3(aq)}$ as well as in our previous low pH work.[21,26]

The film was electrodeposited onto the GDE (Cu/PTFE) from a 10 mM solution of additive in pH = 1 KCl/1.0 M H_3PO_4 electrolyte ($[K^+] = 3$ M) and $E_{applied} = -1.45$ V vs. RHE for 5 minutes. This electrode was submitted for chronopotentiometry (CP) at –100 mA cm^{-2} in the same CO_2-saturated pH = 1 electrolyte at –100 mA cm^{-2} for 35 minutes (Figure 11). **IsqPh** film on Cu GDE yields $FE_{C2+} = 64\%$ and $FE_{CO2R} = 71\%$. No CO_2R products are observed on bare Cu ($FE_{H2} = 95\%$). The crucial role of the film is further emphasized by generation of C_{2+} despite $|j| < 200$ mA cm^{-2}, highlighting an outstanding strategy for boosting selectivity at higher current densities independent of alkali cation concentration.[15,18,19,23]. The present findings at –100 mA cm^{-2} demonstrate that the electrodeposited films enable highly selective CO_2R to C_{2+} products at low pH on Cu (Table 1).[15,20]

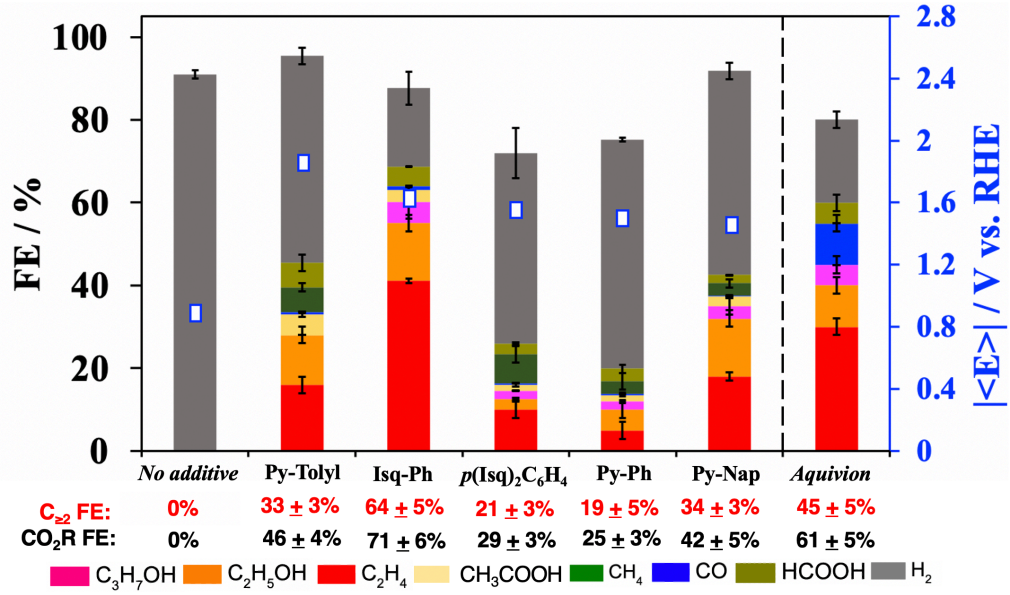

Figure 11. FEs and average corrected potentials (white squares) of additive films on Cu GDEs after 35-min CO_2R chronopotentiometry at –100 mA cm^{-2} in 3 M KCl/1 M H_3PO_4 (pH = 1). CO_2R Faradaic efficiencies from Aquivion on Cu GDE reported by Sinton, Sargent, et al. shown to the right of the dotted line.

Table 1. Comparing selectivity profiles on Cu GDEs from literature

Authors	Electrode	Electrolyte	FE_{C2+}	FE_{CO2R}	$\|j\|$ (mA cm^{-2})
This work	**Isq-Ph** film-modified Cu/PTFE[a]	3 M KCl/1 M H_3PO_4 (pH = 1)	64%	71%	100
Agapie, Peters, and co-workers[21]	**Py-Tolyl** film-modified Cu/PTFE	0.1 M K^+/1 M H_3PO_4, 1.5 mM **Py-Tolyl** (pH = 1)	55%	65%	50
Sinton, Sargent, and co-workers[15]	Aquivion deposited on Cu/PTFE	3 M KCl/1 M H_3PO_4 (pH = 1)	~48%[b]	~55%[b]	1200
Hu and co-workers[20]	Cu nanoparticles deposited on carbon paper	0.8 M K_2SO_4 /0.1 M H_2SO_4 (pH = 1)	~36%[b]	~55%[b]	550
Wang, Sargent, and co-workers[30]	6.2% Pd-Cu/PTFE	0.5 M K_2SO_4/ H_2SO_4 (pH = 2)	80%	84%	550

Creissen, Fontecave, and co-workers[17]	Cu nanoparticles spray-coated	3 M KCl/0.05 M H_2SO_4 (pH = 1.3)	60%	~75%[b]	200

[a] Cu/PTFE = Cu nanoparticles sputtered onto PTFE support

[b] Data obtained from graphics in paper or supporting information.

CONCLUSIONS

High selectivity in CO_2R to C_{2+} products in acidic electrolyte is reported, with the best result on Cu foil from **IsqPh-**derived film at FE_{CO2R} = 87% and FE_{C2+} = 69%, highlighting the broad scope of pyridinium- and isoquinolinium-derived films on Cu electrodes in achieving high selectivity towards CO_2R at low pH. Outstanding HER suppression is also observed relative to bare Cu by a factor of 65. **IsqPh** improves longer-term stability as well as greater tolerance in lower pH electrolyte. RDE and variable partial pressure CO_2 electrolysis studies with **IsqPh** film suggest that the film does not substantially limit proton carrier diffusion but is likely facilitating CO_2 mass transport. Molecular additives have led to improved performance at low pH on Cu GDEs at –100 mA cm^{-2}. Our work highlights the utility of tuning electrocatalyst performance via a molecular approach leading to improved selectivity for chemical feedstocks.

EXPERIMENTAL

Materials and Methods

General Considerations. All solvents and reagents were obtained from commercial sources (Aldrich, Merck, and Combi Blocks) and used as received, unless stated otherwise. Isoquinoline was dried by dissolving in diethyl ether and stirring in calcium hydride under inert atmosphere for 12 h and filtered over a pad of alumina. Diphenyl iodonium triflate, 1,4-bis(phenyliodonium)phenylene triflate, *N*-tolyl pyridinium triflate, *N*-phenyl pyridinium triflate, and *N*-phenyl isoquinolinium triflate, and 1-(2,4-dinitrophenyl)-pyridinium chloride were all prepared using reported procedures, and the ^{13}C and ^{1}H NMR spectra are in agreement.[26,35,36] Dichloromethane was dried by passing over activated alumina by the method of Grubbs[37] and stored over 3 Å molecular sieves in a N_2-filled glovebox.

Copper foil (product number 266744, 99.999% Cu, 25 mm × 50 mm × 1 mm), phosphoric acid (85%, TraceSelect), potassium carbonate (99.995%), potassium hydroxide (semiconductor grade, 99.99% trace metals basis), and potassium chloride (99.999% trace metals basis) were purchased from Sigma Aldrich). The leakless Ag/AgCl reference electrode was purchased from Innovative Instruments. Platinum foil (99.99% Pt, 25 mm × 25 mm × 0.05 mm) was purchased from Alfa Aesar. Carbon rods (99.999% C) were purchased from Strem Chemicals. Perchloric acid (67-72%, TraceSELECT, for trace analysis) was purchased from Fluka Analytical. Natural abundance CO_2 (Research grade) was purchased from Airgas. Deuterium oxide (D 99.96%) and d_6-dimethylsulfoxide (D 99.8%) were purchased from Cambridge Isotope Laboratories. The ^{1}H and ^{13}C NMR spectra were recorded on a Bruker 400 MHz instrument with a prodigy broadband cryoprobe. Shifts were reported relative to the residual solvent peak.

Water was purified by a Nanopure Analytical Ultrapure Water System (Thermo Scientific) or a Milli-Q Advantage A10 Water Purification System (Millipore) with specific resistance of 18.2 MΩ·cm at 25 °C. A VWR sympHony^{TM} pH meter (calibrated with a pH = 1.68 standard) was used to determine the pH of the electrolytes before experiments.

Electrolyte Preparation. Potassium phosphate monobasic in phosphoric acid (KH_2PO_4/H_3PO_4, 0.1 M) was prepared by mixing 0.1 M potassium hydroxide with 0.1 M phosphoric acid. The pH of the solution was adjusted to a value of 2 by adding 4 M H_3PO_4 dropwise.

0.1 M $KClO_4$ (pH = 2.2~2.5) electrolyte was prepared by combining 0.1 M $HClO_4$ and 0.1 M KOH in aqueous solution, pH adjusted using concentrated $HClO_4$.

pH = 1 electrolyte solutions for GDE and Cu foil experiments were prepared by dissolving the appropriate amount of potassium chloride in 1.0 M H_3PO_4. All electrolytes were sparged with $CO_{2(g)}$ for at least 30 minutes prior to electrolysis.

Potassium bicarbonate electrolyte ($KHCO_{3(aq)}$, 0.1 M) was prepared by sparging an aqueous solution of potassium carbonate ($K_2CO_{3(aq)}$, 0.05 M) with CO_2 for at least 1 hour prior to electrolysis. This process converts K_2CO_3 into $KHCO_3$ and saturates the electrolyte solution with CO_2. Potassium hydroxide electrolyte (0.1 M KOH) was prepared by dissolving solid potassium hydroxide into water and sparging for at least 30 minutes prior to electrolysis under CO_2.

Electrode Preparation

Before each experiment, copper foil was polished to a mirror-like finish using diamond paste (3 μm, then 1 μm) followed by rinsing with water and drying with a stream of nitrogen gas. The copper foil was then electropolished using the following method: in an 85% phosphoric acid bath, +400 mA was applied to the Cu foil until a potential of +2.3 V versus carbon rod was reached, and this potential was held for 5 minutes. The foil was subsequently washed with nano-pure water and dried under a

stream of nitrogen gas. Platinum foil as the counter electrode was rinsed with water and flame-annealed using a butane torch for 10 s.

The gas diffusion electrodes (GDEs) were prepared by sputtering 300 nm Cu onto a 5 cm x 5 cm portion of polytetrafluoroethylene membrane (pore size of 450 nm, with polypropylene support on backside) using a pure Cu target (99.99%) at a sputtering rate of 1 Å s^{-1}.

Synthetic Procedures

Synthesis of *N*-(2-anthracenyl)-pyridinium chloride (PyAnthr)

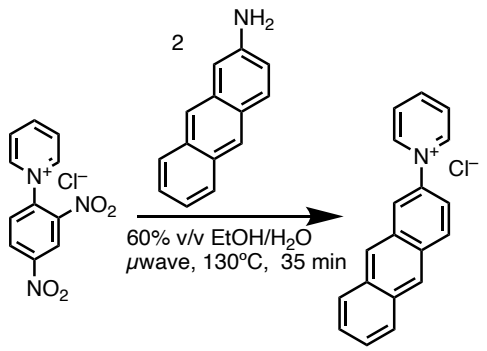

A microwave vial was charged with 2-aminoanthracene (500 mg, 3.49 mmol), 1-(2,4-dinitrophenyl)-pyridinium chloride (394 mg, 1.39 mmol), ethanol (6 mL) and water (4 mL) and sealed under N_2. The vial was submitted for microwave irradiation at 130 ºC for 35 minutes. The vial was allowed to cool to room temperature, and the volatiles were removed on a rotary evaporator. The crude solid was charged with water (4 x 30 mL) to extract the desired product and pumped down on a rotary evaporator. The amber solid was recrystallized from MeOH at –10ºC (Yield: 80%). ^{1}H NMR (400 MHz, D_2O) δ (ppm) = 9.25 (d, 1H, Py*H*), 9.01 (m, 2H, Py*H*), 8.83 (s, 2H, Py*H*), 8.5 (t, 1H, Py*H*), 8.30 (s, 1H, Ar*H*), 8.25 (t, 1H, Ar*H*), 8.00 (m, 2H, Ar*H*), 7.89 (br d, 2H, Ar*H*). Anal. Calcd (%) for $C_{15}H_{12}ClN$: C, 74.54; H, 5.00; N, 5.79. Found: C, 74.60; H, 4.87; N, 5.68

Synthesis of *N*-(2-naphthyl)-pyridinium chloride (Py-Nap)

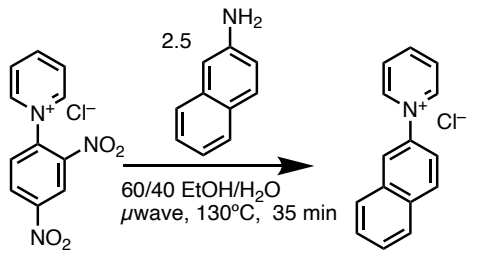

A microwave vial was charged with 2-aminonaphthalene (500 mg, 3.49 mmol), 1-(2,4-dinitrophenyl)-pyridinium chloride (394 mg, 1.39 mmol), ethanol (6 mL) and water (4 mL) and sealed under N_2. The vial was submitted for microwave irradiation at 130 ºC for 35 minutes. The vial was allowed to cool to room temperature, and the volatiles were removed on a rotary evaporator. The crude solid was charged with water (4 x 30 mL) to extract the desired product and pumped down on a rotovap. The amber solid was recrystallized from MeOH at –10ºC (Yield: 80%). ^{1}H NMR (400 MHz, DMSO-d_6) δ (ppm) = 9.50 (d, 2H, Py*H*), 8.83 (t, 1H, Py*H*), 8.54 (s, 1H, Ar*H*), 8.37 (t, 2H, Py*H*), 8.30 (d, 1H, Ar*H*), 8.14 (2, br t, Ar*H*), 8.00 (d, 1H, Ar*H*), 7.77 (br d, 2H, Ar*H*). ^{13}C NMR (126 MHz, DMSO-d_6) δ (ppm) = 146.66, 145.21, 140.16, 133.29, 132.31, 130.33, 128.72, 128.54, 128.19, 128.12, 128.01, 124.30, 121.77. Anal. Calcd (%) for $C_{15}H_{12}ClN$: C, 74.54; H, 5.00; N, 5.79. Found: C, 74.60; H, 4.87; N, 5.68

Synthesis of 1,4-bis(phenyliodonium)phenylene triflate (*p*-(Isq)$_2$-C$_6$H$_4$)

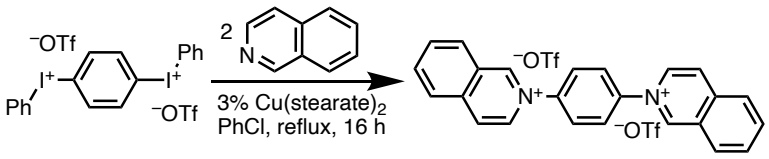

In an N_2-filled glovebox, an oven-dried Schlenk tube was charged with isoquinoline (820 mg, 6.3 mmol), 1,4-bis(*N*-pyridinium)phenylene triflate, (2.0 g, 3.2 mmol), and copper(II) stearate (57 mg, 3 mol%). Chlorobenzene (10 mL) was transferred via syringe under inert atmosphere on the Schlenk line, and the reaction was refluxed under nitrogen for 16 h. The volume of the solution was reduced to about 5 mL, and diethyl ether was added to form a brown precipitate, which was then filtered and washed with ether (3 x 10 mL). The crude solid was recrystallized from ethanol at –10 ºC to yield brown crystals (Yield: 50%). ^{1}H NMR (400 MHz, DMSO-d$_6$) δ (ppm) = 10.39 (s, 2H, Ar*H*), 9.07 (d, 2H, Ar*H*), 8.74 (d, 2H, Ar*H*), 8.63 (d, 2H, Ar*H*), 8.45 (d, 2H, Ar*H*), 8.35 (t, 2H, Ar*H*), 8.16 (t, 2H, Ar*H*), 8.01 (d, 2H, Ar*H*), 7.79 (d, 2H, Ar*H*). ^{13}C NMR (126 MHz, DMSO-d$_6$) δ (ppm) = 150.33, 138.96, 137.71, 134.99, 134.76, 131.55, 131.25, 130.26, 127.31, 126.99, 125.73, 124.98. ^{19}F NMR (471 MHz, DMSO-d$_6$) δ = 78.0 ppm. Anal. Calcd (%) for $C_{26}H_{18}F_6N_2O_6S_2$: C, 49.37; H, 2.87; N, 4.43. Found: C, 49.46; H, 2.68; N, 4.03

Procedure for homogeneous reduction of IsqPh

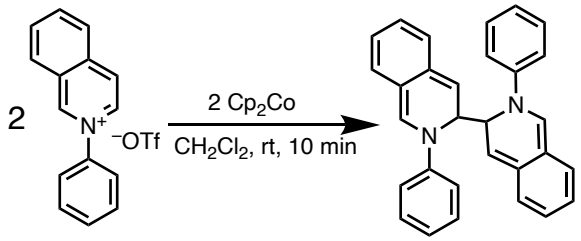

The following is modified from a previously-reported procedure.[22] In a N_2-filled glovebox, a scintillation vial was charged with **Isq-Ph** (50 mg, 0.14 mmol) and suspended in dichloromethane. A solution of Cp_2Co (26.6 mg, 0.14 mmol) was added to the suspension, resulting in a tan, homogeneous solution, which was allowed to stir for 10 minutes at room temperature. The volatiles were removed, and the crude material was rinsed with 1,2-dimethyoxyethane and dried under vacuum. The product was extracted with benzene and volatiles were removed on a rotovap to form a white solid (1). Yield: 25%. ^{1}H NMR (400 MHz, CD_2Cl_2) δ (ppm) = 7.22 (t, 4H, Ar*H*), 7.15 (m, 3H, Ar*H*), 6.96 (br m, 7H, Ar*H*), 6.74 (d, 4H, Ar*H*), 6.36 (d, 2H, Ar*H*), 6.27 (d, 4H, Ar*H*), 5.27 (br m, 2H, benzylic *H*). ^{13}C NMR (126 MHz, CD_2Cl_2) δ (ppm) = 146.21, 129.72, 129.46, 129.05, 128.77, 128.49, 128.27, 126.36, 123.69, 121.34, 117.06, 108.44, 59.27. HRMS (Field Desorption Mass Spectrometry) $([M]/2)^+$ $C_{15}H_{12}N$. Calcd. 206.09643; Found 206.09816.

NMR Characterization

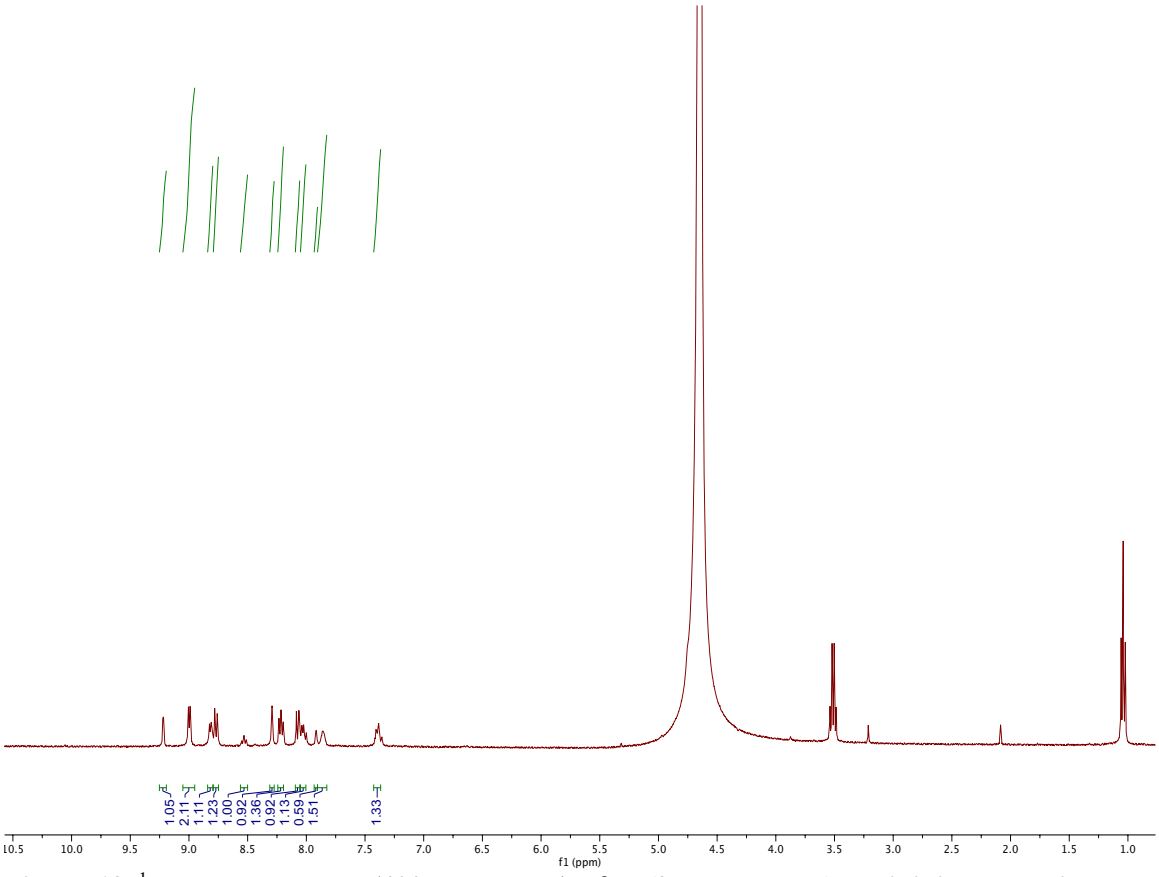

Figure 12. ^{1}H NMR spectrum (400 MHz, D_2O) of ***N*-(2-anthracenyl)-pyridinium chloride [Py-Anthr].**

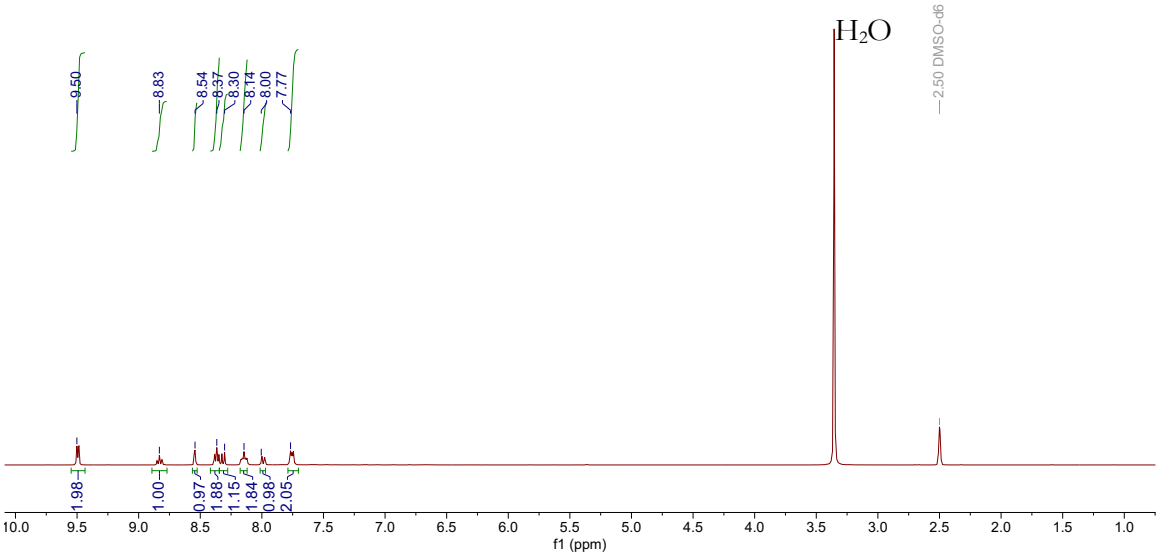

Figure 13. ^{1}H NMR spectrum (400 MHz, DMSO-d_6) of ***N*-(2-naphthyl)-pyridinium chloride [Py-Nap].**

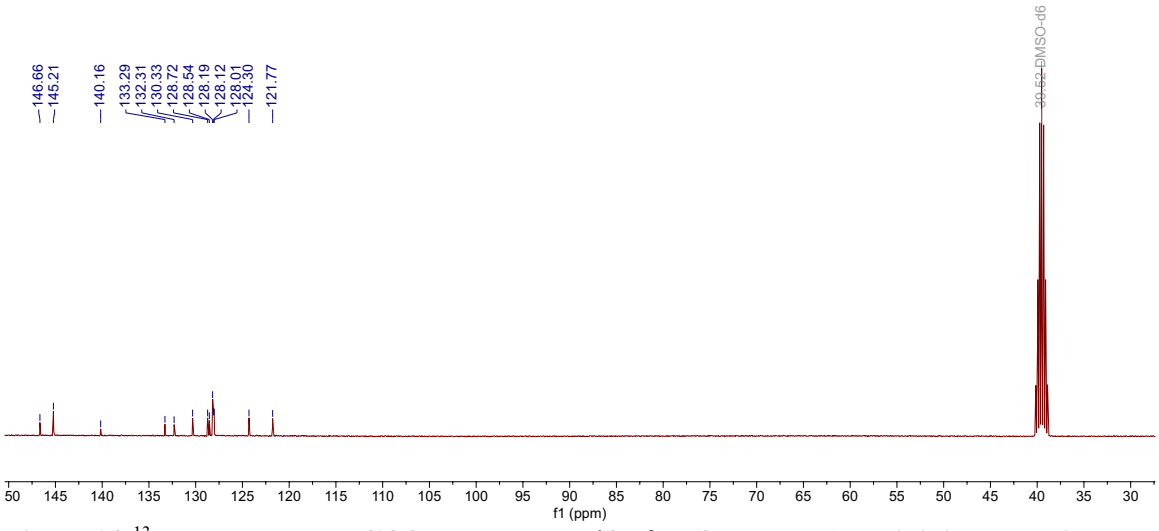

Figure 14. ^{13}C NMR spectrum (126 MHz, DMSO-d_6) of ***N*-(2-naphthyl)-pyridinium chloride [Py-Nap].**

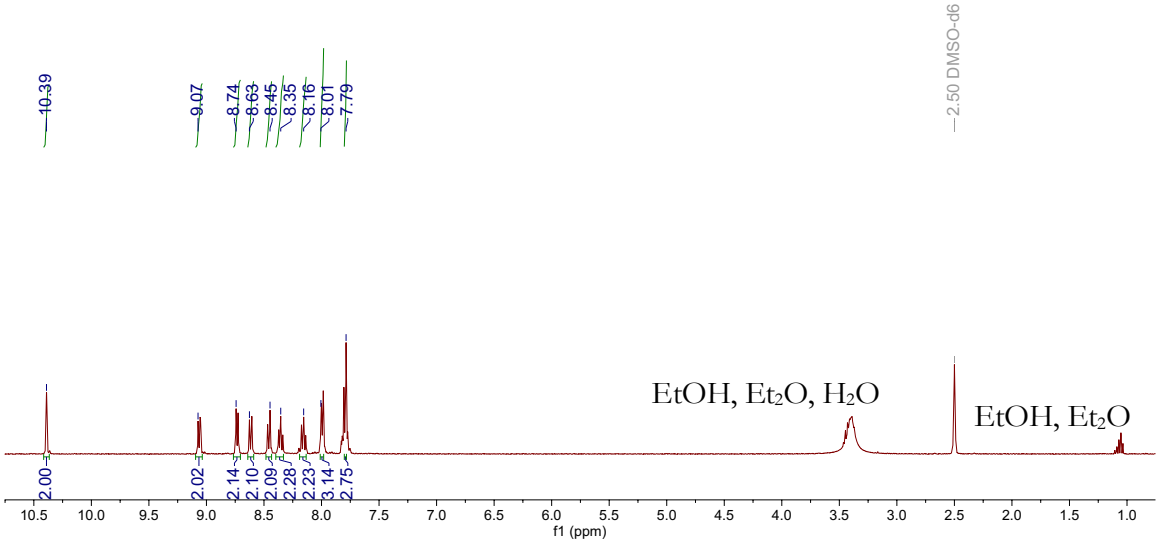

Figure 15. ^{1}H NMR spectrum (400 MHz, DMSO-d_6) of **1,4-bis(phenyliodonium)phenylene triflate [*p*-(Isq)$_2$-C$_6$H$_4$].**

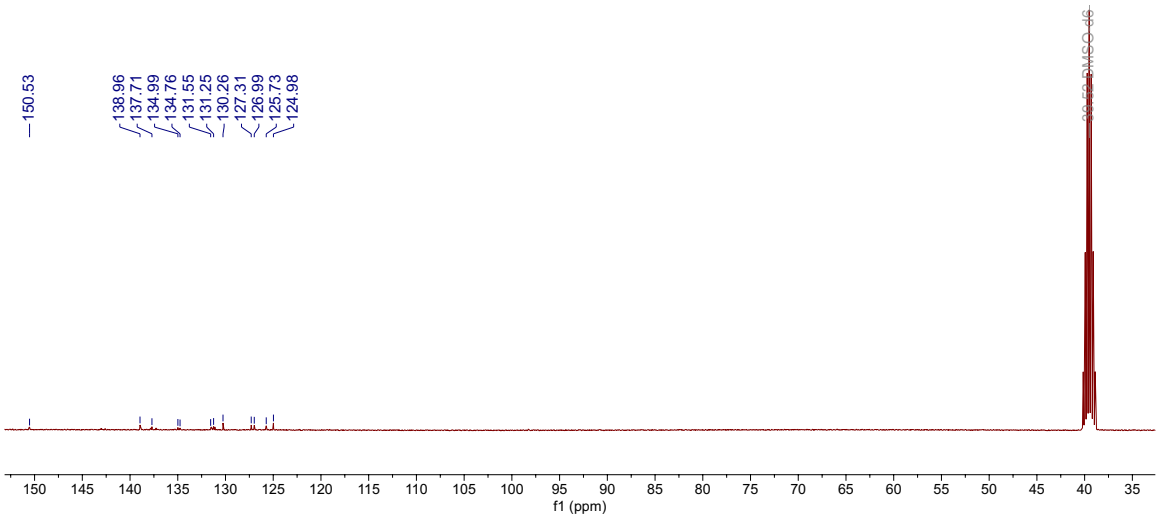

Figure 16. ^{13}C NMR spectrum (126 MHz, DMSO-d_6) of **1,4-bis(phenyliodonium)phenylene triflate [*p*-(Isq)$_2$-C$_6$H$_4$].**

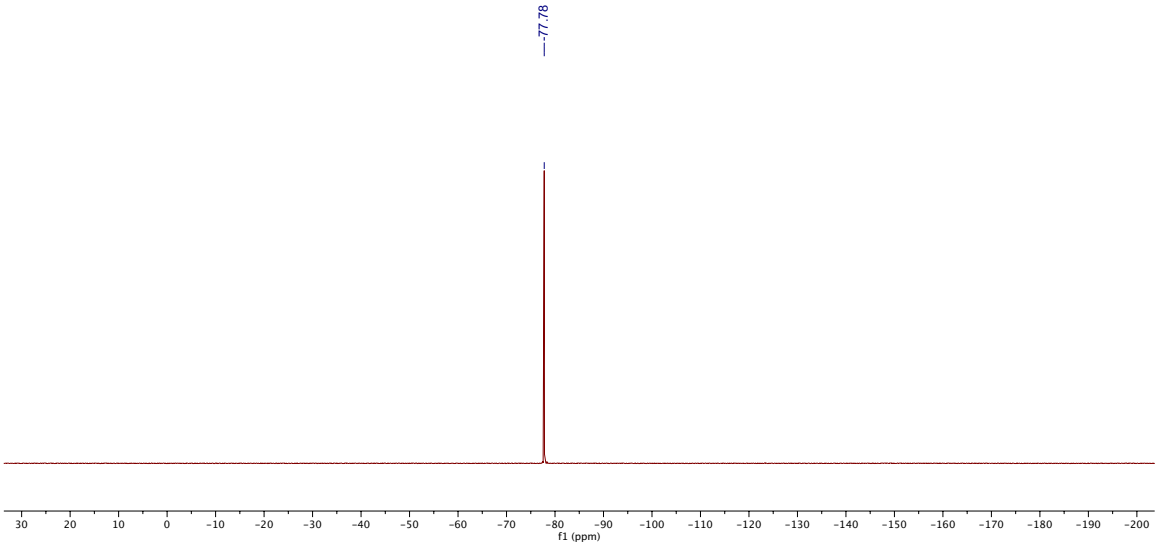

Figure 17. ^{19}F NMR spectrum (471 MHz, DMSO-d_6) of **1,4-bis(phenyliodonium)phenylene triflate (*p*-(Isq)$_2$-C$_6$H$_4$).**

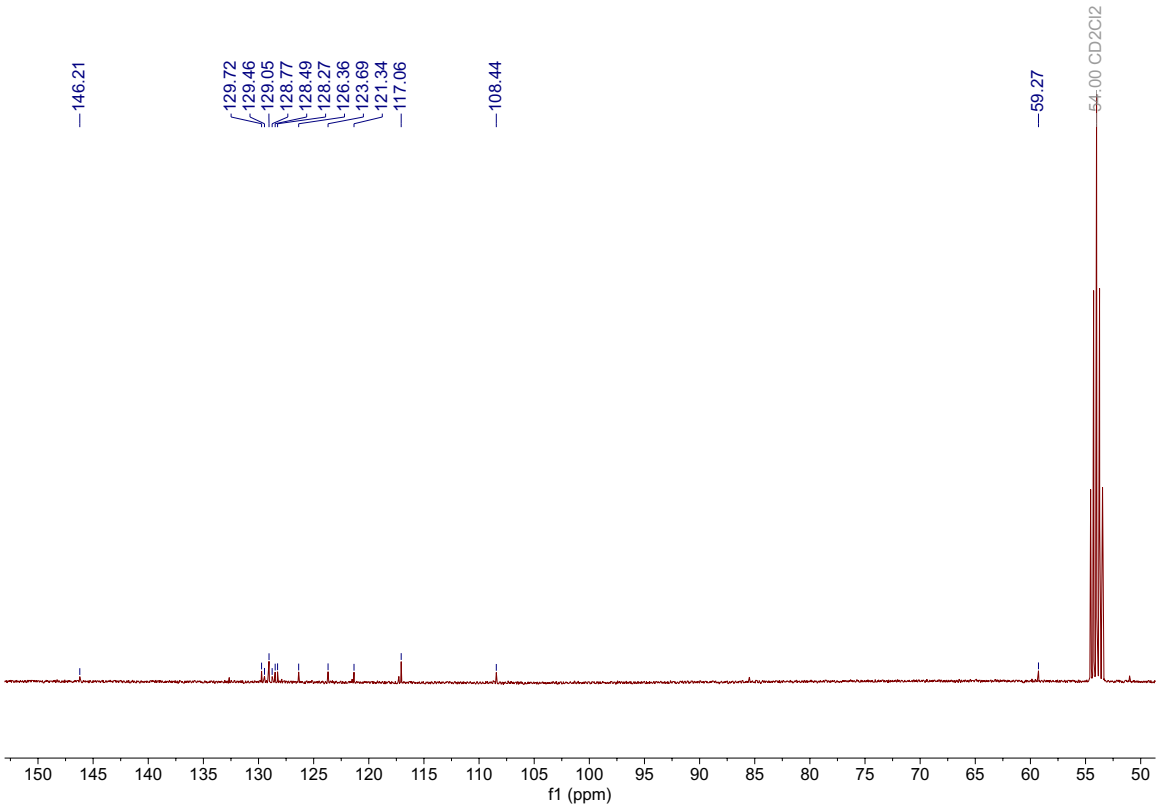

Figure 18. ^{13}C NMR spectrum (126 MHz, CD_2Cl_2) of **1**.

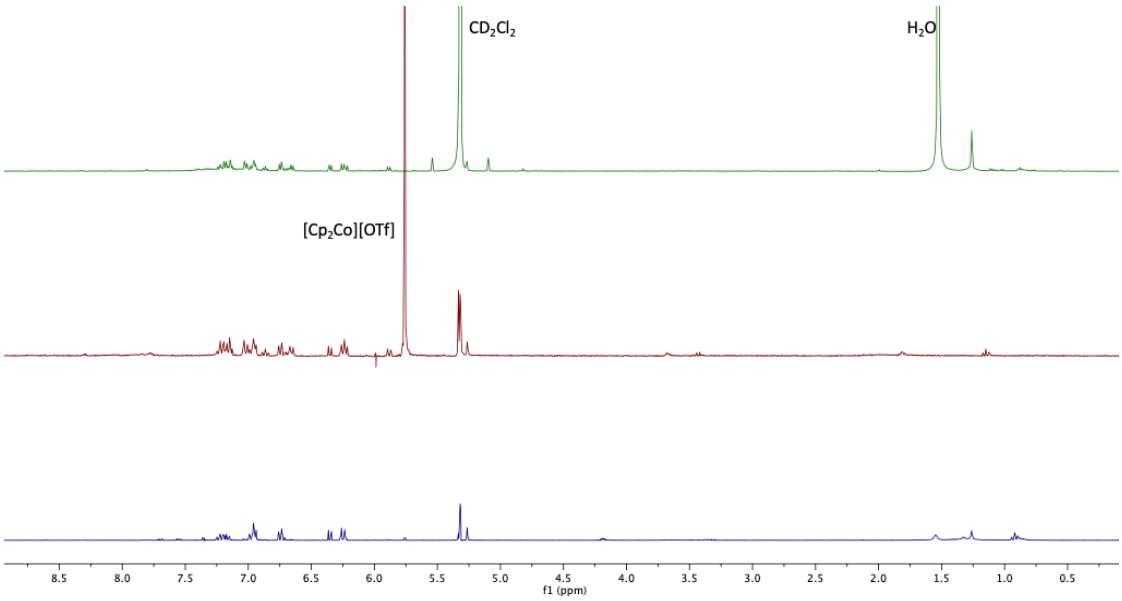

Figure 19. ^{1}H NMR spectra (400 MHz, CD_2Cl_2) of (top) **IsqPh** film post-catalysis after dissolving from Cu electrode, (middle) the crude material after reduction with 1 equivalent of cobaltocene, and (bottom) **1** after purification.

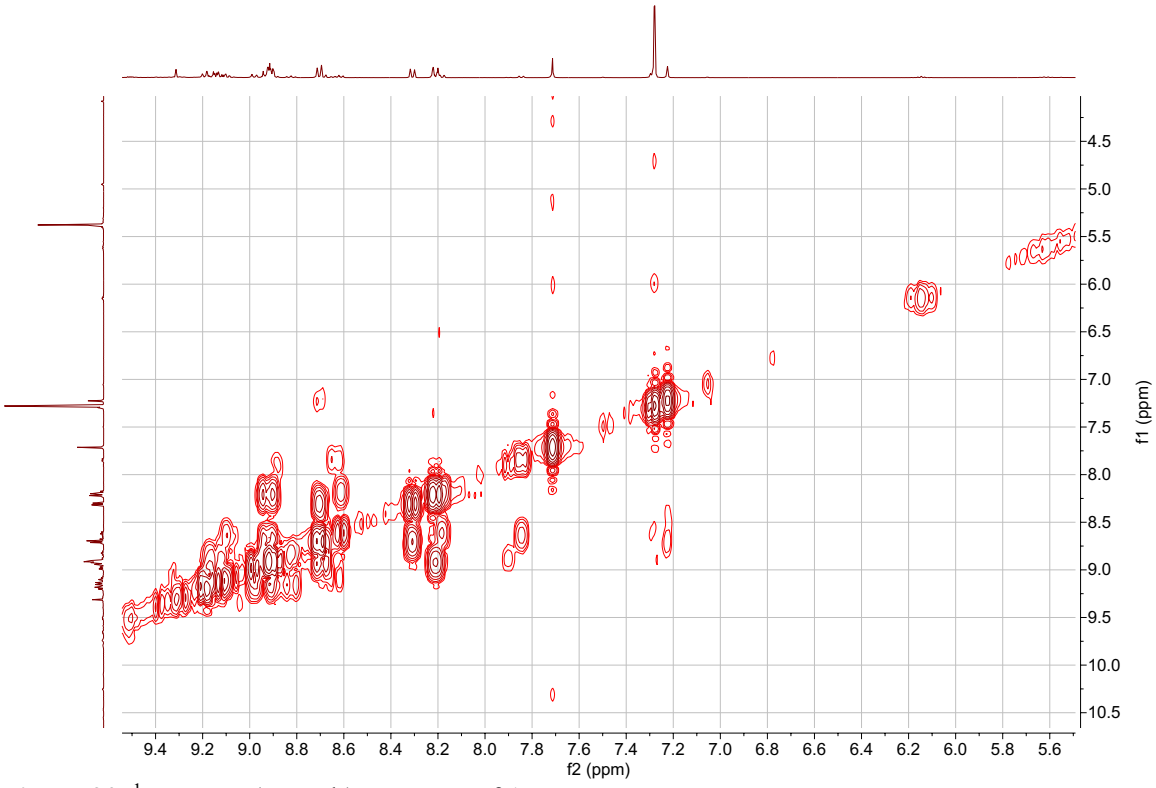

Figure 20. ^{1}H COSY (CD_2Cl_2) spectrum of **1**.

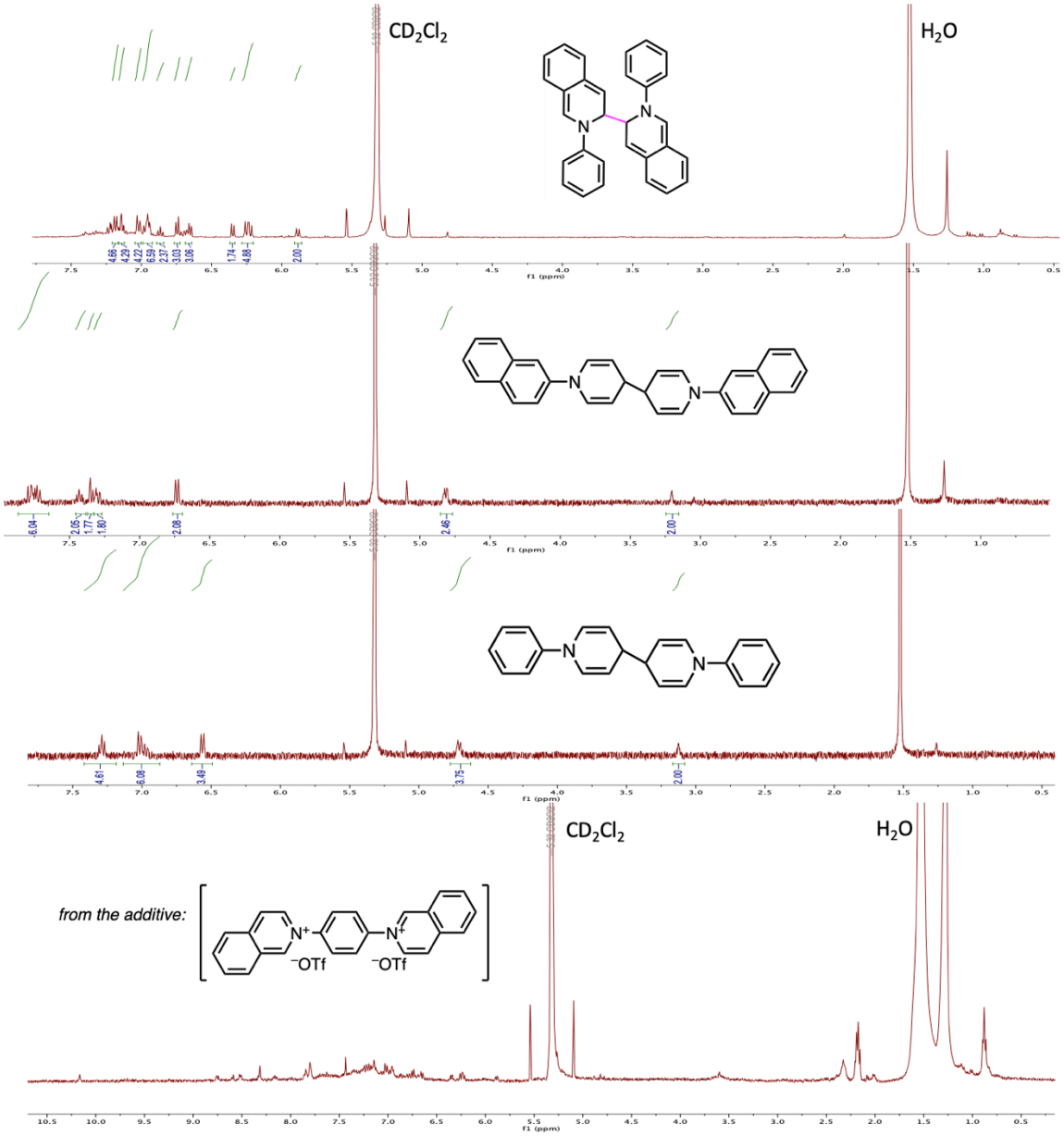

Figure 21. a) ^{1}H NMR spectra (400 MHz, CD_2Cl_2) of films post-catalysis and proposed structures. Films were generated on the Cu electrode *in situ* via chronoamperometry at –1.4 V vs. RHE for 35 minutes in CO_2-saturated 0.1 M KH_2PO_4/H_3PO_4. The ^{1}H NMR of the film of ***p*-(Isq)$_2$(C$_6$H$_4$)** is provided in the bottom spectrum, but its intractable nature complicated analysis.

Electrochemistry

Electrochemical Measurements in the Flow Cell

Chronoamperometry measurements were carried out in a custom-made PEEK flow cell setup similar to the one reported by Ager and co-workers using a copper foil as the working electrode and a platinum foil as the counter electrode.[25] The cathode compartment was separated from the anode compartment by a Selemion AMV anion-exchange membrane (AGC Engineering Co.). All potentials were measured versus a leakless Ag/AgCl reference electrode (Innovative Instruments) with an outer diameter of 5 mm that was inserted into the cathode compartment. The reference electrode was calibrated against H^+/H_2 on Pt in a 0.5 M sulfuric acid solution (0 V vs. standard hydrogen electrode) and saturated calomel electrode (SCE) (+0.241 V saturated vs. standard hydrogen electrode). All electrochemical measurements were carried out using a Biologic VMP3 multichannel potentiostat. The applied potentials were converted to the reversible hydrogen electrode (RHE) scale with iR correction through the following equation:

$$E_{corrected}\,(\text{vs. RHE}) = E_{applied}\,(\text{vs. Ag/AgCl}) + (0.059 \times \text{pH}) + 0.210 + (0.15)\,iR \qquad (1)$$

where i is the current at each applied potential and R is the equivalent series resistance measured via electrochemical impedance spectroscopy (EIS) in the frequency range of 10^5 – 0.1 Hz with an amplitude of 10 mV.

Potentiostatic electrochemical impedance spectroscopy (PEIS) measurements were carried out prior to each electrolysis experiment to determine the Ohmic resistance of the flow cell. The impedance measurements were carried out at frequencies ranging from 200 kHz to 100 MHz to measure the solution resistance. A Nyquist plot was plotted and in the low-frequency part, a linear fit was performed, and the axis intersection was calculated. The value of this intersection represents the

Ohmic resistance of the cell. An average of 3 measurements was taken to calculate the value of R. Typically, resistance measurements ranged from 40 to 50 Ω.

All chronoamperometric experiments were performed for 35 min at 25 °C using a CO_2-saturated electrolyte of choice. In experiments where an additive was used, a 10 mM solution of the materials was prepared and injected into the cathode compartment. The same electrolyte was used in the anode without any additive. The potentiostat was set to compensate for 85 % of the Ohmic drop, with the remaining 15 % being compensated for after the measurements. The effluent gas stream coming from the flow cell (5 mL/min) was flowed into the sample loops of a gas chromatograph (GC-FID/TCD, SRI 8610C, in Multi Gas 5 configuration) equipped with HayeSep D and Molsieve 5A columns. Methane, ethylene, ethane, and carbon monoxide were detected by a methanizer-flame ionization detector (FID) and the hydrogen was detected by a thermal conductivity detector (TCD). Every 15 minutes, 2 mL of gas was sampled to determine the concentration of gaseous products. After electrolysis, the liquid products in both catholytes and anolytes were quantified by both HPLC (Thermo Scientific Ultimate 3000) and ^{1}H NMR spectroscopy (Bruker 400 MHz Spectrometer).

Electrochemical Measurements in the GDE Cell

The CO_2R measurements were conducted in a gas-tight liquid-electrolyte flow cell. Chronopotentiometry experiments were carried out in a custom-made PEEK liquid-electrolyte cell similar to the one reported by Sargent and co-workers.[26] The liquid-electrolyte flow cell consists of three compartments: gas chamber, catholyte chamber, and anolyte chamber. The PTFE electrode was sandwiched between CO_2 gas chamber and catholyte chamber with an exposure area of 0.5 cm^{-2}. Catholyte and anolyte chambers were separated by a cation-exchange membrane (Nafion 115, FuelCellStore). An Autolab PGSTAT204 in a potentiostatic mode was used as electrochemical workstation. The PTFE electrode, leakless Ag/AgCl electrode, and Pt mesh were employed as working, reference and counter electrodes, respectively. The applied potentials were converted to the reversible hydrogen electrode (RHE) scale with iR correction through the following equation:

$$E_{corrected}\ (\text{vs. RHE}) = E_{applied}\ (\text{vs. Ag/AgCl}) + (0.059 \times \text{pH}) + 0.210 + iR \qquad (1)$$

where *i* is the current at each applied potential and R is the equivalent series resistance measured via electrochemical impedance spectroscopy (EIS) in the frequency range of 10^5 – 0.1 Hz with an amplitude of 10 mV. The appropriate CO_2-saturated electrolyte was used as both catholyte and anolyte and was circulated through the flow cell using peristaltic pumps with a silicone Shore A50 tubing. The electrolyte was bubbled with CO_2 during the entire electrolysis process. The electrolyte flow rate was kept at 10 mL min^{-1}. The flow rate of the CO_2 gas flowing into the gas chamber was kept at 50 sccm by a digital mass flow controller.

Potentiostatic electrochemical impedance spectroscopy (PEIS) measurements were carried out prior to and after each electrolysis experiment to determine the Ohmic resistance of the flow cell.[38] The impedance measurements were carried out at frequencies ranging from 200 kHz to 100 MHz to measure the solution resistance. A Nyquist plot was plotted and in the high-frequency part a linear fit was performed, and the axis intersection was calculated. The value of this intersection represents the Ohmic resistance of the cell. An average of 3 measurements was taken to calculate the value of R. Typically, small resistances were measured, ranging from 4 to 7 Ω.

All chronopotentiometric experiments were performed for 35 min at 25 °C using a CO_2-saturated electrolyte of choice. Before each CO_2 electrolysis experiment, the film was deposited via CA at –1.4 V vs. RHE for 5 minutes with 10 mM [*additive*] flowing in the catholyte. The anolyte contained the same electrolyte composition absent of any additive. The catholyte was replaced with fresh electrolyte before the subsequent chronopotentiometry experiment. The entire Ohmic drop was compensated before and after the measurement. The effluent gas stream coming from the flow cell (5 mL/min) was

flowed into the sample loops of a gas chromatograph (GC-FID/TCD, SRI 8610C, in Multi Gas 5 configuration) equipped with HayeSep D and Molsieve 5A columns. Methane, ethylene, ethane, and carbon monoxide were detected by a methanizer-flame ionization detector (FID) and the hydrogen was detected by a thermal conductivity detector (TCD). Every 15 minutes, 2 mL of gas was sampled to determine the concentration of gaseous products. After electrolysis, the liquid products in both catholytes and anolytes were quantified by both HPLC (Thermo Scientific Ultimate 3000) and ^{1}H NMR spectroscopy (Bruker 400 MHz Spectrometer), the latter using 10% v/v D_2O with DMSO and phenol and standards employing a water suppression technique described in our previous report.[22,38] For variable partial pressure CO_2 (pCO_2) experiments, the standard electrolyte mixture (0.1 M KH_2PO_4/H_3PO_4, pH = 2) and applied potential (–1.4 V vs. RHE) were used for each partial pressure. Argon was utilized as the balance gas such that the total flow rate was remained at 10 sccm. For example, in the case where pCO_2 = 0.8 atm, the flow rate of CO_2 was 8 sccm and that of Ar was 2 sccm.

The Faradaic efficiencies for gaseous products was calculated from the following equations:

$$F_m = \frac{pF_v}{RT} \tag{2}$$

$$FE_{prod} = \frac{n_{prod} F x_{prod} F_m}{i}. \tag{3}$$

F_m is the molar flow, defined by the pressure p, the volume flow F_v, the gas constant R, and temperature T. FE_{prod} is the Faradaic efficiency of a gaseous product $prod$, defined by the electron transfer coefficient of the product n_{prod}, Faraday's constant F, the fraction of the product x_{prod}, the molar flow F_m, and the current i.

Error bars shown in all figures and tables represent standard deviations from at least three replicate measurements.

Rotating Disk Electrochemistry Experiments

Rotation disk electrode experiments were done in a single-compartment cell using a Cu disc electrode, a carbon rod as a counter electrode, and a saturated calomel reference electrode using N_2-saturated 0.1 M $KClO_4$ electrolyte (pH = 2.2). Copper disk electrodes were sonicated sequentially in 0.1 M HNO_3, H_2O, acetone, and H_2O again for 3 min, then mechanically polished with 3 μm, and 0.1 μm diamond pastes, and finally sonicated in nanopure H_2O for 5 minutes before use. The film was generated on the Cu disk first via chronoamperometry without rotation for 35 min at –1.4 V vs. RHE with 10 mM additive dissolved in 0.1 M KH_2PO_4/H_3PO_4 (pH = 2) under a blanket of CO_2. This Cu disk was rinsed with water and dried under a stream of N_2. Cyclic voltammograms were collected at different rotation rates (400 rpm, 800 rpm, 1200 rpm, 1600 rpm and 2500 rpm). Potentials were scanned cathodically (0 V to –1.8 V vs. RHE). For each electrode, i_{plateau} was plotted versus square root of rotation rate ($\omega^{1/2}$**,** [rad s^{-1}]$^{1/2}$), and the diffusion coefficient was determined via the Levich equation:[31]

$$i_{plateau} = 0.62nFAD^{2/3}v^{-1/6}C\omega^{1/2} \quad (4)$$

where n is the number of electrons transferred, F is Faraday's constant, A is the electrode area (cm^2), D is the diffusion coefficient (cm^2 s^{-1}), v is the scan rate (cm^2 s^{-1}), C is the analyte concentration (mol cm^{-3}), and ω is the angular rotation rate (rad s^{-1}).

SUPPLEMENTARY FIGURES/DATA

Table 2. Selectivity profile from CO_2R on Cu foil modified by various cationic *N*-heterocycle molecular additives. 35-minute chronoamperometry (CA) with 10 mM [*additive*] dissolved in CO_2-saturated 0.1 M KH_2PO_4/H_3PO_4 in catholyte. $E_{applied}$ = –1.4 V vs. RHE.

Additive	E_{corr} (V vs. RHE)	Faradaic Efficiency (%)[a]										*j* (mA/cm^2)[a]
		H_2	CO	HCOOH	CH_4	C_2H_4	C_2H_5OH	C_3H_7OH	FE_{C2+}	CO_2R FE	Total	
No additve	-1.31	99.0 ± 0.1	0.1 ± 0.1	1.1 ± 0.3	0.0	0.0	0.0	0.0	0.0	1.2 ± 0.2	100 ± 0.2	–18 ± 1
Py-Tolyl	-1.40	20 ± 6	1.0 ± 0.1	5.0 ± 0.9	2 ± 1	22 ± 3	28 ± 4	3 ± 1	55 ± 2	59 ± 5	89 ± 6	–1.4 ± 0.2
***p*-(Isq)$_2$(C_6H_4)**	-1.40	19 ± 3	1.2 ± 0.1	10 ± 1	3 ± 3	34 ± 5	19 ± 5	7± 2	60 ± 7	74 ± 8	92 ± 8	–2.8 ± 0.6
Isq-Ph	-1.40	15 ± 5	3 ± 2	16 ± 5	0.0	40 ± 3	23 ± 4	7 ± 1	69 ± 5	87 ± 7	103 ± 5	–1.86 ± 0.03
Py-Ph	-1.41	37 ± 3	0.8 ± 0.6	7 ± 3	0.0	23 ± 5	23 ± 2	0.0	46 ± 5	55 ± 8	92 ± 7	–1.0 ± 0.1
Py-Nap	-1.40	50 ± 3	1.8 ± 0.1	8 ± 0.3	2 ± 1	17 ± 2	20 ± 1	0.0	37 ± 2	48 ± 3	98.8 ± 0.2	–1.5 ± 0.3

[a] Reported values are averages and standard deviations from three independent measurements.

Table 3. Selectivity profile from CO_2R on Cu foil modified by IsqPh film with and without dissolved additive. 35-minute chronoamperometry (CA) in CO_2-saturated 0.1 M KH_2PO_4/H_3PO_4 in catholyte. $E_{applied}$ = –1.4 V vs. RHE.

Additive	$E_{corrected}$ (V vs. RHE)	Faradaic Efficiency (%)[a]										*j* (mA/cm^2)[a]
		H_2	CO	HCOOH	CH_4	C_2H_4	C_2H_5OH	C_3H_7OH	FE_{C2+}	CO_2R FE	Total	
10 mM IsqPh	-1.40	15 ± 5	3 ± 2	16 ± 5	0.0	40 ± 3	23 ± 4	7 ± 1	69 ± 5	87 ± 7	103 ± 5	–1.86 ± 0.03
0 mM IsqPh; Film on electrode	-1.40	16 ± 2	0.7 ± 0.1	8 ± 3	0.3 ± 0.1	44 ± 3	20 ± 3	5 ± 1	69 ± 5	78 ± 5	95 ± 6	–3.0 ± 0.3

[a] Reported values are averages and standard deviations from three independent measurements

Table 4. Selectivity profile from CO_2R on Cu GDE. 35-minute chronopotentiometry (CP) with film-modified GDE in CO_2-saturated 3 M KCl/ 1 M H_3PO_4 (pH = 1.1) in catholyte. j = –100 mA cm^{-2}.

Additive	Faradaic Efficiency (%)[a]											$E_{corrected}$ (V vs. RHE)[a]
	H_2	CO	HCOOH	CH_4	C_2H_4	C_2H_5OH	C_3H_7OH	CH_3COOH	C_{2+}	CO_2R Products	Total	
No additve	91 ± 1	0.0	0.0	0.0	0.0	0.0	0.0	0.0	0.0	0.0	91 ± 1	–0.9 ± 0.1
Py-Tolyl	50 ± 2	0.5 ± 0.1	6 ± 2	6 ± 1	16 ± 2	12 ± 2	0.0	5.0 ± 0.6	33 ± 3	46 ± 3	96 ± 4	–1.7 ± 0.2
***p*-$(Isq)_2(C_6H_4)$**	46 ± 6	0.4 ± 0.2	2.6 ± 0.3	7 ± 2	10 ± 2	2.6 ± 0.3	2.0 ± 0.1	1.4 ± 0.5	19 ± 3	27 ± 9	75 ± 7	–1.9 ± 0.2
Isq-Ph	19 ± 4	0.8 ± 0.1	4.82 ± 0.03	0.0	41.1 ± 0.5	14 ± 2	5 ± 4	3 ± 1	64 ± 5	71 ± 5	90 ± 6	–1.56 ± 0.03
Py-Ph	55.3 ± 0.4	0.4 ± 0.2	3 ± 1	3 ± 2	5 ± 2	5 ± 2	2.0 ± 0.4	1.5 ± 0.3	21 ± 5	24 ± 6	80 ± 6	–1.8 ± 0.2
Py-Nap	49 ± 2	0.25 ± 0.01	2.04 ± 0.01	3 ± 1	18 ± 1	14 ± 2	3 ± 2	2.3 ± 0.4	34 ± 3	42 ± 3	90 ± 4	–1.68 ± 0.04

[a] Reported values are averages and standard deviations from three independent measurements.

Table 5. Selectivity profile from CO_2R on Cu GDEs. 35-minute CP with film-modified GDE in CO_2-saturated 3 M KCl/ 1 M H_3PO_4 (pH = 1.1) in catholyte. j = –200 mA cm^{-2}.

Additive	Faradaic Efficiency (%)[a]											$E_{corrected}$ (V vs. RHE)[a]
	H_2	CO	HCOOH	CH_4	C_2H_4	C_2H_5OH	C_3H_7OH	CH_3COOH	C_{2+}	CO_2R FE	Total	
No additve	67 ± 1	0.2 ± 0.1	0.7 ± 0.2	0.6 ± 0.1	0.8 ± 0.3	0.7 ± 0.2	0.0	0.7 ± 0.1	2.1 ± 0.2	3.6 ± 0.3	71 ± 1	–2.4 ± 0.1
Isq-Ph	55 ± 2	0.3 ± 0.1	1.8 ± 0.3	5.1 ± 0.2	4.1 ± 0.5	3.8 ± 0.2	1.1 ± 0.1	3.6 ± 0.5	13.0 ± 0.1	15.4 ± 0.5	70 ± 2	–2.2 ± 0.1

[a] Reported values are averages and standard deviations from three independent measurements.

Table 6. Selectivity profile from CO_2R on Cu foil at $p(CO_2)$ = 0.2 atm in 0.1 M $KHCO_3$, 10 mM in catholyte. $E_{applied}$ = –1.1 V vs. RHE

Additive	Faradaic Efficiency (%)[a]											j (mA/ cm^2)[a]
	H_2	CO	HCOOH	CH_4	C_2H_4	C_2H_5OH	C_3H_7OH	CH_3COOH	C_{2+}	CO_2R FE	Total	
No additve	77 ± 2	0.2 ± 0.1	4 ± 1	11 ± 3	1.3 ± 0.3	2.7 ± 0.2	0.0	0.0	4.0 ± 0.2	19 ± 3	96 ± 4	–7.5 ± 0.5
Isq-Ph	81 ± 2	0.2 ± 0.1	1.3 ± 0.3	0.4 ± 0.2	4 ± 1	10 ± 3	0.0	0.0	14 ± 2	16 ± 2	97 ± 2	–2.0 ± 0.1

[a] Reported values are averages and standard deviations from three independent measurements

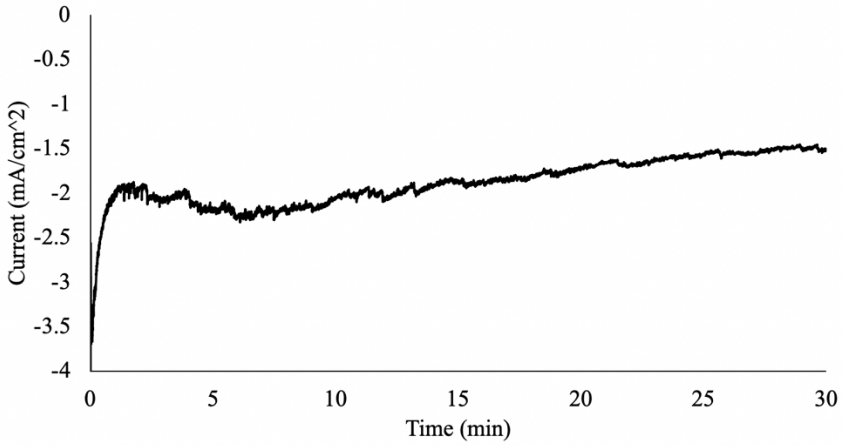

Figure 22. Example chronoamperometry trace in flow cell for **IsqPh.**

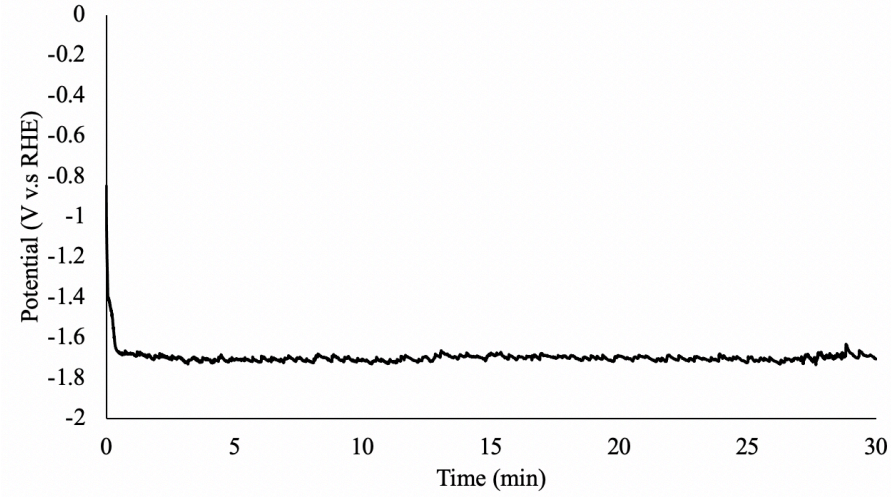

Figure 23. Example chronopotentiometry (CP) trace in GDE cell for **IsqPh.**

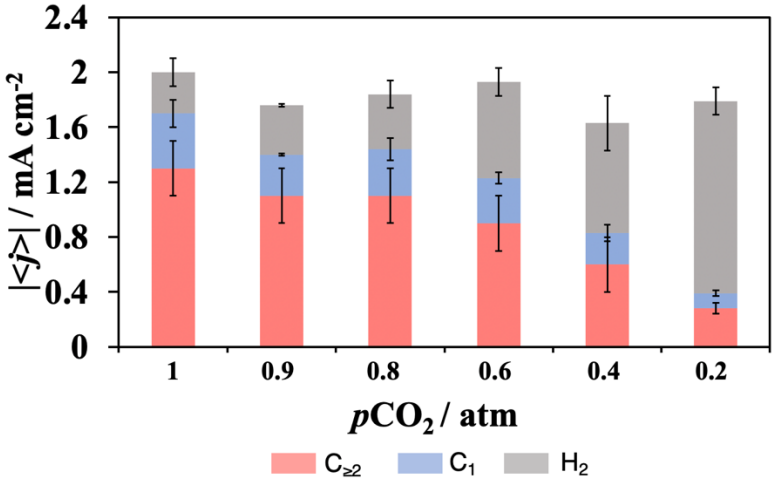

Figure 24. Partial current densities of $C_{\geq 2}$ products (red), C_1 products (blue), and hydrogen (grey) in different partial pressures of CO_2.

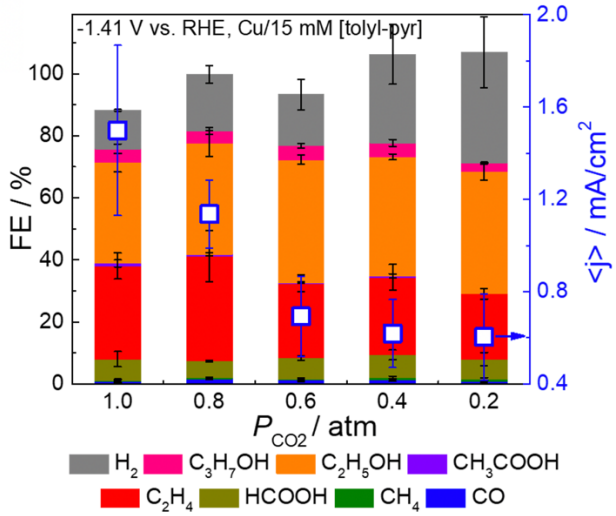

Figure 25. FEs and total current densities (white squares) with varying CO_2 partial pressure in pH = 2 electrolyte (0.1 M KH_2PO_4/H_3PO_4), 10 mM **Py-Tolyl** and $E_{applied}$ = –1.4 V vs. RHE.

REFERENCES

(1) Hori, Y.; Kikuchi, K.; Suzuki, S. Production of CO and CH_4 in Electrochemical Reduction of CO_2 at Metal Electrodes in Aqueous Hydrogencarbonate Solution. *Chem. Lett.* **1985**, *14* (11), 1695–1698.

(2) Murata, A.; Hori, Y. Product Selectivity Affected by Cationic Species in Electrochemical Reduction of CO2 and CO at a Cu Electrode. *Bull. Chem. Soc. Jpn.* **1991**, *64* (1), 123–127.

(3) Chu, S.; Cui, Y.; Liu, N. The Path towards Sustainable Energy. *Nat. Mater.* **2017**, *16* (1), 16–22.

(4) Kuhl, K. P.; Cave, E. R.; Abram, D. N.; Jaramillo, T. F. New Insights into the Electrochemical Reduction of Carbon Dioxide on Metallic Copper Surfaces. *Energy Environ. Sci.* **2012**, *5* (5), 7050–7059.

(5) Chatterjee, T.; Boutin, E.; Robert, M. Manifesto for the Routine Use of NMR for the Liquid Product Analysis of Aqueous CO2 Reduction: From Comprehensive Chemical Shift Data to Formaldehyde Quantification in Water. *Dalt. Trans.* **2020**, *49* (14), 4257–4265.

(6) Deng, B.; Huang, M.; Zhao, X.; Mou, S.; Dong, F. Interfacial Electrolyte Effects on Electrocatalytic CO2 Reduction. *ACS Catal.* **2022**, *12* (1), 331–362.

(7) Nitopi, S.; Bertheussen, E.; Scott, S. B.; Liu, X.; Engstfeld, A. K.; Horch, S.; Seger, B.; Stephens, I. E. L.; Chan, K.; Hahn, C.; et al. Progress and Perspectives of Electrochemical CO2 Reduction on Copper in Aqueous Electrolyte. *Chem. Rev.* **2019**, *119* (12), 7610–7672.

(8) Pelayo, G. de A. F.; Cao-Thang, D.; Adnan, O.; Joshua, W.; Christopher, M.; R., K. A.; Dae-Hyun, N.; Christine, G.; Ali, S.; Xue, W.; et al. CO2 Electrolysis to Multicarbon Products at Activities Greater than 1 A Cm−2. *Science (80-.).* **2020**, *367* (6478), 661–666.

(9) Lees, E. W.; Mowbray, B. A. W.; Parlane, F. G. L.; Berlinguette, C. P. Gas Diffusion Electrodes and Membranes for CO2 Reduction Electrolysers. *Nat. Rev. Mater.* **2021**.

(10) Wang, M.; Zhang, Q.; Xie, Q.; Wan, L.; Zhao, Y.; Zhang, X.; Luo, J. Selective Electrochemical Reduction of Carbon Dioxide to Ethylene on a Copper Hydroxide Nitrate Nanostructure Electrode. *Nanoscale* **2020**, *12* (32), 17013–17019.

(11) Thevenon, A.; Rosas-Hernández, A.; Peters, J. C.; Agapie, T. In-Situ Nanostructuring and Stabilization of Polycrystalline Copper by an Organic Salt Additive Promotes Electrocatalytic CO2 Reduction to Ethylene. *Angew. Chemie Int. Ed.* **2019**, *58* (47), 16952–16958.

(12) Kim, C.; Bui, J. C.; Luo, X.; Cooper, J. K.; Kusoglu, A.; Weber, A. Z.; Bell, A. T. Tailored Catalyst Microenvironments for CO2 Electroreduction to Multicarbon Products on Copper Using Bilayer Ionomer Coatings. *Nat. Energy* **2021**, *6* (11), 1026–1034.

(13) Zhang, B. A.; Ozel, T.; Elias, J. S.; Costentin, C.; Nocera, D. G. Interplay of Homogeneous Reactions, Mass Transport, and Kinetics in Determining Selectivity of the Reduction of CO2 on Gold Electrodes. *ACS Cent. Sci.* **2019**, *5* (6), 1097–1105.

(14) Alerte, T.; Edwards, J. P.; Gabardo, C. M.; O'Brien, C. P.; Gaona, A.; Wicks, J.; Obradović, A.; Sarkar, A.; Jaffer, S. A.; MacLean, H. L.; et al. Downstream of the CO2 Electrolyzer: Assessing the Energy Intensity of Product Separation. *ACS Energy Lett.* **2021**, *6* (12), 4405–4412.

(15) Erick, H. J.; Fengwang, L.; Adnan, O.; Armin, S. R.; Pelayo, G. de A. F.; Shijie, L.; Shuzhen, Z.; Mingchuan, L.; Xue, W.; Yanwei, L.; et al. CO2 Electrolysis to Multicarbon Products in Strong Acid. *Science (80-.).* **2021**, *372* (6546), 1074–1078.

(16) Li, J.; Kornienko, N. Electrocatalytic Carbon Dioxide Reduction in Acid. *Chem Catal.* **2022**, *2* (1), 29–38.

(17) Perazio, A.; Creissen, C. E.; Rivera de la Cruz, J. G.; Schreiber, M. W.; Fontecave, M. Acidic Electroreduction of CO2 to Multi-Carbon Products with CO2 Recovery and Recycling from Carbonate. *ACS Energy Lett.* **2023**, *8* (7), 2979–2985.

(18) Bondue, C. J.; Graf, M.; Goyal, A.; Koper, M. T. M. Suppression of Hydrogen Evolution in Acidic Electrolytes by Electrochemical CO2 Reduction. *J. Am. Chem. Soc.* **2021**, *143* (1), 279–285.

(19) Monteiro, M. C. O.; Philips, M. F.; Schouten, K. J. P.; Koper, M. T. M. Efficiency and Selectivity of CO2 Reduction to CO on Gold Gas Diffusion Electrodes in Acidic Media. *Nat. Commun.* **2021**, *12* (1), 4943.

(20) Gu, J.; Liu, S.; Ni, W.; Ren, W.; Haussener, S.; Hu, X. Modulating Electric Field Distribution by Alkali Cations for CO2 Electroreduction in Strongly Acidic Medium. *Nat. Catal.* **2022**, *5* (4), 268–276.

(21) Nie, W.; Heim, G. P.; Watkins, N. B.; Agapie, T.; Peters, J. Organic Additive-Derived Films on Cu Electrodes Promote Electrochemical CO2 Reduction to C2+ Products Under Strongly Acidic Conditions. *Angew. Chemie Int. Ed.* **2023**, *n/a* (n/a).

(22) Han, Z.; Kortlever, R.; Chen, H.-Y.; Peters, J. C.; Agapie, T. CO2 Reduction Selective for C≥2 Products on Polycrystalline Copper with N-Substituted Pyridinium Additives. *ACS Cent. Sci.* **2017**, *3* (8), 853–859.

(23) Monteiro, M. C. O.; Dattila, F.; Hagedoorn, B.; García-Muelas, R.; López, N.; Koper, M. T. M. Absence of CO2 Electroreduction on Copper, Gold and Silver Electrodes without Metal Cations in Solution. *Nat. Catal.* **2021**, *4* (8), 654–662.

(24) Cheng, B.; Du, J.; Yuan, H.; Tao, Y.; Chen, Y.; Lei, J.; Han, Z. Selective CO2 Reduction to Ethylene Using Imidazolium-Functionalized Copper. *ACS Appl. Mater. Interfaces* **2022**, *14* (24), 27823–27832.

(25) Lobaccaro, P.; Singh, M. R.; Clark, E. L.; Kwon, Y.; Bell, A. T.; Ager, J. W. Effects of Temperature and Gas–Liquid Mass Transfer on the Operation of Small Electrochemical Cells for the Quantitative Evaluation of CO2 Reduction Electrocatalysts. *Phys. Chem. Chem. Phys.* **2016**, *18* (38), 26777–26785.

(26) Li, F.; Thevenon, A.; Rosas-Hernández, A.; Wang, Z.; Li, Y.; Gabardo, C. M.; Ozden, A.; Dinh, C. T.; Li, J.; Wang, Y.; et al. Molecular Tuning of CO2-to-Ethylene Conversion. *Nature*

2020, *577* (7791), 509–513.

(27) Thevenon, A.; Rosas-Hernández, A.; Fontani Herreros, A. M.; Agapie, T.; Peters, J. C. Dramatic HER Suppression on Ag Electrodes via Molecular Films for Highly Selective CO2 to CO Reduction. *ACS Catal.* **2021**, *11* (8), 4530–4537.

(28) Ren, W.; Xu, A.; Chan, K.; Hu, X. A Cation Concentration Gradient Approach to Tune the Selectivity and Activity of CO2 Electroreduction. *Angew. Chemie Int. Ed.* **2022**, *61* (49), e202214173.

(29) Xu, Z.; Xie, Y.; Wang, Y. Pause Electrolysis for Acidic CO2 Reduction on 3-Dimensional Cu. *Mater. Reports Energy* **2023**, *3* (1), 100173.

(30) Xie, Y.; Ou, P.; Wang, X.; Xu, Z.; Li, Y. C.; Wang, Z.; Huang, J. E.; Wicks, J.; McCallum, C.; Wang, N.; et al. High Carbon Utilization in CO2 Reduction to Multi-Carbon Products in Acidic Media. *Nat. Catal.* **2022**, *5* (6), 564–570.

(31) Ooka, H.; Figueiredo, M. C.; Koper, M. T. M. Competition between Hydrogen Evolution and Carbon Dioxide Reduction on Copper Electrodes in Mildly Acidic Media. *Langmuir* **2017**, *33* (37), 9307–9313.

(32) Chen, C.; Khosrowabadi Kotyk, J. F.; Sheehan, S. W. Progress toward Commercial Application of Electrochemical Carbon Dioxide Reduction. *Chem* **2018**, *4* (11), 2571–2586.

(33) Nguyen, T. N.; Dinh, C.-T. Gas Diffusion Electrode Design for Electrochemical Carbon Dioxide Reduction. *Chem. Soc. Rev.* **2020**, *49* (21), 7488–7504.

(34) Liu, K.; Smith, W. A.; Burdyny, T. Introductory Guide to Assembling and Operating Gas Diffusion Electrodes for Electrochemical CO2 Reduction. *ACS Energy Lett.* **2019**, *4* (3), 639–643.

(35) Ge, Q.; Hu, Y.; Li, B.; Wang, B. Synthesis of Conjugated Polycyclic Quinoliniums by Rhodium(III)-Catalyzed Multiple C–H Activation and Annulation of Arylpyridiniums with Alkynes. *Org. Lett.* **2016**, *18* (10), 2483–2486.

(36) Hong, A. Y.; Vanderwal, C. D. A Synthesis of Alsmaphorazine B Demonstrates the Chemical Feasibility of a New Biogenetic Hypothesis. *J. Am. Chem. Soc.* **2015**, *137* (23), 7306–7309.

(37) Pangborn, A. B.; Giardello, M. A.; Grubbs, R. H.; Rosen, R. K.; Timmers, F. J. Safe and Convenient Procedure for Solvent Purification. *Organometallics* **1996**, *15* (5), 1518–1520.

(38) Ma, M.; Zheng, Z.; Yan, W.; Hu, C.; Seger, B. Rigorous Evaluation of Liquid Products in High-Rate CO2/CO Electrolysis. *ACS Energy Lett.* **2022**, *7* (8), 2595–2601.

CHAPTER III

POTASSIUM ION MODULATION OF THE Cu ELECTRODE-ELECTROLYTE INTERFACE WITH IONOMERS ENHANCES CO_2 REDUCTION TO C_{2+} PRODUCTS

This chapter was reproduced from:

Heim, G.P.[†]; Bruening, M.A.[†]; Musgrave III, C.B.; Goddard III, W.A. Peters, J.C.; Agapie, T. *Joule*. **2024**. *Accepted article.*

[†]*Authors contributed equally*

ABSTRACT: Ionomers have shown promise as organic coatings on Cu electrodes to increase the CO_2 reduction (CO_2R) selectivity towards multi-carbon (C_{2+}) products. However, effects of systematic polymer structure modification on electrocatalytic performance have been seldom reported. Herein, we report on a series of polystyrene-based ionomers to probe the effect of local [K^+] in the Cu electrode microenvironment on CO_2R performance. Partial current density towards C_{2+} products ($|j_{C2+}|$) increases with [K^+] in ionomer, up to 225 mA cm^{-2}. Replacing K^+ with $[Me_4N]^+$ lowers performance to the level of bare Cu, highlighting the crucial role of K^+ in improving C_{2+} product selectivity. Molecular dynamics simulations show that CO_2 diffusivity increases with [K^+], implicating CO_2 transport to the electrode as a potential mechanism for improved CO_2R performance. Our results highlight the intersection of synthetic polymer chemistry and electrocatalysis as a promising strategy in electrode modification towards achieving high selectivity of value-added chemicals.

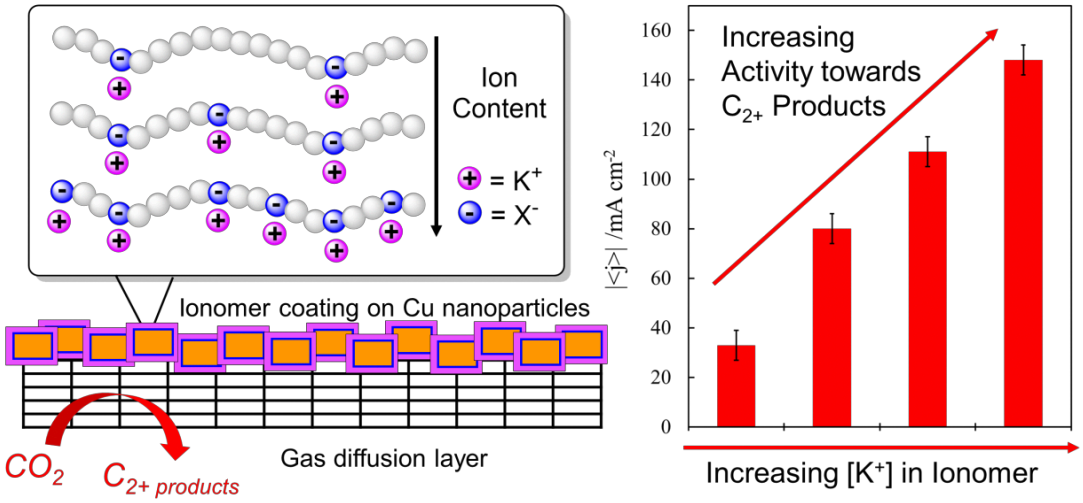

ACKNOWLEDGMENTS

Meaghan A. Bruening and Charles B. Musgrave III (Professor William A. Goddard's student) are tirelessly thanked for their tremendous contributions to this work (polymer synthesis and molecular dynamics simulations, respectively). I am grateful to Dr. Yungchieh Lai (Dr. John Gregoire's research group) for assisting with ICP-MS measurements. This material is based on work performed by the Liquid Sunlight Alliance, which is supported by the U.S. Department of Energy, Office of Science, Office of Basic Energy Sciences, Fuels from Sunlight Hub under Award DE-SC0021266. The Resnick Sustainability Institute at Caltech is acknowledged for support of the laboratory facilities in which lhis research was conducted. This work also used resources of the National Energy Research Scientific Computing Center, a DOE Office of Science User Facility supported by the Office of Science of the U.S. Department of Energy under Contract No. DE-AC02-05CH11231 using NERSC award BES-ERCAP0024109.

INTRODUCTION

Converting CO_2 to value-added chemicals electrochemically using renewable energy is a potential avenue toward achieving a net-zero carbon economy.[1] Cu is the only metallic electrode where multi-carbon (C_{2+}) products, including C_2H_4, C_2H_5OH, and C_3H_7OH are produced from electrochemical CO_2 reduction (CO_2R).[2] However, Cu alone suffers from poor selectivity towards C_{2+} products owing to the significant generation of C_1 products and hydrogen.[2–4] Coating Cu electrodes with organic films is a strategy for steering CO_2R selectivity towards C_{2+} products. Organic coatings derived from molecular precursors such as pyridinium,[5–9] ionic liquids,[10–12] amines,[13,14] and aryl diazonium and iodonium species[15] have shown promise. Although the ease of precursor synthesis and *in situ* film generation are attractive features of general approach, the physical properties of the coating and electrocatalyst microenvironment, including local pH, CO_2 concentration, hydrophobicity, and electric field strength, are not readily predicted.

An alternative approach to organic films is provided by ionomers.[16–23] For example, Bell and co-workers recently examined a combination of ionomers to control local pH and hydrophobicity to achieve high C_{2+} product selectivity on Cu.[16] Also, Sargent and co-workers have demonstrated high current density electrolysis with Nafion on Cu.[17] These examples employing commercial polymers highlight the potential of this approach; however, a dearth of studies of the effects of systematic changes in ionomer structure on CO_2R behavior limit fundamental understanding of the features crucial for electrochemical performance.[21,23] Of note, Grubbs and co-workers synthesized and tested a library of ionomer coatings bearing imidazolium groups and observed high selectivity for C_{2+} products and low HER.[21] Computations suggested that high local [CO_2], as well as an

induced electric field effect from the positively charged functional groups, drove high selectivity towards C_{2+} products. Alkali cations were found to facilitate CO_2R on metallic electrodes.[19,24–28] Their presence in the outer Helmholtz plane was hypothesized to suppress proton carrier mass transport and stabilize CO_2R intermediates.[19,28–30]

With the concentration of alkali metal cations established to affect CO_2R, a systematic investigation of anionic polymers with alkali cations can provide a strategy to facilitate CO_2R and possibly shed light on their impact on the electrode-electrolyte interface. Herein we report the impact of a series of polystyrene-based ionomer films for CO_2R on Cu. A correlation is observed between the content of K^+ in the ionomer and $|j_{C2+}|$. The role of the ionomer has been probed experimentally and computationally.

RESULTS AND DISCUSSION

Ionomers displaying variable K^+ content were prepared based on polystyrene using different ratios of 4-methoxystyrene and potassium (4-styrenesulfonyl)(trifluoromethanesulfonyl)imide (K-STFSI). A mixture of substituted styrene comonomers was treated with 10% azobisisobutyronitrile (AIBN) in MeCN and heated for 3 days at 70 °C (Figure 1A). Upon purification,[31] the resulting polymers were characterized by ^1H, ^{19}F, and ^{13}C NMR spectroscopy. The percent of charged comonomer incorporated was determined by ^1H NMR by integrating the OCH_3 peak for 4-methoxyphenyl at 3.7 ppm versus the protons *ortho* to the sulfonate moiety, centered at 7.6 ppm. Within this series in hand, copolymers were prepared with the content of the K-STFSI ranging from 0-37% (Figure 1B). While polymers with a higher content of charged monomer were accessed synthetically, they were too soluble in the electrolyte solution (1 M $KHCO_{3(aq)}$) to warrant further study as electrode coatings.

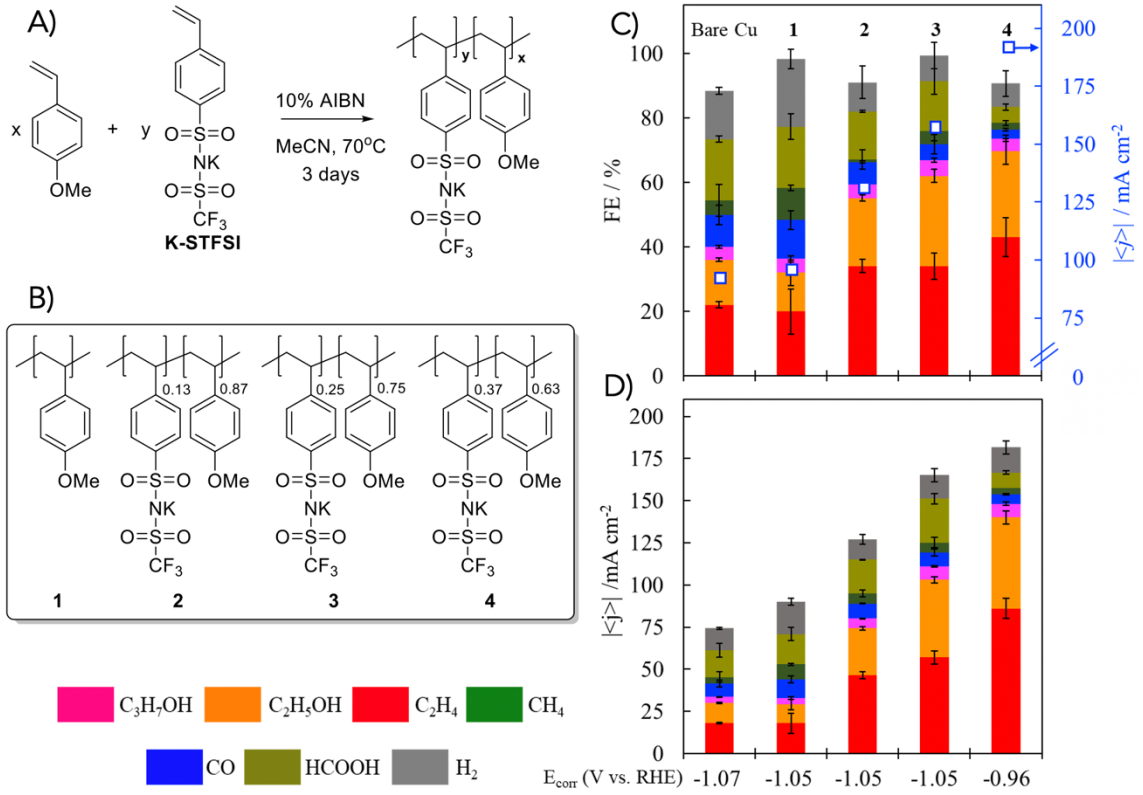

Figure 1. A. Ionomer synthesis. B. Series of prepared ionomers. C. Faradaic efficiency (FE, columns) and current density (white squares) for CO_2R products on Cu/PTFE in the presence of ionomer films casted from solutions of **1**-**4.** Electrolysis performed in 1 M $KHCO_{3(aq)}$ for 30 minutes with $E_{applied}$ = –1.15 V vs. RHE. Corrected potentials (E_{corr}) determined from measured (uncompensated) resistance are reported. D. Partial current densities for trials shown in panel C.

The ionomer film impact on CO_2R was studied in chronoamperometry experiments using a gas diffusion electrode (GDE),[7] at $E_{applied}$ = –1.15 V vs. RHE (1 M $KHCO_{3(aq)}$). The coated electrodes were prepared by drop casting stock solutions of ionomers in alcohol mixture (50% v/v EtOH/^{i}PrOH) onto a Cu GDE, based on Cu sputtered onto PTFE

(Cu/PTFE). All electrolysis experiments were carried out in a flow cell designed specifically for GDEs.[7,9]

Ionomers **2**-**4** each increased C_{2+} product selectivity compared to both bare Cu and Cu coated with **1** (Figure 1C). Analysis of the partial current densities reveals that $|j_{C2+}|$ increases as a function of K^+ content in the ionomer (Figure 1D), where $|j_{C2+}|$ on Cu coated with **4** is greater (150 vs 34 mA cm^{-2}) than bare Cu. The FE for C_{2+} products is improved (75%) using **4** relative to bare Cu (40%). These results suggest that the charged polymer does not act as physical barrier for the substrate. Rather, increased incorporation of K^+ within the microenvironment provided by ionomers at the electrode surface facilitates CO_2 reduction to C_{2+} products. While electric field effects can augment local cation concentration,[32–34] ICP-MS measurements suggest that differences between the local [K^+] is established due to K^+ content provided by the ionomer (Table 9). This effect is reminiscent of previous strategies for enhancing C_{2+} selectivity by increasing K^+ concentration in the bulk electrolyte, up to 4 M; in the present approach, the K^+ concentration is increased at the electrode-electrolyte interface via the ionomer.[19,28,35]

CO_2R performance was further optimized by increasing the ionomer **3** loading from 4.5 µg to 13.5 µg, enabling FE_{C2+} = 82%, $|j_{C2+}|$ = 225 mA cm^{-2} (Figure 2). Notably, there appears to be no decrease of $|j_{H2}|$ (Figure 2) suggesting that the improved selectivity for CO_2R is not solely a consequence of suppressed HER.[5,8,9,16] There is likely insignificant local pH increase (*vide infra*).[16] Greater loadings of **4** were also attempted, leading to similarly high $|j_{C2+}|$ but also significantly greater $|j_{H2}|$ compared to **3** (Figure 8).

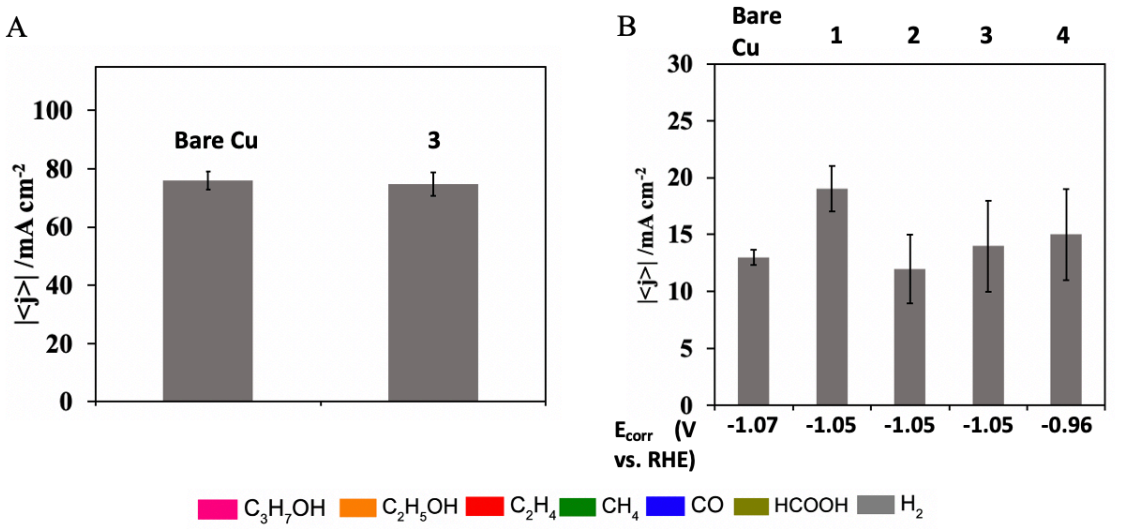

Figure 2. A. Partial current densities from chronoamperometry in 1 M $KHCO_3$ at –1.16 V vs. RHE in the presence of $Ar_{(g)}$ comparing bare Cu/PTFE with **3**-coated Cu. B. Partial current density for H_2 for each ionomer-coated Cu from $CO_{2(g)}$ electrolysis in 1 M $KHCO_3$. $E_{applied}$ = –1.15 V vs. RHE.

Next, CO_2R on a GDE catalyzed by Cu modified with organic films at high current densities ($|j_{C2+}| > 200$ mA cm^{-2}) was compared (Table 1 and Table 10). Focusing on anionic ionomers, Nafion 1100W tested under the CO_2R conditions reported herein (Figure 1) provided 36% FE_{C2+} at a $|j_{C2+}|$ = 25 mA cm^{-2}. In contrast, using ionomer **3** resulted in 82% FE_{C2+} at $|j_{C2+}|$ = 225 mA cm^{-2} (Figure 3). This result highlights the potential designer ionomers can offer to improve CO_2R. For comparison, the best-in-class performance using Nafion-coated electrodes has been previously reported in highly basic, high $[K^+]$ conditions of 7 M KOH, resulting in FE_{C2+} = 79.5 %, $|j_{C2+}|$ at 1232 mA cm^{-2}.[7] Similar FEs are obtained with ionomer **3** in 1 M $KHCO_{3(aq)}$, despite the much lower $[K^+]$ in the electrolyte.

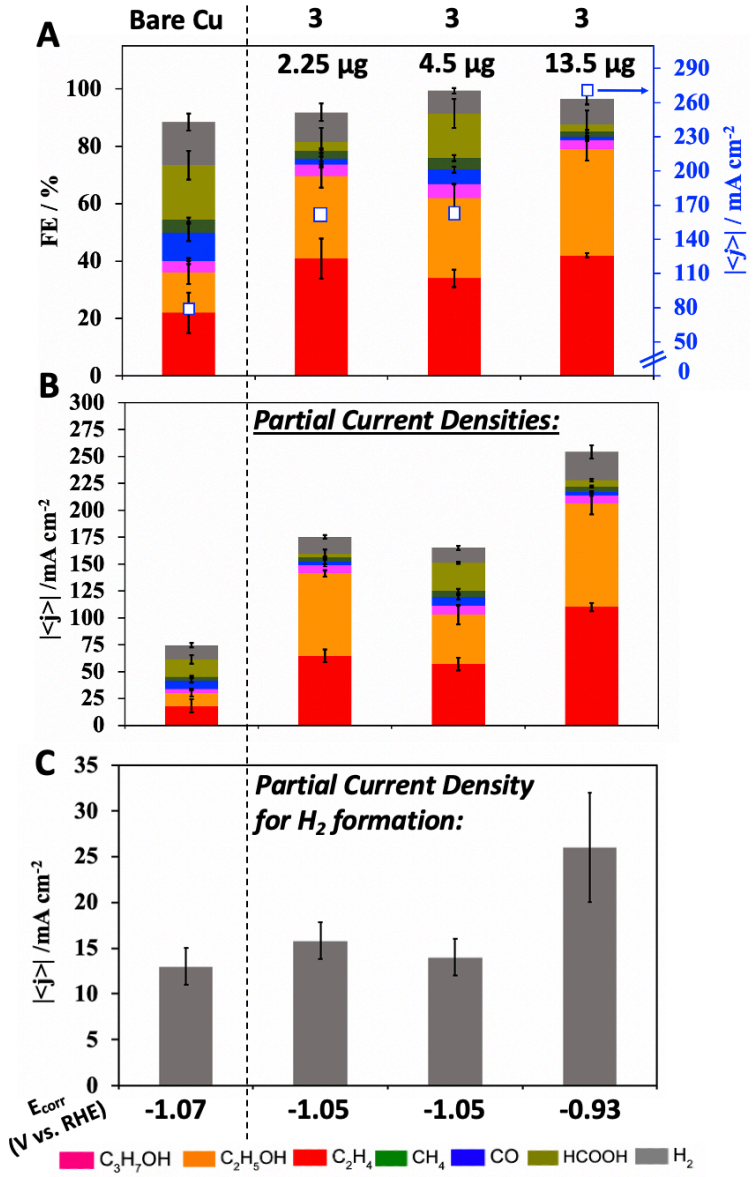

Figure 3. A. Faradaic efficiencies (FEs, columns) and current densities (white squares) and B. partial current densities from CO_2R on **3**-coated Cu at different loadings. C. Partial current density for hydrogen formation. Chronoamperometry performed in 1 M $KHCO_3$ at –1.15 V vs. RHE. E_{corr} represents potentials corrected after compensating for ohmic losses.

Table 1. Comparing CO_2R performance between Cu electrodes coated with ionomer films.

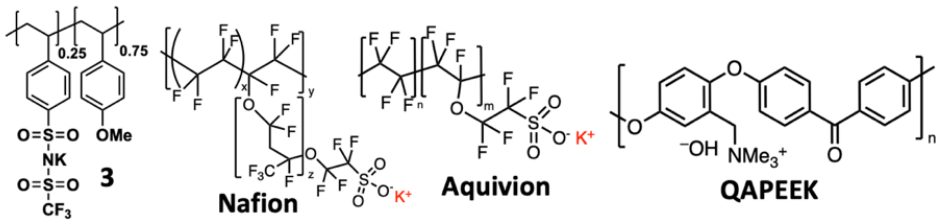

Authors	Ionomer	Electrolyte	$E_{corrected}$ (V vs. RHE)	FE_{C2+}	$\|j_{C2+}\|$ (mA cm^{-2})	FE_{H2}
This work	**3**	1 M $KHCO_3$	–0.96	82%	225	8%
	Nafion 1100W	1 M $KHCO_3$	–1.07	36%	25	25%
Sinton, Sargent, and co-workers[17]	**Nafion 1000W**	7 M KOH	–0.91	79.5%	1232.3	6.8%
	Nafion 1000W	7 M KOH	–1.43	82.5%	420.8	13%
Bell and co-workers[16]	**Nafion 1100W**	0.1 M $CsHCO_3$	–1.15	64%	6.5	12.1%
Sinton, Sargent, and co-workers[19]	**Aquivion**	3 M KCl/1 M H_3PO_4	*Not reported*	~48%	576	35%
Agapie, Peters, Sargent, and co-workers[18]	**Aquivion**	*None* (MEA)	*Not reported*	45%	68	10%
Zhuang, L., et al.[23]	**QAPEEK**	*None* (MEA)	*Not reported*	73.4%	587	10.6%
				65.3%	653	16.4%

To address the critical role of the K^+ ionomer, CO_2R was performed in the absence of any alkali metal. Previous work examining ionomers suggested a critical role of the anionic species in limiting hydroxide diffusion away from the microenvironment, thus facilitating C–C coupling.[16,17] In addition, a bis(sulfonyl)imide anion was found to promote bulk CO_2 solubility.[36] Such a species alone could enhance local CO_2 concentration in the ionomers leading to enhanced CO_2R performance.[21] Therefore, $[Me_4N]^+$ was introduced in both the ionomer and the electrolyte (1 M $Me_4NHCO_{3(aq)}$, pH = 7.8). With 1 M

$Me_4NHCO_{3(aq)}$, H_2 was the exclusive product observed in each experiment, both with bare Cu and **3**-coated Cu (Figure 4). Despite the consumption of proton carriers, we do not expect local pH to increase significantly at relatively low current densities (~–60 mA cm^{-2}), as previously demonstrated.[19,37] While CO_2R was observed with N-aryl pyridinium films in the absence of alkali cations,[9] the results with Me_4N^+ indicate that the ionomer coating alone is not sufficient to compensate for the previously reported detrimental effect of the absence of K^+ in electrolyte.[26,27]

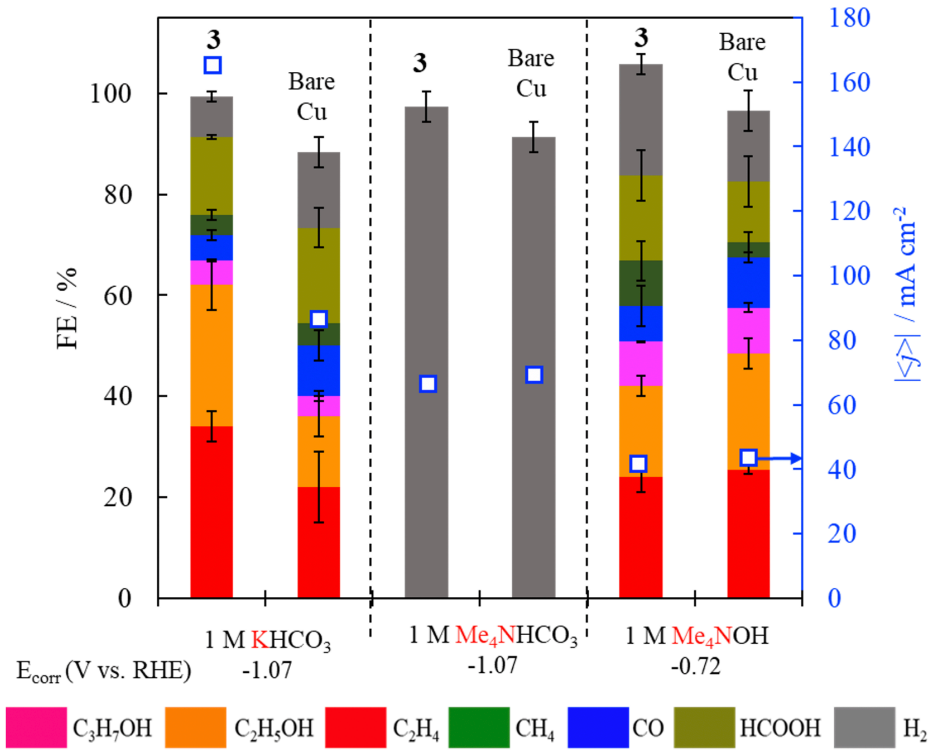

Figure 4. Selectivity profile from CO_2R on Cu/PTFE in the presence of ionomer film **3** (4.5 µg) tested in various electrolyte solutions. $E_{applied}$ = –1.6 V vs. SHE. For 1 M $KHCO_{3(aq)}$ and 1 M $Me_4NHCO_{3(aq)}$, $E_{applied}$ = –1.15 V vs. RHE. For 1 M Me_4NOH, $E_{applied}$ = –0.80 V vs. RHE.

Additionally, no improvement in CO_2R selectivity was observed in the presence of **3** compared to bare Cu in 1 M $Me_4NOH_{(aq)}$, pH = 14. These results underscore the importance of local K^+ content in the electrode microenvironment in improving CO_2R performance; the ionomer in the absence of K^+ is insufficient. Moreover, a pH effect alone stemming from the ionomer accumulating hydroxide in the microenvironment is inconsistent with these observations.

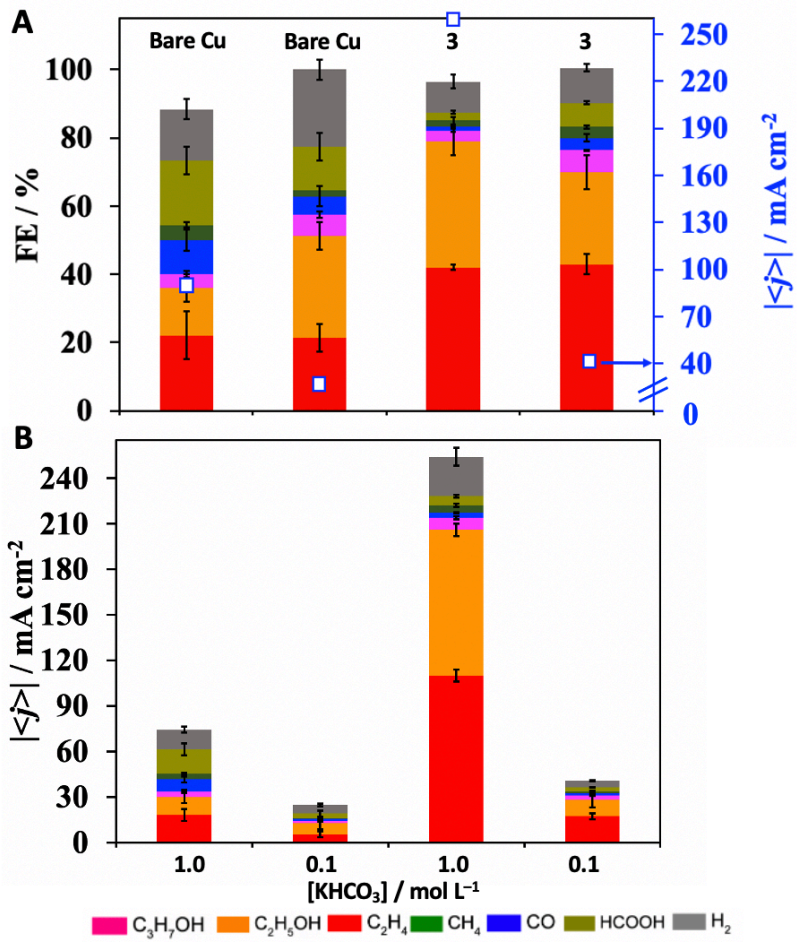

Figure 5. **A.** Faradaic efficiencies (FEs) and current densities (white squares) from CO_2R on bare Cu/PTFE and **3**-coated Cu comparing 0.1 M $KHCO_{3(aq)}$ and 1 M $KHCO_{3(aq)}$ Chronoamperometry performed in 1 M $KHCO_{3(aq)}$ at –1.15 V vs. RHE and 0.1 M $KHCO_{3(aq)}$ at –1.05 V vs. RHE. **B.** Partial current densities of each product.

The impact of K^+ was also probed at lower concentration of electrolyte. High selectivity towards C_{2+} products was still observed in 0.1 M $KHCO_{3(aq)}$, albeit at lower current densities (Figure 5), further demonstrating that high [K^+] in the electrolyte is not necessary to obtain good selectivity from K^+ ionomer-modified electrodes.

Varying the partial pressure of CO_2 (P_{CO2}) provides additional insight into the impact of the ionomer. On bare Cu, a non-linear relationship between P_{CO2} and $|j_{C2+}|$ is observed such that $|j_{C2+}|$ is greatest at 0.4 atm (Figure 6; see Figure 11 for FEs), consistent with previous observations.[38–40] A rationalization of this phenomenon has pointed to surface saturation with *CO, thereby excluding *H and preventing formation of C_{2+} products.[38,40] Another explanation has also been proposed:[39] greater local CO_2 concentration lowers the local pH, thereby promoting HER. This behavior limits CO_2R at higher P_{CO2}. In the presence of **3** on Cu, however, a monotonic increase in $|j_{C2+}|$ as a function of P_{CO2} is observed, effectively overcoming the volcano relationship observed on unmodified Cu. A log-log plot of P_{CO2} and $|j_{C2+}|$ reveals a first-order relationship between C_{2+} product formation and CO_2 in the presence of **3** (Figure 12), suggesting efficient mass transport through the ionomer film (*vide infra*).[5,41,42] In our previous work with pyridinium-derived films on Ag,[5] the relationship between P_{CO2} and j_{CO2R} was unchanged relative to bare Ag, suggesting no effect of the film on CO_2 mass transport. In the present work, the increase in $|j_{C2+}|$ with P_{CO2} in stark contrast to the relationship on bare Cu highlights the ionomers' ability to enhance reactivity with CO_2. While previous reports have suggested other possible effects of alkali cations, including increase in local pH[16,19,28] and modulation of the local electric field,[28,35,43] our data points towards an elevation of CO_2 mass transport in the presence of the ionomer film.

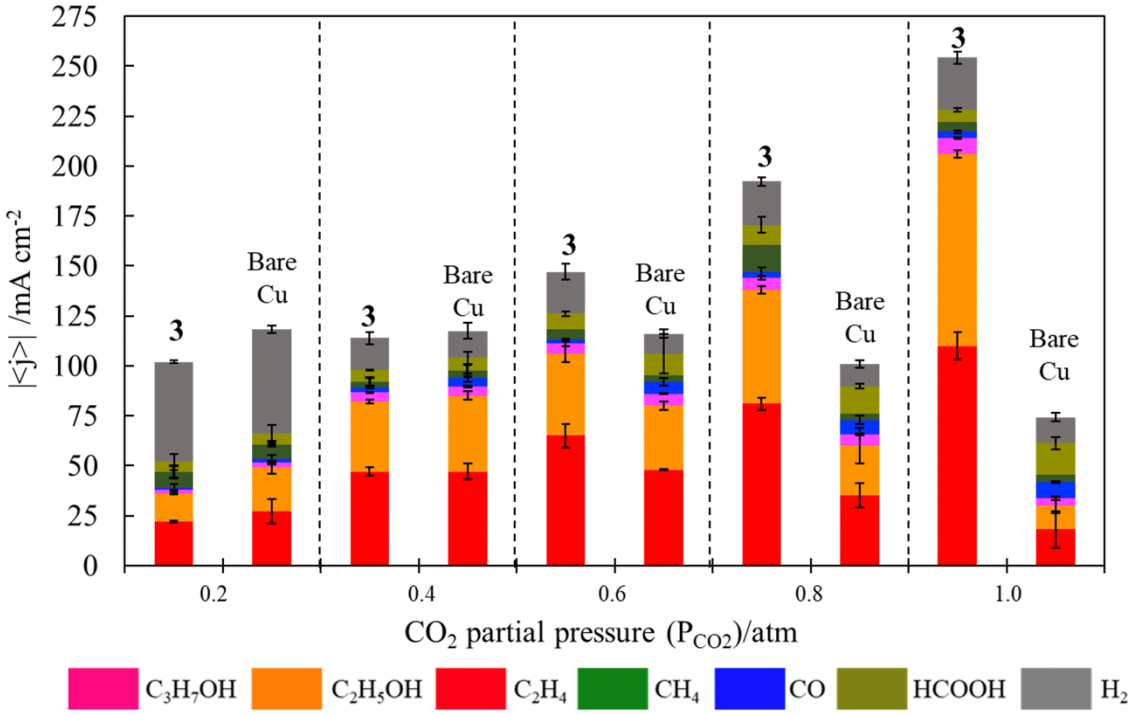

Figure 6. Partial current densities from CO_2R in the presence of the ionomer **3** (ionomer loading: 13.5 μg) tested in 1 M $KHCO_{3(aq)}$ at various CO_2 partial pressures (Ar balance gas). $E_{applied}$ = -1.15 V vs. RHE.

We employed molecular dynamics (MD) calculations examining thermodynamic and mass transport behavior of CO_2 molecules in each polymer **1-4**. From the Fourier transform of the velocity autocorrelation function, we calculated molecular entropies (S), Helmholtz free energies (A_q), and diffusion coefficients (D) via the 2-Phase Thermodynamics (2PT) method.[44] This methodology was previously employed to understand CO transport with pyridinium-derived films.[45] The calculations suggest that increasing the amount of charged monomer units in the polymer enhances CO_2 mass transport within the bulk polymer environment. For instance, 2PT predicts that the CO_2 entropy increases from **1** to **4** (Table 2).

Table 2. Thermodynamic values computed from 2PT method

Polymer	Entropy (*S*, J/mol/K/CO_2)	Helmholtz Free Energy (*A*, kJ/mol/K/CO_2)	Diffusion coefficient (*D*, cm^2/s)	Total number of K^+ [a]	Total volume ($Å^3$)	Polymer volume ($Å^3$)	Open volume ($Å^3$)[b]
1	3.26	-0.95	$3.6*10^{-6}$	0	2504	180.4	2324
2	4.96	-2.09	$2.6*10^{-5}$	16	2629	187.3	2442
3	5.91	-3.22	$1.07*10^{-4}$	32	2769	194.2	2575
4	6.26	-3.58	$1.6*10^{-4}$	48	2945	201.1	2744
4-NMe_4	3.73	-1.13	$1.92*10^{-5}$	0	3267	201	3066
4 (remove charges)[c]	3.33	-0.98	$3.7*10^{-6}$	0	2451	180	2271

[a]160 total monomeric units; one K^+ per monomer; [b](Open volume) = (Total volume) – (Polymer volume); [c]From the optimized structure of polymer **4**, the charged comonomer units were removed and the structure and parameters recalculated.

Table 3. Coordination of CO_2 molecules to ionomers derived from simulations

Polymer	Average number of CO_2 molecules within 5 Å	% CO_2 molecules within 5 Å of K^+
2	1	6
3	7	44
4	9	56

2PT predicts a decrease in CO_2 free energy from **1** to **4**. The enhanced CO_2 stabilization in **4**, relative to **1**-**3**, is related to the increase in favorable coulomb interactions between CO_2 and nearby K^+,[21,46] which is a result of increased proportion of K-STFSI comonomer. CO_2 evidently possesses the most favorable mass transport in the polymer matrix created by **4**, giving rise to the largest D_{CO2} among all of the polymers. The

correlation of D_{CO2} with K^+ concentration trends with an increased $|j_{C2+}|$ observed in the CO_2R experiments (Figure 1D). This suggests that improved CO_2R is due to more facile mass transport of CO_2 to the electrode. This agrees with previous claims that improved CO_2 diffusion leads to higher performance CO_2R towards C_{2+} products.[21,24,47,48] Inspection of the simulation boxes provides insight as to how increasing the amount of charged monomer units may increase interactions with CO_2 to improve mass transport (Figure 7B and Figure 8).

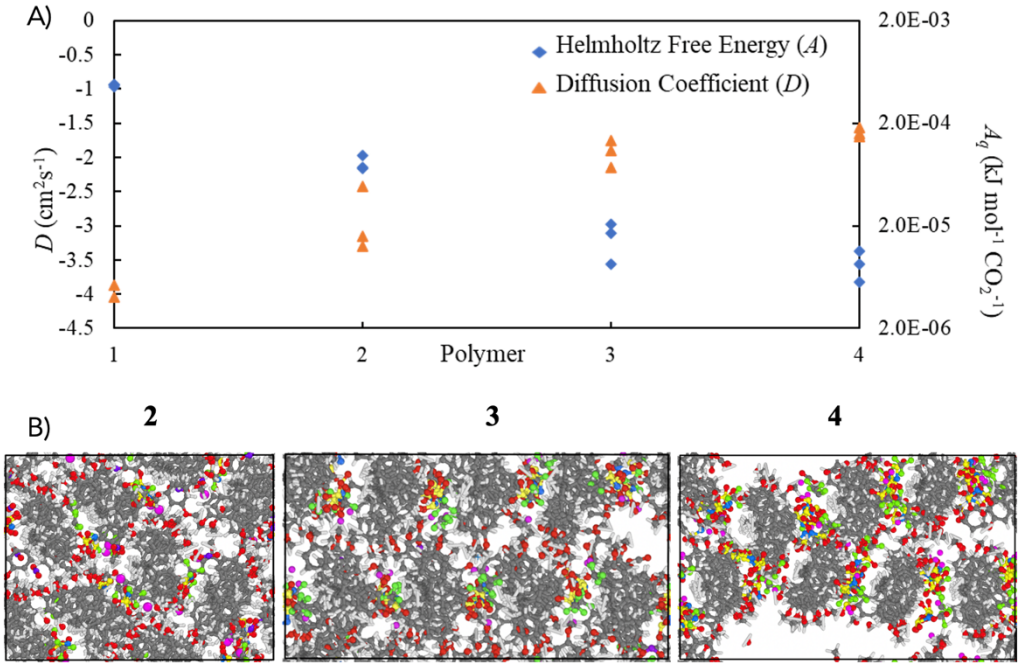

Figure 7. A. Helmholtz free energy (A), and diffusion coefficient (D) for **1** through **4** calculated from molecular dynamics calculations. A is normalized by the number of CO_2 molecules in the simulation box. B. Top view of simulation box (looking down polymer backbone) of **2** through **4**. Atom color legend: gray: carbon; white: hydrogen; red: oxygen; green: fluorine; yellow: sulfur; purple: potassium

Specifically, as the concentration of K-STFSI is increased, we observe increased interactions between CO_2 and K^+. In polymer **2**, only 6% of the CO_2 molecules have a K^+ within 5 Å, whereas in polymer **3**, 44% do, and in polymer **4**, 56% of the CO_2 molecules interact with nearby K^+ (Table 3).

These interactions lower the energy of the CO_2 molecule, shown by the decrease in $A_{q,CO2}$, effectively improving solubility in the ionomer. Despite lower $A_{q,CO2}$ with increasing K^+ content, reaction with CO_2 is not less favorable.[49,50] Rather this gives rise to an enhanced local CO_2 concentration at the ionomer film-electrode interface, providing a possible explanation for improved CO_2R performance with increasing K^+ in the ionomer film. The porosity of the ionomer correlates with the amount of K-STFSI in the polymer due to repulsion from like charges. Figure 4B illustrates a top view (looking down the polymer backbone) of **2** through **4**, showing that **4** has the most substantial porosity derived from larger channels. To quantify porosity, we evaluated the open volume for polymers **1** through **4,** which is the total cell volume minus the volume occupied by the polymer backbone (see **Computations** in Supplemental Information for calculation details). At equilibrium, polymers **1** through **4** have open volumes of 2324, 2442, 2575, and 2744 $Å^3$, respectively (Table 2). Hence polymer **1** has the lowest porosity while polymer **4** has the highest. CO_2 mass transport to the Cu surface is improved due to favorable interactions with K^+, and greater K^+ content leads to greater polymer porosity.[16,21,24,51–53]

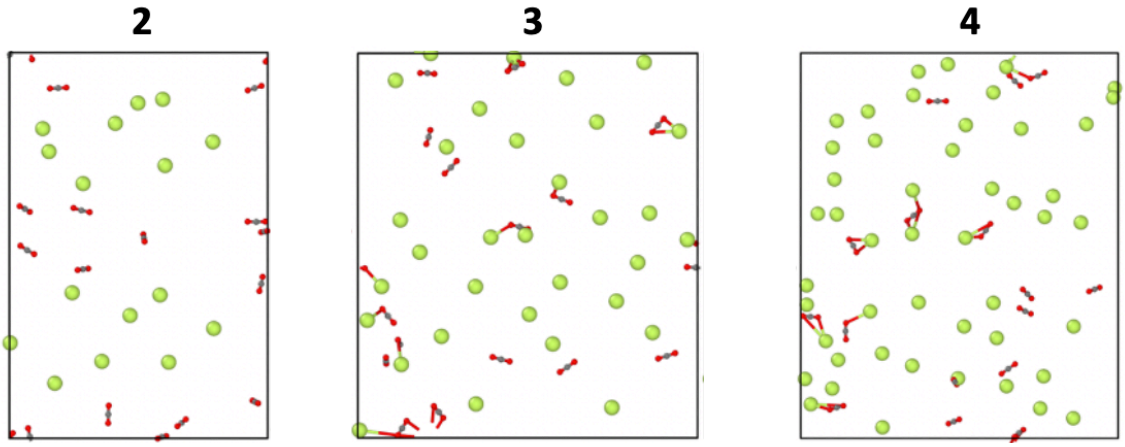

Figure 8. **A**. Computational model representing CO_2 and K^+ in polymers **2** through **4**. The O–K distance cutoff is set to 5 Å.

To further understand how cation identity affects CO_2, K^+ was replaced with $[NMe_4]^+$ in polymer **4** (Table 2). Despite increasing the polymer porosity in **4-NMe$_4$** relative to **4** (3066 vs. 2744 Å^3), CO_2 possesses a weakened interaction between CO_2 and $[Me_4N]^+$ compared to K^+, leading to less favorable mass transport and substantially less cation-induced stabilization. CO_2 diffusion decreases for **4-NMe$_4$** as $A_{q,CO2}$ is raised. These calculations, in addition to the experimental results displaying lack of improved CO_2R in the ionomer films devoid of K^+, (Figure 4) demonstrate the crucial role of the alkali cation in driving CO_2R performance.

CONCLUSIONS

In summary, we demonstrated a novel strategy for modulating local $[K^+]$ at the electrode-electrolyte interface via systematic variation of ionomer structure. We observed that $|j_{C2+}|$ trends with the amount of K^+-containing comonomer, reaching $|j_{C2+}| = 225$ mA cm^{-2} for the ionomer featuring the highest K^+ content. Replacing the cation with $[Me_4N]^+$ eliminates any improvement in selectivity compared to bare Cu, highlighting the indispensable role of K^+ in these polymers for enhanced CO_2R. MD simulations suggest

that increased entropy, diffusivity, and lower free energy of CO_2 in the polymer matrix facilitate CO_2 reactivity at the electrode interface. The combined results from electrochemistry and MD simulations highlight a crucial effect of K^+ within ionomers **2**-**4**, in which the reaction of CO_2R is favored due to enhanced mass transport and stabilization in the ionomer microenvironment. Finally, this study highlights a promising strategy for preparing film-modified electrodes for higher performance CO_2R.

EXPERIMENTAL

Materials and Methods

General Considerations. All solvents and reagents were obtained from commercial sources (Aldrich, Merck, and Combi Blocks) and used as received, unless stated otherwise. 4-Methoxystyrene was dried with CaH_2 and filtered under inert atmosphere. **K-STFSI** was prepared based on a previously reported synthesis.[54] Acetonitrile was dried by passing over activated alumina by the method of Grubbs[55] and stored over 3 Å molecular sieves in a N_2-filled glovebox. Nafion 1100W was purchased from Sigma-Aldrich (Product #274704, 5 wt% in 1-propanol/2-propanol).

Copper nanoparticles, potassium carbonate (99.995%), trimethylammonium hydroxide (semiconductor grade, 99.99% trace metals basis), 4-methoxystyrene, and 1 M aqueous trimethylammonium bicarbonate solution (99%), isopropanol (HPLC grade), and ethanol (HPLC grade) were purchased from Sigma Aldrich. Polytetrafluoroethylene (PTFE) was purchased from McMaster-Carr. The leakless Ag/AgCl reference electrode was purchased from Innovative Instruments. Platinum mesh (99.99% Pt, 25 mm × 25 mm × 0.05 mm) was purchased from Alfa Aesar. CO_2 (research grade) was purchased from Airgas. Deuterium oxide (D 99.96%) and CD_3CN (99.9%) were purchased from Cambridge Isotope Laboratories. The ^{1}H and ^{19}F NMR spectra were recorded on a Bruker 400 MHz with broadband auto-tune OneProbe. ^{13}C NMR spectra were recorded on a Bruker 400 MHz instrument with a prodigy broadband cryoprobe. Shifts were reported relative to the residual solvent peak. Inductively coupled plasma-mass spectrometry (ICP-MS) was performed on a Thermo Fisher Scientific iCAP^{TM} RQ instrument. Each sample was digested/diluted by a factor of 10 with 2% v/v $HNO_{3(aq)}$.

Water was purified by a Nanopure Analytical Ultrapure Water System (Thermo Scientific) or a Milli-Q Advantage A10 Water Purification System (Millipore) with specific resistance of 18.2 MΩ·cm at

25 °C. A VWR sympHony™ pH meter (calibrated with a pH = 1.68 standard) was used to determine the pH of the electrolytes before experiments.

Synthetic Procedures **Carried out by Meaghan A. Bruening*

Synthesis of Methoxystyrene Homopolymer: The reaction was conducted under an inert atmosphere. Methoxystyrene (208 mg, 1.55 mmol, 1.0 equiv) was dissolved in MeCN (4 mL). AIBN (26 mg, 0.1equiv) was added and rinsed with MeCN (1 mL). The vial was sealed, removed from the glovebox, and heated at 70 ºC for 3 days. The reaction was quenched by exposure to air. The crude material concentrated, redissolved in THF, and precipitated into MeOH (100 mL). The polymer was isolate as a fine white solid. Isolated yield: 108 mg. ^{1}H NMR CD_3CN: 7.0-6.5 (br., 4H), 3.71 (br., 3H), 1.8-0.8 (br., multiple peaks, 3H)

General Procedure for Copolymer Synthesis: The reaction was conducted under an inert atmosphere. Methoxystyrene added to a 20-mL scintillation vial and dissolved in MeCN (2 mL) followed by addition of K-TFSI dissolved in MeCN (2 mL). AIBN (0.1 equiv) was added and rinsed with MeCN (1 mL). The vial was sealed, removed from the glovebox, and heated at 70ºC for 3 days. The reaction was quenched by exposure to air. The crude polymer was precipitated into Et_2O (100 mL) and filtered. The precipitate was stirred with 20 mL of an aqueous solution of 1 M $KHCO_3$ at 90ºC for a minimum of 30 minutes. The mixture was filtered hot over a glass frit. An additional 2 washes with 1 M $KHCO_{3(aq)}$ were necessary for most purifications. The solid material was extracted with MeCN, concentrated under reduced vacuum, redissolved in MeCN and filtered. The filtrate was precipitated with Et_2O (100 mL) and filtered. The polymer was isolated as a fine white solid.

Polymer 2: Methoxystyrene (189 mg, 1.416 mmol, 0.9 equiv), K-TFSI (50mg, 0.1416mmol, 0.1equiv), AIBN (26mg, 0.157mmol, 0.1 equiv). Isolated Yield: 146 mg ^{1}H NMR CD_3CN: 7.60, 6.63, 3.72, 1.8-0.8. ^{19}F NMR -79.22

Polymer 3: Methoxystyrene (456 mg, 3.40 mmol, 0.8 equiv), K-TFSI (300mg, 0.8499mmol, 0.2 equiv), AIBN (69.8mg, 0.423mmol, 0.1equiv). Isolated yield: 357 mg ^{1}H NMR CD_3CN: 7.63, 6.63, 3.72, 1.8-0.8. ^{19}F NMR -79.22

Polymer 4: Methoxystyrene (399.2 mg, 2.97 mmol, 0.7 equiv), K-TFSI (450mg, 1.27mmol, 0.3equiv), AIBN (69.8mg, 0.423mmol, 0.1equiv). Isolated yield: 318 mg ^{1}H NMR CD_3CN: 7.60, 6.63, 3.72, 1.8-0.8. ^{19}F NMR -79.22

All polymer representations here and in the main text express the ratio of the monomers as determined by ^{1}H NMR spectroscopy. However, the comonomers are considered to be ordered randomly.

Electrochemistry

Electrolyte Preparation

Potassium bicarbonate electrolyte (1 M $KHCO_{3(aq)}$) was prepared by sparging an aqueous solution of potassium carbonate (0.5 M $K_2CO_{3(aq)}$) with CO_2 for at least 1 hour prior to electrolysis. This process converts K_2CO_3 into $KHCO_3$ and saturates the electrolyte solution with CO_2.

Electrode Preparation

The gas diffusion electrodes (GDEs) were prepared by sputtering 300 nm Cu onto a 5 cm x 5 cm portion of polytetrafluoroethylene membrane (pore size of 450 nm, with polypropylene support on backside) using a pure Cu target (99.99%) at a sputtering rate of 1 Å s^{-1}.

A 0.3 mg mL^{-1} stock solution of the ionomer was prepared in 50% v/v EtOH/^{i}PrOH and sonicated for 30 minutes to ensure complete dissolution. For a standard loading, 15 μL were drop casted (4.5 μg) onto a 2.5 cm^2 electrode, ensuring complete coverage of the Cu nanoparticles, and allowed to dry under ambient conditions for 1 hour.

To test Nafion 1100W, 60 μL of the stock solution (5 wt% in propanol mixture) was drop casted onto a 2.5 cm^2 electrode to match the loading that was reported by Bell and co-workers.[16]

For experiments involving Me_4N^+, 15 μL of the standard 0.3 mg mL^{-1} ionomer solution were drop casted onto Cu/PTFE, and the electrode was dried for 1 hour. The cell was assembled and 1 M $Me_4NHCO_{3(aq)}$ (or 1 M $Me_4NOH_{(aq)}$) was circulated using a peristaltic pump at 10 mL min^{-1} with 30 sccm CO_2 flowing for 30 minutes. Before electrolysis under CO_2, the electrolyte was replaced with fresh electrolyte.

Electrochemical Measurements in the GDE (Flow) Cell

CO_2R and COR measurements were conducted in a gas-tight liquid-electrolyte flow cell. Chronoamperometry experiments were carried out in a custom-made PEEK liquid-electrolyte cell similar to the one reported by Sargent and co-workers.[7] The liquid-electrolyte flow cell consists of three compartments: gas chamber, catholyte chamber, and anolyte chamber. The PTFE electrode was sandwiched between CO_2 gas chamber and catholyte chamber with an exposure area of 0.5 cm^{-2}. Catholyte and anolyte chambers were separated by a Selemion AMV anion-exchange membrane (AGC Engineering Co.). The reference electrode was calibrated against H^+/H_2 on Pt in a 0.5 M sulfuric acid solution (0 V vs. RHE) and saturated calomel electrode (SCE) (+0.241 V saturated vs. RHE). An Autolab PGSTAT204 in a potentiostatic mode was used as electrochemical workstation. The PTFE electrode, leakless Ag/AgCl electrode (Innovative Instruments), and Pt mesh (rinsed with water and annealed with a butane torch) were employed as working, reference and counter electrodes, respectively. The applied potentials were converted to the reversible hydrogen electrode (RHE) scale with iR correction through the following equation:

$$E_{corrected}\,(\text{vs. RHE}) = E\,(\text{vs. Ag/AgCl}) + (0.059 \times \text{pH}) + 0.210 + iR. \qquad (1)$$

$E_{applied}$ in this report is the applied potential without iR compensation. In order to convert from potential vs. Ag/AgCl, we use the following relationship:

$$E_{applied}\,(\text{vs. RHE}) = E\,(\text{vs. Ag/AgCl}) + (0.059 \times \text{pH}) + 0.210 \qquad (2)$$

where i is the current at each applied potential and R is the equivalent series resistance measured via potentioelectrochemical impedance spectroscopy (PEIS) in the frequency range of 10^5 – 0.1 Hz with an amplitude of 10 mV. The appropriate gas-saturated electrolyte was used as both catholyte and

anolyte and was circulated through the flow cell using peristaltic pumps with a silicone Shore A50 tubing. The electrolyte was bubbled with the desired gas during the entire electrolysis process. The electrolyte flow rate was kept at 10 mL min^{-1}. The flow rate of the gas flowing into the gas chamber was kept at 30 sccm by a digital mass flow controller.

Ohmic resistance values were determined with procedures described elsewhere[56,57] and employed in our prior work[7–9] PEIS measurements were carried out prior to and after each electrolysis experiment to determine the Ohmic resistance of the flow cell and ensure it is unchanged during the experiment.[58,59] The impedance measurements were carried out at frequencies ranging from 200 kHz to 100 MHz. A Nyquist plot was obtained, and in the low-frequency region (containing a Warburg element) a line was plotted to determine the value of the intersection with the x-axis, representing the Ohmic resistance (Figure 10).[56] An average of 3 measurements was taken to calculate the value of R. Typically, small resistances were measured, ranging from 4 to 7 Ω. The potentiostat was set to compensate for 85 % of the Ohmic drop, with the remaining 15 % being compensated for after the measurements.[56,57]

All chronoamperometric experiments were performed for 30 min at 25 °C. Before each electrolysis experiment, the ionomer was drop casted onto a 2.5 cm^2 Cu/PTFE electrode. The entire Ohmic drop was compensated before and after the measurement. The effluent gas stream coming from the cell (30 mL min^{-1}) was flowed into the sample loops of a gas chromatograph (GC-FID/TCD, SRI 8610C, in Multi Gas 5 configuration) equipped with HayeSep D and Molsieve 5A columns. Methane, ethylene, ethane, and carbon monoxide were detected by a methanizer-flame ionization detector (FID) and the hydrogen was detected by a thermal conductivity detector (TCD). Every 15 minutes, 2 mL of gas was sampled to determine the concentration of gaseous products. After electrolysis, the

liquid products in the catholytes were quantified by both HPLC (Thermo Scientific Ultimate 3000) and ^{1}H NMR spectroscopy (Bruker 400 MHz Spectrometer).

For ^{1}H NMR analysis, 630 μL of the electrolyte sample were combined with 30 μL of internal standard solution (10 mM DMSO and 50 mM phenol) and 70 μL of D_2O. Water suppression was achieved with a presaturation sequence.[8,59]

The Faradaic efficiencies for gaseous products was calculated from the following equations:

$$F_m = \frac{pF_v}{RT} \tag{3}$$

$$FE_{prod} = \frac{n_{prod}Fx_{prod}F_m}{i}. \tag{4}$$

F_m is the molar flow, defined by the pressure p, the volume flow F_v, the gas constant R, and temperature T. FE_{prod} is the Faradaic efficiency of a gaseous product $prod$, defined by the electron transfer coefficient of the product n_{prod}, Faraday's constant F, the fraction of the product x_{prod}, the molar flow F_m, and the current i.

Error bars shown in all figures and tables represent standard deviations from at least three replicate measurements.

For variable partial pressure $CO_{2(g)}$ (P_{CO2}) experiments, $Ar_{(g)}$ was utilized as the balance gas such that the total flow rate remained at 30 sccm. For example, in the case where pCO_2 = 0.8 atm, the flow rate of $CO_{2(g)}$ was 24 sccm and that of $Ar_{(g)}$ was 6 sccm.

To compare local K^+ between ionomers **2** and **4** each in the presence and absence of applied potential, extraction with 0.1 M $LiHCO_{3(aq)}$ was carried out[34] to exchange K^+ in the ionomer with Li^+, as was carried out in the cation exchange experiments described above.

No applied potential: 45 μL of each ionomer solution was drop casted onto a separate 2.5 cm^2 electrode. Each electrode was placed in a 1 mL solution of 0.1 M $LiHCO_{3(aq)}$ and stirred for 72 hours. The electrodes were rinsed with their extraction solution to ensure complete removal of K^+. The solutions were submitted for ICP-MS.

With applied potential: 45 μL of each ionomer solution was drop casted onto a separate 2.5 cm^2 electrode, and each was submitted for electrolysis in 1 M $KHCO_{3(aq)}$ with $CO_{2(g)}$ in the GDE cell for 30 minutes. Each electrode was rinsed with 500 μL of nanopure water to remove excess K^+ from the electrolyte. Each electrode was placed in a 1 mL solution of 0.1 M $LiHCO_{3(aq)}$ and stirred for 72 hours. The electrodes were rinsed with their extraction solution to ensure complete removal of K^+. The solutions were submitted for ICP-MS.

Computations ***Carried out by Charles B. Musgrave III***

All molecular dynamics calculations were performed using the LAMMPS software package. The Universal Force Field (UFF) was used, along with the qEq charge scheme, which has been shown to accurately capture atomic charges calculated from quantum mechanics. All K^+ charges were fixed at +0.6 and all N^- charges were fixed at -0.6. Polymer chains are bound to themselves at the periodic boundaries, such that the polymers are infinite in length. When adding the charged monomer units to polymers **2** through **4**, spacing was chosen to maximize distance between charged groups.

Calculations were initiated by energy minimization. Minimization was followed by heating via Nose-Hoover NVT molecular dynamics (MD) from 1.0 to 300.0 K over 10 ps. Following heating, the temperature was held at 300 K (still with Nose-Hoover NVT) while the box was deformed to an

energy minima. Finally, the simulation box was equilibrated at 300 K at the new cell volume for 220 ps; the last 120 ps were used for analysis.

The periodic simulation boxes for polymers **1**-**4** each contain 8 polymer chains propagating parallel to each other; the polymer chains are each made of 20 explicit monomeric units. However, the ends of the polymer chains are bound together at the periodic boundary such that the polymers are infinite in length. The simulation boxes also include 16 CO_2 molecules and 16 water molecules.

The 2 Phase Thermodynamics (2PT) method was used to calculate entropies, free energies, and diffusion coefficients from our MD simulations. 2PT tracks atom velocities in order to calculate the velocity autocorrelation function, which in turn can undergo a Fourier transform to yield the density of state function. Entropy and free energy are calculated via weighted integrals over the density of states, and diffusion coefficient is calculated via the density of states at zero frequency. We perform 3 calculations based on the velocity autocorrelation function, which we've found requires 40 ps to converge and yield reasonable statistics (120 ps total).

The polymer open volumes (V_{open}, Equation 3) are defined as the total cell volumes (V_{total}) minus the volumes occupied by the polymer backbone. The polymer backbone volume is computed assuming that all atoms are spheres with radii equivalent to their covalent atomic radius (r_i), as computed from first principles by Clementi et al.[60] n_i in Equation 3 is the number of atoms of type *i*.

$$V_{open} = V_{total} - \sum_i n_i \frac{4}{3}\pi r_i^3 \quad (5)$$

SUPPLEMENTARY FIGURES/DATA

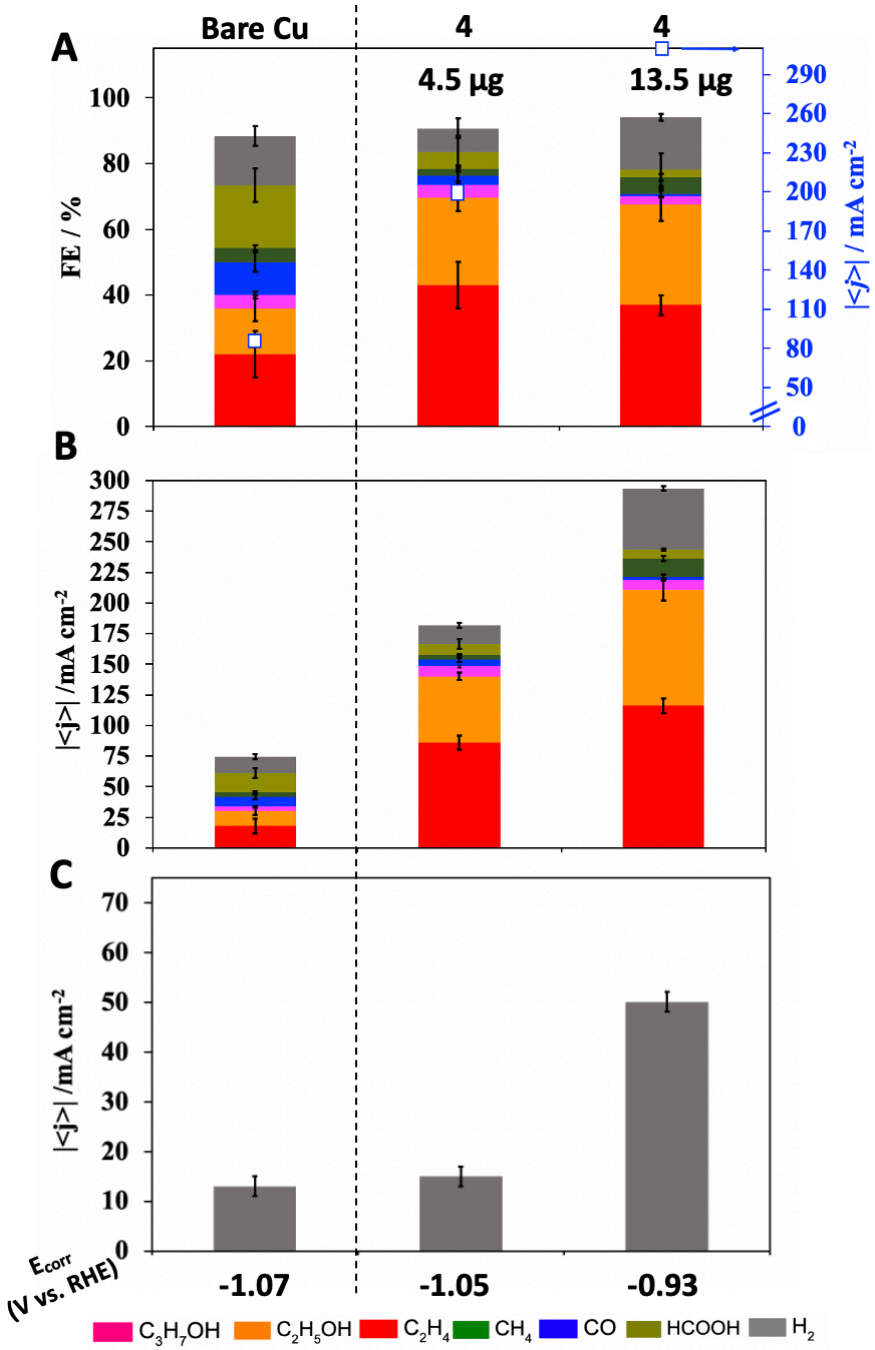

Figure 9. **A.** Faradaic efficiencies (FEs, columns) and current densities (white squares) and **B.** partial current densities from CO_2R on **4**-coated Cu at different loadings. **C.** Partial current density for hydrogen formation. Chronoamperometry performed in 1 M $KHCO_3$ at –1.15 V vs. RHE.

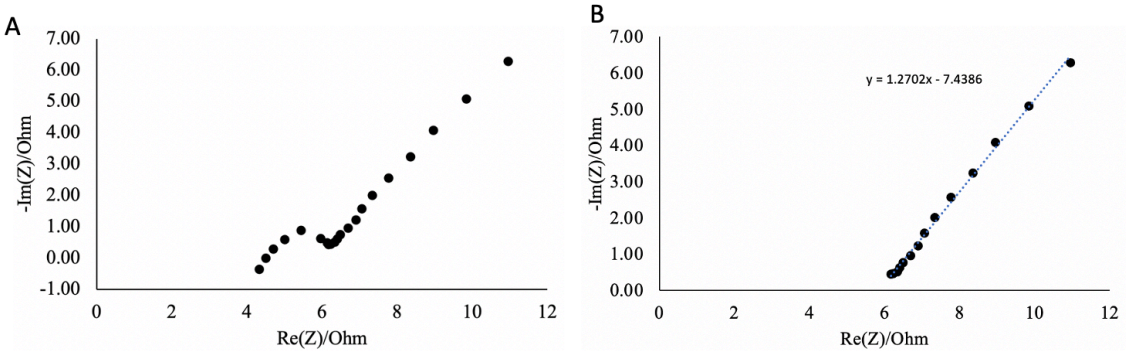

Figure 10. A. Example Nyquist plot from CO_2R electrolysis with **3**-coated Cu (13.5 µg). B. Linear fit of Warburg region.

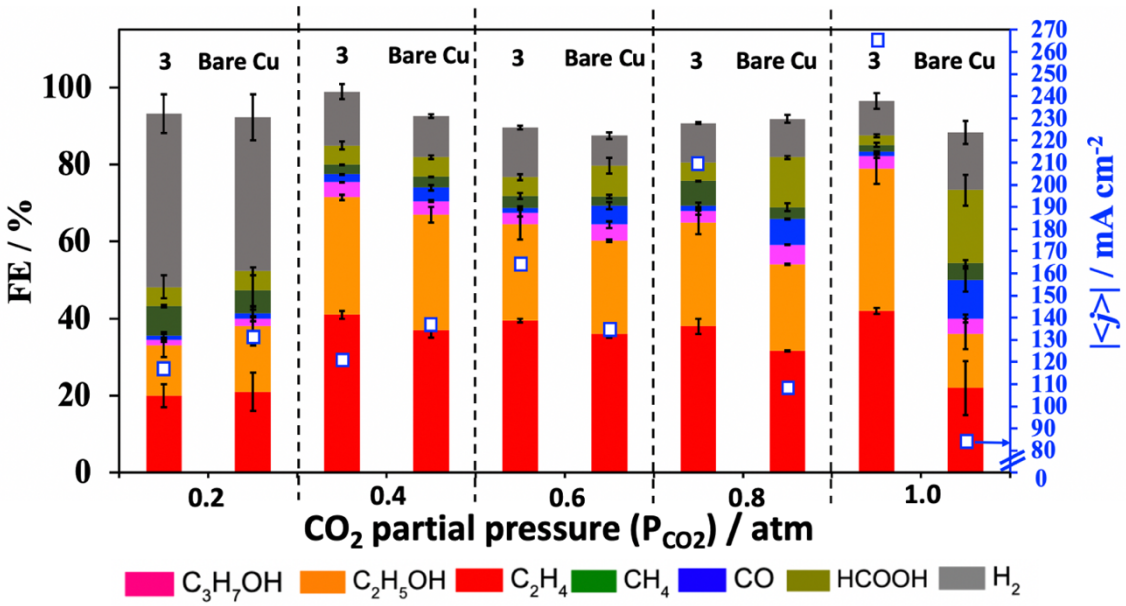

Figure 11. Faradaic efficiencies (FEs) and current densities (white squares) from CO_2R on Cu/PTFE in the presence of film drop casted from **3** (ionomer loading: 13.5 µg) tested in 1 M $KHCO_{3(aq)}$ at various CO_2 partial pressures ($Ar_{(g)}$ balance gas).

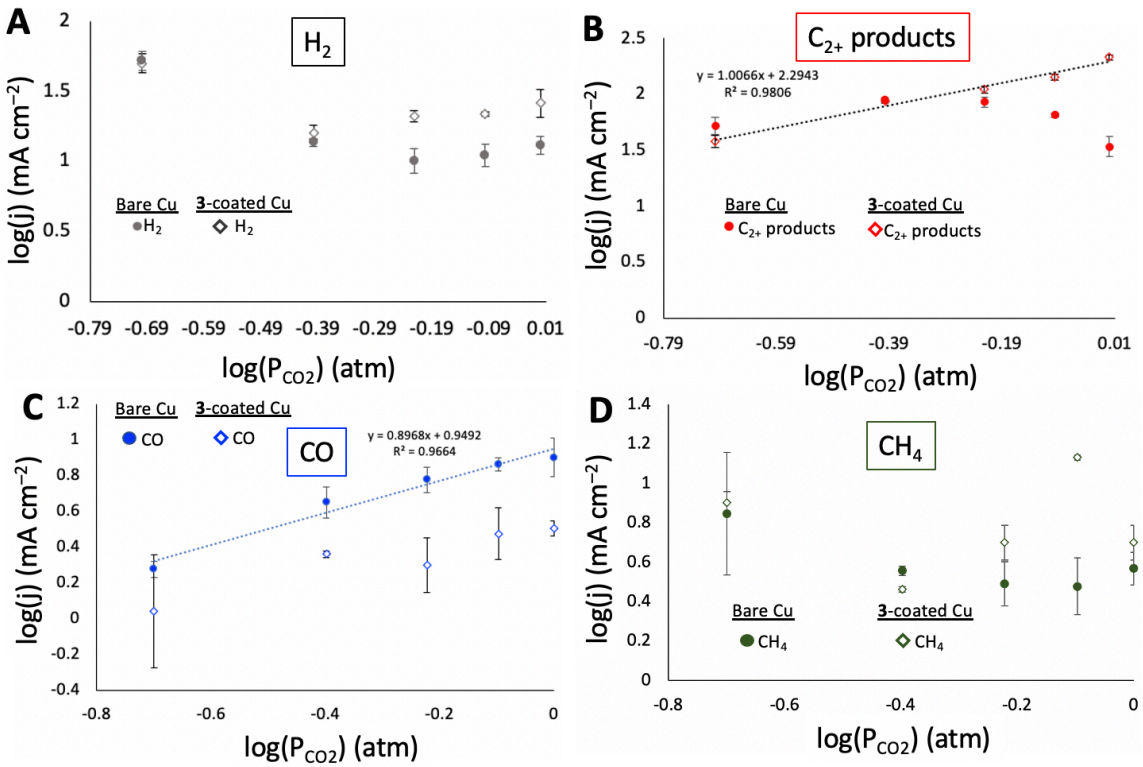

Figure 12. Plots of log(j_{prod}) vs. log(P_{CO2}) from variable partial pressure CO_2 experiments for H_2 (panel A), C_{2+} products (panel B), CO (panel C), CH_4 (panel D). Filled circles represent bare Cu data and hollow diamonds represent **3**-coated Cu.

Table 4. Partial current densities from CO_2R with different alkali cations (Li^+, K^+, and Cs^+) in the ionomer (4.5 µg) and electrolyte

	Electrolyte	$E_{applied}$ (V vs. RHE)	$E_{corrected}$ (V vs. RHE)	|*j*| (mA/cm^2)							
				H_2	CH_4	CO	C_2H_4	$HCOO^-$	C_2H_5OH	C_3H_7OH	$\|j_{C2+}\|$
Bare Cu	0.1 M $LiHCO_{3(aq)}$	-1.10	-0.98	11.2 ± 0.5	2.4 ± 0.6	0.12 ± 0.03	0.31±0.03	0.6 ± 0.1	0	0	0.31± 0.03
4	0.1 M $LiHCO_{3(aq)}$	-1.10	-0.98	2.2 ± 0.2	0.11± 0.09	2.8 ± 0.7	1.9 ± 0.3	3 ± 1	1.3 ± 0.6	1.1 ± 0.6	4.2 ± 0.9
Bare Cu	0.1 M $KHCO_{3(aq)}$	-1.10	-0.92	5.6 ± 0.6	0.4 ± 0.2	1.3 ± 0.3	5 ± 1	3 ± 1	7 ± 1	1.5 ± 0.5	14 ± 2
4	0.1 M $KHCO_{3(aq)}$	-1.10	-0.93	4.2 ± 0.4	1.3 ± 0.4	1.5 ± 0.5	24 ± 1	2.82 ± 0.03	15 ± 2	5.0 ± 0.4	44 ± 3
Bare Cu	0.1 M $CsHCO_{3(aq)}$	-1.10	-0.75	11 ± 2	0	12 ± 1	12.5 ± 0.5	7 ± 2	10 ± 3	5 ± 1	30 ± 3
4	0.1 M $CsHCO_{3(aq)}$	-1.10	-0.5	10 ± 2	0	14.5 ± 0.7	22 ± 1	12 ± 1	23 ± 2	4.9 ± 0.3	50 ± 2

Table 5. Selectivity profile from CO_2R on Cu GDE modified by 1-4; $E_{applied}$ = –0.95 V vs. RHE. 1 M $KHCO_{3(aq)}$

	$E_{corrected}$ (V vs. RHE)	Faradaic Efficiency (%)									
		H_2	CO	HCOOH	CH_4	C_2H_4	C_2H_5OH	C_3H_7OH	Total	FE_{C2+}/FE_{C1}	*j* (mA/cm^2)
Bare Cu	-0.89	22 ± 4	6.7 ± 0.2	17 ± 0.4	17 ± 2	19 ± 4	10 ± 1	3.0 ± 0.4	95 ± 6	1.2 ± 0.5	-45 ± 1
1	-0.88	23 ± 1	9 ± 1	20 ± 1	4 ± 1	18 ± 2	11 ± 1	3 ± 1	98 ± 4	1.0 ± 0.1	-46 ± 1
2	-0.87	20 ± 4	6 ± 1	15 ± 1	4 ± 1	25 ± 6	17 ± 4	2 ± 1	90 ± 4	1.8 ± 0.8	–55 ± 5
3	-0.78	18 ± 2	8 ± 2	19 ± 5	4 ± 3	30 ± 3	15 ± 2	3 ± 1	97 ± 6	1.5 ± 0.7	–65 ± 3
4	-0.85	18 ± 2	4.0 ± 0.7	8 ± 1	2 ± 1	34 ± 3	15 ± 5	4 ± 1	85 ± 4	4.1 ± 0.8	–80 ± 8
Nafion 1100W	-0.92	32 ± 2	15.6 ± 0.7	27 ± 5	4.4 ± 0.7	5 ± 3	19 ± 6	7 ± 1	110 ± 8	1.1 ± 0.5	–17 ± 4

Table 6. Selectivity profile from CO_2R on Cu GDE modified by 1-4; $E_{applied}$ = –1.05 V vs. RHE. 1 M $KHCO_{3(aq)}$

	$E_{corrected}$ (V vs. RHE)	Faradaic Efficiency (%)									
		H_2	CO	HCOOH	CH_4	C_2H_4	C_2H_5OH	C_3H_7OH	Total	FE_{C2+}/FE_{C1}	*j* (mA/cm^2)
Bare Cu	-0.99	27 ± 1	13 ± 3	27 ± 1	4 ± 2	17 ± 1	10.6 ± 0.5	4.5 ± 0.4	103 ± 6	0.7 ± 0.1	–65 ± 1
1	-0.98	23 ± 5	13 ± 3	19.7 ± 0.3	9 ± 3	18 ± 2	12 ± 1	4.30 ± 0.05	99 ± 6	0.82 ± 0.08	–65 ± 1
2	-0.94	13 ± 4	6.2 ± 0.4	11 ± 1	4.5 ± 0.7	40 ± 6	22 ± 4	5 ± 1	102 ± 8	3.1 ± 0.4	–99 ± 5
3	-0.96	14 ± 2	6 ± 2	12 ± 5	4 ± 2	34 ± 3	25 ± 2	4 ± 1	99 ± 7	2.9 ± 0.9	–105 ± 7
4	-0.87	11 ± 2	3.3 ± 0.7	8.4 ± 0.3	2.1 ± 0.2	34 ± 3	20.3 ± 0.2	5.6 ± 0.1	85 ± 6	4.3 ± 0.8	–111 ± 8
Nafion 1100W	-0.96	22 ± 2	6 ± 1	30 ± 2	2.5 ± 0.5	18 ± 3	18 ± 2	5 ± 1	102 ± 5	1.1 ± 0.5	–58 ± 2

Table 7. Selectivity profile from CO_2R on Cu GDE modified by 1-4; $E_{applied}$ = –1.15 V vs. RHE. 1 M $KHCO_{3(aq)}$

	$E_{corrected}$ (V vs. RHE)	Faradaic Efficiency (%)									
		H_2	CO	HCOOH	CH_4	C_2H_4	C_2H_5OH	C_3H_7OH	Total	FE_{C2+}/FE_{C1}	*j* (mA/cm^2)
Bare Cu	-1.07	15 ± 3	10 ± 3	19 ± 4	4.4 ± 0.8	22 ± 2	14 ± 4	4 ± 1	90 ± 8	1.2 ± 0.3	–84 ± 5
1	-1.05	21 ± 4	12 ± 3	19 ± 3	10 ± 3	20 ± 2	12 ± 2	4.3 ± 0.6	98 ± 8	0.9 ± 0.2	–90 ± 1
2	-1.05	9 ± 1	7 ± 1	15 ± 8	1 ± 1	34.1 ± 0.2	21 ± 1	4.23 ± 0.03	92 ± 6	2.6 ± 0.9	–135 ± 5
3	-1.05	8 ± 1	5 ± 1	15.5 ± 0.5	2 ± 1	34 ± 3	25 ± 2	4 ± 1	97 ± 6	3.0 ± 0.3	–166 ± 8
4	-0.96	7.3 ± 8	2.7 ± 0.1	8.4 ± 0.3	2.7 ± 0.5	43 ± 5	28 ± 5	4.86 ± 0.05	90 ± 5	7.5 ± 0.8	–202 ± 9
Nafion 1100W	-1.07	25 ± 2	3 ± 1	30 ± 1	1.0 ± 0.5	22 ± 1	11 ± 2	4 ± 1	96 ± 4	1.1 ± 0.5	-69 ± 2

Table 8. Selectivity profile from CO_2R on Cu GDE modified by 4 with Me_4N^+-containing electrolyte. $E_{applied}$ = –1.6 V vs. SHE

	Electrolyte	$E_{corrected}$ (V vs. RHE)	Faradaic Efficiency (%)								
			H_2	CH_4	CO	C_2H_4	$HCOO^-$	C_2H_5OH	C_3H_7OH	Total	*j* (mA/ cm^2)
Bare Cu	1 M $Me_4NHCO_{3(aq)}$	-1.07	91 ± 3	0	0	0	0	0	0	91 ± 3	-65 ± 1
4	1 M $Me_4NHCO_{3(aq)}$	-1.07	95 ± 3	0	0	0	0	0	0	95 ± 3	-67 ± 1
4-Me_4N[a]	1 M $Me_4NHCO_{3(aq)}$	-1.07	97 ± 1	0	0	0	0	0	0	97 ± 3	-67 ± 1
Bare Cu	1 M $Me_4NOH_{(aq)}$	-0.72	14 ± 4	3 ± 2	10 ± 1	26 ± 1	12 ± 3	23 ± 3	9 ± 1	97 ± 8	-40 ± 3
4	1 M $Me_4NOH_{(aq)}$	-0.72	22 ± 4	9 ± 4	7 ± 4	24 ± 3	17 ± 5	18 ± 2	8.8 ± 0.1	106 ± 8	-40 ± 5

[a]Performed cation exchange with **4** or **3** in 1 M $Me_4NHCO_{3(aq)}$, then drop casted onto Cu GDE.

Table 9. ICP-MS data to determine K^+ concentration from each ionomer with and without electrolysis.

Sample	$[K^+]$ (μg mL^{-1}) [a]
Water	20 ± 1
0.1 M $LiHCO_{3(aq)}$	20 ± 1
4, no electrolysis	53 ± 6
4, with electrolysis	360 ± 10
2, no electrolysis	41 ± 2
2, with electrolysis	210 ± 10

[a]Standard deviations represent error from triplicate measurements.

Table 10. Comparing CO_2R performance between Cu electrodes with various coatings that impart high performance towards C_{2+} products

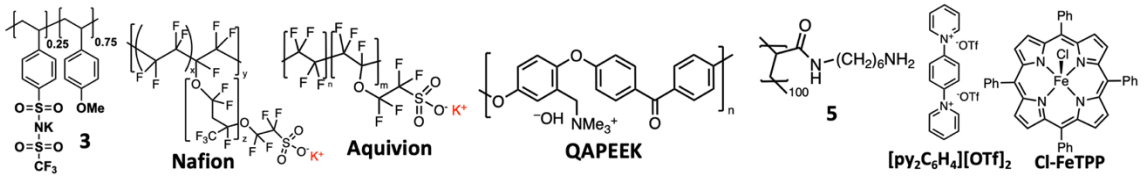

Authors	Ionomer	Electrolyte	$E_{corrected}$ (V vs. RHE)	FE_{C2+}	$\|j_{C2+}\|$ (mA cm^{-2})	FE_{H2}
This work	**3**	1 M $KHCO_3$	–0.96	82%	225	8%
	Nafion 1100W	1 M $KHCO_3$	–1.07	36%	25	25%
Sinton, Sargent, and co-workers[17]	**Nafion 1000W**	7 M KOH	–0.91	79.5%	1232.3	6.8%
	Nafion 1000W	7 M KOH	–1.43	82.5%	420.8	13%
Bell and co-workers[16]	**Nafion 1100W**	0.1 M $CsHCO_3$	–1.15	64%	6.5	12.1%
Sinton, Sargent, and co-workers[19]	**Aquivion**	3 M KCl/1 M H_3PO_4	*Not reported*	~48%	576	35%
Agapie, Peters, Sargent, and co-workers[18]	**Aquivion**	*None* (MEA)	*Not reported*	45%	68	10%
Zhuang, L., et al.[23]	**QAPEEK**	*None* (MEA)	*Not reported*	73.4%	587	10.6%
				65.3%	653	16.4%

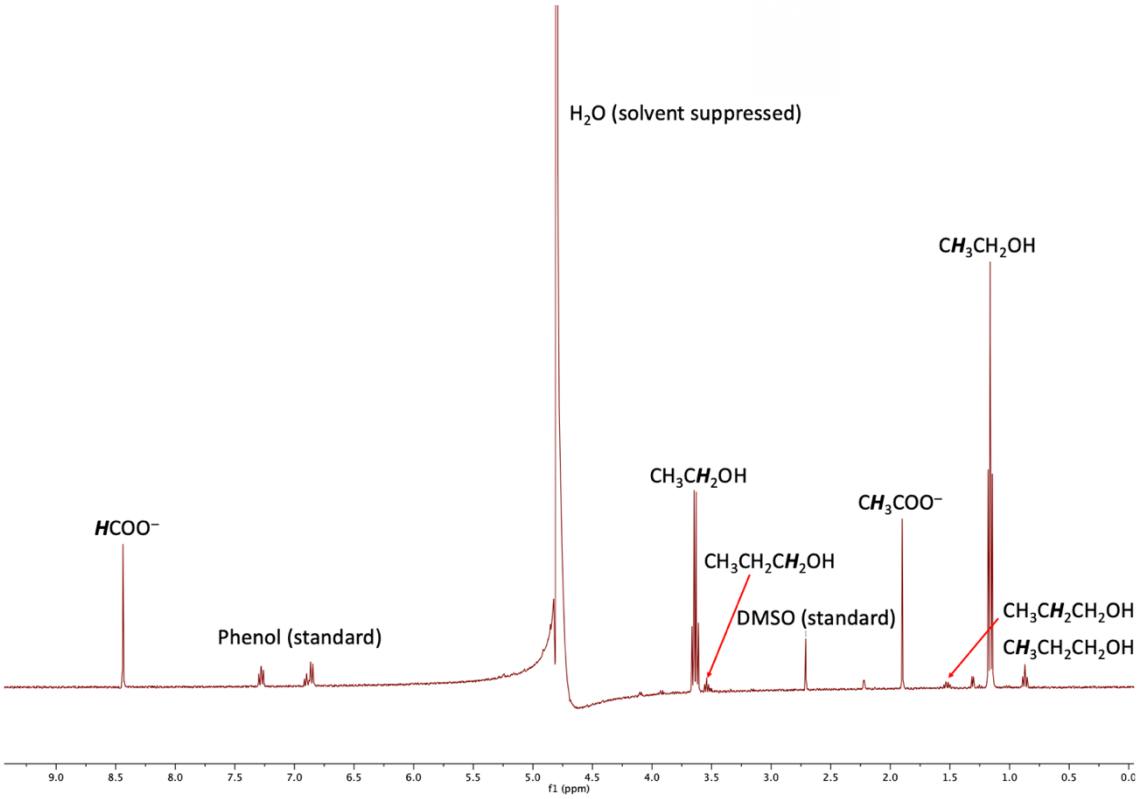

Figure 13. Sample ^{1}H NMR spectrum (400 MHz, 10% v/v D_2O) of catholyte after 30-minute CO_2R chronoamperometry ($E_{applied}$ = –1.15 V vs. RHE) with **3**-coated Cu (4.5 μg). DMSO and phenol were used as standards.

NMR spectra of polymers (**obtained by Meaghan A. Bruening*)

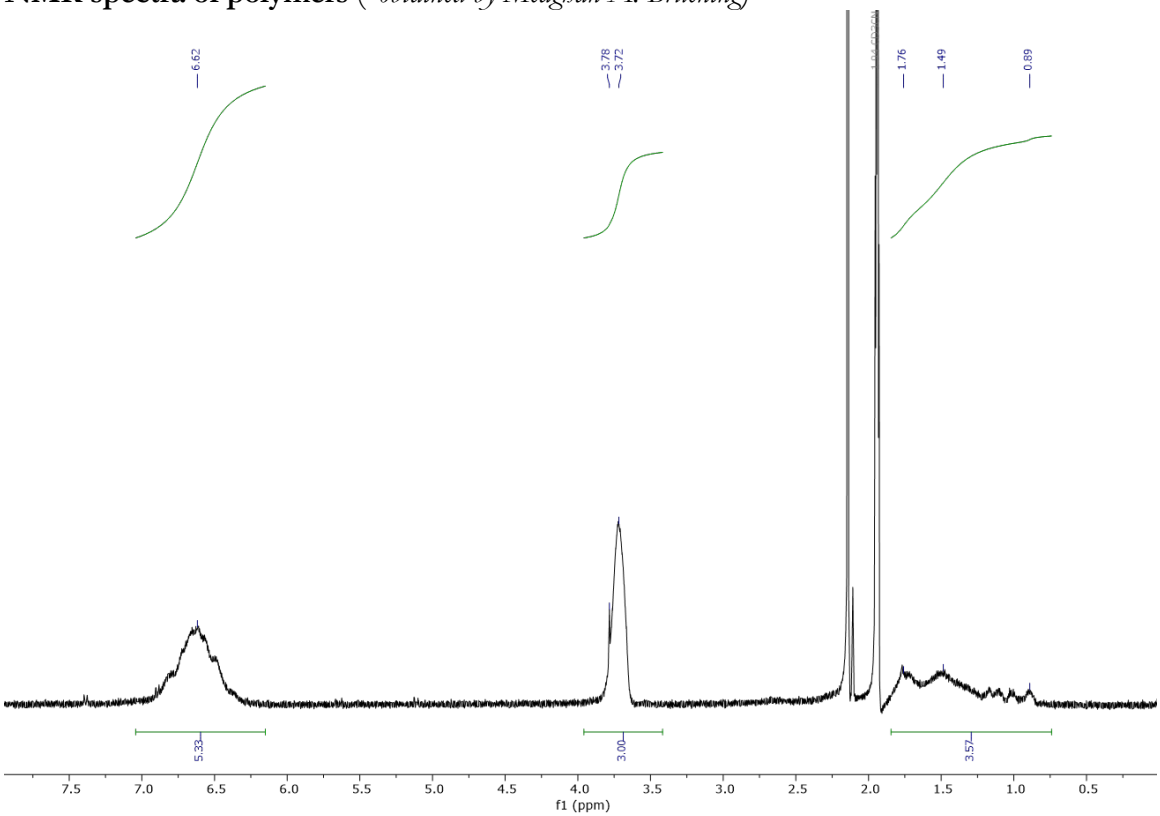

Figure 14. ^{1}H NMR of polymer **1** in CD_3CN.

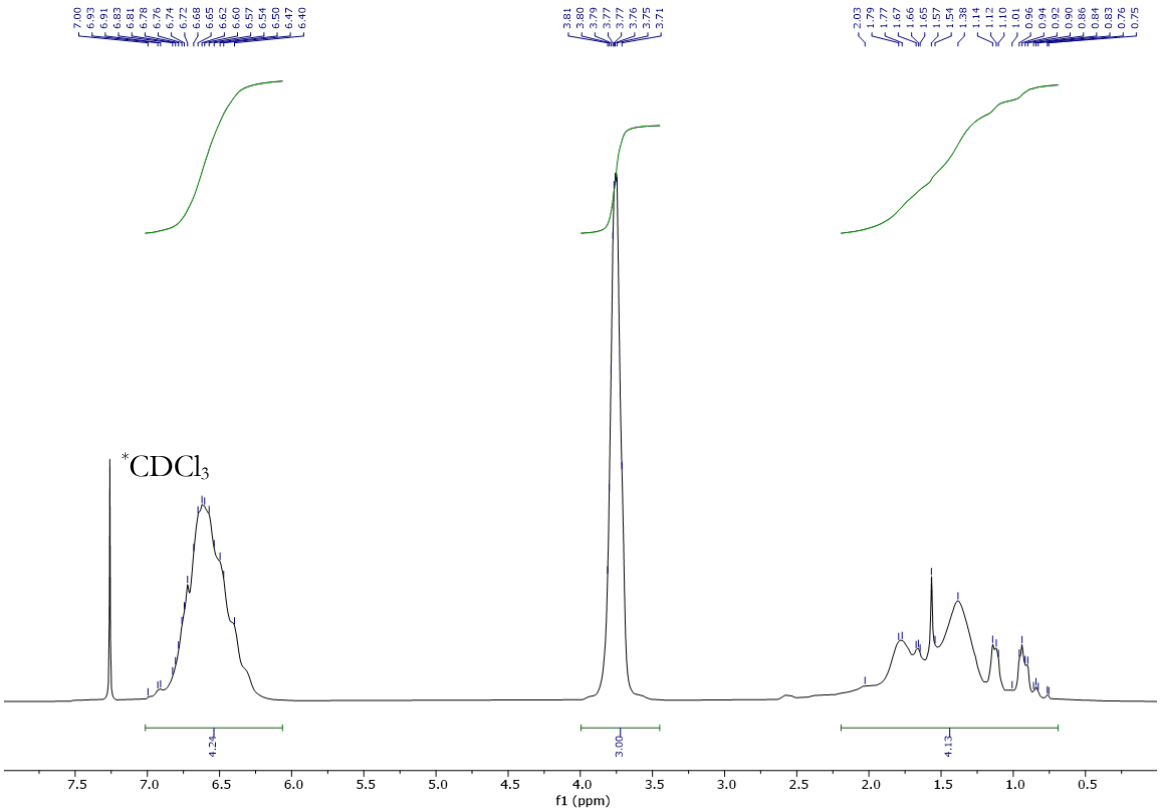

Figure 15. ^{1}H NMR of polymer **1** in $CDCl_3$.

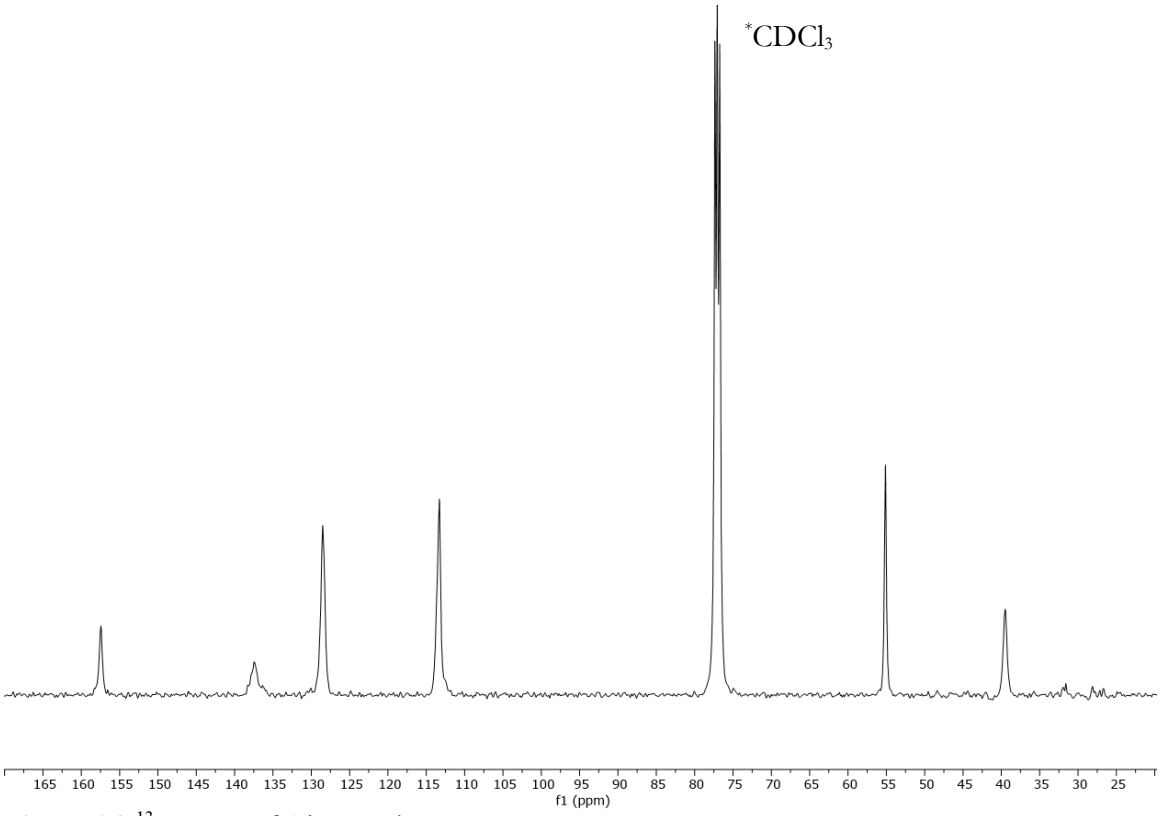

Figure 16. ^{13}C NMR of **1** in $CDCl_3$.

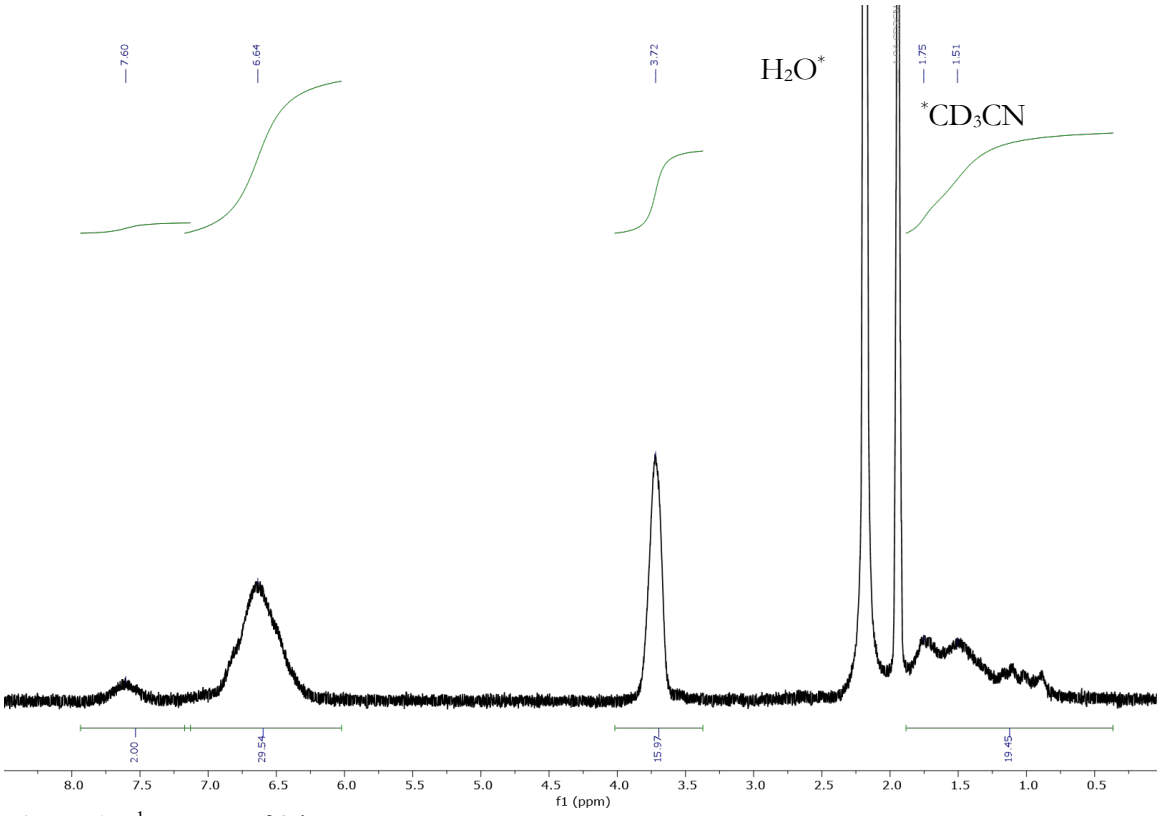

Figure 17. ^{1}H NMR of **2** in CD_3CN.

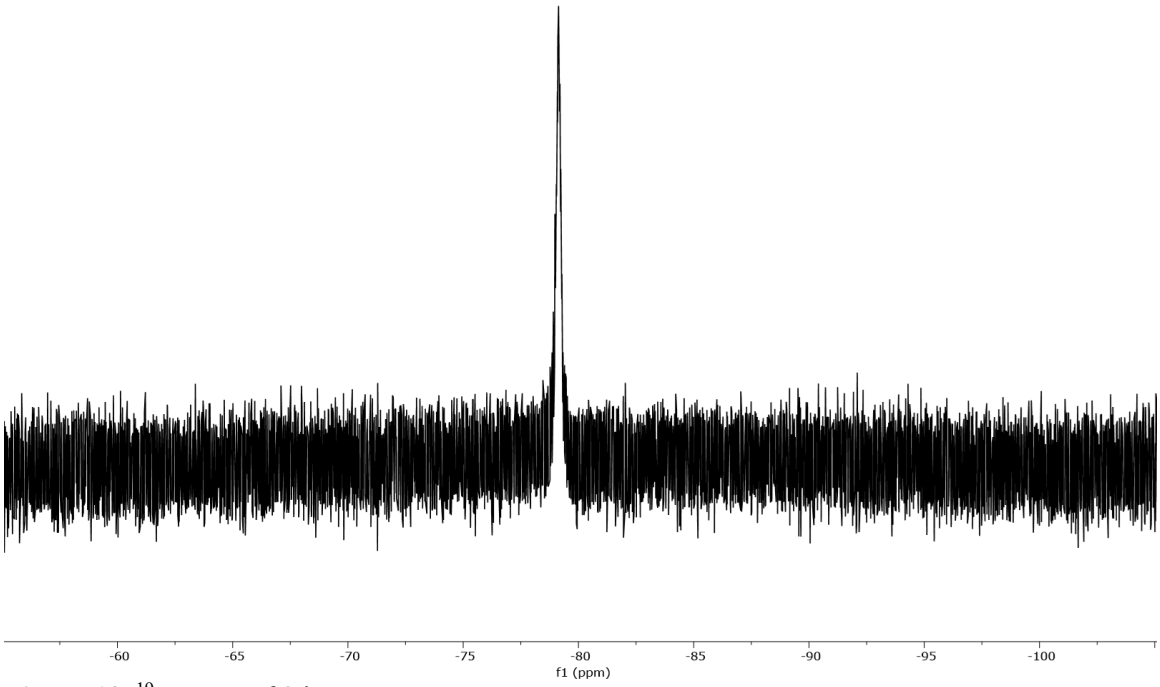

Figure 18. ^{19}F NMR of **2** in CD_3CN.

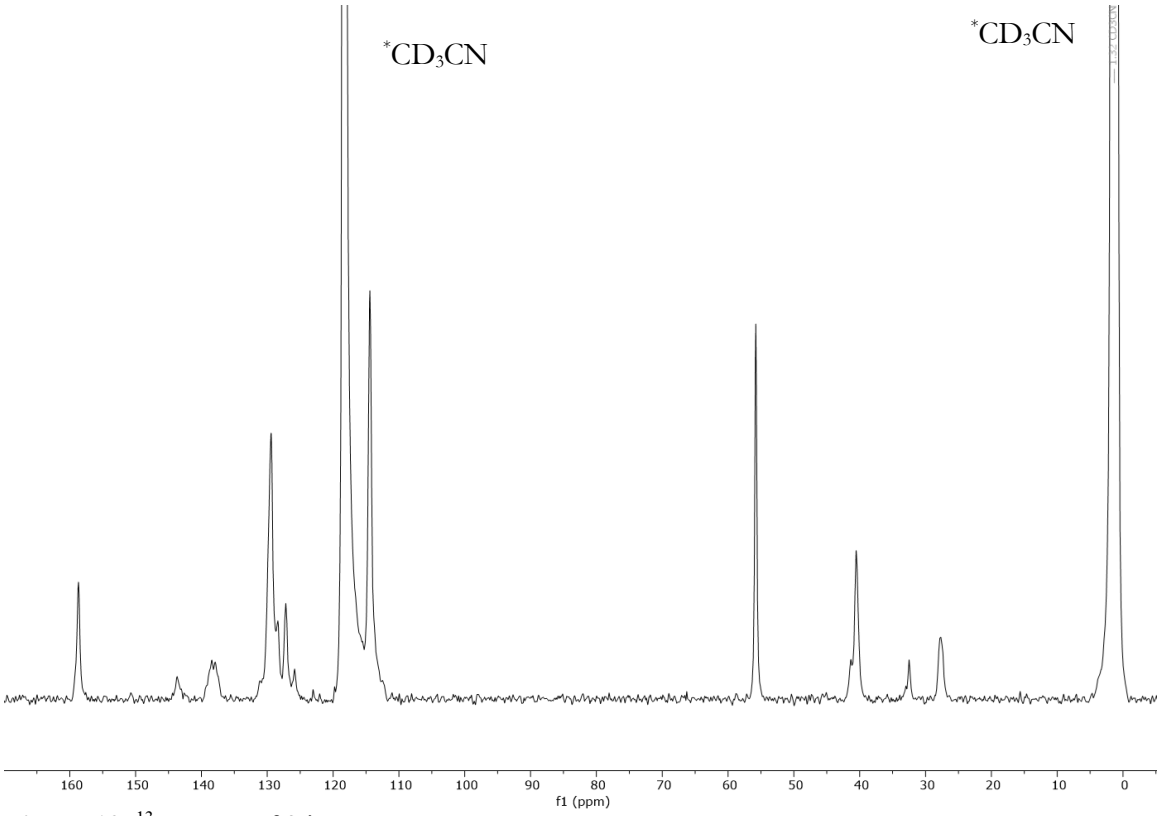

Figure 19. ^{13}C NMR of **2** in CD_3CN.

.

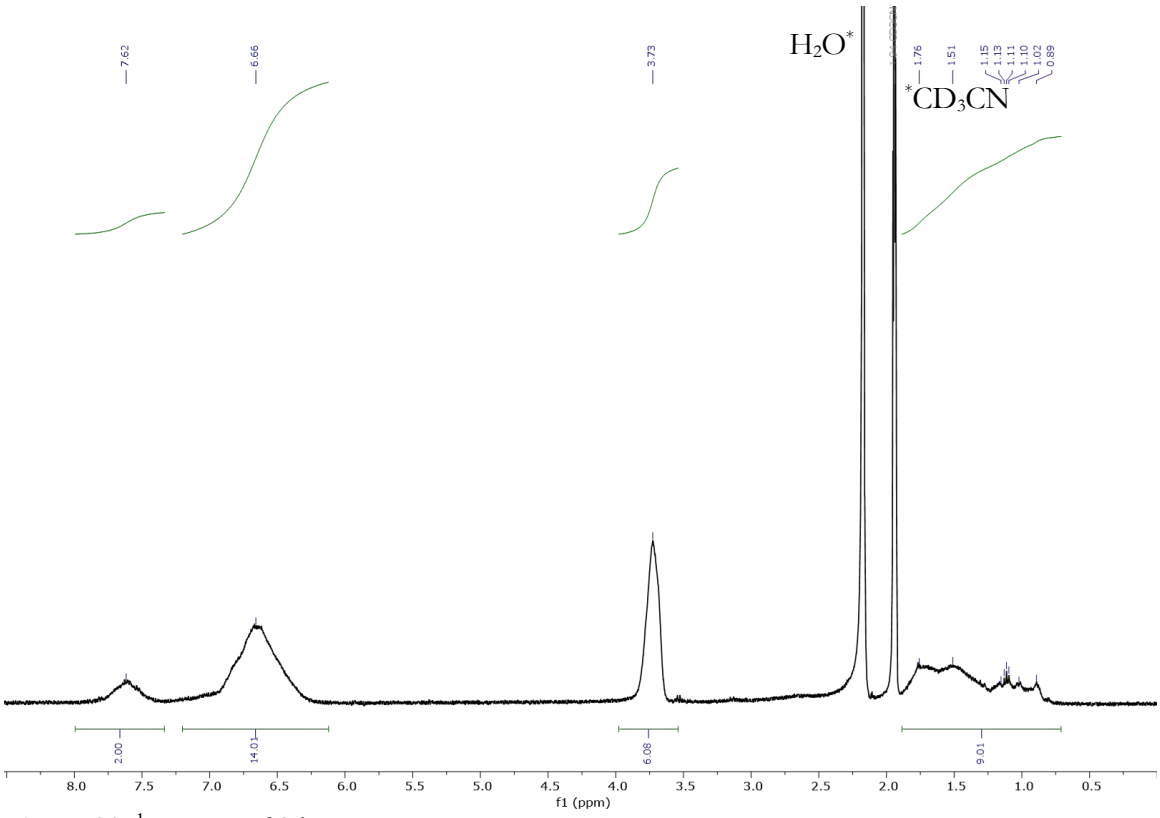

Figure 20. ^{1}H NMR of **3** in CD_3CN.

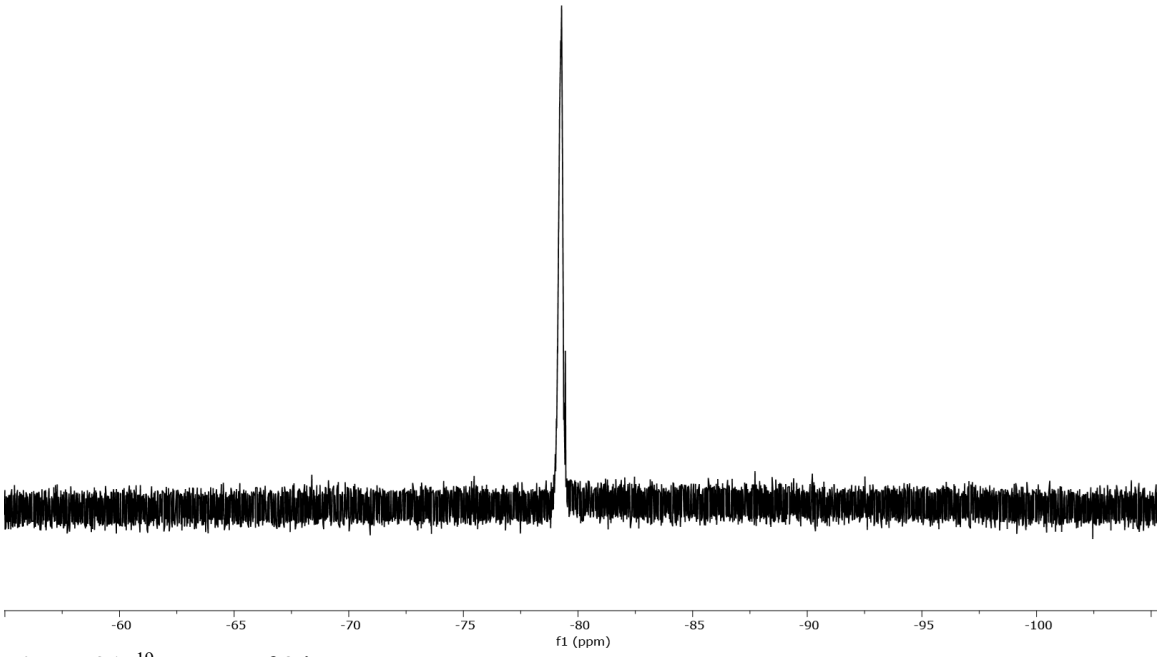

Figure 21. ^{19}F NMR of **3** in CD_3CN.

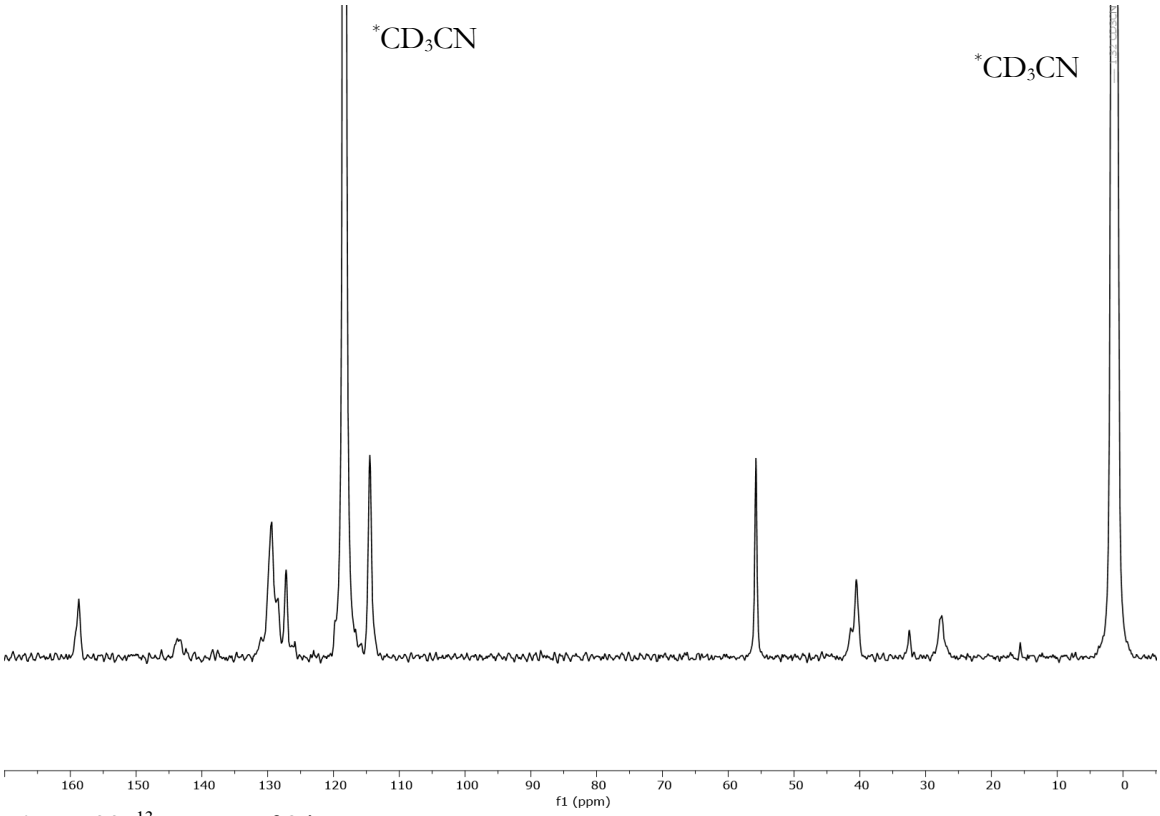

Figure 22. ^{13}C NMR of **3** in CD_3CN.

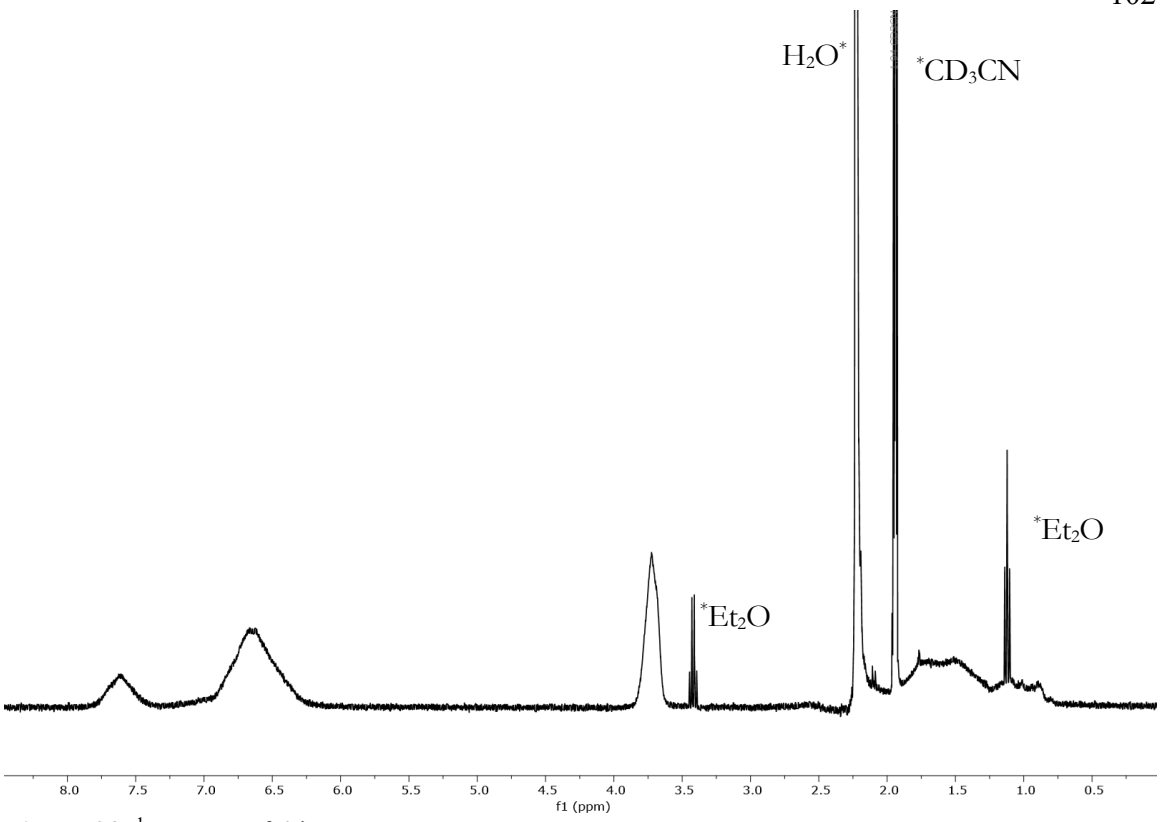

Figure 23. ^{1}H NMR of **4** in CD_3CN.

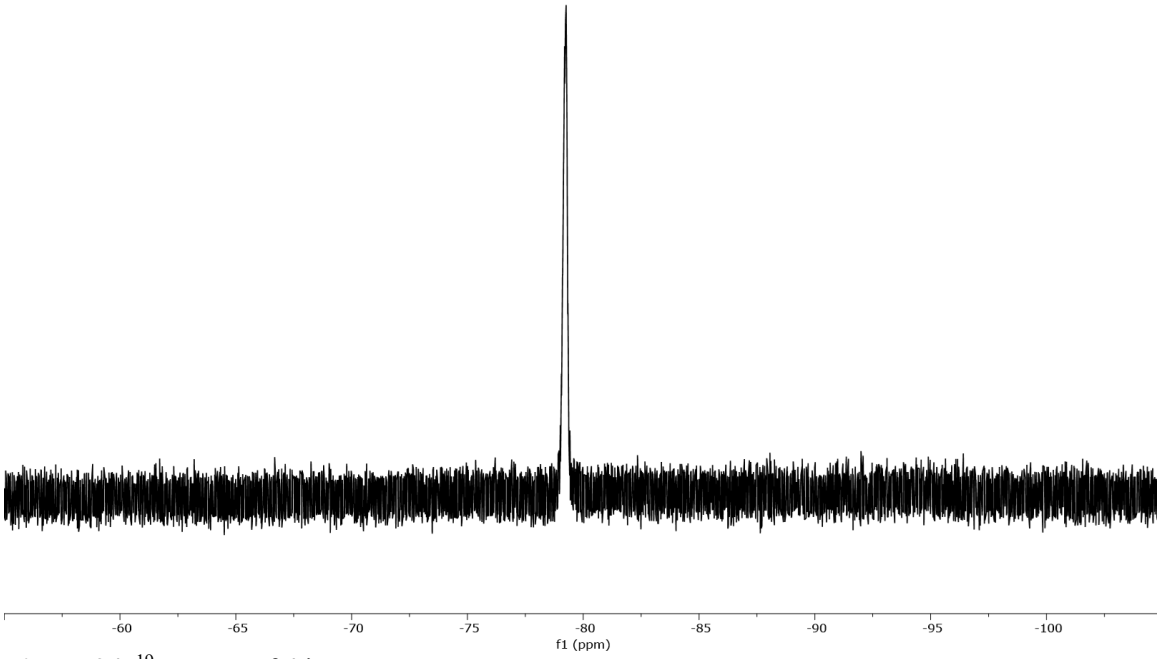

Figure 24. ^{19}F NMR of **4** in CD_3CN.

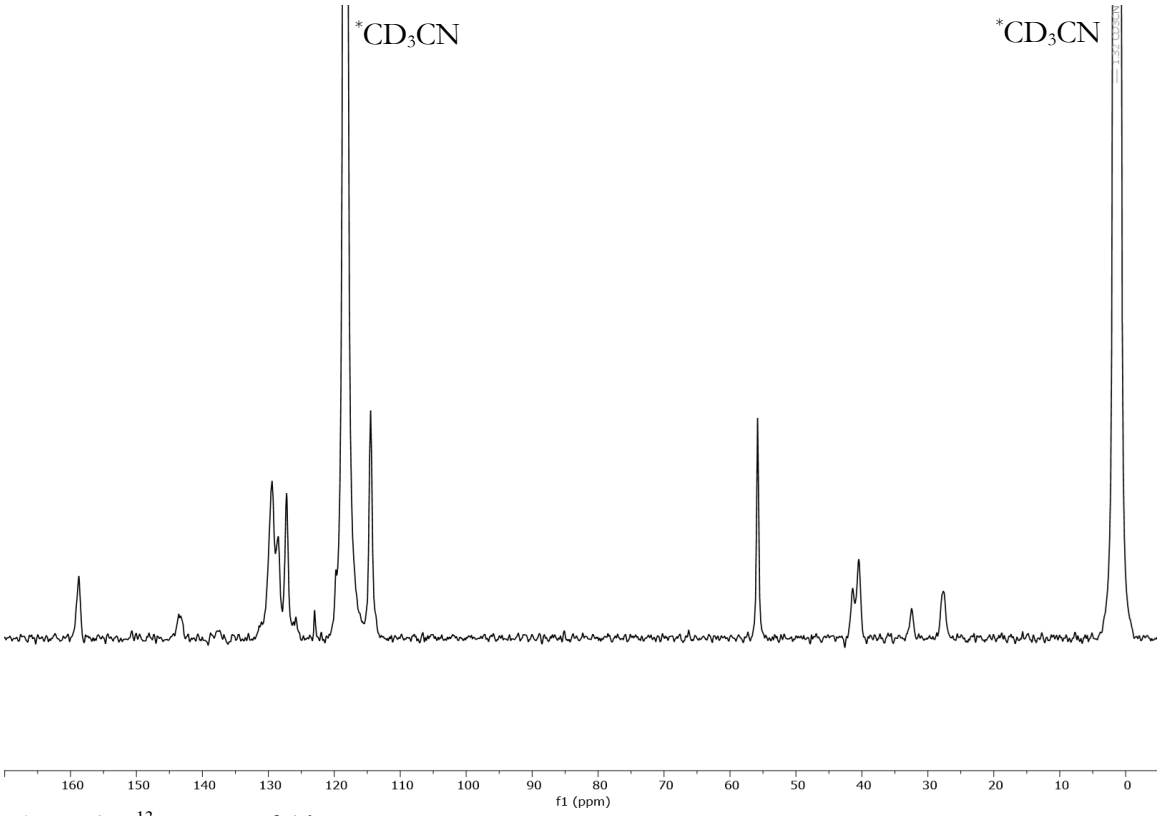

Figure 25. ^{13}C NMR of **4** in CD_3CN.

REFERENCES

(1) Nitopi, S.; Bertheussen, E.; Scott, S. B.; Liu, X.; Engstfeld, A. K.; Horch, S.; Seger, B.; Stephens, I. E. L.; Chan, K.; Hahn, C.; et al. Progress and Perspectives of Electrochemical CO2 Reduction on Copper in Aqueous Electrolyte. *Chem. Rev.* **2019**, *119* (12), 7610–7672.

(2) Hori, Y.; Kikuchi, K.; Suzuki, S. *Chem. Lett.* **1985**, *14* (11), 1695–1698.

(3) Kuhl, K. P.; Cave, E. R.; Abram, D. N.; Jaramillo, T. F. New Insights into the Electrochemical Reduction of Carbon Dioxide on Metallic Copper Surfaces. *Energy Environ. Sci.* **2012**, *5* (5), 7050–7059.

(4) Murata, A.; Hori, Y. Product Selectivity Affected by Cationic Species in Electrochemical Reduction of CO2 and CO at a Cu Electrode. *Bull. Chem. Soc. Jpn.* **1991**, *64* (1), 123–127.

(5) Thevenon, A.; Rosas-Hernández, A.; Fontani Herreros, A. M.; Agapie, T.; Peters, J. C. Dramatic HER Suppression on Ag Electrodes via Molecular Films for Highly Selective CO2 to CO Reduction. *ACS Catal.* **2021**, *11* (8), 4530–4537.

(6) Thevenon, A.; Rosas-Hernández, A.; Peters, J. C.; Agapie, T. In-Situ Nanostructuring and Stabilization of Polycrystalline Copper by an Organic Salt Additive Promotes Electrocatalytic CO2 Reduction to Ethylene. *Angew. Chemie Int. Ed.* **2019**, *58* (47), 16952–16958.

(7) Li, F.; Thevenon, A.; Rosas-Hernández, A.; Wang, Z.; Li, Y.; Gabardo, C. M.; Ozden, A.; Dinh, C. T.; Li, J.; Wang, Y.; et al. Molecular Tuning of CO2-to-Ethylene Conversion. *Nature* **2020**, *577* (7791), 509–513.

(8) Han, Z.; Kortlever, R.; Chen, H.-Y.; Peters, J. C.; Agapie, T. CO2 Reduction Selective for C≥2 Products on Polycrystalline Copper with N-Substituted Pyridinium Additives. *ACS Cent. Sci.* **2017**, *3* (8), 853–859.

(9) Nie, W.; Heim, G. P.; Watkins, N. B.; Agapie, T.; Peters, J. Organic Additive-Derived Films on Cu Electrodes Promote Electrochemical CO2 Reduction to C2+ Products Under Strongly Acidic Conditions. *Angew. Chemie Int. Ed.* **2023**, *n/a* (n/a).

(10) Cheng, B.; Du, J.; Yuan, H.; Tao, Y.; Chen, Y.; Lei, J.; Han, Z. Selective CO2 Reduction to Ethylene Using Imidazolium-Functionalized Copper. *ACS Appl. Mater. Interfaces* **2022**, *14* (24), 27823–27832.

(11) Buckley, A. K.; Cheng, T.; Oh, M. H.; Su, G. M.; Garrison, J.; Utan, S. W.; Zhu, C.; Toste, F. D.; Goddard, W. A. I. I. I.; Toma, F. M. Approaching 100% Selectivity at Low Potential on Ag for Electrochemical CO2 Reduction to CO Using a Surface Additive. *ACS Catal.* **2021**, *11* (15), 9034–9042.

(12) Rosen, B. A.; Salehi-Khojin, A.; Thorson, M. R.; Zhu, W.; Whipple, D. T.; Kenis, P. J. A.; Masel, R. I. Ionic Liquid–Mediated Selective Conversion of CO2 to CO at Low Overpotentials. *Science (80-.).* **2011**, *334* (6056), 643–644.

(13) Chen, X.; Chen, J.; Alghoraibi, N. M.; Henckel, D. A.; Zhang, R.; Nwabara, U. O.; Madsen, K. E.; Kenis, P. J. A.; Zimmerman, S. C.; Gewirth, A. A. Electrochemical CO2-to-Ethylene Conversion on Polyamine-Incorporated Cu Electrodes. *Nat. Catal.* **2021**, *4* (1), 20–27.

(14) Wei, X.; Yin, Z.; Lyu, K.; Li, Z.; Gong, J.; Wang, G.; Xiao, L.; Lu, J.; Zhuang, L. Highly Selective Reduction of CO2 to C2+ Hydrocarbons at Copper/Polyaniline Interfaces. *ACS Catal.* **2020**, *10* (7), 4103–4111.

(15) Watkins, N. B.; Wu, Y.; Nie, W.; Peters, J. C.; Agapie, T. In Situ Deposited Polyaromatic Layer Generates Robust Copper Catalyst for Selective Electrochemical CO2 Reduction at Variable PH. *ACS Energy Lett.* **2023**, *8* (1), 189–195.

(16) Kim, C.; Bui, J. C.; Luo, X.; Cooper, J. K.; Kusoglu, A.; Weber, A. Z.; Bell, A. T. Tailored Catalyst Microenvironments for CO2 Electroreduction to Multicarbon Products on Copper Using Bilayer Ionomer Coatings. *Nat. Energy* **2021**, *6* (11), 1026–1034.

(17) Pelayo, G. de A. F.; Cao-Thang, D.; Adnan, O.; Joshua, W.; Christopher, M.; R., K. A.; Dae-Hyun, N.; Christine, G.; Ali, S.; Xue, W.; et al. CO2 Electrolysis to Multicarbon Products at Activities Greater than 1 A Cm−2. *Science (80-.).* **2020**, *367* (6478), 661–666.

(18) Ozden, A.; Li, F.; García de Arquer, F. P.; Rosas-Hernández, A.; Thevenon, A.; Wang, Y.; Hung, S.-F.; Wang, X.; Chen, B.; Li, J.; et al. High-Rate and Efficient Ethylene Electrosynthesis Using a Catalyst/Promoter/Transport Layer. *ACS Energy Lett.* **2020**, *5* (9), 2811–2818.

(19) Erick, H. J.; Fengwang, L.; Adnan, O.; Armin, S. R.; Pelayo, G. de A. F.; Shijie, L.; Shuzhen, Z.; Mingchuan, L.; Xue, W.; Yanwei, L.; et al. CO2 Electrolysis to Multicarbon Products in Strong Acid. *Science (80-.).* **2021**, *372* (6546), 1074–1078.

(20) Pan, H.; Barile, C. J. Electrochemical CO2 Reduction to Methane with Remarkably High Faradaic Efficiency in the Presence of a Proton Permeable Membrane. *Energy Environ. Sci.* **2020**, *13* (10), 3567–3578.

(21) Wang, J.; Cheng, T.; Fenwick, A. Q.; Baroud, T. N.; Rosas-Hernández, A.; Ko, J. H.; Gan, Q.; Goddard III, W. A.; Grubbs, R. H. Selective CO2 Electrochemical Reduction Enabled by a Tricomponent Copolymer Modifier on a Copper Surface. *J. Am. Chem. Soc.* **2021**, *143* (7), 2857–2865.

(22) Chang, M.; Ren, W.; Ni, W.; Lee, S.; Hu, X. Ionomers Modify the Selectivity of Cu-Catalyzed Electrochemical CO2 Reduction. *ChemSusChem* **2022**, *n/a* (n/a), e202201687.

(23) Li, W.; Yin, Z.; Gao, Z.; Wang, G.; Li, Z.; Wei, F.; Wei, X.; Peng, H.; Hu, X.; Xiao, L.; et al. Bifunctional Ionomers for Efficient Co-Electrolysis of CO2 and Pure Water towards Ethylene Production at Industrial-Scale Current Densities. *Nat. Energy* **2022**, *7* (9), 835–843.

(24) Shin, S.-J.; Choi, H.; Ringe, S.; Won, D. H.; Oh, H.-S.; Kim, D. H.; Lee, T.; Nam, D.-H.; Kim, H.; Choi, C. H. A Unifying Mechanism for Cation Effect Modulating C1 and C2 Productions from CO2 Electroreduction. *Nat. Commun.* **2022**, *13* (1), 5482.

(25) Ringe, S.; Clark, E. L.; Resasco, J.; Walton, A.; Seger, B.; Bell, A. T.; Chan, K. Understanding Cation Effects in Electrochemical CO2 Reduction. *Energy Environ. Sci.* **2019**, *12* (10), 3001–3014.

(26) Resasco, J.; Chen, L. D.; Clark, E.; Tsai, C.; Hahn, C.; Jaramillo, T. F.; Chan, K.; Bell, A. T. Promoter Effects of Alkali Metal Cations on the Electrochemical Reduction of Carbon Dioxide. *J. Am. Chem. Soc.* **2017**, *139* (32), 11277–11287.

(27) Monteiro, M. C. O.; Dattila, F.; Hagedoorn, B.; García-Muelas, R.; López, N.; Koper, M. T. M. Absence of CO2 Electroreduction on Copper, Gold and Silver Electrodes without Metal Cations in Solution. *Nat. Catal.* **2021**, *4* (8), 654–662.

(28) Gu, J.; Liu, S.; Ni, W.; Ren, W.; Haussener, S.; Hu, X. Modulating Electric Field Distribution by Alkali Cations for CO2 Electroreduction in Strongly Acidic Medium. *Nat. Catal.* **2022**, *5* (4), 268–276.

(29) Qin, H.-G.; Li, F.-Z.; Du, Y.-F.; Yang, L.-F.; Wang, H.; Bai, Y.-Y.; Lin, M.; Gu, J. Quantitative Understanding of Cation Effects on the Electrochemical Reduction of CO2 and H+ in Acidic Solution. *ACS Catal.* **2023**, *13* (2), 916–926.

(30) Waegele, M. M.; Gunathunge, C. M.; Li, J.; Li, X. How Cations Affect the Electric Double Layer and the Rates and Selectivity of Electrocatalytic Processes. *J. Chem. Phys.* **2019**, *151* (16), 160902.

(31) Residual styrene starting materials were removed from the ionomers by precipitation of polymer from a concentrated MeCN solution with Et_2O, washing with hot 1 M $KHCO_{3(aq)}$, and followed by reprecipitation with MeCN and Et_2O. Due to the difference in solubility, a modified purification procedure was employed for the methoxystyrene homopolymer, with residual starting material removed by precipitation of a concentrated THF solution into MeOH.

(32) Weitzner, S. E.; Akhade, S. A.; Varley, J. B.; Wood, B. C.; Otani, M.; Baker, S. E.; Duoss, E. B. Toward Engineering of Solution Microenvironments for the CO2 Reduction Reaction: Unraveling PH and Voltage Effects from a Combined Density-Functional–Continuum Theory. *J. Phys. Chem. Lett.* **2020**, *11* (10), 4113–4118.

(33) Zhao, Y.; Hao, L.; Ozden, A.; Liu, S.; Miao, R. K.; Ou, P.; Alkayyali, T.; Zhang, S.; Ning, J.; Liang, Y.; et al. Conversion of CO2 to Multicarbon Products in Strong Acid by Controlling the Catalyst Microenvironment. *Nat. Synth.* **2023**, *2* (5), 403–412.

(34) Zi, X.; Zhou, Y.; Zhu, L.; Chen, Q.; Tan, Y.; Wang, X.; Sayed, M.; Pensa, E.; Geioushy, R. A.; Liu, K.; et al. Breaking K+ Concentration Limit on Cu Nanoneedles for Acidic Electrocatalytic CO2 Reduction to Multi-Carbon Products. *Angew. Chemie Int. Ed.* **2023**, *62* (42), e202309351.

(35) Ren, W.; Xu, A.; Chan, K.; Hu, X. A Cation Concentration Gradient Approach to Tune the Selectivity and Activity of CO2 Electroreduction. *Angew. Chemie Int. Ed.* **2022**, *61* (49), e202214173.

(36) Ramdin, M.; de Loos, T. W.; Vlugt, T. J. H. State-of-the-Art of CO2 Capture with Ionic Liquids. *Ind. Eng. Chem. Res.* **2012**, *51* (24), 8149–8177.

(37) Li, L.; Liu, Z.; Yu, X.; Zhong, M. Achieving High Single-Pass Carbon Conversion Efficiencies in Durable CO2 Electroreduction in Strong Acids via Electrode Structure Engineering. *Angew. Chemie Int. Ed.* **2023**, *62* (21), e202300226.

(38) Song, H.; Song, J. T.; Kim, B.; Tan, Y. C.; Oh, J. Activation of C2H4 Reaction Pathways in Electrochemical CO2 Reduction under Low CO2 Partial Pressure. *Appl. Catal. B Environ.* **2020**, *272*, 119049.

(39) Moradzaman, M.; Martínez, C. S.; Mul, G. Effect of Partial Pressure on Product Selectivity in Cu-Catalyzed Electrochemical Reduction of CO2. *Sustain. Energy Fuels* **2020**, *4* (10), 5195–5202.

(40) Moradzaman, M.; Mul, G. Optimizing CO Coverage on Rough Copper Electrodes: Effect of the Partial Pressure of CO and Electrolyte Anions (PH) on Selectivity toward Ethylene. *J. Phys. Chem. C* **2021**, *125* (12), 6546–6554.

(41) Lu, S.; Wang, Y.; Xiang, H.; Lei, H.; Xu, B. Bin; Xing, L.; Yu, E. H.; Liu, T. X. Mass Transfer Effect to Electrochemical Reduction of CO2: Electrode, Electrocatalyst and Electrolyte. *J. Energy Storage* **2022**, *52*, 104764.

(42) Yano, H.; Tanaka, T.; Nakayama, M.; Ogura, K. Selective Electrochemical Reduction of CO2 to Ethylene at a Three-Phase Interface on Copper(I) Halide-Confined Cu-Mesh Electrodes in Acidic Solutions of Potassium Halides. *J. Electroanal. Chem.* **2004**, *565* (2), 287–293.

(43) Chen, L. D.; Urushihara, M.; Chan, K.; Nørskov, J. K. Electric Field Effects in Electrochemical CO2 Reduction. *ACS Catal.* **2016**, *6* (10), 7133–7139.

(44) Lin, S.-T.; Blanco, M.; Goddard III, W. A. The Two-Phase Model for Calculating Thermodynamic Properties of Liquids from Molecular Dynamics: Validation for the Phase Diagram of Lennard-Jones Fluids. *J. Chem. Phys.* **2003**, *119* (22), 11792–11805.

(45) Watkins, N. B.; Schiffer, Z. J.; Lai, Y.; Musgrave, C. B. I. I. I.; Atwater, H. A.; Goddard, W. A. I. I. I.; Agapie, T.; Peters, J. C.; Gregoire, J. M. Hydrodynamics Change Tafel Slopes in Electrochemical CO2 Reduction on Copper. *ACS Energy Lett.* **2023**, *8* (5), 2185–2192.

(46) Prasetyo, N.; Hofer, T. S. Structure, Dynamics, and Hydration Free Energy of Carbon Dioxide in Aqueous Solution: A Quantum Mechanical/Molecular Mechanics Molecular Dynamics Thermodynamic Integration (QM/MM MD TI) Simulation Study. *J. Chem. Theory Comput.* **2018**, *14* (12), 6472–6483.

(47) Goyal, A.; Marcandalli, G.; Mints, V. A.; Koper, M. T. M. Competition between CO2 Reduction and Hydrogen Evolution on a Gold Electrode under Well-Defined Mass Transport Conditions. *J. Am. Chem. Soc.* **2020**, *142* (9), 4154–4161.

(48) Richard, D.; Tom, M.; Jang, J.; Yun, S.; Christofides, P. D.; Morales-Guio, C. G. Quantifying Transport and Electrocatalytic Reaction Processes in a Gastight Rotating Cylinder Electrode Reactor via Integration of Computational Fluid Dynamics Modeling and Experiments. *Electrochim. Acta* **2023**, *440*, 141698.

(49) Qiao, Y.; Lai, W.; Huang, K.; Yu, T.; Wang, Q.; Gao, L.; Yang, Z.; Ma, Z.; Sun, T.; Liu, M.; et al. Engineering the Local Microenvironment over Bi Nanosheets for Highly Selective Electrocatalytic Conversion of CO2 to HCOOH in Strong Acid. *ACS Catal.* **2022**, 2357–2364.

(50) Liang, Y.; Zhao, J.; Yang, Y.; Hung, S.-F.; Li, J.; Zhang, S.; Zhao, Y.; Zhang, A.; Wang, C.; Appadoo, D.; et al. Stabilizing Copper Sites in Coordination Polymers toward Efficient Electrochemical C-C Coupling. *Nat. Commun.* **2023**, *14* (1), 474.

(51) Sato, Y.; Takikawa, T.; Sorakubo, A.; Takishima, S.; Masuoka, H.; Imaizumi, M. Solubility and Diffusion Coefficient of Carbon Dioxide in Biodegradable Polymers. *Ind. Eng. Chem. Res.* **2000**, *39* (12), 4813–4819.

(52) We acknowledge the complicated relationship between gas solubility and diffusivity as models have previously highlighted an inverse relationship when comparing ionomers (ref. 16) while others have experimentally observed direct correlations (ref. 51) Other models have invoked both improved mass transport and greater local CO_2 concentration as phenomena to explain greater FE_{C2+} and $|j_{C2+}|$ with Cu electrodes (ref. 21). In our system, minimization of Helmholtz free energy is attributed to increased CO_2 entropy (S_{CO2}, Table 2) which is a result of increased diffusion, as well as decreased internal energy due to enhanced K+-related coulomb stabilization.

(53) Soniat, M.; Tesfaye, M.; Brooks, D.; Merinov, B.; Goddard, W. A.; Weber, A. Z.; Houle, F. A. Predictive Simulation of Non-Steady-State Transport of Gases through Rubbery Polymer Membranes. *Polymer (Guildf).* **2018**, *134*, 125–142.

(54) Luo, G.; Yuan, B.; Guan, T.; Cheng, F.; Zhang, W.; Chen, J. Synthesis of Single Lithium-Ion Conducting Polymer Electrolyte Membrane for Solid-State Lithium Metal Batteries. *ACS Appl. Energy Mater.* **2019**, *2* (5), 3028–3034.

(55) Pangborn, A. B.; Giardello, M. A.; Grubbs, R. H.; Rosen, R. K.; Timmers, F. J. Safe and Convenient Procedure for Solvent Purification. *Organometallics* **1996**, *15* (5), 1518–1520.

(56) Lazanas, A. C.; Prodromidis, M. I. Electrochemical Impedance Spectroscopy─A Tutorial. *ACS Meas. Sci. Au* **2023**, *3* (3), 162–193.

(57) Zheng, W. IR Compensation for Electrocatalysis Studies: Considerations and Recommendations. *ACS Energy Lett.* **2023**, *8* (4), 1952–1958.

(58) Heenan, A. R.; Hamonnet, J.; Marshall, A. T. Why Careful IR Compensation and Reporting of Electrode Potentials Are Critical for the CO2 Reduction Reaction. *ACS Energy Lett.* **2022**, *7* (7), 2357–2361.

(59) Ma, M.; Zheng, Z.; Yan, W.; Hu, C.; Seger, B. Rigorous Evaluation of Liquid Products in High-Rate CO2/CO Electrolysis. *ACS Energy Lett.* **2022**, *7* (8), 2595–2601.

(60) Clementi, E.; Raimondi, D. L.; Reinhardt, W. P. Atomic Screening Constants from SCF Functions. II. Atoms with 37 to 86 Electrons. *J. Chem. Phys.* **2004**, *47* (4), 1300–1307.

CHAPTER IV

POTASSIUM-CONTAINING IONOMERS AS ELECTRODE COATINGS ELECTRODES FACILITATE HIGH PERFORMANCE CO_2 REDUCTION

ABSTRACT: This chapter discusses variation of the ionomer/polymer structures to maximize CO_2R performance and enhance our understanding of effects of organic moieties. Incorporation of neutral comonomers bearing cross-linking units rich in biphenyl and terphenyl motifs result in high current densities, maximizing at ~330 mA cm^{-2} towards C_{2+} products with 82% Faradaic Efficiency (FE), surpassing the minimum 200 mA cm^{-2} necessary for application on an industrial scale. The analogous neutral variants (i.e., those lacking the charged comonomer) show comparable $|j_{C2+}|$ to the K^+-containing polymers, suggesting a non-innocent role of the aryl-rich polymers. More insoluble comonomers were envisioned to allow incorporation of greater amounts of the charged comonomer, thus permitting development of a broad relationship between $[K^+]$ and $|j_{C2+}|$. However, it was observed that increased $[K^+]$ beyond 40-50 mol% did not facilitate greater $|j_{C2+}|$.

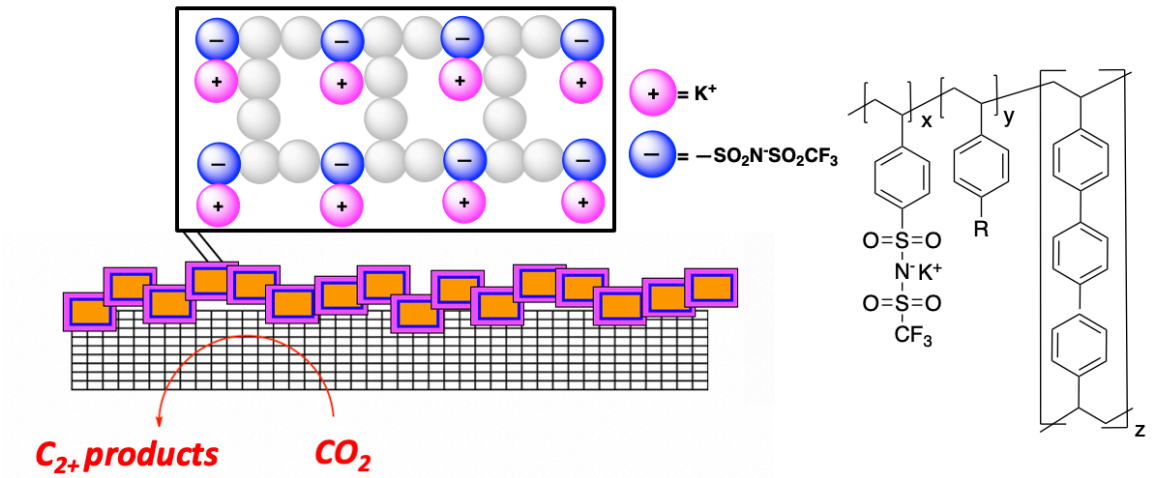

ACKNOWLEDGMENTS

Meaghan A. Bruening is thanked for synthesizing the polymers. This material is based on work performed by the Liquid Sunlight Alliance, which is supported by the U.S. Department of Energy, Office of Science, Office of Basic Energy Sciences, Fuels from Sunlight Hub under Award DE-SC0021266. The Resnick Sustainability Institute at Caltech is acknowledged for support of the laboratory facilities in which this research was conducted.

INTRODUCTION

Converting CO_2 to value-added chemicals electrochemically using renewable energy is a potential avenue toward achieving a net-zero carbon economy.[1] Cu is the only metallic electrode where multi-carbon (C_{2+}) products, including C_2H_4, C_2H_5OH, and C_3H_7OH are produced from electrochemical CO_2 reduction (CO_2R).[2] However, Cu alone suffers from poor selectivity towards C_{2+} products owing to the significant generation of C_1 products and hydrogen.[2–4] Coating Cu electrodes with organic films is a strategy for steering CO_2R selectivity towards C_{2+} products. Organic coatings derived from molecular precursors such as pyridinium,[5–9] ionic liquids,[10–12] amines,[13,14] and aryl diazonium and iodonium species[15] have shown promise. Although the ease of precursor synthesis and *in situ* film generation are attractive features of general approach, the physical properties of the coating and electrocatalyst microenvironment, including local pH, CO_2 concentration, hydrophobicity, and electric field strength, are not readily predicted.

An alternative approach to organic films is provided by ionomers.[16–23] For example, Bell and co-workers recently examined a combination of ionomers to control local pH and hydrophobicity to achieve high C_{2+} product selectivity on Cu.[16] Also, Sargent and co-workers have demonstrated high current density electrolysis with Nafion on Cu.[17] These examples employing commercial polymers highlight the potential of this approach; however, a dearth of studies of the effects of systematic changes in ionomer structure on CO_2R behavior limit fundamental understanding of the features crucial for electrochemical performance.[21,23] Of note, Grubbs and co-workers synthesized and tested a library of ionomer coatings bearing imidazolium groups and observed high selectivity for C_{2+} products and low HER.[21] Computations suggested that high local [CO_2], as well as an

induced electric field effect from the positively charged functional groups, drove high selectivity towards C_{2+} products. Alkali cations were found to facilitate CO_2R on metallic electrodes.[19,24–28] Their presence in the outer Helmholtz plane was hypothesized to suppress proton carrier mass transport and stabilize CO_2R intermediates.[19,28–30]

As discussed in Chapter III, we observed a correlation between K^+ content provided by ionomer films and $|j_{C2+}|$. Experiments and simulations are consistent with elevated mass transport of CO_2 to the electrode surface. It is also of interest to prepare ionomers with greater $[K^+]$ than was possible in this series to expand these observations; ionomers with content beyond 37 mol% K^+ were soluble in water and therefore not suitable for investigation as films on electrodes. Less polar neutral comonomers are envisioned to allow for greater K^+ content without increasing solubility under aqueous conditions.

In this chapter is discussed results from investigating greater $[K^+]$ films. Continuous increase in $|j_{C2+}|$ could not be extended beyond ~40 mol% $[K^+]$. This phenomenon is possibly due to inhibited CO_2 mass transport with high alkali cation content in the double layer, consistent with previous reports investigating high alkali cation concentrations in bulk electrolyte. Separately, lower $[K^+]$ ionomers with poly(aryl) cross-linking motifs were found to impart high $|j_{C2+}|$, surpassing 300 mA cm^{-2}. The potassium-free analogues were found to similarly provide high activity, suggesting a non-innocent role of the uncharged, poly(aryl) motif and outperforming previous attempts to similar films via *in situ* electrodeposition.

RESULTS AND DISCUSSION

i) Ionomers bearing poly(aryl) comonomers

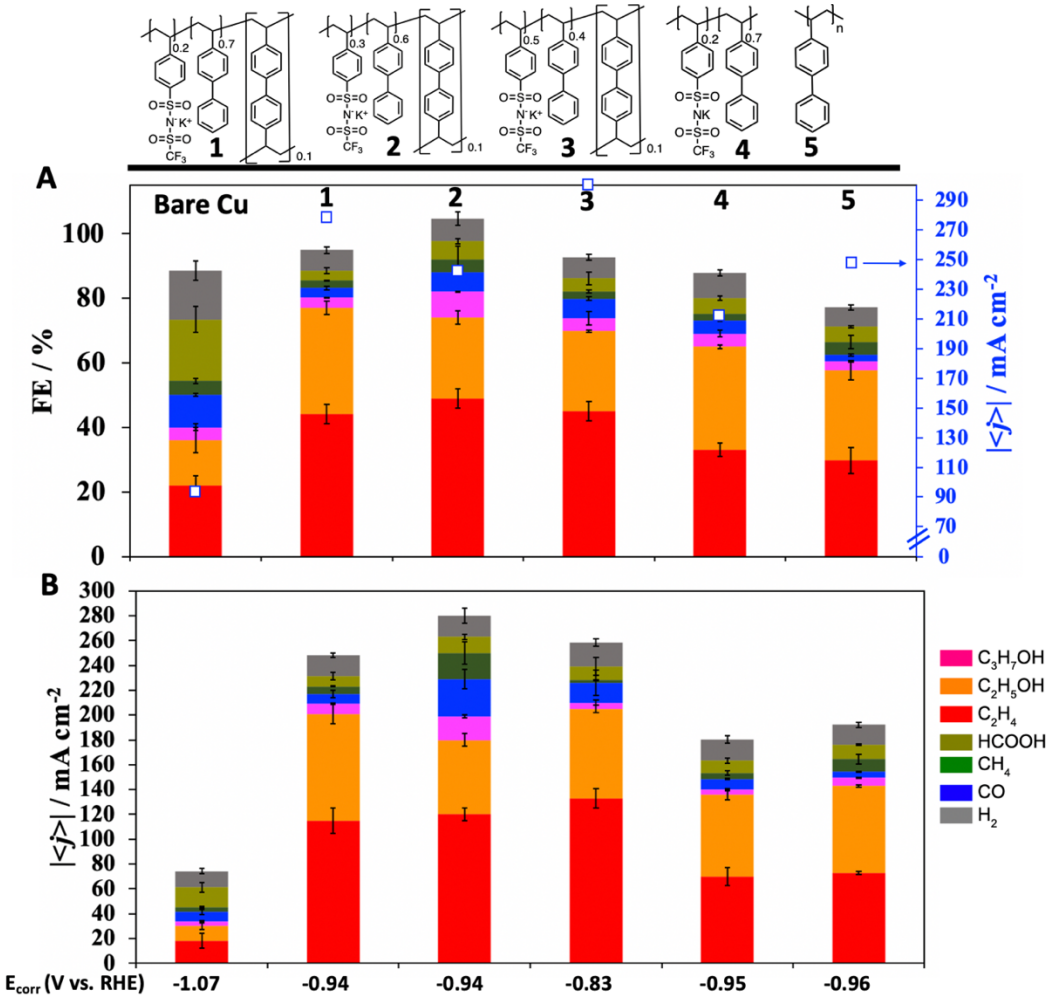

Figure 1. A. Faradaic efficiency (FE, columns) and current density (white squares) for CO_2R products on Cu/PTFE in the presence of ionomer films casted from solutions of **1-5.** Electrolysis performed in 1 M $KHCO_{3(aq)}$ for 30 minutes with $E_{applied}$ = –1.15 V vs. RHE. Corrected potentials (E_{corr}) determined from measured (uncompensated) resistance are reported. B. Partial current densities for trials shown in panel A.

Ionomers were prepared by performing copolymerizations initiated via radical generation with azobisisobutyronitrile. Styrene comonomer precursors capable of forming

cross-linking motifs were utilized (4,4'-divinyl-1,1'-biphenyl and 4,4"-divinyl-1,1':4',1"-terphenyl); these compounds were constructed from Pd-catalyzed cross-couplings or condensation reactions or (see **Synthetic Procedures** under **EXPERIMENTAL**).[31]

Ionomers **1**-**3** were studied as films on Cu/PTFE, and effects on CO_2R performance were investigated in a gas diffusion electrode flow cell, as described in Chapter III. Faradaic efficiency for C_{2+} products (FE_{C2+}) with **3** was not significantly greater than with **1** despite the greater K^+ content (Figure 1, ~210 mA cm^{-2}). Similar FE_{C2+} was observed in **2**. Moreover, $|j_{C2+}|$ does not increase monotonically with increasing $[K^+]$. The apparent inconsistency with the results from the methoxystyrene series (see Chapter III) could be due to two possible phenomena: 1) high alkali cation concentration beyond a certain limit in electrolytes was found to be detrimental for $|j_{CO2R}|$,[32] possibly due to attenuated CO_2 diffusion by a double layer saturated with alkali cations. 2) $[K^+]$ cannot be decoupled from an apparent effect of poly(aryl) species as comonomers, which seem to significantly boost CO_2R selectivity/activity on Cu towards C_{2+} products (Figure 1, ionomer **5**). This effect is reminiscent of poly(aryl) films generated from electrodeposition of bis(aryl)iodonium triflate salts, albeit demonstrating worse activity than the species investigated in Figure 1.[15] While poly(4-methoxy)styrene on Cu yields similar performance to bare Cu, poly(4-phenyl)styrene elevates both FE_{C2+} and $|j_{C2+}|$ (Figure 2, **10**).

In order to develop polymers lacking solubility in water but attempting to decouple the effects of 4-phenylstyrene, a similar series of ionomers were constructed with 4-methoxystyrene as a precursor along with **K-STFSI** and 4,4'-divinyl-1,1'-biphenyl. Ionomer **8** possessed lower $|j_{C2+}|$ compared to **6** (110 mA cm^{-2} vs. 180 mA cm^{-2}); ionomers

7-9 gave similar CO_2R performance to each other (Figure 2). Notably, each of ionomers **6-9** increase performance relative to both bare Cu and **10**. These results suggest that a significant effect of the cross-linking bi(aryl) motif on CO_2R performance cannot be ruled out.

A series of ionomers were developed with poly(4-phenyl)styrene as neutral comonomer to determine if CO_2R effects from K^+ were significant in the absence of a cross-linking motif (Figure 3). When $E_{applied} = -1.05$ V vs. RHE in 1 M $KHCO_{3(aq)}$, a correlation is observed in $[K^+]$ with $|j_{C2+}|$, with **14** imparting 100 mA cm^{-2}. When $E_{applied} = -1.15$ V vs. RHE, a linear increase in $|j_{C2+}|$ is not observed, but **14** drives $|j_{C2+}|$ to 190 mA cm^{-2}. Under certain conditions, the trend is reminiscent of observations from examining the methoxystyrene series as films on Cu (Chapter III). Notably, poly(4-phenyl)styrene as a coating generates high selectivity for C_{2+} products (FE_{C2+} = 61%), while poly(4-methoxyphenyl)styrene does not improve performance relative to bare Cu (Figure 2).

Additional ionomers with terphenyl and poly(ethylene glycol)-based linkers were prepared and tested as films on Cu to maximize performance (Figure 4). Ionomer **16** demonstrates a record amongst all polymers discussed, observing $|j_{C2+}| = 270$ mA cm^{-2}, more than 9-fold greater than bare Cu. High performance was also observed in a poly(ethylene glycol)-containing ionomer ($|j_{C2+}| = 180$ mA cm^{-2}). Notably, each ionomer's potassium-free analogue demonstrated high CO_2R performance, suggesting that these motifs can facilitate CO_2R possibly due to a cation-π effect (thus enhancing local $[K^+]$ from the electrolyte)[33,34] or elevated CO_2 mass transport.[35]

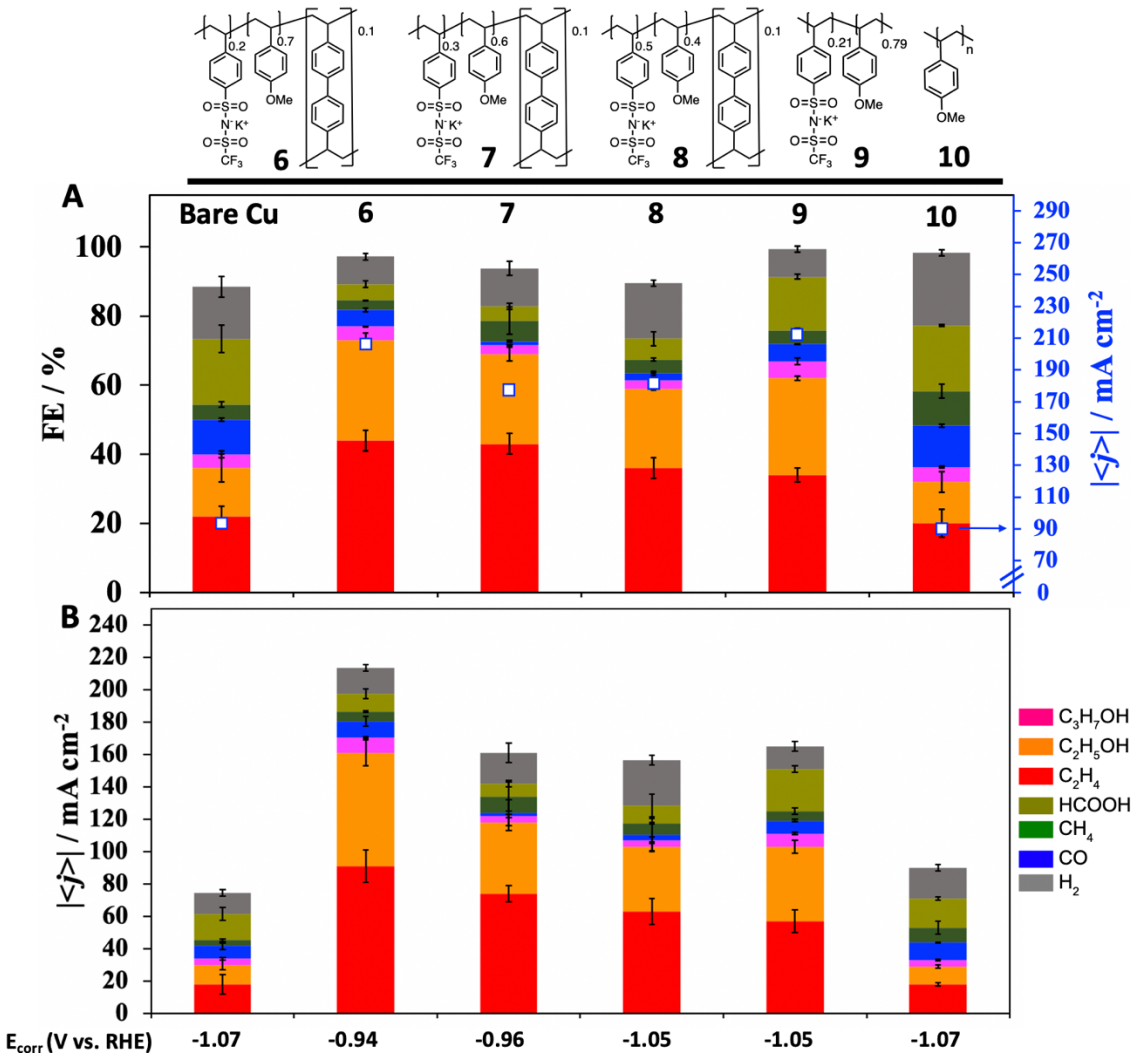

Figure 2. A. Faradaic efficiency (FE, columns) and current density (white squares) for CO_2R products on Cu/PTFE in the presence of ionomer films casted from solutions of **6-10.** Electrolysis performed in 1 M $KHCO_{3(aq)}$ for 30 minutes with $E_{applied}$ = –1.15 V vs. RHE. Corrected potentials (E_{corr}) determined from measured (uncompensated) resistance are reported. B. Partial current densities for trials shown in panel A.

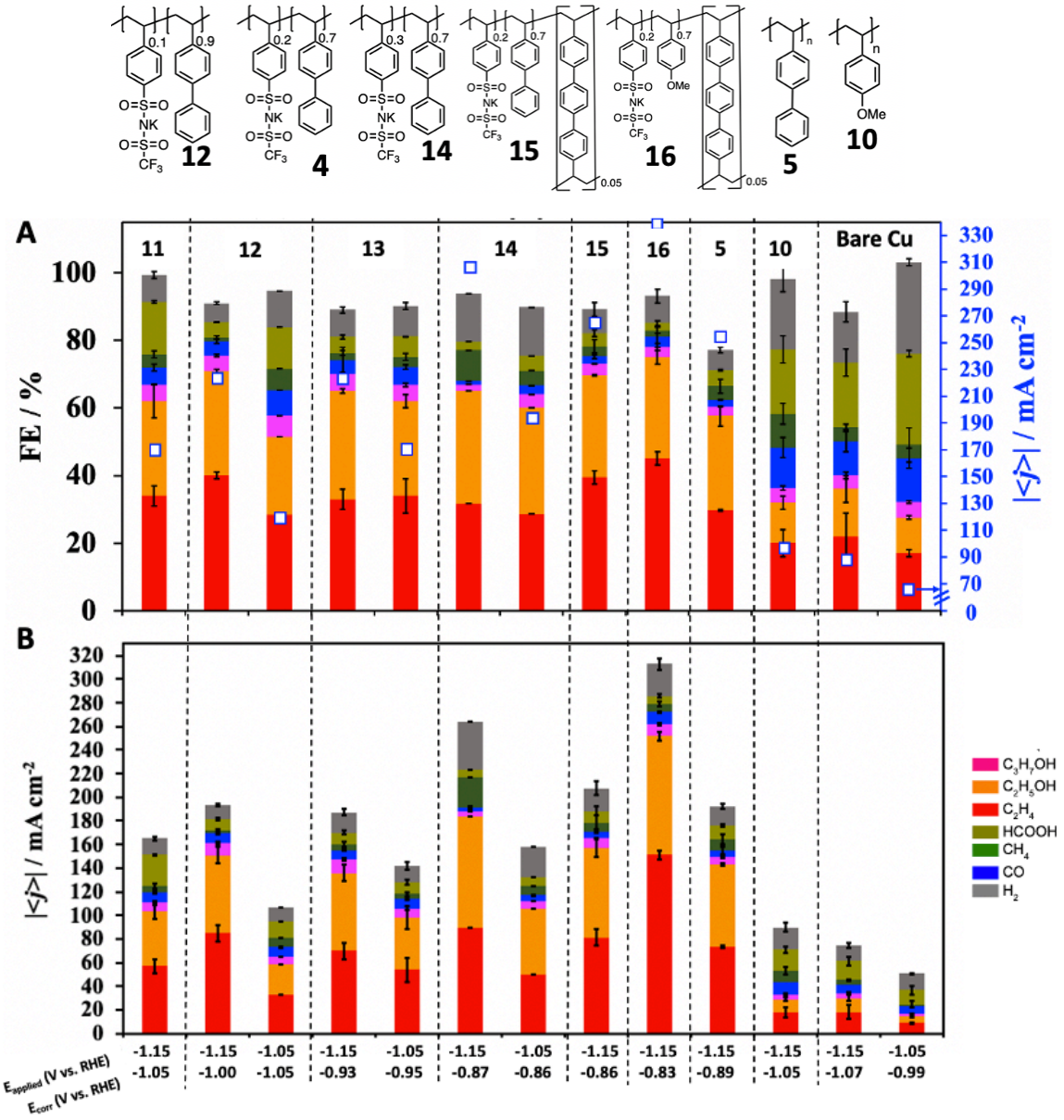

Figure 3. A. Faradaic efficiency (FE, columns) and current density (white squares) for CO_2R products on Cu/PTFE in the presence of ionomer films casted from various solutions of ionomers**.** Electrolysis performed in 1 M $KHCO_{3(aq)}$ for 30 minutes. Corrected potentials (E_{corr}) determined from measured (uncompensated) resistance are reported. B. Partial current densities for trials shown in panel A.

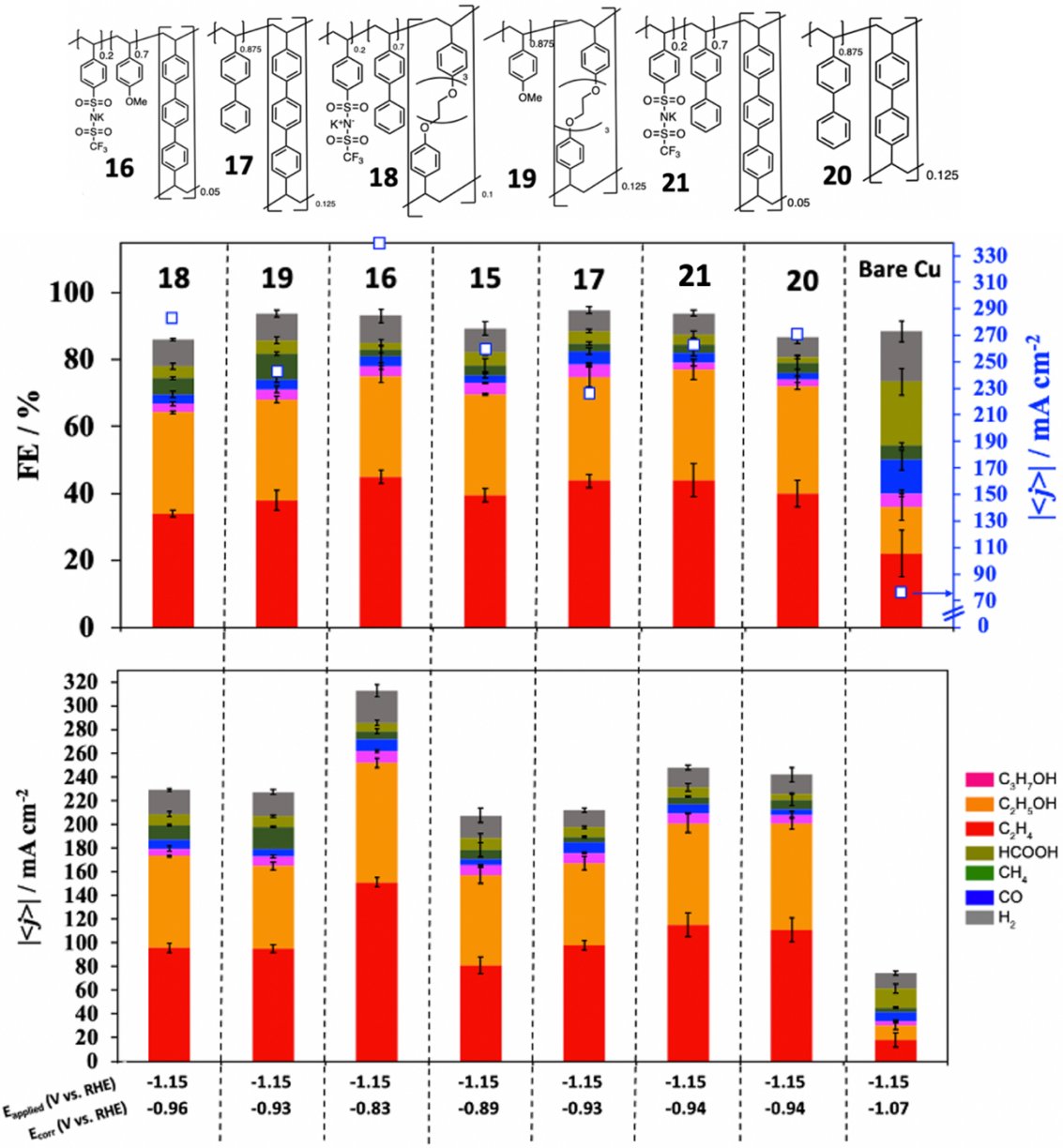

Figure 4. A. Faradaic efficiency (FE, columns) and current density (white squares) for CO_2R products on Cu/PTFE in the presence of ionomer films casted from various solutions of ionomers**.** Electrolysis performed in 1 M $KHCO_{3(aq)}$ for 30 minutes. Corrected potentials (E_{corr}) determined from measured (uncompensated) resistance are reported. B. Partial current densities for trials shown in panel A.

CONCLUSIONS

To summarize, several series of ionomers along with their neutral analogues were developed and examined as coatings on Cu for high current density for C_{2+} products (270 mA cm^{-2}). While materials bearing K^+ content greater than 40 mol% were accessible synthetically, this aspect alone was not beneficial in driving high CO_2R activity. The neutral comonomers bearing aryl-rich styrene precursors were found to impart outstanding improvement in performance relative to bare Cu (as much as 10x increase in $|j_{C2+}|$); K^+-free analogues in most cases also provided high performance. Current and future work is dedicated understanding how these polymers facilitate CO_2R performance on Cu. To rule out morphological changes to Cu, scattered angle X-ray spectroscopy measurements (SAXS) will be carried out. Electrochemical measurements will also be performed to determine CO_2 diffusion coefficients. Finally, effects on CO reduction performance corroborated with MD simulations of CO residence time could suggest the films' effects on CO_2R intermediates.

EXPERIMENTAL

Materials and Methods

General Considerations. All solvents and reagents were obtained from commercial sources (Aldrich, Merck, and Combi Blocks) and used as received, unless stated otherwise. 4-Methoxystyrene was dried with CaH_2 and filtered under inert atmosphere. Azobisisobutyronitrile (AIBN) was dried under vacuum for 16 hr. 4-vinylbiphenyl was dried under vacuum for 16 hr. **K-STFSI** was prepared based on a previously reported synthesis.[36] Acetonitrile was dried by passing over activated alumina by the method of Grubbs[37] and stored over 3 Å molecular sieves in a N_2-filled glovebox. Anhydrous dimethylformamide (DMF) was degassed and stored over 3 Å molecular sieves in a N_2-filled glovebox. $KHCO_3$ (grade) for polymer purification was purchased from Sigma Aldrich.

Copper nanoparticles, potassium carbonate (99.995%), 4-methoxystyrene, solution (99%), isopropanol (HPLC grade), and ethanol (HPLC grade) were purchased from Sigma Aldrich. Polytetrafluoroethylene (PTFE) was purchased from McMaster-Carr. The leakless Ag/AgCl reference electrode was purchased from Innovative Instruments. Platinum mesh (99.99% Pt, 25 mm × 25 mm × 0.05 mm) was purchased from Alfa Aesar. CO_2 (research grade) was purchased from Airgas. Deuterium oxide (D 99.96%) and CD_3CN (99.9%) were purchased from Cambridge Isotope Laboratories. The ^{1}H and ^{19}F NMR solution-state NMR spectra were recorded on a Bruker 400 MHz with broadband auto-tune OneProbe. ^{13}C solution-state NMR spectra were recorded on a Bruker 400 MHz instrument with a prodigy broadband cryoprobe. Shifts were reported relative to the residual solvent peak.

Water was purified by a Nanopure Analytical Ultrapure Water System (Thermo Scientific) or a Milli-Q Advantage A10 Water Purification System (Millipore) with specific resistance of 18.2 MΩ·cm at

25 °C. A VWR sympHony™ pH meter (calibrated with a pH = 1.68 standard) was used to determine the pH of the electrolytes before experiments.

Synthetic Procedures **Carried out by Meaghan A. Bruening*

Preparation of Monomers:

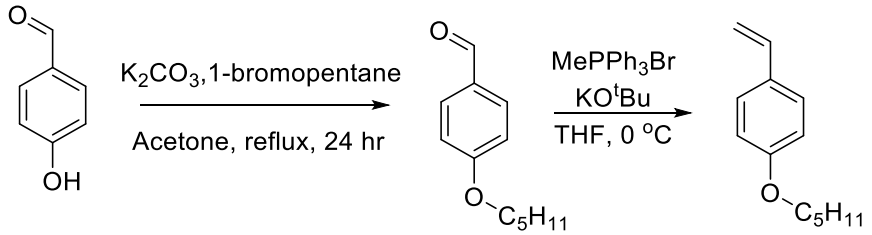

4-Pentoxystyrene was prepared in two steps from 4-hydroxybenzaldehyde based on literature procedures.[38] Product isolated as an oil. ^{1}H $CDCl_3$ 7.34 (m, 2 H, Ar-*H*), 6.85 (m, 2 H, Ar-*H*), 6.65 (dd, 1 H, vinyl-*H*), 5.60 (dd, 1 H, vinyl-*H*), 5.11 (dd, 1 H, vinyl-*H*), 3.95 (t, 2 H, Ar-O-C*H*$_2$CH$_2$CH$_2$CH$_2$CH$_3$), 1.78 (m, 2 H, Ar-O-CH$_2$C*H*$_2$CH$_2$CH$_2$CH$_3$), 1.36 (m, 4 H, Ar-O-CH$_2$CH$_2$C*H*$_2$C*H*$_2$CH$_3$), 0.92 (m, 3 H, Ar-O-CH$_2$CH$_2$CH$_2$CH$_2$C*H*$_3$).

Preparation of Cross-Linking Monomers:

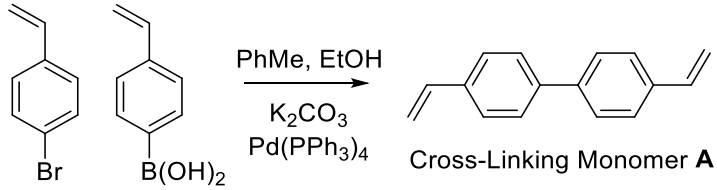

4-Bromostyrene (3.36 g, 18.35 mmol, 1.0 equiv) and 4-vinylphenylbornoic acid (xx g, mmol, equiv) were added as solids to a Schlenk tube and suspended in toluene (mL), ethanol (mL) and 2 M aqueous K_2CO_3 (mL). The reaction mixture was thoroughly degassed 3x before addition of $Pd(PPh_3)_4$ (mg, mmol, equiv), and the reaction was heated to 70 °C for 16 hr. The reaction was quenched with exposure to air, and the reaction was filtered over a silica plug and extracted with DCM. The volatiles were concentrated *in vacuo*, dissolved in DCM, and the mixture was washed 3x with water. The organic layer was dried with $MgSO_4$, and the volatiles were removed *in vacuo*. The product was

purified by column chromatography. The product was isolated as a light-yellow solid. Characterization is consistent with previous reports.[31]

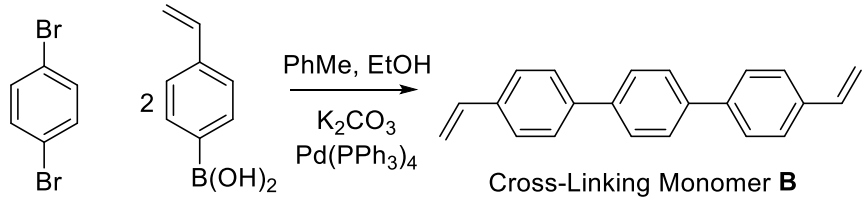

1,4 dibromobenzene (3.98 g, 16.89 mmol, 1.0 eqiv) and 4-vinylphenylbornoic acid (5 g, 33.79 mmol) were added as solids to a Schlenk tube and suspended in toluene (120 mL), ethanol (40 mL), and 2 M aqueous K_2CO_3 (66 mL). The reaction mixture was thoroughly degassed 3x before addition of $Pd(PPh_3)_4$ (400 mg, 0.3379 mmol, 0.02 equiv), and the reaction was heated to 70 °C for 16 hr. The reaction was quenched with exposure to air, and the reaction was filtered over a silica plug and extracted with DCM. The volatiles were concentrated *in vacuo*, dissolved in DCM, and the mixture was washed 3x with water. The organic layer was dried with $MgSO_4$, and the volatiles were removed *in vacuo*. The product was purified by column chromatography. The product was isolated as a light-yellow solid. Characterization is consistent with previous reports.

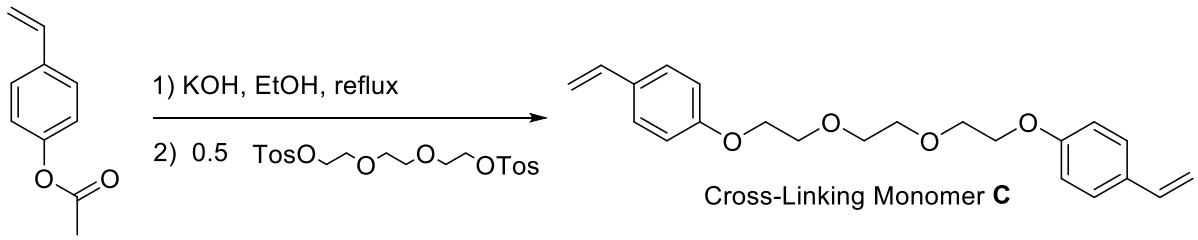

4-Acetoxystyrene (1.965 g, 12.12 mmol, 2.0 equiv) was dissolved in EtOH followed by addition of KOH (0.85 g, 15.15 mmol, 2.5 equiv). The reaction was heated to 70 °C for 1.5 hr, followed by addition of triethylene glycol di(*p*-toluenesulfonate) (2.77 g, 6.05 mmol, 1.0 equiv). The reaction was stirred for 16 hr at RT. The volatiles were concentrated *in vacuo*, dissolved in DCM, and the mixture was washed 3x with water. The product was purified by column chromatography. The product was isolated at a white solid. Characterization is consistent with previous reports.

General Procedure for Synthesis of Neutral Homopolymer: The reaction was conducted under an inert atmosphere. The neutral monomer (methoxystyrene or vinylbiphenyl) was dissolved in MeCN (4 mL). AIBN (26 mg, 0.1equiv) was added and rinsed with MeCN (1 mL). The vial was sealed, removed from the glovebox, and heated at 70 ºC for 3 days. The reaction was quenched by exposure to air. The crude material concentrated, redissolved in THF, and precipitated into MeOH (100 mL). The polymer was isolate as a fine white solid.

General Procedure for Copolymer Synthesis: The reaction was conducted under an inert atmosphere. The neutral monomer (methoxystyrene or vinylbiphenyl) was added to a 20-mL scintillation vial and dissolved in MeCN (2 mL) followed by addition of K-STFSI dissolved in MeCN (2 mL). AIBN (0.1 equiv) was added and rinsed with MeCN (1mL). The vial was sealed, removed from the glovebox, and heated at 70ºC for 3 days. The reaction was quenched by exposure to air. The crude polymer was precipitated into Et_2O (100 mL) and filtered. The precipitate was stirred with 20 mL of an aqueous solution of 1 M $KHCO_3$ at 90ºC for a minimum of 30 minutes. The mixture was filtered hot over a glass frit. An additional 2 washes with 1 M $KHCO_{3(aq)}$ were necessary for most purifications. The solid material was extracted with MeCN, concentrated under reduced vacuum, redissolved in MeCN, and filtered. The filtrate was precipitated with Et_2O (100 mL) and filtered. The polymer dried under vacuum and was isolated as a fine white solid.

General Procedure for Cross-Linking Copolymers Synthesis with Cross-Linking Monomer A: The reaction was conducted under an inert atmosphere. The neutral monomer (methoxystyrene or vinylbiphenyl) was added to a 20-mL scintillation vial and dissolved in MeCN (2 mL) followed by addition of cross-linking comonomer and K-STFSI dissolved in MeCN (1 mL, each). AIBN (0.1 equiv) was added and rinsed with MeCN (1mL). The vial was sealed, removed from the glovebox, and heated at 70ºC for 3 days. The reaction was quenched by exposure to air. The polymer was

precipitated into Et_2O (100 mL) and filtered. The precipitate was stirred with 20 mL of an aqueous solution of 1 M $KHCO_3$ at 90ºC for a minimum of 30 minutes. The mixture was filtered hot over a glass frit. An additional 2 washes with 1 M $KHCO_{3(aq)}$ were necessary for most purifications. The solid material was extracted with MeCN, concentrated under reduced vacuum, redissolved in MeCN, and filtered. The filtrate was precipitated with Et_2O (100 mL) and filtered. The polymer dried under vacuum and was isolated as a fine white solid.

General Procedure for Cross-Linking Copolymers Synthesis with Cross-Linking Monomers B and C: The reaction was conducted under an inert atmosphere. The neutral monomer (methoxystyrene or vinylbiphenyl) was added to a 20-mL scintillation vial and dissolved in DMF (2 mL) followed by addition of cross-linking comonomer and K-STFSI dissolved in DMF (1 mL, each). AIBN (0.1 equiv) was added and rinsed with DMF (1mL). The vial was sealed, removed from the glovebox, and heated at 70ºC for 3 days. The reaction was quenched by exposure to air. DMF was removed *in vacuo*, and the crude polymer was redissolved in minimal MeCN (~5 mL). The polymer was precipitated into Et_2O (100 mL) and filtered. The precipitate was stirred with 20 mL of an aqueous solution of 1 M $KHCO_3$ at 90ºC for a minimum of 30 minutes. The mixture was filtered hot over a glass frit. An additional 2 washes with 1 M $KHCO_{3(aq)}$ were necessary for most purifications. The solid material was extracted with MeCN, concentrated under reduced vacuum, redissolved in MeCN, and filtered. The filtrate was precipitated with Et_2O (100 mL) and filtered. The polymer dried under vacuum and was isolated as a fine white solid.

Note about Polymer Purification: For some copolymers with a higher content of charged comonomer where some moderate solubility in 90 ºC 1 M $KHCO_3$ is observed, an alternative purification was used to removed unreacted K-STFSI. The crude polymer was dissolved in minimal MeCN (< 5 mL) and precipitated by addition to 1 M aqueous $KHCO_3$ (25 mL). The purification was

repeated until residual unreacted monomer was removed (generally 3-5 washes). The polymer was then further purified with the same procedure described above (redissolved in MeCN, filtered, and precipitated with Et_2O).

Electrochemistry

Electrolyte Preparation

Potassium bicarbonate electrolyte (1 M $KHCO_{3(aq)}$) was prepared by sparging an aqueous solution of potassium carbonate (0.5 M $K_2CO_{3(aq)}$) with CO_2 for at least 1 hour prior to electrolysis. This process converts K_2CO_3 into $KHCO_3$ and saturates the electrolyte solution with CO_2.

Electrode Preparation

The gas diffusion electrodes (GDEs) were prepared by sputtering 300 nm Cu onto a 5 cm x 5 cm portion of polytetrafluoroethylene membrane (pore size of 450 nm, with polypropylene support on backside) using a pure Cu target (99.99%) at a sputtering rate of 1 Å s^{-1}.

A 0.3 mg mL^{-1} stock solution of the ionomer was prepared in 50% v/v EtOH/^{i}PrOH and sonicated for 30 minutes to ensure complete dissolution. For a standard loading, 15 µL were drop casted (4.5 µg) onto a 2.5 cm^2 electrode, ensuring complete coverage of the Cu nanoparticles, and allowed to dry under ambient conditions for 1 hour.

Electrochemical Measurements in the GDE (Flow) Cell

CO_2R and COR measurements were conducted in a gas-tight liquid-electrolyte flow cell. Chronoamperometry experiments were carried out in a custom-made PEEK liquid-electrolyte cell similar to the one reported by Sargent and co-workers.[7] The liquid-electrolyte flow cell consists of three compartments: gas chamber, catholyte chamber, and anolyte chamber. The PTFE electrode was sandwiched between CO_2 gas chamber and catholyte chamber with an exposure area of 0.5 cm^{-2}. Catholyte and anolyte chambers were separated by a Selemion AMV anion-exchange membrane

(AGC Engineering Co.). The reference electrode was calibrated against H^+/H_2 on Pt in a 0.5 M sulfuric acid solution (0 V vs. RHE) and saturated calomel electrode (SCE) (+0.241 V saturated vs. RHE). An Autolab PGSTAT204 in a potentiostatic mode was used as electrochemical workstation. The PTFE electrode, leakless Ag/AgCl electrode (Innovative Instruments), and Pt mesh (rinsed with water and annealed with a butane torch) were employed as working, reference and counter electrodes, respectively. The applied potentials were converted to the reversible hydrogen electrode (RHE) scale with iR correction through the following equation:

$$E_{corrected}\ (\text{vs. RHE}) = E\ (\text{vs. Ag/AgCl}) + (0.059 \times \text{pH}) + 0.210 + iR. \quad (1)$$

$E_{applied}$ in this report is the applied potential without iR compensation. In order to convert from potential vs. Ag/AgCl, we use the following relationship:

$$E_{applied}\ (\text{vs. RHE}) = E\ (\text{vs. Ag/AgCl}) + (0.059 \times \text{pH}) + 0.210 \quad (2)$$

where i is the current at each applied potential and R is the equivalent series resistance measured via potentioelectrochemical impedance spectroscopy (PEIS) in the frequency range of 10^5 – 0.1 Hz with an amplitude of 10 mV. The appropriate gas-saturated electrolyte was used as both catholyte and anolyte and was circulated through the flow cell using peristaltic pumps with a silicone Shore A50 tubing. The electrolyte was bubbled with the desired gas during the entire electrolysis process. The electrolyte flow rate was kept at 10 mL min^{-1}. The flow rate of the gas flowing into the gas chamber was kept at 30 sccm by a digital mass flow controller.

Ohmic resistance values were determined with procedures described elsewhere[39,40] and employed in our prior work[7–9] PEIS measurements were carried out prior to and after each electrolysis experiment

to determine the Ohmic resistance of the flow cell and ensure it is unchanged during the experiment.[41,42] The impedance measurements were carried out at frequencies ranging from 200 kHz to 100 MHz. A Nyquist plot was obtained, and in the low-frequency region (containing a Warburg element) a line was plotted to determine the value of the intersection with the x-axis, representing the Ohmic resistance.[39] An average of 3 measurements was taken to calculate the value of R. Typically, small resistances were measured, ranging from 4 to 7 Ω. The potentiostat was set to compensate for 85 % of the Ohmic drop, with the remaining 15 % being compensated for after the measurements.[39,40]

All chronoamperometric experiments were performed for 30 min at 25 °C. Before each electrolysis experiment, the ionomer was drop casted onto a 2.5 cm^2 Cu/PTFE electrode. The entire Ohmic drop was compensated before and after the measurement. The effluent gas stream coming from the cell (30 mL min^{-1}) was flowed into the sample loops of a gas chromatograph (GC-FID/TCD, SRI 8610C, in Multi Gas 5 configuration) equipped with HayeSep D and Molsieve 5A columns. Methane, ethylene, ethane, and carbon monoxide were detected by a methanizer-flame ionization detector (FID) and the hydrogen was detected by a thermal conductivity detector (TCD). Every 15 minutes, 2 mL of gas was sampled to determine the concentration of gaseous products. After electrolysis, the liquid products in the catholytes were quantified by both HPLC (Thermo Scientific Ultimate 3000) and ^{1}H NMR spectroscopy (Bruker 400 MHz Spectrometer).

For ^{1}H NMR analysis, 630 µL of the electrolyte sample were combined with 30 µL of internal standard solution (10 mM DMSO and 50 mM phenol) and 70 µL of D_2O. Water suppression was achieved with a presaturation sequence.[8,42]

The Faradaic efficiencies for gaseous products was calculated from the following equations:

$$F_m = \frac{pF_v}{RT} \qquad (3)$$

$$FE_{prod} = \frac{n_{prod}Fx_{prod}F_m}{i}. \qquad (4)$$

F_m is the molar flow, defined by the pressure p, the volume flow F_v, the gas constant R, and temperature T. FE_{prod} is the Faradaic efficiency of a gaseous product $prod$, defined by the electron transfer coefficient of the product n_{prod}, Faraday's constant F, the fraction of the product x_{prod}, the molar flow F_m, and the current i.

Error bars shown in all figures and tables represent standard deviations from at least three replicate measurements.

SUPPLEMENTARY FIGURES/DATA

NMR spectra of polymers (**obtained by Meaghan A. Bruening*)

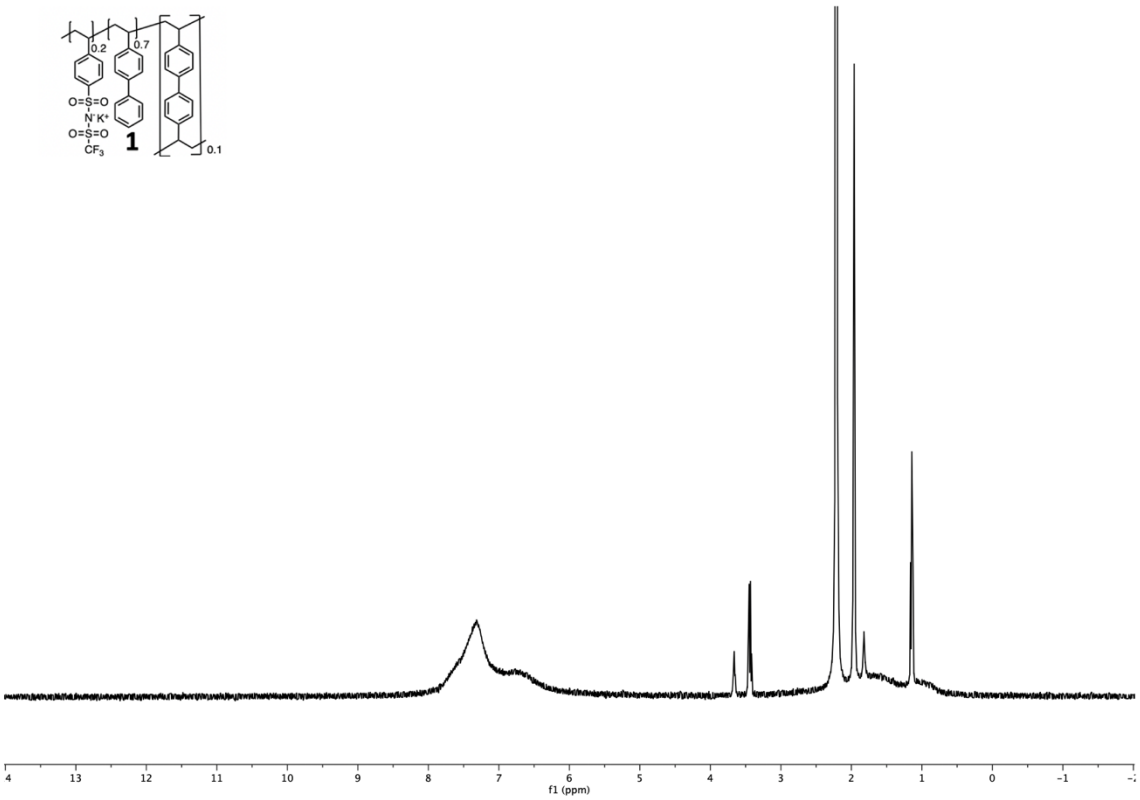

Figure 5. ^{1}H NMR spectrum of **1**.

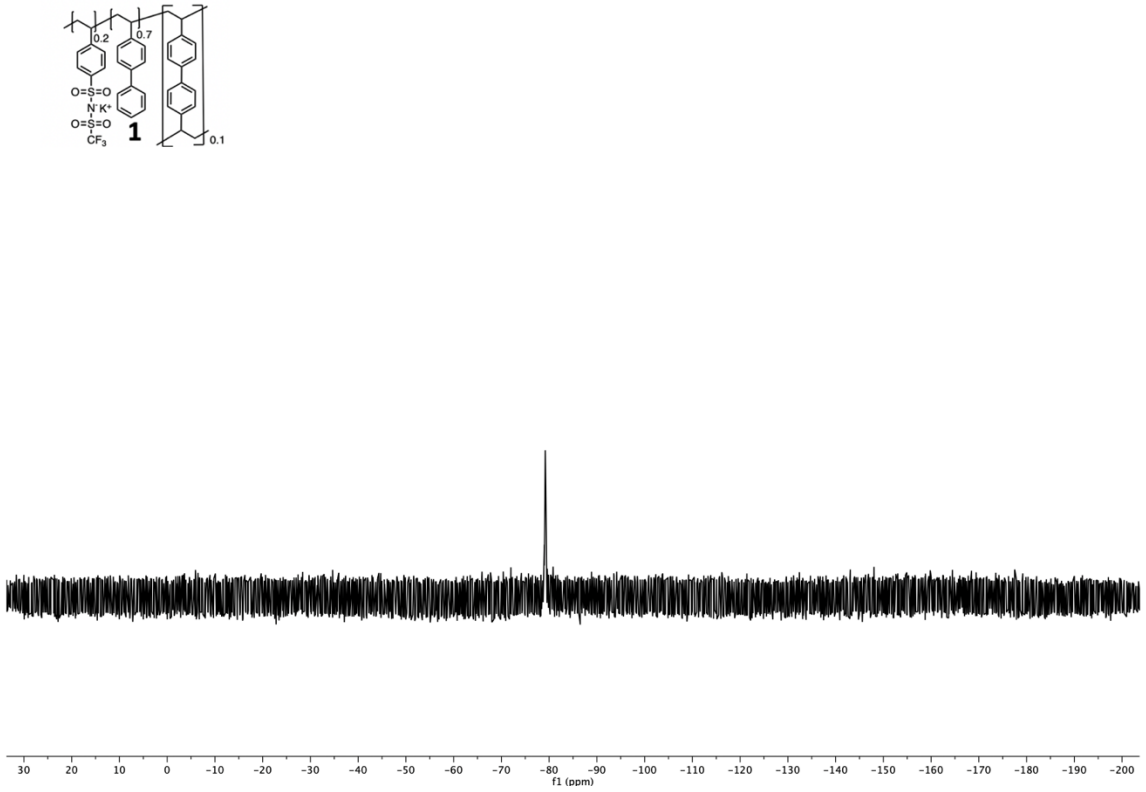

Figure 6. ^{19}F NMR spectrum of **1**.

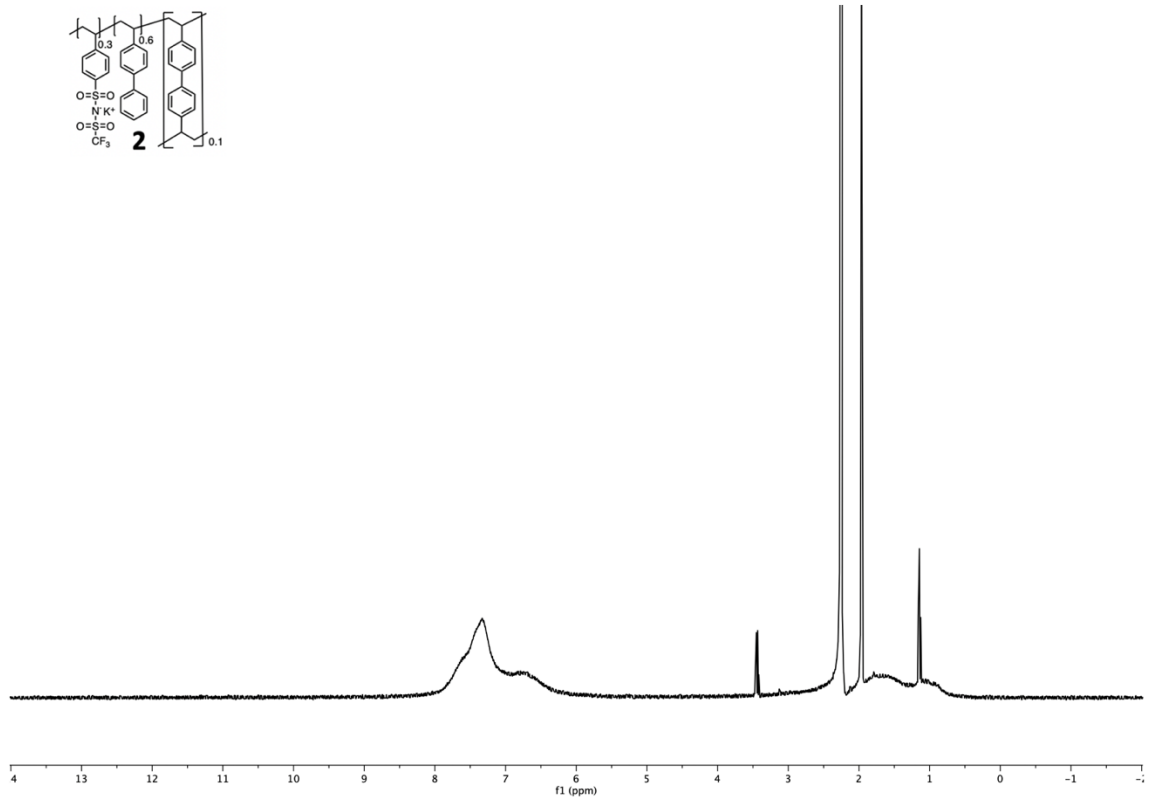

Figure 7. ^{1}H NMR spectrum of **2**.

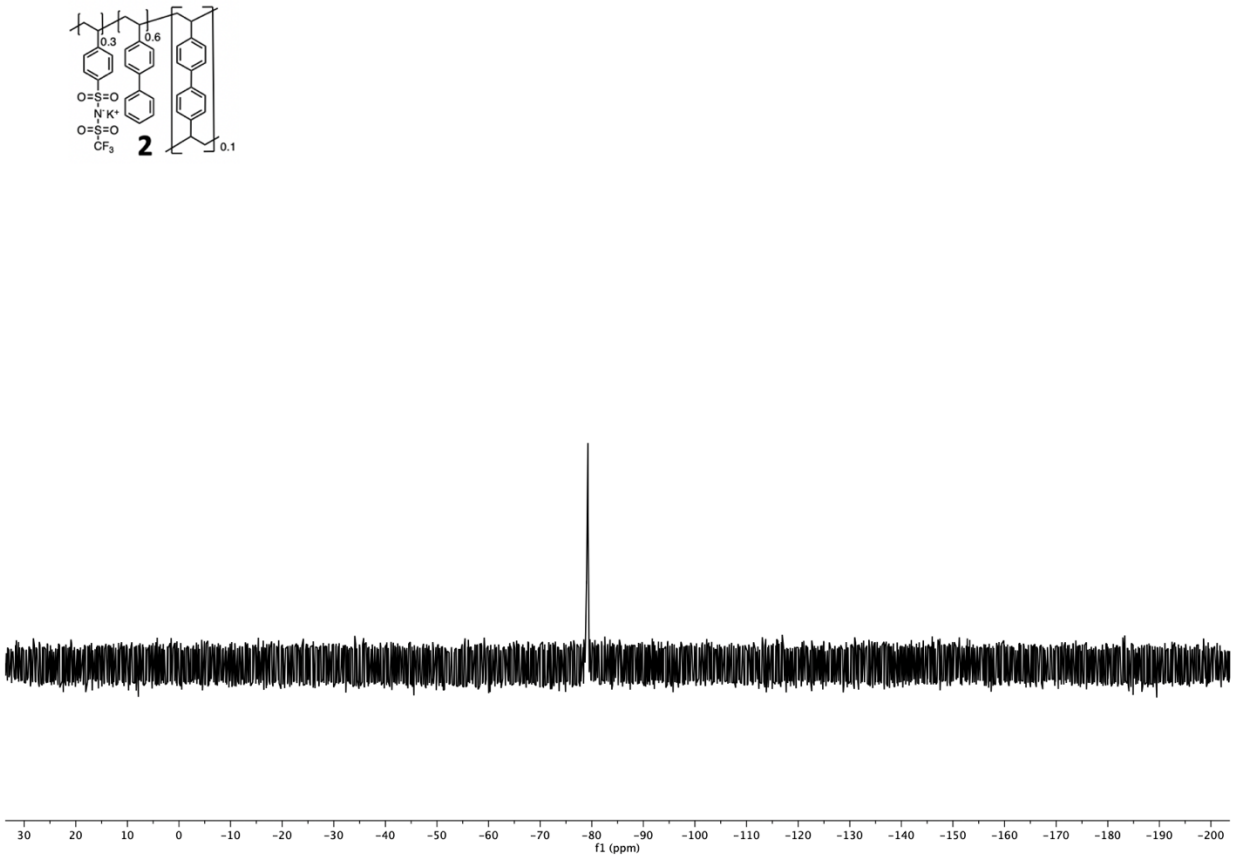

Figure 8. ^{19}F NMR spectrum of **2**.

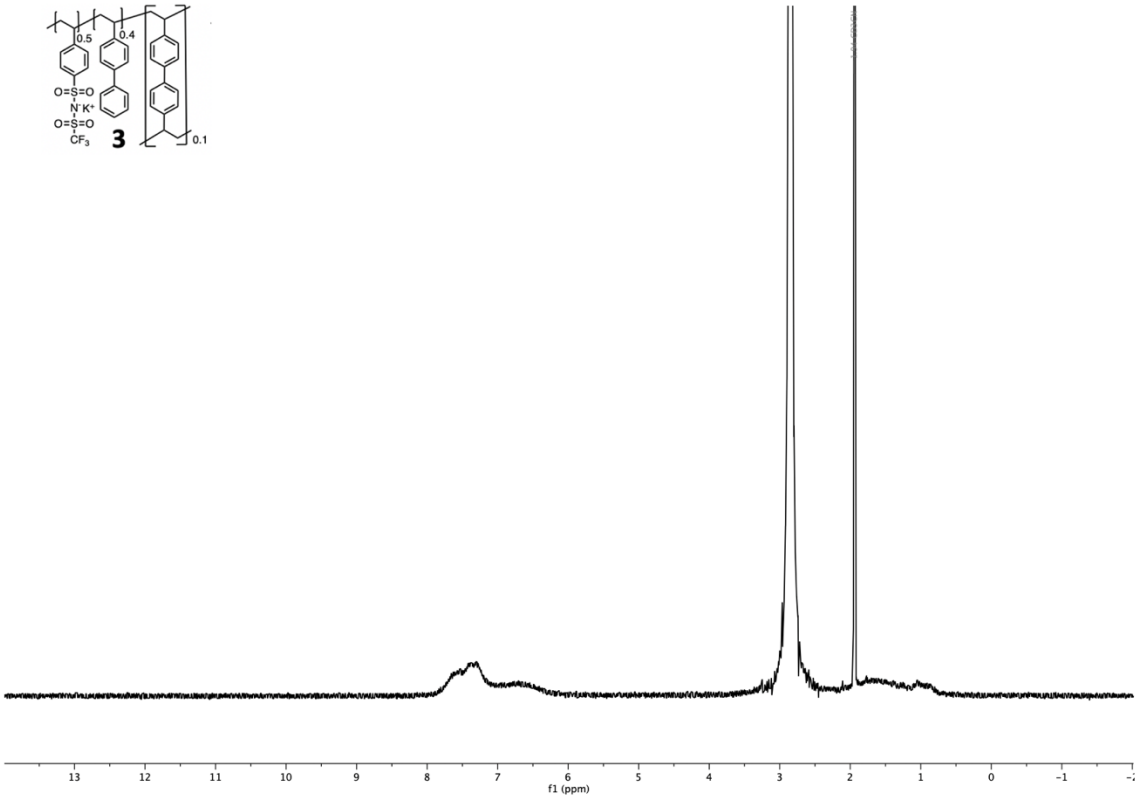

Figure 9. ^{1}H NMR spectrum of **3**.

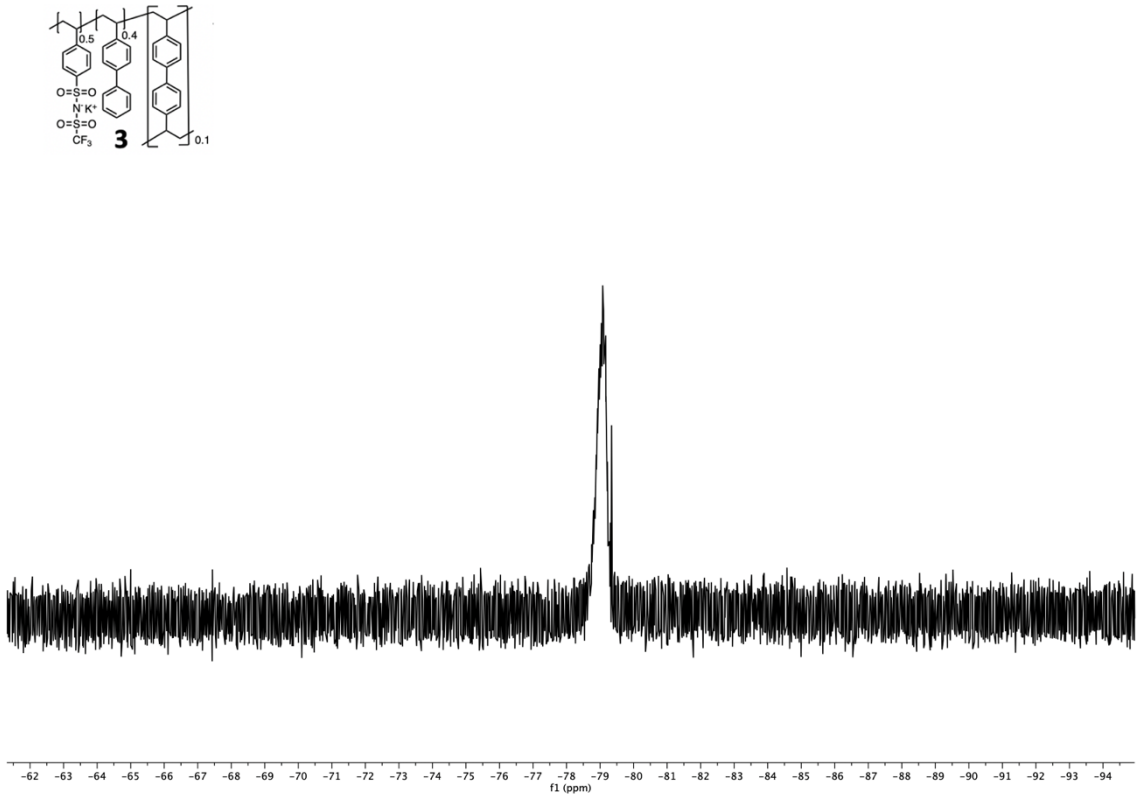

Figure 10. ^{19}F NMR spectrum of **3**.

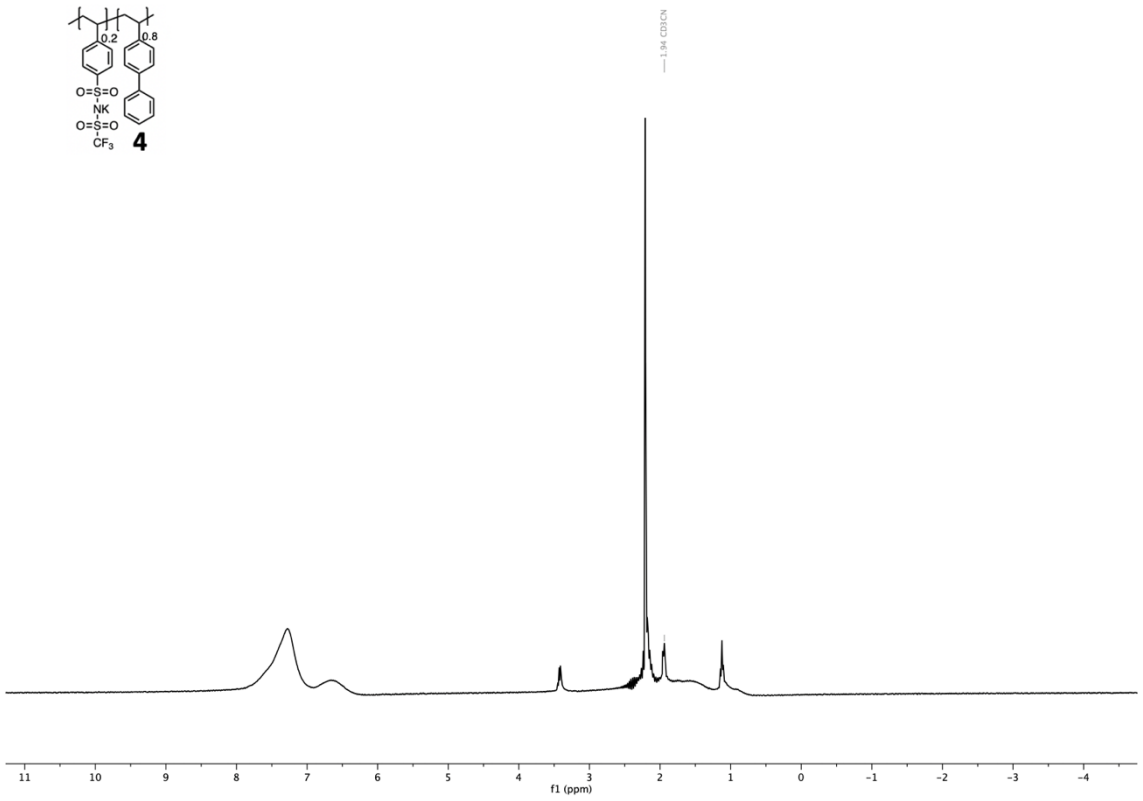

Figure 11. ^{1}H NMR spectrum of **4**.

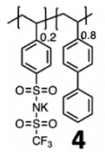

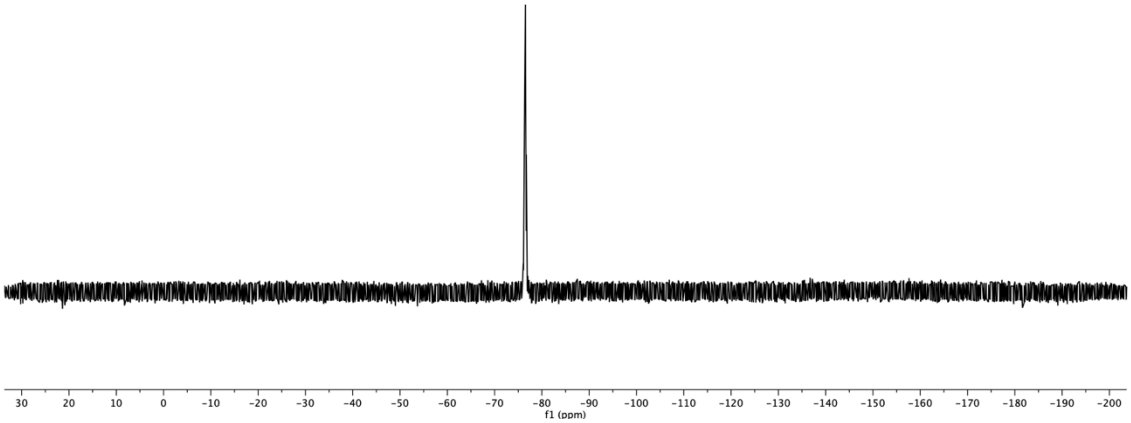

Figure 12. ^{19}F NMR spectrum of **4**.

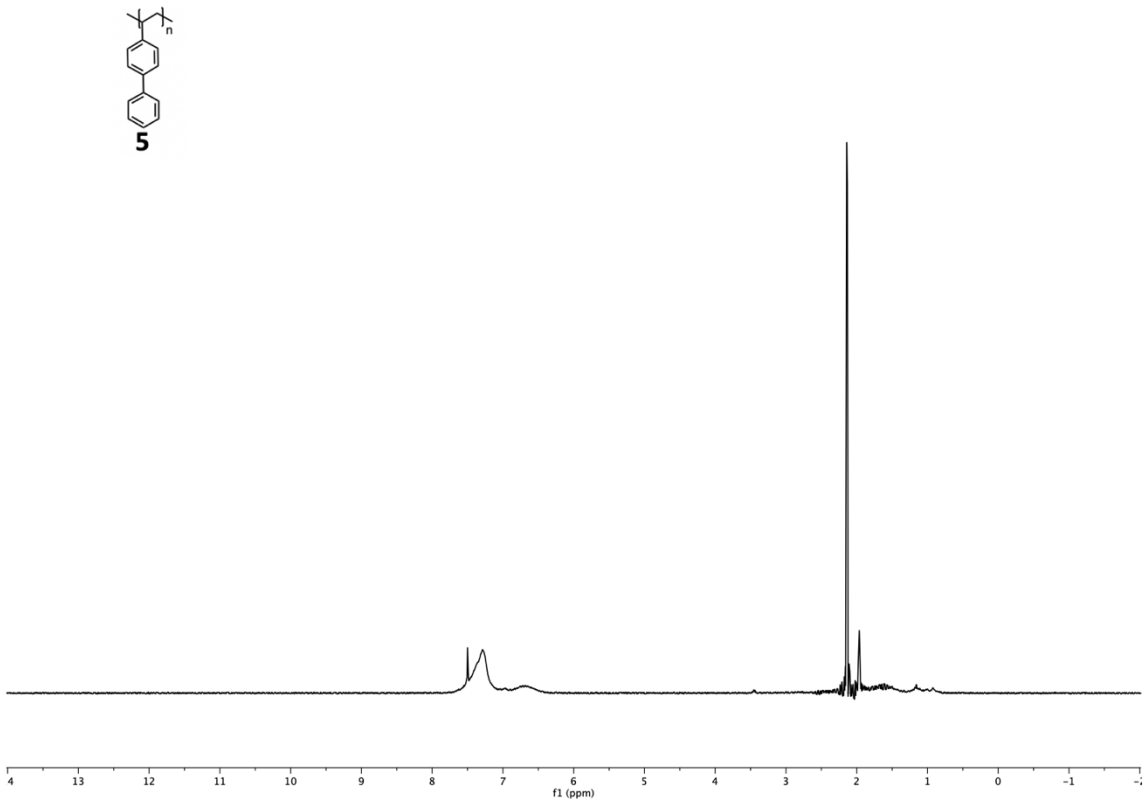

Figure 13. ^{1}H NMR spectrum of **5**.

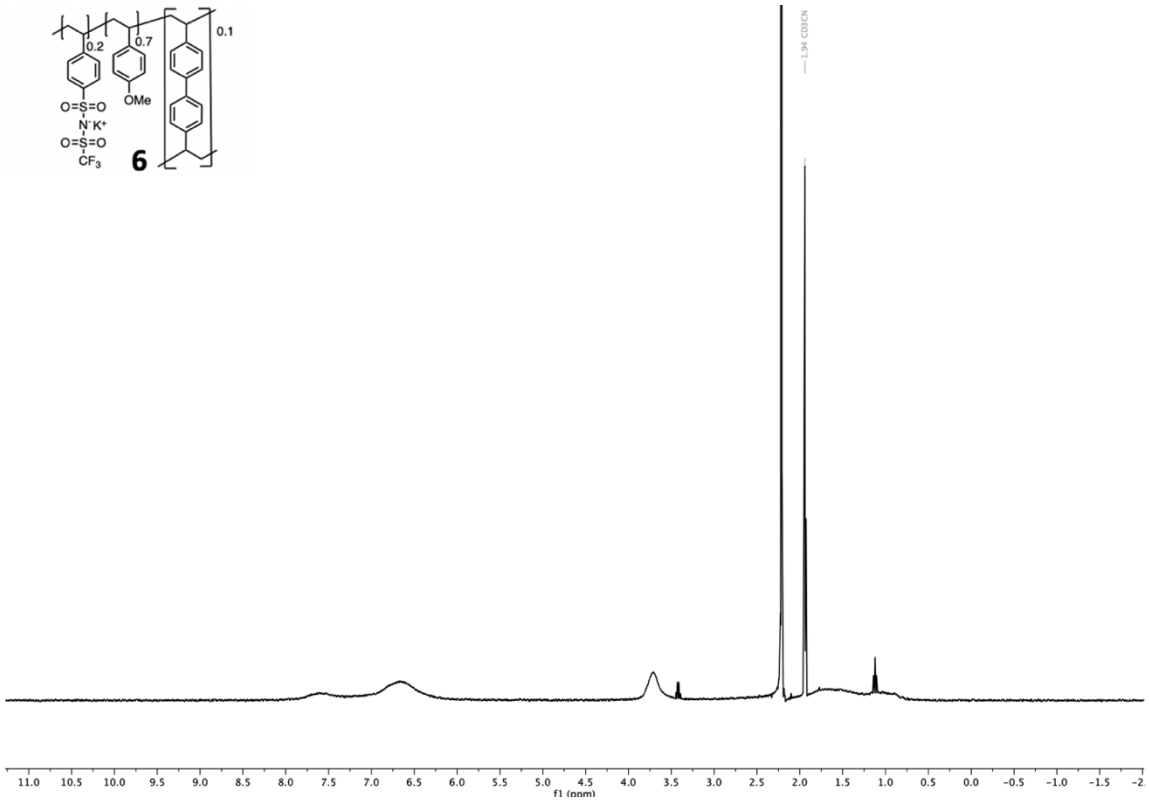

Figure 14. ^{1}H NMR spectrum of **6**.

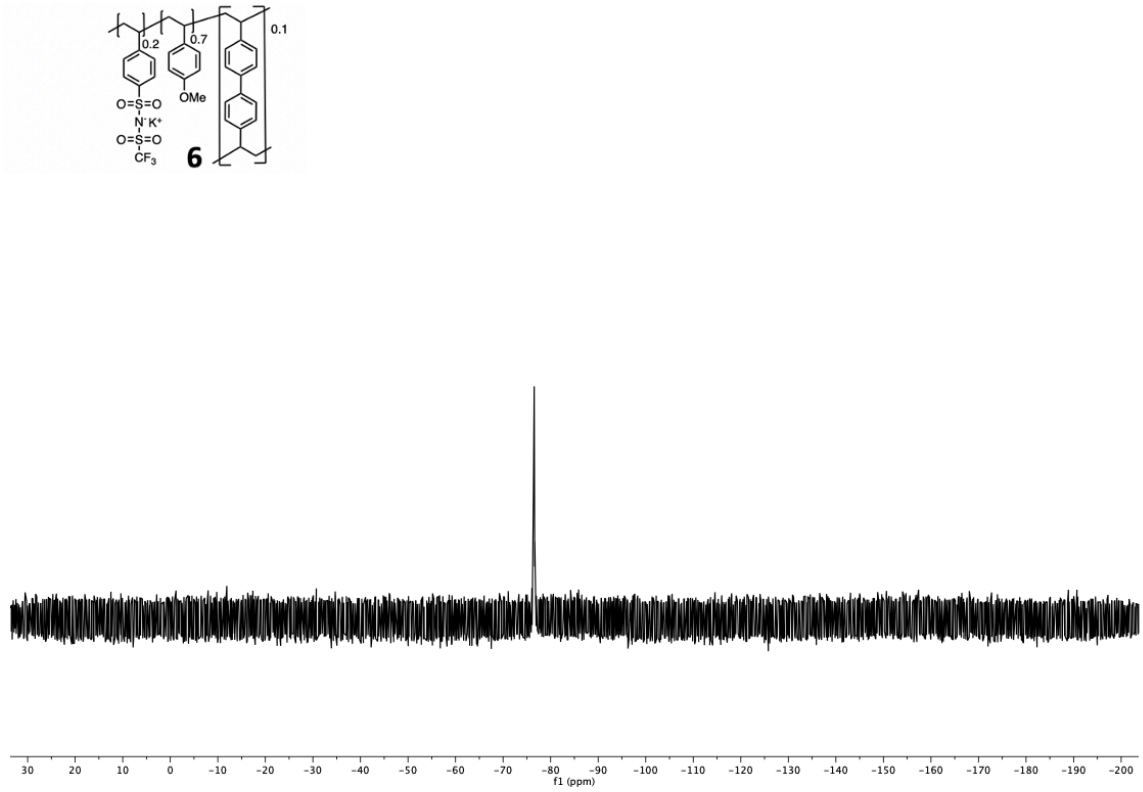

Figure 15. ^{19}F NMR spectrum of **6**.

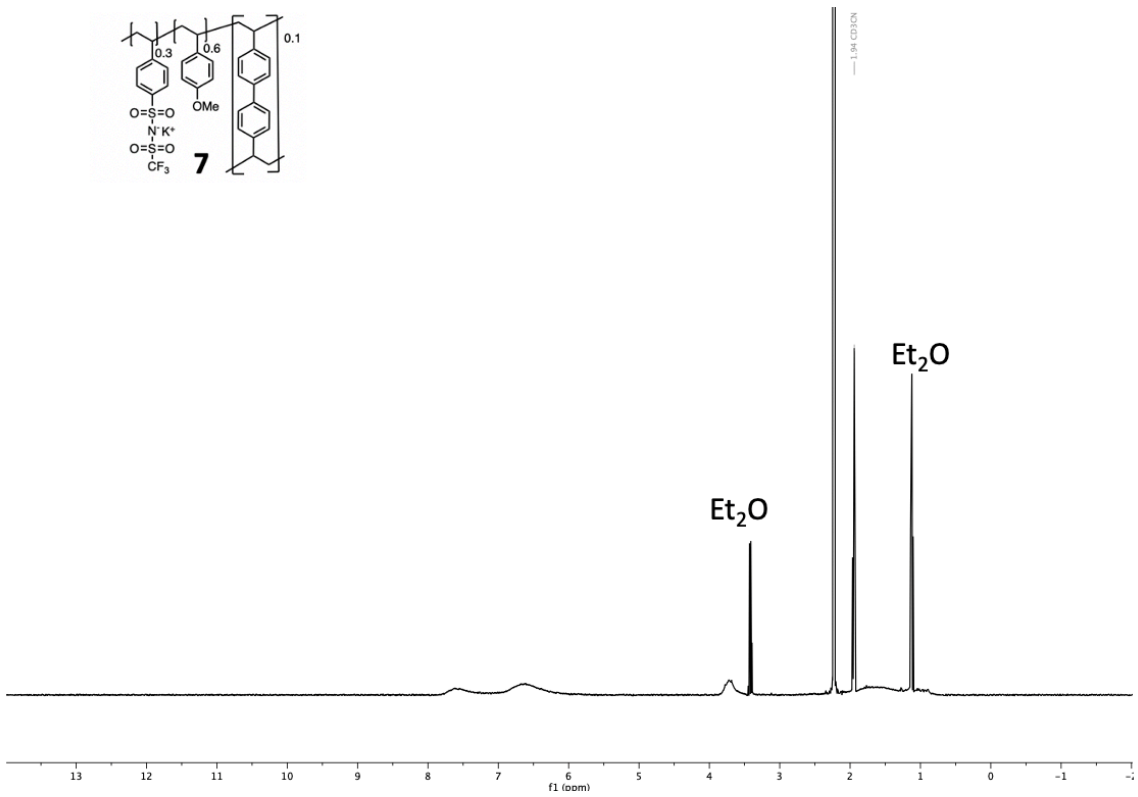

Figure 16. ^{1}H NMR spectrum of **7**.

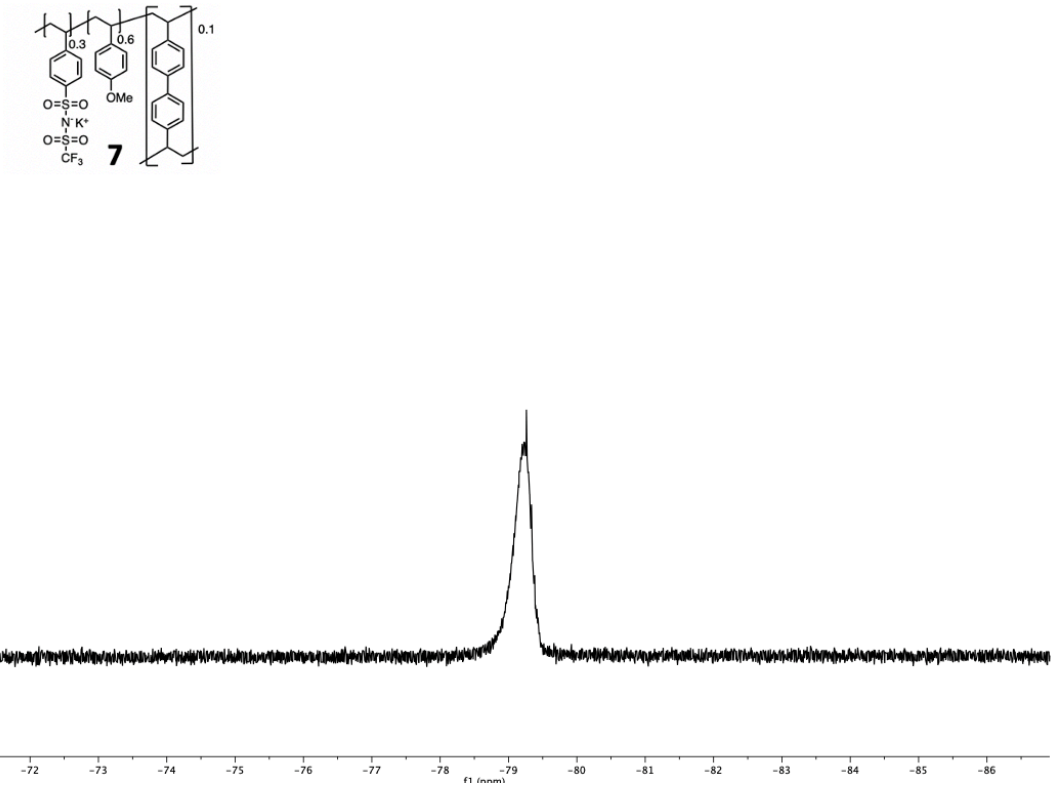

Figure 17. ^{19}F NMR spectrum of **7**.

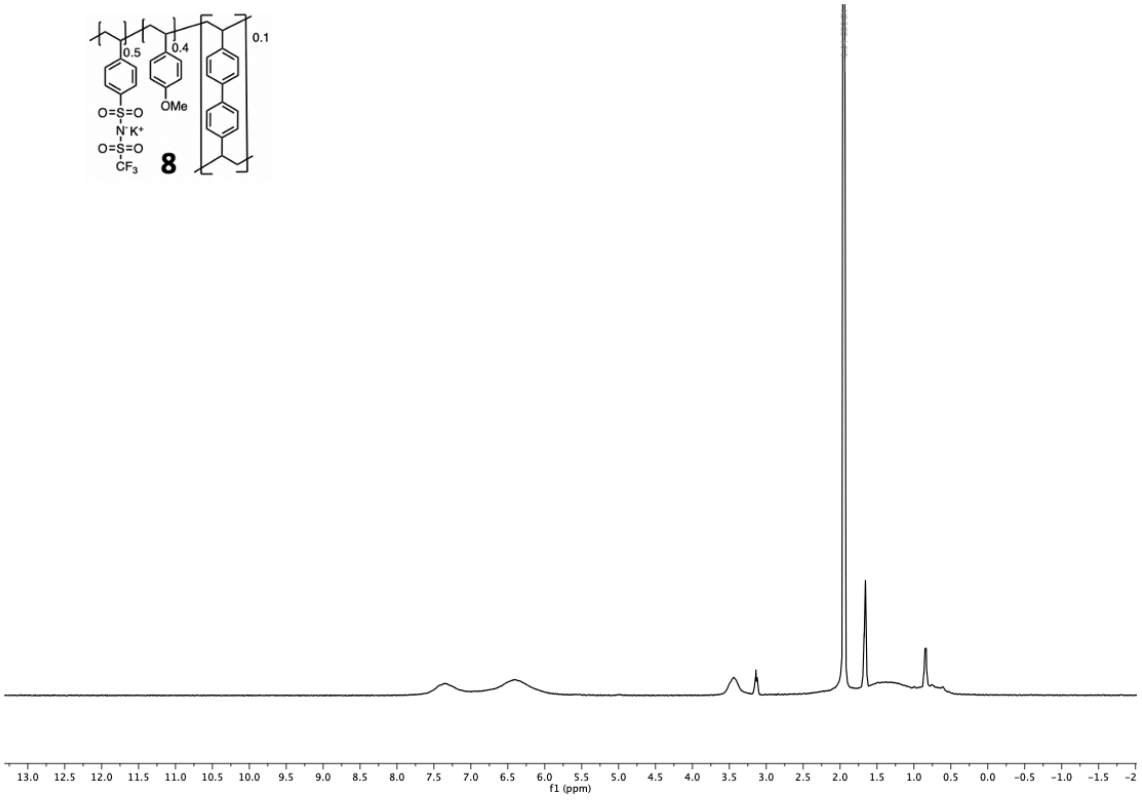

Figure 18. ^{1}H NMR spectrum of **8.**

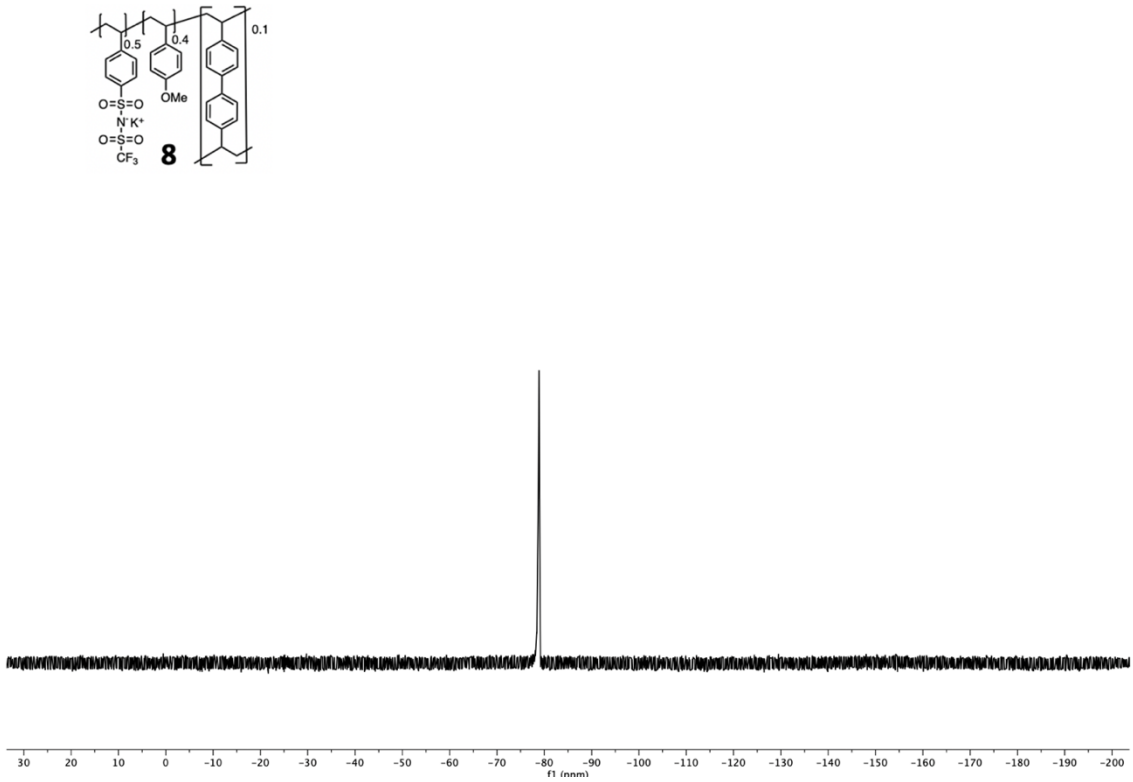

Figure 19. ^{19}F NMR spectrum of **8.**

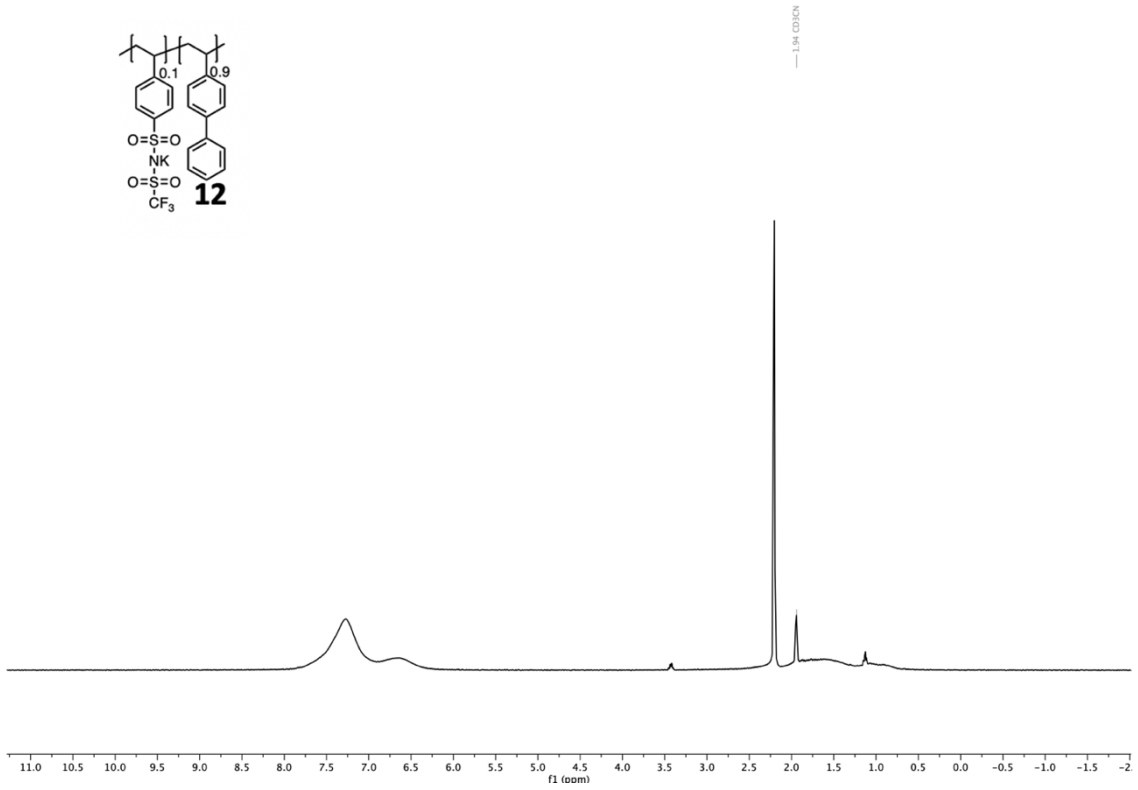

Figure 20. ^{1}H NMR spectrum **12**.

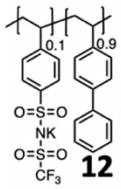

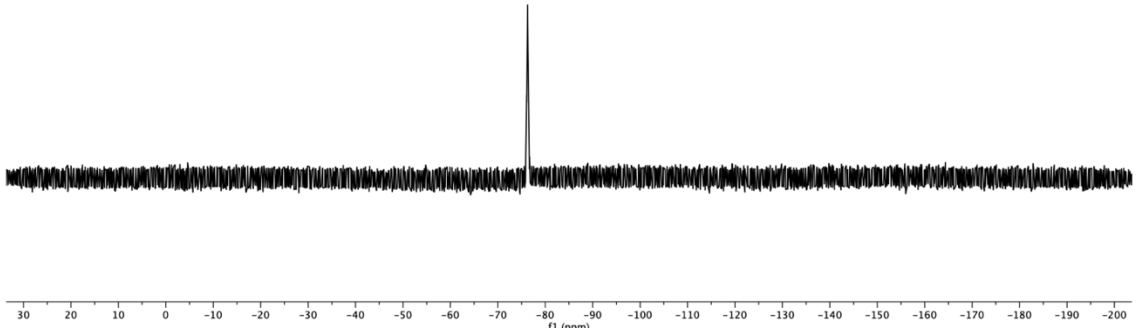

Figure 21. ^{19}F NMR spectrum **12**.

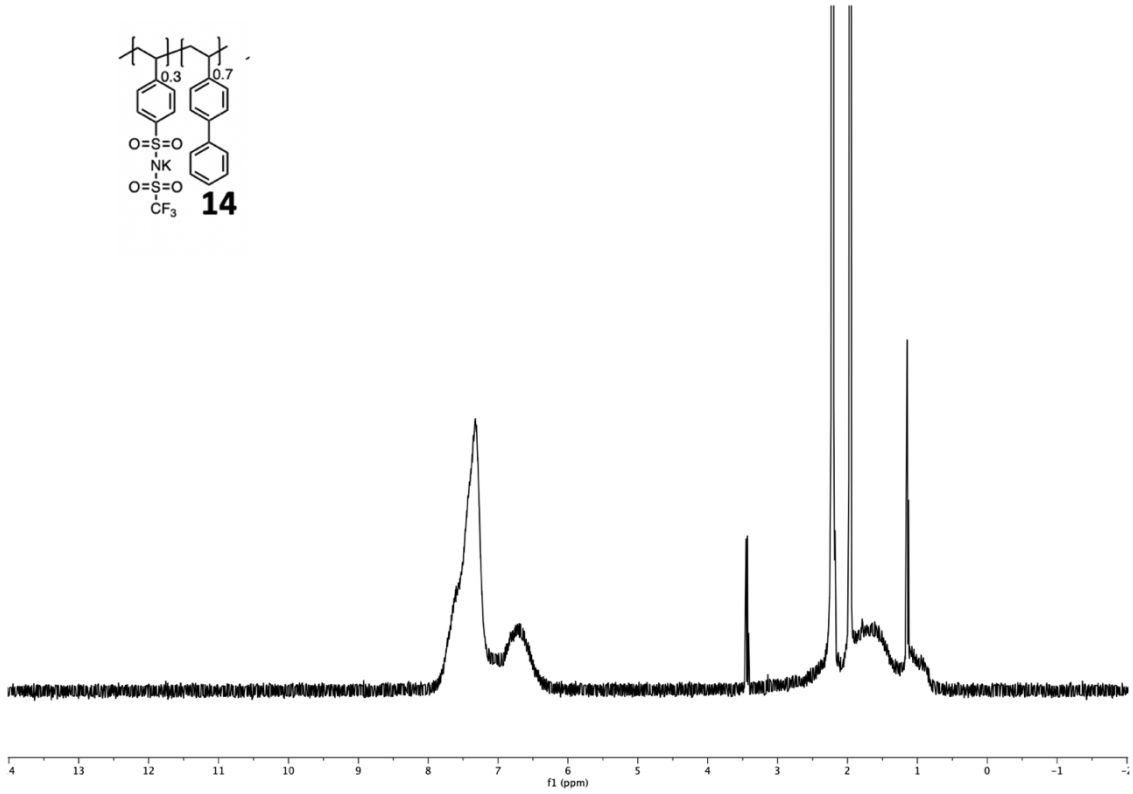

Figure 22. ^{1}H NMR spectrum **14**.

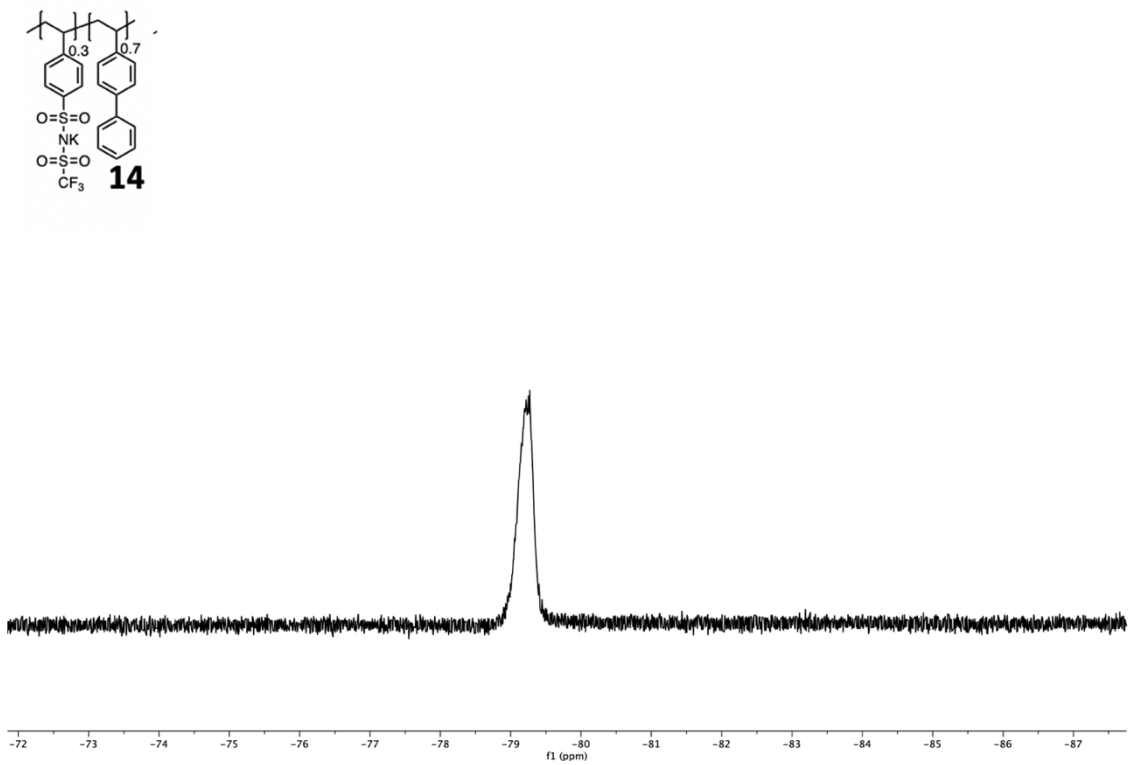

Figure 23. ^{19}F NMR spectrum **14**.

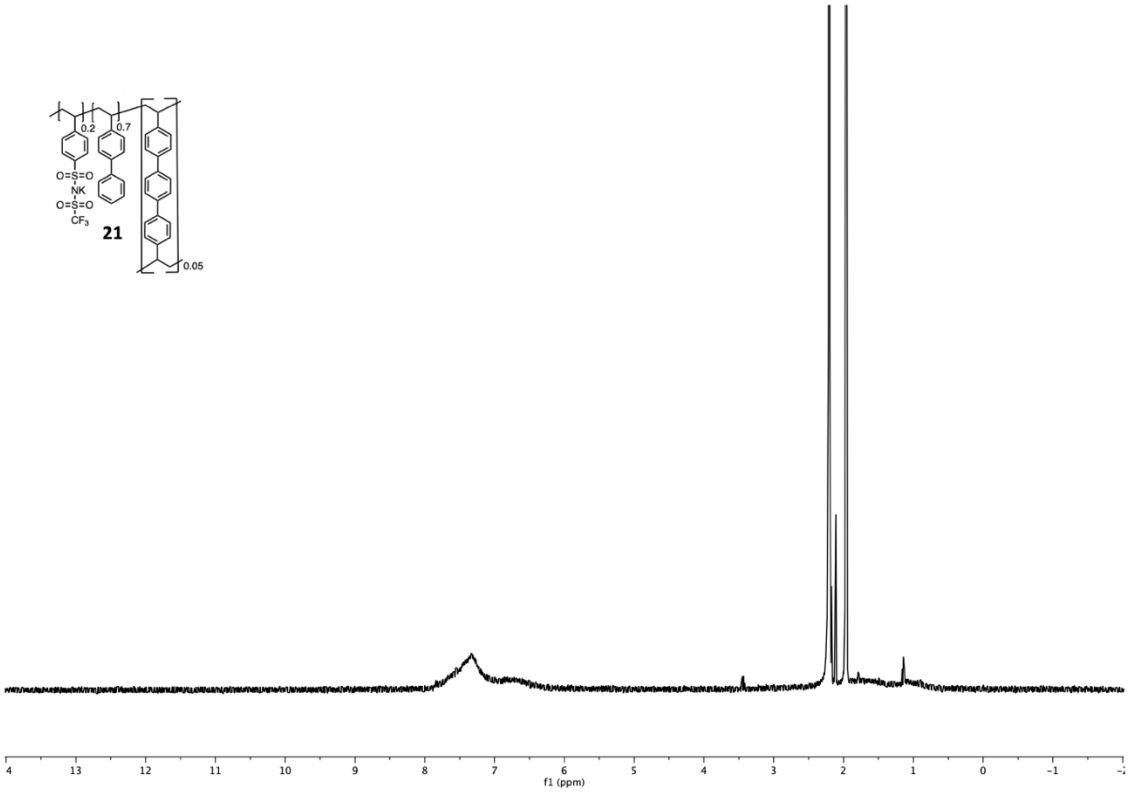

Figure 24. ^{1}H NMR spectrum **21**.

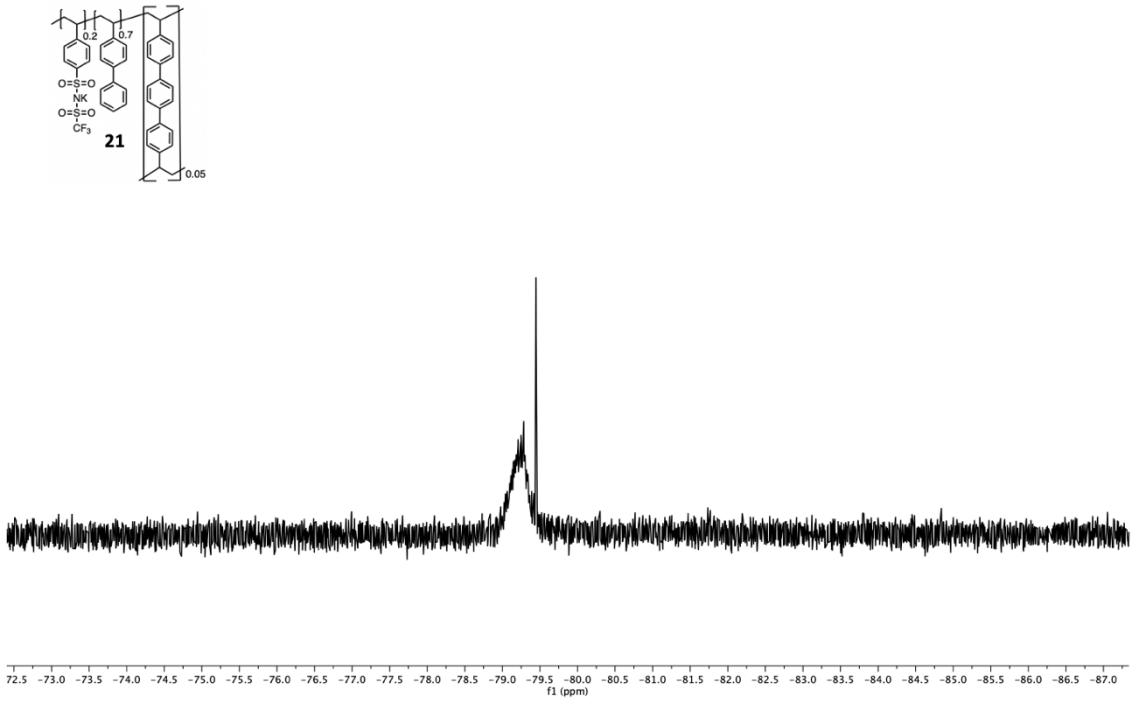

Figure 25. ^{19}F NMR spectrum **21**.

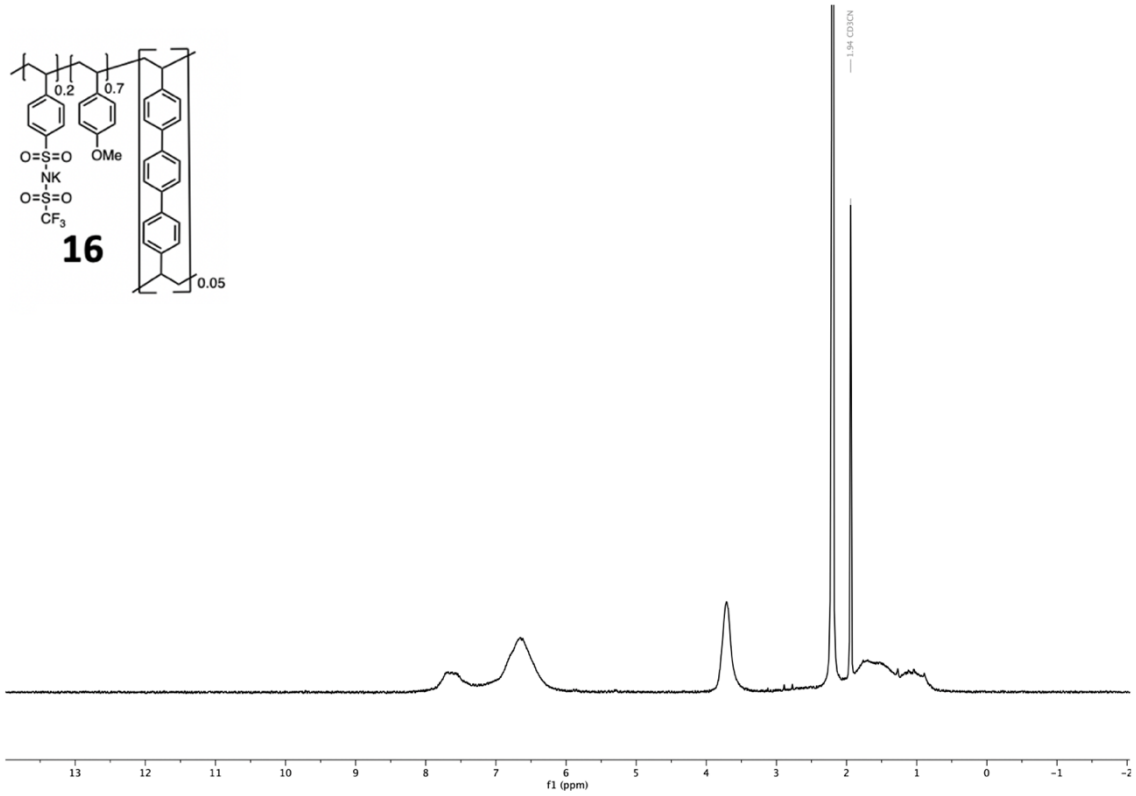

Figure 26. ^{1}H NMR spectrum **16**.

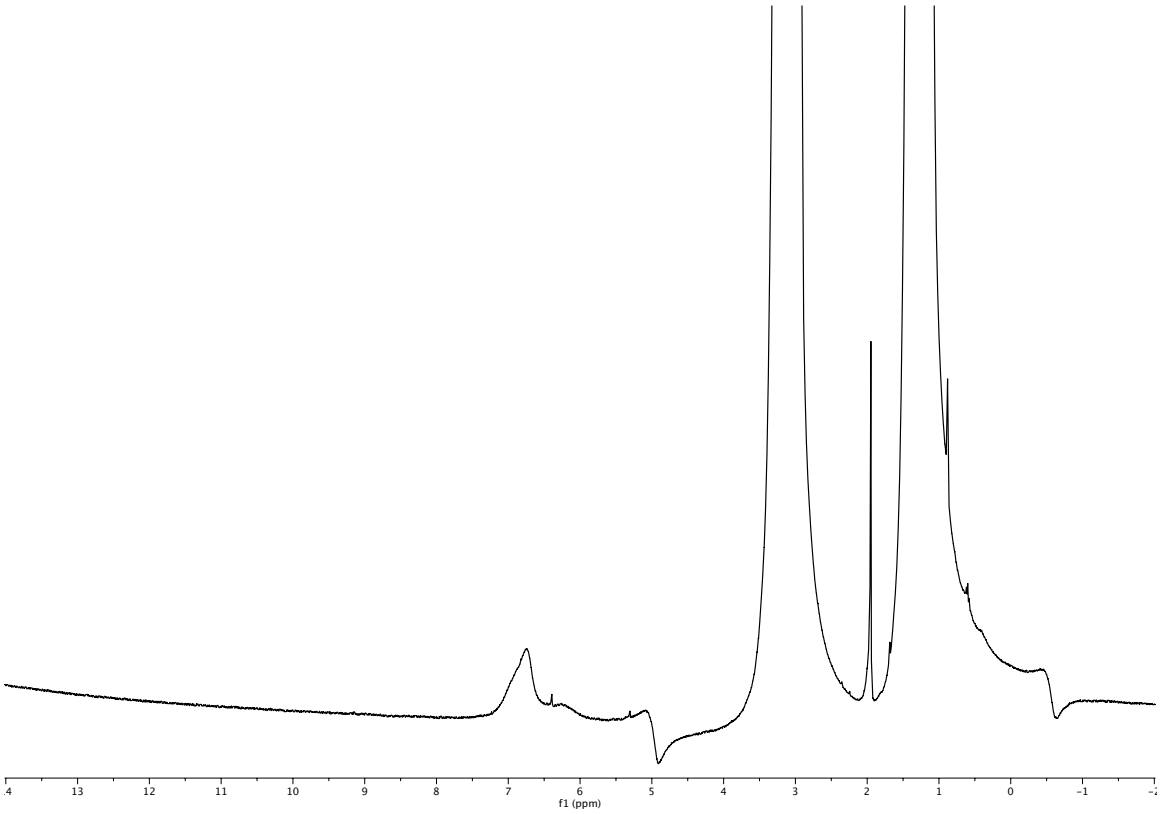

Figure 27. ^{1}H NMR spectrum **17**.

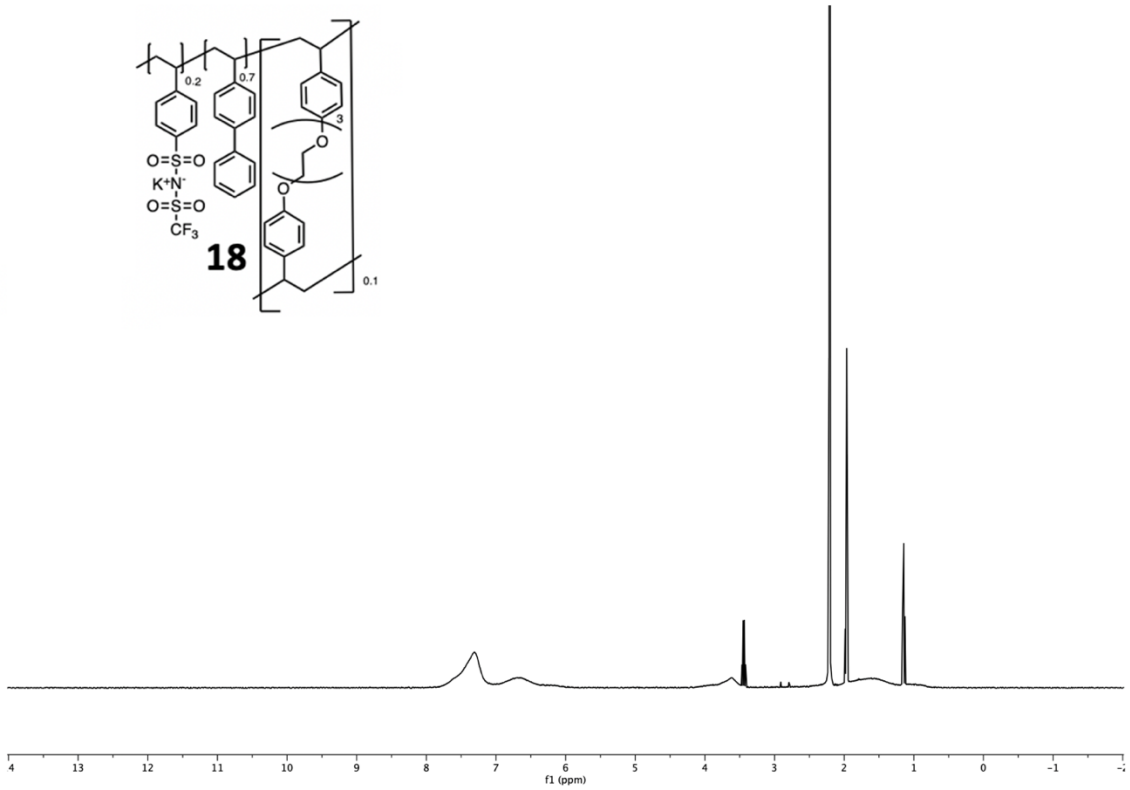

Figure 28. ^{1}H NMR spectrum **18**.

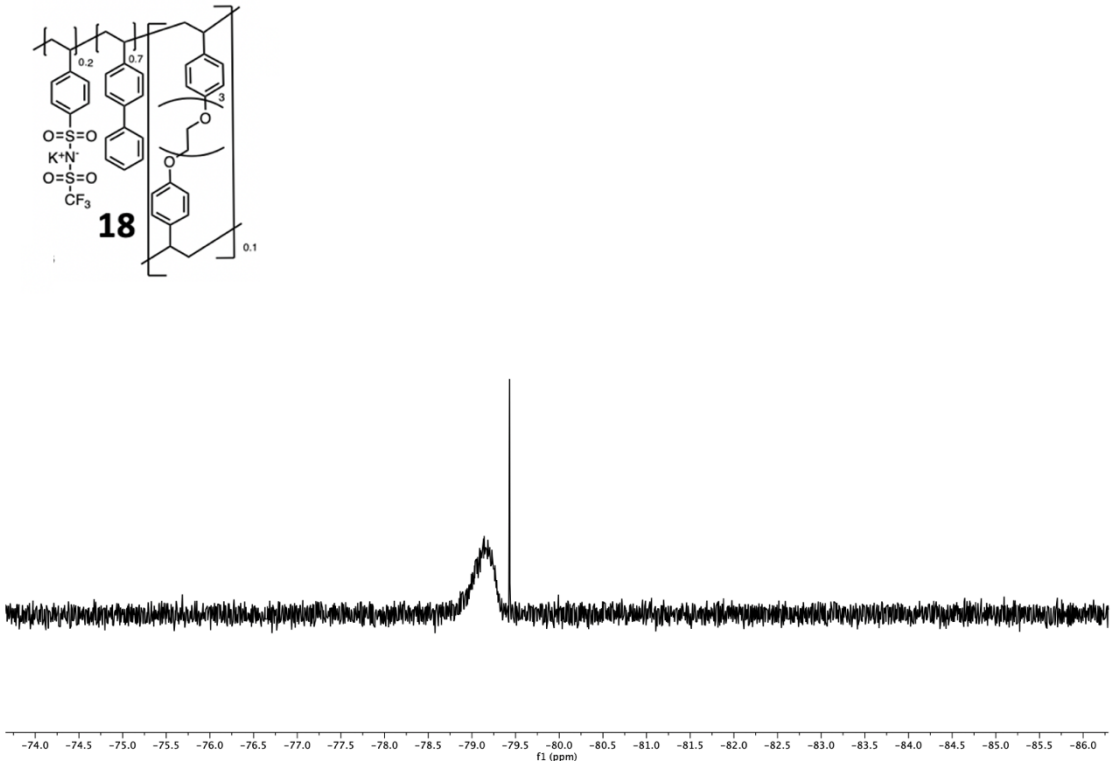

Figure 29. ^{19}F NMR spectrum **18**.

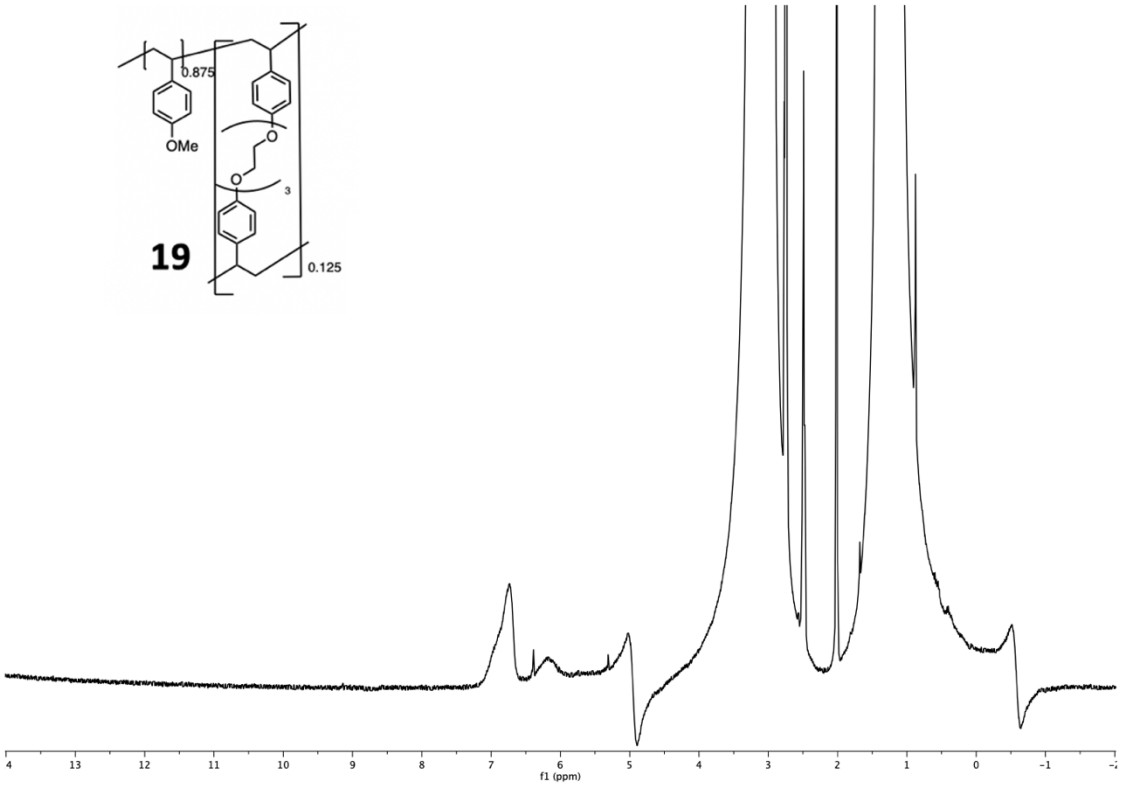

Figure 30. ^{1}H NMR spectrum of **19.**

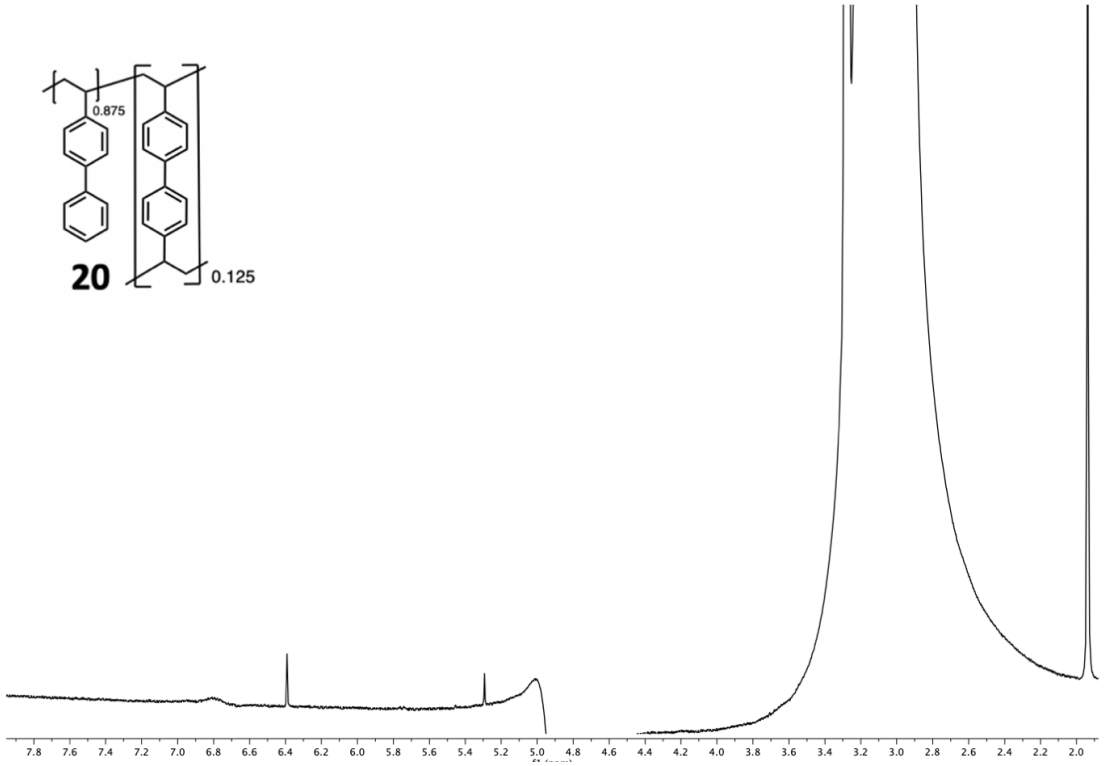

Figure 31. ^{1}H NMR spectrum of **20.**

REFERENCES

(1) Nitopi, S.; Bertheussen, E.; Scott, S. B.; Liu, X.; Engstfeld, A. K.; Horch, S.; Seger, B.; Stephens, I. E. L.; Chan, K.; Hahn, C.; et al. Progress and Perspectives of Electrochemical CO2 Reduction on Copper in Aqueous Electrolyte. *Chem. Rev.* **2019**, *119* (12), 7610–7672.

(2) Hori, Y.; Kikuchi, K.; Suzuki, S. *Chem. Lett.* **1985**, *14* (11), 1695–1698.

(3) Kuhl, K. P.; Cave, E. R.; Abram, D. N.; Jaramillo, T. F. New Insights into the Electrochemical Reduction of Carbon Dioxide on Metallic Copper Surfaces. *Energy Environ. Sci.* **2012**, *5* (5), 7050–7059.

(4) Murata, A.; Hori, Y. Product Selectivity Affected by Cationic Species in Electrochemical Reduction of CO2 and CO at a Cu Electrode. *Bull. Chem. Soc. Jpn.* **1991**, *64* (1), 123–127.

(5) Thevenon, A.; Rosas-Hernández, A.; Fontani Herreros, A. M.; Agapie, T.; Peters, J. C. Dramatic HER Suppression on Ag Electrodes via Molecular Films for Highly Selective CO2 to CO Reduction. *ACS Catal.* **2021**, *11* (8), 4530–4537.

(6) Thevenon, A.; Rosas-Hernández, A.; Peters, J. C.; Agapie, T. In-Situ Nanostructuring and Stabilization of Polycrystalline Copper by an Organic Salt Additive Promotes Electrocatalytic CO2 Reduction to Ethylene. *Angew. Chemie Int. Ed.* **2019**, *58* (47), 16952–16958.

(7) Li, F.; Thevenon, A.; Rosas-Hernández, A.; Wang, Z.; Li, Y.; Gabardo, C. M.; Ozden, A.; Dinh, C. T.; Li, J.; Wang, Y.; et al. Molecular Tuning of CO2-to-Ethylene Conversion. *Nature* **2020**, *577* (7791), 509–513.

(8) Han, Z.; Kortlever, R.; Chen, H.-Y.; Peters, J. C.; Agapie, T. CO2 Reduction Selective for C≥2 Products on Polycrystalline Copper with N-Substituted Pyridinium Additives. *ACS Cent. Sci.* **2017**, *3* (8), 853–859.

(9) Nie, W.; Heim, G. P.; Watkins, N. B.; Agapie, T.; Peters, J. Organic Additive-Derived Films on Cu Electrodes Promote Electrochemical CO2 Reduction to C2+ Products Under Strongly Acidic Conditions. *Angew. Chemie Int. Ed.* **2023**, *n/a* (n/a).

(10) Cheng, B.; Du, J.; Yuan, H.; Tao, Y.; Chen, Y.; Lei, J.; Han, Z. Selective CO2 Reduction to Ethylene Using Imidazolium-Functionalized Copper. *ACS Appl. Mater. Interfaces* **2022**, *14* (24), 27823–27832.

(11) Buckley, A. K.; Cheng, T.; Oh, M. H.; Su, G. M.; Garrison, J.; Utan, S. W.; Zhu, C.; Toste, F. D.; Goddard, W. A. I. I. I.; Toma, F. M. Approaching 100% Selectivity at Low Potential on Ag for Electrochemical CO2 Reduction to CO Using a Surface Additive. *ACS Catal.* **2021**, *11* (15), 9034–9042.

(12) Rosen, B. A.; Salehi-Khojin, A.; Thorson, M. R.; Zhu, W.; Whipple, D. T.; Kenis, P. J. A.; Masel, R. I. Ionic Liquid–Mediated Selective Conversion of CO2 to CO at Low Overpotentials. *Science (80-.).* **2011**, *334* (6056), 643–644.

(13) Chen, X.; Chen, J.; Alghoraibi, N. M.; Henckel, D. A.; Zhang, R.; Nwabara, U. O.; Madsen, K. E.; Kenis, P. J. A.; Zimmerman, S. C.; Gewirth, A. A. Electrochemical CO2-to-Ethylene Conversion on Polyamine-Incorporated Cu Electrodes. *Nat. Catal.* **2021**, *4* (1), 20–27.

(14) Wei, X.; Yin, Z.; Lyu, K.; Li, Z.; Gong, J.; Wang, G.; Xiao, L.; Lu, J.; Zhuang, L. Highly Selective Reduction of CO2 to C2+ Hydrocarbons at Copper/Polyaniline Interfaces. *ACS Catal.* **2020**, *10* (7), 4103–4111.

(15) Watkins, N. B.; Wu, Y.; Nie, W.; Peters, J. C.; Agapie, T. In Situ Deposited Polyaromatic Layer Generates Robust Copper Catalyst for Selective Electrochemical CO2 Reduction at Variable PH. *ACS Energy Lett.* **2023**, *8* (1), 189–195.

(16) Kim, C.; Bui, J. C.; Luo, X.; Cooper, J. K.; Kusoglu, A.; Weber, A. Z.; Bell, A. T. Tailored Catalyst Microenvironments for CO2 Electroreduction to Multicarbon Products on Copper Using Bilayer Ionomer Coatings. *Nat. Energy* **2021**, *6* (11), 1026–1034.

(17) Pelayo, G. de A. F.; Cao-Thang, D.; Adnan, O.; Joshua, W.; Christopher, M.; R., K. A.; Dae-Hyun, N.; Christine, G.; Ali, S.; Xue, W.; et al. CO2 Electrolysis to Multicarbon Products at Activities Greater than 1 A Cm−2. *Science (80-.).* **2020**, *367* (6478), 661–666.

(18) Ozden, A.; Li, F.; García de Arquer, F. P.; Rosas-Hernández, A.; Thevenon, A.; Wang, Y.; Hung, S.-F.; Wang, X.; Chen, B.; Li, J.; et al. High-Rate and Efficient Ethylene Electrosynthesis Using a Catalyst/Promoter/Transport Layer. *ACS Energy Lett.* **2020**, *5* (9), 2811–2818.

(19) Erick, H. J.; Fengwang, L.; Adnan, O.; Armin, S. R.; Pelayo, G. de A. F.; Shijie, L.; Shuzhen, Z.; Mingchuan, L.; Xue, W.; Yanwei, L.; et al. CO2 Electrolysis to Multicarbon Products in Strong Acid. *Science (80-.).* **2021**, *372* (6546), 1074–1078.

(20) Pan, H.; Barile, C. J. Electrochemical CO2 Reduction to Methane with Remarkably High Faradaic Efficiency in the Presence of a Proton Permeable Membrane. *Energy Environ. Sci.* **2020**, *13* (10), 3567–3578.

(21) Wang, J.; Cheng, T.; Fenwick, A. Q.; Baroud, T. N.; Rosas-Hernández, A.; Ko, J. H.; Gan, Q.; Goddard III, W. A.; Grubbs, R. H. Selective CO2 Electrochemical Reduction Enabled by a Tricomponent Copolymer Modifier on a Copper Surface. *J. Am. Chem. Soc.* **2021**, *143* (7), 2857–2865.

(22) Chang, M.; Ren, W.; Ni, W.; Lee, S.; Hu, X. Ionomers Modify the Selectivity of Cu-Catalyzed Electrochemical CO2 Reduction. *ChemSusChem* **2022**, *n/a* (n/a), e202201687.

(23) Li, W.; Yin, Z.; Gao, Z.; Wang, G.; Li, Z.; Wei, F.; Wei, X.; Peng, H.; Hu, X.; Xiao, L.; et al. Bifunctional Ionomers for Efficient Co-Electrolysis of CO2 and Pure Water towards Ethylene Production at Industrial-Scale Current Densities. *Nat. Energy* **2022**, *7* (9), 835–843.

(24) Shin, S.-J.; Choi, H.; Ringe, S.; Won, D. H.; Oh, H.-S.; Kim, D. H.; Lee, T.; Nam, D.-H.; Kim, H.; Choi, C. H. A Unifying Mechanism for Cation Effect Modulating C1 and C2 Productions from CO2 Electroreduction. *Nat. Commun.* **2022**, *13* (1), 5482.

(25) Ringe, S.; Clark, E. L.; Resasco, J.; Walton, A.; Seger, B.; Bell, A. T.; Chan, K. Understanding Cation Effects in Electrochemical CO2 Reduction. *Energy Environ. Sci.* **2019**, *12* (10), 3001–3014.

(26) Resasco, J.; Chen, L. D.; Clark, E.; Tsai, C.; Hahn, C.; Jaramillo, T. F.; Chan, K.; Bell, A. T. Promoter Effects of Alkali Metal Cations on the Electrochemical Reduction of Carbon Dioxide. *J. Am. Chem. Soc.* **2017**, *139* (32), 11277–11287.

(27) Monteiro, M. C. O.; Dattila, F.; Hagedoorn, B.; García-Muelas, R.; López, N.; Koper, M. T. M. Absence of CO2 Electroreduction on Copper, Gold and Silver Electrodes without Metal Cations in Solution. *Nat. Catal.* **2021**, *4* (8), 654–662.

(28) Gu, J.; Liu, S.; Ni, W.; Ren, W.; Haussener, S.; Hu, X. Modulating Electric Field Distribution by Alkali Cations for CO2 Electroreduction in Strongly Acidic Medium. *Nat. Catal.* **2022**, *5* (4), 268–276.

(29) Qin, H.-G.; Li, F.-Z.; Du, Y.-F.; Yang, L.-F.; Wang, H.; Bai, Y.-Y.; Lin, M.; Gu, J. Quantitative Understanding of Cation Effects on the Electrochemical Reduction of CO2 and H+ in Acidic Solution. *ACS Catal.* **2023**, *13* (2), 916–926.

(30) Waegele, M. M.; Gunathunge, C. M.; Li, J.; Li, X. How Cations Affect the Electric Double Layer and the Rates and Selectivity of Electrocatalytic Processes. *J. Chem. Phys.* **2019**, *151* (16), 160902.

(31) Majchrzak, M.; Kostera, S.; Kubicki, M.; Kownacki, I. Synthesis of New Styrylarenes via Suzuki–Miyaura Coupling Catalysed by Highly Active, Well-Defined Palladium Catalysts. *Dalt. Trans.* **2013**, *42* (44), 15535–15539.

(32) Ren, W.; Xu, A.; Chan, K.; Hu, X. A Cation Concentration Gradient Approach to Tune the Selectivity and Activity of CO2 Electroreduction. *Angew. Chemie Int. Ed.* **2022**, *61* (49), e202214173.

(33) Sun, D.; Lindeman, S. V; Rathore, R.; Kochi, J. K. Intramolecular (Electron) Delocalization between Aromatic Donors and Their Tethered Cation–Radicals. Application of Electrochemical and Structural Probes. *J. Chem. Soc. Perkin Trans. 2* **2001**, No. 9, 1585–1594.

(34) Dougherty, D. A. The Cation−π Interaction. *Acc. Chem. Res.* **2013**, *46* (4), 885–893.

(35) Richard, D.; Tom, M.; Jang, J.; Yun, S.; Christofides, P. D.; Morales-Guio, C. G. Quantifying Transport and Electrocatalytic Reaction Processes in a Gastight Rotating Cylinder Electrode Reactor via Integration of Computational Fluid Dynamics Modeling and Experiments. *Electrochim. Acta* **2023**, *440*, 141698.

(36) Luo, G.; Yuan, B.; Guan, T.; Cheng, F.; Zhang, W.; Chen, J. Synthesis of Single Lithium-Ion Conducting Polymer Electrolyte Membrane for Solid-State Lithium Metal Batteries. *ACS Appl. Energy Mater.* **2019**, *2* (5), 3028–3034.

(37) Pangborn, A. B.; Giardello, M. A.; Grubbs, R. H.; Rosen, R. K.; Timmers, F. J. Safe and Convenient Procedure for Solvent Purification. *Organometallics* **1996**, *15* (5), 1518–1520.

(38) Buchs, J.; Geßner, A.; Heyne, B.; Janietz, D.; Sawade, H. Fluorescent Liquid Crystals with Rod-Shaped π-Conjugated Hydrocarbon Core. *Liq. Cryst.* **2019**, *46* (2), 281–298.

(39) Lazanas, A. C.; Prodromidis, M. I. Electrochemical Impedance Spectroscopy─A Tutorial. *ACS Meas. Sci. Au* **2023**, *3* (3), 162–193.

(40) Zheng, W. IR Compensation for Electrocatalysis Studies: Considerations and Recommendations. *ACS Energy Lett.* **2023**, *8* (4), 1952–1958.

(41) Heenan, A. R.; Hamonnet, J.; Marshall, A. T. Why Careful IR Compensation and Reporting of Electrode Potentials Are Critical for the CO2 Reduction Reaction. *ACS Energy Lett.* **2022**, *7* (7), 2357–2361.

(42) Ma, M.; Zheng, Z.; Yan, W.; Hu, C.; Seger, B. Rigorous Evaluation of Liquid Products in High-Rate CO2/CO Electrolysis. *ACS Energy Lett.* **2022**, *7* (8), 2595–2601.

CHAPTER V

CO_2 REDUCTION TO METHANOL CATALYZED BY MACROCYCLIC MOLECULAR COBALT COMPLEXES

ABSTRACT: Cobalt phthalocyanine (**CoPc**), a proposed molecular mimic of single atom catalysts, has demonstrated electrochemical CO_2 conversion to MeOH, a six-electron process rarely observed with molecular catalysts. Modularity over the **CoPc** ligand framework is difficult to realize, thus precluding the development of thorough structure-function relationships. Development of molecular species capable of CO_2 to MeOH conversion can be undertaken to understand molecular properties crucial for the transformation. Dicationic Co complexes **CoL^{tBu}** and **CoL^{mes}** were immobilized on carbon nanotubes and submitting for electrochemical CO_2 reduction, yielding MeOH (FE = 12%) at a range of applied potentials. Electrolysis in the presence of CO also leads to formation of MeOH, suggesting CO-bound complexes to be significant intermediates in CO_2R to MeOH. CO is the exclusive CO_2R product in CH_3CN; decomposition of solvent is evident from observation of ethylamine by ^{1}H NMR. This work highlights molecular systems facilitating multi-electron electrochemical transformations to highly reduced CO_2R products.

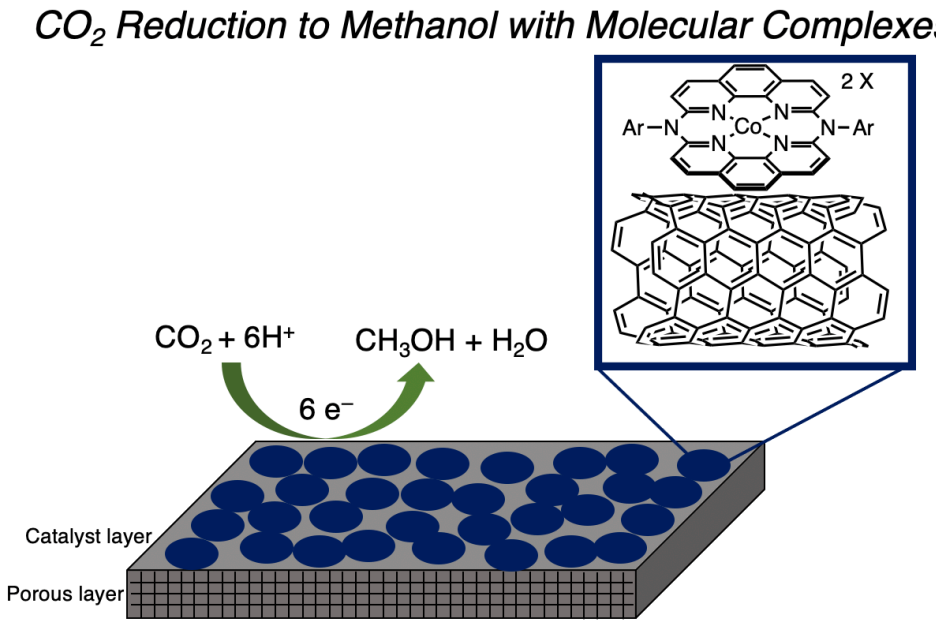

ACKNOWLEDGEMENTS

Dr. Matthew Espinosa, Fernando Guerrero, and Alexandria Hong are thanked for their preparations of the [Co] complexes. I am grateful to Mike Foley from Cheap Tubes, Inc. for providing a free sample (50 mg) of single-walled carbon nanotubes. This material is based on work performed by the Liquid Sunlight Alliance, which is supported by the U.S. Department of Energy, Office of Science, Office of Basic Energy Sciences, Fuels from Sunlight Hub under Award DE-SC0021266. The Resnick Sustainability Institute at Caltech is acknowledged for support of the laboratory facilities in which this research was conducted.

INTRODUCTION

Previous work in electrocatalysis has utilized single-atom catalysts (SACs) demonstrating high selectivity at low overpotentials,[1–5] where the proposed active metal site is embedded in a heteroatom-doped graphene. Description of the active site has been often limited to models developed from images or spectroscopic data.[6] Recent work has investigated well-defined molecular mimics of SACs able to demonstrate high electrocatalytic performance for electrochemically converting CO_2 to CO.[7–11] Molecular CO_2 reduction (CO_2R) electrocatalysts typically yield CO, a syngas component utilized in Fisher-Tropsch chemistry.[12–16] The most promising molecular systems perform CO_2R at high turnover frequencies and low overpotentials.[17] However, molecular complexes are kinetically limited and typically do not facilitate CO_2R beyond 2 electrons.

Recent work with cobalt phthalocyanine (**CoPc**) has yielded MeOH from CO_2R when supported on carbon nanotubes (CNTs).[18,19] MeOH is of interest as a liquid fuel in overseas shipping.[20] Wang and co-workers obtained 40% Faradaic efficiency for MeOH (FE_{MeOH}) with hybrid **CoPc**/CNT.[21] Ye, Goddard, and co-workers investigated the effects of strain on **CoPc** induced by CNTs of different diameters, observing FE_{MeOH} = 60%.[22] Significant selectivity for MeOH via photoelectrochemical CO_2R has also been observed.[23] All successful examples of electrochemical CO_2R to MeOH have been observed with **CoPc**. While few reports have functionalized the phthalocyanine ligand on **CoPc**, it remains challenging the isolation of variants with well-defined substituents,[11,21] thus precluding investigation into the effects of ligand/second sphere effects on MeOH

generation. Moreover, given the dearth of examples of molecular electrocatalysts that reduce CO_2 to MeOH, there remains a potentially large space of molecules to explore.

Presented herein is electrochemical CO_2R to MeOH with Co complexes bearing neutral, macrocyclic ligands, where variation in the ligand framework is achieved by the choice of aniline. Cyclic voltammetry of each novel [Co] complex dissolved in organic solvent reveals a catalytic current, and high selectivity for CO is evident from bulk electrolysis. **CoL^{mes}** supported on multi-walled CNTs (MWCNTs) for electrolysis in 1 M $KHCO_{3(aq)}$ results in FE_{MeOH} = 12.1% at –0.7 V vs. RHE in 1 M $KHCO_{3(aq)}$; no MeOH was observed under the same conditions for **CoPc**. CO reduction to MeOH is also observed, suggesting CO as an intermediate in CO_2R.

RESULTS AND DISCUSSION

i) Electrolysis with [Co] supported on carbon nanotubes

Novel molecular cobalt complexes were investigated as potential electrocatalysts. The coordination environment around cobalt consists of four neutral, nitrogen donors, resulting in a dicationic macrocycle.[24] Single-crystal X-ray diffraction highlights the planarity of the phenanthroline motifs with the aryl groups possessing significant dihedral angles. The overall +2 charge provides a complex likely electronically distinct from **CoPc**, where cobalt is ligand by neutral anionic donors.

Methodologies for immobilization onto MWCNTs were employed for **[CoL^{mes}][2 OTf] [CoL^{tBu}][2 OTf]**, where each complex was dissolved in 2-propanol followed by suspension with MWCNTs. This slurry was sonicated for 60 minutes before drop casting onto a carbon paper electrode (38 BC, Fuel Cell Store),[25] yielding a nominal [Co] loading of 50 μg cm^{-2}.

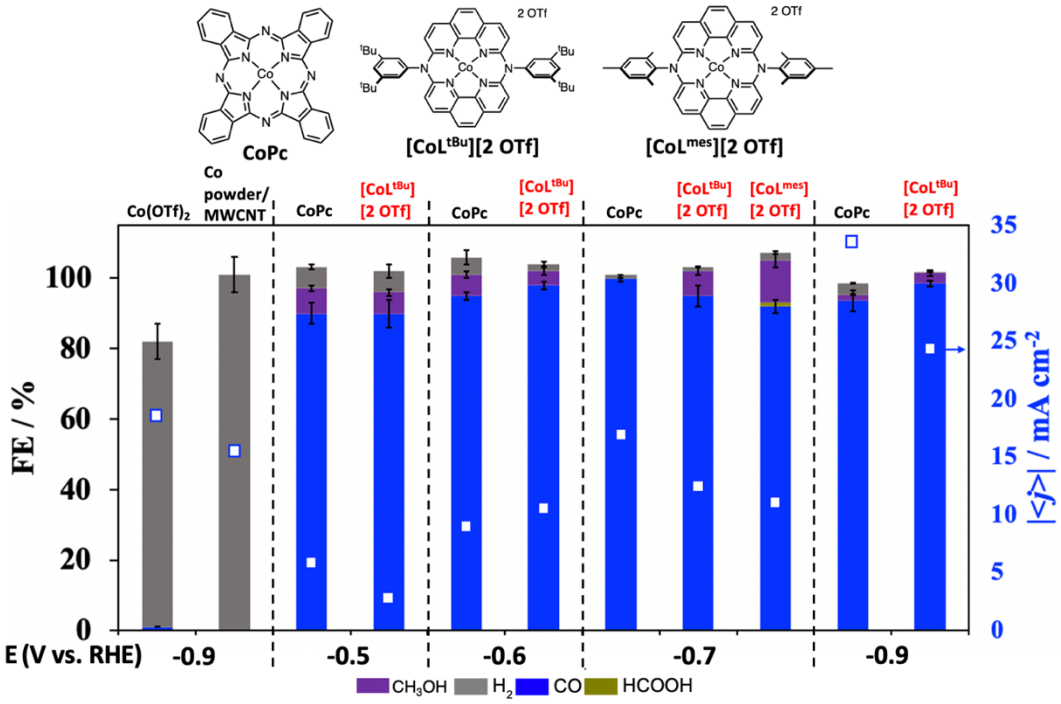

Figure 1. Selectivity profile from constant potential electrolysis with $CO_{2(g)}$ in gas diffusion electrode flow cell with [Co] supported on MWCNT highlighting Faradaic efficiencies (columns) and total current density (white squares). 1:2 mass ratio of [Co] to MWNCTs was prepared and drop casted onto C paper (nominal [Co] loading: 50 μg cm^{-1}).

This electrode was allowed to dry under ambient conditions for 2 hours before assembling in a gas diffusion electrode (GDE) cell.[26,27] $CO_{2(g)}$ was provided to the inlet of the cell at a constant 20 standard cubic centimeters per minute (sccm), where online gas chromatography detection of products was employed. 1 M $KHCO_{3(aq)}$ was employed as electrode at a constant recirculation rate in cathode and anode of 10 mL min^{-1}.

[CoL^{mes}][2 OTf] and **[CoL^{tBu}][2 OTf]** were each tested at several applied potentials (chronoamperometry) and compared to **CoPc**, which was immobilized following a similar preparation. CO is the major product under most conditions, with minimal Faradaic efficiency (FE) for H_2 observed (Figure 1). MeOH is observed via ^{1}H NMR spectroscopy of

a sample of the electrolyte, yielding two additional, distinct molecular complexes capable of catalyzing the six-electron process of converting CO_2 to MeOH. Before now, **CoPc** was the only reported example. **[CoL^{mes}][2 OTf]** appears to outperform **CoPc** at –0.7 V vs. RHE. To rule out possible molecular decomposition into Co^0, Co powder was mixed with MWCNTs and drop casted onto carbon paper, finding that exclusively H_2 is generated under similar CO_2R conditions. A similar observation was made with $Co(OTf)_2$/MWCNT. Electrolysis was performed in the presence of $^{13}CO_{2(g)}$ with 1 M $KH^{13}CO_{3(aq)}$. ^1H NMR of the electrolyte sample shows a doublet centered at 3.3 ppm ($J_{H\text{-}C}$ = 144 Hz) confirming the presence of $^{13}CH_3OH$ (Figure 3). Therefore, MeOH generated in the electrolysis originates from CO_2.

The turnover frequency (TOF) for CO provided by **CoL^{mes}**/MWCNT either surpass or are comparable to that of **CoPc**/MWCNT at potentials more negative than –0.5 V vs. RHE (Figure 2). Activity for MeOH formation was compared to values reported in the literature (Table 1). Despite lower TOF, **CoPc** was the only reported molecular species capable of converting CO_2 to MeOH electrochemically. Demonstrating a novel series of compounds capable of enacting this transformation paves the way for enriching the space of molecular complexes able generate highly reduced products from CO_2R.

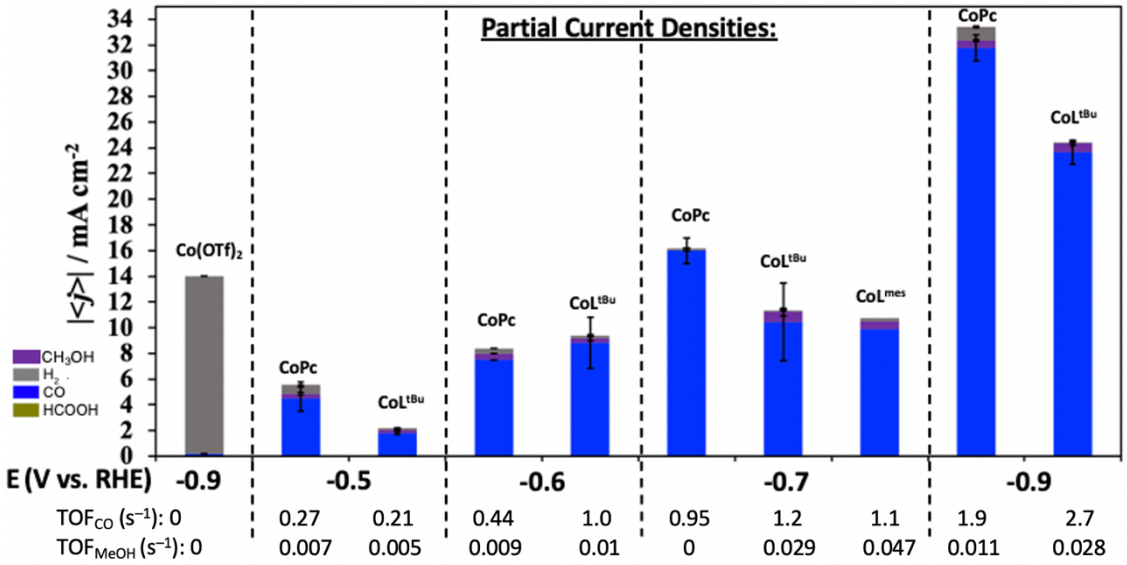

Figure 2. Partial current densities (columns) calculated from Faradaic efficiencies in Figure 1. Turnover frequencies (TOFss) are provided for each CO and MeOH for each set of conditions.

Table 1. Comparing CO_2R performance between complexes

Authors	Complex/support	E (V vs. RHE)	FE_{MeOH}	Electrolyte	TOF_{MeOH} (s^{-1})
This work	**CoL^{mes}/MWCNT**	–0.7	12.1%	1 M $KHCO_3$	0.05
	CoPc/MWCNT	–0.7	0%	1 M $KHCO_3$	0
Wang, H. and co-workers.[21]	**CoPc/MWCNT**	–0.94	40%	0.1 M $KHCO_3$	1.05
Ye, R. and coworkers.[22]	**CoPc/SWCNT**	–0.8	60%	0.1 M $KHCO_3$	14.8
Rooney, Wang, and co-workers[23]	**CoPc/GO**	–0.93	25%	0.5 M $KHCO_3$	0.21

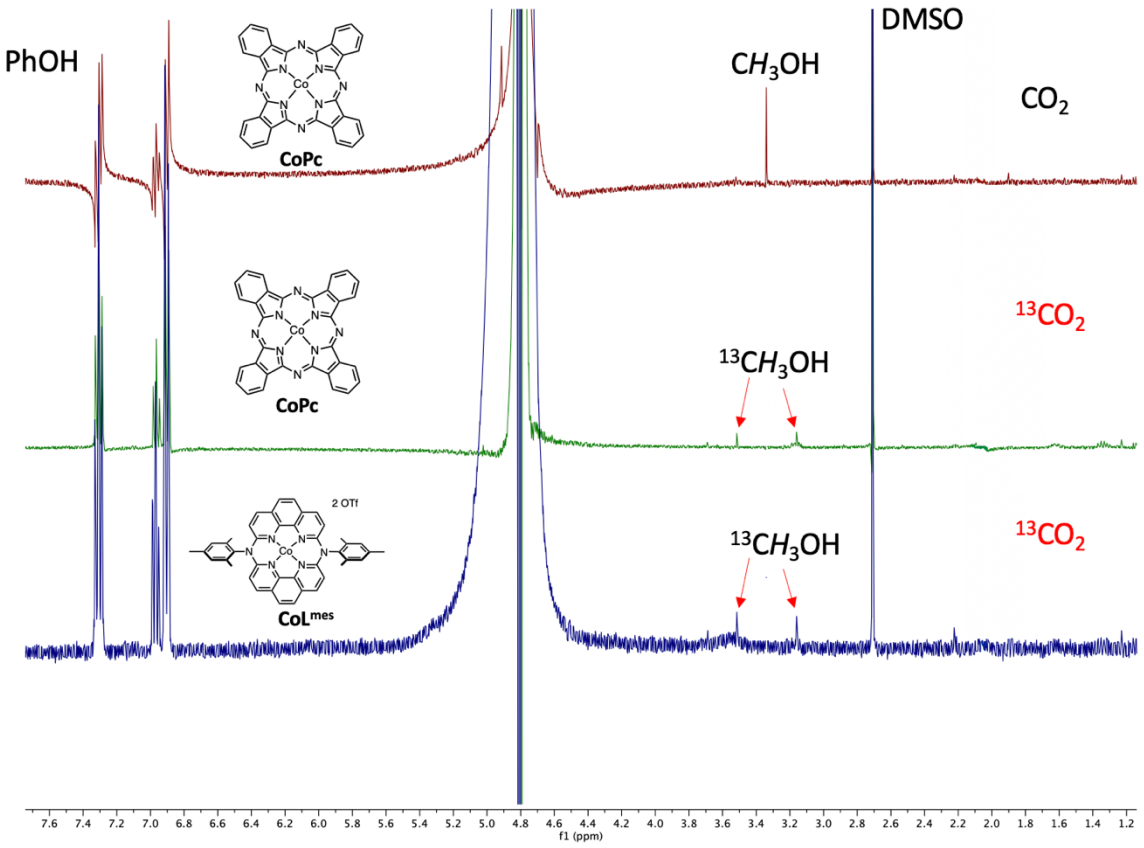

Figure 3. ^{1}H NMR spectra (400 MHz) of electrolyte sample post-electrolysis (–0.6 V vs. RHE for 30 minutes) with either natural abundance $CO_{2(g)}$ (electrolyte: 1 M $KHCO_{3(aq)}$) or $^{13}CO_{2(g)}$ (1 M $KH^{13}CO_{3(aq)}$), the latter yielding $^{13}CH_3OH$ ($J_{H\text{-}C}$ = 144 Hz).

Variants of the ligand primary and secondary coordination spheres were investigated. A more open variant (**CoL^{mes,open}**) appeared to lessen the rigidity of the ligand. Immobilization onto MWCNTs and submission for CO_2R experiments demonstrate no generation of MeOH and poor selectivity for CO (Figure 4). This complex likely does not bind favorably to MWCNTs, thus yielding worse CO_2R performance.[28] Switching out $^{-}$OTf for Cl^{-} shuts down MeOH generation; selectivity for CO is not attenuated relative to $^{-}$OTf. Instead, $|j_{CO}|$ increases by as much as 2-fold. Stronger axial donors were found in prior work to increase TOF for CO formation by as much as a factor of 2.[29] It is hypothesized that the

presence of Cl^- in **[CoL^{mes}][Cl]** as an axial donor inhibits MeOH generation by virtue enhancing the rate of CO formation.

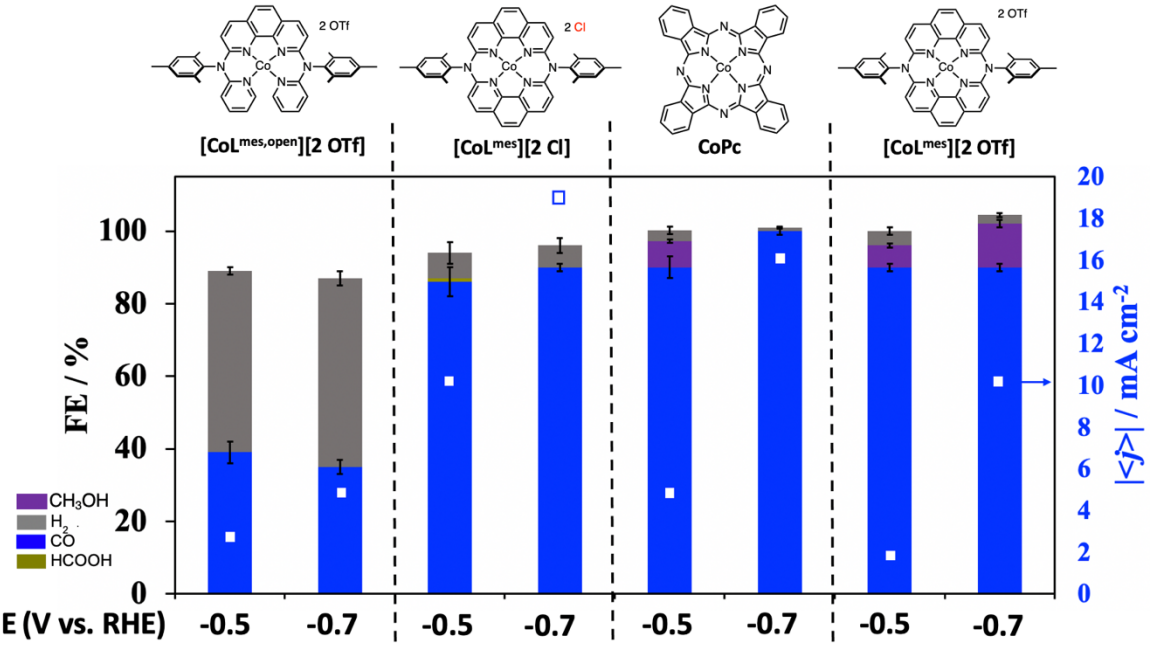

Figure 4. Selectivity profile from constant potential electrolysis with $CO_{2(g)}$ with [Co] derivatives supported on MWCNT highlighting Faradaic efficiencies (columns) and total current density (white squares).

Single-walled carbon nanotubes (SWCNTs) were systematically investigated in previous work to elevate FE_{MeOH}.[21,22] Enhanced curvature in **CoPc** was found computationally to stabilize the CO-bound intermediate, thus favoring the pathway for MeOH formation. Mixing [Co] with SWCNTs (sourced from Cheap tubes, Inc.) via sonication in 2-propanol provides a catalyst ink for drop casting onto carbon paper. MeOH was not observed from CO_2R with either **CoPc** or **[CoL^{mes}][2 OTf]** (Figure 5). $|j_{CO}|$ increases by at most a factor of 5 for **[CoL^{mes}][2 OTf]** when incorporating SWCNT; such a phenomenon could be related to the lack of MeOH formation from CO_2.[29,30]

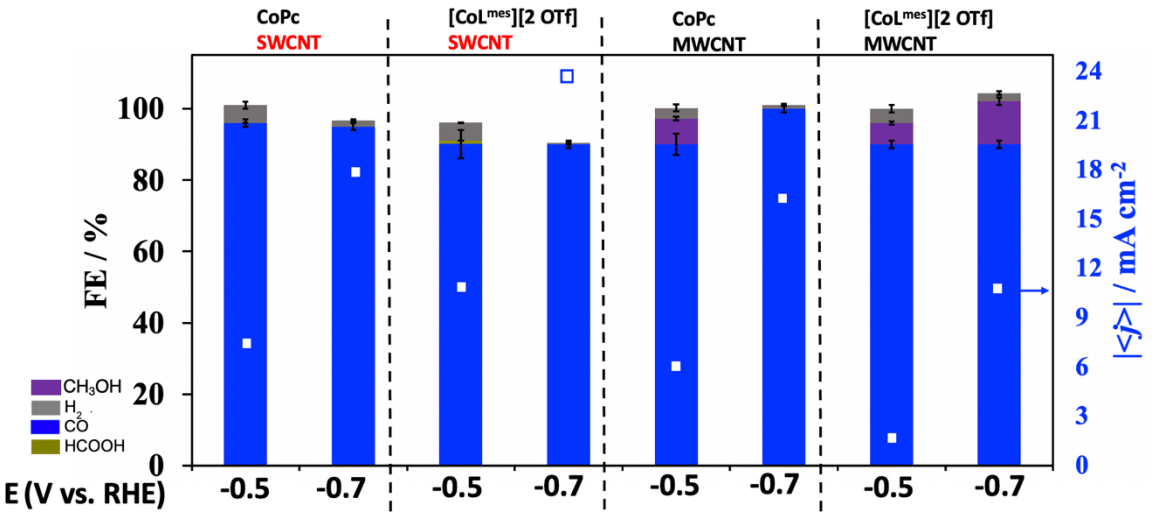

Figure 5. Selectivity profile from constant potential electrolysis with $CO_{2(g)}$ with [Co] derivatives supported on either SWCNT or MWCNT.

Electrolysis was instead attempted with $CO_{(g)}$ (Figure 6). FE_{MeOH} was enhanced with SWCNTs compared to MWCNTs (3% vs. 10%, for **CoL^{mes}**/SWCNT). These results also suggest that CO bound to **CoL^{mes}** is an intermediate in the formation of MeOH, consistent with previous reports examining **CoPc**.[21,22,30]

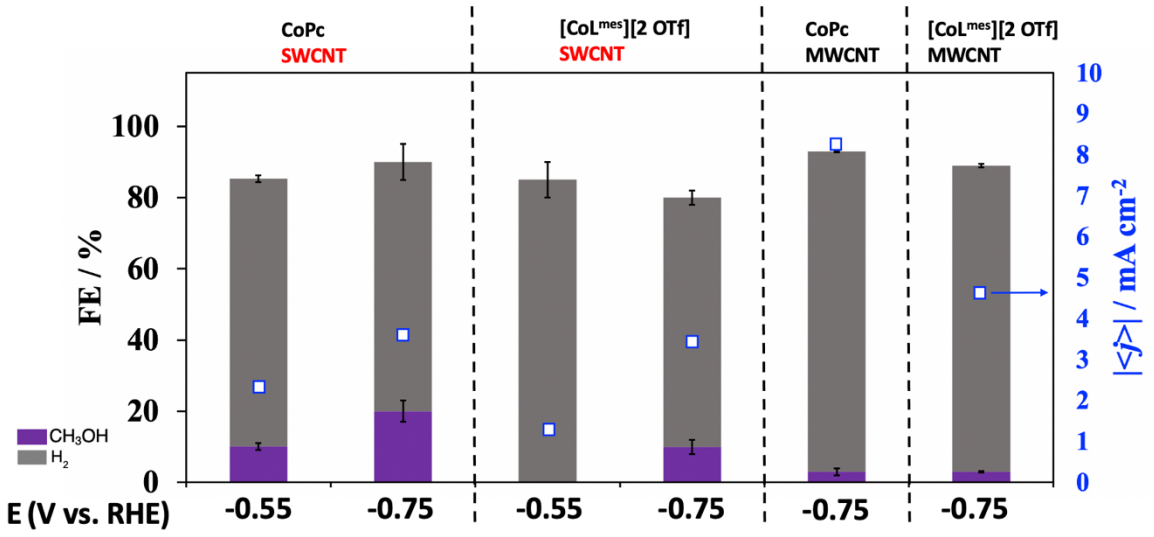

Figure 6. Selectivity profile from constant potential electrolysis with CO with [Co] derivatives supported on either SWCNT or MWCNT.

ii) Homogeneous electrochemistry

Cyclic voltammetry was carried out to ascertain the redox features of **[CoL^{mes}][2 OTf]** (1 mM) in 0.1 M $^{n}Bu_4NPF_6/CH_3CN$. A three-electrode setup was employed in a single-compartment cell with glassy carbon (working electrode), Ag wire (reference electrode), and Pt wire. A reversible feature was observed at –1.1 V vs. $Fc^{+/0}$, assigned as the $Co^{II/I}$ feature based on CVs obtained with the analogous Zn complex (Figure 8), where such a feature is not evident. Three additional redox features at cathodic potentials are observed between –1.5 and –3 V vs. $Fc^{+/0}$ assigned as ligand-based events. Replacing $Ar_{(g)}$ with $CO_{2(g)}$ and adding MeOH reveals a rising current demonstrative of CO_2 reduction. The feature at –1.9 V could be reduction of the ligand followed by electron transfer to the metal center,[31,32] leading to a formally Co^0 species capable of binding CO_2 and performing CO_2R.[33] **[ZnL^{mes}][Cl]** possesses minimal CO_2R activity, suggesting the Co center to be the active site.

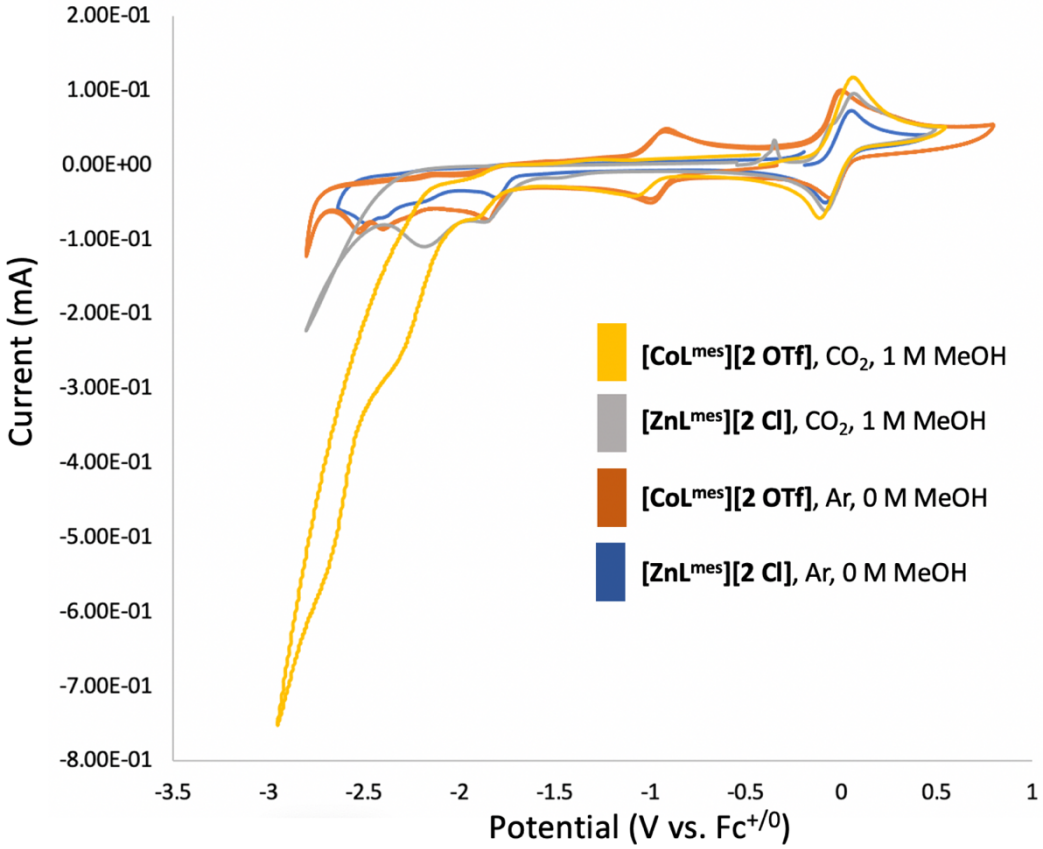

Figure 7. Cyclic voltammograms of **[CoL^{mes}][2 OTf]** and **[ZnL^{mes}][2 OTf]** in the presence of either $Ar_{(g)}$ or $CO_{2(g)}$. Electrolyte: 0.1 M $^{n}Bu_4NPF_6/CH_3CN$. Working electrode: glassy carbon. Reference electrode: Ag wire. Counter electrode: Pt wire. Most positive redox featured centered at 0 V is oxidation of ferrocene (Fc).

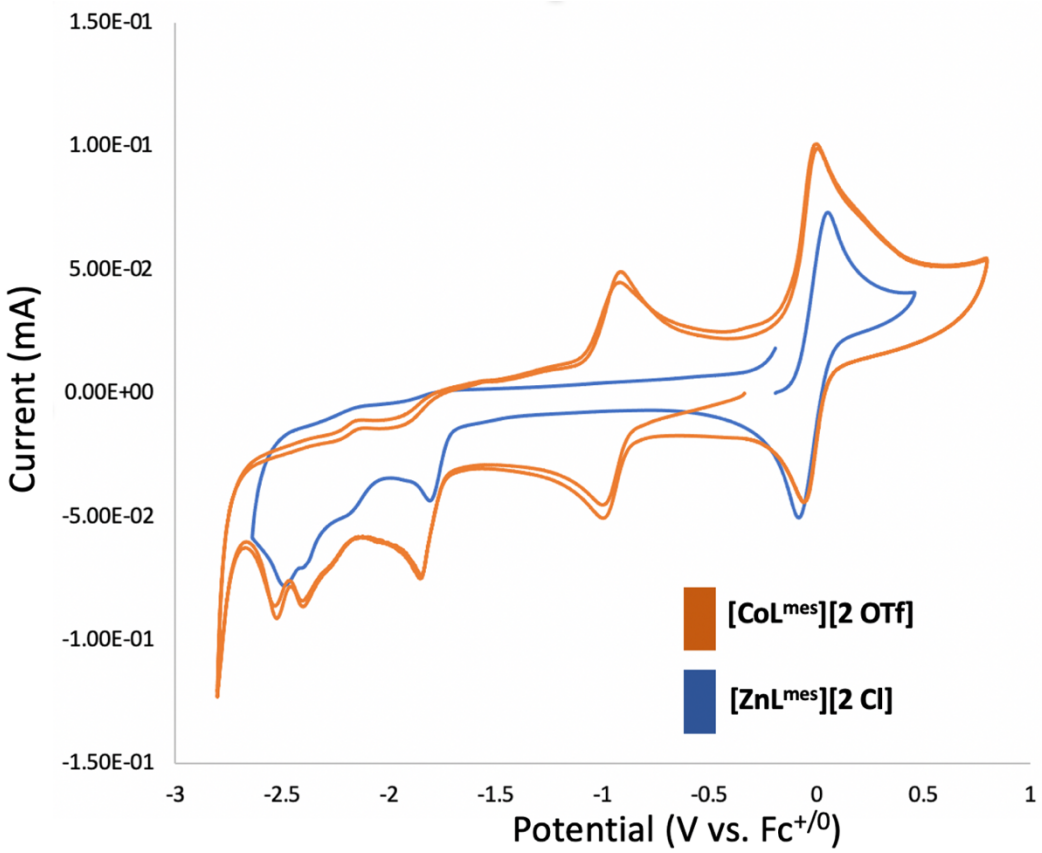

Figure 8. Cyclic voltammograms of **[CoL^{mes}][2 OTf]** and **[ZnL^{mes}][2 OTf]** in the presence of $Ar_{(g)}$. Electrolyte: 0.1 M $^{n}Bu_4NPF_6/CH_3CN$. Working electrode: glassy carbon. Reference electrode: Ag wire. Counter electrode: Pt wire.

Compared to **CoPc**, CO_2R activity is worse as measured by catalytic current divided by current measured in the presence of argon (i_{CO2R}/i_{Ar}). The onset potential of CO_2R is more positive by ~100 mV (Figure 9). Dicationic Co complexes bearing a tetrakis(pyridine) ligand possessed 43-fold greater current than the CV in the presence of $N_{2(g)}$ (Table 4).

Bulk electrolysis was carried out in 0.1 M $^{n}Bu_4NPF_6/CH_3CN$, with CO being the major product along with formation of hydrogen and ethylamine (Table 3). Ethylamine is generated from electrochemical reduction of CH_3CN, consistent with literature reports.[34,35] While molecular electrocatalysts have not been reported carrying out this transformation,[36]

stable acetonitrile-bound Co^{II} macrocycles have been studied.[37] **[CoL^{mes}][OTf]** can plausibly allow competitive CH_3CN binding given the weak coordination abilities of $^{-}$OTf.[38] Finally, no MeOH was observed; electrolysis in the presence of CO also did not yield MeOH.

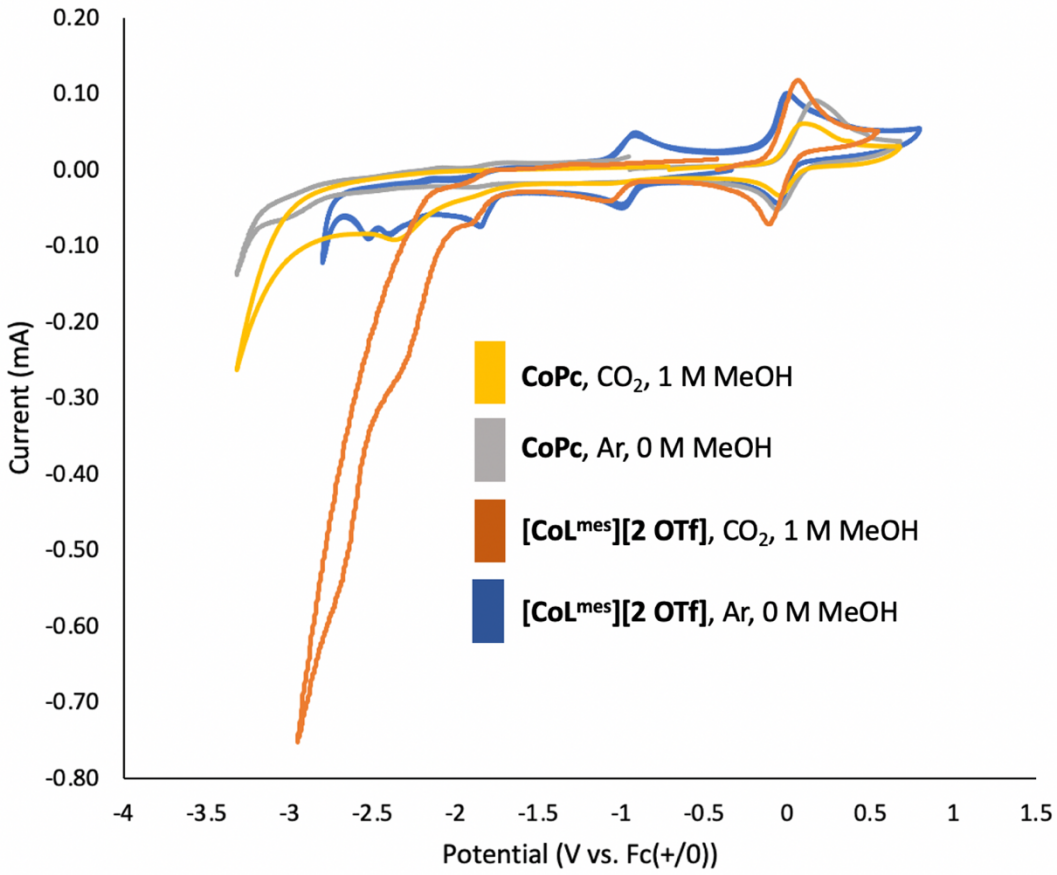

Figure 9. Cyclic voltammograms of **[CoL^{mes}][2 OTf]** and **CoPc**. Electrolyte: 0.1 M $^{n}Bu_4NPF_6/CH_3CN$. Working electrode: glassy carbon. Reference electrode: Ag wire. Counter electrode: Pt wire.

CONCLUSIONS

In summary, novel Co complexes **CoL^{tBu}** and **CoL^{mes}** yield MeOH at a range of potentials, finding the most optimal selectivity (FE = 12%) at –0.7 V vs. RHE in 1 M $KHCO_{3(aq)}$; **CoPc** does not produce MeOH under similar conditions. TOF_{CO} for **CoL^{tBu}** and **CoL^{mes}** is similar or exceeds that of **CoPc**. Electrolysis in the presence of CO also leads to

formation of MeOH, suggesting CO-bound complexes to be significant intermediates in CO_2R to MeOH. CO is the exclusive CO_2R product in CH_3CN; decomposition of solvent is evident from observation of ethylamine by ^1H NMR. Immobilization onto SWNCTs elevates activity for CO generation but does not facilitate MeOH formation in from CO_2. These results highlight a series of novel compounds facilitating electrochemical CO_2R to MeOH, which has reportedly been limited exclusively to **CoPc**. These compounds are currently being investigated via X-ray absorption spectroscopy in comparison to previous examples of immobilized CO_2R electrocatalysts in order to shed light onto electronic properties responsible for MeOH generation.[28]

EXPERIMENTAL

General Considerations. CoPc, **CoTPP**, and $^{13}CO_2$ (99.9% ^{13}C, <3% ^{18}O) were purchased from Millipore Sigma. Deuterated solvents were purchased from Cambridge Isotope Laboratories and used as received. The syntheses of **[CoL^{mes}][2 OTf]**, **[ZnL^{mes}][2 OTf]**, **[CoL^{tBu}][2 OTf]**, **[CoL^{mes,open}][2 OTf]**, **[CoL^{mes}][2 Cl]** are reported.[24] ^1H and $^{13}C\{^1H\}$ spectra were recorded on Varian Mercury 300 MHz or Varian 400 MHz spectrometers at ambient temperatures, unless otherwise denoted. ^1H and $^{13}C\{^1H\}$ NMR spectra are reported referenced internally to residual solvent peaks reported relative to tetramethylsilane. Water suppression for ^1H NMR was carried out on a Varian 400 MHz spectrometer in samples containing 90% H_2O.

Electrochemical measurements of immobilized complexes. All electrochemical measurements were carried out using a Biologic VMP3 multichannel potentiostat. CO_2R and COR measurements were conducted in a gas-tight liquid-electrolyte flow cell. Chronoamperometry experiments were carried out in a custom-made PEEK liquid-electrolyte cell similar to the one reported by Sargent and co-workers.[26] The liquid-electrolyte flow cell consists of three compartments: gas chamber, catholyte chamber, and anolyte chamber. The PTFE electrode was sandwiched between CO_2 gas chamber and catholyte chamber with an exposure area of 0.5 cm^{-2}. Catholyte and anolyte chambers were separated by a Selemion AMV anion-exchange membrane (AGC Engineering Co.). The reference electrode was calibrated against H^+/H_2 on Pt in a 0.5 M sulfuric acid solution (0 V vs. RHE) and saturated calomel electrode (SCE) (+0.241 V saturated vs. RHE). An Autolab PGSTAT204 in a potentiostatic mode was used as electrochemical workstation. The PTFE electrode, leakless Ag/AgCl electrode (Innovative Instruments), and Pt mesh (rinsed with water and annealed with a butane torch) were employed as working, reference and counter electrodes, respectively. The applied potentials were converted to the reversible hydrogen electrode (RHE) scale with iR correction through the following equation:

$$E_{corrected}\ (\text{vs. RHE}) = E\ (\text{vs. Ag/AgCl}) + (0.059 \times \text{pH}) + 0.210 + iR. \quad (1)$$

$E_{applied}$ in this report is the applied potential without iR compensation. In order to convert from potential vs. Ag/AgCl, we use the following relationship:

$$E_{applied}\ (\text{vs. RHE}) = E\ (\text{vs. Ag/AgCl}) + (0.059 \times \text{pH}) + 0.210 \quad (2)$$

where i is the current at each applied potential and R is the equivalent series resistance measured via potentioelectrochemical impedance spectroscopy (PEIS) in the frequency range of 10^5 – 0.1 Hz with an amplitude of 10 mV. The appropriate gas-saturated electrolyte was used as both catholyte and anolyte and was circulated through the flow cell using peristaltic pumps with a silicone Shore A50 tubing. The electrolyte was bubbled with the desired gas during the entire electrolysis process. The electrolyte flow rate was kept at 10 mL min^{-1}. The flow rate of the gas flowing into the gas chamber was kept at 30 sccm by a digital mass flow controller.

Ohmic resistance values were determined with procedures described elsewhere[39,40] and employed in our prior work[26,41,42] PEIS measurements were carried out prior to and after each electrolysis experiment to determine the Ohmic resistance of the flow cell and ensure it is unchanged during the experiment.[43,44] The impedance measurements were carried out at frequencies ranging from 200 kHz to 100 MHz. A Nyquist plot was obtained, and in the low-frequency region (containing a Warburg element) a line was plotted to determine the value of the intersection with the x-axis, representing the Ohmic resistance.[39] An average of 3 measurements was taken to calculate the value of R. Typically, small resistances were measured, ranging from 4 to 7 Ω. The potentiostat was set to compensate for 85 % of the Ohmic drop, with the remaining 15 % being compensated for after the measurements.[39,40]

All chronoamperometric experiments were performed for 30 min at 25 °C. Before each electrolysis experiment, the carbon paper electrode (38 BC, Fuel Cell Store) was prepared with the catalyst ink (see **Cathode Preparation** below). The entire Ohmic drop was compensated before and after the measurement. The effluent gas stream coming from the cell (20 mL min^{-1}) was flowed into the sample loops of a gas chromatograph (GC-FID/TCD, SRI 8610C, in Multi Gas 5 configuration) equipped with HayeSep D and Molsieve 5A columns. Methane, ethylene, ethane, and carbon monoxide were detected by a methanizer-flame ionization detector (FID) and the hydrogen was detected by a thermal conductivity detector (TCD). Every 15 minutes, 2 mL of gas was sampled to determine the concentration of gaseous products. After electrolysis, the liquid products in the catholyte were quantified by ^{1}H NMR spectroscopy (Bruker 400 MHz Spectrometer).

For labeled experiments, $^{13}CO_{2(g)}$ was introduced to the GDE cell at 10 mL/min for 30 minutes. Electrolyte sample was removed, and an NMR sample was prepared to determine the presence of $^{13}CH_3OH$ (see **Preparation of NMR samples**).

Cathode Preparation: The preparation of the catalyst ink was adapted from previous work investigating supported molecular electrocatalysts.[21,28,45] The carbon paper (38 BC, Fuel Cell Store) was dried under vacuum on a Schlenk line for 12 h prior to use. 1.0 mg of [Co] was dissolved in 2 mL of 2-propanol. 2.0 mg of CNTs were added to this solution to form a black suspension, which was sonicated for 60 minutes. 120 μL of this ink was drop casted onto 2.5 cm^2 carbon paper and allowed to dry under ambient conditions for 2 hours.

Electrolyte preparation: Potassium bicarbonate electrolyte (1 M $KHCO_{3(aq)}$) was prepared by sparging an aqueous solution of potassium carbonate (0.5 M $K_2CO_{3(aq)}$) with CO_2 for at least 1 hour

prior to electrolysis. This process converts K_2CO_3 into $KHCO_3$ and saturates the electrolyte solution with CO_2. For isotope labeling experiments the same experimental configurations as described above were employed except $KH^{13}CO_{3(aq)}$ solution and $^{13}CO_2$ were used as the electrolyte and CO_2 source, respectively. To prepare the 0.1 M $KH^{13}CO_{3(aq)}$ solution, 50 mL of nanopure water was sparged with nitrogen for 1 h and was added to potassium hydroxide (0.32 g containing 12.6% water) in a Schlenk flask under nitrogen atmosphere. The headspace was evacuated for a few seconds, and $^{13}CO_2$ was introduced. The solution was stirred vigorously for 5 h and an aliquot was extracted to make sure the pH was ~7.[41]

Preparation of NMR samples:[41] After electrolysis samples were taken from the catholyte. For ^1H NMR, 30 µl internal standard solution, consisting of 10 mM DMSO and 50 mM phenol in water, and 70 µL D2O was added to 0.63 mL electrolyte. The NMR experiments were performed on a Varian 400 MHz NMR spectrometer, using a presaturation sequence to suppress the water signal.

Electrochemical measurements of homogeneous complexes. All electrochemical measurements were carried out using a Biologic VMP3 multichannel potentiostat. All cyclic voltammetry (CV) measurements were performed in a three-electrode cell, which consisted of glassy carbon (working; 3.0 mm diameter), silver wire (reference) and bare platinum wire (counter). Acetonitrile that contained 0.1 M $(^nBu)_4NPF_6$ was used as the electrolyte solution. The ferrocene/ferrocenium (Fc/Fc^+) redox wave was used as an internal standard for all measurements (1 mM). The glassy carbon electrode was polished with alumina paste (0.05 µm, Buehler) and rinsed with nanopure water followed by drying under a stream of nitrogen. The platinum wire was flame dried and rinsed with acetonitrile prior to use. All solutions for CV were loaded with 3 mL of a 1 mM-solution of [Co] in the electrolyte in a 20-mL scintillation vial containing a magnetic stir bar. The solution was sparged

with stirring with the appropriate gas ($Ar_{(g)}$ or $CO_{2(g)}$) for 10 minutes at 25 ºC before performing any electrochemical measurements.

Bulk electrolysis experiments measurements were carried out at constant potential in a custom-made PEEK flow cell setup similar to the one reported by Ager and co-workers using carbon paper (38 BC) as the working electrode, platinum foil as the counter electrode, and Ag/AgCl leakless electrode (eDaq) as the reference electrode.[46] Concentration of [Co] was 1 mM; concentration of phenol was 2.0 M. The cathode compartment was separated from the anode compartment by a Selemion AMV anion-exchange membrane (AGC Engineering Co.). All potentials were measured versus a leakless Ag/AgCl reference electrode (Innovative Instruments) with an outer diameter of 5 mm that was inserted into the cathode compartment. The reference electrode was calibrated against ferrocenecarboxylic acid in a 0.2 M phosphate buffer solution at pH 7.0 (+0.239 V vs. Ag/AgCl). Potentiostatic electrochemical impedance spectroscopy (PEIS) measurements were carried out prior to each electrolysis experiment to determine the Ohmic resistance of the flow cell. The impedance measurements were carried out at frequencies ranging from 200 kHz to 100 MHz to measure the solution resistance. A Nyquist plot was plotted and in the high-frequency part a linear fit was performed, and the axis intersection was calculated. The value of this intersection represents the Ohmic resistance of the cell. An average of 3 measurements was taken to calculate the value of R. Typical resistance values ranged from 50 to 80 Ω. Each chronoamperometry experiment was performed in triplicate.

All chronoamperometric experiments were performed for 30 min at 25 °C using 100 mM $(^{n}Bu)_4NPF_6$ in CH_3CN as the electrolyte. The potentiostat was set to compensate for 85 % of the Ohmic drop, with the remaining 15% being compensated for after the measurements. The effluent gas stream coming from the flow cell (10 mL/min) was flowed into the sample loops of a gas chromatograph

(GC-FID/TCD, SRI 8610C, in Multi Gas 5 configuration) equipped with HayeSep D and molecular sieve 5 Å columns. Carbon monoxide was detected by a S4 methanizer-flame ionization detector (FID), and the hydrogen was detected by a thermal conductivity detector (TCD). Every 10 minutes, 2 mL of gas was sampled to determine the concentration of gaseous products.

Preparation of NMR samples: After electrolysis samples were taken from the catholyte. For ^{1}H NMR, 30 μL internal standard solution, consisting of 10 mM DMSO and 50 mM phenol in CH_3CN, and 70 μL of CD_3CN was added to 0.63 mL electrolyte. The NMR experiments were performed on a Varian 400 MHz NMR spectrometer, using a presaturation sequence to suppress the signal for methyl protons (CH_3CN).

SUPPLEMENTARY FIGURES/DATA

Table 2. Selectivity profile from CO_2 or CO electrolysis in H-cell

Complex/ support	E (V vs. RHE)	Reagent	FE_{H2} (%)	FE_{CO} (%)	FE_{MeOH} (%)	Total FE	$\langle j \rangle$ (mA cm^{-2})
CoPc/ MWCNT	-0.91	CO_2	40 ± 2	44 ± 3	1.0 ± 0.3	85 ± 4	-11.4 ± 0.8
		CO	90 ± 2	N/A	0.24 ± 0.01	90 ± 2	-5.0 ± 0.7
[CoL^{mes}][2 OTf]/ MWCNT	-0.91	CO_2	23 ± 1	63 ± 1	3.5 ± 0.2	90 ± 1	-5.1 ± 0.5
		CO	90 ± 1	N/A	7 ± 1	97 ± 1	-2.5 ± 0.5
CoTPP/ MWCNT	-0.91	CO_2	74 ± 3	24 ± 1	2.0 ± 0.5	100 ± 2	-8.8 ± 0.6
		CO	85 ± 2	N/A	2.3 ± 0.1	87 ± 2	-4.4 ± 0.3

Table 3. Selectivity profile from CO_2R in 0.1 M $^nBu_4NPF_6/CH_3CN$

Complex	Acid	E (V vs. Ag/AgCl)	FE_{H2} (%)	FE_{CO} (%)	$FE_{ethylamine}$ (%)	Total FE (%)	TOF_{CO} (s^{-1})	<*j*> (mA cm^{-2})
[CoL^{mes}] [2 OTf]	2.6 M PhOH	-1.67	16.2 ± 0.5	81.4 ± 0.3	0	97.6 ± 0.4	0.000045	-3.2 ± 0.8
		-1.87	12 ± 2	80 ± 1	6 ± 1	98 ± 2	0.000058	-4.2 ± 0.7
		-1.97	6 ± 1	75 ± 1	10 ± 2	91 ± 2	0.00012	-9.80 ± 0.001
[CoL^{mes}] [2 OTf]	2.6 M CH_3COOH	-1.97	80 ± 3	4 ± 1	0	84 ± 3	$8.1x10^{-7}$	-12 ± 1
[CoL^{mes}] [2 Cl]	2.6 M PhOH	-1.97	6 ± 1	86 ± 1	1.0 ± 0.2	93 ± 1	0.00015	-9.8 ± 0.5

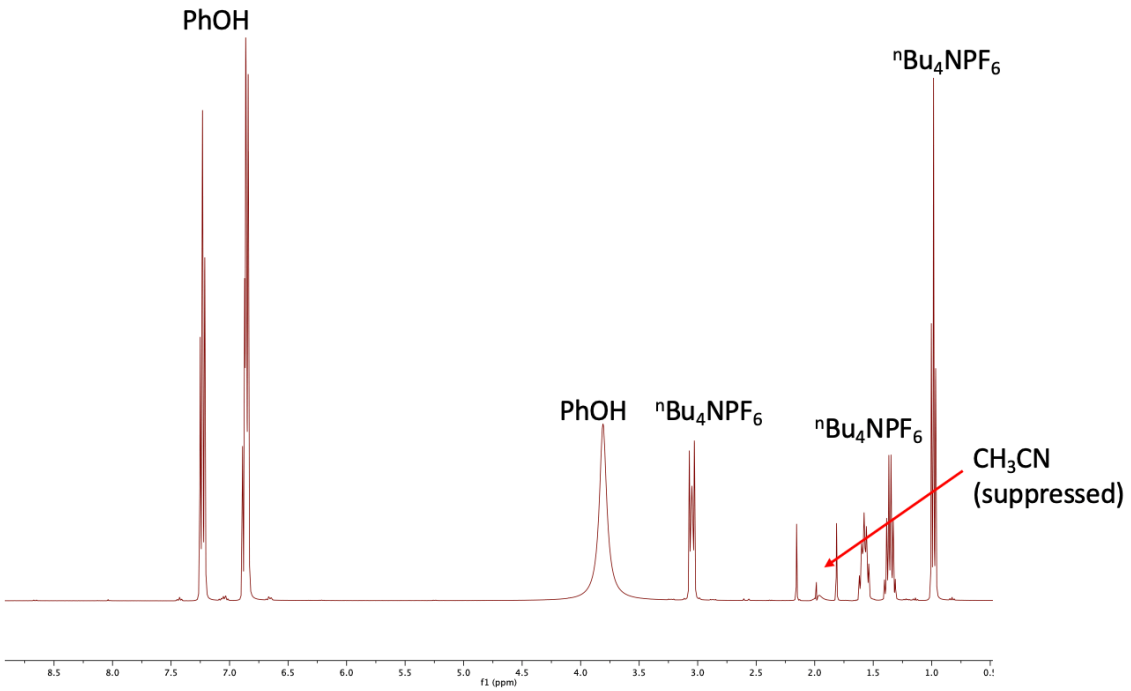

Figure 10. Sample ^{1}H NMR (400 MHz, 10% v/v CD_3CN/CH_3CN) of electrolyte from Table 2, entry 1.

Table 4. Comparing current enhancement from CO_2R between molecular electrocatalysts.

Complex	**E_{CO2R} (V vs. $Fc^{+/0}$)**	**i_{CO2R}/i_{N2}**	**[MeOH] (mol L^{-1})**
[CoL^{mes}][2 OTf]	-2.4	3.3	1.0
CoPc	-2.5	23.1	1.0
[$Co(py)_4$][2 X]	-2.36	43	4.0

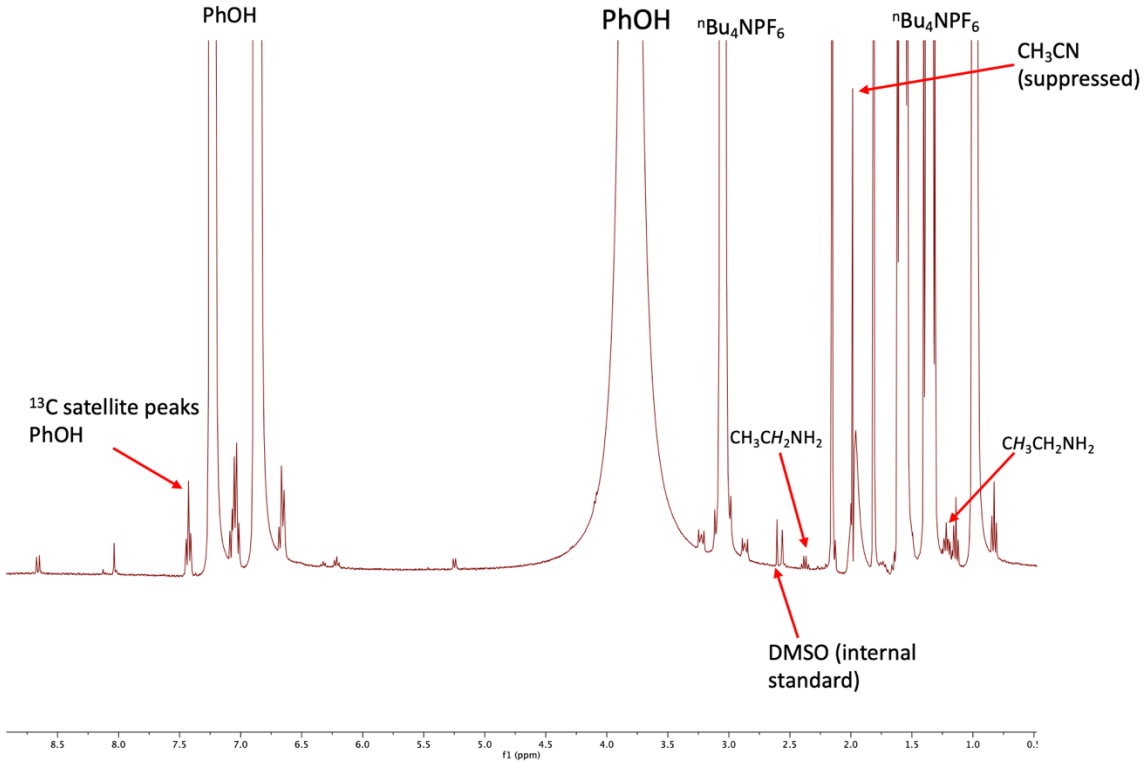

Figure 11. Increased vertical scale of ^{1}H NMR from Figure 9.

REFERENCES

(1) Nguyen, T. N.; Salehi, M.; Le, Q. Van; Seifitokaldani, A.; Dinh, C. T. Fundamentals of Electrochemical CO2 Reduction on Single-Metal-Atom Catalysts. *ACS Catal.* **2020**, *10* (17), 10068–10095.

(2) Guo, D.; Shibuya, R.; Akiba, C.; Saji, S.; Kondo, T.; Nakamura, J. Active Sites of Nitrogen-Doped Carbon Materials for Oxygen Reduction Reaction Clarified Using Model Catalysts. *Science (80-.).* **2016**, *351* (6271), 361 LP – 365.

(3) Jiang, K.; Siahrostami, S.; Zheng, T.; Hu, Y.; Hwang, S.; Stavitski, E.; Peng, Y.; Dynes, J.; Gangisetty, M.; Su, D.; et al. Isolated Ni Single Atoms in Graphene Nanosheets for High-Performance CO2 Reduction. *Energy Environ. Sci.* **2018**, *11* (4), 893–903.

(4) Liu, K.; Fu, J.; Lin, Y.; Luo, T.; Ni, G.; Li, H.; Lin, Z.; Liu, M. Insights into the Activity of Single-Atom Fe-N-C Catalysts for Oxygen Reduction Reaction. *Nat. Commun.* **2022**, *13* (1), 2075.

(5) Liu, J.; Zhang, G.; Ye, K.; Xu, K.; Sheng, Y.; Yu, C.; Zhang, H.; Li, Q.; Liang, Z.; Jiang, K. Top-down Manufacturing of Efficient CO2 Reduction Catalysts from the Gasification Residue Carbon. *Chem. Commun.* **2023**, *59* (5), 611–614.

(6) Zhang, L.; Fischer, J. M. T. A.; Jia, Y.; Yan, X.; Xu, W.; Wang, X.; Chen, J.; Yang, D.; Liu, H.; Zhuang, L.; et al. Coordination of Atomic Co–Pt Coupling Species at Carbon Defects as Active Sites for Oxygen Reduction Reaction. *J. Am. Chem. Soc.* **2018**, *140* (34), 10757–10763.

(7) Qiao, X.; Li, Q.; Schaugaard, R. N.; Noffke, B. W.; Liu, Y.; Li, D.; Liu, L.; Raghavachari, K.; Li, L. Well-Defined Nanographene–Rhenium Complex as an Efficient Electrocatalyst and Photocatalyst for Selective CO2 Reduction. *J. Am. Chem. Soc.* **2017**, *139* (11), 3934–3937.

(8) Li, Q.; Noffke, B. W.; Wang, Y.; Menezes, B.; Peters, D. G.; Raghavachari, K.; Li, L. Electrocatalytic Oxygen Activation by Carbanion Intermediates of Nitrogen-Doped Graphitic Carbon. *J. Am. Chem. Soc.* **2014**, *136* (9), 3358–3361.

(9) Koenig, J. D. B.; Dubrawski, Z. S.; Rao, K. R.; Willkomm, J.; Gelfand, B. S.; Risko, C.; Piers, W. E.; Welch, G. C. Lowering Electrocatalytic CO2 Reduction Overpotential Using N-Annulated Perylene Diimide Rhenium Bipyridine Dyads with Variable Tether Length. *J. Am. Chem. Soc.* **2021**, *143* (40), 16849–16864.

(10) Schaugaard, R. N.; Raghavachari, K.; Li, L. Redox "Innocence" of Re(I) in Electrochemical CO2 Reduction Catalyzed by Nanographene–Re Complexes. *Inorg. Chem.* **2018**, *57* (17), 10548–10556.

(11) Wang, M.; Torbensen, K.; Salvatore, D.; Ren, S.; Joulié, D.; Dumoulin, F.; Mendoza, D.; Lassalle-Kaiser, B.; Işci, U.; Berlinguette, C. P.; et al. CO2 Electrochemical Catalytic Reduction with a Highly Active Cobalt Phthalocyanine. *Nat. Commun.* **2019**, *10* (1), 3602.

(12) Seh, Z. W.; Kibsgaard, J.; Dickens, C. F.; Chorkendorff, I.; Nørskov, J. K.; Jaramillo, T. F. Combining Theory and Experiment in Electrocatalysis: Insights into Materials Design. *Science (80-.).* **2017**, *355* (6321), eaad4998.

(13) Chu, S.; Cui, Y.; Liu, N. The Path towards Sustainable Energy. *Nat. Mater.* **2017**, *16* (1), 16–22.

(14) Sapountzi, F. M.; Gracia, J. M.; Weststrate, C. J. (Kees-J.; Fredriksson, H. O. A.; Niemantsverdriet, J. W. (Hans). Electrocatalysts for the Generation of Hydrogen, Oxygen and Synthesis Gas. *Prog. Energy Combust. Sci.* **2017**, *58*, 1–35.

(15) Ail, S. S.; Dasappa, S. Biomass to Liquid Transportation Fuel via Fischer Tropsch Synthesis – Technology Review and Current Scenario. *Renew. Sustain. Energy Rev.* **2016**, *58*, 267–286.

(16) Lu, S.; Shi, Y.; Meng, N.; Lu, S.; Yu, Y.; Zhang, B. Electrosynthesis of Syngas via the Co-Reduction of CO2 and H2O. *Cell Reports Phys. Sci.* **2020**, *1* (11), 100237.

(17) Francke, R.; Schille, B.; Roemelt, M. Homogeneously Catalyzed Electroreduction of Carbon Dioxide—Methods, Mechanisms, and Catalysts. *Chem. Rev.* **2018**, *118* (9), 4631–4701.

(18) Wu, Y.; Liang, Y.; Wang, H. Heterogeneous Molecular Catalysts of Metal Phthalocyanines for Electrochemical CO2 Reduction Reactions. *Acc. Chem. Res.* **2021**, *54* (16), 3149–3159.

(19) Ren, X.; Zhao, J.; Li, X.; Shao, J.; Pan, B.; Salamé, A.; Boutin, E.; Groizard, T.; Wang, S.; Ding, J.; et al. In-Situ Spectroscopic Probe of the Intrinsic Structure Feature of Single-Atom Center in Electrochemical CO/CO2 Reduction to Methanol. *Nat. Commun.* **2023**, *14* (1), 3401.

(20) Ammar, N. R. An Environmental and Economic Analysis of Methanol Fuel for a Cellular Container Ship. *Transp. Res. Part D Transp. Environ.* **2019**, *69*, 66–76.

(21) Wu, Y.; Jiang, Z.; Lu, X.; Liang, Y.; Wang, H. Domino Electroreduction of CO2 to Methanol on a Molecular Catalyst. *Nature* **2019**, *575* (7784), 639–642.

(22) Su, J.; Musgrave, C. B.; Song, Y.; Huang, L.; Liu, Y.; Li, G.; Xin, Y.; Xiong, P.; Li, M. M.-J.; Wu, H.; et al. Strain Enhances the Activity of Molecular Electrocatalysts via Carbon Nanotube Supports. *Nat. Catal.* **2023**, *6* (9), 818–828.

(23) Shang, B.; Rooney, C. L.; Gallagher, D. J.; Wang, B. T.; Krayev, A.; Shema, H.; Leitner, O.; Harmon, N. J.; Xiao, L.; Sheehan, C.; et al. Aqueous Photoelectrochemical CO2 Reduction to CO and Methanol over a Silicon Photocathode Functionalized with a Cobalt Phthalocyanine Molecular Catalyst. *Angew. Chemie Int. Ed.* **2023**, *62* (4), e202215213.

(24) Matthew Espinosa, Fernando Guerrero, Alexandria Hong, and Theodor Agapie. *Manuscript in preparation.*

(25) Fenwick, A. Q.; Welch, A. J.; Li, X.; Sullivan, I.; DuChene, J. S.; Xiang, C.; Atwater, H. A. Probing the Catalytically Active Region in a Nanoporous Gold Gas Diffusion Electrode for Highly Selective Carbon Dioxide Reduction. *ACS Energy Lett.* **2022**, *7* (2), 871–879.

(26) Li, F.; Thevenon, A.; Rosas-Hernández, A.; Wang, Z.; Li, Y.; Gabardo, C. M.; Ozden, A.; Dinh, C. T.; Li, J.; Wang, Y.; et al. Molecular Tuning of CO2-to-Ethylene Conversion. *Nature* **2020**, *577* (7791), 509–513.

(27) Lees, E. W.; Mowbray, B. A. W.; Parlane, F. G. L.; Berlinguette, C. P. Gas Diffusion Electrodes and Membranes for CO2 Reduction Electrolysers. *Nat. Rev. Mater.* **2021**.

(28) Zoric, M. R.; Chan, T.; Musgrave III, C. B.; Goddard III, W. A.; Kubiak, C. P.; Cordones, A. A. In Situ X-Ray Absorption Investigations of a Heterogenized Molecular Catalyst and Its Interaction with a Carbon Nanotube Support. *J. Chem. Phys.* **2023**, *158* (7), 74703.

(29) Rivera Cruz, K. E.; Liu, Y.; Soucy, T. L.; Zimmerman, P. M.; McCrory, C. C. L. Increasing the CO2 Reduction Activity of Cobalt Phthalocyanine by Modulating the σ-Donor Strength of Axially Coordinating Ligands. *ACS Catal.* **2021**, *11* (21), 13203–13216.

(30) Yao, L.; Rivera-Cruz, K. E.; Zimmerman, P. M.; Singh, N.; McCrory, C. C. L. Electrochemical CO2 Reduction to Methanol by Cobalt Phthalocyanine: Quantifying CO2 and CO Binding Strengths and Their Influence on Methanol Production. *ACS Catal.* **2024**, *14* (1), 366–372.

(31) Smieja, J. M.; Kubiak, C. P. Re(Bipy-TBu)(CO)3Cl−improved Catalytic Activity for Reduction of Carbon Dioxide: IR-Spectroelectrochemical and Mechanistic Studies. *Inorg. Chem.* **2010**, *49* (20), 9283–9289.

(32) Smieja, J. M.; Benson, E. E.; Kumar, B.; Grice, K. A.; Seu, C. S.; Miller, A. J. M.; Mayer, J. M.; Kubiak, C. P. Kinetic and Structural Studies, Origins of Selectivity, and Interfacial Charge Transfer in the Artificial Photosynthesis of CO. *Proc. Natl. Acad. Sci.* **2012**, *109* (39), 15646–15650.

(33) Costentin, C.; Robert, M.; Savéant, J.-M. Catalysis of the Electrochemical Reduction of Carbon Dioxide. *Chem. Soc. Rev.* **2013**, *42* (6), 2423–2436.

(34) Xia, R.; Tian, D.; Kattel, S.; Hasa, B.; Shin, H.; Ma, X.; Chen, J. G.; Jiao, F. Electrochemical Reduction of Acetonitrile to Ethylamine. *Nat. Commun.* **2021**, *12* (1), 1949.

(35) Kim, C.; Bui, J. C.; Luo, X.; Cooper, J. K.; Kusoglu, A.; Weber, A. Z.; Bell, A. T. Tailored Catalyst Microenvironments for CO2 Electroreduction to Multicarbon Products on Copper Using Bilayer Ionomer Coatings. *Nat. Energy* **2021**, *6* (11), 1026–1034.

(36) Martinez, J. L.; Schneider, J. E.; Anferov, S. W.; Anderson, J. S. Electrochemical Reduction of N2O with a Molecular Copper Catalyst. *ACS Catal.* **2023**, *13* (19), 12673–12680.

(37) Creutz, E. F. and C. C-H Bond Activation by Cobalt(I) Macrocycles: Rapid H/D Exchange between Macrocycle and Acetonitrile Solvent. *Inorg. Chem.* **1994**, *33*, 1729–1730.

(38) Britovsek, G. J. P.; England, J.; Spitzmesser, S. K.; White, A. J. P.; Williams, D. J. Synthesis of Iron(Ii), Manganese(Ii) Cobalt(Ii) and Ruthenium(Ii) Complexes Containing Tridentate Nitrogen Ligands and Their Application in the Catalytic Oxidation of Alkanes. *Dalt. Trans.* **2005**, No. 5, 945–955.

(39) Lazanas, A. C.; Prodromidis, M. I. Electrochemical Impedance Spectroscopy─A Tutorial. *ACS Meas. Sci. Au* **2023**, *3* (3), 162–193.

(40) Zheng, W. IR Compensation for Electrocatalysis Studies: Considerations and Recommendations. *ACS Energy Lett.* **2023**, *8* (4), 1952–1958.

(41) Han, Z.; Kortlever, R.; Chen, H.-Y.; Peters, J. C.; Agapie, T. CO2 Reduction Selective for C≥2 Products on Polycrystalline Copper with N-Substituted Pyridinium Additives. *ACS Cent. Sci.* **2017**, *3* (8), 853–859.

(42) Nie, W.; Heim, G. P.; Watkins, N. B.; Agapie, T.; Peters, J. Organic Additive-Derived Films on Cu Electrodes Promote Electrochemical CO2 Reduction to C2+ Products Under Strongly Acidic Conditions. *Angew. Chemie Int. Ed.* **2023**, *n/a* (n/a).

(43) Heenan, A. R.; Hamonnet, J.; Marshall, A. T. Why Careful IR Compensation and Reporting of Electrode Potentials Are Critical for the CO2 Reduction Reaction. *ACS Energy Lett.* **2022**, *7* (7), 2357–2361.

(44) Ma, M.; Zheng, Z.; Yan, W.; Hu, C.; Seger, B. Rigorous Evaluation of Liquid Products in High-Rate CO2/CO Electrolysis. *ACS Energy Lett.* **2022**, *7* (8), 2595–2601.

(45) Zhanaidarova, A.; Jones, S. C.; Despagnet-Ayoub, E.; Pimentel, B. R.; Kubiak, C. P. Re(TBu-Bpy)(CO)3Cl Supported on Multi-Walled Carbon Nanotubes Selectively Reduces CO2 in Water. *J. Am. Chem. Soc.* **2019**, *141* (43), 17270–17277.

(46) Lobaccaro, P.; Singh, M. R.; Clark, E. L.; Kwon, Y.; Bell, A. T.; Ager, J. W. Effects of Temperature and Gas–Liquid Mass Transfer on the Operation of Small Electrochemical Cells for the Quantitative Evaluation of CO2 Reduction Electrocatalysts. *Phys. Chem. Chem. Phys.* **2016**, *18* (38), 26777–26785.

CHAPTER VI

LIGANDS WITH EXTENDED π SYSTEMS: LOWER OVERPOTENTIALS IN ELECTROCATALYTIC CO_2 REDUCTION WITH Re

This chapter was reproduced from:

Heim, G.P.; Dev, V.M.; Agapie, T. *Manuscript submitted.*

ABSTRACT: We report molecular CO_2 reduction (CO_2R) electrocatalysts bearing novel polyaromatic ligands (**2-Re(CO)$_3$Br** and **3-Re(CO)$_3$Br**) that display lower electrocatalytic potential (E_{cat}) of CO_2R to CO by ~310 mV compared to **^{tBu}bpyRe(CO)$_3$Br**. Bulk electrolysis experiments reveal improved selectivity for CO at 600 mV more positive potential than obtained with **^{tBu}bpyRe(CO)$_3$Br**. This study demonstrates that molecular electrocatalysts bearing polyaromatic ligands proximal to the metal center improve electrocatalytic performance.

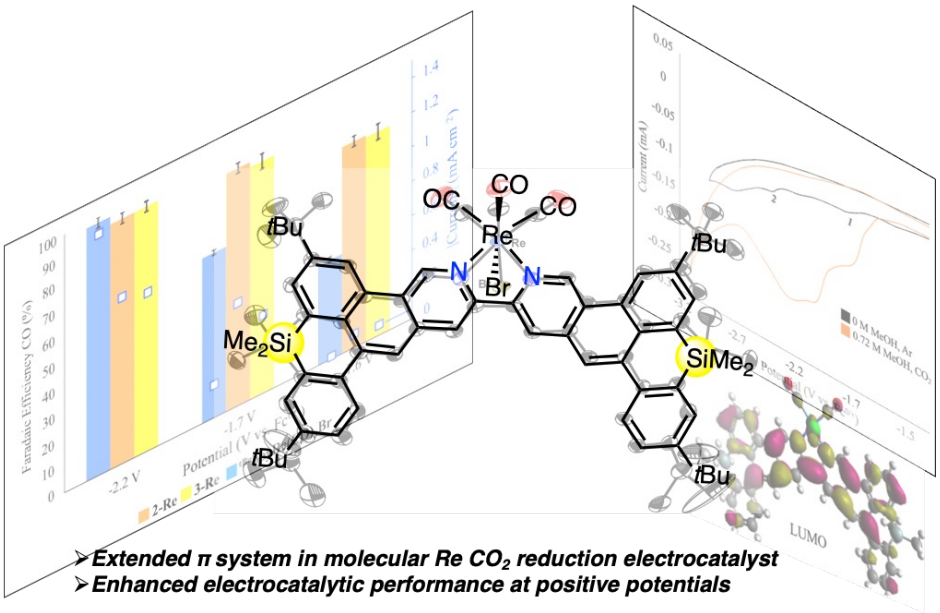

ACKNOWLEDGMENTS

I thank Michael Takase for assistance with X-ray crystallography. Vidhya Dev is acknowledged for her assistance with density functional theory computations. This material is based on work performed by the Liquid Sunlight Alliance, which is supported by the U.S. Department of Energy, Office of Science, Office of Basic Energy Sciences, Fuels from Sunlight Hub under Award DE-SC0021266. The Resnick Sustainability Institute at Caltech is acknowledged for support of the laboratory facilities in which this research was conducted. I am grateful for the Beckman Institute for instrumentation support.

INTRODUCTION

Carbon-supported single-atom catalysts (SACs) have demonstrated improved electrocatalytic performance, including high selectivity at low overpotentials.[1–5] Description of the actives site as metal centers embedded in a heteroatom-doped graphene has been developed from images or spectroscopic data.[6] To address limitations in obtaining atomic resolution characterization, recent work has investigated molecular mimics of SACs which show high performance for electrochemical reduction of CO_2 to CO,[7–11] the typical product for molecular CO_2 reduction (CO_2R) electrocatalysts.[12–16] Modifications to 2,2'-bipyridine ligand in Lehn complexes with polycyclic aromatic hydrocarbons (PAHs) have been reported to lower the potential for CO_2R by up to 800 mV (Figure 1).[7,9,10] However, the scarcity of examples with structural diversity of such systems limits understanding of the impact conjugated π systems on the catalytic site.

We set out to prepare ligands with that could enhance electronic communication between a catalytic metal center (Re) and an extended π system and to probe their impact on for CO_2R. Herein, we report complexes based on the $Re(bpy)(CO)_3$ motif supported by novel ligand frameworks displaying extended π systems. Constant-potential CO_2R electrolysis reveals high selectivity for CO up to 600 mV more positive relative to E_{cat} for **^{tBu}bpyRe(CO)$_3$Br**. Density functional theory (DFT) calculations suggest greater delocalization across the ligand scaffold in the frontier molecular orbitals (MOs) compared to **^{tBu}bpyRe(CO)$_3$Br**, thus leading to CO_2R occurring at more positive potentials.

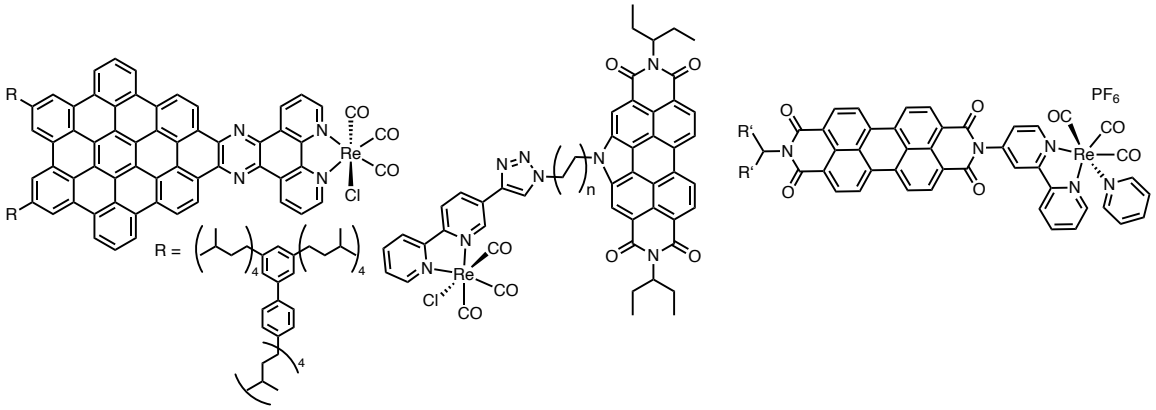

Figure 1. Extended π system ligands supporting Re for electrochemical CO_2R.

RESULTS AND DISCUSSION

Scheme 1. Synthesis of **2-Re(CO)$_3$Br** and **3-Re(CO)$_3$Br**

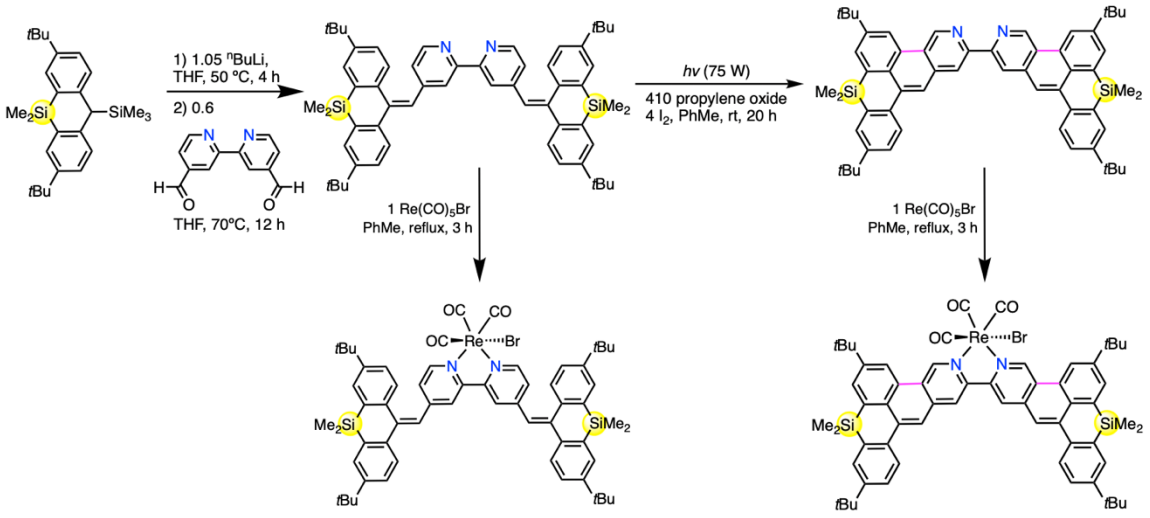

Compound **1** was prepared in four steps from diphenylmethane following procedures reported by Wagner and co-workers.[17–20] **2** was prepared via deprotonation of **1** with *n*-butyllithium followed by addition of 2,2'-bipyridine-4,4'-dicarbaldehyde (Scheme 1).[18] **2** was converted to **3** using excess iodine and (±)propylene oxide under UV irradiation (75-W arc lamp).[18] Metalation of **2** and **3** each with $Re(CO)_5Br$ in refluxing toluene results in the corresponding metal complexes **2-Re(CO)$_3$Br** and **3-Re(CO)$_3$Br**.[21] The complexes were purified by recrystallization: **2-Re(CO)$_3$Br** from room temperature

evaporation of a concentrated C_6H_6 solution into hexamethyldisiloxane (HMDSO) and **3-Re(CO)$_3$Br** from room temperature evaporation of hexanes into a concentrated THF solution. The solid-state structures confirm the identity of the target molecules (Figure 2). The crystal structure of **2-Re(CO)$_3$Br** highlights the bipyridine π system conjugated with that of the olefins and arenes olefin and flexibility of the backbone of the ligand at the vinylic positions with the two large substituents pointing in, likely broadening the ^{1}H NMR resonances (Figure 13). The complex **3-Re(CO)$_3$Br** possesses mirror symmetry between each silanthracene moiety (Figure 30).[17]

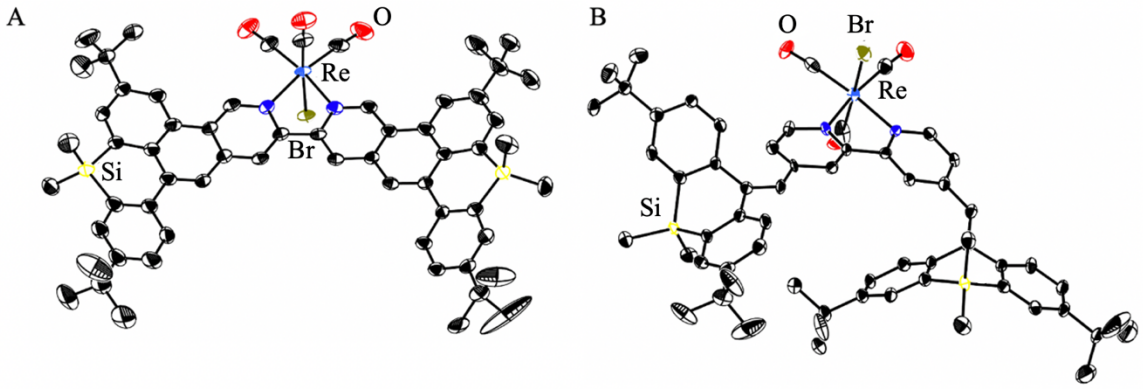

Figure 2. Solid state structures of (A) **3-Re(CO)$_3$Br** and (B) **2-Re(CO)$_3$Br** as determined by single-crystal X-ray diffraction. Carbon atoms are black and nitrogen atoms are blue. Hydrogen atoms as well as solvent molecules are omitted for clarity. Thermal ellipsoids are displayed at 50% probability.

2-Re(CO)$_3$Br and **3-Re(CO)$_3$Br** were investigated by cyclic voltammetry (CV) with in a 0.1 M [N^n(Bu)$_4$][PF$_6$] solution in CH_3CN. Solutions were sparged with argon to remove oxygen. The features observed are similar to those of **^{tBu}bpyRe(CO)$_3$Br.**[21–23] Scanning to negative potentials from open circuit voltage (100 mV vs. Fc$^{+/0}$), the CV of **2-Re(CO)$_3$Br** reveals two quasi-reversible reductions (Figure 3), which are assigned as 1) 1-

electron reduction of the ligand scaffold, and 2) reduction of a halide-dissociated complex formed after step 1, resulting in formation of an anionic species, with a five-coordinate metal center. These assignments are supported by previous work investigating infrared spectroelectrochemistry of Lehn complexes.[21–23] A third reduction observed at more negative potentials is assigned to reduction of bipyridine, similarly reported in complexes bearing electron deficient ligands.[24,25] A similar electrochemical profile is observed for **3-Re(CO)$_3$Br** (Figure 4).

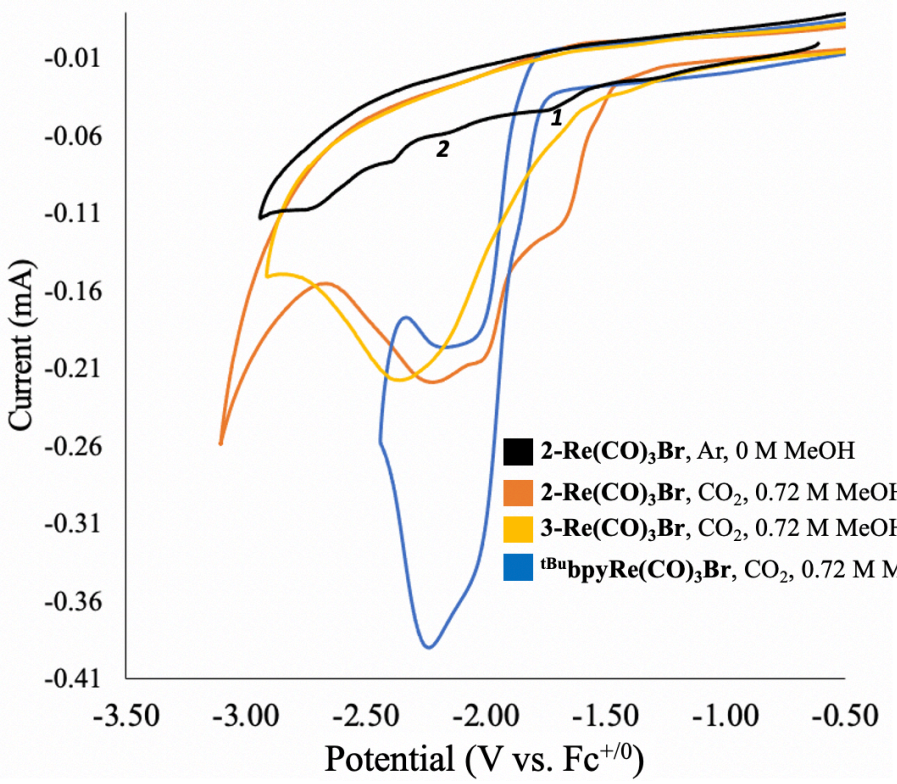

Figure 3. CVs of **2-Re(CO)$_3$Br**, **3-Re(CO)$_3$Br**, and **^{tBu}bpyRe(CO)$_3$Br** (1.5 mM) in CO_2-saturated or Ar-saturated electrolyte (0.1 M $[N^n(Bu)_4][PF_6]/CH_3CN$) with 0.72 M MeOH or 0 M MeOH at 200 mV/s scan rate. Working electrode: glassy carbon rod (3 mm diameter), reference electrode: Ag/AgCl wire, and counter electrode: Pt wire. Scan rate: 200 mV/s. Potentials referenced to 1 mM ferrocene$^{0/+}$ ($Fc^{0/+}$) redox couple.

Sparging the electrochemistry solutions of each **2-Re(CO)$_3$Br** and **3-Re(CO)$_3$Br** with CO_2 and introducing MeOH reveals an enhancement in current at negative potentials (Figure 3 and 5), demonstrating electrocatalytic CO_2R (Figure 2). As [MeOH] increased, the onset potential became more positive, suggesting a dependence of the onset potential of CO_2R on the proton concentration (Figure 5).[9,26] In 0.72 M MeOH, the onset potential and half-wave potential ($E_{cat/2}$) of **2-Re(CO)$_3$Br** are more positive than that of **^{tBu}bpyRe(CO)$_3$Br** by ~310 mV (Figure 3). While different electrolyte conditions can complicate comparison, **2-Re(CO)$_3$Br** and **3-Re(CO)$_3$Br,** possess among the most positive values of $E_{cat/2}$ relative to published molecular CO_2R electrocatalysts (Table 1).[27–32] The Re-hexabenzocoronene complex reported by Li and co-workers (**bpy^{HBC}Re(CO)$_3$Cl**) catalyzes CO_2R at the most positive potential (–1.04 V vs. $Fc^{+/0}$).[7] The lower onset potentials observed for **2-Re(CO)$_3$Br** and **3-Re(CO)$_3$Br** relative to **^{tBu}bpyRe(CO)$_3$Br** are likely due to combined electron-withdrawing effects from the vinyl-silanthracene moiety and greater delocalization imparted by the polyaromatic framework. Despite the polyaromatic ligand in **3-Re(CO)$_3$Br**, the onset potential is not significantly more positive than that of **2-Re(CO)$_3$Br**; the number of π-electrons is the same for both compounds. Additionally, the lack of energetically accessible orbitals for reduction in the dimethylsilane moiety precludes further reduction of the extended π system.[17]

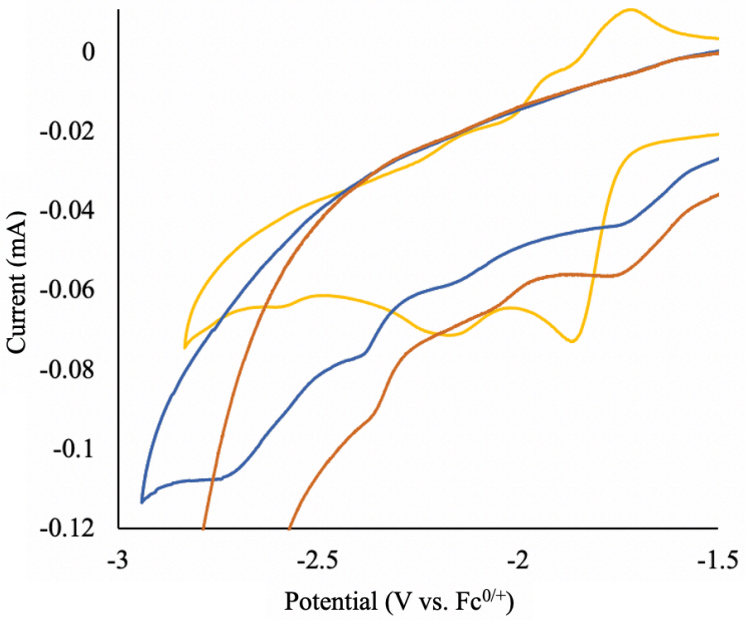

Figure 4. CVs of **2-Re(CO)$_3$Br** (blue), **3-Re(CO)$_3$Br** (orange), and **^{tBu}bpyRe(CO)$_3$Br** under $Ar_{(g)}$.

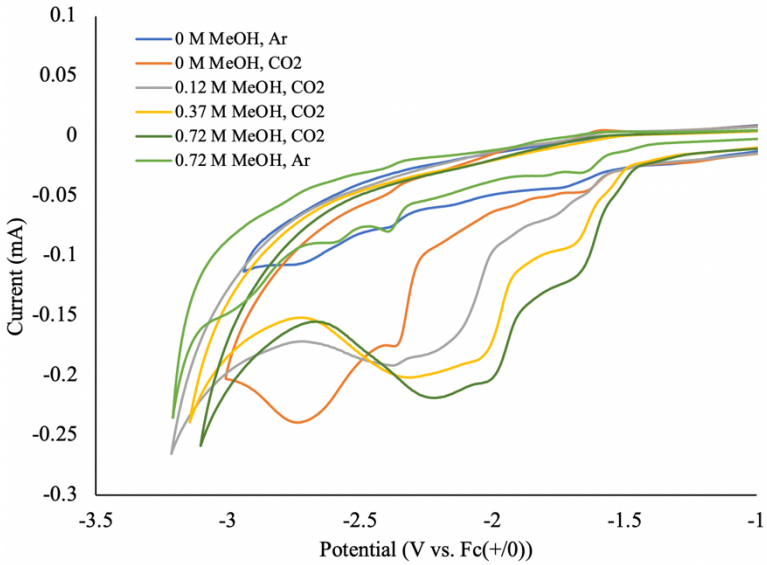

Figure 5. CVs of **2-Re(CO)$_3$Br** with various [MeOH] under $CO_{2(g)}$ or $Ar_{(g)}$.

Table 1. Comparing $E_{cat/2}$ derived from cyclic voltammetry between molecular CO_2R catalysts

Authors	Complex	Electrolyte	Proton source	$E_{cat/2}$ (V vs. $Fc^{+/0}$)[a]
This work	**2-Re(CO)$_3$Br**	0.1 M $(^nBu)_4PF_6/CH_3CN$	0.72 M MeOH	-1.47
This work	**3-Re(CO)$_3$Br**	0.1 M $(^nBu)_4PF_6/CH_3CN$	0.72 M MeOH	-1.53
This work	**^{tBu}bpyRe(CO)$_3$Br**	0.1 M $(^nBu)_4PF_6/CH_3CN$	0.72 M MeOH	-1.78
Li and co-workers[7]	**bpy^{HBC}Re(CO)$_3$Cl**	0.1 M $(^nBu)_4PF_6$/THF	1.2 M MeOH	-1.04
Welch and co-workers[9]	**Re(py-C0-NPDI)**	0.1 M $(^nBu)_4PF_6$/DMF	0.5 M CF_3CH_2OH	-2.08
Kubiak and co-workers[22]	**^{tBu}bpyRe(CO)$_3$Cl**	0.1 M $(^nBu)_4PF_6/CH_3CN$	1 M PhOH	-1.85
Kubiak and co-workers[22]	**4,4'-CF$_3$bpyRe(CO)$_3$Cl**	0.1 M $(^nBu)_4PF_6/CH_3CN$	1 M PhOH	-2.5
McCrory and co-workers[29]	**[Co(PDI-PyCH$_3$I)]$^+$**	0.1 M $(^nBu)_4PF_6/CH_3CN$	11 M H_2O	-1.55
Marinescu and co-workers[27]	**[Co(py)$_4$]$^{2+}$**	0.1 M $(^nBu)_4PF_6$/DMF	1.2 M CF_3CH_2OH	-2.2
Deronzier and co-workers[25]	**dmbpyMn(CO)$_3$Cl**	0.1 M $(^nBu)_4ClO_4/CH_3CN$	2.8 M H_2O	-1.78
Kubiak and co-workers[30]	**[bpy^{mes}Mn(CO)$_3$NCCH$_3$][OTf]**	0.1 M $(^nBu)_4PF_6/CH_3CN$	0.12 M $Mg(OTf)_2$	-1.5
Savéant and co-workers[26]	**FeTDHPP**	0.1 M $(^nBu)_4PF_6$/DMF	2 M H_2O	-2.0
Peters and co-workers[28]	**[Co^{III}N$_4$H(Br)$_2$]$^+$**	0.1 M $(^nBu)_4PF_6/CH_3CN$	10 M H_2O	-1.68

[a]Onset potential

Comparing the apex of the catalytic waves reveals that the value of the catalytic current ($|i_{cat}|$) is significantly lower for **2-Re(CO)$_3$Br** and **3-Re(CO)$_3$Br** than **^{tBu}bpyRe(CO)$_3$Br** (Figure 3). Electrocatalysis with molecular systems occurring at lower overpotential has often led to decrease in $|i_{cat}|$.[7,22,31–35] The greater delocalization provided by the extended π system in **2-Re(CO)$_3$Br** and **3-Re(CO)$_3$Br** renders the Re center less nucleophilic, thus attenuating the reactivity with CO_2 and the rate of CO_2R.[7]

Bulk electrolysis experiments confirm that CO is the exclusive CO_2R product for all Re complexes tested in the presence of MeOH at –2.2 V vs. $Fc^{+/0}$, with no detectable H_2 (Figure 6 and Table 2). Electrolysis experiments were also carried out at more positive potentials. The Faradaic efficiency for CO (FE_{CO}) when employing **^{tBu}bpyRe(CO)$_3$Br** is lower compared to either **2-Re(CO)$_3$Br** or **3-Re(CO)$_3$Br** at –1.6 V vs. $Fc^{+/0}$ (39% vs. 90%) in addition to having a lower partial current density for CO ($|j_{CO}|$, 0.08 mA cm^{-2} vs. 0.54 mA cm^{-2}) by a factor of 6.8. These data indicate that the extended π system ligands improve CO_2R performance over state-of-the-art **^{tBu}bpyRe(CO)$_3$Br** at more positive potentials.

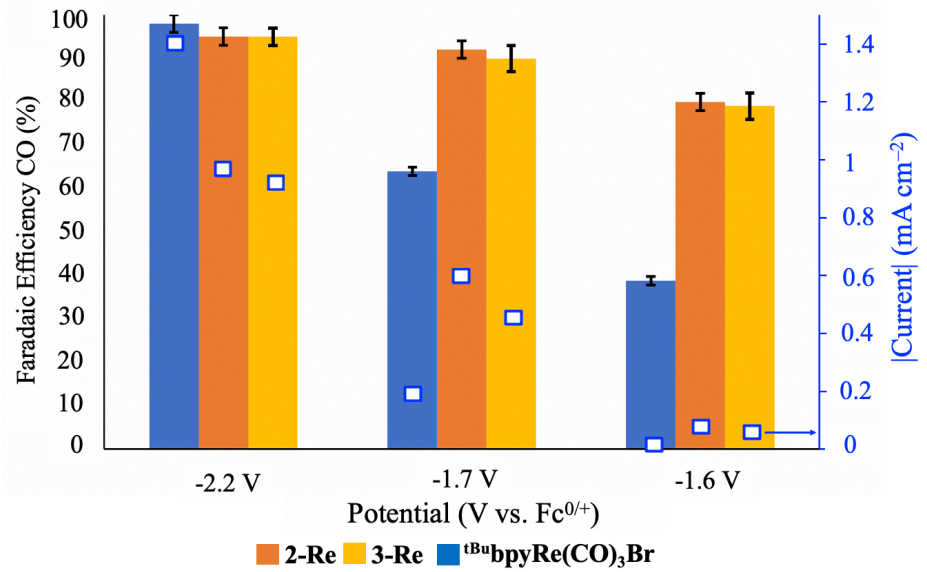

Figure 6. FE_{CO} at different applied potentials for each Re complex. Bulk electrolysis carried out for 30 minutes with 1.5 mM [Re] and 0.72 M MeOH. Error bars represent standard deviations from triplicate measurements.

To understand how structure impacts the electronic structure, DFT calculations were carried out. Model structures were analyzed, where hydrogen atoms were employed instead of *tert*-butyl groups and chloride instead of bromide (heretofore labeled as **2^{H}-Re(CO)$_3$Cl** and **3^{H}-Re(CO)$_3$Cl**, respectively). Each structure was optimized using B3LYP functionals.[36] LANL2DZ basis set was employed for the Re atom[37–39] and 6-311G(d,p) for all other atoms (Figures 19-29).[37,40]

The LUMOs of **2^{H}-Re(CO)$_3$Cl** and **3^{H}-Re(CO)$_3$Cl** reveal orbital contributions from the bipyridine ligand and little contribution from Re (0.8% and 0.5%, respectively), with the orbitals on **3^{H}-Re(CO)$_3$Cl** delocalized more extensively on the extended π system (Figure 7). A similar phenomenon is observed in the LUMO of **^{tBu}bpyRe(CO)$_3$Cl**, but greater contribution from Re is evident (3.0%). The most positive reduction event has been

previously assigned in **^{tBu}bpyRe(CO)$_3$Br** as ligand-based,[23,41] and the ligand-based nature of the LUMOs from **2^{H}-Re(CO)$_3$Cl** and **3^{H}-Re(CO)$_3$Cl** are consistent with a similar phenomenon in the compounds reported herein. The positive shift in the redox features for **2-Re(CO)$_3$Br** and **3-Re(CO)$_3$Br** relative to **^{tBu}bpyRe(CO)$_3$Br** (Figure 4) are explained in terms of the former species exhibiting more extended π systems for the nitrogen-containing ligands making them easier to reduce by affording greater delocalization of the reduced state.[7,9,10] HOMO and HOMO-1 are exclusively Re-based, with d_{xz} and d_{yz} parentage, consistent to previous reports.[9,41]

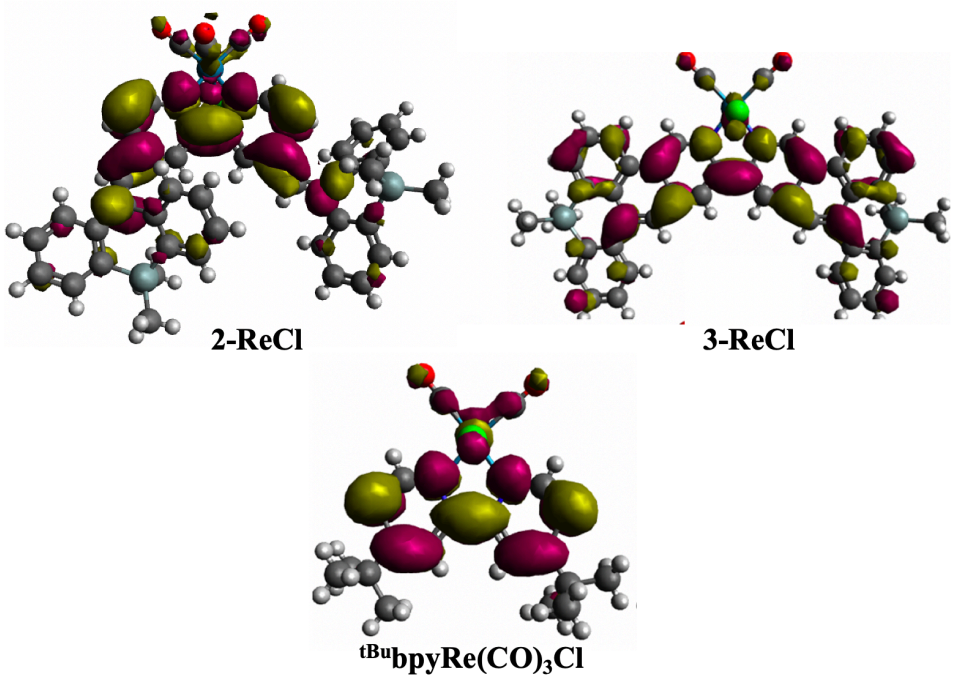

Figure 7. LUMOs of **2-ReCl**, **3-ReCl**, and **^{tBu}bpyRe(CO)$_3$Cl**. Isovalues set to 0.02.

The redox states proposed in the mechanism of CO_2R,[23,41] 1-electron reduced, halide-dissociated and 2-electron reduced halide-dissociated, were investigated computationally. The significant delocalization onto the bipyridine ligand in the HOMOs of **[2^{H}-Re(CO)$_3$]$^{-}$** and **[3^{H}-Re(CO)$_3$]$^{-}$** suggests that the metal center is less nucleophilic

relative to [^{tBu}**bpyRe(CO)$_3$**]$^-$, thus leading to attenuated CO_2R activity.[7,10,22] This phenomenon explains the lower $|i_{cat}|$ for **2-Re** and **3-Re** compared to ^{tBu}**bpyRe(CO)$_3$Br** (Figure 2).

CONCLUSIONS

In summary, we report Lehn complexes displaying novel conjugated polyaromatic ligands. CV studies demonstrate lower onset potential for CO_2R relative to ^{tBu}**bpyRe(CO)$_3$Br**. Bulk electrolysis experiments show high selectivity for CO (FE_{CO} = 80%) and 6.8 fold increase in CO_2R activity at potentials up to 600 mV more positive than the optimal potential for ^{tBu}**bpyRe(CO)$_3$Br**. DFT studies suggest that this improved electrochemical performance is due to significant electron delocalization over the π-conjugated ligand.

EXPERIMENTAL

Materials and Methods

General Considerations. Unless otherwise specified, all operations involving air- or water-sensitive reagents were carried out in an MBraun drybox under a nitrogen atmosphere or using standard Schlenk and vacuum line techniques. Glassware was oven-dried at 140 ºC for 2 h prior to use on the Schlenk line or in the MBraun drybox. Tetrahydrofuran (THF), diethyl ether (Et_2O) , toluene, pentane, and hexanes for air- and moisture-sensitive reactions were dried by the method of Grubbs.[40] Dry *N,N*-dimethylformamide (DMF) was purchased from Millipore Sigma and cannula transferred to freshly-activated 3 Å molecular sieves and stored in a Teflon-sealed Schlenk tube under N_2 atmosphere for 12 hours prior to use. Deuterated solvents were purchased from Cambridge Isotope Laboratories and $CDCl_3$ was used as received. C_6D_6 was dried with Na/benzophenone and vacuum transferred once the solution was purple. Bis(4-(*tert*-butyl)phenyl)methane, bis(2-bromo-4-(*tert*-butyl)phenyl)methane were prepared following literature procedures[20,19], 3,7-di-*tert*-butyl-5,5-dimethyl-5,10-dihydrodibenzo[*b*,*e*]siline, and **1** were each prepared following literature procedures.[17] **^{tBu}bpyRe(CO)$_3$Br** was prepared following a reported procedure, but $Re(CO)_5Br$ was used instead of $Re(CO)_5Cl$.[21] All solvents, once dried and degassed, were stored under a nitrogen atmosphere over activated 3 Å molecular sieves. ^1H, and $^{13}C\{^1H\}$ spectra were recorded on Varian Mercury 300 MHz or Varian 400 MHz spectrometers at ambient temperatures, unless otherwise denoted. ^1H and $^{13}C\{^1H\}$ NMR spectra are reported referenced internally to residual solvent peaks reported relative to tetramethylsilane. Gas chromatography-mass spectrometry (GC-MS) were performed on an Agilent 6890A instrument using a HP-5MS column (30 m length, 0.25 mm diameter, 0.50 μm film) and an Agilent 5973N mass-selective EI detector. Infrared (IR) spectra were collected on a Thermo Fischer Nicolet 6700 FTIR spectrometer. Absorption spectra were recorded on a Varian Cary Bio 50 spectrophotometer. Fast atom bombardment-mass spectrometry (FAB-MS) analyses were performed

with a JEOL JMS-600H high resolution mass spectrometer. Photolyses were conducted using an Oriel Instruments arc lamp housing and a Osram 75 W Xe arc lamp set to a current of 5.4 A

Electrochemical measurements. All electrochemical measurements were carried out using a Biologic VMP3 multichannel potentiostat. All cyclic voltammetry (CV) measurements were performed in a three-electrode cell, which consisted of glassy carbon (working; 3.0 mm diameter), silver wire (reference) and bare platinum wire (counter). Dry acetonitrile that contained 100 mM $(^{n}Bu)_4NPF_6$ was used as the electrolyte solution. The ferrocene/ferrocenium (Fc/Fc^{+}) redox wave was used as an internal standard for all measurements (1 mM). The glassy carbon electrode was polished with alumina paste (0.05 μm, Buehler) and rinsed with nanopure water followed by drying under a stream of nitrogen. The platinum wire was flame dried and rinsed with acetonitrile prior to use. All solutions for CV were loaded with 5 mL of a 1.5 mM-solution of [Re] in the electrolyte in a 20-mL scintillation vial containing a magnetic stir bar. The solution was sparged with stirring with the appropriate gas ($Ar_{(g)}$ or $CO_{2(g)}$) for 10 minutes at 25 ºC with stirring before performing any electrochemical measurements.

Bulk electrolysis experiments measurements were carried out at constant potential in a custom-made PEEK flow cell setup similar to the one reported by Ager and co-workers using a glassy carbon plate as the working electrode and a platinum foil as the counter electrode.[41] Concentration of [Re] was 1.5 mM; concentration of MeOH was 0.72 M. The cathode compartment was separated from the anode compartment by a Selemion AMV anion-exchange membrane (AGC Engineering Co.). All potentials were measured versus a leakless Ag/AgCl reference electrode (Innovative Instruments) with an outer diameter of 5 mm that was inserted into the cathode compartment. The reference electrode was calibrated against ferrocenecarboxylic acid in a 0.2 M phosphate buffer solution at pH 7.0 (+0.239 V vs. Ag/AgCl). Potentiostatic electrochemical impedance spectroscopy (PEIS) measurements were

carried out prior to each electrolysis experiment to determine the Ohmic resistance of the flow cell. The impedance measurements were carried out at frequencies ranging from 200 kHz to 100 MHz to measure the solution resistance. A Nyquist plot was plotted and in the high-frequency part a linear fit was performed, and the axis intersection was calculated. The value of this intersection represents the Ohmic resistance of the cell. An average of 3 measurements was taken to calculate the value of R. Typical resistance values ranged from 50 to 80 Ω. Each chronoamperometry experiment was performed in triplicate.

All chronoamperometric experiments were performed for 30 min at 25 °C using 100 mM $(^{n}Bu)_4NPF_6$ as the electrolyte. The potentiostat was set to compensate for 85 % of the Ohmic drop, with the remaining 15% being compensated for after the measurements. The effluent gas stream coming from the flow cell (10 mL/min) was flowed into the sample loops of a gas chromatograph (GC-FID/TCD, SRI 8610C, in Multi Gas 5 configuration) equipped with HayeSep D and molecular sieve 5 Å columns. Carbon monoxide was detected by a S4 methanizer-flame ionization detector (FID), and the hydrogen was detected by a thermal conductivity detector (TCD). Every 10 minutes, 2 mL of gas was sampled to determine the concentration of gaseous products.

Synthesis

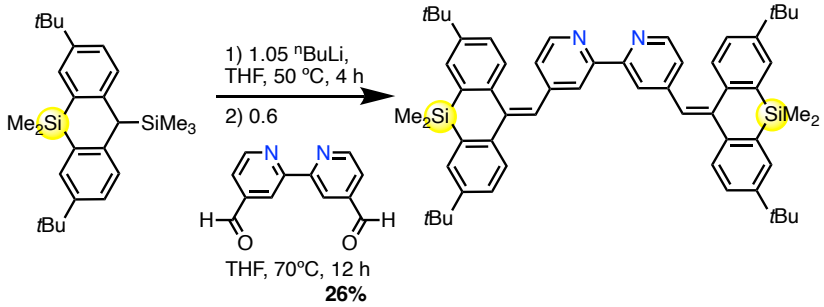

In an inert atmosphere glove box, a 100-mL Schlenk tube fitted with a screw-in Teflon stopper was charged with **1** (626 mg, 1.53 mmol) and 30 mL of THF. *N*-butyllithium (0.61 mL 1.53 mmol) was added dropwise via syringe at room temperature, resulting in a red solution. The flask was sealed and heated under N_2 flow at 50 ºC for 4 h. The flask was cooled to room temperature, sealed, and brought back into the glove box. 2,2'-bipyridine-4,4'-dicarbaldehyde (195 mg, 0.92 mmol) was suspended in THF and added to the Schlenk tube at room temperature. The flask was sealed and heated under N_2 flow to reflux for 12 h, causing the suspension to turn orange. The reaction was quenched with water and allowed to stir for 30 min at room temperature. Dichloromethane was added to the mixture to partition the organic and aqueous layers. The organic layer was washed with water (6 x 25 mL), brine (2 x 25 mL) and dried with magnesium sulfate. The volatiles were removed on the rotary evaporator, and the orange oil was purified via silica gel column chromatography (15% EtOAc/Hexanes). The white solid **2** was dried at 60ºC under vacuum for 12 h and brought into the glove box (200 mg, 26% yield). ^{1}H NMR (400 MHz, $CDCl_3$) δ= 8.42 (app d, 2H, Ar*H*), 8.38 (br s, 1H, Ar*H*), 7.70 (app d, 2H, Ar*H*), 7.66 (br s, 2H, Ar*H*), 7.50 (dd, 2H, Ar*H*), 7.17 (s, 2H, Ar*H*), 7.15 (d, 2H, Ar*H*), 6.94 (s, 2H, Ar*H*), 6.92 (s, 2H, Ar*H*), 1.39 (s, 18H, -C(CH_3)$_3$), 1.34 (s, 18H, -C(CH_3)$_3$), 0.59 (br s, 12H, -Si(CH_3)$_3$). ^{13}C{^{1}H} NMR (101 MHz, $CDCl_3$) δ 155.77 (aryl-*C*), 152.41 (aryl-*C*), 151.23 (aryl-*C*), 150.27 (aryl-*C*), 148.87 (aryl-*C*), 145.14 (aryl-*C*), 142.65 (aryl-*C*), 139.73 (aryl-*C*), 138.39 (aryl-*C*), 136.77 (aryl-*C*), 134.74 (aryl-*C*), 130.32 (aryl-*C*), 129.68 (aryl-*C*), 129.31 (aryl-*C*), 127.52 (aryl-*C*), 126.89 (aryl-*C*), 124.84 (aryl-*C*), 124.07 (aryl-*C*), 123.03 (aryl-*C*), 34.99 (-*C*(CH$_3$)$_3$), 34.88 (-*C*(CH$_3$)$_3$),

34.50 (-C(CH_3)$_3$), 29.85 (-C(CH_3)$_3$), -1.08 (-Si(CH_3)$_3$). HRMS (FAB+) m/z Calcd. for [M + H^+] $C_{58}H_{68}N_2Si_2$ 849.5012., found 849.5033.

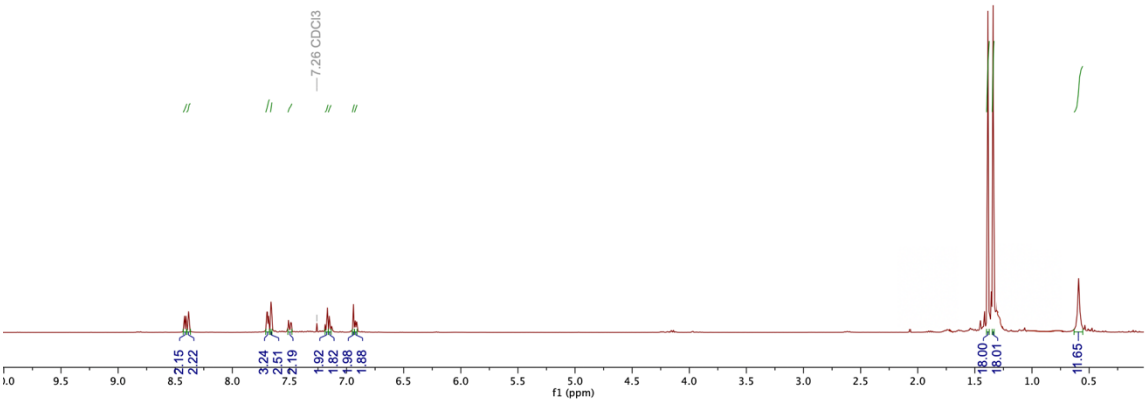

Figure 9. ^{1}H NMR spectrum (400 MHz, $CDCl_3$) of **2**.

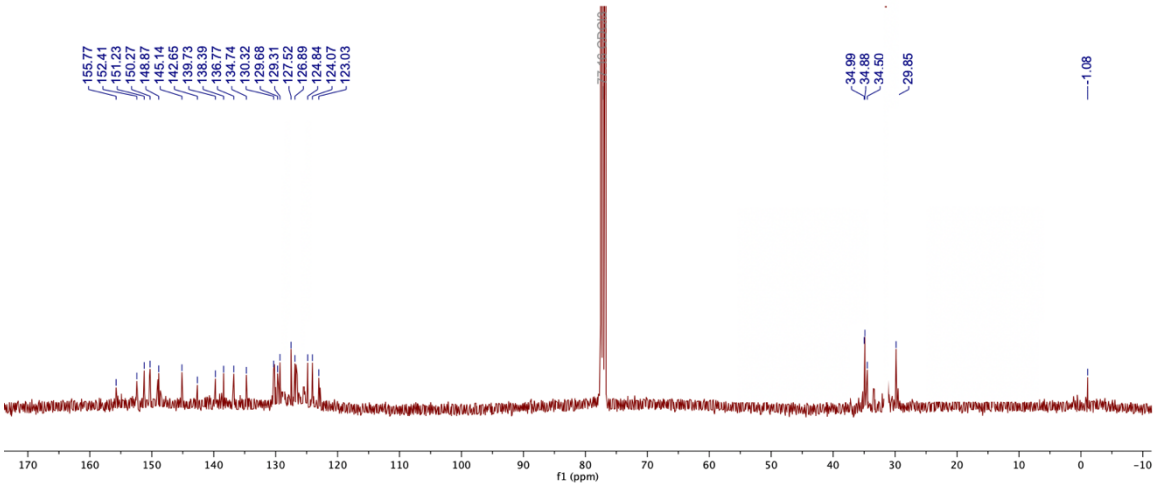

Figure 10. $^{13}C\{^1H\}$ NMR spectrum (101 MHz, $CDCl_3$) of **2**.

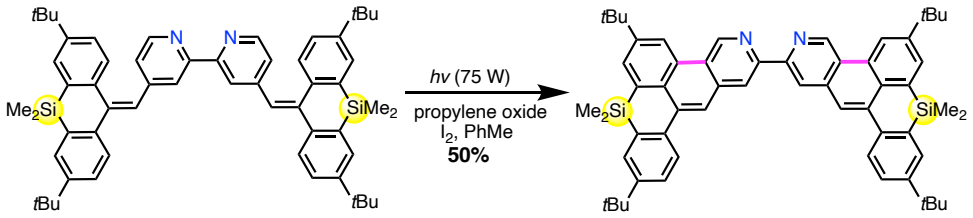

In an inert-atmosphere glovebox, a 50-mL quartz Schlenk tube fitted with a screw-in Teflon stopper was charged with **2** (50 mg, 0.059 mmol) dissolved in toluene (50 mL). To this mixture was added (±) propylene oxide (0.6 mL, 8.9 mmol). Under positive N_2 on the Schlenk line, iodine (90 mg, 0.35 mmol) was added to form a ruby-colored solution. The reaction vessel was sealed and stirred at room temperature under UV irradiation for 20 h. The reaction mixture was quenched with saturated $Na_2S_2O_{3(aq)}$ to form a yellow solution. The organic layer was separated, washed with water (3 x 10 mL), brine (1 x 5 mL), dried over magnesium sulfate. Volatiles were removed from the filtrate on the rotary evaporator to yield a yellow oil. Purification via silica gel column chromatography was carried out with 30% EtOAc/hexanes eluent, yielding **3**. The yellow solid was heated under vacuum at 60ºC for 12 h and stored in a glove box for further chemistry. (25 mg, 50%).^{1}H NMR (400 MHz, $CDCl_3$) δ = 10.21 (s, 2H, Ar*H*), 9.09 (s, 2H, Ar*H*), 9.01 (s, 2H, Ar*H*), 8.60 (s, 2H, Ar*H*), 8.25 (d, 2H, Ar*H*), 8.06 (s, 2H, Ar*H*), 7.78 (s, 2H, Ar*H*), 7.66 (s, 2H, Ar*H*), 1.58 (s, 18H, C(CH_3)$_3$), 1.45 (s, 18H, -C(CH_3)$_3$), 0.56 (s, 12H, -Si(CH_3)$_3$). ^{13}C{^{1}H} NMR (101 MHz, $CDCl_3$). δ = 154.90 (aryl-*C*), 152.42 (aryl-*C*), 151.23 (aryl-*C*), 150.27 (aryl-*C*), 148.87 (aryl-*C*), 145.14 (aryl-*C*), 142.65 (aryl-*C*), 140.71 (aryl-*C*), 139.74 (aryl-*C*), 138.39 (aryl-*C*), 135.71 (aryl-*C*), 134.74 (aryl-*C*), 130.01 (aryl-*C*), 129.61 (aryl-*C*), 127.53 (aryl-*C*), 126.47 (aryl-*C*), 122.84 (aryl-*C*), 31.29 (-*C*(CH_3)$_3$), 31.09 (-*C*(CH_3)$_3$), 23.03 (-C(CH_3)$_3$), 22.85 (-C(CH_3)$_3$), -1.08 (-Si(*C*H_3)$_2$). HRMS (FAB+) m/z Calcd. for [M + H$^+$] $C_{58}H_{64}N_2Si_2$ 845.4686, found 845.4672.

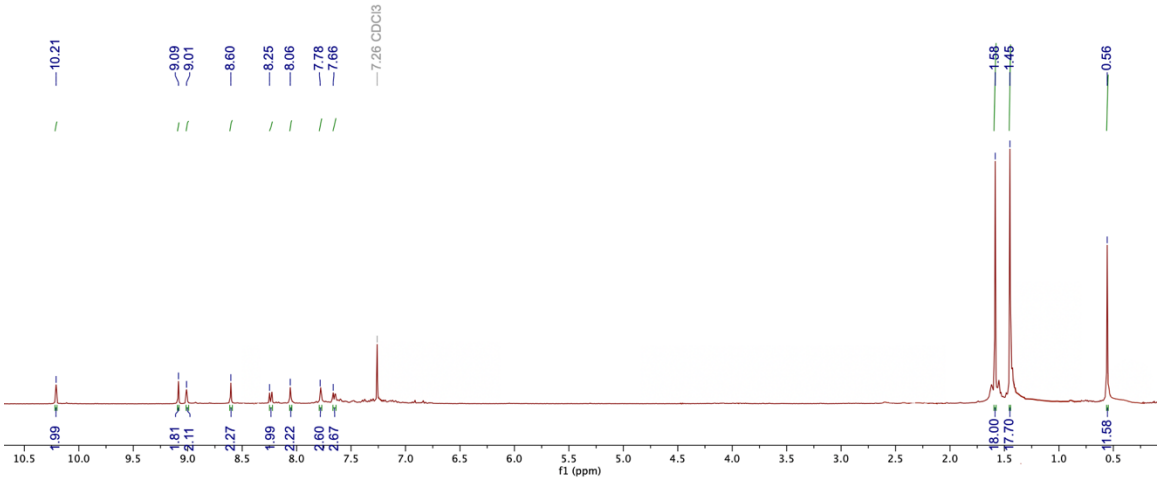

Figure 11. ^{1}H NMR spectrum (400 MHz, $CDCl_3$) of **3.**

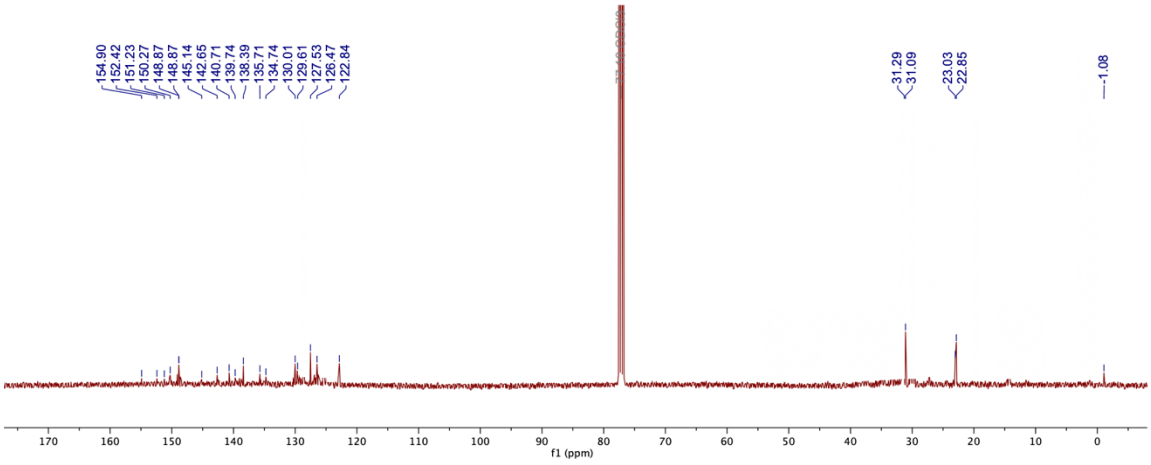

Figure 12. $^{13}C\{^{1}H\}$ NMR spectrum (101 MHz, $CDCl_3$) of **3.**

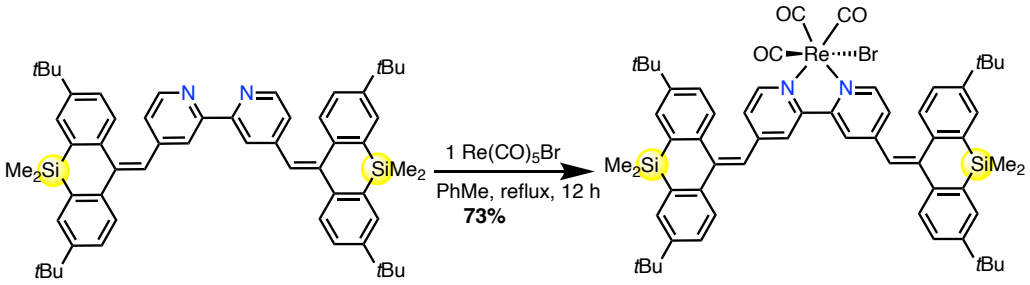

In an inert-atmosphere glove box, a 50-mL Schlenk flask fitted with a screw-in Teflon stopper was charged with **2** (50 mg, 0.058 mmol) and 15 mL toluene. Pentacarbonylbromorhenium(I) (24 mg, 0.058 mmol) was added to the flask via suspension in toluene. The flask was sealed, brought out of the box, and heated to reflux under N_2 flow for 12 h, resulting in a red homogeneous solution. The volatiles were removed under reduced pressure, and the red-yellow solid was lyophilized with benzene. X-ray quality single crystals were grown from slow evaporation of benzene into hexamethyldisiloxane at room temperature, yielding **2-Re(CO)$_3$Br** (73%, 50.8 mg). ^{1}H NMR (400 MHz, $CDCl_3$) δ = 8.16 (br s, 2H, Ar*H*), 8.03 (s, 2H, Ar*H*), 7.88 (br s, 4H, Ar*H*), 7.79 (s, 2H, Ar*H*), 7.68 (d, 4H, Ar*H*), 7.10 (br mult, 2H, Ar*H*), 6.95 (br mult, 2H, Ar*H*), 6.69 (s, 2H, Ar*H*), 6.58 (s, 2H, vinyl-*H*), 1.38 (s, 18H, -C(CH_3)$_3$), 1.21 (s, 18H, -C(CH_3)$_3$), 0.57 (br s, 12H, -Si(CH_3)$_3$). ^{13}C NMR (101 MHz, $CDCl_3$) δ = 196.97 (-*C*O) 192.34 (-*C*O), 152.41 (aryl-*C*), 151.22 (aryl-*C*), 150.27 (aryl-*C*), 148.87 (aryl-*C*), 145.12 (aryl-*C*), 142.64 (aryl-*C*), 139.72 (aryl-*C*), 138.39 (aryl-*C*), 136.77 (aryl-*C*), 134.72 (aryl-*C*), 130.21 (aryl-*C*), 129.70 (aryl-*C*), 129.30 (aryl-*C*), 127.52 (aryl-*C*), 126.90 (aryl-*C*), 126.46 (aryl-*C*), 125.31 (aryl-*C*), 124.05 (aryl-*C*), 123.03 (aryl-*C*), 34.98 (-*C*(CH$_3$)$_3$), 34.87 ((-*C*(CH$_3$)$_3$), 31.21 (-C(*C*H$_3$)$_3$), 29.84 (-C(*C*H$_3$)$_3$), 0.90 (-Si(*C*H$_3$)$_3$), -1.09 (-Si(*C*H$_3$)$_3$). Anal. calcd. (%) for $C_{61}H_{68}BrN_2O_3ReSi_2$: C, 61.08; H, 5.71; N, 2.34. Found: C, 61.20; H, 5.81; N, 2.15.

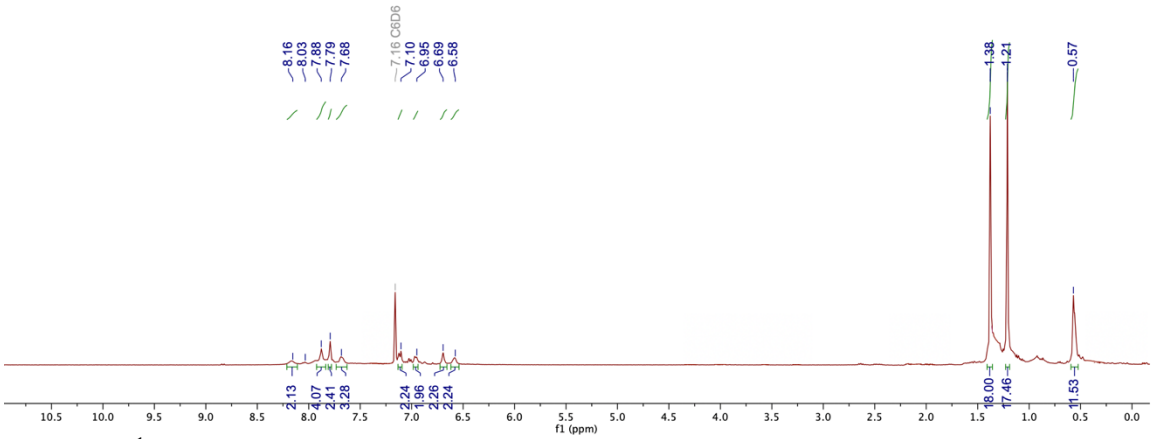

Figure 13. ^{1}H NMR spectrum (400 MHz, $CDCl_3$) of **2-Re(CO)$_3$Br**.

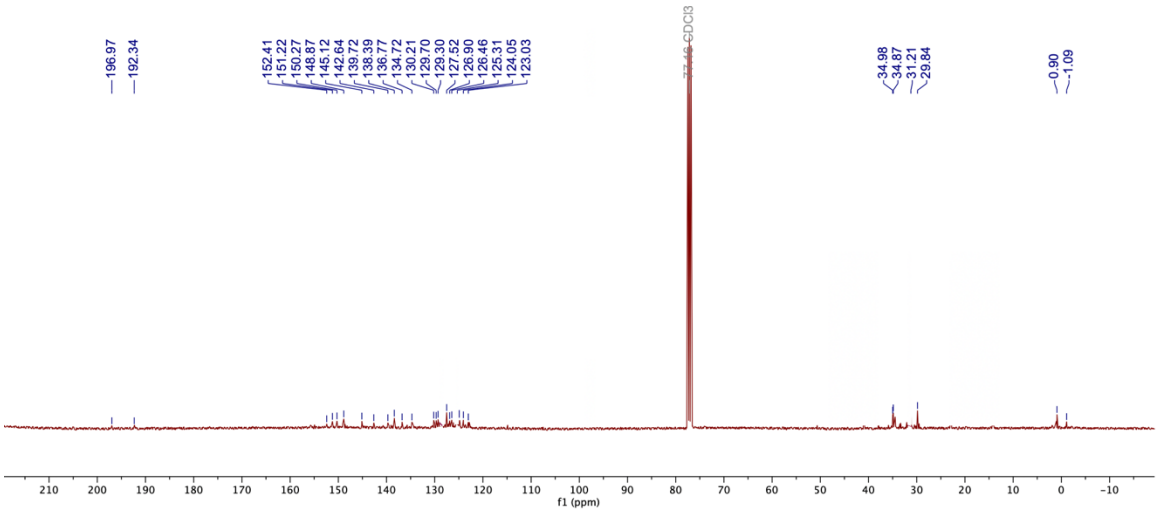

Figure 14. $^{13}C\{^{1}H\}$ NMR spectrum (101 MHz, $CDCl_3$) of **2-Re(CO)$_3$Br**.

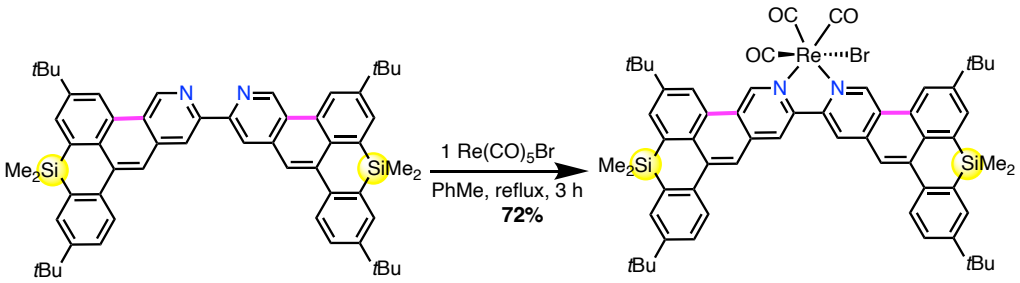

In an inert-atmosphere glove box, a 50-mL Schlenk flask fitted with a screw-in Teflon stopper was charged with **3** (25 mg, 0.029 mmol) and 15 mL toluene. Pentacarbonylbromorhenium(I) (12 mg, 0.029 mmol) was added to the flask via a suspension in toluene. The flask was sealed, brought out of the box, and heated to reflux under N_2 counterflow for 12 h. The volatiles were removed under reduced pressure, and the red-yellow solid was lyophilized with benzene. X-ray quality single crystals were grown from slow diffusion of hexanes into a saturated THF solution of the crude material at room temperature, yielding **3-Re(CO)$_3$Br** (72%, 20.8 mg). ^{1}H NMR (400 MHz, $CDCl_3$) δ = 8.16 (br s, 2H, Ar*H*), 8.03 (s, 2H, Ar*H*), 7.88 (br s, 4H, Ar*H*), 7.79 (s, 2H, Ar*H*), 7.68 (d, 4H, Ar*H*), 7.10 (br mult, 2H, Ar*H*), 6.95 (br mult, 2H, Ar*H*), 6.69 (s, 2H, Ar*H*), 6.58 (s, 2H, vinyl-*H*), 1.38 (s, 18H, -C(CH_3)$_3$), 1.21 (s, 18H, -C(CH_3)$_3$), 0.57 (br s, 12H, -Si(CH_3)$_3$). ^{13}C NMR (101 MHz, $CDCl_3$) δ = 192.59 (-*C*O) 187.78 (-*C*O), 154.96 (aryl-*C*), 150.28 (aryl-*C*), 148.42 (aryl-*C*), 147.76 (aryl-*C*), 145.14 (aryl-*C*), 143.37 (aryl-*C*), 140.56 (aryl-*C*), 139.74 (aryl-*C*), 139.10 (aryl-*C*), 138.40 (aryl-*C*), 135.60 (aryl-*C*), 134.04 (aryl-*C*), 131.07 (aryl-*C*), 130.43 (aryl-*C*), 128.67 (aryl-*C*), 127.51 (aryl-*C*), 126.13 (aryl-*C*), 125.46 (aryl-*C*), 122.84 (aryl-*C*), 31.59 (-*C*(CH$_3$)$_3$), 29.86 (-C(*C*H$_3$)$_3$), 22.49 ((-*C*(CH$_3$)$_3$), 14.22 (-C(*C*H$_3$)$_3$), 2.13 (-Si(*C*H$_3$)$_3$) , -1.08 (-Si(*C*H$_3$)$_3$). calcd. (%) for $C_{61}H_{64}BrN_2O_3ReSi_2$: C, 61.29; H, 5.40; N, 2.34. Found: C, 61.34; H, 5.70; N, 2.45.

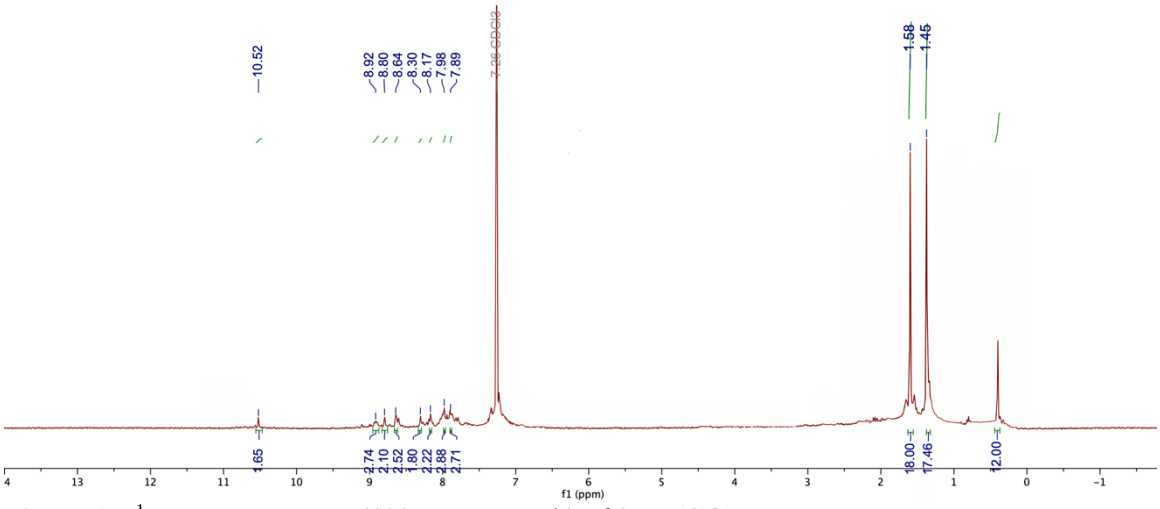

Figure 15. ^{1}H NMR spectrum (400 MHz, $CDCl_3$) of **3-Re(CO)$_3$Br**.

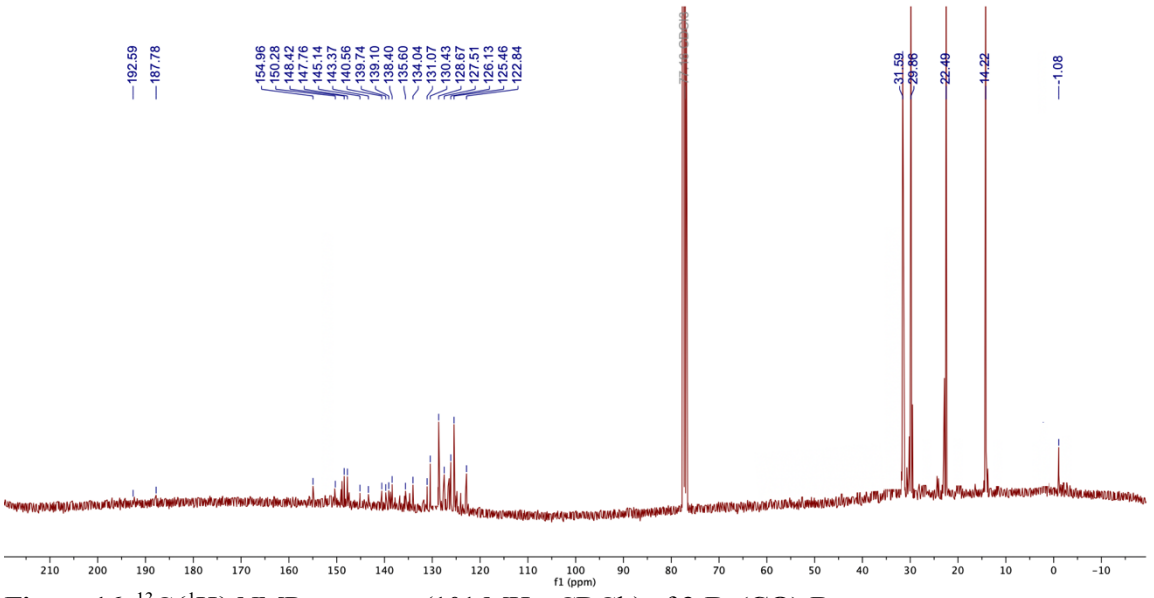

Figure 16. ^{13}C{^{1}H} NMR spectrum (101 MHz, $CDCl_3$) of **3-Re(CO)$_3$Br**.

SUPPLEMENTARY FIGURES/DATA

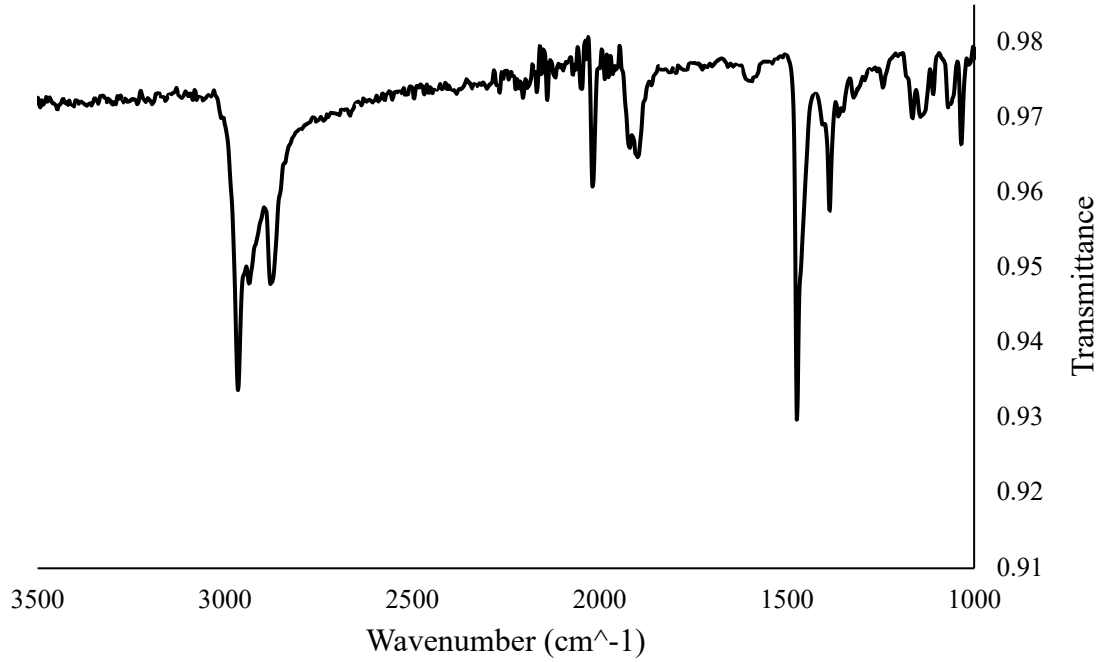

Figure 17. FT-IR spectrum of **2-Re(CO)$_3$Br** in $CHCl_3$.

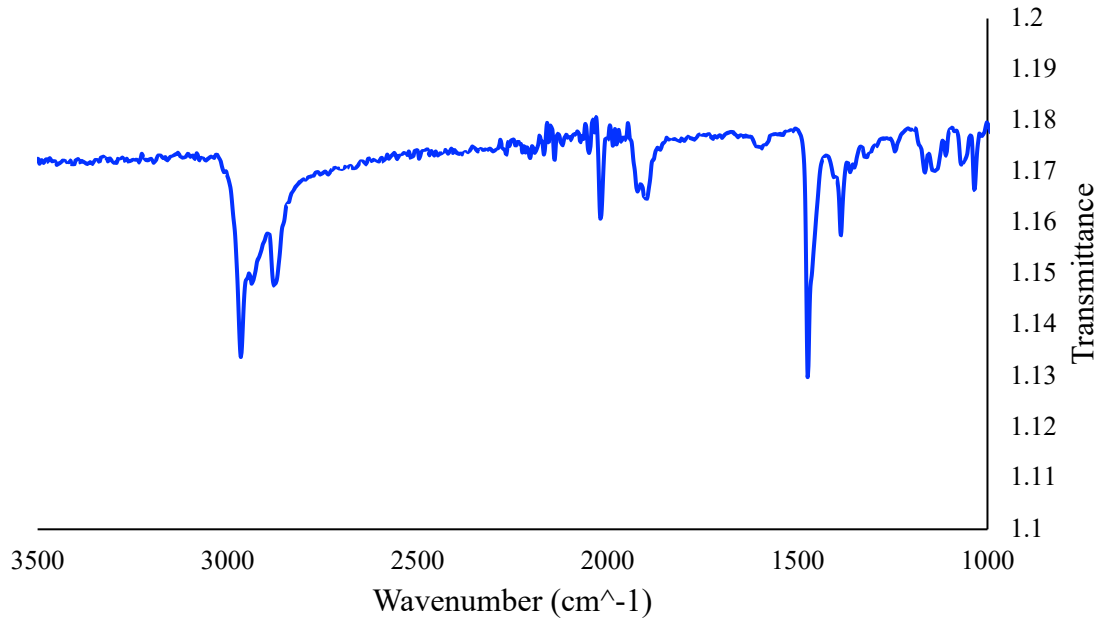

Figure 18. FT-IR spectrum of **3-Re(CO)$_3$Br** in $CHCl_3$.

Table 2. Selectivity profiles from bulk CO_2 electrolysis experiments

Complex	Applied potential (V vs. $Fc^{0/+}$)	FE_{CO} (%)	FE_{H2} (%)	Current (mA cm^{-2})
2-Re(CO)$_3$Br	–2.2	95 ± 2	0	-1.0 ± 0.1
	–1.7	92 ± 1	0	-0.6 ± 0.1
	–1.6	80 ± 1	0	-0.04 ± 1
3-Re(CO)$_3$Br	–2.2	95 ± 2	0	-1.0 ± 0.3
	–1.7	90 ± 2	0	-0.4 ± 0.1
	–1.6	79 ± 1	0	-0.03 ± 0.01
^{tBu}bpyRe(CO)$_3$Br	–2.2	98 ± 2	0	-1.4 ± 0.2
	–1.7	64 ± 2	30 ± 5	-0.2 ± 0.1
	–1.6	39 ± 3	55 ± 5	-0.02 ± 0.01

Density Functional Theory (DFT) Calculations

All computations were performed using ORCA software[42] version 4.1.2 on the High-Performance Computing Cluster at Caltech. Geometry optimizations and orbital energies were calculated using the B3LYP functional[34] and the LANL2DZ basis set for Re and 6-311G(d,p) basis set for all other atoms.[35] UV-vis spectra and first 50 excited states thereof were computed via time-dependent DFT calculations with the CAM-B3LYP/LANL2DZ level of theory.[43] Orbitals and optimized structures were visualized with the Avogadro software.[44] The input files for the initial optimizations of the neutral-state complexes were generated from their respective X-ray crystal structures. In each Re complexes, bromine was replaced with chlorine and *tert*-butyl groups were replaced with hydrogen atoms for simplification (e.g., **2-Re** becomes **2-ReCl**). Isovalues for all orbital representations are set to 0.02.

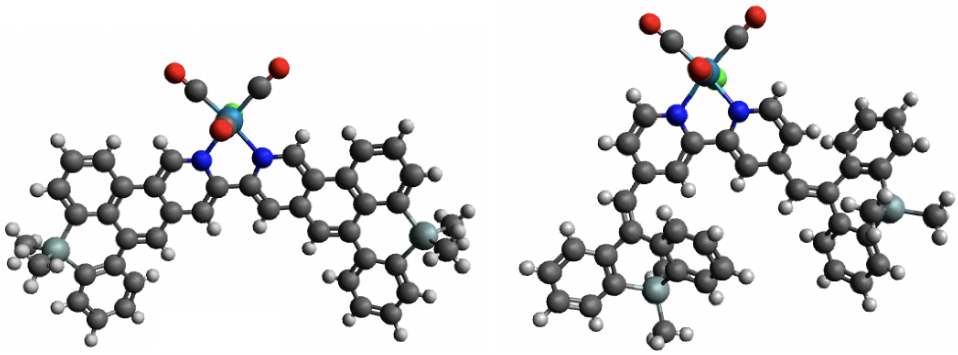

Figure 19. Optimized structures of **3^{H}-Re(CO)$_3$Cl** (left) and **2^{H}-Re(CO)$_3$Cl** (right).

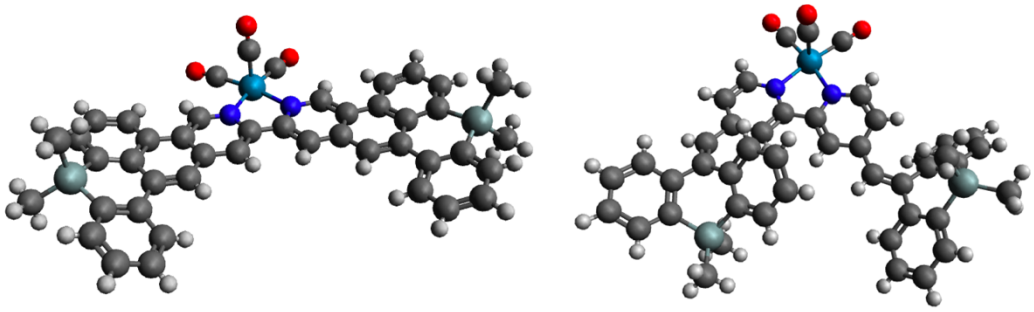

Figure 20. Optimized structures of **3^{H}-Re(CO)$_3$** (left) and **2^{H}-Re(CO)$_3$** (right).

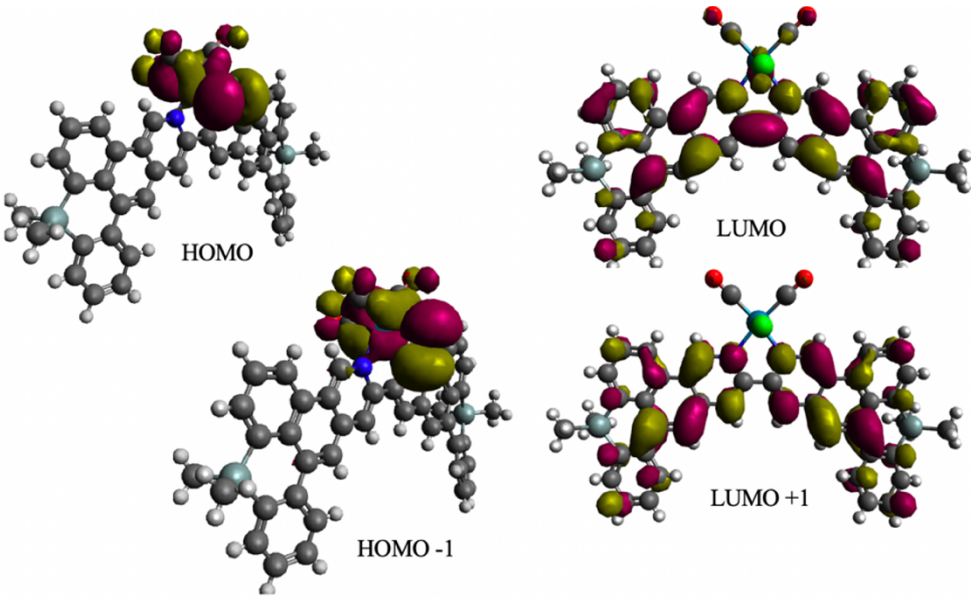

Figure 21. Frontier molecular orbitals for **3^{H}-Re(CO)$_3$Cl**.

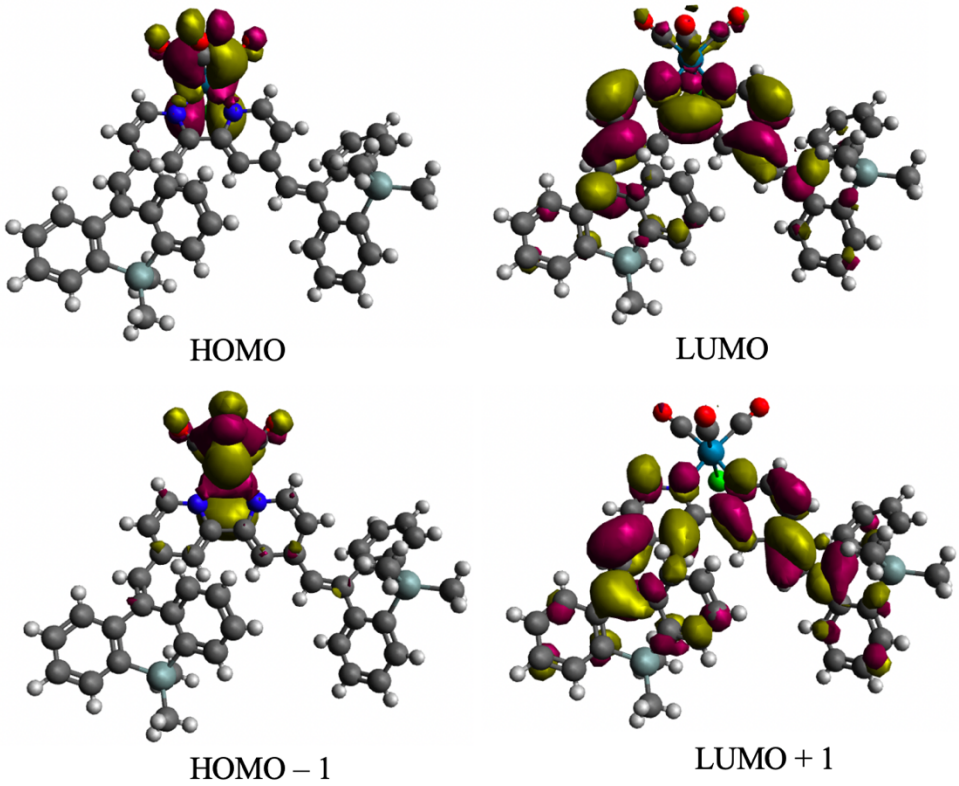

Figure 22. Frontier molecular orbitals for **2^{H}-Re(CO)$_3$Cl**.

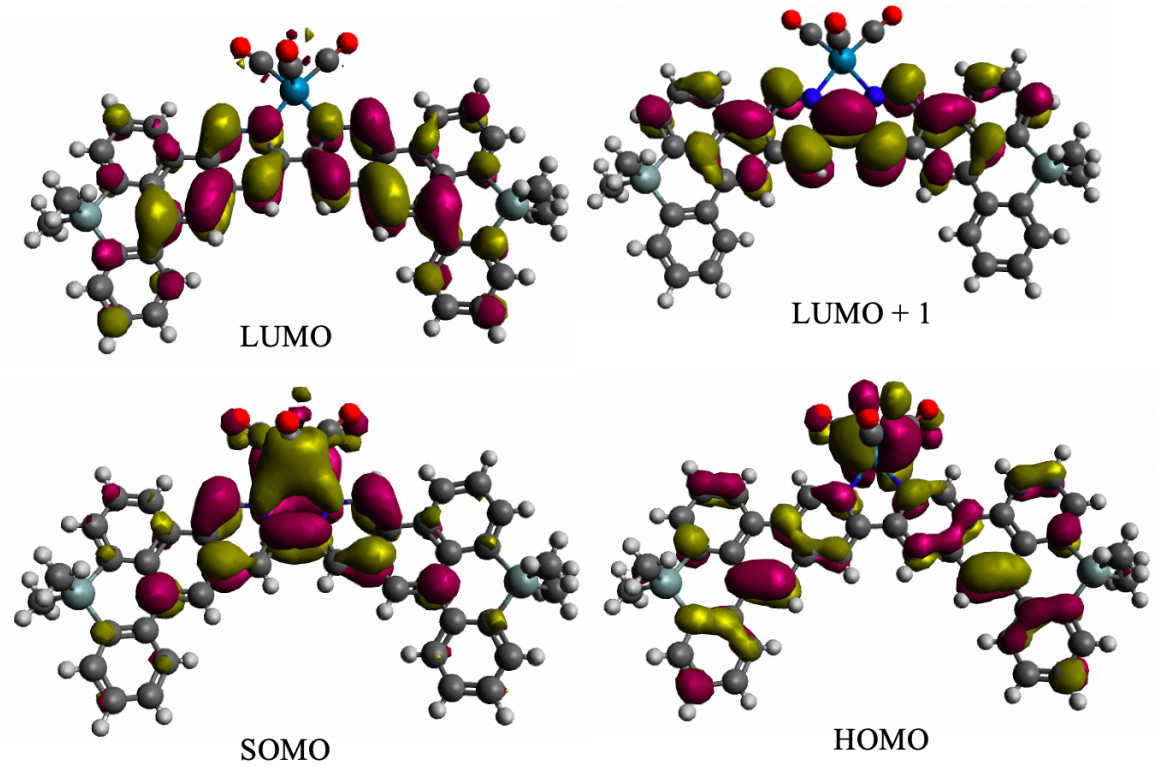

Figure 23. Frontier molecular orbitals for $\mathbf{3^{H}\text{-}Re(CO)_3}$.

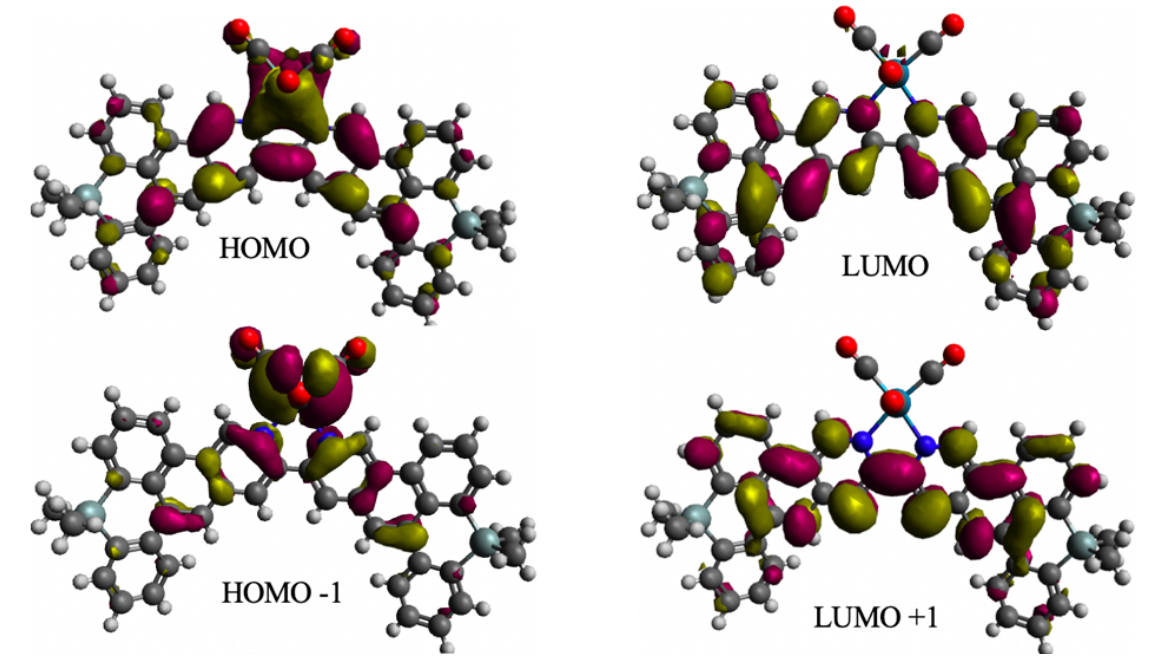

Figure 24. Frontier molecular orbitals for $\mathbf{[3^{H}\text{-}Re(CO)_3]^{-}}$.

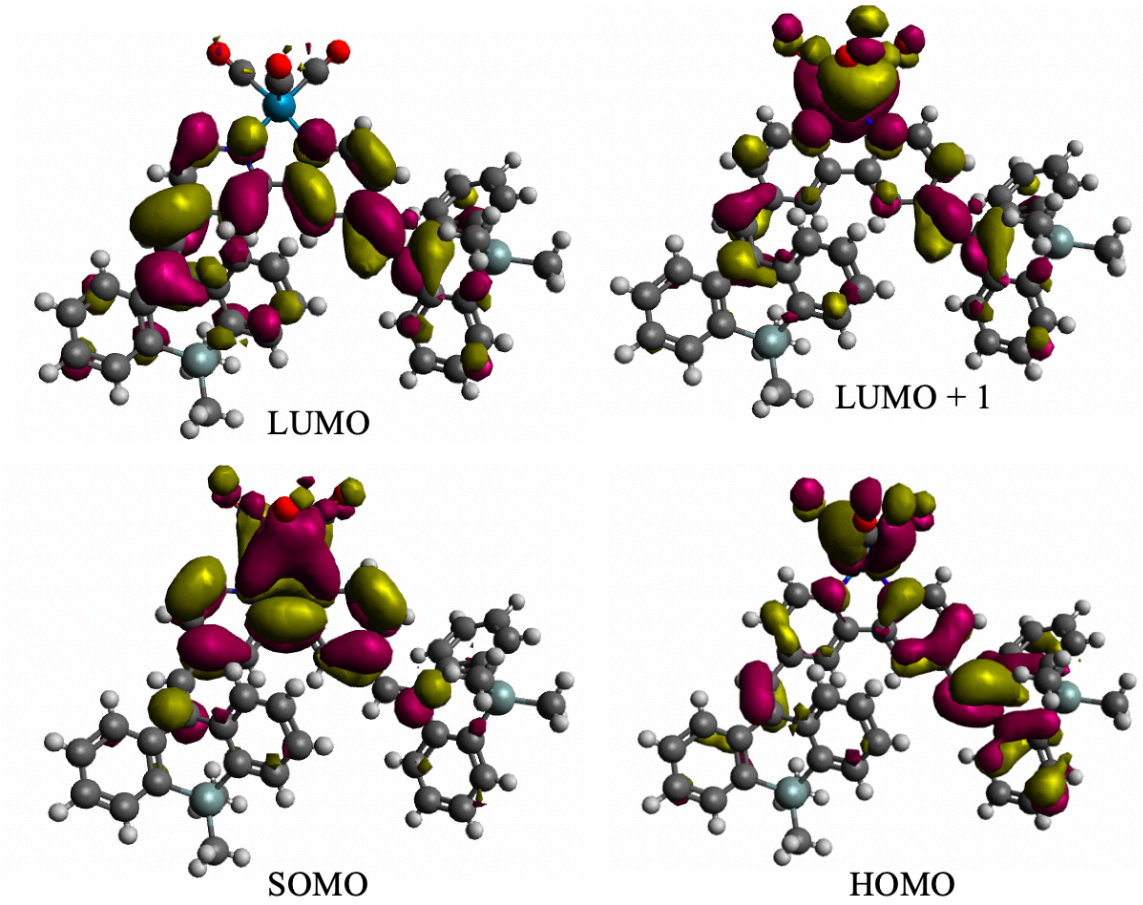

Figure 25. Frontier molecular orbitals for $\mathbf{2^{H}\text{-}Re(CO)_3}$.

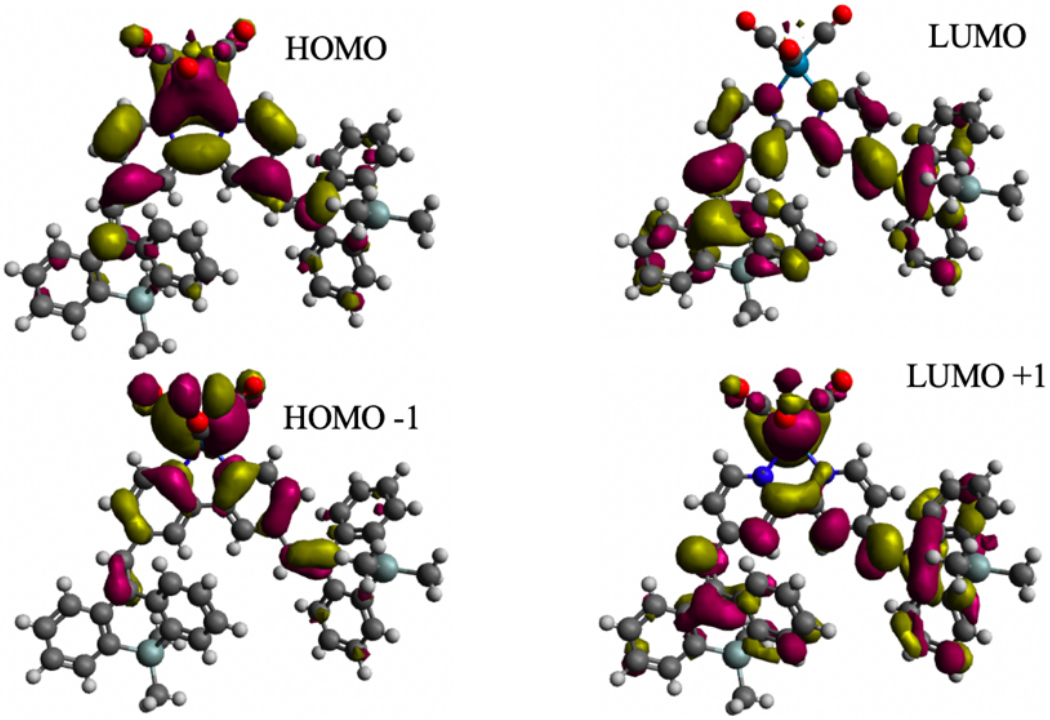

Figure 26. Frontier molecular orbitals for $[\mathbf{2^{H}\text{-}Re(CO)_3}]^-$.

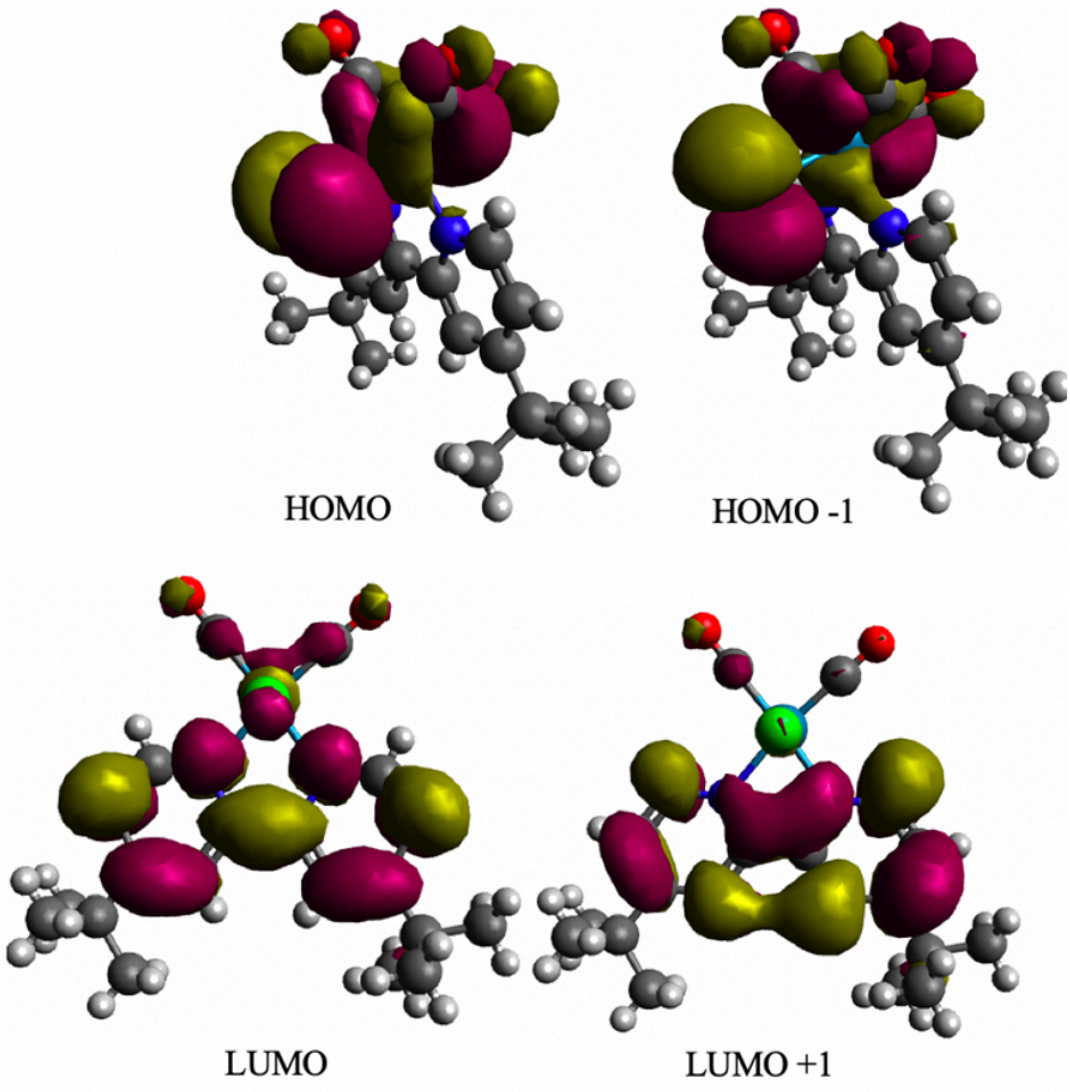

Figure 27. Frontier molecular orbitals for **bpy^{tBu}Re(CO)$_3$Cl**.

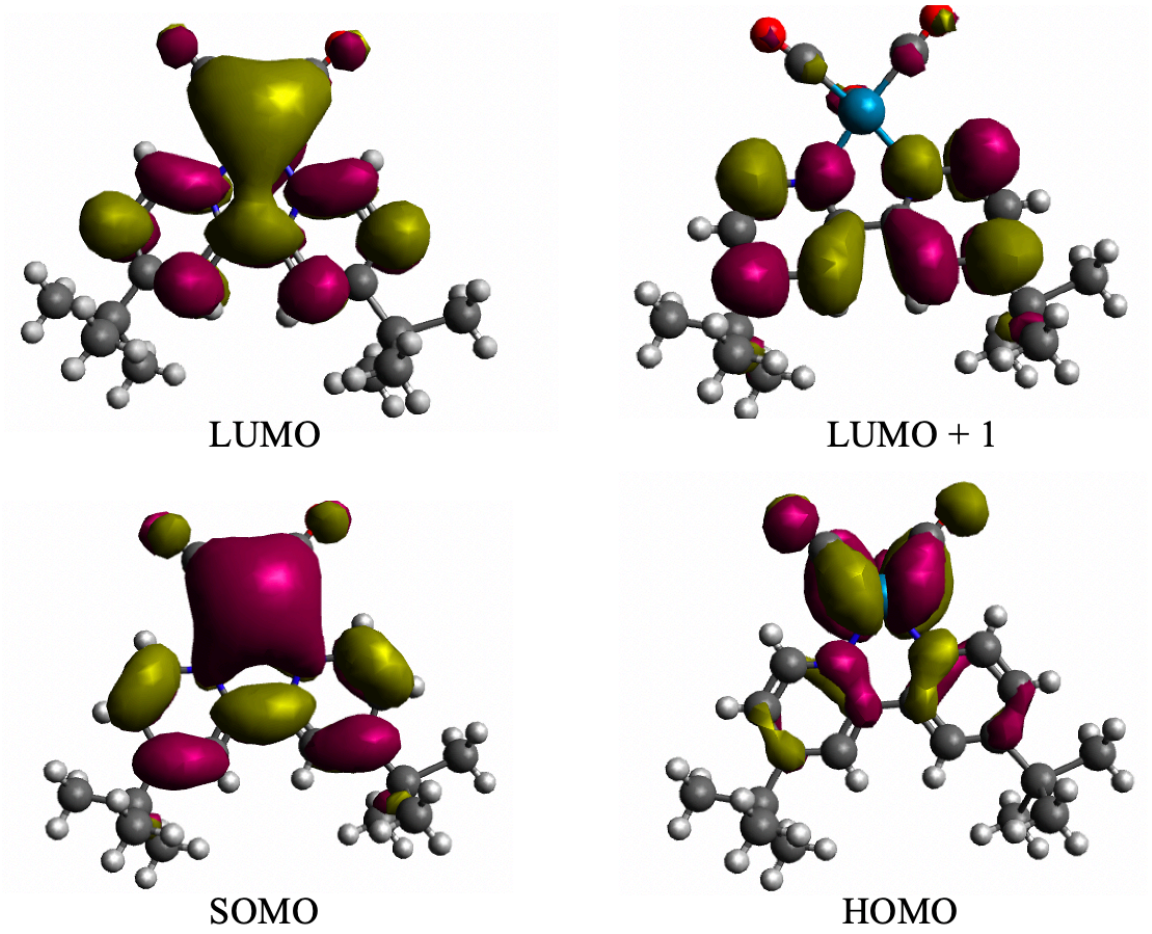

Figure 28. Frontier molecular orbitals for **bpy^{tBu}Re(CO)$_3$**.

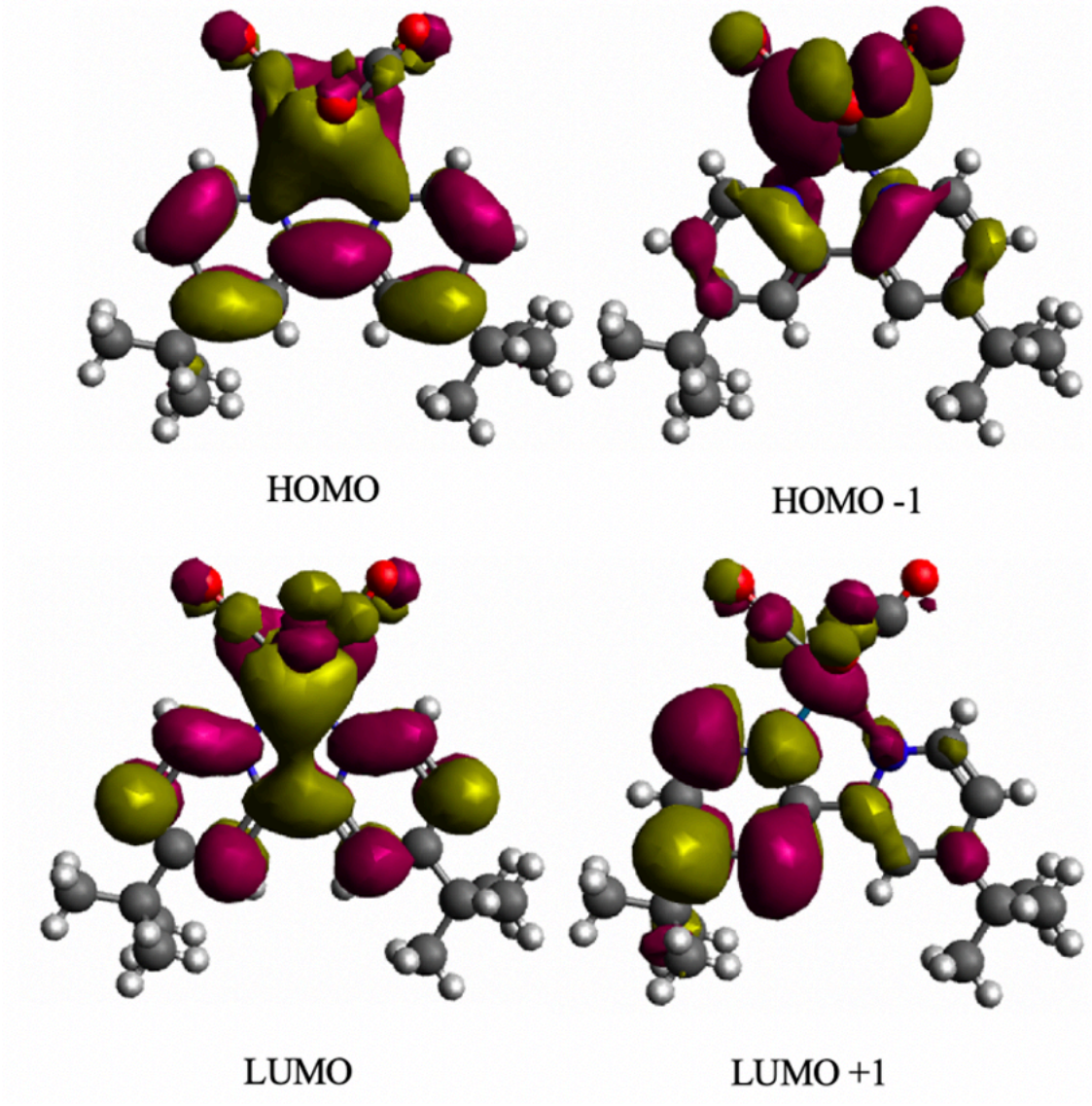

Figure 29. Frontier molecular orbitals for [**bpy^{tBu}Re(CO)$_3$**]$^-$.

Table 3: Coordinates for **3^{H}-Re(CO)$_3$Cl:**

Re	1.44600	10.53700	11.65600
Cl	1.07900	9.16100	9.45500
Si	10.01100	6.22400	13.13100
Si	2.20700	18.96400	6.68700
N	3.52700	9.99100	11.39300
N	2.25100	12.08400	10.35400
O	-1.44100	11.58600	11.61700
O	1.99600	11.99400	14.28100
C	7.52800	7.28200	12.21700
C	5.47100	8.60500	11.77200
O	0.65200	8.04000	13.27700
C	8.24300	8.11000	11.24300
C	8.15200	6.30200	13.01500
C	10.15100	8.45800	9.66400
H	9.53800	8.86700	9.06400
C	6.13900	7.49800	12.43100
C	3.46100	13.96900	8.67000
C	9.67700	7.88200	10.86900
C	6.23100	9.45400	10.93200
C	5.59100	10.55100	10.32200
H	6.07700	11.11600	9.73200
C	4.16400	12.85600	9.15600
H	5.07100	12.73000	8.90200
C	7.60600	9.16900	10.68200
H	8.09400	9.74200	10.10200
C	2.12400	14.13500	9.06000
C	-0.36200	11.17400	11.65500
C	4.27600	10.80300	10.57800
C	10.58800	7.18600	11.67900
C	4.11800	8.93900	11.94500
H	3.59000	8.37200	12.49500
C	11.50600	8.43100	9.35500
H	11.79500	8.81200	8.53400
C	0.12100	15.57800	9.08600
H	-0.31800	14.90800	9.59600
C	3.56400	11.94400	9.99300
C	1.57200	13.17100	9.88600
H	0.66400	13.27200	10.14300
C	2.09600	16.31300	7.82200
C	4.08700	14.93500	7.83000
H	4.98400	14.77900	7.56100
C	5.41600	6.65700	13.32500
H	4.47700	6.77500	13.41000
C	1.43100	15.32500	8.63100
C	3.47700	16.06700	7.39200
C	0.92800	9.01200	12.68300
C	1.40000	17.53300	7.55000
C	12.46100	7.86000	10.21000
C	-0.55300	16.75300	8.82500
C	4.28800	17.00900	6.55500
C	3.90400	18.32000	6.25400
C	0.12000	17.70500	8.02700
H	-0.33600	18.50800	7.80800

C	7.40300	5.54800	13.91000
H	7.85100	4.90300	14.44400
C	6.02800	5.69100	14.06100
C	1.78900	11.45100	13.26600
C	11.93200	7.21000	11.32100
H	12.54000	6.74400	11.88200
C	6.04700	18.80800	5.15300
C	4.79200	19.17300	5.57400
H	4.50400	20.06000	5.39300
C	1.23500	19.45300	5.16600
H	1.04900	18.65600	4.62700
H	1.75700	20.09100	4.63600
H	0.39000	19.86900	5.43800
C	6.40900	17.48100	5.39800
H	7.25400	17.16300	5.10100
C	5.54200	16.61000	6.07500
H	5.81700	15.71200	6.21500
C	10.50900	7.03700	14.72000
H	10.10100	7.92600	14.77500
H	11.48500	7.12300	14.75100
H	10.20600	6.49100	15.47600
C	10.59700	4.47800	13.04600
H	10.13000	3.94400	13.72200
H	11.56200	4.44900	13.21400
H	10.40900	4.11400	12.15600
C	2.31900	20.42200	7.86100
H	1.43400	20.60500	8.24000
H	2.63500	21.21100	7.37300
H	2.94700	20.21200	8.58400
H	5.46400	5.05500	14.74100
H	-1.55300	16.93700	9.21400
H	6.71800	19.50900	4.65900
H	13.53100	7.92100	10.01900

*

Table 4: Coordinates for **2^{H}-$Re(CO)_3Cl$:**

Re	-2.07000	3.99100	11.97400
Cl	-4.17600	5.49600	11.66600
Si	2.70000	10.01100	6.30200
Si	-3.49600	2.02600	2.55800
N	-1.35900	5.15200	10.31200
N	-2.72000	2.91300	10.19600
O	-3.34800	2.06700	13.99400
C	-3.56700	0.77700	6.59300
H	-4.24700	0.12600	6.71900
C	-1.82300	4.83000	9.07300
C	-3.06400	0.79900	5.34600
C	-0.88600	6.84900	8.08300
O	-0.94200	5.79100	14.20200
C	0.17300	9.27600	5.32400
C	1.62000	10.33400	7.80700
C	-3.61400	-0.15400	4.34400
C	-0.64700	7.59500	6.88400
H	-0.94500	7.17400	6.08600
C	-0.06400	8.80400	6.70500
C	-2.78200	2.86900	7.79200
H	-2.64300	3.32100	6.96800
C	1.40200	9.87800	4.97800
C	1.92900	11.22300	8.84000
H	2.78500	11.63500	8.84200
C	-1.61200	5.63700	7.98100
H	-1.96100	5.37500	7.13700
C	0.34600	9.73300	7.80600
C	-3.27300	1.56600	7.80100
C	-3.80200	0.23200	3.00400
C	-0.57900	6.24300	10.40300
H	-0.21300	6.45900	11.25300
C	0.24700	2.66200	5.24600
H	1.04000	2.70800	5.76800
C	-0.78500	1.82400	5.65500
H	-0.69400	1.32300	6.45800
C	-2.49700	3.50700	8.99800
C	-1.95700	1.71000	4.89800
C	-0.28100	7.06400	9.34300
H	0.33500	7.77900	9.45600
C	-4.46100	-2.05600	2.42500
C	-0.56800	10.09500	8.78900
H	-1.44200	9.72200	8.76700
C	-2.87000	2.83100	13.25600
C	-1.00900	3.26700	3.31800
H	-1.09100	3.76100	2.51000
C	-2.04600	2.40800	3.68300
C	0.15000	3.43300	4.09200
C	-3.91000	-1.46200	4.71300
H	-3.82800	-1.72200	5.62300
C	-0.81200	9.12500	4.34000
H	-1.64000	8.71900	4.57000
C	-4.22000	-0.73400	2.07800
H	-4.34300	-0.47200	1.17300

C	1.03900	11.53300	9.86700
C	3.61500	8.40000	6.45200
H	4.31400	8.48300	7.13400
H	4.02500	8.17600	5.59000
H	2.98900	7.69100	6.71000
C	-0.24100	10.98200	9.79700
H	-0.89300	11.21800	10.44600
C	1.59300	10.30100	3.65500
H	2.42000	10.70200	3.41700
C	-1.40200	5.11800	13.39800
C	0.59800	10.15100	2.66200
C	-3.25700	1.68300	10.20300
H	-3.44700	1.27000	11.03700
C	-4.32700	-2.40600	3.75800
H	-4.52000	-3.29500	4.03100
C	-3.54200	0.99700	9.03800
H	-3.92600	0.12900	9.08400
C	3.89000	11.41500	6.01600
H	3.38800	12.24200	5.85800
H	4.44700	11.21700	5.23400
H	4.46200	11.52500	6.80400
C	-0.60700	9.55000	3.04900
H	-1.29600	9.43300	2.40500
C	-4.97900	3.08500	3.01300
H	-5.77000	2.76500	2.53000
H	-4.80200	4.01700	2.76800
H	-5.14000	3.02600	3.97800
C	-3.05400	2.17600	0.76300
H	-2.34500	1.53600	0.54600
H	-2.74100	3.08600	0.57900
H	-3.84400	1.98700	0.21500
O	0.63090	2.31897	12.10686
C	-0.25600	2.88900	12.03700
H	1.32537	12.29532	10.72151
H	-4.82108	-2.82088	1.74567
H	0.50620	10.80136	1.94791
H	0.74766	4.07956	4.06206

Table 5: Coordinates for ^{tBu}**bpyRe(CO)$_3$Cl:**

C	-1.41800	-1.94600	3.95200
H	-1.80200	-2.75700	3.64000
C	-2.06400	-1.24900	4.95500
H	-2.87600	-1.58300	5.31800
C	-1.52600	-0.05900	5.43600
C	-0.31900	0.35800	4.88700
C	0.29100	-0.37300	3.87300
C	3.17900	-0.53000	1.67800
H	3.51100	-1.13000	1.01800
C	3.89600	0.62100	1.94300
H	4.70300	0.79900	1.47300
C	3.43300	1.51900	2.89900
C	2.22900	1.19900	3.54400
H	1.87100	1.78800	4.19700
C	1.56100	0.02500	3.23200
C	-0.07500	-1.81200	0.38900
C	-0.34000	-4.12200	1.68200
C	2.10600	-3.45400	0.71500
N	-0.26200	-1.52100	3.39800
N	2.03800	-0.84000	2.30500
O	-0.60600	-1.44700	-0.46500
O	-1.08700	-4.96500	1.49900
O	2.88100	-3.90900	-0.00400
Cl	1.91000	-3.59700	3.94200
Re	0.85800	-2.61900	1.90900
C	-2.39900	0.78300	6.62500
C	-4.08300	-0.01700	6.82300
C	-2.52600	2.61800	6.16400
C	-1.49700	0.54200	8.18200
C	4.30000	2.75200	3.40300
C	5.08700	2.22200	4.77800
C	3.29000	4.17600	3.74300
C	5.58700	3.00900	2.25100
H	-4.58000	0.08000	5.88000
H	-4.63400	0.51400	7.57200
H	-4.02300	-1.05100	7.09000
H	-1.43700	-0.49200	8.44900
H	-2.04700	1.07200	8.93100
H	-0.51000	0.94900	8.10900
H	0.13000	1.22000	5.23600
H	-3.06400	2.71900	5.24400
H	-1.53900	3.01400	6.04600
H	-3.03600	3.15700	6.93500
H	6.22900	2.17300	2.06800
H	6.17000	3.83900	2.59000
H	5.08100	3.27400	1.34600
H	4.36800	2.04400	5.55000
H	5.73600	3.02100	5.07200
H	5.66400	1.33600	4.61700
H	2.54500	3.90300	4.46100
H	2.81600	4.46800	2.83000
H	3.86800	4.99300	4.12200

Crystallographic Information

CCDC deposition number 2335089 and 2335090 contains the supplementary crystallographic data for this paper.[45] These data can be obtained free of charge from The Cambridge Crystallographic Data Centre via www.ccdc.cam.ac.uk/data_request/cif.

Refinement Details. In each case, crystals were mounted on a glass fiber or MiTeGen loop using Paratone oil, then placed on the diffractometer under a nitrogen stream. Low temperature (175 K) X-ray data were obtained on a Bruker D8 VENTURE Kappa Duo PHOTON 100 CMOS based diffractometer (Mo IμS HB micro-focus sealed X-ray tube, Kα = 0.71073 Å or Cu IμS HB micro-focused X-ray tube, Kα = 1.54178). All diffractometer manipulations, including data collection, integration, and scaling were carried out using the Bruker APEXII software.[46] Absorption corrections were applied using SADABS.[47] Space groups were determined on the basis of systematic absences and intensity statistics and the structures were solved in the Olex 2 software interface[48] by intrinsic phasing using XT (incorporated into SHELXTL)[49] and refined by full-matrix least squares on F2. All non-hydrogen atoms were refined using anisotropic displacement parameters, except in some cases with heavily distorted solvent. Hydrogen atoms were placed in the idealized positions and refined using a riding model. The structure was refined (weighed least squares refinement on F2) to convergence. Graphical representation of structures with 50% probability thermal ellipsoids was generated using Diamond 3 visualization software.[50]

Table 6. Crystal data and structure refinement for 2-Re(CO)$_3$Br

CCDC Number	2335089
Empirical formula	$C_{61}H_{68}B_2N_2O_3Si_2ReBr_{0.5}$
Formula weight	1181.12
Temperature/K	106.0
Crystal system	Triclinic
Space group	P-1
a/Å	12.5794(10)
b/Å	16.884(2)
c/Å	16.9262(16)
α/°	104.436(8)
β/°	109.588(5)
γ/°	95.695(11)
Volume/Å^3	3213.5(6)
Z	2
ρ_{calc} g/cm^3	1.221
μ/mm^{-1}	4.724
Abs. Correction	Semi-empirical
Crystal size/mm^3	0.05 × 0.05 × 0.2
Radiation	CuKα (λ = 1.54178)
2Θ range/°	5.516 to 150.344
GOF	1.132
Diffractometer	PHOTON
R_1[a], wR_2[b] [I>2σ(I)]	0.0688, 0.1477

[a]$R_1 = \Sigma||F_0| - |F_c||/\Sigma|F_0|$. [b]w$R_2 = [\Sigma[w(F_0^2 - F_c^2)^2]/\Sigma[w(F_0^2)^2]]^{1/2}$

Table 7. Crystal data and structure refinement for 3-Re(CO)$_3$Br

CCDC Number	2335090
Empirical formula	$C_{61}H_{64}N_2O_3Si_2BrRe$
Formula weight	1135.43
Temperature/K	100.0
Crystal system	Monoclinic
Space group	$P2_1/n$
a/Å	17.220(4)
b/Å	21.088(18)
c/Å	19.067(12)
α/°	90
β/°	115.95(2)
γ/°	90
Volume/Å^3	6226(7)
Z	4
ρ_{calc} g/cm^3	1.275
μ/mm^{-1}	2.673
Abs. Correction	Semi-empirical
Crystal size/mm^3	0.1 × 0.1 × 0.15
Radiation	MoKα (λ = 0.71073)
2Θ range/°	3.862 to 72.564
GOF	1.136
Diffractometer	PHOTON
R_1[a], wR_2[b] [I>2σ(I)]	0.0593, 0.1636

[a]$R_1 = \Sigma||F_0| - |F_c||/\Sigma|F_0|$. [b]w$R_2 = [\Sigma[w(F_0^2 - F_c^2)^2]/\Sigma[w(F_0^2)^2]]^{1/2}$

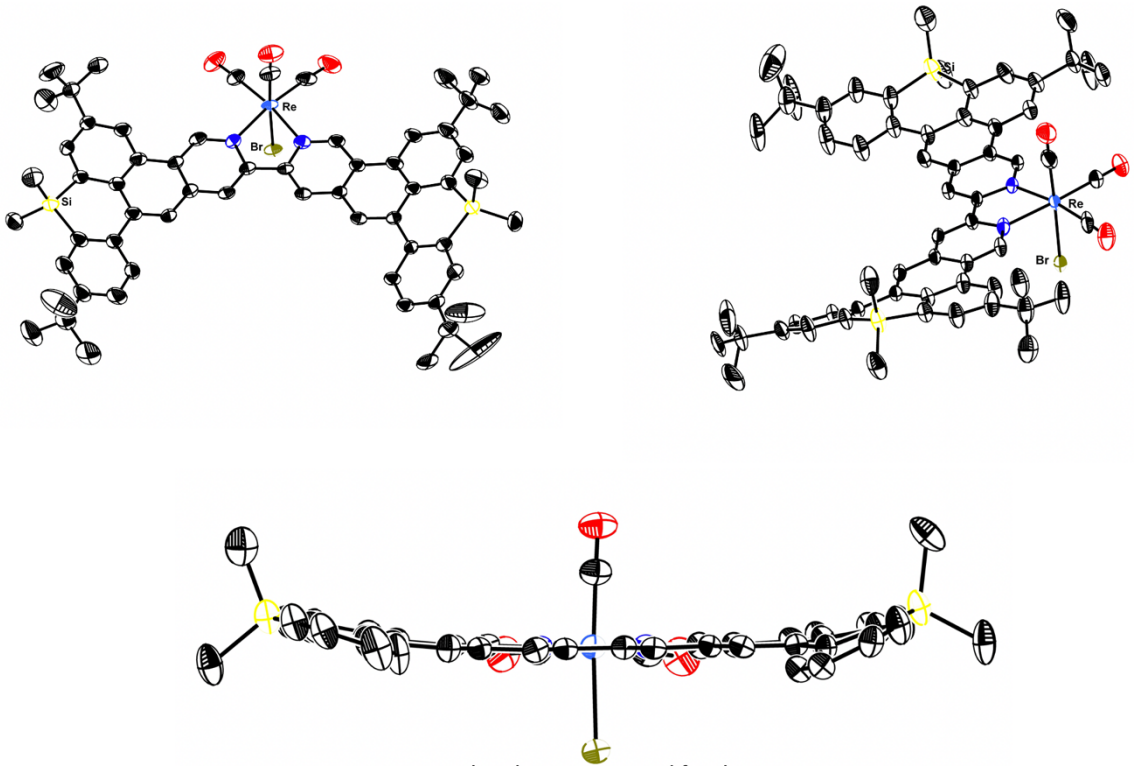

Figure 30. Solid state structure determined from single crystal X-ray diffraction of **3-Re(CO)$_3$Br**. Bottom panel: *tert*-Butyl groups omitted for clarity.

REFERENCES

(1) Nguyen, T. N.; Salehi, M.; Le, Q. Van; Seifitokaldani, A.; Dinh, C. T. Fundamentals of Electrochemical CO2 Reduction on Single-Metal-Atom Catalysts. *ACS Catal.* **2020**, *10* (17), 10068–10095.

(2) Guo, D.; Shibuya, R.; Akiba, C.; Saji, S.; Kondo, T.; Nakamura, J. Active Sites of Nitrogen-Doped Carbon Materials for Oxygen Reduction Reaction Clarified Using Model Catalysts. *Science (80-.).* **2016**, *351* (6271), 361 LP – 365.

(3) Jiang, K.; Siahrostami, S.; Zheng, T.; Hu, Y.; Hwang, S.; Stavitski, E.; Peng, Y.; Dynes, J.; Gangisetty, M.; Su, D.; et al. Isolated Ni Single Atoms in Graphene Nanosheets for High-Performance CO2 Reduction. *Energy Environ. Sci.* **2018**, *11* (4), 893–903.

(4) Liu, K.; Fu, J.; Lin, Y.; Luo, T.; Ni, G.; Li, H.; Lin, Z.; Liu, M. Insights into the Activity of Single-Atom Fe-N-C Catalysts for Oxygen Reduction Reaction. *Nat. Commun.* **2022**, *13* (1), 2075.

(5) Liu, J.; Zhang, G.; Ye, K.; Xu, K.; Sheng, Y.; Yu, C.; Zhang, H.; Li, Q.; Liang, Z.; Jiang, K. Top-down Manufacturing of Efficient CO2 Reduction Catalysts from the Gasification Residue Carbon. *Chem. Commun.* **2023**, *59* (5), 611–614.

(6) Zhang, L.; Fischer, J. M. T. A.; Jia, Y.; Yan, X.; Xu, W.; Wang, X.; Chen, J.; Yang, D.; Liu, H.; Zhuang, L.; et al. Coordination of Atomic Co–Pt Coupling Species at Carbon Defects as Active Sites for Oxygen Reduction Reaction. *J. Am. Chem. Soc.* **2018**, *140* (34), 10757–10763.

(7) Qiao, X.; Li, Q.; Schaugaard, R. N.; Noffke, B. W.; Liu, Y.; Li, D.; Liu, L.; Raghavachari, K.; Li, L. Well-Defined Nanographene–Rhenium Complex as an Efficient Electrocatalyst and Photocatalyst for Selective CO2 Reduction. *J. Am. Chem. Soc.* **2017**, *139* (11), 3934–3937.

(8) Li, Q.; Noffke, B. W.; Wang, Y.; Menezes, B.; Peters, D. G.; Raghavachari, K.; Li, L. Electrocatalytic Oxygen Activation by Carbanion Intermediates of Nitrogen-Doped Graphitic Carbon. *J. Am. Chem. Soc.* **2014**, *136* (9), 3358–3361.

(9) Koenig, J. D. B.; Dubrawski, Z. S.; Rao, K. R.; Willkomm, J.; Gelfand, B. S.; Risko, C.; Piers, W. E.; Welch, G. C. Lowering Electrocatalytic CO2 Reduction Overpotential Using N-Annulated Perylene Diimide Rhenium Bipyridine Dyads with Variable Tether Length. *J. Am. Chem. Soc.* **2021**, *143* (40), 16849–16864.

(10) Schaugaard, R. N.; Raghavachari, K.; Li, L. Redox "Innocence" of Re(I) in Electrochemical CO2 Reduction Catalyzed by Nanographene–Re Complexes. *Inorg. Chem.* **2018**, *57* (17), 10548–10556.

(11) Wang, M.; Torbensen, K.; Salvatore, D.; Ren, S.; Joulié, D.; Dumoulin, F.; Mendoza, D.; Lassalle-Kaiser, B.; Işci, U.; Berlinguette, C. P.; et al. CO2 Electrochemical Catalytic Reduction with a Highly Active Cobalt Phthalocyanine. *Nat. Commun.* **2019**, *10* (1), 3602.

(12) Seh, Z. W.; Kibsgaard, J.; Dickens, C. F.; Chorkendorff, I.; Nørskov, J. K.; Jaramillo, T. F. Combining Theory and Experiment in Electrocatalysis: Insights into Materials Design. *Science (80-.).* **2017**, *355* (6321), eaad4998.

(13) Chu, S.; Cui, Y.; Liu, N. The Path towards Sustainable Energy. *Nat. Mater.* **2017**, *16* (1), 16–22.

(14) Sapountzi, F. M.; Gracia, J. M.; Weststrate, C. J. (Kees-J.; Fredriksson, H. O. A.; Niemantsverdriet, J. W. (Hans). Electrocatalysts for the Generation of Hydrogen, Oxygen and Synthesis Gas. *Prog. Energy Combust. Sci.* **2017**, *58*, 1–35.

(15) Ail, S. S.; Dasappa, S. Biomass to Liquid Transportation Fuel via Fischer Tropsch Synthesis – Technology Review and Current Scenario. *Renew. Sustain. Energy Rev.* **2016**, *58*, 267–286.

(16) Lu, S.; Shi, Y.; Meng, N.; Lu, S.; Yu, Y.; Zhang, B. Electrosynthesis of Syngas via the Co-Reduction of CO2 and H2O. *Cell Reports Phys. Sci.* **2020**, *1* (11), 100237.

(17) Hertz, V. M.; Bolte, M.; Lerner, H.-W.; Wagner, M. Boron-Containing Polycyclic Aromatic Hydrocarbons: Facile Synthesis of Stable, Redox-Active Luminophores. *Angew. Chemie Int. Ed.* **2015**, *54* (30), 8800–8804.

(18) Hertz, V. M.; Massoth, J. G.; Bolte, M.; Lerner, H.-W.; Wagner, M. En Route to Stimuli-Responsive Boron-, Nitrogen-, and Sulfur-Doped Polycyclic Aromatic Hydrocarbons. *Chem. – A Eur. J.* **2016**, *22* (37), 13181–13188.

(19) Hirao, Y.; Konishi, A.; Kubo, T. Anthroxyl-Based Biradical: Toward the Construction of Highly Stable Multi-Spin Systems. *Org. Chem. Front.* **2017**, *4* (5), 828–833.

(20) Ageshina, A. A.; Sterligov, G. K.; Rzhevskiy, S. A.; Topchiy, M. A.; Chesnokov, G. A.; Gribanov, P. S.; Melnikova, E. K.; Nechaev, M. S.; Asachenko, A. F.; Bermeshev, M. V. Mixed Er-NHC/Phosphine Pd(Ii) Complexes and Their Catalytic Activity in the Buchwald–Hartwig Reaction under Solvent-Free Conditions. *Dalt. Trans.* **2019**, *48* (10), 3447–3452.

(21) Smieja, J. M.; Kubiak, C. P. Re(Bipy-TBu)(CO)3Cl−improved Catalytic Activity for Reduction of Carbon Dioxide: IR-Spectroelectrochemical and Mechanistic Studies. *Inorg. Chem.* **2010**, *49* (20), 9283–9289.

(22) Clark, M. L.; Cheung, P. L.; Lessio, M.; Carter, E. A.; Kubiak, C. P. Kinetic and Mechanistic Effects of Bipyridine (Bpy) Substituent, Labile Ligand, and Brønsted Acid on Electrocatalytic CO2 Reduction by Re(Bpy) Complexes. *ACS Catal.* **2018**, *8* (3), 2021–2029.

(23) Machan, C. W.; Sampson, M. D.; Chabolla, S. A.; Dang, T.; Kubiak, C. P. Developing a Mechanistic Understanding of Molecular Electrocatalysts for CO2 Reduction Using Infrared Spectroelectrochemistry. *Organometallics* **2014**, *33* (18), 4550–4559.

(24) Elgrishi, N.; Kurtz, D. A.; Dempsey, J. L. Reaction Parameters Influencing Cobalt Hydride Formation Kinetics: Implications for Benchmarking H2-Evolution Catalysts. *J. Am. Chem. Soc.* **2017**, *139* (1), 239–244.

(25) Bourrez, M.; Molton, F.; Chardon-Noblat, S.; Deronzier, A. [Mn(Bipyridyl)(CO)3Br]: An Abundant Metal Carbonyl Complex as Efficient Electrocatalyst for CO2 Reduction. *Angew. Chemie Int. Ed.* **2011**, *50* (42), 9903–9906.

(26) Costentin, C.; Drouet, S.; Robert, M.; Savéant, J.-M. A Local Proton Source Enhances CO2 Electroreduction to CO by a Molecular Fe Catalyst. *Science (80-.).* **2012**, *338* (6103), 90–94.

(27) Chapovetsky, A.; Welborn, M.; Luna, J. M.; Haiges, R.; Miller, T. F. I. I. I.; Marinescu, S. C. Pendant Hydrogen-Bond Donors in Cobalt Catalysts Independently Enhance CO2 Reduction. *ACS Cent. Sci.* **2018**, *4* (3), 397–404.

(28) Lacy, D. C.; McCrory, C. C. L.; Peters, J. C. Studies of Cobalt-Mediated Electrocatalytic CO2 Reduction Using a Redox-Active Ligand. *Inorg. Chem.* **2014**, *53* (10), 4980–4988.

(29) Nie, W.; Tarnopol, D. E.; McCrory, C. C. L. Enhancing a Molecular Electrocatalyst's Activity for CO2 Reduction by Simultaneously Modulating Three Substituent Effects. *J. Am. Chem. Soc.* **2021**, *143* (10), 3764–3778.

(30) Sampson, M. D.; Kubiak, C. P. Manganese Electrocatalysts with Bulky Bipyridine Ligands: Utilizing Lewis Acids To Promote Carbon Dioxide Reduction at Low Overpotentials. *J. Am. Chem. Soc.* **2016**, *138* (4), 1386–1393.

(31) Barlow, J. M.; Yang, J. Y. Thermodynamic Considerations for Optimizing Selective CO2 Reduction by Molecular Catalysts. *ACS Cent. Sci.* **2019**, *5* (4), 580–588.

(32) Azcarate, I.; Costentin, C.; Robert, M.; Savéant, J.-M. Dissection of Electronic Substituent Effects in Multielectron–Multistep Molecular Catalysis. Electrochemical CO2-to-CO Conversion Catalyzed by Iron Porphyrins. *J. Phys. Chem. C* **2016**, *120* (51), 28951–28960.

(33) Sampson, M. D.; Nguyen, A. D.; Grice, K. A.; Moore, C. E.; Rheingold, A. L.; Kubiak, C. P. Manganese Catalysts with Bulky Bipyridine Ligands for the Electrocatalytic Reduction of Carbon Dioxide: Eliminating Dimerization and Altering Catalysis. *J. Am. Chem. Soc.* **2014**, *136* (14), 5460–5471.

(34) Stephens, P. J.; Devlin, F. J.; Chabalowski, C. F.; Frisch, M. J. Ab Initio Calculation of Vibrational Absorption and Circular Dichroism Spectra Using Density Functional Force Fields. *J. Phys. Chem.* **1994**, *98* (45), 11623–11627.

(35) Krishnan, R.; Binkley, J. S.; Seeger, R.; Pople, J. A. Self-consistent Molecular Orbital Methods. XX. A Basis Set for Correlated Wave Functions. *J. Chem. Phys.* **1980**, *72* (1), 650–654.

(36) Hehre, W. J.; Ditchfield, R.; Pople, J. A. Self—Consistent Molecular Orbital Methods. XII. Further Extensions of Gaussian—Type Basis Sets for Use in Molecular Orbital Studies of Organic Molecules. *J. Chem. Phys.* **2003**, *56* (5), 2257–2261.

(37) Hay, P. J.; Wadt, W. R. Ab Initio Effective Core Potentials for Molecular Calculations. Potentials for the Transition Metal Atoms Sc to Hg. *J. Chem. Phys.* **1985**, *82* (1), 270–283.

(38) McLean, A. D.; Chandler, G. S. Contracted Gaussian Basis Sets for Molecular Calculations. I. Second Row Atoms, Z=11–18. *J. Chem. Phys.* **2008**, *72* (10), 5639–5648.

(39) Smieja, J. M.; Benson, E. E.; Kumar, B.; Grice, K. A.; Seu, C. S.; Miller, A. J. M.; Mayer, J. M.; Kubiak, C. P. Kinetic and Structural Studies, Origins of Selectivity, and Interfacial Charge Transfer in the Artificial Photosynthesis of CO. *Proc. Natl. Acad. Sci.* **2012**, *109* (39), 15646–15650.

(40) Pangborn, A. B.; Giardello, M. A.; Grubbs, R. H.; Rosen, R. K.; Timmers, F. J. Safe and Convenient Procedure for Solvent Purification. *Organometallics* **1996**, *15* (5), 1518–1520.

(41) Lobaccaro, P.; Singh, M. R.; Clark, E. L.; Kwon, Y.; Bell, A. T.; Ager, J. W. Effects of Temperature and Gas–Liquid Mass Transfer on the Operation of Small Electrochemical Cells for the Quantitative Evaluation of CO2 Reduction Electrocatalysts. *Phys. Chem. Chem. Phys.* **2016**, *18* (38), 26777–26785.

(42) Neese, F. The ORCA Program System. *WIREs Comput. Mol. Sci.* **2012**, *2* (1), 73–78.
(43) Shcherbin, D.; Ruud, K. The Use of Coulomb-Attenuated Methods for the Calculation of Electronic Circular Dichroism Spectra. *Chem. Phys.* **2008**, *349* (1), 234–243.
(44) Hanwell, M. D.; Curtis, D. E.; Lonie, D. C.; Vandermeersch, T.; Zurek, E.; Hutchison, G. R. Avogadro: An Advanced Semantic Chemical Editor, Visualization, and Analysis Platform. *J. Cheminform.* **2012**, *4* (1), 17.
(45) Schäfer, J.; Holzapfel, M.; Mladenova, B.; Kattnig, D.; Krummenacher, I.; Braunschweig, H.; Grampp, G.; Lambert, C. Hole Transfer Processes in Meta- and Para-Conjugated Mixed Valence Compounds: Unforeseen Effects of Bridge Substituents and Solvent Dynamics. *J. Am. Chem. Soc.* **2017**, *139* (17), 6200–6209.
(46) APEX2, Version 2 User Manual, M86-E01078, Bruker Analytical X-Ray Systems, Madison, WI, June 2006.
(47) Sheldrick, G. M. *SADABS (Version 2008/1): Program for Absorption Correction for Data from Area Detector Frames.*; University of Göttingen: 2008, 2008.
(48) Dolomanov, O. V.; Bourhis, L. J.; Gildea, R. J.; Howard, J. A. K.; Puschmann, H. No. *J. Appl. Crystallogr.* **2009**, *42*, 339–341.
(49) Sheldrick, G. M. No Title. *Acta Crystallogr. Sect. A* **2008**, *64*, 112–122.
(50) Brandenburg, K. (1999). Diamond. Crystal Impact GbR, Bonn, Germany.

CHAPTER VII

SYNTHESIS AND ELECTRONIC PROPERTIES OF A NITROGEN-RICH NANOGRAPHENE

This chapter was reproduced from:

Heim, G.P.; Hirahara, M.; Dev, V.M.; Agapie, T. *Manuscript submitted.*

ABSTRACT: A polycyclic aromatic hydrocarbon bearing twelve edge nitrogen atoms for a 42 π-electron system is reported. The compounds are synthesized via Sonogashira coupling of pyrimidine precursors, [2+2+2] cycloaddition of bis(aryl) alkynes, and anionic cyclodehydrogenation. Spectroscopy, electrochemistry, and computational results suggest a significant narrowing of the HOMO-LUMO gap compared to the N-free analogue owing to the electron-deficient extended π system imposed by the nitrogen dopants. Coordination to metals and electronic structure modification of the extended π system were observed.

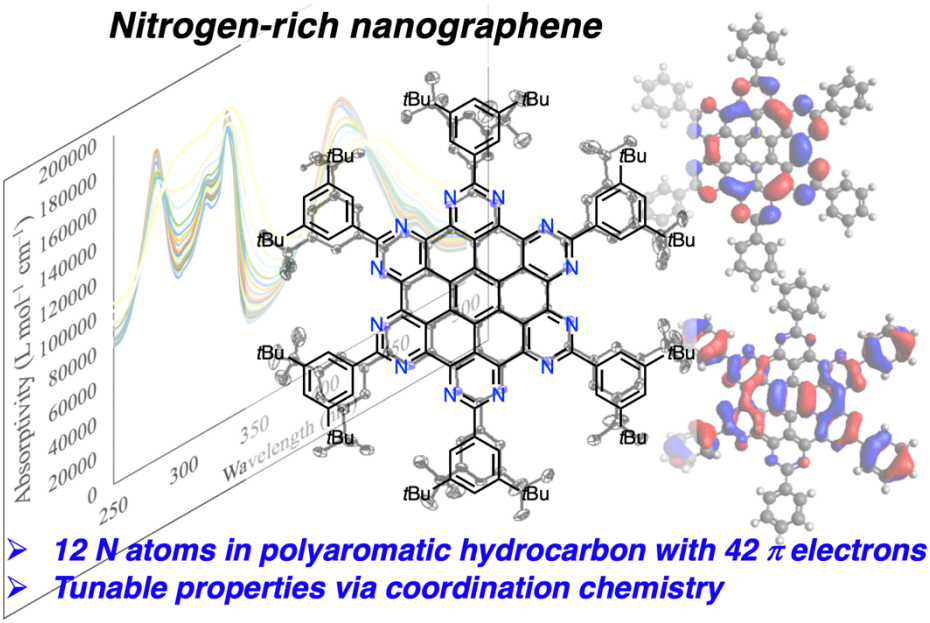

ACKNOWLEDGEMENTS

This material is based on work performed by the Liquid Sunlight Alliance, which is supported by the U.S. Department of Energy, Office of Science, Office of Basic Energy Sciences, Fuels from Sunlight Hub under Award DE-SC0021266. Dr. Masanari Hirahara and Vidhya Dev are thanked for their contributions to this project. I acknowledge the Beckman Institute for instrumentation support. I thank Dr. Michael Takase for assistance with X-ray crystallography and Maryann Morales for assistance with fluorescence spectroscopy. I am grateful to Dr. Matthew Espinosa for assisting with MALDI-TOF.

INTRODUCTION

Polycyclic aromatic hydrocarbons (PAHs) have attracted substantial interest in the development of charge-carrying materials owing to their optical and electronic properties.[1–6] Bottom-up preparation affords molecular nanographenes that are amenable to well-defined characterization via solution-state spectroscopy and X-ray crystallography.[4,7] Hexabenzocoronenes (HBCs) in particular have received much attention due to high thermal stability and modular preparations.[1,2,8,9] Facile tunability of electronic structure is of interest to ascertain the ability of nanographene molecules as candidate materials for organic electronics;[3] strategies include incorporation of heteroatom dopants,[10,11] functionalization with electron-withdrawing/donating substituents,[4,12,13] and coordination to metal centers.[14–16] Moreover, nitrogen-containing polyaromatics have displayed desirable photophysical properties.[6,10,15–17]

Although maximizing the nitrogen content of nanographenes has been proposed to lead to enhanced photophysics,[18,19] direct comparisons of structural analogs are rare.[15,16] While several reports exist investigating higher nitrogen content PAHs (Scheme 1),[18–23] we set out to maximize nitrogen content as a means of tuning electronic properties of nanographenes bearing HBC motifs[6,10,11,14–17] and systematically compare with nitrogen-free analogues.

We report the synthesis and electronic structure of an N-rich HBC variant based on a hexa-pyrimido-coronene, **HPC-N$_{12}$(Ar^{tBu})$_6$** each bearing twelve edge nitrogen atoms. Functionalization at the 2-position of the pyrimidine allows variation of the aryl substituent on the extended π system, which provides an additional platform for tailoring the electronic properties of the HBC. Cyclodehydrogenation to generate the fused polyaromatic system

required alkali metal reduction followed by exposure to dioxygen,[24] whereas all-carbon variants are typically amenable to Scholl oxidation conditions.[25] The electrochemistry, electronic spectra, and DFT computations are reported, highlighting a significant narrowing of the HOMO-LUMO gap when the nitrogen content is increased.

Scheme 1. Literature examples of N-containing PAHs and compound reported in this work.

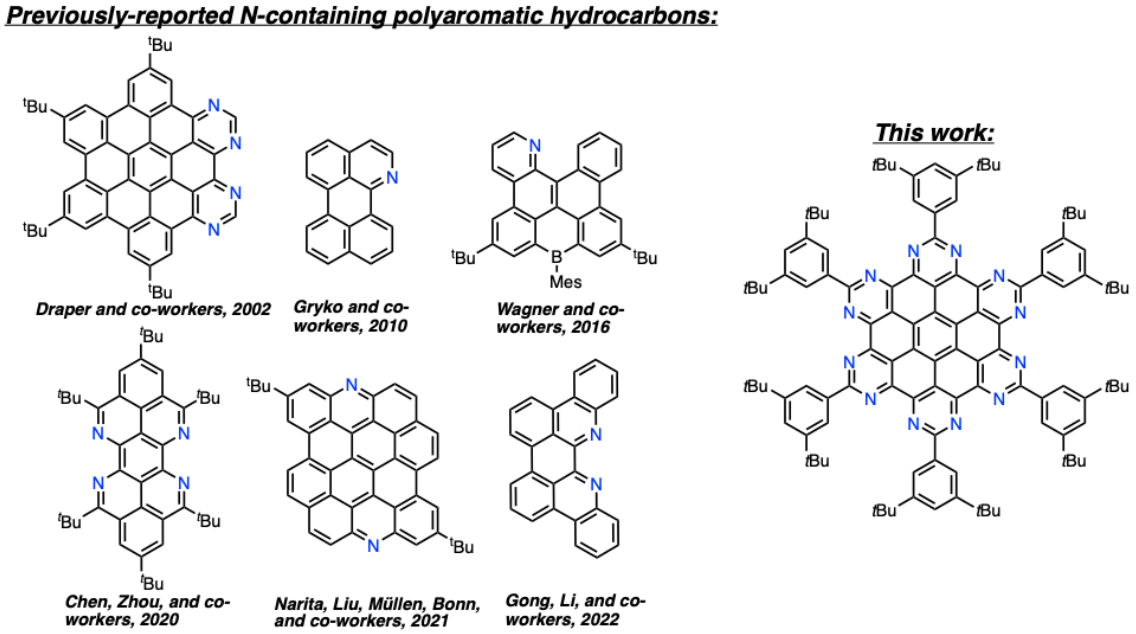

RESULTS AND DISCUSSION

HPC-$N_{12}(Ar^{tBu})_6$ was prepared in four steps from commercially available starting materials (Scheme 2). The aryl pyrimidine **1** was prepared via a Negishi coupling (see ESI).[26] A modified Sonogashira coupling of **1** with trimethylsilylacetylene in the presence [Cu(Xantphos)I] and $Pd(OAc)_2$ leads to the generation of the bis(aryl)alkyne **2** in a single pot, in 50% yield.[27] **3** was generated from the [2+2+2] cycloaddition of **2** utilizing a mixture of $Ni(OAc)_2$, $^{i}PrMgCl$, and 1,3-bis(2,4,6-trimethylphenyl)imidazolium chloride (IMesHCl) in 77% yield.[28] All steps were performed on multigram-scales without affecting the purities of products.

Scheme 2. Synthesis of **HPC-N$_{12}$(Ar^{tBu})$_6$**.

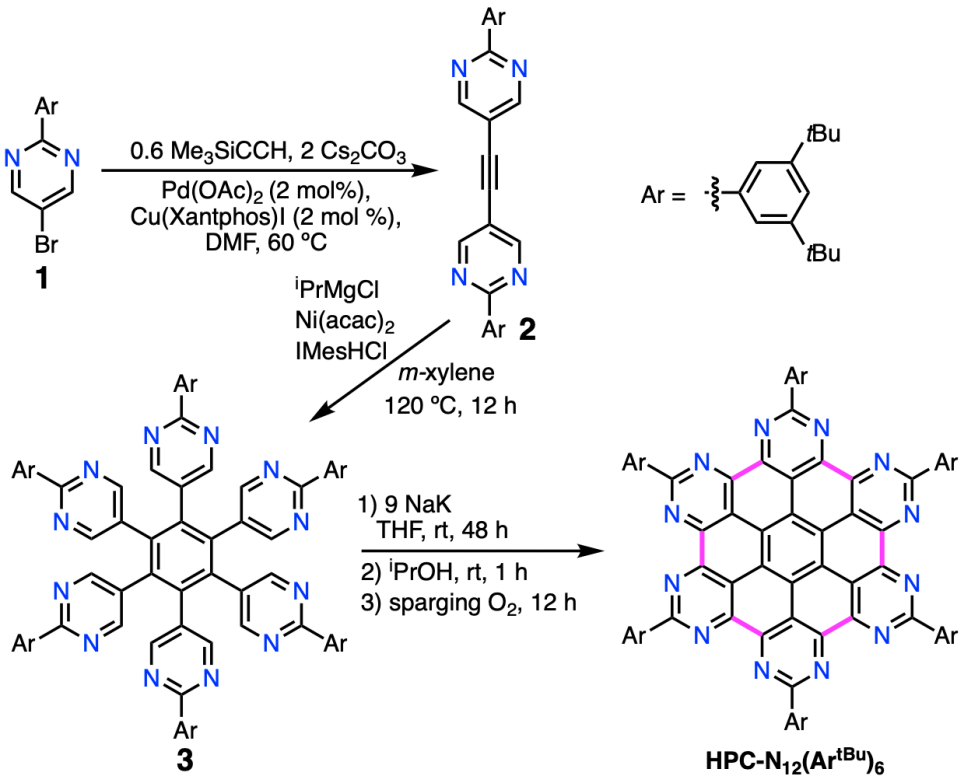

Cyclodehydrogenation reactions of polycyclic aromatic hydrocarbon precursors are typically performed under oxidative conditions, where the proposed intermediate is an arenium cation.[24,25] Treatment of **3** with DDQ/triflic acid in CH_2Cl_2 did not result in the desired product likely due to the electron-deficient nature of the nitrogen-containing heterocycles in **3**, increasing the energy of putative cationic intermediates.[29] Another methodology involves formation of radical-anionic species prone to C-C coupling with strong reducing agents. Subsequent oxidation results in the desired PAH, route previously reported for ring closure of naphthylisoquinolines to N-containing perylenes.[24,30]

Treatment of **3** with 9 equivalents of 1:1 molar ratio of sodium and potassium metal (NaK) for 48 h causes the suspension to turn from colorless to dark red. The solution was quenched with ^{i}PrOH, then MeOH, followed by sparging with O_2 for 12 h to promote

aromatization, yielding a dark brown solution. The ^{1}H NMR spectrum of this material (Figure 12) reveals two aromatic resonances at 9.25 and 7.83 ppm that integrate in a 2:1 ratio corresponding to *ortho* and *para* protons, respectively, on the 3,5-di-*tert*-butylphenyl substituent. In addition, there is only one peak in the aliphatic region corresponding to the *tert*-butyl groups (1.65 ppm) owing to the six-fold rotational symmetry in the desired **HPC-N$_{12}$(Ar^{tBu})$_6$.**

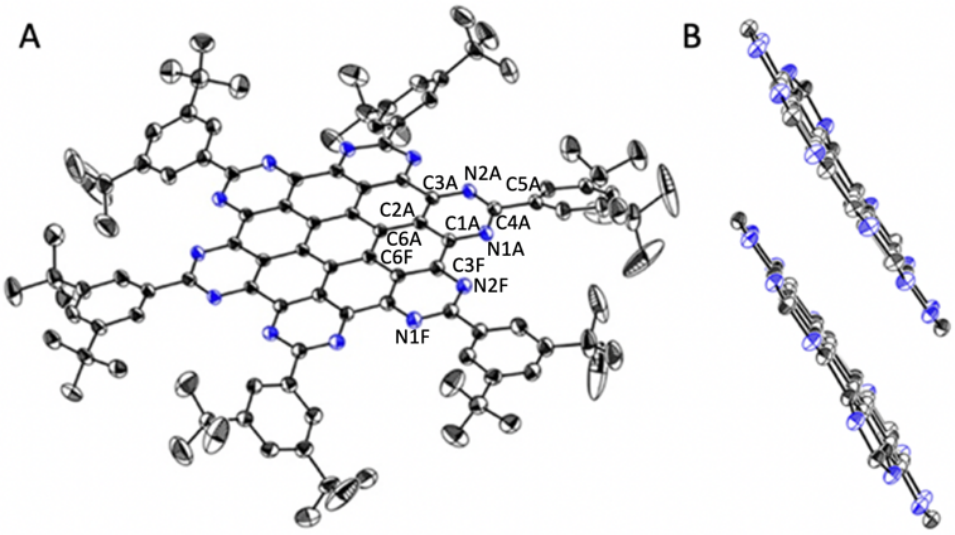

Figure 1. A. Solid-state structure of **HPC-N$_{12}$(Ar^{tBu})$_6$**. B. π-stacking as evident in the unit cell. 3,5-di-*tert*-butylaryl groups omitted for clarity. Thermal ellipsoids shown at 50% probability. Blue: Nitrogen, black: carbon. Chloroform molecules and hydrogen atoms are omitted for clarity.

Deep-red single crystals of **HPC-N$_{12}$(Ar^{tBu})$_6$** suitable for single-crystal X-ray diffraction were grown by slow evaporation at room temperature of a concentrated chloroform solution. The crystal structure (Figure 1) confirms the identity of **HPC-N$_{12}$(Ar^{tBu})$_6$** as a planar, nitrogen-rich HBC. The distance of 3.37 Å between two **HPC-N$_{12}$(Ar^{tBu})$_6$** molecules in the unit cell is evidence of intermolecular π stacking; typical π stacking distances are less than 3.8 Å.[31] The 3,5-di-*tert*-butylphenyl groups cause the HPC

motifs to be offset to optimize the π stacking interaction (Figure 23). Analysis of the bond lengths in comparison to 2,9-bis(2,6-dimethoxyphenyl)-1,10-phenanthroline show significant differences (Table 7).[32] Contraction of bonds between C6A and C2A is observed by 0.03 Å in **HPC-N$_{12}$(Ar^{tBu})$_6$**. By contrast, C6A-C6F and C3F-C1A lengthen by 0.05 and 0.02 Å, respectively, highlighting greater double bond character towards the nitrogen atoms away from the core of the π system. C17'-C27' in decamethylphenanthrene is shorter than C6A-C6F in **HPC-N$_{12}$(Ar^{tBu})$_6$** by 0.06 Å. **HPC-N$_{12}$(Ar^{tBu})$_6$** represents the first example of an HBC bearing twelve peripheral nitrogen atoms. Prior examples of N-containing HBC display only four N.[15,16]

The cyclic voltammogram (CV) of **HPC-N$_{12}$(Ar^{tBu})$_6$** in THF is shown in Figure 2. There are two quasireversible reduction features at –1.3 V and –1.5 V vs. $Fc^{0/+}$ as well as an irreversible feature at –2.2 V. The first reduction of a heteroatom-free HBC with six *tert*-butyl substituents is –2.1 V vs $Fc^{0/+}$ in THF (Table 1).[33–36] The positive shift in the reduction potentials in **HPC-N$_{12}$(Ar^{tBu})$_6$** is due to the presence of nitrogen atoms, resulting in a more electron-deficient π system.[15,16] For comparison, simple heterocycle show a similar trend, with benzo[e]pyrene vs 1,8-diazabenzo[e]pyrene showing one-electron reduction at –2.6 V vs –2.02 V vs. $Fc^{+/0}$, respectively.[20] Notably, HPC can be reduced by three electrons positive of the potential for the first reduction of HBC.

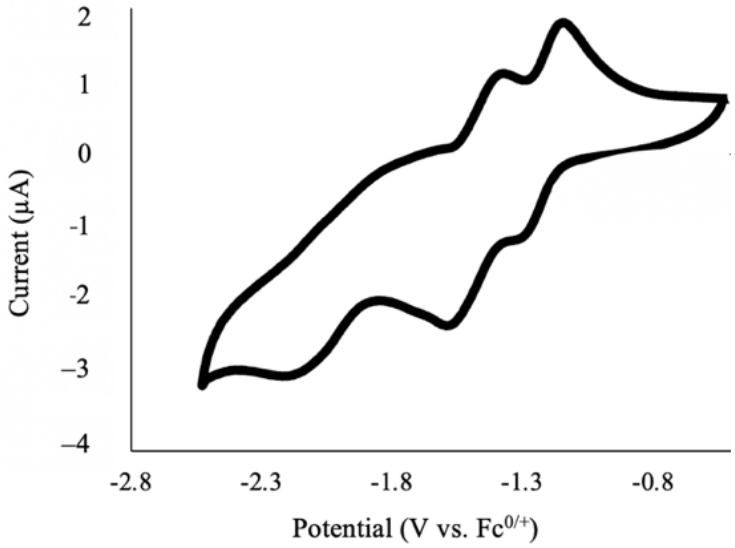

Figure 2. CV of **LN_{12}** (1 mM) collected at 200 mV/s. 0.1 M ($^{n}Bu)_4NPF_6$ in THF. Working electrode: glassy carbon. Reference electrode: Ag/AgCl. Counter electrode: Pt wire.

Table 1. Comparing most positive reduction determined by cyclic voltammetry between hexabenzocoronene variants

Compound	$E_{1/2}$ (V vs. $Fc^{0/+}$)	Electrolyte	Reference
HPC-N_{12}(Ar^{tBu})$_6$	-1.3	0.1 M $^{n}(Bu)_4PF_6$/THF	*This work*
N_4-HBC	-1.6	0.1 M $^{n}(Bu)_4PF_6$/CH_3CN	Draper and co-workers[16]
^{tBu}HBC	-2.1	0.1 M $^{n}(Bu)_4PF_6$/THF	Müllen and co-workers[33]
^{tBu}HBC	-1.7	0.1 M $^{n}(Bu)_4PF_6$/CH_2Cl_2	Guldi, Jux, and co-workers[36]

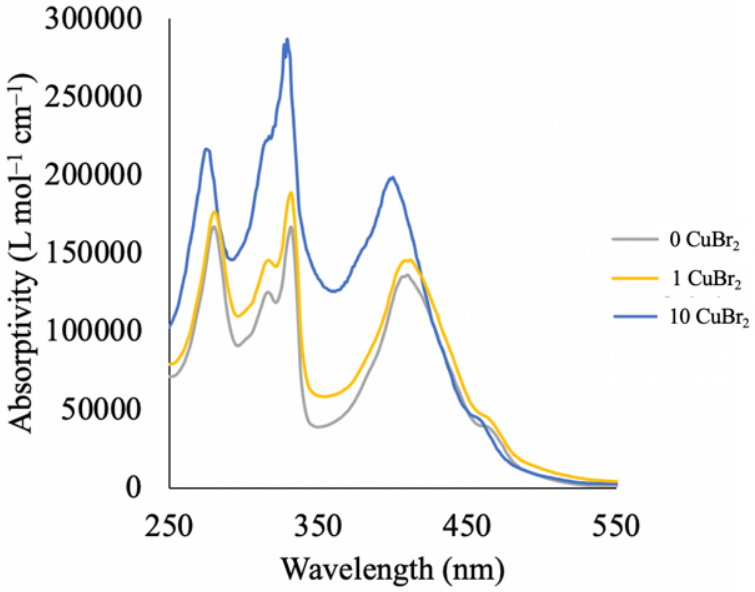

Figure 3. Absorption spectra of **HPC-N$_{12}$(Ar^{tBu})$_6$** (0.060 mM in THF) recorded after adding successive equivalents of $CuBr_2$.

Nitrogen incorporation appears to shrink the band gap when comparing to all-carbon HBC (Figure 3). Three prominent features are observed in 0.060 mM **HPC-N$_{12}$(Ar^{tBu})$_6$** in $CHCl_3$ at 410 nm, 330 nm, and 279 nm. These peaks are redshifted from those of a previously-reported hexaaryl HBC (~190, ~250, and ~370 nm).[37,38] Nitrogen-containing PAHs have provided opportunities for investigating coordination chemistry effects on photophysics.[6,15,16,39–41] To probe a similar phenomenon with our system, UV-vis spectra were recorded after addition of a single equivalent of $CuBr_2$ to **HPC-N$_{12}$(Ar^{tBu})$_6$**, finding enhancement in intensity in the absorption in all features up to 30 equivalents (Figure 3). The feature with the lowest wavelength redshifts by blueshifts by 20 nm. This finding suggests widening of HOMO-LUMO gap provided by metal complexation (*vide infra)*.[45,46] Attenuation in fluorescence ($\lambda_{excited}$ = 410 nm) is observed from adding $CuBr_2$ (Figure 4), consistent with prior reports adding Cu^{2+} to N-containing PAHs;[40,41] shifting to higher energy

is also observed. Matrix-assisted laser desorption time of flight (MALDI-TOF) mass spectrometry of the solution after 20 equivalents of $CuBr_2$ suggests a mixture of metal complexes in addition to **HPC-N_{12}(Ar^{tBu})$_6$**: **Br_2Cu-HPC-N_{12}(Ar^{tBu})$_6$** and (**Br_2Cu)$_3$-HPC-N_{12}(Ar^{tBu})$_6$**.[44–47] While purification efforts have not yielded an isolated metal complex, these results suggest the ability of metals in tuning the HOMO-LUMO gap of nitrogen-rich PAHs. Binding to $ZnCl_2$ is also evident based on spectroscopy and MALDI-TOF data (Figures 14 and 16, respectively). Addition of trifluoromethanesulfonic acid (TfOH) to **HPC-N_{12}(Ar^{tBu})$_6$** provides redshifted absorption features by up to 20 nm (65 equivalents). The emission spectrum intensity is attenuated and also redshifts by up to 36 nm (Figure 15), consistent with previous reports demonstrating attenuated emission intensity due to protonation.[6,15,16,41] **HPC-N_{12}(Ar^{tBu})$_6$** could serve as a possible pH sensing material.[6]

To better understand the electronic structures of the nanographene molecules DFT calculations were performed. Geometry optimization was performed with the B3LYP functional[48] and 6-311G(d,p) basis set.[49] Few studies have been carried out to compare heteroatom-containing extended π systems and all-carbon analogues.[50] A model with the *tert*-butyl groups replaced with hydrogen atoms (**HPC-N_{12}Ph$_6$**) was employed for **HPC-N_{12}(Ar^{tBu})$_6$**.

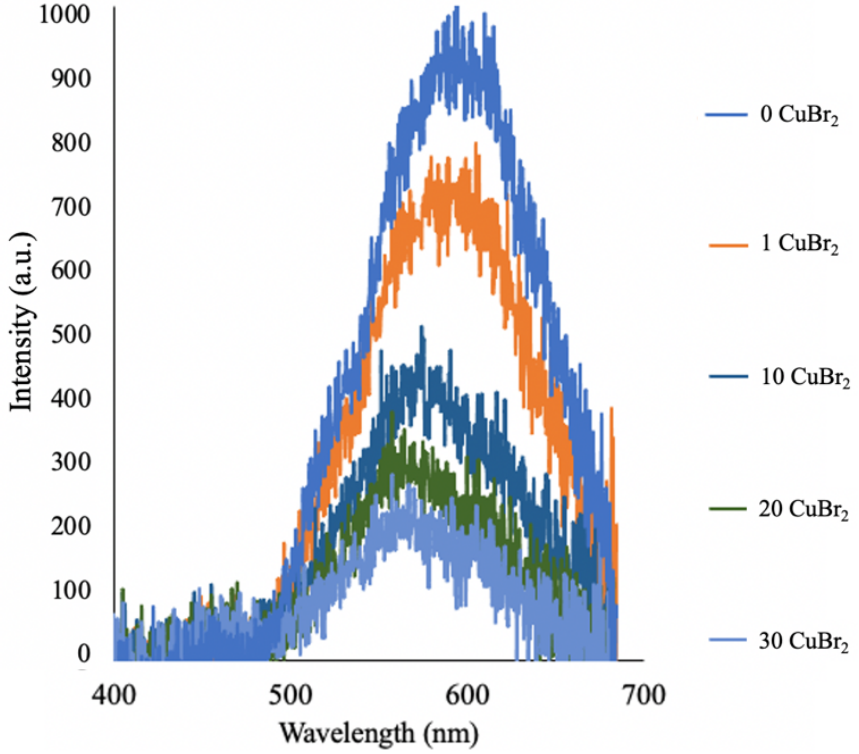

Figure 4. Emission spectra (excitation wavelength: 410 nm) of **HPC-N$_{12}$(Ar^{tBu})$_6$** (0.060 mM in THF) recorded after adding successive equivalents of $CuBr_2$.

An analogous model was studied for HBC (**HBC-Ph$_6$**). The HOMO-LUMO gap is narrower by 328 meV in **HPC-N$_{12}$Ph$_6$** than in the nitrogen-free analogue **HBC-Ph$_6$** (Table S2), suggesting that nitrogen doping is a viable strategy in preparing lower band gap materials.[1,2,6,10,20,42,43] HOMO-LUMO energy gap shrinking due to N incorporation is attributed to significant electron-accepting character.[10,51] The LUMO of **HPC-N$_{12}$Ph$_6$** (Figure 5) possesses significant N character. In addition, delocalization onto the aryl substituents is observed in the HOMO and HOMO-1 for **HPC-N$_{12}$Ph$_6$** (Figure 19).[52]

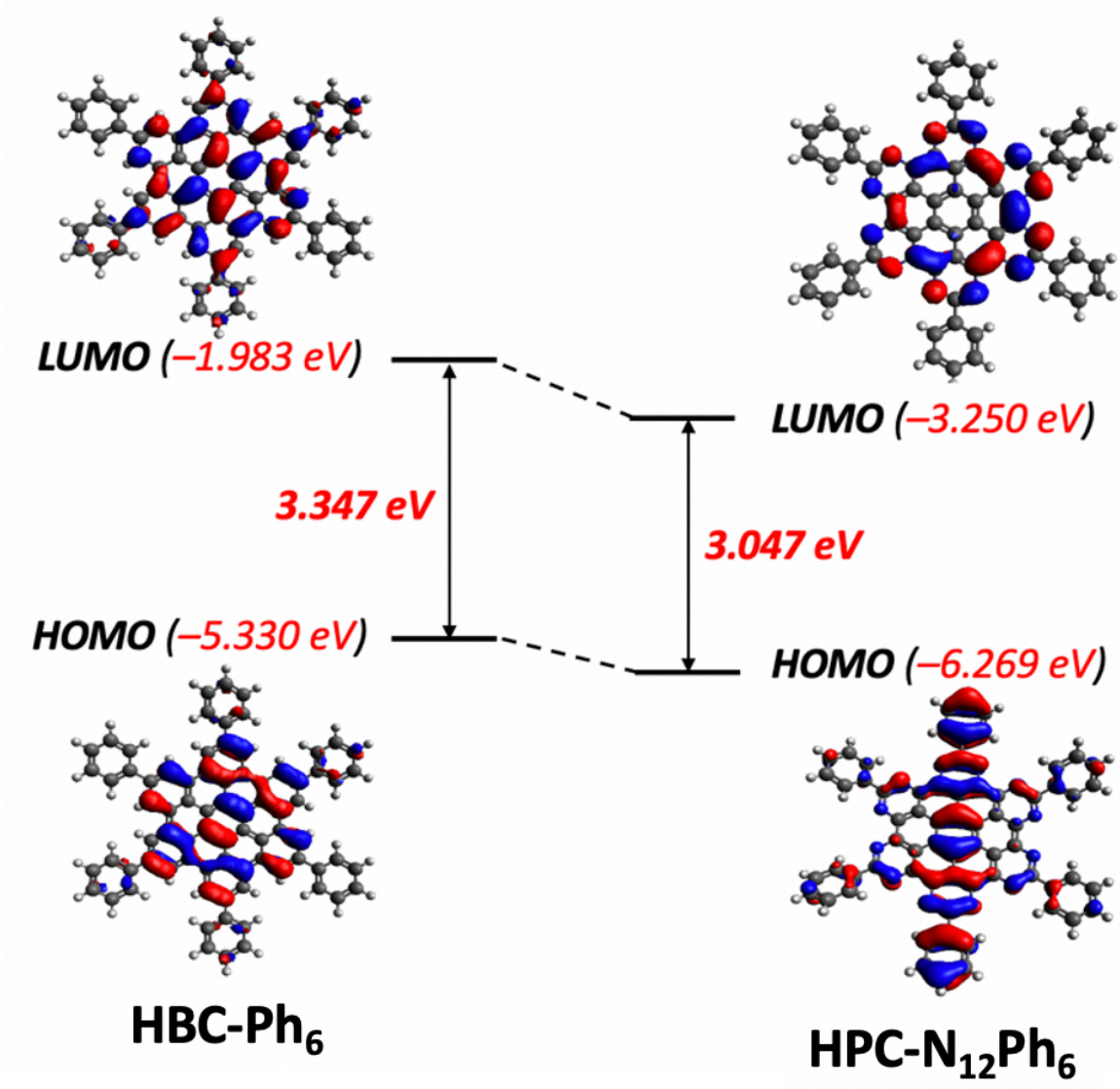

Figure 5. HOMO and LUMO each for **HBC-Ph$_6$** and **HPC-N$_{12}$Ph$_6$**, comparing energy levels and energy gap. Orbitals are calculated at the B3LYP/6-311G(d,p) level of theory. Isosurfaces are shown at 0.02 value.

CONCLUSIONS

Synthesis and electronic structure of nitrogen-rich PAH **HPC-N$_{12}$(Ar^{tBu})$_6$** is reported. Preparation of the compound was achieved via anionic cyclodehydrogenation. Characterization in the solid-state in addition to NMR spectroscopy is obtained, highlighting

substantial development in preparing heteroatom-containing nanographenes with well-defined characterization. The energy gaps between the HOMO and LUMO are significantly narrower resulting from substantial electron-accepting character of the nitrogen dopants, evident by electrochemistry as well as experimental and computed electronic spectra. Metal binding suggests that coordination chemistry can be utilized to tune electronic structure of this extended π system. This report unlocks a new paradigm in synthesizing N-rich nanographenes with potential application in optoelectronics.

EXPERIMENTAL

General considerations. Unless otherwise specified, all operations involving air- or water-sensitive reagents were carried out in an MBraun drybox under a nitrogen atmosphere or using standard Schlenk and vacuum line techniques. Glassware was oven-dried at 140 ºC for 2 h prior to use on the Schlenk line or in the MBraun drybox. Tetrahydrofuran (THF), diethyl ether, toluene, pentane, and hexanes for air- and moisture-sensitive reactions were dried by the method of Grubbs.[53] Dry *N,N*-dimethylformamide (DMF) was purchased from Millipore Sigma and cannula transferred to freshly-activated 3 Å molecular sieves and stored in a Teflon-sealed Schlenk tube under N_2 atmosphere for 12 h prior to use. *Meta*-xylene was vacuum transferred from sodium benzophenone ketyl. Deuterated solvents were purchased from Cambridge Isotope Laboratories and $CDCl_3$ was used as received. All solvents, once dried and degassed, were stored under a nitrogen atmosphere over 3 Å molecular sieves. Iodo[bis(diphenylphosphino)-9,9-dimethylxanthene]copper(I) was prepared following a previously reported procedure.[54] All other reagents were used as received. ^{1}H, and $^{13}C\{^{1}H\}$ spectra were recorded on Varian Mercury 300 MHz or Varian 400 MHz spectrometers at ambient temperatures, unless otherwise denoted. ^{1}H and $^{13}C\{^{1}H\}$ NMR spectra are reported referenced internally to residual solvent peaks reported relative to tetramethylsilane. Gas chromatography-mass spectrometry (GC-MS) were performed on an Agilent 6890A instrument using a HP-5MS column

(30 m length, 0.25 mm diameter, 0.50 μm film) and an Agilent 5973N mass-selective EI detector. Absorption spectra were recorded on a Varian Cary Bio 50 spectrophotometer.

Electrochemical measurements: CVs were recorded with a Pine Instrument Company AFCBP1 biopotentiostat with the AfterMath software package. All measurements were performed in a three electrode cell, which consisted of glassy carbon (working; ø = 3.0 mm), silver wire (counter) and bare platinum wire (reference), in an N_2-filled MBraun glovebox at RT. Dry tetrahydrofuran that contained ~100 mM [^{n}Bu$_4$N][PF_6] was used as the electrolyte solution. The ferrocene/ferrocenium (Fc/Fc^+) redox wave was used as an internal standard for all measurements.

Preparation of pre-reduced magnetic stir bars: Sodium mirror (10-20 mg) is prepared in a 20-mL scintillation vial along with 200-300 mg of benzophenone dissolved in THF to form a purple solution, which is then added to a 20-mL vial containing 10-20 Teflon-coated magnetic stir bars and stirred for 12 h. The solution is decanted, and the stir bars are rinsed with THF until the mother liquor is colorless, resulting in black, pre-reduced magnetic stir bars that are dried under vacuum for 1 h and are to be used for reactions involving Na and NaK.

Absorption spectroscopy: UV-vis spectra were recorded on a Varian Cary Bio 50 spectrophotometer in a 1 mm cuvette. Single equivalents of $ZnCl_2$ (103 mM in $CHCl_3$) were added to 0.060 mM **HPC-N$_{12}$(Ar^{tBu})$_6$**. After addition of an equivalent, a spectrum was recorded.

Emission spectroscopy: Corrected room temperature emission spectra were collected in the Beckman Institute Laser Resource Center using a modified Jobin Yvon Spec Fluorolog-3 instrument. Samples were excited with a xenon arc lamp, employing a monochromator for wavelength selection, and emission was detected at 90° using two Ocean Optics EQDPro CCD spectrometers spanning

300–930 nm. Single equivalents of metal salt or trifluoromethane sulfonic acid (103 mM) were added to 0.060 mM **HPC-N$_{12}$(Ar^{tBu})$_6$**. After addition of an equivalent, a spectrum was recorded. The entrance and exit slits were 5 nm, and voltage was set to 400 V.

MALDI-TOF: Mass spectra were recorded on a Bruker Autoflex MALDI TOF/TOF. Dithranol (0.091 mM in $CHCl_3$) was employed as the matrix. 3 μL of the dithranol solution were combined with 1 μL of 0.060 mM **HPC-N$_{12}$(Ar^{tBu})$_6$** + metal salt mixture. This mixture was drop casted onto a MALDI plate and allowed to dry under ambient conditions.

Synthesis

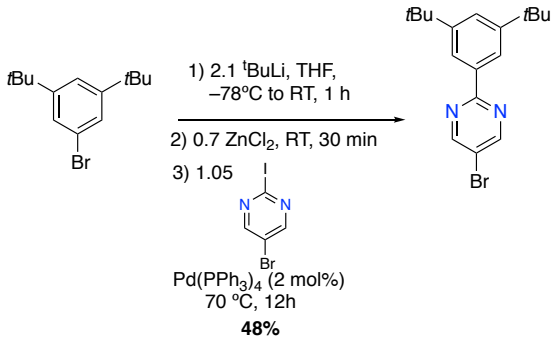

5-bromo-2-(3,5-di-*tert*-butylphenyl)pyrimidine (1a). Adapted from a previously-reported procedure:[26] In an N_2-purged glove box, a Schlenk flask fitted with a screw-in Teflon stopper was charged with a solution of 3,5-di-*tert*-butylbromobenzene (20 g, 75 mmol) in THF (250 mL). The flask was sealed, brought outside of the box and cooled to –78 °C with a dry ice/acetone bath. A pentane solution of tert-butyllithium (80 mL, 2.0 M, 160 mmol) was added dropwise via cannula. The reaction was allowed to warm to room temperature and stirred for 1 h forming a yellow solution. The reaction was then brought back into an N_2-purged glovebox and $ZnCl_2$ (7.2 g, 53 mmol) was added slowly to the reaction resulting in the loss of the yellow coloration and formation of a white precipitate. The mixture was allowed to stir at room temperature for 30 min. 5-bromo-2-iodopyrimidine (22.3 g, 78 mmol) was added to the mixture. The flask was then placed in the cold

well previously cooled with liquid nitrogen. $Pd(PPh_3)_4$ (1.3 g, 1.0 mmol) was added slowly, the flask sealed, and brought outside of the box. The vessel was fitted with an oven-dried reflux condenser and warmed to 70 °C for 12 h. After cooling to room temperature, water (100 mL) was added to quench the reaction, and the mixture concentrated in vacuo to about 100 mL. The resulting suspension was taken up in CH_2Cl_2 (200 mL) and washed with 5 x 100 mL of water. The organic layer was washed with brine (2 x 100 mL), dried over $MgSO_4$, and filtered. Removal of the volatiles under a reduced pressure afforded an orange solid, which was charged with 200 mL of hexanes and heated to reflux. The mixture was filtered, and the filtrate was concentrated under a reduced pressure, allowing a white solid to crash out, which was filtered and washed with cold hexanes. The off-white solid was determined to be analytically pure **1a.** 15 g (50% yield). ^{1}H NMR (400 MHz, $CDCl_3$): δ = 8.84 (s, 2H, Ar*H*), 8.31 (app d, 2H, Ar*H*), 7.62 (t, 1H, Ar*H*), 1.43 (s, 18H, C(CH_3)$_3$). ^{13}C{^{1}H} NMR (101 MHz, $CDCl_3$) δ = 163.75 (aryl-*C*), 157.84 (aryl-*C*), 151.40 (aryl-*C*), 135.93 (aryl-*C*), 125.6 (aryl-*C*), 122.65 (aryl-*C*), 118.05 (aryl-*C*), 35.18 (*C*(CH_3)$_3$), 31.64 (C(*C*H_3)$_3$). HRMS (FAB+) m/z Calcd. for [M + H$^+$] $C_{18}H_{13}BrN_2$ 347.1123, found 347.1122.

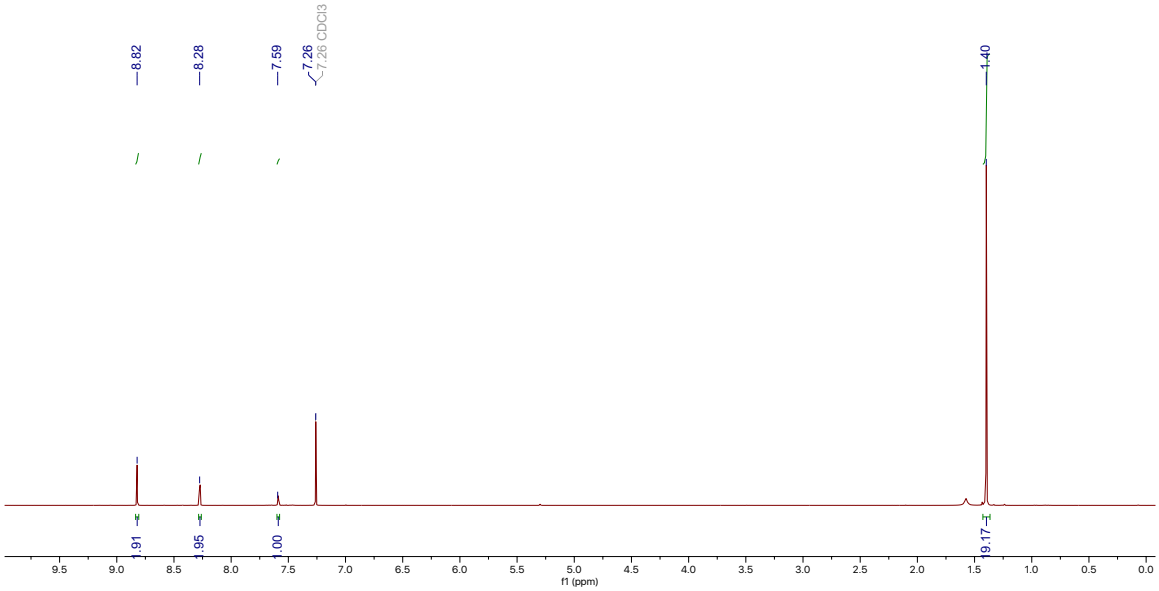

Figure 6. ^{1}H NMR spectrum (400 MHz, $CDCl_3$) of 5-bromo-2-(3,5-di-*tert*-butylphenyl)pyrimidine **(1a)**.

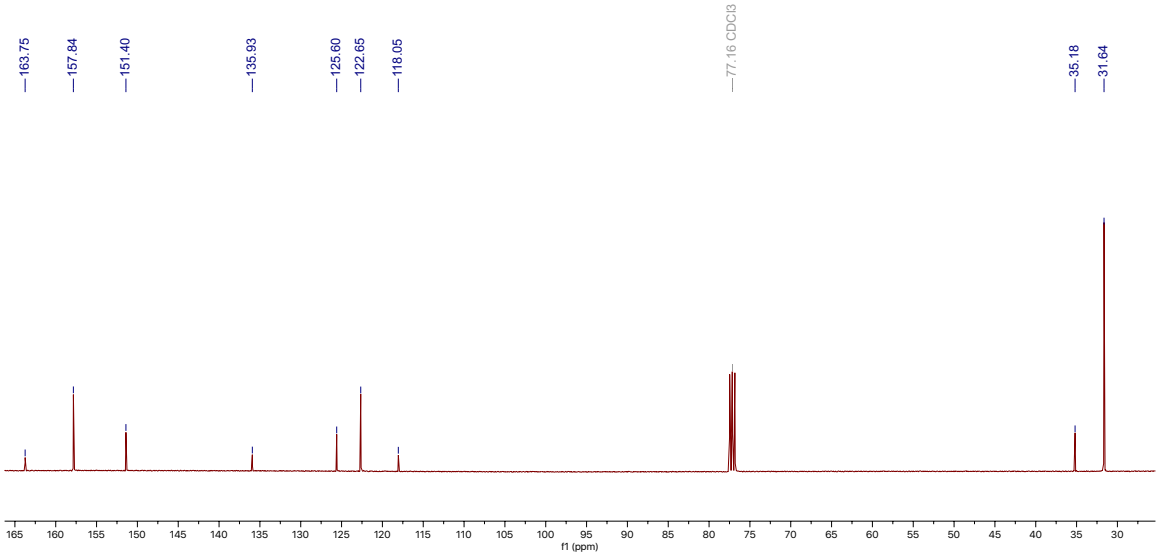

Figure 7. $^{13}C\{^{1}H\}$ NMR spectrum (101 MHz, $CDCl_3$) of 5-bromo-2-(3,5-di-*tert*-butylphenyl)pyrimidine **(1a)**.

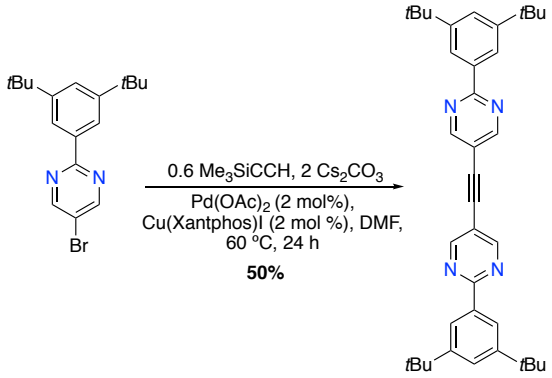

1,2-bis(2-(3,5-di-*tert*-butylphenyl)pyrimidin-5-yl)ethyne (2a). Adapted from a previously-reported procedure:[27] A 1-L, oven-dried Schlenk flask was allowed to cool under vacuum on the Schlenk line. Under a positive pressure of N_2, the Schlenk flask was charged with of 5-bromo-2-(3,5-di-*tert*-butylphenyl)pyrimidine (**1a**) (12.8 g, 37 mmol), cesium carbonate (24.1 g, 74 mmol), and palladium (II) acetate (165 mg , 0.73 mmol). DMF (250 mL) was added to the Schlenk flask via cannula. To this mixture was added trimethylsilylacetylene (3.14 mL, 22 mmol) under positive N_2. The reaction mixture was degassed via one cycle of freeze-pump-thaw. Iodo[bis(diphenylphosphino)-9,9-dimethylxanthene]copper(I) (566 mg, 0.73 mmol) was added under positive N_2. The reaction mixture was subject to two more cycles of freeze-pump-thaw, and the mixture was heated to 60 ºC for 12 h. Volatiles were removed under a reduced pressure, and the crude solid was charged with CH_2Cl_2 (300 mL) and filtered to remove excess cesium carbonate. The filtrate was concentrated under a reduced pressure and purified via column chromatography with CH_2Cl_2 as the eluent. The white solid was dried under vacuum for 12 h at room temperature prior to the next step. (5 g, 50%). ^{1}H NMR (400 MHz, $CDCl_3$) δ= 8.95 (s, 4H, Ar*H*), 8.36 (app d, 4H, Ar*H*), 7.61 (t, 2H, Ar*H*), 1.42 (s, 36H, C(C*H*$_3$)$_3$). ^{13}C{^{1}H} NMR (101 MHz, $CDCl_3$) δ= 164.02 (aryl-*C*), 159.13 (aryl-*C*), 151.45 (aryl-*C*), 136.22 (aryl-*C*), 125.93 (aryl-*C*), 123.02 (aryl-*C*), 115.89 (aryl-*C*), 90.03 (alkyne-*C*C), 35.22 (*C*(CH$_3$)$_3$) 31.65 (C(*C*H$_3$)$_3$). HRMS (FAB+) m/z Calcd. for [M + H$^+$] $C_{38}H_{47}N_4$ 559.3801, found 559.3813.

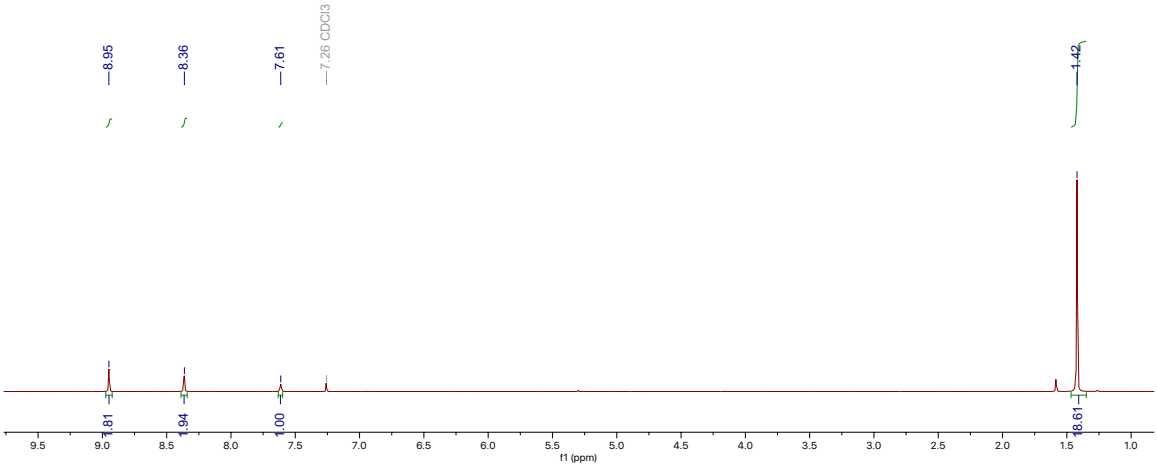

Figure 8. ^{1}H NMR spectrum (400 MHz, $CDCl_3$) of 1,2-bis(2-(3,5-di-*tert*-butylphenyl)pyrimidin-5-yl)ethyne **(2a)**

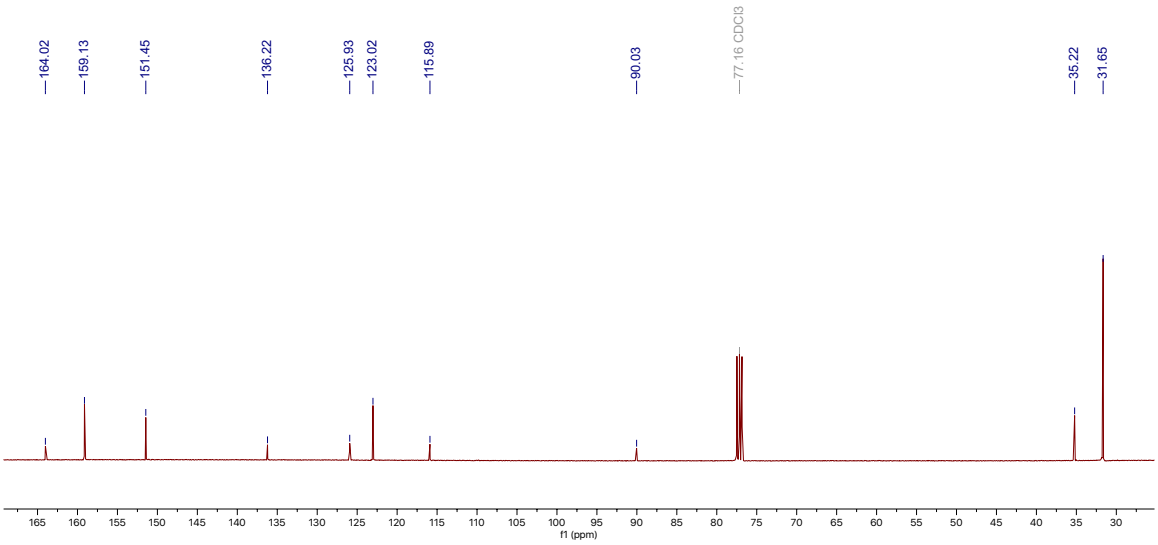

Figure 9. $^{13}C\{^{1}H\}$ NMR spectrum (101 MHz, $CDCl_3$) of 1,2-bis(2-(3,5-di-*tert*-butylphenyl)pyrimidin-5-yl)ethyne **(2a)**

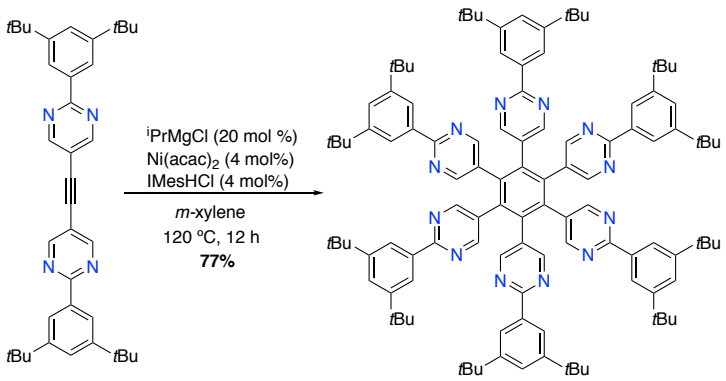

1,2,3,4,5,6-hexakis(2-(3,5-di-*tert*-butylphenyl)pyrimidin-5-yl)benzene (3a). Adapted from a previously-reported procedure:[28] An oven-dried Schlenk tube fitted with a screw-in Teflon stopper was charged with 1,2-bis(2-(3,5-di-*tert*-butylphenyl)pyrimidin-5-yl)ethyne (**2a**) (2.00 g, 4 mmol), IMesHCl (54 mg, 0.16 mmol), and acetylacetonatonickel (II) (41 mg, 0.16 mmol). The flask was then charged with 10 mL of *m*-xylene via syringe. The solution was subject to three cycles of freeze-pump-thaw and left under nitrogen. Isopropylmagnesium chloride (0.5 mL, 1.39 M in THF, 0.7 mmol) was added via syringe, and the solution was warmed to 120 ºC for 16 h. Volatiles were removed under a reduced pressure. The crude solid was purified via column chromatography, and the fractions containing the desired product precipitated a white solid, which was filtered and washed with ethyl acetate and hexanes to yield the desired cyclotrimer **3a** (1.65 g, 77%). ^{1}H NMR (400 MHz, $CDCl_3$) δ = 8.49 (s, 2H, Ar*H*), 8.09 (s, 2H, Ar*H*), 7.47 (s, 1H, Ar*H*), 1.28 (s, 18H, C(CH_3)$_3$). ^{13}C{^{1}H} NMR (101 MHz, $CDCl_3$) δ = 164.15 (aryl-*C*), 157.82 (aryl-*C*), 151.25 (aryl-*C*), 138.07 (aryl-*C*), 135.64 (aryl-*C*), 128.94 (aryl-*C*), 125.91 (aryl-*C*), 122.81 (aryl-*C*), 34.82 (*C*(CH$_3$)$_3$), 31.53 (C(*C*H$_3$)$_3$). Anal. calcd. (%) for $C_{114}H_{138}N_{12}$: C, 81.68; H, 8.30; N, 10.03. Found: C, 80.99; H, 8.14; N, 9.89.

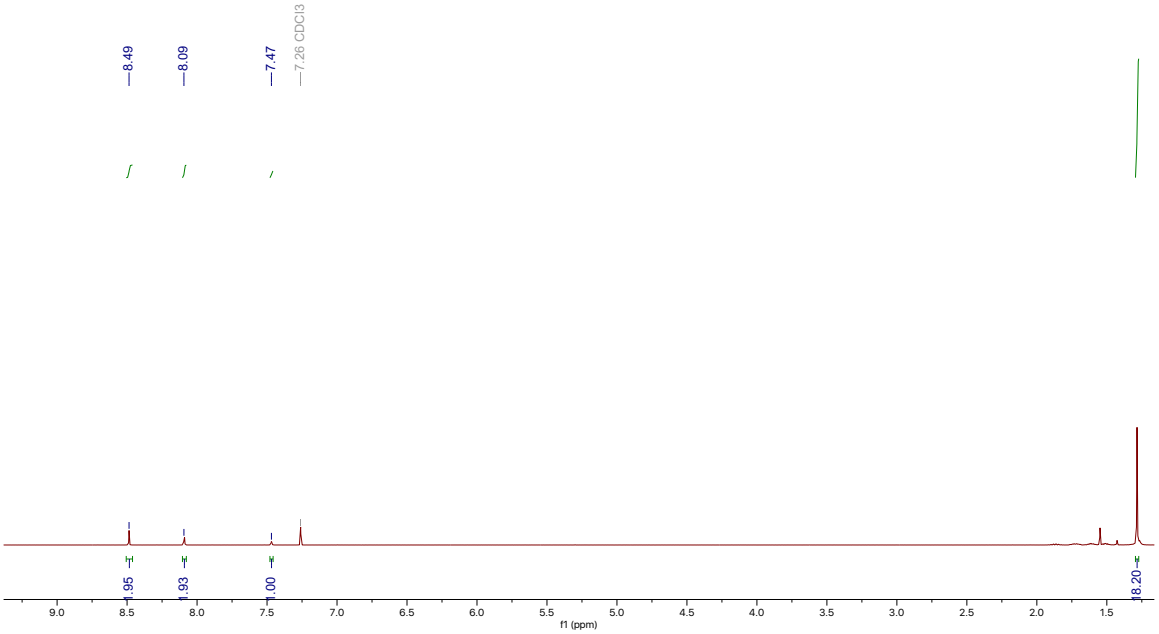

Figure 10. ^{1}H NMR spectrum (400 MHz, $CDCl_3$) of 1,2,3,4,5,6-hexakis(2-(3,5-di-*tert*-butylphenyl)pyrimidin-5-yl)benzene **(3a)**.

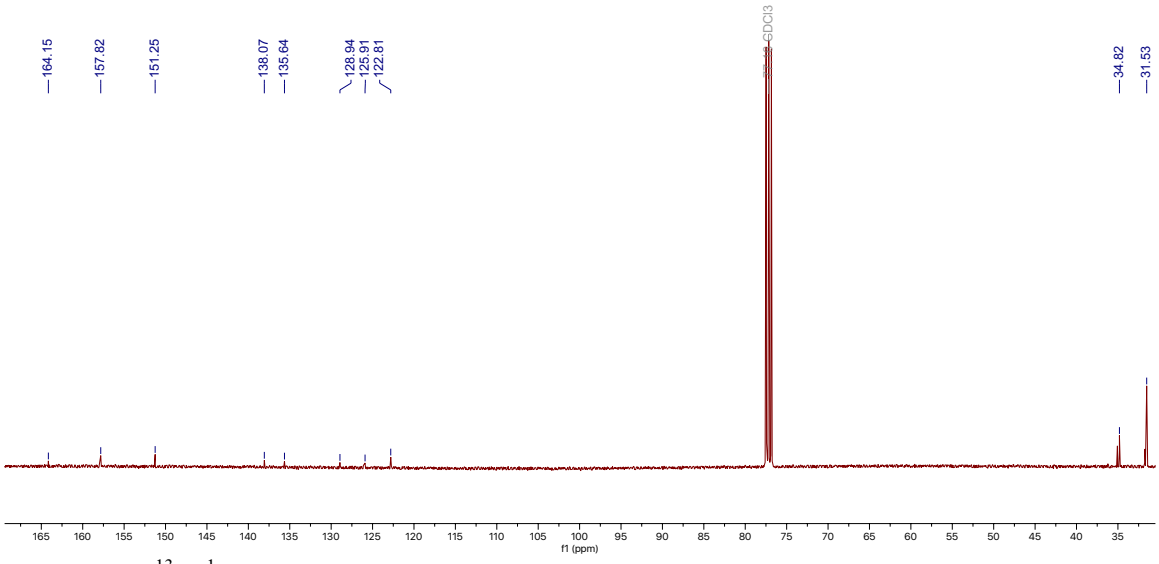

Figure 11. $^{13}C\{^{1}H\}$ NMR spectrum (101 MHz, $CDCl_3$) of 1,2,3,4,5,6-hexakis(2-(3,5-di-*tert*-butylphenyl)pyrimidin-5-yl)benzene **(3a)**.

Monitoring the ring closure of 3a and 3b. In an N_2-purged glovebox, a 1-2 mL aliquot was removed from the reduction of **3** and quenched slowly with isopropanol on the benchtop. This mixture was then charged with a minimal amount of DDQ to oxidize the putative anionic intermediate,[30] resulting in a red-yellow solution. The volatiles were removed on the rotary evaporator, and the crude solid was taken up in $CDCl_3$ and filtered to record the ^1H NMR spectrum.

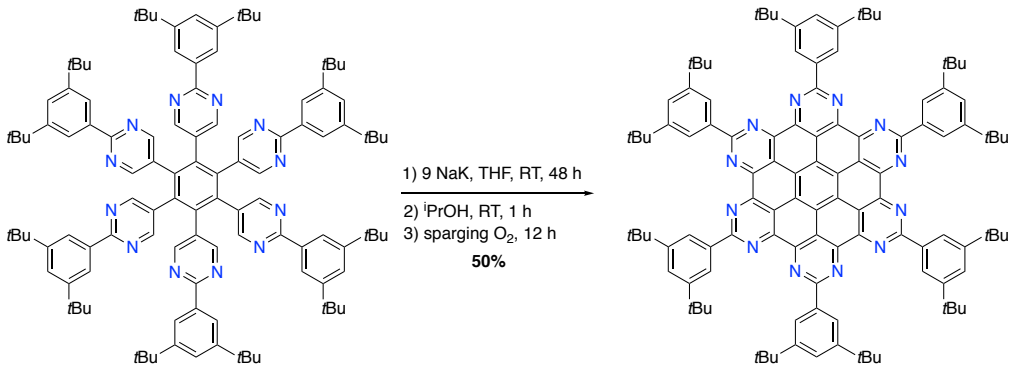

HPC-N$_{12}$(Ar^{tBu})$_6$. In an N_2-purged glovebox, a 20-mL scintillation vial is charged with 1,2,3,4,5,6-hexakis(2-(3,5-di-*tert*-butylphenyl)pyrimidin-5-yl)benzene (200 mg, 0.12 mmol). In a separate vial, sodium (24.7 mg, 1.07 mmol) and potassium (42 mg, 1.07 mmol) are weighed out and carefully mixed with a spatula. The alloy is suspended in THF and charged with a magnetic pre-reduced stir bar. Compound **3a** is suspended in THF and added to the sodium and potassium alloy to immediately form a purple suspension. This mixture is stirred at room temperature for 48 h. The dark brown solution is transferred to a Teflon-sealed Schlenk tube and quenched with isopropanol over 1 h to form a dark yellow mixture. This solution is then sparged with dioxygen for 12 h, concentrated under a reduced pressure, and extracted with chloroform and filtered. The filtrate is allowed to sit at –20 ºC for 7 h to form deep-red crystals. The mother liquor is decanted, and the crystals are rinsed with cold chloroform. **HPC-N$_{12}$(Ar^{tBu})$_6$** is then dried in vacuo at room temperature for 12 h before further use (100 mg, 50%). Single crystals suitable for X-ray diffraction were grown from slow evaporation at room temperature of a saturated chloroform solution. ^{1}H NMR (400 MHz, $CDCl_3$) δ= 9.25 (br s, 2H, Ar*H*), 7.83 (s, 1H, Ar*H*), 1.65 (s, 18H, C(C*H*$_3$)$_3$). ^{13}C{^{1}H} NMR (101 MHz, $CDCl_3$). δ= 153.82 (aryl-*C*), 150.40 (aryl-*C*), 136.74 (aryl-*C*), 124.85 (aryl-*C*), 123.48 (aryl-*C*), 119.67 (aryl-*C*), 116.22 (aryl-*C*), 115.35 (aryl-*C*), 34.27 (*C*(CH$_3$)$_3$), 31.04 (C(*C*H$_3$)$_3$). Anal. calcd. (%) for $C_{114}H_{126}N_{12}$: C, 82.27; H, 7.63; N, 10.10. Found: C, 82.00; H, 7.43; N, 9.90.

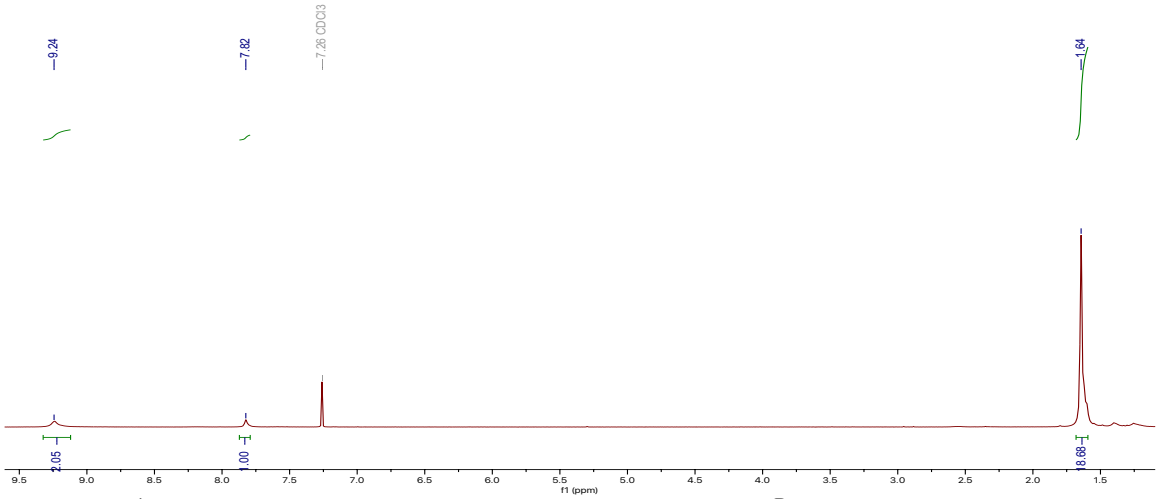

Figure 12. ^{1}H NMR spectrum (400 MHz, $CDCl_3$) of **HPC-N$_{12}$(Ar^{tBu})$_6$.**

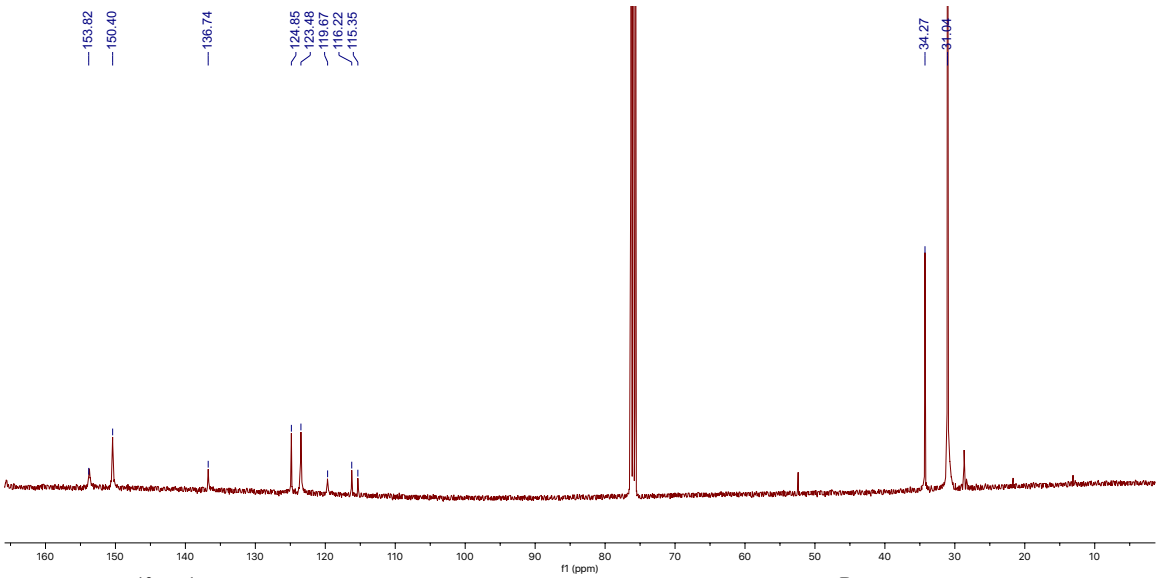

Figure 13. $^{13}C\{^{1}H\}$ NMR spectrum (101 MHz, $CDCl_3$) of **HPC-N$_{12}$(Ar^{tBu})$_6$.**

SUPPLEMENTARY FIGURES/DATA

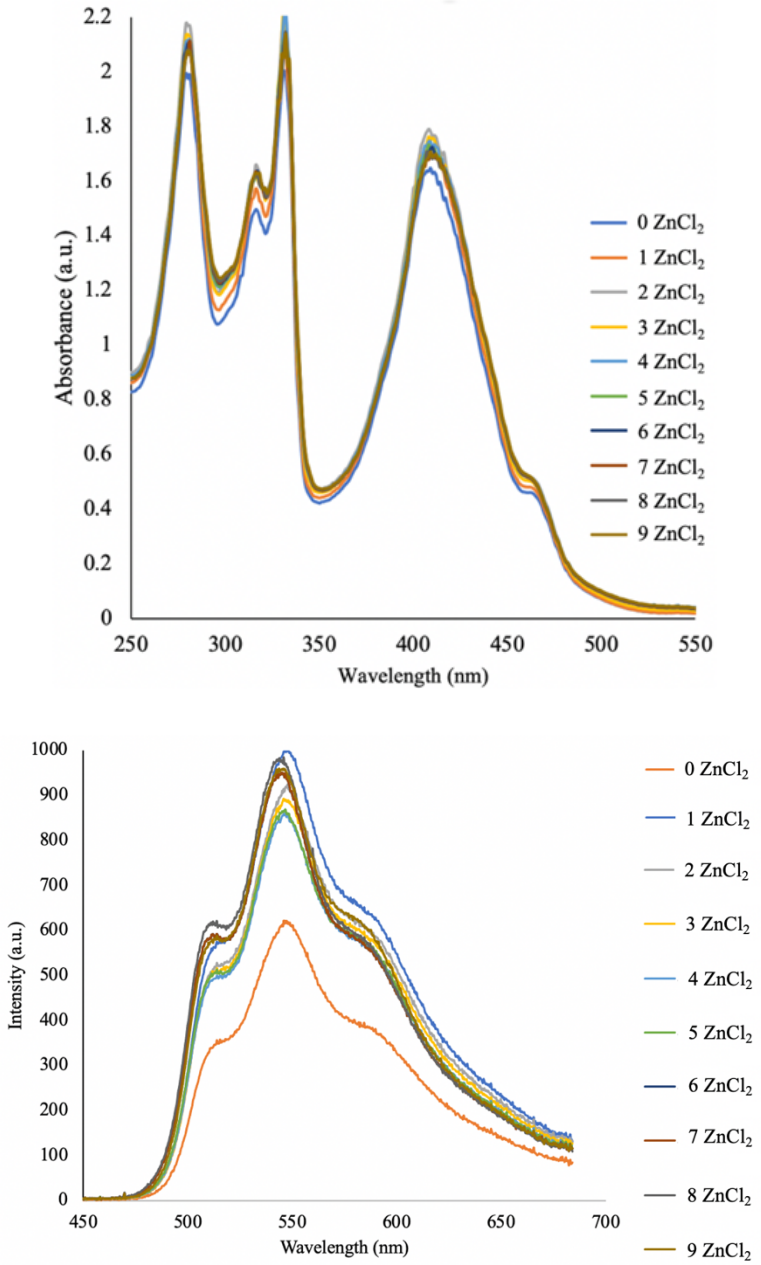

Figure 14. A. Absorption spectra of **HPC-N$_{12}$(Ar^{tBu})$_6$** (0.060 mM in $CHCl_3$). B. Emission spectra (excitation wavelength: 410 nm) of **HPC-N$_{12}$(Ar^{tBu})$_6$** recorded after adding successive equivalents of $ZnCl_2$.

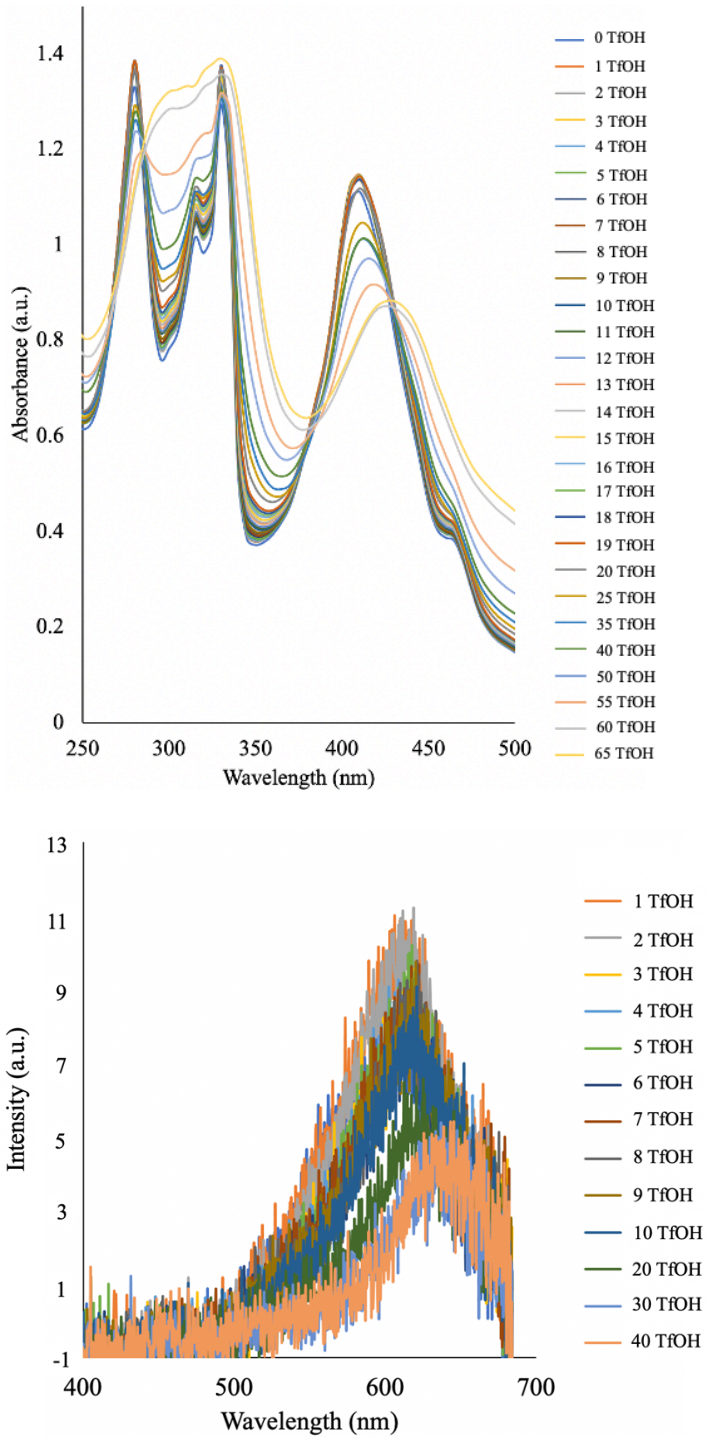

Figure 15. A. Absorption spectra of **HPC-N$_{12}$(Ar^{tBu})$_6$** (0.060 mM in $CHCl_3$). B. Emission spectra (excitation wavelength: 410 nm) of **HPC-N$_{12}$(Ar^{tBu})$_6$** recorded after adding successive equivalents of TfOH (100 mM in $CHCl_3$).

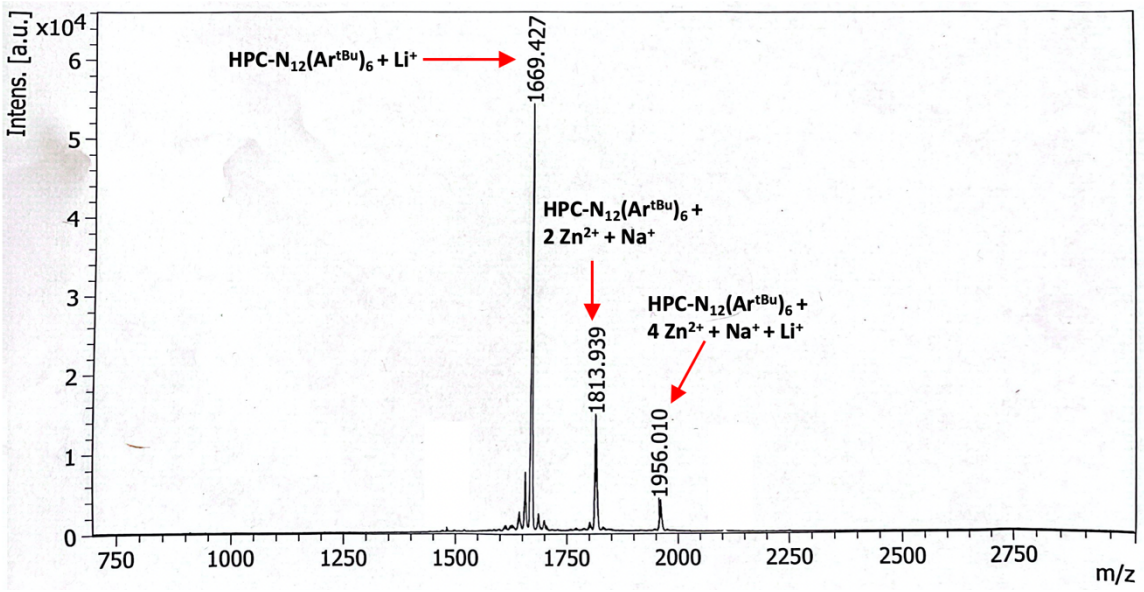

Figure 16. MALDI-TOF of 20 $ZnCl_2$ added to **HPC-N12(Ar^{tBu})6** in $CHCl_3$. Matrix: dithranol.

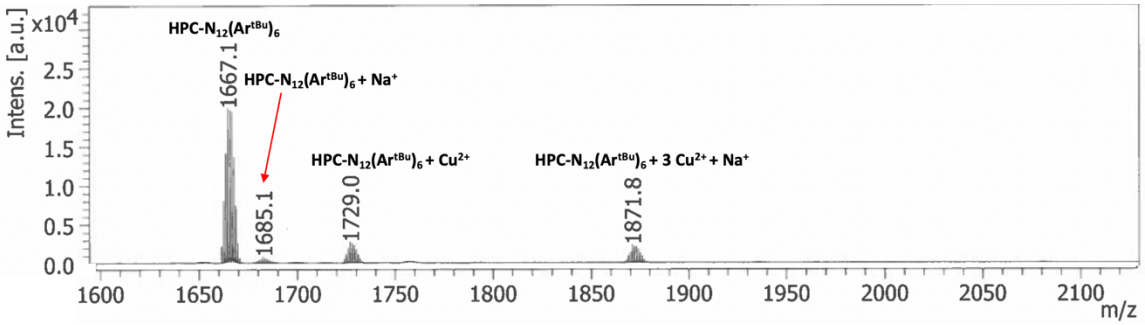

Figure 17. MALDI-TOF of 20 $CuBr_2$ added to **HPC-N12(Ar^{tBu})6** in THF Matrix: dithranol.

Density Functional Theory (DFT) Calculations

All computations were performed using ORCA software[55] version 4.1.2 on the Resnick High-Performance Computing Cluster at Caltech. Geometry optimizations and orbital energies were performed using the restricted Kohn-Sham formalism with the B3LYP functional[48] and the 6-311G(d,p) basis set.[49]

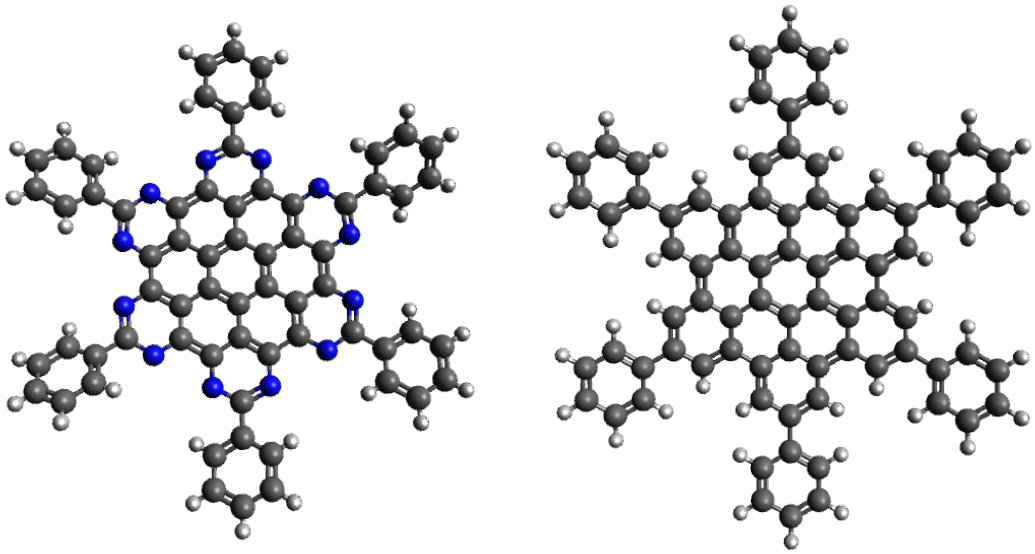

Figure 18. Geometry-optimized structures of **HPC-N_{12}Ph$_6$** (left) and **HBC-Ph$_6$** (right).

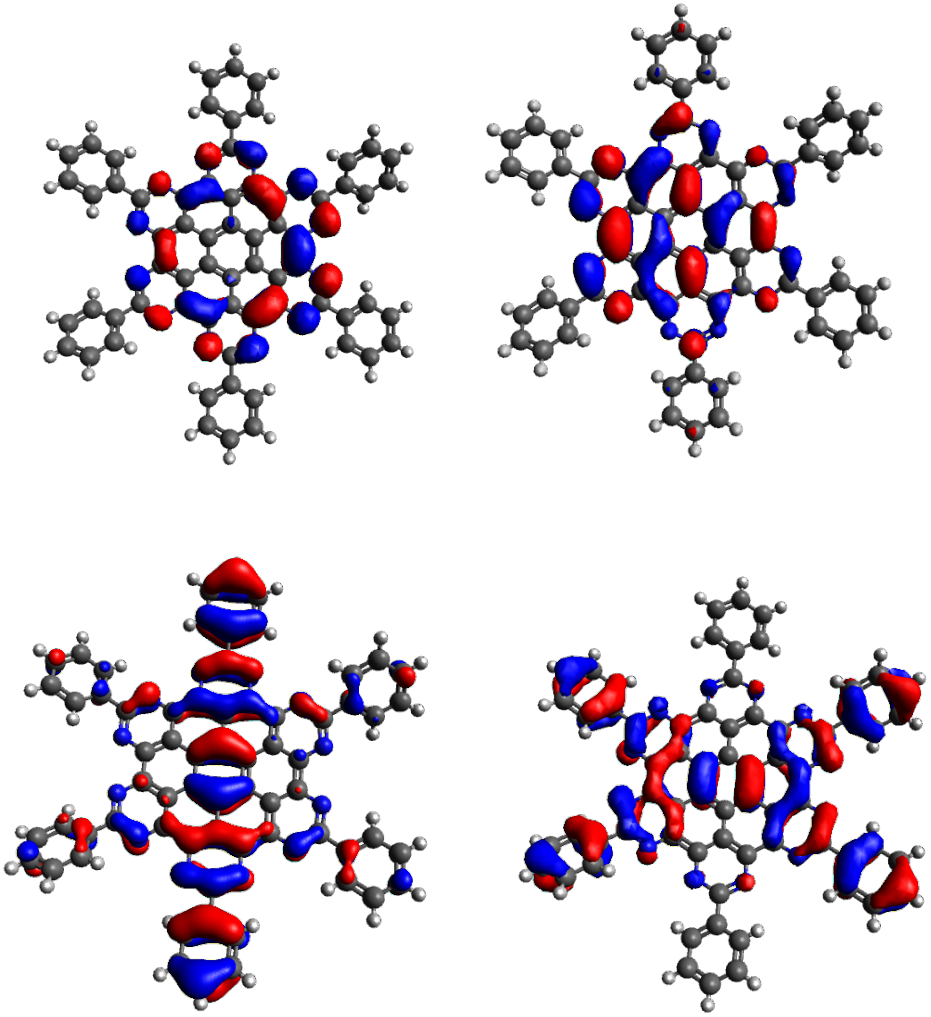

Figure 19. Clockwise from top left: LUMO (–3.250 eV), LUMO+1 (–3.190 eV), HOMO-1 (–6.296 eV), and HOMO (–6.269 eV) of **HPC-N_{12}Ph$_6$**. Isosurfaces are shown at 0.02 value.

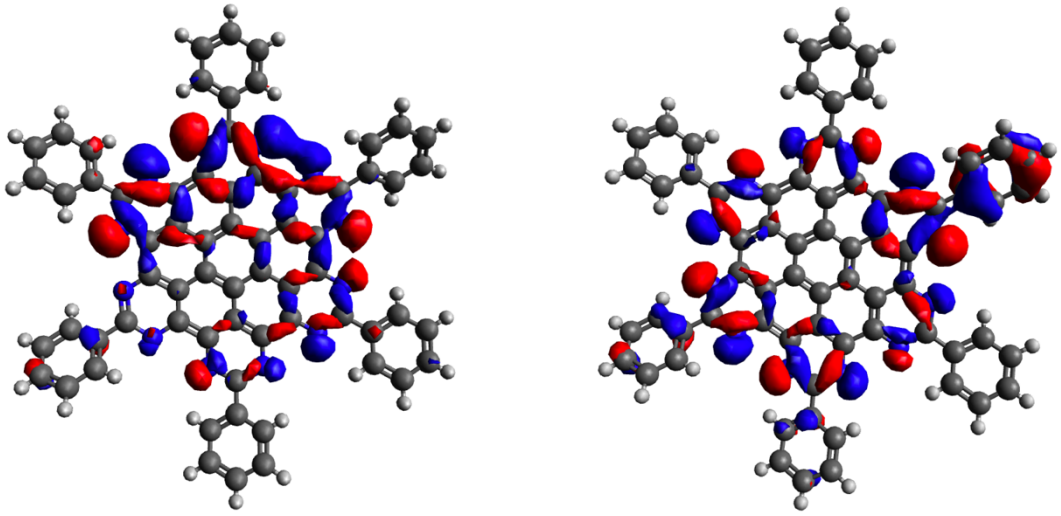

Figure 20. HOMO-6 (left) and HOMO-2 (right) for **HPC-$N_{12}Ph_6$**. Isovalues set to 0.02.

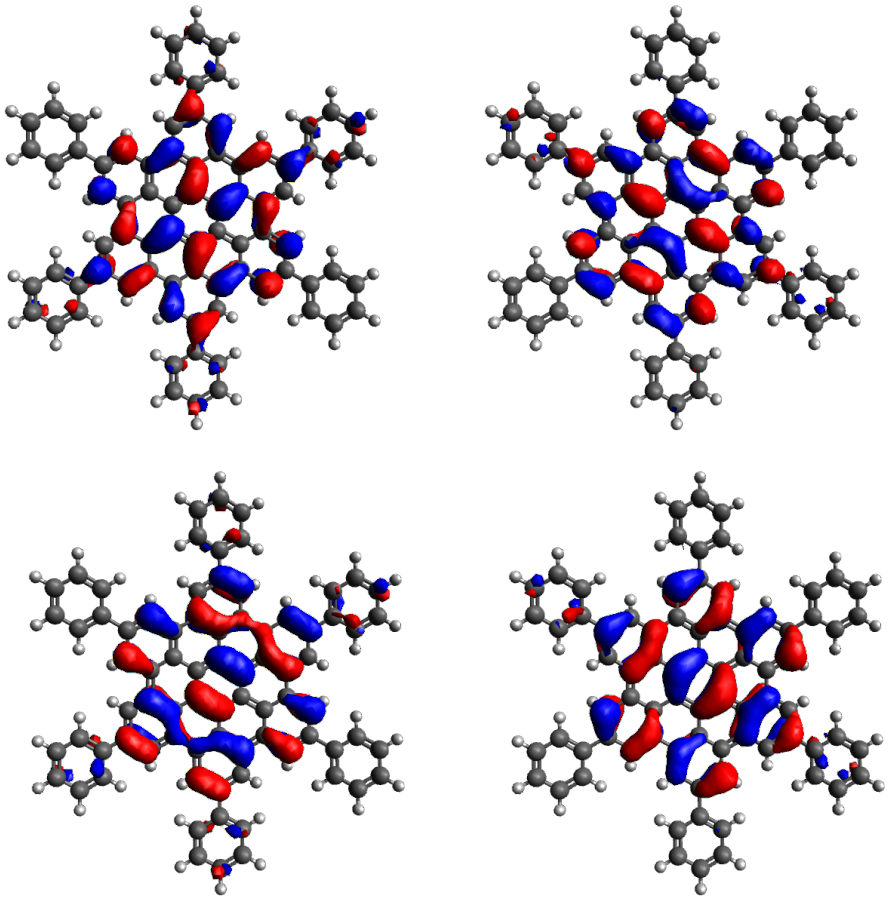

Figure 21. Clockwise from top left: LUMO (–1.983 eV), LUMO+1 (–1.953 eV), HOMO-1 (–5.350 eV), and HOMO (–5.330 eV) of **HBC-Ph$_6$**. Isosurfaces are shown at 0.02 value.

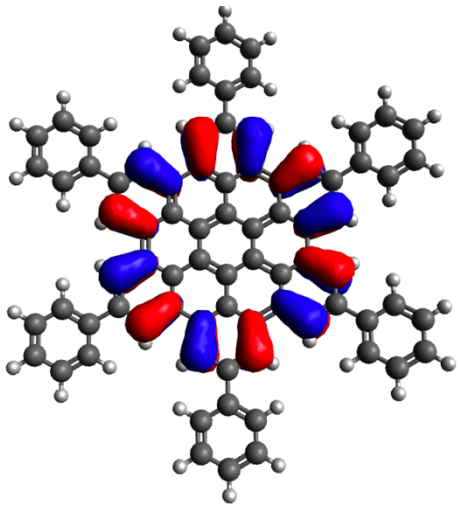

Figure 22. HOMO-2 for **HBC-Ph$_6$**. Isovalue set to 0.02.

Table 2. HOMO-LUMO energy differences (eV) (computed from B3LYP/6-311G(d,p)).

HBC	3.568
HBC-Ph_6	3.347
HPC-N_{12}	3.635
HPC-$N_{12}Ph_6$	3.019

Table 3. Cartesian coordinates obtained for the optimized geometry of **HPC-N_{12}.**

N	10.210694	1.114678	9.574955
N	4.182042	8.128486	13.773238
N	8.907951	3.602846	16.345539
N	10.726567	1.035419	12.359151
N	3.665661	8.207244	10.989105
N	5.484301	5.639819	7.002708
N	4.095899	7.384091	8.750411
N	5.377297	7.188247	15.660537
N	9.015201	2.054679	7.687723
N	7.282290	5.365938	16.696740
N	10.296512	1.858772	14.597805
N	7.110462	3.877184	6.651460
C	9.554088	1.939529	10.408885
C	5.282938	6.454228	10.632569
C	9.823511	1.898285	11.862209
C	9.109130	2.788294	12.715713
C	8.146520	3.710214	12.191837
C	4.568675	7.344359	11.486059
C	6.677092	4.700446	8.876330
C	4.838244	7.303238	12.939371
C	6.938026	4.660570	10.283795
C	7.453865	4.581809	13.064524
C	8.590254	2.867646	9.917997
C	5.801847	6.374925	13.430302
C	6.503278	5.492904	12.546907
C	7.714957	4.542111	14.471962
C	7.888627	3.749469	10.801424
C	6.191116	4.774809	6.253476
C	9.391221	2.725330	14.111279
C	6.039302	6.358789	14.835419
C	8.352990	2.883939	8.512857
C	7.033321	5.407073	15.376327
C	10.904036	1.071718	13.691949
C	3.488260	8.171009	9.656268
C	6.245377	5.532156	11.156467
C	5.725453	5.606683	8.324809
C	8.201579	4.468408	17.094717
C	8.666700	3.635924	15.023524
C	5.000981	6.517318	9.236968
C	4.493438	8.017452	15.077064
C	7.358978	3.835693	7.971888
C	9.899255	1.225653	8.271144

H	8.401195	4.437979	18.171098
H	3.956183	8.691225	15.752899
H	2.751358	8.875174	9.255691
H	5.991070	4.804538	5.177153
H	10.436929	0.552341	7.595187
H	11.640963	0.367628	14.092615

Table 4. Cartesian coordinates obtained for the optimized geometry of **HPC-$N_{12}Ph_6$.**

N	10.27700	1.23800	9.58400
N	4.27400	8.17000	13.74800
N	8.88900	3.59600	16.32200
N	10.74900	1.11200	12.34700
N	3.71900	8.21300	10.97900
N	5.47200	5.61200	7.03500
N	4.13900	7.38400	8.76200
N	5.49400	7.24600	15.61000
N	9.07500	2.16000	7.70900
N	7.24200	5.31800	16.66100
N	10.28800	1.87600	14.57600
C	9.52400	1.96000	10.42500
C	5.26000	6.40900	10.64000
C	9.78300	1.90300	11.87300
C	9.02700	2.72900	12.73200
C	13.04900	-0.16400	13.34700
H	12.98600	0.01900	12.41700
C	8.02800	3.61300	12.20600
C	4.58100	7.32100	11.47900
C	6.61100	4.63800	8.90800
C	4.84700	7.28300	12.93300
C	6.84800	4.57200	10.31100
C	7.34500	4.47500	13.07100
C	8.51800	2.82100	9.93800
C	5.76500	6.31800	13.42900
C	6.41700	5.40000	12.55400
C	2.59900	9.21000	9.07800
C	7.63000	4.45700	14.46900
C	7.78200	3.65800	10.83100
C	8.47900	4.48700	18.54100
C	2.51400	9.39800	7.70700
H	3.03000	8.85200	7.12500
C	9.33700	2.69000	14.09900
C	11.29200	1.31500	6.13900
H	10.91800	2.16200	5.92400
C	6.03100	6.33100	14.81000
C	8.31400	2.87300	8.55100
C	6.98300	5.33900	15.35600
C	5.99600	4.85300	4.79400
C	10.94700	1.12000	13.67200

C	1.85300	10.00800	9.94200
H	1.91400	9.87300	10.88000
C	10.94900	0.69800	7.33600
C	3.53900	8.20500	9.64400
C	6.17500	5.45100	11.17700
C	5.70100	5.55700	8.34600
C	12.09600	-0.05300	15.54800
H	11.39700	0.23100	16.12400
C	12.17100	0.71300	5.25600
C	8.18500	4.45400	17.08700
C	8.60500	3.59100	15.02000
C	12.04400	0.26500	14.20000
C	14.15800	-0.86300	13.84200
C	4.99800	6.48900	9.26100
C	4.64900	8.13500	15.04300
C	7.28500	3.78400	8.00300
C	3.35900	11.34700	17.48300
H	3.08400	12.07900	18.02300
C	4.15700	9.23300	15.92000
C	1.67500	10.38500	7.16800
C	5.45600	6.01500	4.23900
H	5.10500	6.68800	4.81100
C	10.03600	1.39600	8.27100
C	2.87500	9.75800	15.76400
H	2.29100	9.39300	15.11000
C	12.29400	-1.23200	6.75400
C	11.46900	-0.55500	7.65500
H	11.26100	-0.95200	8.49200
C	9.04800	4.64600	21.23900
H	9.23900	4.69200	22.16800
C	8.01100	5.42800	20.72000
C	12.63500	-0.57600	5.58900
H	13.21400	-1.01600	4.97900
C	6.47500	3.84400	3.96400
H	6.82600	3.04800	4.34500
C	2.44700	10.81500	16.56500
C	1.01900	11.00000	9.43900
C	13.16900	-0.78900	16.07000
C	14.17500	-1.15400	15.19300
H	14.92000	-1.63200	15.53900
C	4.65000	10.85300	17.64100
C	5.42300	6.20100	2.86100
C	5.03000	9.77100	16.86500
H	5.89400	9.39200	16.97700
C	9.51100	3.72100	19.08300
H	10.01200	3.14000	18.52200
C	7.74300	5.32700	19.36600
H	7.03900	5.84400	18.99300
C	6.44400	3.99200	2.57900
C	0.94100	11.15400	8.05800

H	0.35700	11.81700	7.70900
C	9.81100	3.80200	20.43400
C	5.91600	5.17300	2.06100
H	5.89000	5.28200	1.11700
C	6.16300	4.74600	6.25800
H	1.60700	10.53300	6.14900
H	0.47300	11.60500	10.07200
H	14.93200	-1.14900	13.22200
H	13.20700	-1.04800	17.06800
H	10.58400	3.24800	20.83600
H	7.46400	6.05900	21.32600
H	5.30400	11.28000	18.31600
H	1.49000	11.19200	16.48400
H	5.04700	7.06800	2.44700
H	6.80100	3.25000	1.95600
H	12.47400	1.18700	4.39100
H	12.63500	-2.18600	6.95200
N	7.05400	3.82700	6.70200

Table 5. Cartesian coordinates obtained for the optimized geometry of **HBC-Ph$_6$.**

C	4.25600	0.22000	6.32600
H	4.08400	0.62700	5.48500
C	5.05200	0.89000	7.26000
C	5.33700	0.25500	8.46800
H	5.88400	0.70100	9.10300
C	5.94100	-1.02000	11.02600
H	6.32200	-0.17400	10.82300
C	6.19300	-1.57700	12.26500
C	5.64000	-2.82000	12.53300
H	5.77700	-3.20600	13.39100
C	4.67100	-5.53100	13.07300
H	5.12300	-5.05000	13.75600
C	4.30200	-6.85100	13.31100
C	3.61300	-7.51900	12.30500
H	3.40400	-8.43900	12.42400
C	1.68000	-8.74000	10.52700
H	1.92100	-9.16800	11.34000
C	0.72200	-9.33100	9.71100
C	0.43800	-8.72300	8.48800
H	-0.15700	-9.15400	7.88500
C	-0.40500	-7.30700	6.05100
H	-0.75600	-8.17300	6.23200
C	-0.90000	-6.60800	4.96100
C	-0.29900	-5.38300	4.65900
H	-0.59800	-4.90000	3.89700
C	0.98000	-2.89000	3.92400
H	0.38700	-3.31500	3.31600
C	1.46300	-1.61800	3.61000
C	2.37800	-1.04100	4.48300

H	2.73700	-0.18700	4.27700
C	2.79200	-1.68300	5.65900
C	3.70900	-1.03800	6.60700
C	4.00900	-1.67700	7.83600
C	4.84300	-1.01000	8.77800
C	5.14800	-1.64700	10.06100
C	4.61500	-2.92900	10.33900
C	4.88500	-3.53000	11.59000
C	4.40300	-4.88500	11.86200
C	3.65400	-5.56100	10.87300
C	3.21800	-6.87900	11.12300
C	2.29800	-7.53100	10.18500
C	1.92900	-6.86800	9.00000
C	1.00200	-7.49600	8.11900
C	0.58500	-6.79600	6.89800
C	1.15100	-5.52800	6.59800
C	0.73000	-4.84700	5.44300
C	1.33500	-3.55900	5.09500
C	2.25200	-2.95300	5.98800
C	2.61400	-3.61800	7.21400
C	3.47000	-2.97900	8.13900
C	3.79400	-3.61100	9.36500
C	3.29400	-4.90300	9.63800
C	2.45400	-5.55600	8.70700
C	2.09000	-4.90000	7.50600
C	-2.06500	-7.15900	4.11700
C	-2.54000	-6.43100	3.02600
C	-2.64400	-8.38500	4.44300
C	-3.59500	-6.93000	2.26200
H	-2.08400	-5.46400	2.76900
C	-3.69800	-8.88400	3.67800
H	-2.26900	-8.95900	5.30400
C	-4.17400	-8.15700	2.58800
H	-3.97000	-6.35700	1.40100
H	-4.15400	-9.85100	3.93500
H	-5.00500	-8.55000	1.98500
C	-0.00400	-10.61800	10.14400
C	-0.96200	-11.19400	9.30900
C	0.29600	-11.21000	11.37100
C	-1.62000	-12.35900	9.70100
H	-1.19800	-10.72700	8.34100
C	-0.36100	-12.37600	11.76300
H	1.05100	-10.75600	12.03000
C	-1.31900	-12.95100	10.92800
H	-2.37400	-12.81300	9.04200
H	-0.12400	-12.84200	12.73000
H	-1.83700	-13.87000	11.23700
C	4.64400	-7.54700	14.64100
C	4.26200	-8.87300	14.85300
C	5.33700	-6.85400	15.63400

C	4.57200	-9.50400	16.05800
H	3.71600	-9.41900	14.07000
C	5.64800	-7.48600	16.83800
H	5.63900	-5.81000	15.46700
C	5.26500	-8.81000	17.05000
H	4.27100	-10.54800	16.22500
H	6.19400	-6.93900	17.62100
H	5.51000	-9.30800	18.00000
C	7.05600	-0.84500	13.30900
C	7.29400	-1.43200	14.55300
C	7.60000	0.40500	13.01300
C	8.07500	-0.76900	15.49900
H	6.86500	-2.41700	14.78700
C	8.38300	1.06700	13.95900
H	7.41300	0.86800	12.03300
C	8.62000	0.48100	15.20200
H	8.26300	-1.23100	16.47900
H	8.81200	2.05200	13.72500
H	9.23600	1.00300	15.94800
C	5.60100	2.29700	6.96100
C	6.39400	2.95100	7.90500
C	5.30700	2.91800	5.74700
C	6.89200	4.22600	7.63500
H	6.62600	2.46200	8.86200
C	5.80600	4.19300	5.47700
H	4.68200	2.40300	5.00300
C	6.59800	4.84700	6.42000
H	7.51700	4.74100	8.37800
H	5.57400	4.68200	4.52000
H	6.99100	5.85100	6.20700
C	0.99800	-0.88000	2.34100
C	1.49700	0.39100	2.05100
C	0.07900	-1.48200	1.48100
C	1.07600	1.05900	0.90100
H	2.22100	0.86500	2.72900
C	-0.34100	-0.81300	0.33000
H	-0.31400	-2.48300	1.70900
C	0.15700	0.45700	0.04100
H	1.46900	2.06000	0.67200
H	-1.06500	-1.28800	-0.34800
H	-0.17400	0.98400	-0.86600

Crystallographic Information

CCDC deposition number 2335088 contains the supplementary crystallographic data for this paper.[56] These data can be obtained free of charge from The Cambridge Crystallographic Data Centre via www.ccdc.cam.ac.uk/data_request/cif.

Refinement Details In each case, crystals were mounted on a glass fiber or MiTeGen loop using Paratone oil, then placed on the diffractometer under a constant nitrogen stream. Low temperature (175 K) X-ray data were obtained on a Bruker D8 VENTURE Kappa Duo PHOTON 100 CMOS based diffractometer (Mo IμS HB micro-focus sealed X-ray tube, Kα = 0.71073 Å or Cu IμS HB micro-focused X-ray tube, Kα = 1.54178). All diffractometer manipulations, including data collection, integration, and scaling were carried out using the Bruker APEXII software.[57] Absorption corrections were applied using SADABS.[58] Space groups were determined on the basis of systematic absences and intensity statistics and the structures were solved in the Olex 2 software interface[59] by intrinsic phasing using XT (incorporated into SHELXTL)[60] and refined by full-matrix least squares on F2. All non-hydrogen atoms were refined using anisotropic displacement parameters, except in some cases with heavily distorted solvent. Hydrogen atoms were placed in the idealized positions and refined using a riding model. The structure was refined (weighed least squares refinement on F2) to convergence. Graphical representation of structures with 50% probability thermal ellipsoids was generated using Diamond 3 visualization software.[61]

Table 6. Crystal data and structure refinement for **HPC-N_{12}(Ar^{tBu})$_6$.**

CCDC Number[6]	2335088
Empirical formula	$C_{116.94}H_{128.94}Cl_{8.84}N_{12}$
Formula weight	2015.80
Temperature/K	175.0
Crystal system	Triclinic
Space group	P-1
a/Å	14.3540(6)
b/Å	18.2341(6)
c/Å	23.2636(10)
α/°	110.586(3)
β/°	101.322(3)
γ/°	93.081(3)
Volume/Å^3	5538.9(4)
Z	2
ρ_{calc} g/cm^3	1.209
μ/mm^{-1}	2.448
Abs. Correction	Semi-empirical
Crystal size/mm^3	$0.2 \times 0.2 \times 0.1$
Radiation	CuKα (λ = 1.54178)
2Θ range/°	5.344 to 133.268
GOF	1.050
Diffractometer	PHOTON
R_1[a], wR_2[b] [I>2σ(I)]	0.0747, 0.2025

[a]$R_1 = \Sigma||F_0| - |F_c||/\Sigma|F_0|$. [b]w$R_2 = [\Sigma[w(F_0^2 - F_c^2)^2]/\Sigma[w(F_0^2)^2]]^{1/2}$

Table 7. Comparison of select bond lengths between **2,9-bis(2,6-dimethoxyphenyl)-1,10-phenanthroline** (left) and **HPC-N_{12}(Ar^{tBu})$_6$** (right, truncated structure).

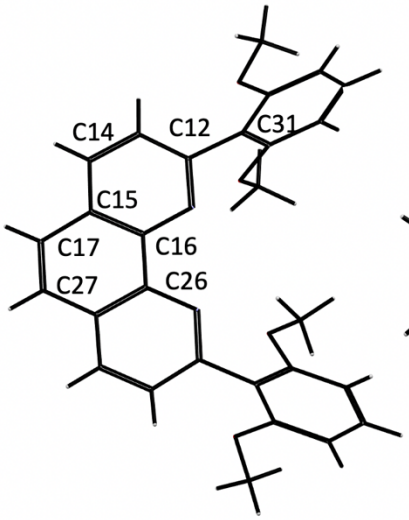

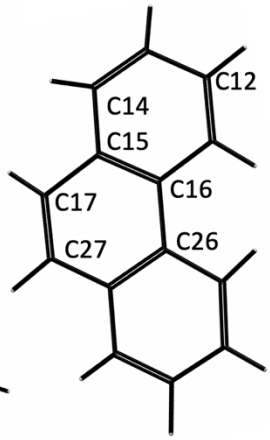

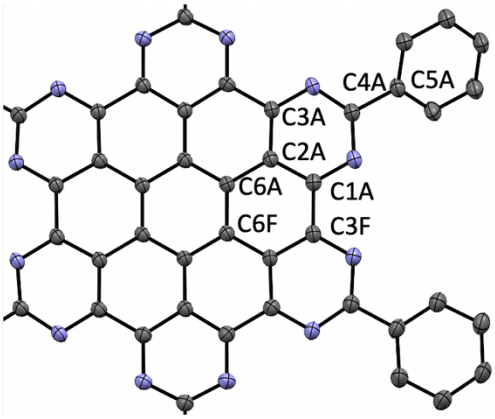

2,9-bis(2,6-dimethoxyphenyl)-1,10-phenanthroline bond lengths (Å)[19]	**Decamethylphenanthrene** bond lengths (Å)[20]	**HPC-N_{12}(Ar^{tBu})$_6$** bond lengths (Å)
C16-C26: 1.457	C16'-C26' 1.453	C3F-C1A: 1.480(2)
C12-C31: 1.508	*N/A*	C4A-C5A: 1.486(2)
C15-C14: 1.415	C15'-C14': 1.420	C3A-C2A: 1.412(4)
C17-C27: 1.356	C17'-C27': 1.332	C6A-C6F: 1.408(4)
C17-C15: 1.461	C17'-C15': 1.446	C6A-C2A: 1.427(3)
C15-C16: 1.425	C15'-C16': 1.393	C2A-C1A: 1.406(3)

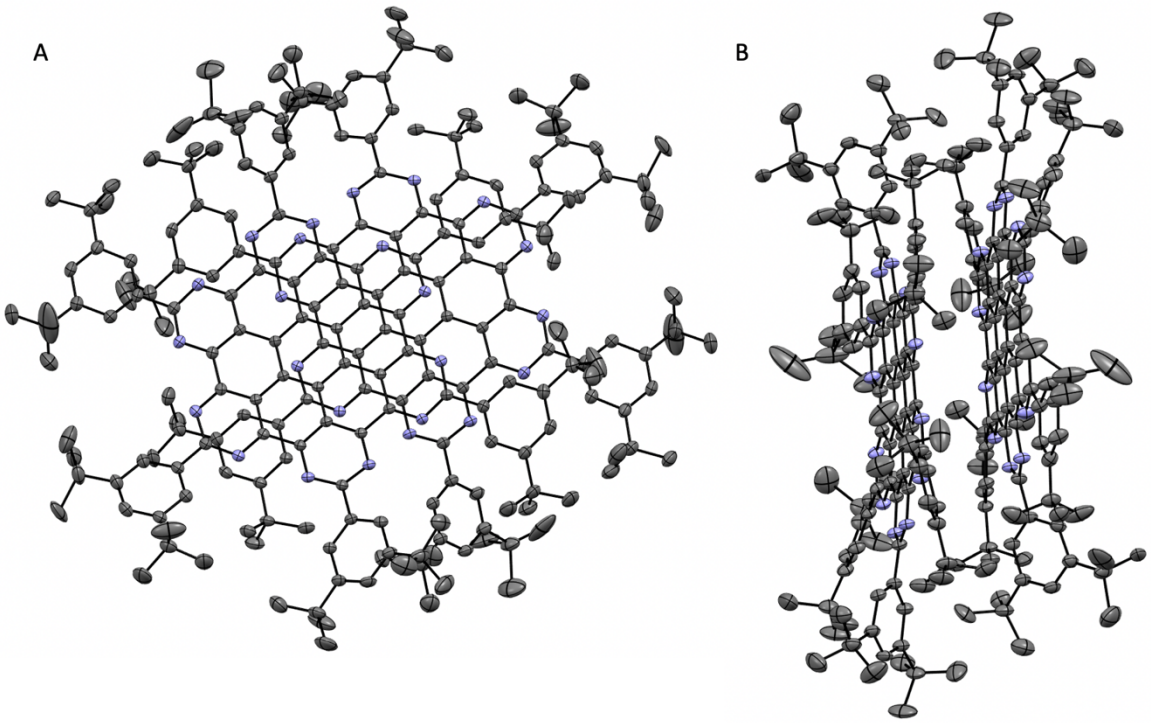

Figure 23. A. Top-down view of **HPC-N_{12}(Ar^{tBu})$_6$** unit cell and B. side-on view, each highlighting optimal π stacking requires each unit to be offset.

REFERENCES

(1) Narita, A.; Verzhbitskiy, I. A.; Frederickx, W.; Mali, K. S.; Jensen, S. A.; Hansen, M. R.; Bonn, M.; De Feyter, S.; Casiraghi, C.; Feng, X.; et al. Bottom-Up Synthesis of Liquid-Phase-Processable Graphene Nanoribbons with Near-Infrared Absorption. *ACS Nano* **2014**, *8* (11), 11622–11630.

(2) Wu, J.; Pisula, W.; Müllen, K. Graphenes as Potential Material for Electronics. *Chem. Rev.* **2007**, *107* (3), 718–747.

(3) Narita, A.; Wang, X.-Y.; Feng, X.; Müllen, K. New Advances in Nanographene Chemistry. *Chem. Soc. Rev.* **2015**, *44* (18), 6616–6643.

(4) Liu, Y.-M.; Hou, H.; Zhou, Y.-Z.; Zhao, X.-J.; Tang, C.; Tan, Y.-Z.; Müllen, K. Nanographenes as Electron-Deficient Cores of Donor-Acceptor Systems. *Nat. Commun.* **2018**, *9* (1), 1901.

(5) Fantuzzi, P.; Candini, A.; Chen, Q.; Yao, X.; Dumslaff, T.; Mishra, N.; Coletti, C.; Müllen, K.; Narita, A.; Affronte, M. Color Sensitive Response of Graphene/Graphene Quantum Dot Phototransistors. *J. Phys. Chem. C* **2019**, *123* (43), 26490–26497.

(6) Jin, E.; Yang, Q.; Ju, C.-W.; Chen, Q.; Landfester, K.; Bonn, M.; Müllen, K.; Liu, X.; Narita, A. A Highly Luminescent Nitrogen-Doped Nanographene as an Acid- and Metal-Sensitive Fluorophore for Optical Imaging. *J. Am. Chem. Soc.* **2021**, *143* (27), 10403–10412.

(7) Luo, H.; Liu, J. Facile Synthesis of Nitrogen-Doped Nanographenes with Joined Nonhexagons via a Ring Expansion Strategy. *Angew. Chemie Int. Ed.* **2023**, *62* (21), e202302761.

(8) Watson, M. D.; Fechtenkötter, A.; Müllen, K. Big Is Beautiful−"Aromaticity" Revisited from the Viewpoint of Macromolecular and Supramolecular Benzene Chemistry. *Chem. Rev.* **2001**, *101* (5), 1267–1300.

(9) Clar, E.; Ironside, C. T.; Zander, M. 28. The Electronic Interaction between Benzenoid Rings in Condensed Aromatic Hydrocarbons. 1 : 12-2 : 3-4 : 5-6 : 7-8 : 9-10 : 11-Hexabenzocoronene, 1 : 2-3 : 4-5 : 6-10 : 11-Tetrabenzoanthanthrene, and 4 : 5-6 : 7-11 : 12-13 : 14-Tetrabenzoperopyrene. *J. Chem. Soc.* **1959**, No. 0, 142–147.

(10) Hertz, V. M.; Massoth, J. G.; Bolte, M.; Lerner, H.-W.; Wagner, M. En Route to Stimuli-Responsive Boron-, Nitrogen-, and Sulfur-Doped Polycyclic Aromatic Hydrocarbons. *Chem. – A Eur. J.* **2016**, *22* (37), 13181–13188.

(11) Hertz, V. M.; Bolte, M.; Lerner, H.-W.; Wagner, M. Boron-Containing Polycyclic Aromatic Hydrocarbons: Facile Synthesis of Stable, Redox-Active Luminophores. *Angew. Chemie Int. Ed.* **2015**, *54* (30), 8800–8804.

(12) Yamaguchi, R.; Ito, S.; Lee, B. S.; Hiroto, S.; Kim, D.; Shinokubo, H. Functionalization of Hexa-Peri-Hexabenzocoronenes: Investigation of the Substituent Effects on a Superbenzene. *Chem. – An Asian J.* **2013**, *8* (1), 178–190.

(13) Yamaguchi, R.; Hiroto, S.; Shinokubo, H. Synthesis of Oxygen-Substituted Hexa-Peri-Hexabenzocoronenes through Ir-Catalyzed Direct Borylation. *Org. Lett.* **2012**, *14* (10), 2472–2475.

(14) Qiao, X.; Li, Q.; Schaugaard, R. N.; Noffke, B. W.; Liu, Y.; Li, D.; Liu, L.; Raghavachari, K.; Li, L. Well-Defined Nanographene–Rhenium Complex as an Efficient Electrocatalyst and Photocatalyst for Selective CO2 Reduction. *J. Am. Chem. Soc.* **2017**, *139* (11), 3934–3937.

(15) Draper, S. M.; Gregg, D. J.; Madathil, R. Heterosuperbenzenes: A New Family of Nitrogen-Functionalized, Graphitic Molecules. *J. Am. Chem. Soc.* **2002**, *124* (14), 3486–3487.

(16) Draper, S. M.; Gregg, D. J.; Schofield, E. R.; Browne, W. R.; Duati, M.; Vos, J. G.; Passaniti, P. Complexed Nitrogen Heterosuperbenzene: The Coordinating Properties of a Remarkable Ligand. *J. Am. Chem. Soc.* **2004**, *126* (28), 8694–8701.

(17) Krzeszewski, M.; Dobrzycki, Ł.; Sobolewski, A. L.; Cyrański, M. K.; Gryko, D. T. Bowl-Shaped Pentagon- and Heptagon-Embedded Nanographene Containing a Central Pyrrolo[3,2-b]Pyrrole Core. *Angew. Chemie Int. Ed.* **2021**, *60* (27), 14998–15005.

(18) Bunz, U. H. F. The Larger Linear N-Heteroacenes. *Acc. Chem. Res.* **2015**, *48* (6), 1676–1686.

(19) Cortizo-Lacalle, D.; Gozalvez, C.; Olano, M.; Sun, X.; Melle-Franco, M.; Hueso, L. E.; Mateo-Alonso, A. Bisthiadiazole-Fused Tetraazapentacenequinone: An Air-Stable Solution-Processable n-Type Organic Semiconductor. *Org. Lett.* **2015**, *17* (23), 5902–5905.

(20) Schneider, J. A.; Perepichka, D. F. A New Approach to Polycyclic Azaarenes: Visible-Light Photolysis of Vinyl Azides in the Synthesis of Diazabenzopyrene and Diazaperylene. *J. Mater. Chem. C* **2016**, *4* (30), 7269–7276.

(21) Nakazato, T.; Kamatsuka, T.; Inoue, J.; Sakurai, T.; Seki, S.; Shinokubo, H.; Miyake, Y. The Reductive Aromatization of Naphthalene Diimide: A Versatile Platform for 2,7-Diazapyrenes. *Chem. Commun.* **2018**, *54* (41), 5177–5180.

(22) Wei, J.; Han, B.; Guo, Q.; Shi, X.; Wang, W.; Wei, N. 1,5,9-Triazacoronenes: A Family of Polycyclic Heteroarenes Synthesized by a Threefold Pictet–Spengler Reaction. *Angew. Chemie Int. Ed.* **2010**, *49* (44), 8209–8213.

(23) Würthner, F.; Sautter, A.; Thalacker, C. Substituted Diazadibenzoperylenes: New Functional Building Blocks for Supramolecular Chemistry. *Angew. Chemie Int. Ed.* **2000**, *39* (7), 1243–1245.

(24) Gryko, D. T.; Piechowska, J.; Gałęzowski, M. Strongly Emitting Fluorophores Based on 1-Azaperylene Scaffold. *J. Org. Chem.* **2010**, *75* (4), 1297–1300.

(25) Grzybowski, M.; Skonieczny, K.; Butenschön, H.; Gryko, D. T. Comparison of Oxidative Aromatic Coupling and the Scholl Reaction. *Angew. Chemie Int. Ed.* **2013**, *52* (38), 9900–9930.

(26) Low, C. H.; Rosenberg, J. N.; Lopez, M. A.; Agapie, T. Oxidative Coupling with Zr(IV) Supported by a Noninnocent Anthracene-Based Ligand: Application to the Catalytic Cotrimerization of Alkynes and Nitriles to Pyrimidines. *J. Am. Chem. Soc.* **2018**, *140* (38), 11906–11910.

(27) Qiu, S.; Zhang, C.; Qiu, R.; Yin, G.; Huang, J. One-Pot Domino Synthesis of Diarylalkynes/1,4-Diaryl-1,3-Diynes by [9,9-Dimethyl-4,5-Bis(Diphenylphosphino)Xanthene] (Xantphos)–Copper(I) Iodide–Palladium(II) Acetate-Catalyzed Double Sonogashira-Type Reaction. *Adv. Synth. Catal.* **2018**, *360* (2), 313–321.

(28) Stolley, R. M.; Maczka, M. T.; Louie, J. Nickel-Catalyzed [2+2+2] Cycloaddition of Diynes and Cyanamides. *European J. Org. Chem.* **2011**, *2011* (20-21), 3815–3824.

(29) Dou, X.; Yang, X.; Bodwell, G. J.; Wagner, M.; Enkelmann, V.; Müllen, K. Unexpected Phenyl Group Rearrangement during an Intramolecular Scholl Reaction Leading to an Alkoxy-Substituted Hexa-Peri-Hexabenzocoronene. *Org. Lett.* **2007**, *9* (13), 2485–2488.

(30) Rickhaus, M.; Belanger, A. P.; Wegner, H. A.; Scott, L. T. An Oxidation Induced by Potassium Metal. Studies on the Anionic Cyclodehydrogenation of 1,1′-Binaphthyl to Perylene. *J. Org. Chem.* **2010**, *75* (21), 7358–7364.

(31) Janiak, C. A Critical Account on π–π Stacking in Metal Complexes with Aromatic Nitrogen-Containing Ligands. *J. Chem. Soc. Dalt. Trans.* **2000**, No. 21, 3885–3896.

(32) Bolte, M. CCDC 2001096. *CSD Commun.* **2020**.

(33) Herwig, P. T.; Enkelmann, V.; Schmelz, O.; Müllen, K. Synthesis and Structural Characterization of Hexa-Tert-Butyl- Hexa-Peri-Hexabenzocoronene, Its Radical Cation Salt and Its Tricarbonylchromium Complex. *Chem. – A Eur. J.* **2000**, *6* (10), 1834–1839.

(34) Pavlishchuk, V. V; Addison, A. W. Conversion Constants for Redox Potentials Measured versus Different Reference Electrodes in Acetonitrile Solutions at 25°C. *Inorganica Chim. Acta* **2000**, *298* (1), 97–102.

(35) In CH_2Cl_2, the reduction was reported at –1.7 V vs $Fc^{0/+}$.

(36) Haines, P.; Reger, D.; Träg, J.; Strauss, V.; Lungerich, D.; Zahn, D.; Jux, N.; Guldi, D. M. On the Photophysics of Nanographenes – Investigation of Functionalized Hexa-Peri-Hexabenzocoronenes as Model Systems. *Nanoscale* **2021**, *13* (2), 801–809.

(37) Pisula, W.; Tomović, Ž.; Watson, M. D.; Müllen, K.; Kussmann, J.; Ochsenfeld, C.; Metzroth, T.; Gauss, J. Helical Packing of Discotic Hexaphenyl Hexa-Peri-Hexabenzocoronenes: Theory and Experiment. *J. Phys. Chem. B* **2007**, *111* (26), 7481–7487.

(38) Hendel, W.; Khan, Z. H.; Schmidt, W. Hexa-Peri-Benzocoronene, a Candidate for the Origin of the Diffuse Interstellar Visible Absorption Bands ? *Tetrahedron* **1986**, *42* (4), 1127–1134.

(39) Wang, F.-F.; Wang, Y.-X.; Wu, Q.; Chai, L.; Chen, X.-W.; Tan, Y.-Z. Nanographene with a Nitrogen-Doped Cavity. *Angew. Chemie Int. Ed.* **2024**, *63* (2), e202315302.

(40) Bai, J.; Xu, X.; Wang, X.-Y.; Sun, X.; Liang, J.; Liang, T.; Gong, H.-Y. Pentatomic Carbon Ring Conjugated Nitrogen-Doped Nanographene. *Mater. Adv.* **2024**, *5* (3), 1028–1032.

(41) Xu, X.; Xia, T.; Chen, X.-L.; Hao, X.; Liang, T.; Li, H.-R.; Gong, H.-Y. Tetrabenzo[b,de,Gh,j][1,10]Phenanthroline: A Nitrogen-Doped Nanographene as a Selective Metal Cation and Proton Fluorophore. *New J. Chem.* **2022**, *46* (24), 11835–11839.

(42) Pham, N. N. T. Nitrogen Doping Effects on the Physical and Chemical Properties of Bilayer Graphdiyne: A Density Functional Theory Approach. *Appl. Surf. Sci. Adv.* **2022**, *11*, 100301.

(43) Zhang, H.; Zhou, P.; Daaoub, A.; Sangtarash, S.; Zhao, S.; Yang, Z.; Zhou, Y.; Zou, Y.-L.; Decurtins, S.; Häner, R.; et al. Atomically Well-Defined Nitrogen Doping for Cross-Plane Transport through Graphene Heterojunctions. *Chem. Sci.* **2023**, *14* (22), 6079–6086.

(44) Nishikaze, T.; Takayama, M. Disappearance of Interfering Alkali-Metal Adducted Peaks from Matrix-Assisted Laser Desorption/Ionization Mass Spectra of Peptides with Serine Addition to α-Cyano-4-Hydroxycinnamic Acid Matrix. *Rapid Commun. Mass Spectrom.* **2007**, *21* (20), 3345–3351.

(45) Contamination from Li^+ and Na^+ is often observed MALDI-TOF samples (ref. 44).

(46) Eom, G. H.; Park, H. M.; Hyun, M. Y.; Jang, S. P.; Kim, C.; Lee, J. H.; Lee, S. J.; Kim, S.-J.; Kim, Y. Anion Effects on the Crystal Structures of ZnII Complexes Containing 2,2′-Bipyridine: Their Photoluminescence and Catalytic Activities. *Polyhedron* **2011**, *30* (9), 1555–1564.

(47) Zhang, J.; Frankevich, V.; Knochenmuss, R.; Friess, S. D.; Zenobi, R. Reduction of Cu(II) in Matrix-Assisted Laser Desorption/Ionization Mass Spectrometry. *J. Am. Soc. Mass Spectrom.* **2003**, *14* (1), 42–50.

(48) Stephens, P. J.; Devlin, F. J.; Chabalowski, C. F.; Frisch, M. J. Ab Initio Calculation of Vibrational Absorption and Circular Dichroism Spectra Using Density Functional Force Fields. *J. Phys. Chem.* **1994**, *98* (45), 11623–11627.

(49) Krishnan, R.; Binkley, J. S.; Seeger, R.; Pople, J. A. Self-consistent Molecular Orbital Methods. XX. A Basis Set for Correlated Wave Functions. *J. Chem. Phys.* **1980**, *72* (1), 650–654.

(50) Rouillé, G.; Steglich, M.; Huisken, F.; Henning, T.; Müllen, K. UV/Visible Spectroscopy of Matrix-Isolated Hexa-Peri-Hexabenzocoronene: Interacting Electronic States and Astrophysical Context. *J. Chem. Phys.* **2009**, *131* (20), 204311.

(51) Hoffend, C.; Diefenbach, M.; Januszewski, E.; Bolte, M.; Lerner, H.-W.; Holthausen, M. C.; Wagner, M. Effects of Boron Doping on the Structural and Optoelectronic Properties of 9,10-Diarylanthracenes. *Dalt. Trans.* **2013**, *42* (38), 13826–13837.

(52) Hu, Y.; Dössel, L. F.; Wang, X.-Y.; Mahesh, S.; Pisula, W.; De Feyter, S.; Feng, X.; Müllen, K.; Narita, A. Synthesis, Photophysical Characterization, and Self-Assembly of Hexa-Peri-Hexabenzocoronene/Benzothiadiazole Donor–Acceptor Structure. *Chempluschem* **2017**, *82* (7), 1030–1033.

(53) Pangborn, A. B.; Giardello, M. A.; Grubbs, R. H.; Rosen, R. K.; Timmers, F. J. Safe and Convenient Procedure for Solvent Purification. *Organometallics* **1996**, *15* (5), 1518–1520.

(54) Huang, J.; Chan, J.; Chen, Y.; Borths, C. J.; Baucom, K. D.; Larsen, R. D.; Faul, M. M. A Highly Efficient Palladium/Copper Cocatalytic System for Direct Arylation of Heteroarenes: An Unexpected Effect of Cu(Xantphos)I. *J. Am. Chem. Soc.* **2010**, *132* (11), 3674–3675.

(55) Neese, F. The ORCA Program System. *WIREs Comput. Mol. Sci.* **2012**, *2* (1), 73–78.

(56) Schäfer, J.; Holzapfel, M.; Mladenova, B.; Kattnig, D.; Krummenacher, I.; Braunschweig, H.; Grampp, G.; Lambert, C. Hole Transfer Processes in Meta- and Para-Conjugated Mixed Valence Compounds: Unforeseen Effects of Bridge Substituents and Solvent Dynamics. *J. Am. Chem. Soc.* **2017**, *139* (17), 6200–6209.

(57) APEX2, Version 2 User Manual, M86-E01078, Bruker Analytical X-Ray Systems, Madison, WI, June 2006.

(58) Sheldrick, G. M. *SADABS (Version 2008/1): Program for Absorption Correction for Data from Area Detector Frames.*; University of Göttingen: 2008, 2008.

(59) Dolomanov, O. V.; Bourhis, L. J.; Gildea, R. J.; Howard, J. A. K.; Puschmann, H. No. *J. Appl. Crystallogr.* **2009**, *42*, 339–341.

(60) Sheldrick, G. M. No Title. *Acta Crystallogr. Sect. A* **2008**, *64*, 112–122.

(61) Brandenburg, K. (1999). Diamond. Crystal Impact GbR, Bonn, Germany.

(62) Ermer, O.; Neudörfl, J. Comparative Supramolecular Chemistry of Coronene and Hexahelicene: Helix Alignment in Crystalline Complexes with Trimesic Acid (=Benzene-1,3,5-Tricarboxylic Acid) and π-Acceptor Compounds. *Helv. Chim. Acta* **2001**, *84* (6), 1268–1313.

APPENDIX A

INVESTIGATING CO_2 REDUCTION ON Cu WITH CASCADE CATALYSIS INVOLVING SUPPORTED MOLECULAR COMPLEXES

ACKNOWLEDGEMENTS

I thank Thomas Chan, Byunghoon Lee, and Prof. Cliff Kubiak for providing the molecular complexes, **CoPc** and **^{tBu}bpyRe(CO)$_3$Cl**, as well as insightful discussions. This material is based on work performed by the Liquid Sunlight Alliance, which is supported by the U.S. Department of Energy, Office of Science, Office of Basic Energy Sciences, Fuels from Sunlight Hub under Award DE-SC0021266. The Resnick Sustainability Institute at Caltech is acknowledged for support of the laboratory facilities in which this research was conducted.

INTRODUCTION

Converting carbon dioxide to value-added chemicals at high activities and efficiencies is of interest towards achieving a net zero carbon economy.[1–3] Achieving highly selective CO_2 reduction on Cu to C_{2+} products is of interest at relatively positive potentials since less energy would be expended; few strategies have been reported.[4–6]

Immobilization of molecular complexes that are highly active for CO_2R to CO (Table 1) onto Cu electrodes has demonstrably elevated selectivity/activity for C_{2+} products.[7–11] Some work has proposed spillover of CO into *CO, whereby enhanced population on Cu facilitates C_{2+} generation.[8] Up to 40% Faradaic efficiency (FE) for C_{2+} products at –0.5 V vs. RHE in 0.1 M $KHCO_{3(aq)}$ was achieved by Sargent and co-workers with immobilized **Cl-FeTPP**.[8]

Table 1. Comparing CO_2R data between supported molecular complexes

Compound/support	Weight percent metal complex (wt%)	E (V vs. RHE)	FE_{CO} (%)	TOF (s^{-1})
^{tBu}bpyRe(CO)$_3$Cl/MWCNT[12]	23.1	–0.56	99	1.6
CoPc/MWCNT[13]	3.5	–0.68	92	4.1
TPPFe-Cl/MWCNT[14]	3.6	–0.63	96	0.94

Previous work with pyridinium films highlighted elevated FE_{C2+} due to HER suppression.[15–17] In addition, molecular dynamics simulations have suggested enhanced CO residence time provided by the film relative to bare Cu.[18] It is envisioned that incorporation of a pyridinium-derived film with a highly active CO_2R to CO molecular at

potentials more positive than –1.1 V vs. RHE[19] (Table 1) would enhance formation of C_{2+} due to CO spillover (Figure 1).

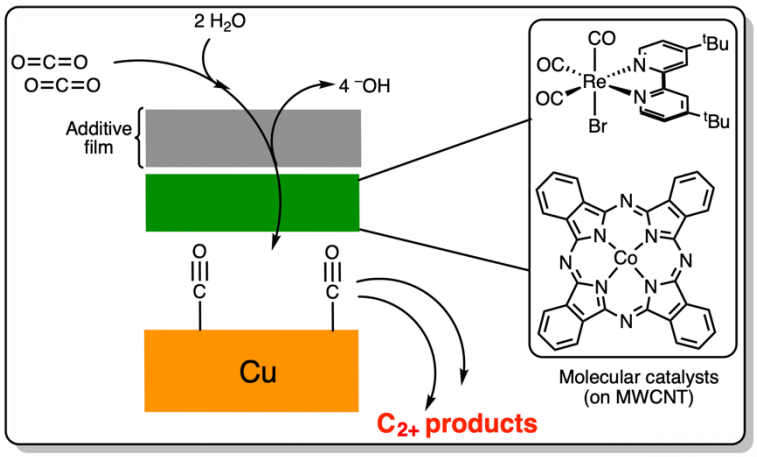

Figure 1. Proposed scheme for generation of C_{2+} products from enhanced CO spillover with immobilized molecular CO_2R complexes on Cu.

RESULTS AND DISCUSSION

i) Layer-by-layer deposition of molecular complex inks and pyridinium-derived film

Several deposition strategies are illustrated in Figure 2 to account for possible insulation of film with respect to potential CO spillover.[20] The film can be electrodeposited from 30-minute chronoamperometry in 0.1 M $KHCO_{3(aq)}$. **CoPc**/MWCNT (1 mg each per mL ^{i}PrOH) can then be drop casted onto Cu foil; this material is one of the most active supported molecular complexes for CO_2R to CO.[13,21] An additional "layer" of **IsqPh** film can be electrodeposited after incorporating **CoPc**/MWCNT to form a "sandwiched" film-**CoPc**/MWCNT-film coating. Alternatively, **CoPc**/MWCNT can be drop casted onto bare Cu foil followed by electrodeposition of **IsqPh** film.

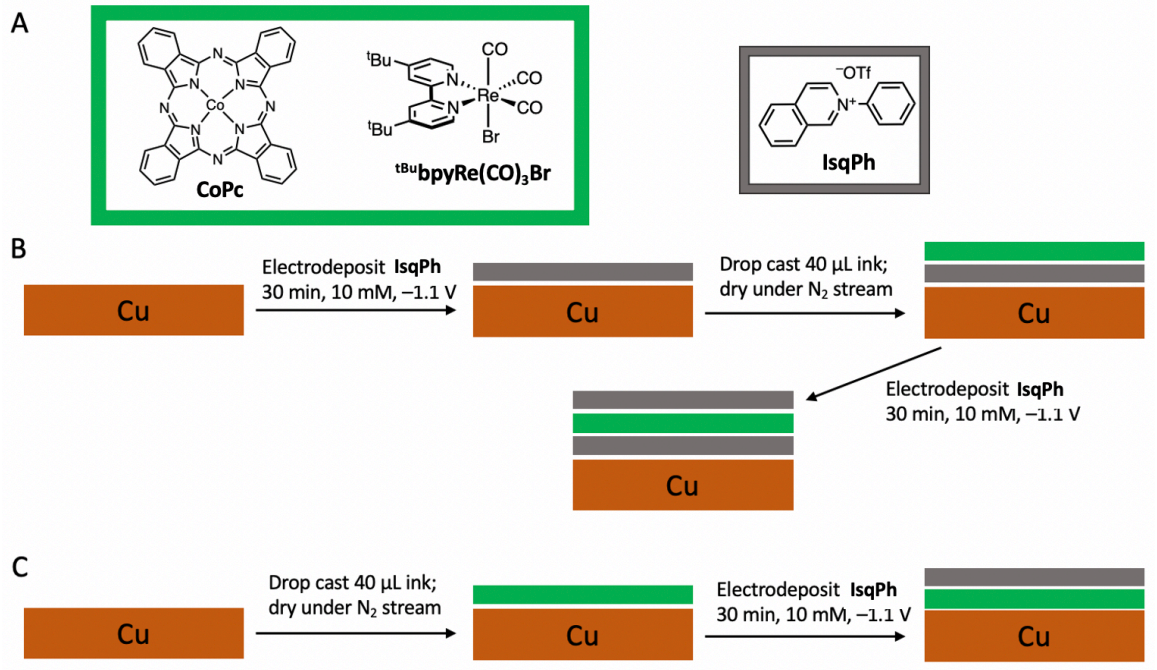

Figure 2. A. Molecular complexes (green box) and film precursor **IsqPh** (gray box). B. Electrodeposition of film following by drop casting of ink (molecular complex + MWCNTs). C. Drop casting following by electrodeposition.

CoPc/MWCNT without film (Figure 2C, first intermediate) led to high Faradaic efficiency for CO and minimal formation of H_2 compared to bare Cu (Figure 3). CO_2 electrolysis with film-**CoPc**/MWCNT-film on Cu (Figure 2B, last intermediate) at –1.1 V vs. RHE revealed the greatest selectivity for C_{2+} products compared to all other conditions tested, but the activity was substantially less than bare Cu and Cu bearing **IsqPh** film (Figure 2B, first intermediate). The high activity towards CO suggests that cascade catalysis involving CO conversion to C_{2+} products is not taking place. It is evident that this strategy does not enhance CO residence time at the Cu foil surface to facilitate enhanced *CO-*CO coupling.

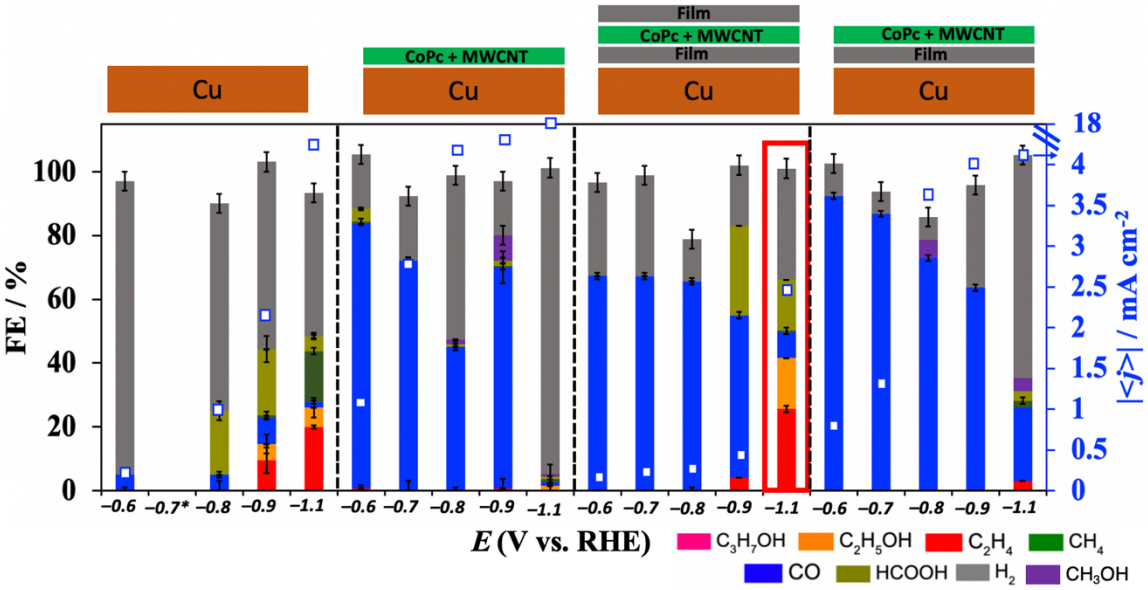

Figure 3. Selectivity profile showing FEs (columns, left axis) and total current density (white squares, right axis) for various immobilization/electrodeposition conditions on Cu foil. Electrolyte: 0.1 M $KHCO_{3(aq)}$. Column boxed in red (Film-[Co]-film, –1.1 V vs. RHE) represents highest FE_{C2+} relative to bare Cu.

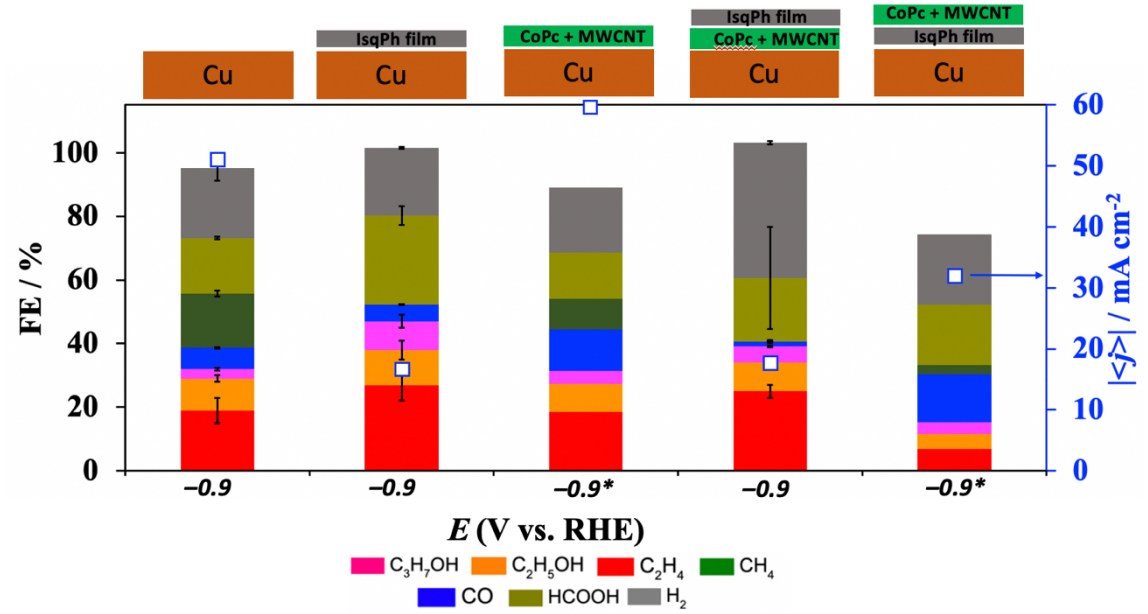

Figure 4. Selectivity profile from **CoPc**/MWCNT + **IsqPh** film on Cu/PTFE in a GDE configuration. Starred (*) data points represent a single electrolysis experiment.

It was hypothesized that polycrystalline Cu foil does not bear sufficient activity to convert high local [CO] to C_{2+} products. Attention was then to Cu gas diffusion electrodes (GDEs). Electrodes were prepared via sputtering of Cu nanoparticles onto poly(tetrafluoroethylene) (Cu/PTFE), and experiments were carried out in a Cu GDE flow cell (Figure 4).[17] No improvement in performance relative to either bare Cu or film was observed despite incorporation of **CoPc**/MWCNT. Reports in the literature have demonstrated up to 2-fold increase in $|j_{C2+}|$ with **CoPc**/MWCNT as a coating on bare Cu.[11] Significant increase in j is observed in the present work (Figure 4). The lack of further increase in activity could be due to HER suppression by the film, leading to ~4-fold attenuation in j.[15,16] The inability of CO to penetrate the film cannot be ruled out.[18]

Experiments with **^{tBu}bpyRe(CO)$_3$Br**/MWCNT were carried out on polycrystalline Cu foil (Figure 5); this material has demonstrated highly active CO_2R to CO in $KHCO_{3(aq)}$ electrolyte. Significant improvement was observed at –0.82 V vs. RHE with film-**^{tBu}bpyRe(CO)$_3$Br**/MWCNT-film (FE_{C2+} = 45%) compared to bare Cu (FE_{C2+} = 0%). Despite the improvement in FE_{C2+}, cascade catalysis is not evident due to significant formation of formic acid (FE_{HCOOH} = 40%) observed with **^{tBu}bpyRe(CO)$_3$Br**/MWCNT on Cu, which differs from high FE_{CO} (80%) catalyzed by **CoPc**/MWCNT (Figure 2). Conversion of CO_2 to formate on Cu cannot further on lead to generation of C_{2+} products as determined by previously investigated reaction pathways on Cu.[22] These observations do not support the CO spillover hypothesis.

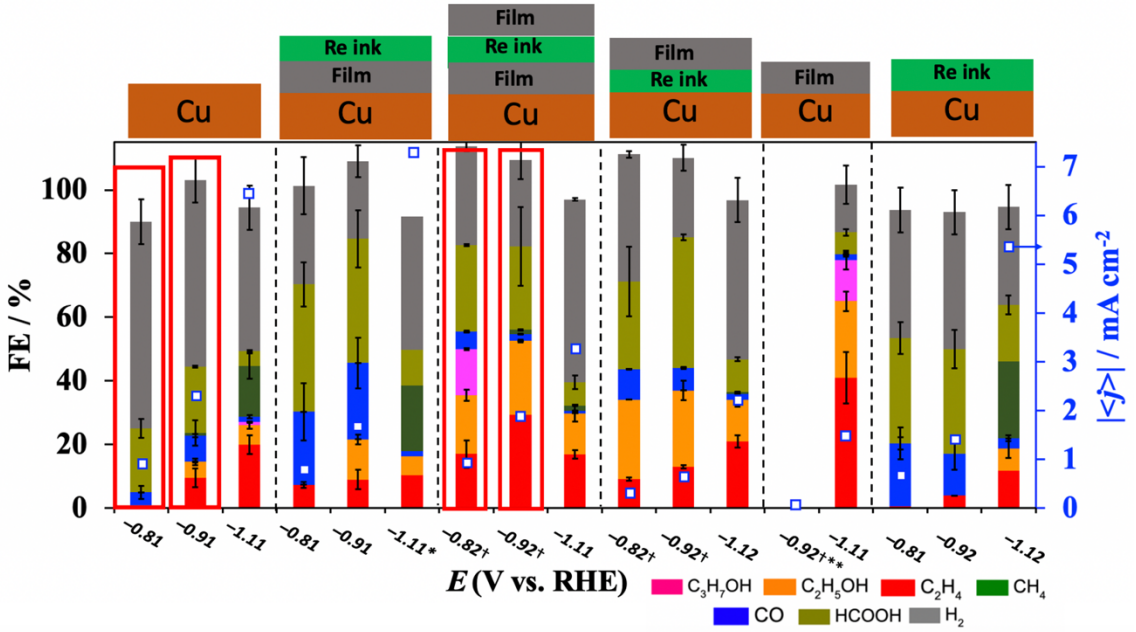

Figure 5. Selectivity profile from ^{tBu}**bpyRe(CO)$_3$Br**/MWCNT + **IsqPh** film on Cu foil. Electrolyte: 0.1 M $KHCO_{3(aq)}$. Red boxes compare data with greatest improvement in FE_{C2+}. Starred (*) data points represent a single electrolysis experiment. Double-starred (**): no gaseous or liquid products were observed from electrolysis (j = –40 μA). Dagger (†) represents electrolysis experiments run for 60 minutes.

Next, CO_2R experiments were carried out with the chloride analogue ^{tBu}**bpyRe(CO)$_3$Cl**/MWCNT (Figure 6). The bromide anion was hypothesized to play a signficant role in improving CO_2R activity; previous reports found that bromide restructuring of Cu surface as evident by atomic force microscopy (AFM) enhanced CO_2R performance.[23] Elevation in FE_{C2+} was found with ^{tBu}**bpyRe(CO)$_3$Cl**/MWCNT, albeit less significantly activity enhancement with the bromide analogue. These findings suggest that the halide was responsible for improvement in CO_2R, rather than CO spillover.

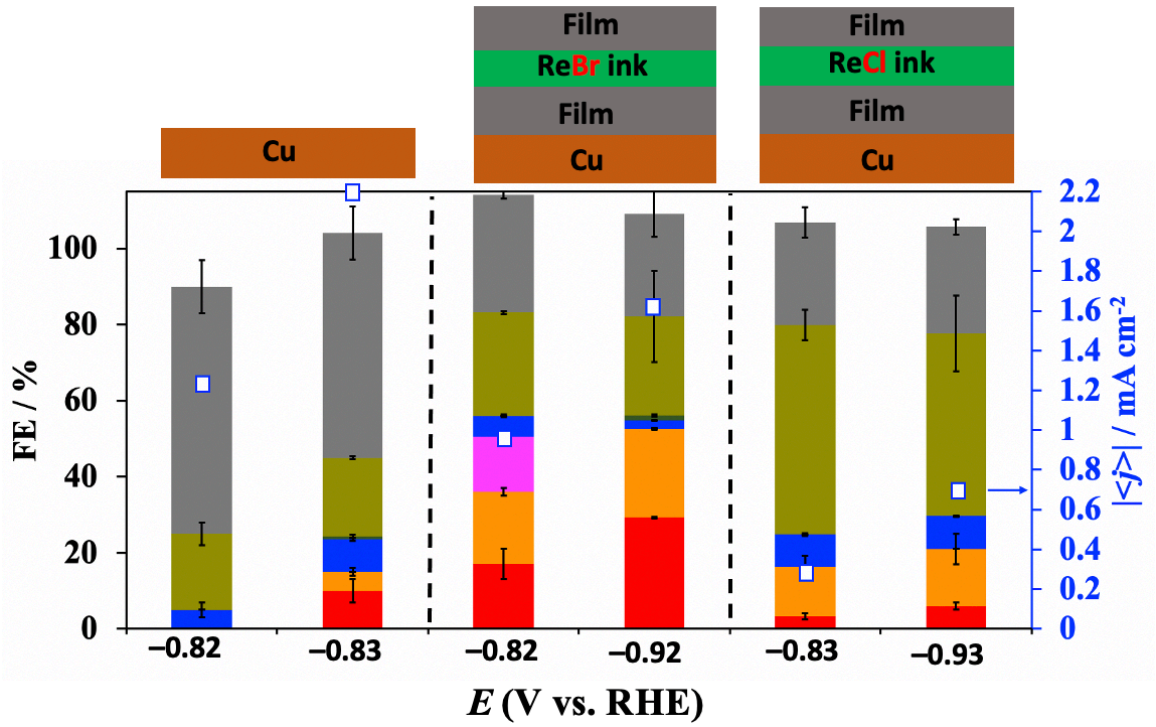

Figure 6. Selectivity profile from ^{tBu}**bpyRe(CO)$_3$Cl**/MWCNT + **IsqPh** film on Cu foil. Electrolyte: 0.1 M $KHCO_{3(aq)}$.

ii) Mixing films/molecular complexes with Cu nanoparticles

Additional experiments were carried out mixing Cu nanoparticles (CuNPs) with molecular electrocatalyst inks prior to deposition onto carbon paper (38 BC, Fuel Cell Store). Prior work mixing AgNPs and CuNPs followed by drop casting suggested that this approach might be preferred for cascade catalysis.[7]

While there was improvement in FE_{C2+} with the **CoPc** ink + CuNP + **IsqPh** film set of conditions (Table 2, Entry 1) relative to the absence of film (Entry 3), this did not outperform CuNPs coated with **IsqPh** film, suggesting improvement in performance due to **IsqPh** film rather than cascade catalysis. Entry 1 displayed high FE_{CO} relative to Entry 3, suggesting that CO did not spillover to yield C_{2+} products. In any set of conditions

utilizing **IsqPh** film, the current density magnitude is lower by up to a factor of 6.5 relative to the film-absent experiments.

Table 2. Selectivity profile from various ink compositions of **CoPc**/MWCNT + CuNPs + **IsqPh** film.

	E (V vs. RHE)	H_2	CO	HCOOH	CH_4	C_2H_4	C_2H_5OH	C_3H_7OH	CH_3OH	Total	j (mA/cm^2)
CoPc ink + **CuNP** + **IsqPh** film	-0.9	18 ± 7	54 ± 5	9 ± 3	0	8 ± 2	23 ± 5	0	0	111 ± 10	–0.7 ± 0.2
CuNP + **IsqPh** film	-0.9	10 ± 4	0.8 ± 0.5	24 ± 6	0	10 ± 5	22 ± 5	19 ± 10	0	85 ± 10	–1.1 ± 0.7
CoPc ink + **CuNP**	-0.9	13.5	63.0	0.07	0	1.0	4.3	0	0	82	–4.6
CoPc ink	-0.9	5.3 ± 0.8	42 ± 4	6 ± 6	0	0	0	0	13 ± 2	67 ± 7	–7.3 ± 0.3
CuNP	-0.9	37.7	12.6	13.3	6.6	15.1	14.0	7.1	0	97.4	–3.4

CONCLUSIONS

In summary, tandem catalysis involving highly active CO-generating CO_2R electrocatalysts coupled with Cu electrodes was investigated. No elevation in CO_2R performance was evident wih **IsqPh** film and **CoPc** ink. Improvement in performance from **^{tBu}bpyRe(CO)$_3$Br**/MWCNT is due to the bromide anion likely restructuring the Cu surface, leading to improved CO_2R performance. Mixing CuNPs with **CoPc**/MWCNT and/or **IsqPh** film did not lead to successful establishment of cascade catalysis involving CO spillover. Future work could be dedicated to more judicious electrode engineering, where the electrode is prepared such that certain film(s) could be appliedertain geometric area of the electrode, thus localizing CO to facilitate *CO-*CO coupling for enhance C_{2+} product.

EXPERIMENTAL

Materials and Methods

General Considerations. All solvents and reagents were obtained from commercial sources (Aldrich, Merck, and Combi Blocks) and used as received, unless stated otherwise. Isoquinoline was dried by dissolving in diethyl ether and stirring in calcium hydride under inert atmosphere for 12 h and filtered over a pad of alumina. *N*-phenyl isoquinolinium triflate was prepared using reported procedures, and the ^{13}C and ^{1}H NMR spectra are in agreement.[17,24,25] **^{tBu}bpyRe(CO)$_3$Br** and **^{tBu}bpyRe(CO)$_3$Cl** were prepared following a reported procedure; ^{1}H NMR spectra are in agreement.[26] Dichloromethane was dried by passing over activated alumina by the method of Grubbs[27] and stored over 3 Å molecular sieves in a N_2-filled glovebox.

Copper foil (product number 266744, 99.999% Cu, 25 mm × 50 mm × 1 mm), phosphoric acid (85%, TraceSelect), potassium carbonate (99.995%), potassium hydroxide (semiconductor grade, 99.99% trace metals basis), and potassium chloride (99.999% trace metals basis) were purchased from Sigma Aldrich). The leakless Ag/AgCl reference electrode was purchased from Innovative Instruments. Platinum foil (99.99% Pt, 25 mm × 25 mm × 0.05 mm) was purchased from Alfa Aesar. Carbon rods (99.999% C) were purchased from Strem Chemicals. Perchloric acid (67-72%, TraceSELECT, for trace analysis) was purchased from Fluka Analytical. Natural abundance CO_2 (Research grade) was purchased from Airgas. Deuterium oxide (D 99.96%) and d_6-dimethylsulfoxide (D 99.8%) were purchased from Cambridge Isotope Laboratories. The ^{1}H and ^{13}C NMR spectra were recorded on a Bruker 400 MHz instrument with a prodigy broadband cryoprobe. Shifts were reported relative to the residual solvent peak.

Water was purified by a Nanopure Analytical Ultrapure Water System (Thermo Scientific) or a Milli-Q Advantage A10 Water Purification System (Millipore) with specific resistance of 18.2 MΩ·cm at 25 °C. A VWR sympHony^{TM} pH meter (calibrated with a pH = 1.68 standard) was used to determine the pH of the electrolytes before experiments.

Electrolyte Preparation.

Potassium bicarbonate electrolyte ($KHCO_{3(aq)}$, 0.1 M) was prepared by sparging an aqueous solution of potassium carbonate ($K_2CO_{3(aq)}$, 0.05 M) with CO_2 for at least 1 hour prior to electrolysis. This process converts K_2CO_3 into $KHCO_3$ and saturates the electrolyte solution with CO_2.

Electrode Preparation

Before each experiment, copper foil was polished to a mirror-like finish using diamond paste (3 μm, then 1 μm) followed by rinsing with water and drying with a stream of nitrogen gas. The copper foil was then electropolished using the following method: in an 85% phosphoric acid bath, +400 mA was applied to the Cu foil until a potential of +2.3 V versus carbon rod was reached, and this potential was held for 5 minutes. The foil was subsequently washed with nano-pure water and dried under a stream of nitrogen gas. Platinum foil as the counter electrode was rinsed with water and flame-annealed using a butane torch for 10 s.

The gas diffusion electrodes (GDEs) were prepared by sputtering 300 nm Cu onto a 5 cm x 5 cm portion of polytetrafluoroethylene membrane (pore size of 450 nm, with polypropylene support on backside) using a pure Cu target (99.99%) at a sputtering rate of 1 Å s^{-1}.

The preparation of the catalyst ink was adapted from previous work investigating supported molecular electrocatalysts.[12,28,29] 8.0 mg of metal complex (**CoPc** or **^{tBu}bpyRe(CO)$_3$X**, where **X** = Br or Cl) was dissolved in 8 mL of 2-propanol. 8.0 mg of MWCNTs were added to this solution to form a black suspension, which was sonicated for 60 minutes. 40 μL of this ink was drop casted onto 5 cm^2 of either 1) freshly polished polycrystalline Cu foil or 2) Cu foil bearing electrodeposited **IsqPh** film.

After drop casting, the electrode was allowed to dry under ambient conditions for 2 hours. A similar protocol was carried out with Cu/PTFE.

Electrochemical Measurements in the Flow Cell

Chronoamperometry measurements were carried out in a custom-made PEEK flow cell setup similar to the one reported by Ager and co-workers using a copper foil as the working electrode and a platinum foil as the counter electrode.[30] The cathode compartment was separated from the anode compartment by a Selemion AMV anion-exchange membrane (AGC Engineering Co.). All potentials were measured versus a leakless Ag/AgCl reference electrode (Innovative Instruments) with an outer diameter of 5 mm that was inserted into the cathode compartment. The reference electrode was calibrated against H^+/H_2 on Pt in a 0.5 M sulfuric acid solution (0 V vs. standard hydrogen electrode) and saturated calomel electrode (SCE) (+0.241 V saturated vs. standard hydrogen electrode). All electrochemical measurements were carried out using a Biologic VMP3 multichannel potentiostat. The applied potentials were converted to the reversible hydrogen electrode (RHE) scale with iR correction through the following equation:

$$E_{corrected}\,(\text{vs. RHE}) = E_{applied}\,(\text{vs. Ag/AgCl}) + (0.059 \times \text{pH}) + 0.210 + (0.15)\,iR$$

where i is the current at each applied potential and R is the equivalent series resistance measured via electrochemical impedance spectroscopy (EIS) in the frequency range of 10^5 – 0.1 Hz with an amplitude of 10 mV.

Potentiostatic electrochemical impedance spectroscopy (PEIS) measurements were carried out prior to each electrolysis experiment to determine the Ohmic resistance of the flow cell. The impedance measurements were carried out at frequencies ranging from 200 kHz to 100 MHz to measure the

solution resistance. A Nyquist plot was plotted and in the low-frequency part, a linear fit was performed, and the axis intersection was calculated. The value of this intersection represents the Ohmic resistance of the cell. An average of 3 measurements was taken to calculate the value of R. Typically, resistance measurements ranged from 40 to 50 Ω.

All chronoamperometric experiments were performed for 30 min (unless otherwise stated) at 25 °C using a CO_2-saturated electrolyte of choice. In experiments where an additive was used, a 10 mM solution of the materials was prepared and injected into the cathode compartment. The same electrolyte was used in the anode without any additive. The potentiostat was set to compensate for 85 % of the Ohmic drop, with the remaining 15 % being compensated for after the measurements. The effluent gas stream coming from the flow cell (5 mL/min) was flowed into the sample loops of a gas chromatograph (GC-FID/TCD, SRI 8610C, in Multi Gas 5 configuration) equipped with HayeSep D and Molsieve 5A columns. Methane, ethylene, ethane, and carbon monoxide were detected by a methanizer-flame ionization detector (FID) and the hydrogen was detected by a thermal conductivity detector (TCD). Every 15 minutes, 2 mL of gas was sampled to determine the concentration of gaseous products. After electrolysis, the liquid products in both catholytes and anolytes were quantified by both HPLC (Thermo Scientific Ultimate 3000) and ^{1}H NMR spectroscopy (Bruker 400 MHz Spectrometer).

Electrochemical Measurements in the GDE Cell

The CO_2R measurements were conducted in a gas-tight liquid-electrolyte flow cell. Chronopotentiometry experiments were carried out in a custom-made PEEK liquid-electrolyte cell similar to the one reported by Sargent and co-workers.[17] The liquid-electrolyte flow cell consists of three compartments: gas chamber, catholyte chamber, and anolyte chamber. The PTFE electrode was sandwiched between CO_2 gas chamber and catholyte chamber with an exposure area of 0.5 cm^{-2}.

Catholyte and anolyte chambers were separated by a cation-exchange membrane (Nafion 115, FuelCellStore). An Autolab PGSTAT204 in a potentiostatic mode was used as electrochemical workstation. The PTFE electrode, leakless Ag/AgCl electrode, and Pt mesh were employed as working, reference and counter electrodes, respectively. The applied potentials were converted to the reversible hydrogen electrode (RHE) scale with iR correction through the following equation:

$$E_{corrected}\,(\text{vs. RHE}) = E_{applied}\,(\text{vs. Ag/AgCl}) + (0.059 \times \text{pH}) + 0.210 + iR$$

where i is the current at each applied potential and R is the equivalent series resistance measured via electrochemical impedance spectroscopy (EIS) in the frequency range of 10^5 – 0.1 Hz with an amplitude of 10 mV. The appropriate CO_2-saturated electrolyte was used as both catholyte and anolyte and was circulated through the flow cell using peristaltic pumps with a silicone Shore A50 tubing. The electrolyte was bubbled with CO_2 during the entire electrolysis process. The electrolyte flow rate was kept at 10 mL min^{-1}. The flow rate of the CO_2 gas flowing into the gas chamber was kept at 50 sccm by a digital mass flow controller.

Potentiostatic electrochemical impedance spectroscopy (PEIS) measurements were carried out prior to and after each electrolysis experiment to determine the Ohmic resistance of the flow cell.[31] The impedance measurements were carried out at frequencies ranging from 200 kHz to 100 MHz to measure the solution resistance. A Nyquist plot was plotted and in the high-frequency part a linear fit was performed, and the axis intersection was calculated. The value of this intersection represents the Ohmic resistance of the cell. An average of 3 measurements was taken to calculate the value of R. Typically, small resistances were measured, ranging from 4 to 7 Ω.

All chronoamperometric experiments were performed for 30 min at 25 °C using a CO_2-saturated electrolyte of choice. Before each CO_2 electrolysis experiment, the film was deposited via CA at –1.1 V vs. RHE for 5 minutes with 10 mM [*additive*] flowing in the catholyte. The anolyte contained the same electrolyte composition absent of any additive. The catholyte was replaced with fresh electrolyte before the subsequent chronopotentiometry experiment. The entire Ohmic drop was compensated before and after the measurement. The effluent gas stream coming from the flow cell (5 mL/min) was flowed into the sample loops of a gas chromatograph (GC-FID/TCD, SRI 8610C, in Multi Gas 5 configuration) equipped with HayeSep D and Molsieve 5A columns. Methane, ethylene, ethane, and carbon monoxide were detected by a methanizer-flame ionization detector (FID) and the hydrogen was detected by a thermal conductivity detector (TCD). Every 15 minutes, 2 mL of gas was sampled to determine the concentration of gaseous products. After electrolysis, the liquid products in both catholytes and anolytes were quantified by both HPLC (Thermo Scientific Ultimate 3000) and ^{1}H NMR spectroscopy (Bruker 400 MHz Spectrometer), the latter using 10% v/v D_2O with DMSO and phenol and standards employing a water suppression technique described in our previous report.[15,31]

The Faradaic efficiencies for gaseous products was calculated from the following equations:

$$F_m = \frac{pF_v}{RT} \qquad (1)$$

$$FE_{prod} = \frac{n_{prod}Fx_{prod}F_m}{i}. \qquad (2)$$

$F_m$is the molar flow, defined by the pressure p, the volume flow F_v, the gas constant R, and temperature T. FE_{prod} is the Faradaic efficiency of a gaseous product $prod$, defined by the electron transfer coefficient of the product n_{prod}, Faraday's constant F, the fraction of the product x_{prod}, the molar flow F_m, and the current i.

Error bars shown in all figures and tables represent standard deviations from at least three replicate measurements.

SUPPLEMENTARY DATA/FIGURES

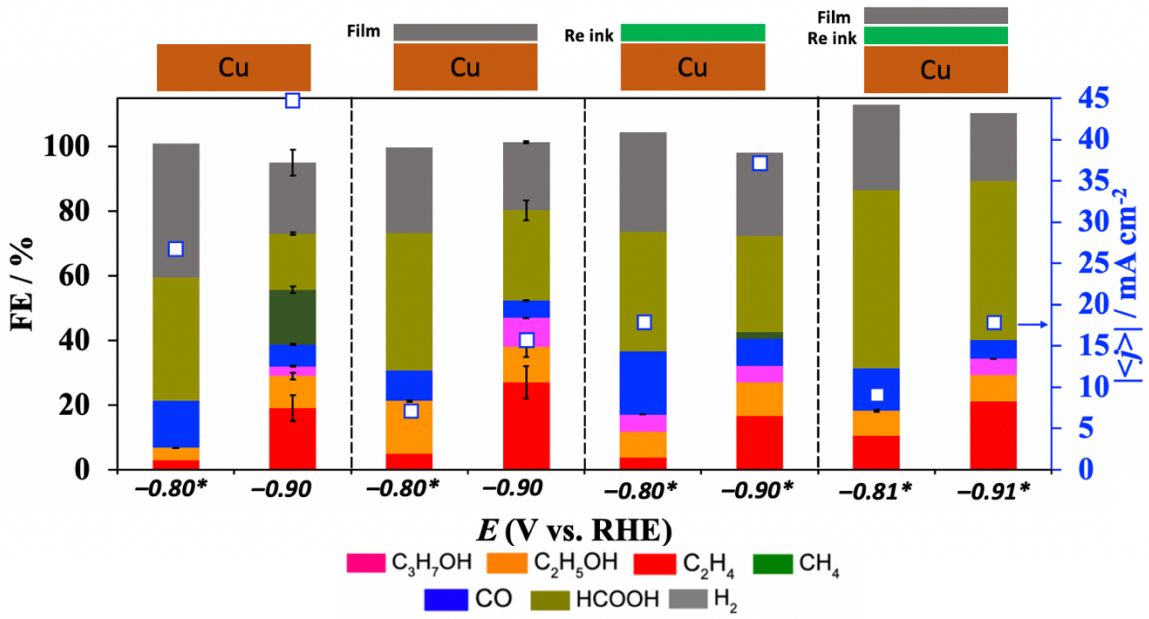

Figure 7. Selectivity profile from ^{tBu}**bpyRe(CO)$_3$Br**/MWCNT + **IsqPh** film on Cu/PTFE in GDE cell configuration. Electrolyte: 0.1 M $KHCO_{3(aq)}$. Starred (*) data points represent a single electrolysis experiment.

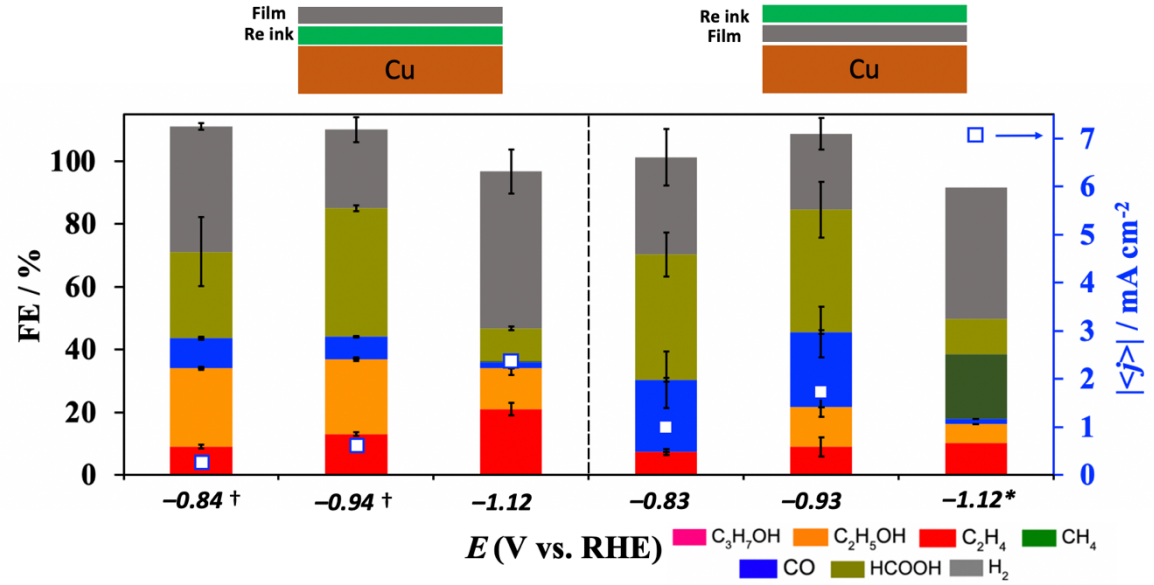

Figure 8. Selectivity profile from ^{tBu}**bpyRe(CO)$_3$Br**/MWCNT + **IsqPh** film (single layer) on Cu foil in GDE cell configuration. Electrolyte: 0.1 M $KHCO_{3(aq)}$. Starred (*) data points represent a single electrolysis experiment.

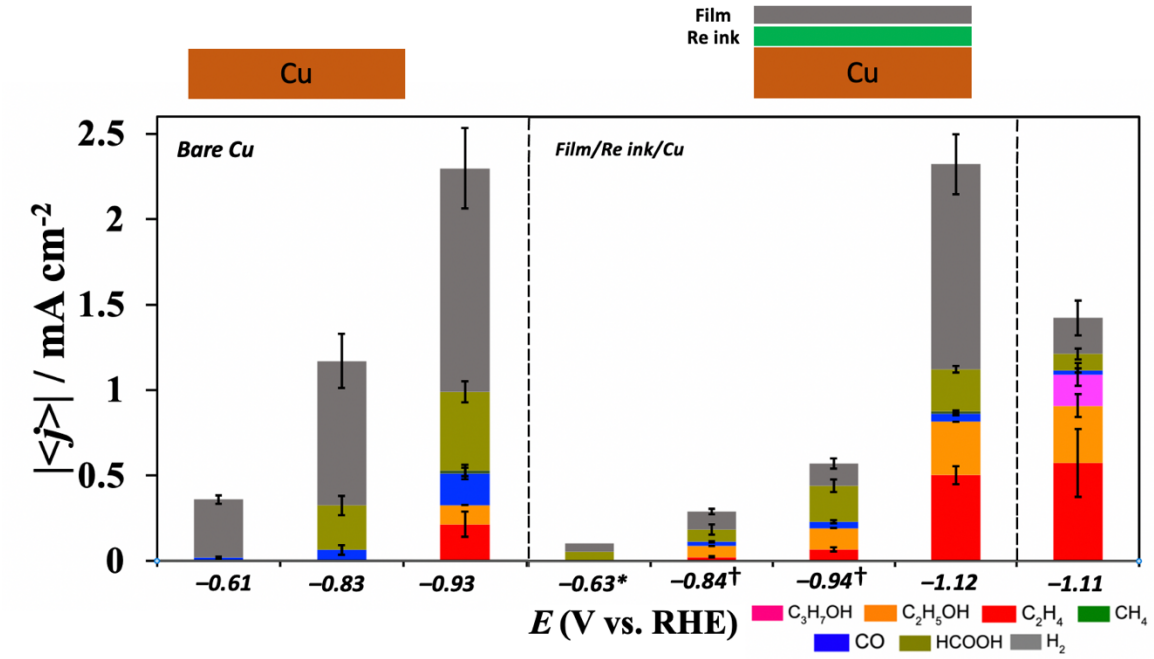

Figure 9. Partial current densities of ^{tBu}**bpyRe(CO)$_3$Br**/MWCNT + **IsqPh** film (single layer) on Cu foil compared to **IsqPh** film. Dagger (†) represents electrolysis experiments run for 60 minutes.

REFERENCES

(1) Hori, Y.; Kikuchi, K.; Suzuki, S. *Chem. Lett.* **1985**, *14* (11), 1695–1698.

(2) Murata, A.; Hori, Y. Product Selectivity Affected by Cationic Species in Electrochemical Reduction of CO2 and CO at a Cu Electrode. *Bull. Chem. Soc. Jpn.* **1991**, *64* (1), 123–127.

(3) Chu, S.; Cui, Y.; Liu, N. The Path towards Sustainable Energy. *Nat. Mater.* **2017**, *16* (1), 16–22.

(4) Zhu, Q.; Sun, X.; Yang, D.; Ma, J.; Kang, X.; Zheng, L.; Zhang, J.; Wu, Z.; Han, B. Carbon Dioxide Electroreduction to C2 Products over Copper-Cuprous Oxide Derived from Electrosynthesized Copper Complex. *Nat. Commun.* **2019**, *10* (1), 3851.

(5) Sha, Y.; Zhang, J.; Cheng, X.; Xu, M.; Su, Z.; Wang, Y.; Hu, J.; Han, B.; Zheng, L. Anchoring Ionic Liquid in Copper Electrocatalyst for Improving CO2 Conversion to Ethylene. *Angew. Chemie Int. Ed.* **2022**, *61* (13), e202200039.

(6) Zhang, G.-R.; Straub, S.-D.; Shen, L.-L.; Hermans, Y.; Schmatz, P.; Reichert, A. M.; Hofmann, J. P.; Katsounaros, I.; Etzold, B. J. M. Probing CO2 Reduction Pathways for Copper Catalysis Using an Ionic Liquid as a Chemical Trapping Agent. *Angew. Chemie Int. Ed.* **2020**, *59* (41), 18095–18102.

(7) Chen, C.; Li, Y.; Yu, S.; Louisia, S.; Jin, J.; Li, M.; Ross, M. B.; Yang, P. Cu-Ag Tandem Catalysts for High-Rate CO2 Electrolysis toward Multicarbons. *Joule* **2020**, *4* (8), 1688–1699.

(8) Li, F.; Li, Y. C.; Wang, Z.; Li, J.; Nam, D.-H.; Lum, Y.; Luo, M.; Wang, X.; Ozden, A.; Hung, S.-F.; et al. Cooperative CO2-to-Ethanol Conversion via Enriched Intermediates at Molecule–Metal Catalyst Interfaces. *Nat. Catal.* **2020**, *3* (1), 75–82.

(9) Zhang, T.; Bui, J. C.; Li, Z.; Bell, A. T.; Weber, A. Z.; Wu, J. Highly Selective and Productive Reduction of Carbon Dioxide to Multicarbon Products via in Situ CO Management Using Segmented Tandem Electrodes. *Nat. Catal.* **2022**, *5* (3), 202–211.

(10) Wang, M.; Loiudice, A.; Okatenko, V.; Sharp, I. D.; Buonsanti, R. The Spatial Distribution of Cobalt Phthalocyanine and Copper Nanocubes Controls the Selectivity towards C2 Products in Tandem Electrocatalytic CO2 Reduction. *Chem. Sci.* **2023**, *14* (5), 1097–1104.

(11) Kong, X.; Zhao, J.; Ke, J.; Wang, C.; Li, S.; Si, R.; Liu, B.; Zeng, J.; Geng, Z. Understanding the Effect of *CO Coverage on C–C Coupling toward CO2 Electroreduction. *Nano Lett.* **2022**, *22* (9), 3801–3808.

(12) Zhanaidarova, A.; Jones, S. C.; Despagnet-Ayoub, E.; Pimentel, B. R.; Kubiak, C. P. Re(TBu-Bpy)(CO)3Cl Supported on Multi-Walled Carbon Nanotubes Selectively Reduces CO2 in Water. *J. Am. Chem. Soc.* **2019**, *141* (43), 17270–17277.

(13) Zhang, X.; Wu, Z.; Zhang, X.; Li, L.; Li, Y.; Xu, H.; Li, X.; Yu, X.; Zhang, Z.; Liang, Y.; et al. Highly Selective and Active CO2 Reduction Electrocatalysts Based on Cobalt Phthalocyanine/Carbon Nanotube Hybrid Structures. *Nat. Commun.* **2017**, *8* (1), 14675.

(14) Smith, P. T.; Benke, B. P.; Cao, Z.; Kim, Y.; Nichols, E. M.; Kim, K.; Chang, C. J. Iron Porphyrins Embedded into a Supramolecular Porous Organic Cage for Electrochemical CO2 Reduction in Water. *Angew. Chemie Int. Ed.* **2018**, *57* (31), 9684–9688.

(15) Han, Z.; Kortlever, R.; Chen, H.-Y.; Peters, J. C.; Agapie, T. CO2 Reduction Selective for C≥2 Products on Polycrystalline Copper with N-Substituted Pyridinium Additives. *ACS Cent. Sci.* **2017**, *3* (8), 853–859.

(16) Nie, W.; Heim, G. P.; Watkins, N. B.; Agapie, T.; Peters, J. Organic Additive-Derived Films on Cu Electrodes Promote Electrochemical CO2 Reduction to C2+ Products Under Strongly Acidic Conditions. *Angew. Chemie Int. Ed.* **2023**, *n/a* (n/a).

(17) Li, F.; Thevenon, A.; Rosas-Hernández, A.; Wang, Z.; Li, Y.; Gabardo, C. M.; Ozden, A.; Dinh, C. T.; Li, J.; Wang, Y.; et al. Molecular Tuning of CO2-to-Ethylene Conversion. *Nature* **2020**, *577* (7791), 509–513.

(18) Watkins, N. B.; Schiffer, Z. J.; Lai, Y.; Musgrave, C. B. I. I. I.; Atwater, H. A.; Goddard, W. A. I. I. I.; Agapie, T.; Peters, J. C.; Gregoire, J. M. Hydrodynamics Change Tafel Slopes in Electrochemical CO2 Reduction on Copper. *ACS Energy Lett.* **2023**, *8* (5), 2185–2192.

(19) Kuhl, K. P.; Cave, E. R.; Abram, D. N.; Jaramillo, T. F. New Insights into the Electrochemical Reduction of Carbon Dioxide on Metallic Copper Surfaces. *Energy Environ. Sci.* **2012**, *5* (5), 7050–7059.

(20) Thevenon, A.; Rosas-Hernández, A.; Fontani Herreros, A. M.; Agapie, T.; Peters, J. C. Dramatic HER Suppression on Ag Electrodes via Molecular Films for Highly Selective CO2 to CO Reduction. *ACS Catal.* **2021**, *11* (8), 4530–4537.

(21) Boutin, E.; Wang, M.; Lin, J. C.; Mesnage, M.; Mendoza, D.; Lassalle-Kaiser, B.; Hahn, C.; Jaramillo, T. F.; Robert, M. Aqueous Electrochemical Reduction of Carbon Dioxide and Carbon Monoxide into Methanol with Cobalt Phthalocyanine. *Angew. Chemie Int. Ed.* **2019**, *58* (45), 16172–16176.

(22) Garza, A. J.; Bell, A. T.; Head-Gordon, M. Mechanism of CO2 Reduction at Copper Surfaces: Pathways to C2 Products. *ACS Catal.* **2018**, *8* (2), 1490–1499.

(23) Thevenon, A.; Rosas-Hernández, A.; Peters, J. C.; Agapie, T. In-Situ Nanostructuring and Stabilization of Polycrystalline Copper by an Organic Salt Additive Promotes Electrocatalytic CO2 Reduction to Ethylene. *Angew. Chemie Int. Ed.* **2019**, *58* (47), 16952–16958.

(24) Ge, Q.; Hu, Y.; Li, B.; Wang, B. Synthesis of Conjugated Polycyclic Quinoliniums by Rhodium(III)-Catalyzed Multiple C–H Activation and Annulation of Arylpyridiniums with Alkynes. *Org. Lett.* **2016**, *18* (10), 2483–2486.

(25) Hong, A. Y.; Vanderwal, C. D. A Synthesis of Alsmaphorazine B Demonstrates the Chemical Feasibility of a New Biogenetic Hypothesis. *J. Am. Chem. Soc.* **2015**, *137* (23), 7306–7309.

(26) Smieja, J. M.; Kubiak, C. P. Re(Bipy-TBu)(CO)3Cl−improved Catalytic Activity for Reduction of Carbon Dioxide: IR-Spectroelectrochemical and Mechanistic Studies. *Inorg. Chem.* **2010**, *49* (20), 9283–9289.

(27) Pangborn, A. B.; Giardello, M. A.; Grubbs, R. H.; Rosen, R. K.; Timmers, F. J. Safe and Convenient Procedure for Solvent Purification. *Organometallics* **1996**, *15* (5), 1518–1520.

(28) Wu, Y.; Jiang, Z.; Lu, X.; Liang, Y.; Wang, H. Domino Electroreduction of CO2 to Methanol on a Molecular Catalyst. *Nature* **2019**, *575* (7784), 639–642.

(29) Zoric, M. R.; Chan, T.; Musgrave III, C. B.; Goddard III, W. A.; Kubiak, C. P.; Cordones, A. A. In Situ X-Ray Absorption Investigations of a Heterogenized Molecular Catalyst and Its Interaction with a Carbon Nanotube Support. *J. Chem. Phys.* **2023**, *158* (7), 74703.

(30) Lobaccaro, P.; Singh, M. R.; Clark, E. L.; Kwon, Y.; Bell, A. T.; Ager, J. W. Effects of Temperature and Gas–Liquid Mass Transfer on the Operation of Small Electrochemical Cells for the Quantitative Evaluation of CO2 Reduction Electrocatalysts. *Phys. Chem. Chem. Phys.* **2016**, *18* (38), 26777–26785.

(31) Ma, M.; Zheng, Z.; Yan, W.; Hu, C.; Seger, B. Rigorous Evaluation of Liquid Products in High-Rate CO2/CO Electrolysis. *ACS Energy Lett.* **2022**, *7* (8), 2595–2601.

APPENDIX B

INVESTIGATING IMIDAZOLIUM-DERIVED FILMS AS MOLECULAR COATINGS ON Cu ELECTRODES IN CO_2 REDUCTION

ACKNOWLEDGEMENTS

I am grateful to Jake Evans for carrying out X-ray photoelectron spectroscopy and providing insightful discussions. This material is based on work performed by the Liquid Sunlight Alliance, which is supported by the U.S. Department of Energy, Office of Science, Office of Basic Energy Sciences, Fuels from Sunlight Hub under Award DE-SC0021266. The Resnick Sustainability Institute at Caltech is acknowledged for support of the laboratory facilities in which this research was conducted. I am grateful for the Beckman Institute for instrumentation support.

INTRODUCTION

Converting CO_2 to value-added chemicals electrochemically using renewable energy is a potential avenue toward achieving a net-zero carbon economy.[1] Cu is the only metallic electrode where multi-carbon (C_{2+}) products, including C_2H_4, C_2H_5OH, and C_3H_7OH are produced from electrochemical CO_2 reduction (CO_2R).[2] However, Cu alone suffers from poor selectivity towards C_{2+} products owing to the significant generation of C_1 products and hydrogen.[2–4] Coating Cu electrodes with organic films is a strategy for steering CO_2R selectivity towards C_{2+} products. Organic coatings derived from molecular precursors such as pyridinium,[5–9] ionic liquids,[10–12] amines,[13,14] and aryl diazonium and iodonium species[15] have shown promise. Few strategies have been judiciously employed to affect reactivity of Cu with CO_2. Ionic liquids increase bulk CO_2 concentration relative to organic solvents and water.[16,17] Ionic liquids and imidazolium-containing films have demonstrably elevated [CO_2] locally at the Cu surface, thus improving CO_2R activity to C_{2+} products.[10–12,18,19]

Pyridinium-derived films boosted FE_{C2+} relative to bare Cu foil via suppression of the hydrogen evolution reaction (HER).[5,8,9] Moreover, the partial current for all CO_2R products ($|j_{CO2R}|$) is attenuated, suggesting that reaction with CO_2 is not directly affected by the films. It was hypothesized that coupling imidazolium-based films with the microenvironment provided by pyridinium films on Cu would enhance $|j_{C2+}|$ and FE_{C2+} due to both 1) elevated local [CO_2] and 2) inhibited HER. Two variants of imidazolium films were investigated 1) ionomers and 2) imidazolium-bearing styrene compounds for potential electrodeposition of the vinyl motif.

RESULTS AND DISCUSSION

Scheme 1. Synthesis of imidazolium-containing styrene and ionomer

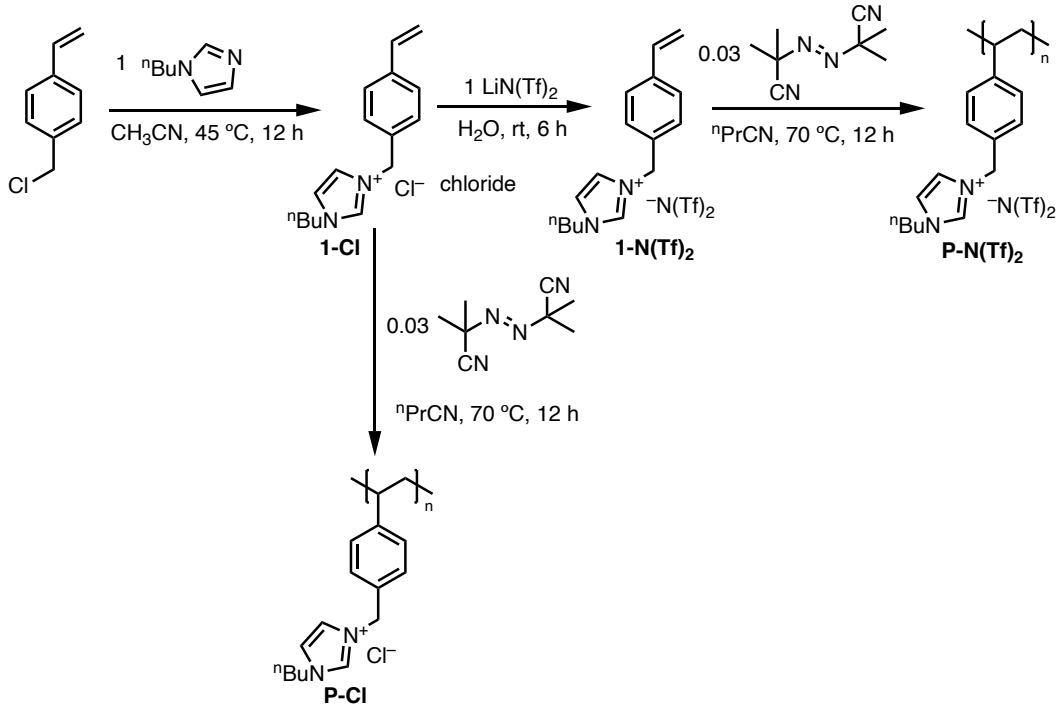

Polystyrene ionomers **P-N(Tf)$_2$** and **P-Cl** were prepared in 2-3 steps (Scheme 1).[20] 4-vinylbenzyl chloride was reacted with 1-butyl-1*H*-imidazole to form the imidazolium chloride, **1-Cl**, followed by anion exchange with lithium bis(trifluoromethylsulfonyl)imide, yielding **1-N(Tf)$_2$**. Polymerization was carried out in the presence azabis(isobutyronitrile). Broadened ^{1}H NMR resonances relative to **1-N(Tf)$_2$** suggest formation of polymer.[20] A similar preparation was carried out for the polymerization of **1-Cl**.

Each polymer was dissolved in CH_3CN (10 mg mL^{-1}), and 40 μL were drop casted onto 5 cm^2 Cu foil and submitted for chronoamperometry (–1.1 V vs. RHE) with $CO_{2(g)}$ in 0.1 M $KHCO_{3(aq)}$ (Figure 1). Each polymer marginally diminished Faradaic efficiency (FE) for CO_2R products relative to bare Cu (55% vs. 20-30%). These polymers did not further elevate performance of films either derived from **PyTolyl** or **IsqPh**. Similar ionomers were

coated on Ag foil, finding boosted HER activity due to proposed enhancement of local [HCO_3^-] by the film.[21]

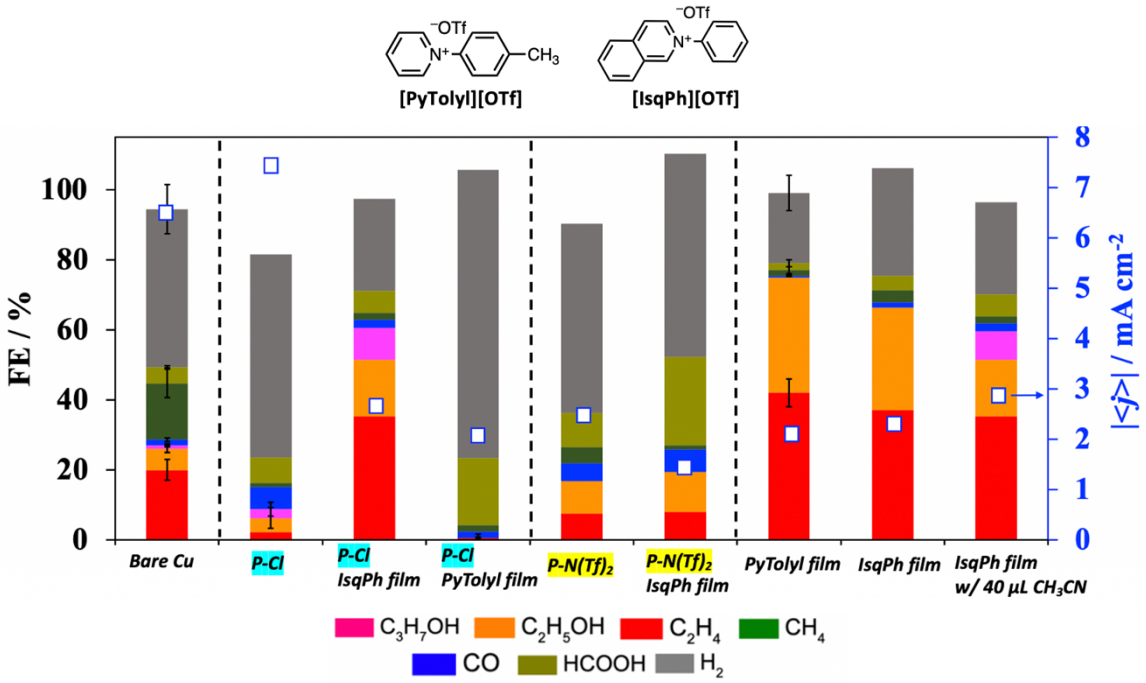

Figure 1. Selectivity profile showing FEs (columns, left axis) and total current density (white squares, right axis) for various ionomers and films derived from **IsqPh** or **PyTolyl**. on Cu foil. Electrolyte: 0.1 M $KHCO_{3(aq)}$.

Next, the styrene compound **1-Cl** was employed as a film precursor. Vinyl species have been investigated for electrodeposition onto Cu, proposed to form a grafted species (Scheme 2).[22] A 10 mM solution of **1-Cl** in 0.1 M $KHCO_{3(aq)}$ was prepared and subject to electrolysis in the presence of CO_2 (Figure 2). Improvement in FE_{C2+} at –1.1 V vs. RHE is observed relative to bare Cu (26% vs. 50%). $|j_{C2+}|$ decreases by ~1.4-fold (1.8 mA cm^{-2} vs. 1.2 mA cm^{-2}). Electrolysis with 10 mM **1-Cl** and 5 mM **IsqPh** boosts FE_{C2+} (70% vs. 50% and 61%) compared to each film precursor by itself. Similar improvement is observed from electrolysis at –1.2 V vs. RHE.

Scheme 2. Proposed interaction of **1-X** upon electrodeposition.

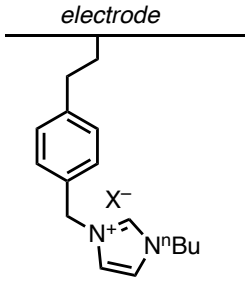

Analysis of partial current densities reveals improvement in $|j_{C2+}|$ by a factor of 2 during electrolysis of both **1-Cl** and **IsqPh** relative to bare Cu and **IsqPh** (Figure 3). The rate of HER decreases by a factor of 4 relative to bare Cu; $|j_{H2}|$ is attenuated 3-fold relative to **IsqPh**. These observations suggest two possible impacts on the microenvironment from co-electrodeposition: 1) proton carrier diffusion limitation[5,9] and/or 2) elevation of local CO_2 concentration imposed by imidazolium-derived species (*vide infra*).[18]

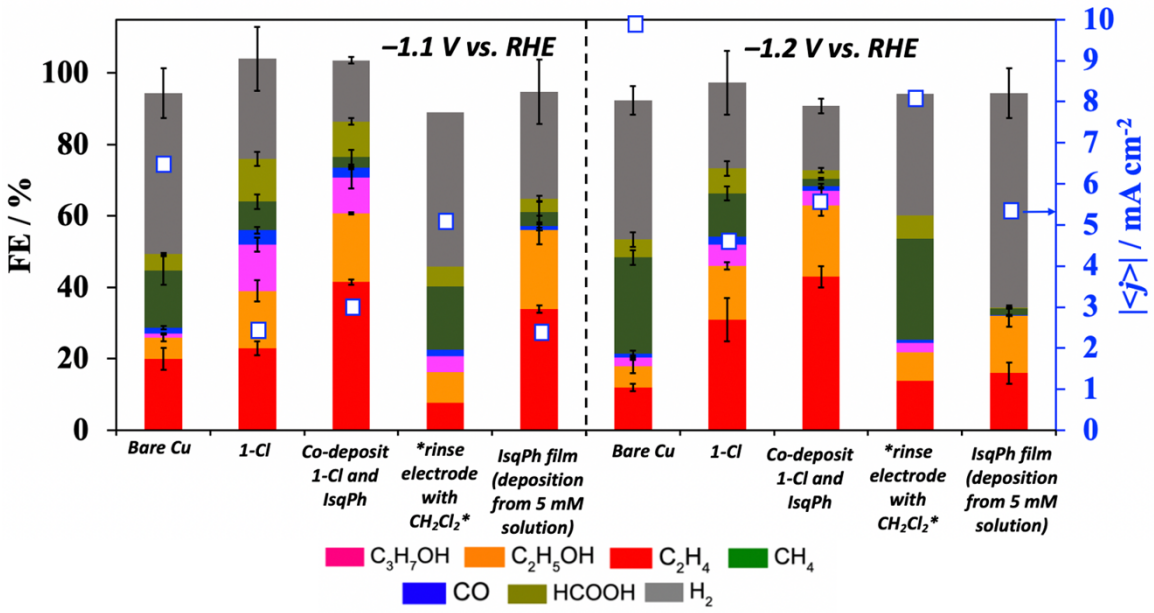

Figure 2. Selectivity profile from various conditions involving **IsqPh** and **1-Cl**. on Cu foil. Electrolyte: 0.1 M $KHCO_{3(aq)}$.

Formation of the species illustrated in Scheme 2 was hypothesized upon performing electrolysis with **1-Cl**, based on previous work investigating electrodeposition of vinyl species to generate grafted motifs.[22] A film is evident on the Cu foil after electrolysis in the presence of **1-Cl**; this material is insoluble in CH_3CN, CH_2Cl_2, and dimethylsulfoxide (DMSO). Rinsing the film observed from co-electrolysis of **1-Cl** and **IsqPh** with CH_2Cl_2 results in a selectivity profile similar to that of bare Cu (Figure 2) at both –1.1 V and –1.2 V. This observation suggests that a new species is formed distinct from either film derived from **1-Cl** or **IsqPh**.

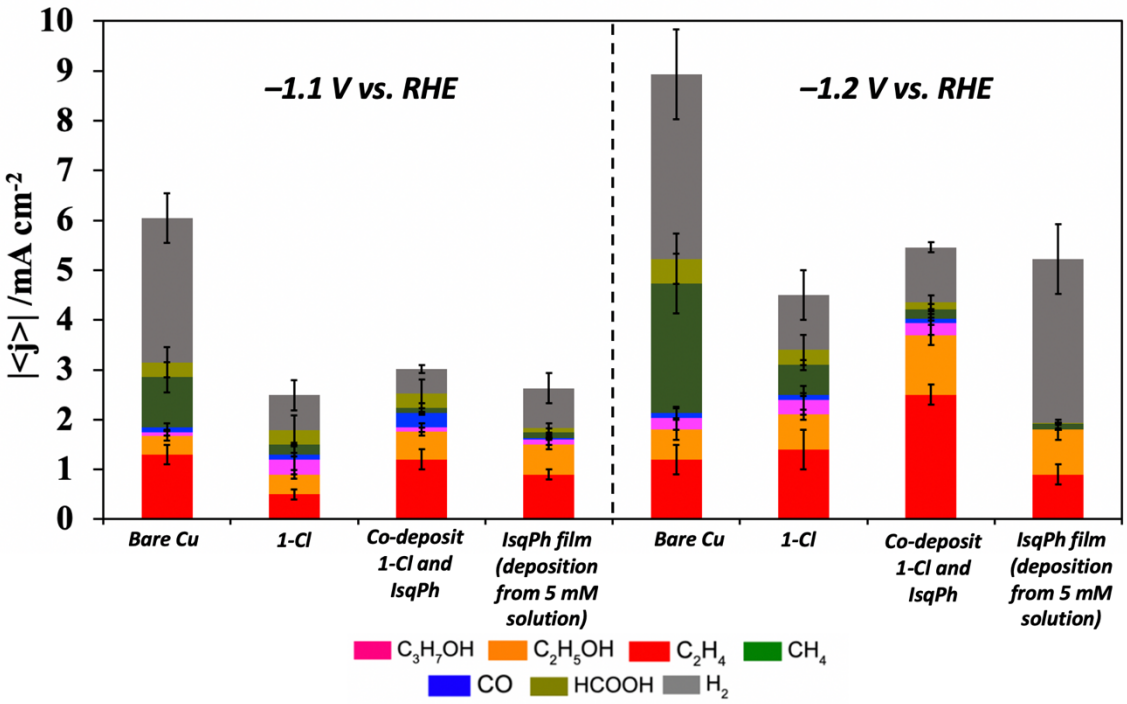

Figure 3. Partial current densities from various conditions involving **IsqPh** and **1-Cl**. on Cu foil. Electrolyte: 0.1 M $KHCO_{3(aq)}$.

^{1}H NMR spectrum of the film generated from co-electrolysis in CD_2Cl_2 reveals an intractable mixture (Figure 4, second from the top), making the exact film structure difficult to elucidate. Three multiplets appear between 5.8 and 6.2 ppm, which show up in the NMR

of the film recorded from electrodeposition of **IsqPh**. New multiplets at 7.2 and 5.7 ppm appear in the film generated from co-electrolysis as well as a singlet at 4.8 ppm. Thus, a mixture of compounds is evident, including the **IsqPh** film and a new species evident from co-electrolysis. Finally, the film from electrolysis of **1-Cl** was not soluble in CD_2Cl_2, consistent with previous reports finding imidazolium-derived films insoluble in conventional organic solvents.[10] X-ray photoelectron spectroscopy (XPS) was employed to ascertain the structure of the film on Cu foil. A single N 1s peak assigned as a tertiary amine is observed; instead, a feature possessing two distinct features would be assigned as a intact imidazolium motif.[21]

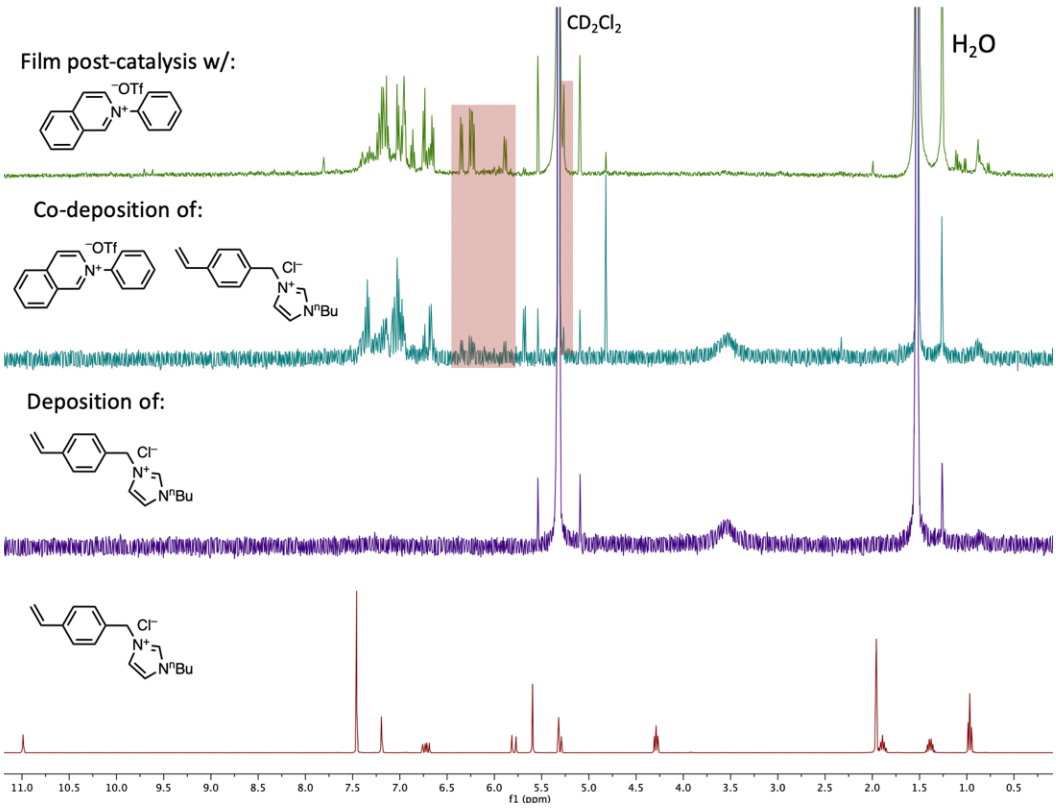

Figure 4. ^{1}H NMR spectra (400 MHz) of films observed from electrolysis (0.1 M $KHCO_{3(aq)}$, –1.1 V vs. RHE) in the presence of CO_2 and **1-Cl**.

XPS investigations of the film from electrolysis of **1-Cl** on the Cu electrode surface reveal a single N 1s peak (Figure 5), similar to the report by Han and co-workers investigating electrodeposited films from imidazoliums.[10] While this peak could conceivably be fit to two Gaussian features, an intact imidazolium would possess two distinct N features in the raw data based on previously reported XPS spectra of imidazolium-containing ionomers drop casted on Ag foil.[21]

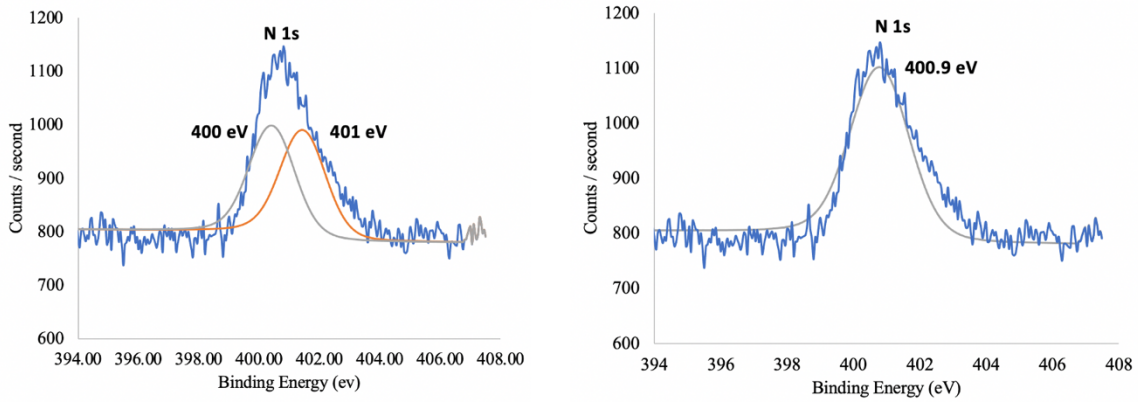

Figure 5. N 1s peak from XPS spectrum of film derived from **1-Cl** illustrating two possible fits.

Possible decomposition products are illustrated in Figure 6.[23,24] Given the non-innocent reactivity of imidazolium species under reducing conditions (Table 1), formation of these decomposition products cannot be precisely elucidated and are certainly not ruled. However, it is unlikely that electrodeposition of **1-Cl** leads to formation of the desired grafted imidazolium-styrene species (Figure 6, top left).[25]

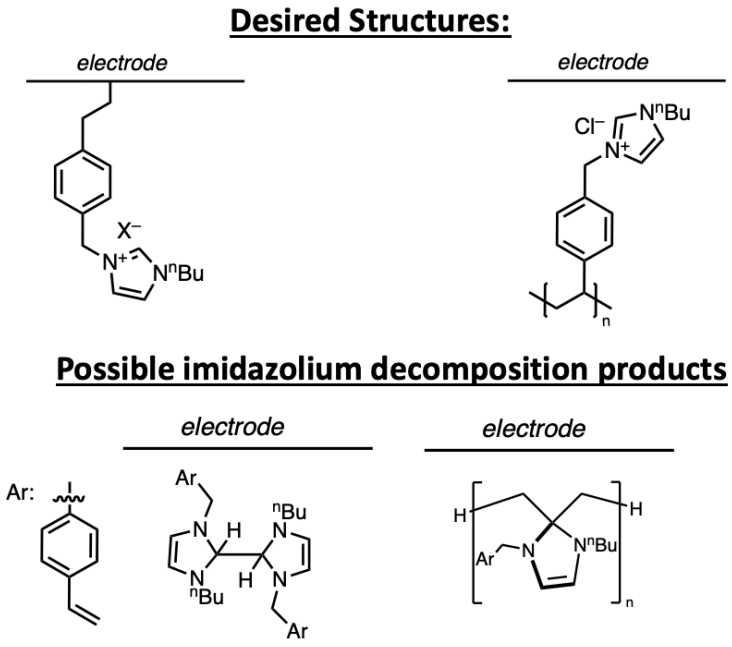

Figure 6. Possible products from electrodeposition of **1-Cl**.

Attention was turned to understanding how the co-electrodeposited film affects reactivity with CO_2. To that end, electrolysis was carried out at various partial pressures of $CO_{2(g)}$ (pCO_2). **IsqPh** film in pH = 2 electrolyte to yields mostly hydrogen with minimal selectivity towards CO_2R products when pCO_2 = 0.2 atm (see Chapter II, Figure 8). In addition, monotonic increase in $|j_{C2+}|$ was observed as a function of increasing pCO_2. A similar phenomenon is observed in 0.1 M $KHCO_{3(aq)}$ with **IsqPh** film (Figure 7). When **1-Cl** is co-electrodeposited, both FE_{C2+} and $|j_{C2+}|$ are elevated relative to exclusively **IsqPh** film (5 mM).

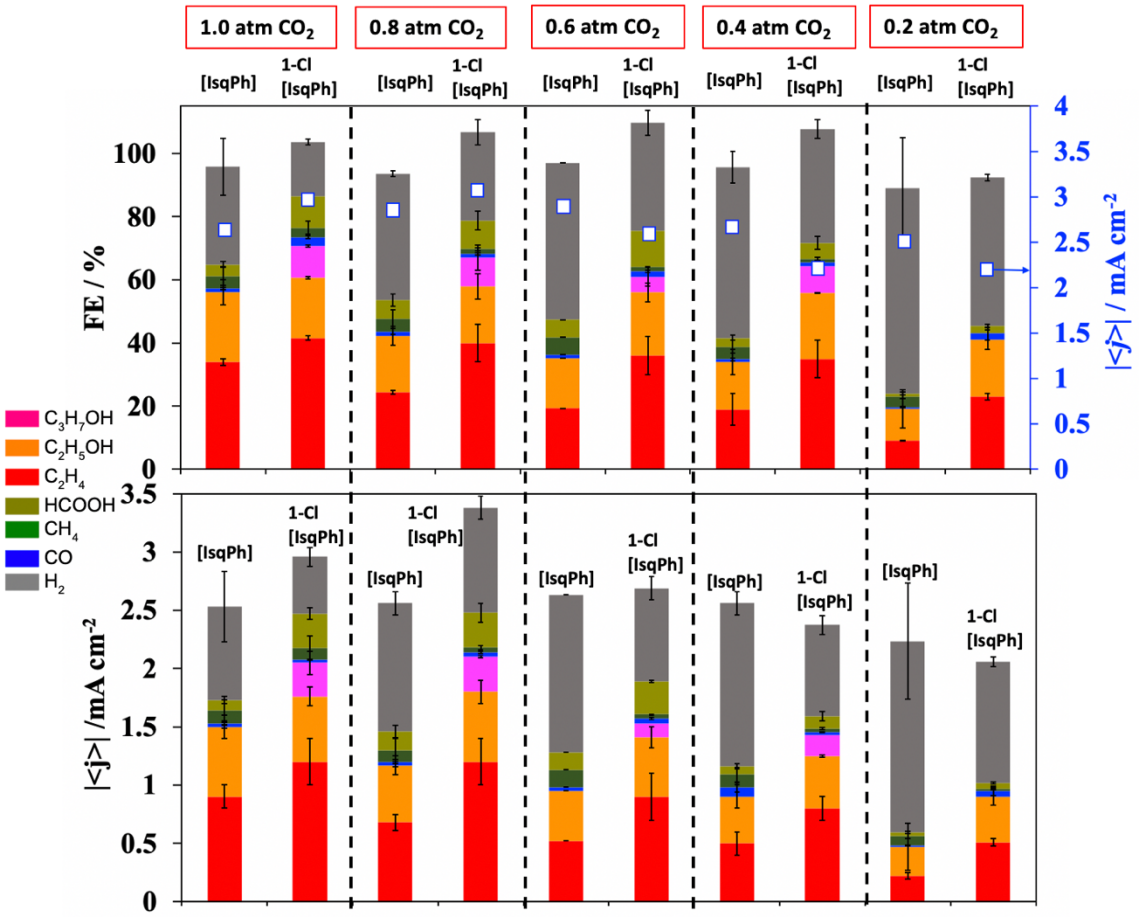

Figure 7. Selectivity profile (top panel) and partial current densities (bottom panel) from CO_2R at various partial pressures of $CO_{2(g)}$.

In addition, $|j_{H2}|$ is attenuated relative to **IsqPh** film. $|j_{C2+}|$ increases until 0.8 atm, wherein a plateau is observed (Figure 7). These data are inconsistent with elevated CO_2 mass transport provided by the film.[5,26,27] The trend in decreasing $|j_{H2}|$ is more consistent with proton carrier mass transport limitation.[5,9] Rotating disk electrochemistry experiments will be carried out to validate this hypothesis, where a decrease in proton carrier diffusion coefficient is expected from the film.[5,9,28] Furthermore, experiments on Cu gas diffusion electrodes (GDE) could elevate performance and shed further light on mass transport implications of these films (see Chapter III).

CONCLUSIONS

To summarize, elevated performance for CO_2R on Cu is observed upon performing co-electrodeposition of **1-Cl** and **IsqPh** (FE_{C2+} = 70%). Improvement in the presence of **1-Cl** film is observed under low pCO_2. Characterization data are consistent with a decomposed N-heterocycle species derived from imidazolium upon exposure to reducing conditions.

EXPERIMENTAL

Materials and Methods

General Considerations. All solvents and reagents were obtained from commercial sources (Aldrich, Merck, and Combi Blocks) and used as received, unless stated otherwise. Isoquinoline was dried by dissolving in diethyl ether and stirring in calcium hydride under inert atmosphere for 12 h and filtered over a pad of alumina. Diphenyl iodonium triflate, 1,4-bis(phenyliodonium)phenylene triflate, *N*-tolyl pyridinium triflate, *N*-phenyl isoquinolinium triflate, 1-(2,4-dinitrophenyl)-pyridinium chloride, **1-Cl**, **P-Cl**, **1-N(Tf)$_2$**, and **P-N(Tf)$_2$** were all prepared using reported procedures, and the ^{13}C and ^{1}H NMR spectra are in agreement.[7,20,29,30] Dichloromethane was dried by passing over activated alumina by the method of Grubbs[31] and stored over 3 Å molecular sieves in a N_2-filled glovebox.

Copper foil (product number 266744, 99.999% Cu, 25 mm × 50 mm × 1 mm), phosphoric acid (85%, TraceSelect), potassium carbonate (99.995%), potassium hydroxide (semiconductor grade, 99.99% trace metals basis), and potassium chloride (99.999% trace metals basis) were purchased from Sigma Aldrich). The leakless Ag/AgCl reference electrode was purchased from Innovative Instruments. Platinum foil (99.99% Pt, 25 mm × 25 mm × 0.05 mm) was purchased from Alfa Aesar. Carbon rods (99.999% C) were purchased from Strem Chemicals. Perchloric acid (67-72%, TraceSELECT, for trace analysis) was purchased from Fluka Analytical. Natural abundance CO_2 (Research grade) was purchased from Airgas. Deuterium oxide (D 99.96%) and d_6-dimethylsulfoxide (D 99.8%) were purchased from Cambridge Isotope Laboratories. The ^{1}H and ^{13}C NMR spectra were recorded on a Bruker 400 MHz instrument with a prodigy broadband cryoprobe. Shifts were reported relative to the residual solvent peak.

Water was purified by a Nanopure Analytical Ultrapure Water System (Thermo Scientific) or a Milli-Q Advantage A10 Water Purification System (Millipore) with specific resistance of 18.2

MΩ·cm at 25 °C. A VWR sympHony^{TM} pH meter (calibrated with a pH = 1.68 standard) was used to determine the pH of the electrolytes before experiments.

Electrolyte Preparation

Potassium bicarbonate electrolyte ($KHCO_{3(aq)}$, 0.1 M) was prepared by sparging an aqueous solution of potassium carbonate ($K_2CO_{3(aq)}$, 0.05 M) with CO_2 for at least 1 hour prior to electrolysis. This process converts K_2CO_3 into $KHCO_3$ and saturates the electrolyte solution with CO_2. Potassium hydroxide electrolyte (0.1 M KOH) was prepared by dissolving solid potassium hydroxide into water and sparging for at least 30 minutes prior to electrolysis under CO_2.

Electrode Preparation

Before each experiment, copper foil was polished to a mirror-like finish using diamond paste (3 μm, then 1 μm) followed by rinsing with water and drying with a stream of nitrogen gas. The copper foil was then electropolished using the following method: in an 85% phosphoric acid bath, +400 mA was applied to the Cu foil until a potential of +2.3 V versus carbon rod was reached, and this potential was held for 5 minutes. The foil was subsequently washed with nano-pure water and dried under a stream of nitrogen gas. Platinum foil as the counter electrode was rinsed with water and flame-annealed using a butane torch for 10 s.

Electrochemistry

Electrochemical Measurements in the Flow Cell

Chronoamperometry measurements were carried out in a custom-made PEEK flow cell setup similar to the one reported by Ager and co-workers using a copper foil as the working electrode and a platinum foil as the counter electrode.[32] The cathode compartment was separated from the anode compartment by a Selemion AMV anion-exchange membrane (AGC Engineering Co.). All potentials

were measured versus a leakless Ag/AgCl reference electrode (Innovative Instruments) with an outer diameter of 5 mm that was inserted into the cathode compartment. The reference electrode was calibrated against H^+/H_2 on Pt in a 0.5 M sulfuric acid solution (0 V vs. standard hydrogen electrode) and saturated calomel electrode (SCE) (+0.241 V saturated vs. standard hydrogen electrode). All electrochemical measurements were carried out using a Biologic VMP3 multichannel potentiostat. The applied potentials were converted to the reversible hydrogen electrode (RHE) scale with iR correction through the following equation:

$$E_{corrected}\ (\text{vs. RHE}) = E_{applied}\ (\text{vs. Ag/AgCl}) + (0.059 \times \text{pH}) + 0.210 + (0.15)\ iR$$

where i is the current at each applied potential and R is the equivalent series resistance measured via electrochemical impedance spectroscopy (EIS) in the frequency range of 10^5 – 0.1 Hz with an amplitude of 10 mV.

Potentiostatic electrochemical impedance spectroscopy (PEIS) measurements were carried out prior to each electrolysis experiment to determine the Ohmic resistance of the flow cell. The impedance measurements were carried out at frequencies ranging from 200 kHz to 100 MHz to measure the solution resistance. A Nyquist plot was plotted and in the low-frequency part, a linear fit was performed, and the axis intersection was calculated. The value of this intersection represents the Ohmic resistance of the cell. An average of 3 measurements was taken to calculate the value of R. Typically, resistance measurements ranged from 40 to 50 Ω.

All chronoamperometric experiments were performed for 35 min at 25 °C using a CO_2-saturated electrolyte of choice. In experiments where an additive was used, a 10 mM solution of the materials was prepared and injected into the cathode compartment. The same electrolyte was used in the anode without any additive. The potentiostat was set to compensate for 85 % of the Ohmic drop, with the remaining 15 % being compensated for after the measurements. The effluent gas stream coming from

the flow cell (5 mL/min) was flowed into the sample loops of a gas chromatograph (GC-FID/TCD, SRI 8610C, in Multi Gas 5 configuration) equipped with HayeSep D and Molsieve 5A columns. Methane, ethylene, ethane, and carbon monoxide were detected by a methanizer-flame ionization detector (FID) and the hydrogen was detected by a thermal conductivity detector (TCD). Every 15 minutes, 2 mL of gas was sampled to determine the concentration of gaseous products. After electrolysis, the liquid products in both catholytes and anolytes were quantified by both HPLC (Thermo Scientific Ultimate 3000) and ^{1}H NMR spectroscopy (Bruker 400 MHz Spectrometer).

For variable partial pressure CO_2 (pCO_2) experiments, the standard electrolyte mixture (0.1 M KH_2PO_4/H_3PO_4, pH = 2) and applied potential (–1.4 V vs. RHE) were used for each partial pressure. Argon was utilized as the balance gas such that the total flow rate was remained at 10 sccm. For example, in the case where pCO_2 = 0.8 atm, the flow rate of CO_2 was 8 sccm and that of Ar was 2 sccm.

The Faradaic efficiencies for gaseous products was calculated from the following equations:

$$F_m = \frac{pF_v}{RT} \tag{1}$$

$$FE_{prod} = \frac{n_{prod}Fx_{prod}F_m}{i}. \tag{2}$$

F_m is the molar flow, defined by the pressure p, the volume flow F_v, the gas constant R, and temperature T. FE_{prod} is the Faradaic efficiency of a gaseous product $prod$, defined by the electron transfer coefficient of the product n_{prod}, Faraday's constant F, the fraction of the product x_{prod}, the molar flow F_m, and the current i.

Error bars shown in all figures and tables represent standard deviations from at least three replicate measurements.

X-ray photoelectron spectroscopy

XPS data were collected using a Kratos Axis Nova system with a base pressure of 1 × 10−9 Torr. The X-ray source was a monochromatic Al Kα line at 1486.6 eV. Data were analyzed using CasaXPS. Spectral energy for all spectra were calibrated using the Cu 2p3/2 peak (932.63 eV). To calculate the atomic ratio of elements, a Shirley background was subtracted. The core-level intensities were corrected by the analyzer transmission function and relative sensitivity factors to obtain corrected peak intensities, which were used to calculate the atomic ratios.

SUPPLEMENTARY FIGURES/DATA

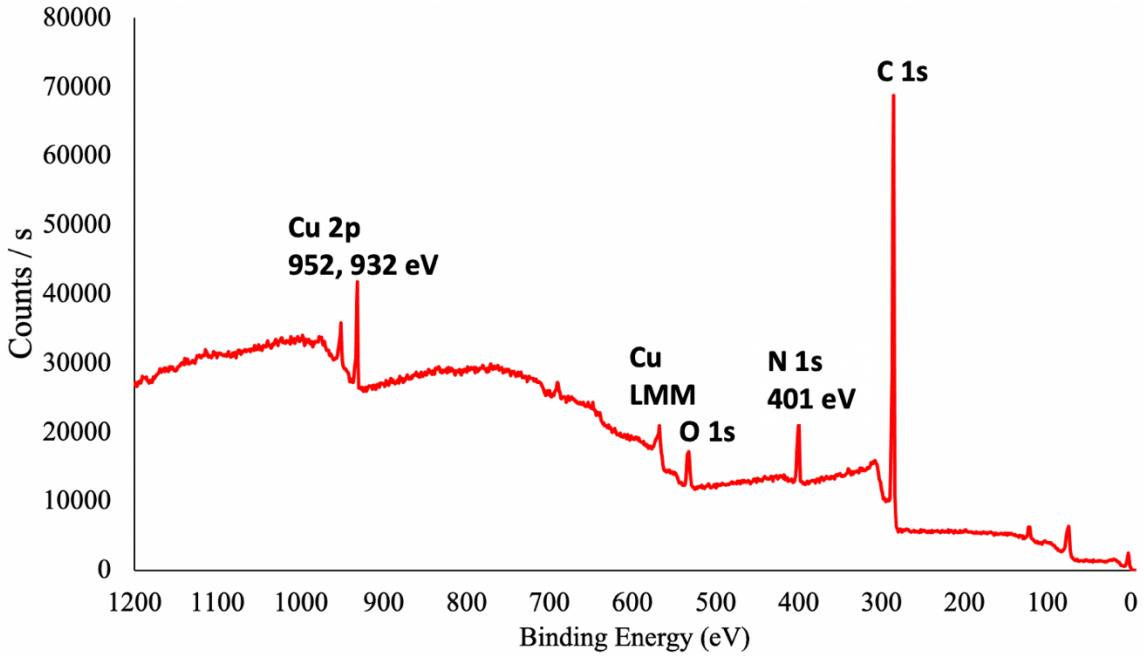

Figure 8. Complete XPS spectrum of film derived from electrodeposition of **1-Cl**.

Table 1. Selectivity profiles from electrolysis with various imidazolium species

	E (V vs. RHE)	H_2	CO	HCOOH	CH_4	C_2H_4	C_2H_5OH	C_3H_7OH	Total	j (mA/cm^2)
1-Cl	-1.1	28 ± 9	4 ± 1	12 ± 2	8 ± 2	23 ± 2	16 ± 3	13 ± 2	104 ± 10	–2.4 ± 0.4
Benzyl imidazolium	-1.1	86.0	1.6	7.1	1.7	0.8	0	0	97.1	–4.2
2	-1.1	31.1	4.6	20.5	1.5	15.2	11.0	14.0	98.1	–1.4
Bare Cu	-1.1	45 ± 7	1.7 ± 0.5	4.7 ± 0.3	16 ± 4	20 ± 3	6 ± 1	1.0 ± 0.2	98 ± 6	–6.4 ± 0.3

REFERENCES

(1) Nitopi, S.; Bertheussen, E.; Scott, S. B.; Liu, X.; Engstfeld, A. K.; Horch, S.; Seger, B.; Stephens, I. E. L.; Chan, K.; Hahn, C.; et al. Progress and Perspectives of Electrochemical CO2 Reduction on Copper in Aqueous Electrolyte. *Chem. Rev.* **2019**, *119* (12), 7610–7672.

(2) Hori, Y.; Kikuchi, K.; Suzuki, S. PRODUCTION OF CO AND CH4 IN ELECTROCHEMICAL REDUCTION OF CO2 AT METAL ELECTRODES IN AQUEOUS HYDROGENCARBONATE SOLUTION. *Chem. Lett.* **1985**, *14* (11), 1695–1698.

(3) Kuhl, K. P.; Cave, E. R.; Abram, D. N.; Jaramillo, T. F. New Insights into the Electrochemical Reduction of Carbon Dioxide on Metallic Copper Surfaces. *Energy Environ. Sci.* **2012**, *5* (5), 7050–7059.

(4) Murata, A.; Hori, Y. Product Selectivity Affected by Cationic Species in Electrochemical Reduction of CO2 and CO at a Cu Electrode. *Bull. Chem. Soc. Jpn.* **1991**, *64* (1), 123–127.

(5) Thevenon, A.; Rosas-Hernández, A.; Fontani Herreros, A. M.; Agapie, T.; Peters, J. C. Dramatic HER Suppression on Ag Electrodes via Molecular Films for Highly Selective CO2 to CO Reduction. *ACS Catal.* **2021**, *11* (8), 4530–4537.

(6) Thevenon, A.; Rosas-Hernández, A.; Peters, J. C.; Agapie, T. In-Situ Nanostructuring and Stabilization of Polycrystalline Copper by an Organic Salt Additive Promotes Electrocatalytic CO2 Reduction to Ethylene. *Angew. Chemie Int. Ed.* **2019**, *58* (47), 16952–16958.

(7) Li, F.; Thevenon, A.; Rosas-Hernández, A.; Wang, Z.; Li, Y.; Gabardo, C. M.; Ozden, A.; Dinh, C. T.; Li, J.; Wang, Y.; et al. Molecular Tuning of CO2-to-Ethylene Conversion. *Nature* **2020**, *577* (7791), 509–513.

(8) Han, Z.; Kortlever, R.; Chen, H.-Y.; Peters, J. C.; Agapie, T. CO2 Reduction Selective for C≥2 Products on Polycrystalline Copper with N-Substituted Pyridinium Additives. *ACS Cent. Sci.* **2017**, *3* (8), 853–859.

(9) Nie, W.; Heim, G. P.; Watkins, N. B.; Agapie, T.; Peters, J. Organic Additive-Derived Films on Cu Electrodes Promote Electrochemical CO2 Reduction to C2+ Products Under Strongly Acidic Conditions. *Angew. Chemie Int. Ed.* **2023**, *n/a* (n/a).

(10) Cheng, B.; Du, J.; Yuan, H.; Tao, Y.; Chen, Y.; Lei, J.; Han, Z. Selective CO2 Reduction to Ethylene Using Imidazolium-Functionalized Copper. *ACS Appl. Mater. Interfaces* **2022**, *14* (24), 27823–27832.

(11) Buckley, A. K.; Cheng, T.; Oh, M. H.; Su, G. M.; Garrison, J.; Utan, S. W.; Zhu, C.; Toste, F. D.; Goddard, W. A. I. I. I.; Toma, F. M. Approaching 100% Selectivity at Low Potential on Ag for Electrochemical CO2 Reduction to CO Using a Surface Additive. *ACS Catal.* **2021**, *11* (15), 9034–9042.

(12) Rosen, B. A.; Salehi-Khojin, A.; Thorson, M. R.; Zhu, W.; Whipple, D. T.; Kenis, P. J. A.; Masel, R. I. Ionic Liquid–Mediated Selective Conversion of CO2 to CO at Low Overpotentials. *Science (80-.).* **2011**, *334* (6056), 643–644.

(13) Chen, X.; Chen, J.; Alghoraibi, N. M.; Henckel, D. A.; Zhang, R.; Nwabara, U. O.; Madsen, K. E.; Kenis, P. J. A.; Zimmerman, S. C.; Gewirth, A. A. Electrochemical CO2-to-Ethylene Conversion on Polyamine-Incorporated Cu Electrodes. *Nat. Catal.* **2021**, *4* (1), 20–27.

(14) Wei, X.; Yin, Z.; Lyu, K.; Li, Z.; Gong, J.; Wang, G.; Xiao, L.; Lu, J.; Zhuang, L. Highly Selective Reduction of CO2 to C2+ Hydrocarbons at Copper/Polyaniline Interfaces. *ACS Catal.* **2020**, *10* (7), 4103–4111.

(15) Watkins, N. B.; Wu, Y.; Nie, W.; Peters, J. C.; Agapie, T. In Situ Deposited Polyaromatic Layer Generates Robust Copper Catalyst for Selective Electrochemical CO2 Reduction at Variable PH. *ACS Energy Lett.* **2023**, *8* (1), 189–195.

(16) Han, X.; Yu, Z.; Qu, J.; Qi, T.; Guo, W.; Zhang, G. Measurement and Correlation of Solubility Data for CO2 in NaHCO3 Aqueous Solution. *J. Chem. Eng. Data* **2011**, *56* (4), 1213–1219.

(17) Pérez-Salado Kamps, Á.; Tuma, D.; Xia, J.; Maurer, G. Solubility of CO2 in the Ionic Liquid [Bmim][PF6]. *J. Chem. Eng. Data* **2003**, *48* (3), 746–749.

(18) Wang, J.; Cheng, T.; Fenwick, A. Q.; Baroud, T. N.; Rosas-Hernández, A.; Ko, J. H.; Gan, Q.; Goddard III, W. A.; Grubbs, R. H. Selective CO2 Electrochemical Reduction Enabled by a Tricomponent Copolymer Modifier on a Copper Surface. *J. Am. Chem. Soc.* **2021**, *143* (7), 2857–2865.

(19) Kim, C.; Bui, J. C.; Luo, X.; Cooper, J. K.; Kusoglu, A.; Weber, A. Z.; Bell, A. T. Tailored Catalyst Microenvironments for CO2 Electroreduction to Multicarbon Products on Copper Using Bilayer Ionomer Coatings. *Nat. Energy* **2021**, *6* (11), 1026–1034.

(20) He, H.; Zhong, M.; Adzima, B.; Luebke, D.; Nulwala, H.; Matyjaszewski, K. A Simple and Universal Gel Permeation Chromatography Technique for Precise Molecular Weight Characterization of Well-Defined Poly(Ionic Liquid)S. *J. Am. Chem. Soc.* **2013**, *135* (11), 4227–4230.

(21) Koshy, D. M.; Akhade, S. A.; Shugar, A.; Abiose, K.; Shi, J.; Liang, S.; Oakdale, J. S.; Weitzner, S. E.; Varley, J. B.; Duoss, E. B.; et al. Chemical Modifications of Ag Catalyst Surfaces with Imidazolium Ionomers Modulate H2 Evolution Rates during Electrochemical CO2 Reduction. *J. Am. Chem. Soc.* **2021**, *143* (36), 14712–14725.

(22) Bélanger, D.; Pinson, J. Electrografting: A Powerful Method for Surface Modification. *Chem. Soc. Rev.* **2011**, *40* (7), 3995–4048.

(23) Shkrob, I. A. Deprotonation and Oligomerization in Photo-, Radiolytically, and Electrochemically Induced Redox Reactions in Hydrophobic Alkylalkylimidazolium Ionic Liquids. *J. Phys. Chem. B* **2010**, *114* (1), 368–375.

(24) Michez, R.; Doneux, T.; Buess-Herman, C.; Luhmer, M. NMR Study of the Reductive Decomposition of [BMIm][NTf2] at Gold Electrodes and Indirect Electrochemical Conversion of CO2. *ChemPhysChem* **2017**, *18* (16), 2208–2216.

(25) Characterization is ongoing of the film derived from **1-Cl** in addition to the product of co-electrolysis of **IsqPh** and **1-Cl**, where XPS is yet to be performed on 1-Cl drop casted on a surface; this compound is a viscous oil at room temperature, thus it would be most appropriate to measure at ambient pressure. No Title.

(26) Lu, S.; Wang, Y.; Xiang, H.; Lei, H.; Xu, B. Bin; Xing, L.; Yu, E. H.; Liu, T. X. Mass Transfer Effect to Electrochemical Reduction of CO2: Electrode, Electrocatalyst and Electrolyte. *J. Energy Storage* **2022**, *52*, 104764.

(27) Yano, H.; Tanaka, T.; Nakayama, M.; Ogura, K. Selective Electrochemical Reduction of CO2 to Ethylene at a Three-Phase Interface on Copper(I) Halide-Confined Cu-Mesh Electrodes in Acidic Solutions of Potassium Halides. *J. Electroanal. Chem.* **2004**, *565* (2), 287–293.

(28) Ooka, H.; Figueiredo, M. C.; Koper, M. T. M. Competition between Hydrogen Evolution and Carbon Dioxide Reduction on Copper Electrodes in Mildly Acidic Media. *Langmuir* **2017**, *33* (37), 9307–9313.
(29) Ge, Q.; Hu, Y.; Li, B.; Wang, B. Synthesis of Conjugated Polycyclic Quinoliniums by Rhodium(III)-Catalyzed Multiple C–H Activation and Annulation of Arylpyridiniums with Alkynes. *Org. Lett.* **2016**, *18* (10), 2483–2486.
(30) Hong, A. Y.; Vanderwal, C. D. A Synthesis of Alsmaphorazine B Demonstrates the Chemical Feasibility of a New Biogenetic Hypothesis. *J. Am. Chem. Soc.* **2015**, *137* (23), 7306–7309.
(31) Pangborn, A. B.; Giardello, M. A.; Grubbs, R. H.; Rosen, R. K.; Timmers, F. J. Safe and Convenient Procedure for Solvent Purification. *Organometallics* **1996**, *15* (5), 1518–1520.
(32) Lobaccaro, P.; Singh, M. R.; Clark, E. L.; Kwon, Y.; Bell, A. T.; Ager, J. W. Effects of Temperature and Gas–Liquid Mass Transfer on the Operation of Small Electrochemical Cells for the Quantitative Evaluation of CO2 Reduction Electrocatalysts. *Phys. Chem. Chem. Phys.* **2016**, *18* (38), 26777–26785.

APPENDIX C

APPLICATIONS IN COORDINATION CHEMISTRY OF HETEROATOM-CONTAINING POLYAROMATIC HYDROCARBONS

ACKNOWLEDGEMENTS

I am grateful to Mike Takase and the Beckman Institute for assistance with X-ray crystallography. This material is based on work performed by the Liquid Sunlight Alliance, which is supported by the U.S. Department of Energy, Office of Science, Office of Basic Energy Sciences, Fuels from Sunlight Hub under Award DE-SC0021266.

INTRODUCTION

The incorporation of nitrogen moieties has allowed nanographene mimics to serve as ligands to metal complexes, creating unprecedented electrocatalytic and photophysical properties. Draper and co-workers reported one of the first syntheses of a nitrogen-doped hexabenzocoronene (HBC) and demonstrated its ability to serve as a ligand.[1,2] The authors were able to characterize the HBC ligand via NMR spectroscopy and examine the absorption and emission spectra, but no solid state characterization from single-crystal X-ray diffraction was obtained.

Addition of a metal impacted photophysics of the HBC.[3] The $[Ru(bpy)_2]^{2+}$ complex of **iii** was prepared and characterized via NMR (Scheme 1). This complex possessed a broad emission feature at λ_{max} = 880 nm, lower in energy than that of $[Ru(bpy)_3]^{2+}$. The phenomenon is explained by the remarkable electron delocalization provided by the nanographene ligand.

Metal complexes of nitrogen-doped nanographenes have also been prepared in the context of electrocatalysis. The role of metal atoms as dopants in nitrogen-doped graphene has been investigated to understand how single atom catalysts (SACs) facilitate electrochemical transformations.[4–11] However, this nomenclature does not consider the putative role of the graphene environment in facilitating electrocatalysis. To gain further insight into the effects of metal centers on the properties of N-containing extended π systems, discrete molecular species can be prepared and investigated for electrocatalysis. Li and co-workers synthesized an HBC-containing ligand coordinated to $[Re(CO)_3Cl]$ (Figure 1), facilitating CO_2 reduction (CO_2R) at 800-mV lower overpotentials.[4,7]

Scheme 1. Metalations reported by Draper and co-workers. Conditions: (i) $[Ru(bpy)_2Cl_2]$. (ii) $[Pd(\eta^3\text{-}C_3H_5)(CH_3CN)_2](NO_3)$

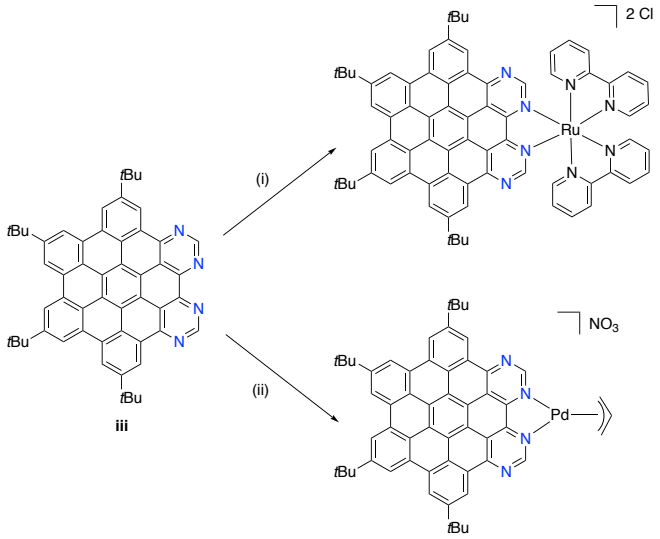

Nanographene bearing other main group heteroatoms has been explored by Wagner and co-workers to explore effects on photoluminescence (Figure 2).[12,13] Their work has highlighted a facile, modular synthesis that involves oxidative photocyclization for graphene doped with either nitrogen, boron, silicon, or different combinations thereof (Scheme 2). Notably, the coordinating properties of these systems are underexplored.

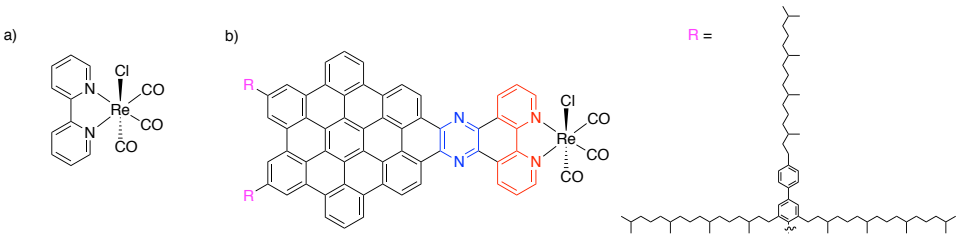

Figure 1. Lehn complexes for CO_2R. a) Tricarbonylbipyridinechlororhenium(I) catalyst for CO_2 reduction. b) Analogous rhenium complex reported by Li and co-workers in which the "bipyridine" ligand is linked to a substituted hexabenzocoronene via a pyrazine.

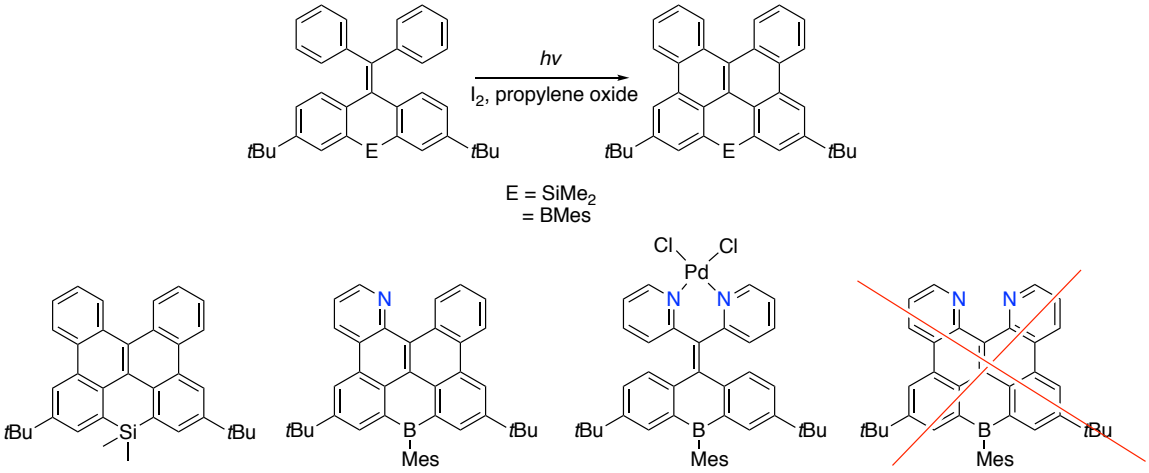

Figure 2. Top: Oxidative photocyclization of a generic compound explored by the Wagner group. Bottom: Representative previously reported extended π systems. Note that the compound on the far right (crossed-out in red) was not observed.

The targeted synthesis of **12b** (Scheme 2) resulted in the half-cyclized compound **12a**. Attempts to run the photolysis longer were unsuccessful in yielding **12b**; attempting to lock the pyridines into a *syn* conformation via protonation of **11a** were also unsuccessful.[12] Although **11a-PdCl₂** was isolated, photocyclization was not feasible owing to the complex's insolubility in choice appropriate solvents (benzene, cyclohexane, and toluene).[14]

Scheme 2. 11a is photocyclized into **12a** instead of **12b**.[12]

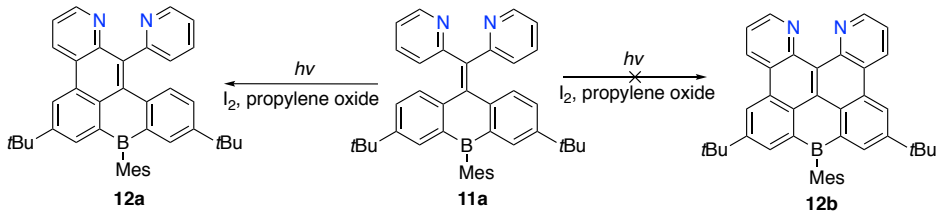

RESULTS AND DISCUSSION

i) Coordination chemistry of heteroatom-containing polyaromatic hydrocarbons

Scheme 3. Synthesis of compound **6a**.

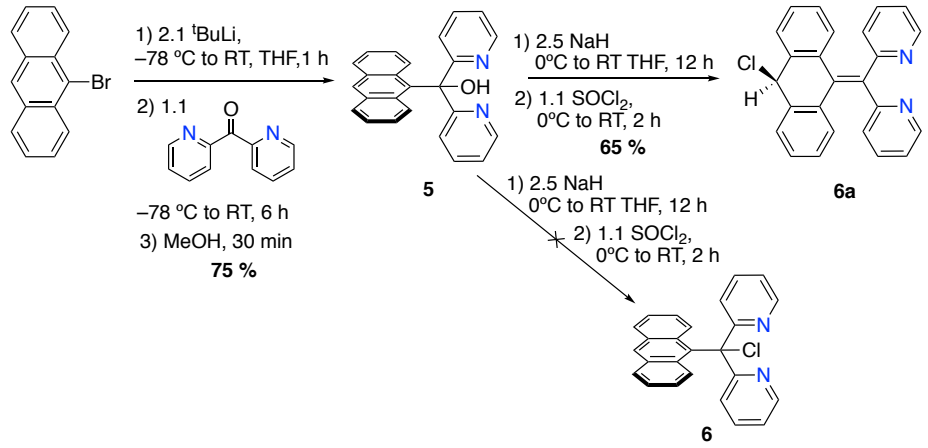

Compound **6** was targeted as an intermediate for cyclodehydrogenation into an extended π system by forming carbon-carbon bonds between the anthracene and the 3 position of pyridines (Scheme 3). 9-bromoanthracene is lithiated with *tert*-butyllithium and quenched with di-2-pyridyl ketone. Addition of methanol results in anthracen-9-yldi(pyridin-2-yl)methanol (**5**). Deprotonation of **5** with sodium hydride followed by addition of thionyl chloride provided compound **6a** instead of compound **6**. The ^{1}H NMR spectrum in C_6D_6 reveals a singlet at 5.91 ppm, which is assigned as the benzylic proton at the 10 position of the hydroanthracene backbone, geminal to the chloride. Single-crystal XRD also unambiguously reveals that the structure is appropriately represented as **6a** rather than **6** (Figure 3). Chlorinations with thionyl chloride typically proceed via an ion-paired intermediate, which leaves the carbon partially positive.[15] The carbocation initially forms at the tertiary carbon, but it is likely unstable here because of the pyridines and rearranges to the 10 position of the anthracene. Attempts to ring-close **6a** via either oxidative photocyclization or anionic radical coupling have thus far been unsuccessful.

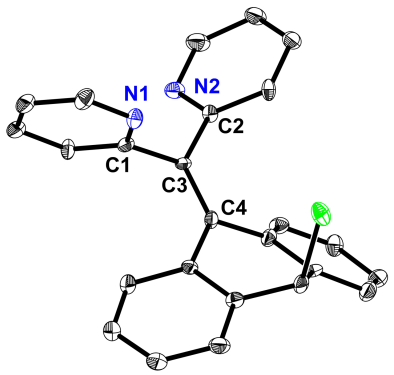

C1-N1: 1.354(7) Å
C2-N2: 1.347(7) Å
C1-C3: 1.470 (5) Å
C2-C3: 1.470 (5) Å
C3-C4: 1.369 (5) Å

Figure 3. Solid state structure of **6a** as determined by single-crystal XRD. Thermal ellipsoids shown at 50% probability. Hydrogen atoms are omitted for clarity.

Metalations of **6a** with Zn^{2+} precursors were carried out to understand the coordination chemistry of the 2,2'-dipyridyl motif and to begin developing potential dioxygen-activating complexes. Similar dipyridyl olefin ligands have been successfully metalated with zinc chloride, palladium(II) chloride, and iridium precursors.[16,17]

Scheme 4. Synthesis of **6a-ZnCl$_2$** from **6a**.

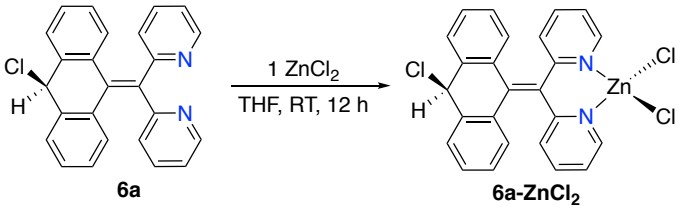

6a **6a-ZnCl$_2$**

Stirring **6a** with 1 equivalent of $ZnCl_2$ in THF at room temperature (Scheme 4) yields a pink suspension. Upon filtration, concentration of filtrate, and extraction with benzene results in a colorless solid. Crystals grown from vapor diffusion of pentane into a saturated dichloromethane solution were submitted for single crystal XRD studies. The solid-state structure reveals a four-coordinate tetrahedral zinc complex with the pyridines bound to the zinc center (Figure 4). The C3 and C4 distance of 1.342 Å is indicative of a double bond. Stilbene-type oxidative photocyclization has been unsuccessful so far. Metalations of **6a** with

$Zn(OTf)_2$ have been attempted, but intractable mixtures were typically observed in the ^1H NMR spectra.

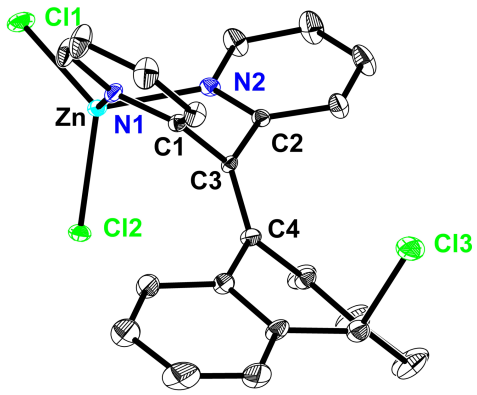

Zn-N1: 2.051(4) Å
Zn-N2: 2.051(4) Å
Zn-Cl1: 2.201(18) Å
Zn-Cl2: 2.235(16) Å
C1-N1: 1.345(5) Å
C2-N2: 1.345(5) Å
C1-C3: 1.498 (7) Å
C2-C3: 1.498 (6) Å
C3-C4: 1.342 (7) Å

∠C1-C3-C2: 115.0(4)º

Figure 4. Solid state structure of **6a-ZnCl₂** as determined by single-crystal XRD. Thermal ellipsoids shown at 50% probability. Dichloromethane molecules and hydrogen atoms are omitted for clarity.

Generation of an anionic dipyridylmethanide motif was investigated from complex **6a-ZnCl₂** by adding 3 equivalents of benzyl potassium in THF at room temperature (Scheme 5). ^1H NMR analysis suggest **6a-ZnBn** to be the major product. Extraction of the crude solid with benzene and crystallization from slow pentane diffusion into a saturated dichloromethane solution resulted in X-ray quality crystals. The solid-state structure of **6a-ZnBn** is provided in Figure 5. Notably, the chloride is not evident; instead, a 9-anthracenyl substituent is generated. The bond angle C1-C3-C2 is significantly more open in **6a-ZnBn** by 14.6º compared to **6a-ZnCl₂**. There are slight contractions of ~0.05 Å in the C1-C3 and C2-C3 distances and elongation of the C3-C4 distance by 0.17 Å.

Scheme 5. Synthesis of **6a-ZnBn** from **6a-ZnCl$_2$**.

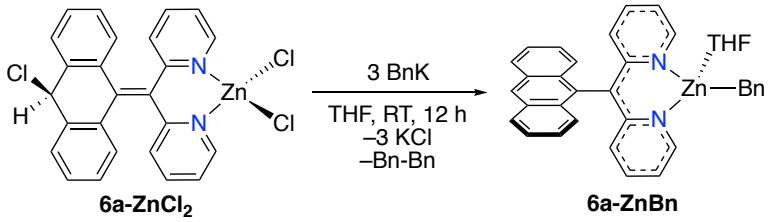

To explain the formation of **6a-ZnBn**, it is proposed that benzyl potassium performs a nucleophilic attack at each chloride bound to the zinc center to release two equivalents of potassium chloride. Dibenzyl zinc is reportedly prepared from reaction of $ZnCl_2$ and 2 equivalents of benzyl magnesium chloride;[18] it is plausible that benzyl potassium will exhibit similar reactivity to the analogous benzyl Grignard. Bibenzyl is observed via gas chromatography-mass spectrum (GC-MS) of the crude reaction mixture (m/z: 182.11, retention time: 10.637 min), suggesting that all three equivalents of BnK are required to generate **6a-ZnBn**. Reacting 2 equivalents of benzyl potassium with **6a-ZnCl$_2$** to make the proposed dibenzyl zinc intermediate was unsuccessful and lead to intractable mixtures.

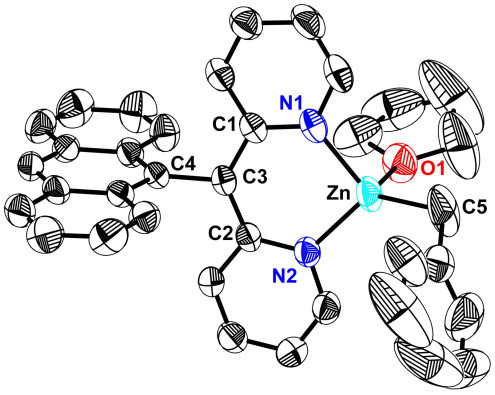

Zn-N1: 1.986(1) Å
Zn-N2: 1.979(2) Å
C1-N1: 1.365(1) Å
C2-N2: 1.368(4) Å
C1-C3: 1.427(5) Å
C2-C3: 1.419(4) Å
C3-C4: 1.510(5) Å
Zn-C5: 1.992(5) Å
Zn-O1: 2.154(5) Å
∠C1-C3-C2: 129.54(4)°

Figure 5. Solid state structure of **6a-ZnBn** as determined by single-crystal XRD. Thermal ellipsoids displayed at 50% probability. Hydrogen atoms omitted for clarity.

Despite being unable so far to annulate the pyridines with the 9-anthracenyl substituent, the delocalization across the pyridines can serve as a model of an SAC active site.[19] Alkyl zinc complexes are non-innocent in reactions with dioxygen; an oxygen insertion compound is typically generated.[20-21] Before pursuing reactivity studies with O_2, attempts to provide substituents with greater steric bulk than benzyl were carried out (Scheme 5). Reacting a benzene solution of **6a-ZnBn** with dibenzoylmethane, 2,4,6-trimethylphenol, 4-*tert*-butylbenzoic acid, or phenanthrolinium triflate results in the formation of an orange precipitate bearing resonances of the 9-anthracenyldipyridylmethanide motife; no resonances originating from the protonolysis reagent is observed. ^{1}H NMR of the mother liquor in each case reveals an intractable mixture. Further characterization with single crystal XRD is ongoing.

Given previously reported success of photocyclization into heteroatom-doped nanographene, attention was turned to compounds explored by Wagner and co-workers.[12,13] Furthermore, coordination chemistry of the annulated species was not reported. Towards preparation of the ligand, diphenylmethane is reacted with an excess of *tert*-butyl chloride in the presence of aluminum trichloride to install *tert*-butyl groups in the 4 and 4' positions, respectively (Scheme 6). 4,4'-di-*tert*-butyl-diphenylmethane **7** is dissolved in dichloromethane and treated with bromine in the presence of iron powder to yield the dibromide **8**. Lithium-halogen exchange followed by quenching with dichlorodimethylsilane results in **9**. The dimethylsilyl group can be exchanged for an aryl borane in a stepwise fashion, which is initiated by stirring **9** in neat boron tribromide to yield the bromoboranthracene **9-BBr**. Nucleophilic attack from mesityl magnesium bromide provides a bulky substituent to facilitate the stability in air of **9a** and subsequent intermediates.

Silylation with trimethylsilyl chloride provides **10a**, and Peterson olefination with di-2-pyridyl ketone results in **11a**. The synthesis of **12a** was reproduced from the literature.

Scheme 6. Synthesis of **12a** and **11a**.

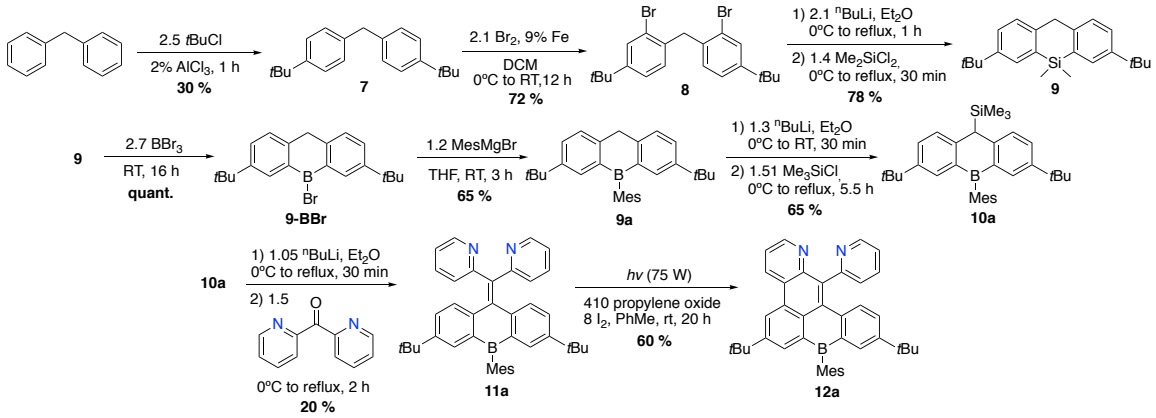

Next, the coordination chemistry of **11a** was investigated. Stirring 1 equivalent of $ZnCl_2$ in a THF solution of **11a** (Scheme 7) results in the formation a pale-yellow solid upon extraction with benzene. The ^1H NMR spectrum is indicative of formation of **11a-$ZnCl_2$**, and it possesses a similar pattern to the NMR spectrum of **11a-$PdCl_2$**. Significant structural distortion to the olefin is brought about by metalation. Particularly, the benzylic protons on the mesityl group are all chemically inequivalent due to the lack of front-back symmetry (Figure 6). **11a-$ZnCl_2$** is entirely soluble in THF, benzene, and toluene in contrast to **11a-$PdCl_2$**. Single-crystals grown from slow evaporation of pentane into a saturated THF solution are awaiting XRD studies, but the photolysis of **11a-$ZnCl_2$** was investigated to determine if a fully annulated species could be realized in the presence of a metal.

Scheme 7. Synthesis of **11a-ZnCl$_2$** and **13a-ZnCl$_2$**.

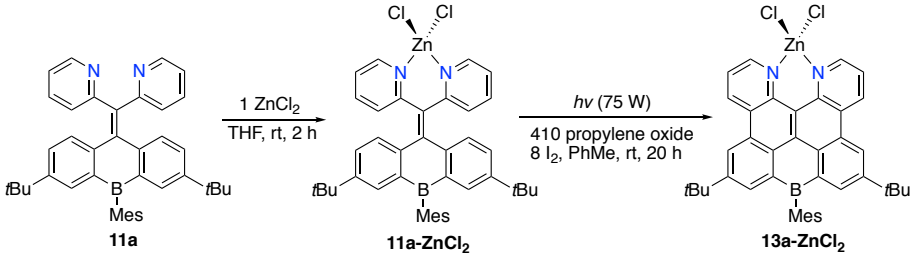

Investigating the oxidative photocyclization of **11a-ZnCl$_2$** by ^{1}H NMR for 24 h under the same conditions as for the synthesis of **12a** reveals the generation of a single species with greater symmetry than **11a-ZnCl$_2$.** Notably, the *ortho* benzylic protons on the mesityl group are now represented by one resonance (Figure 6). The ^{1}H NMR spectrum is assigned to the compound **13a-ZnCl$_2$** (Scheme 7).

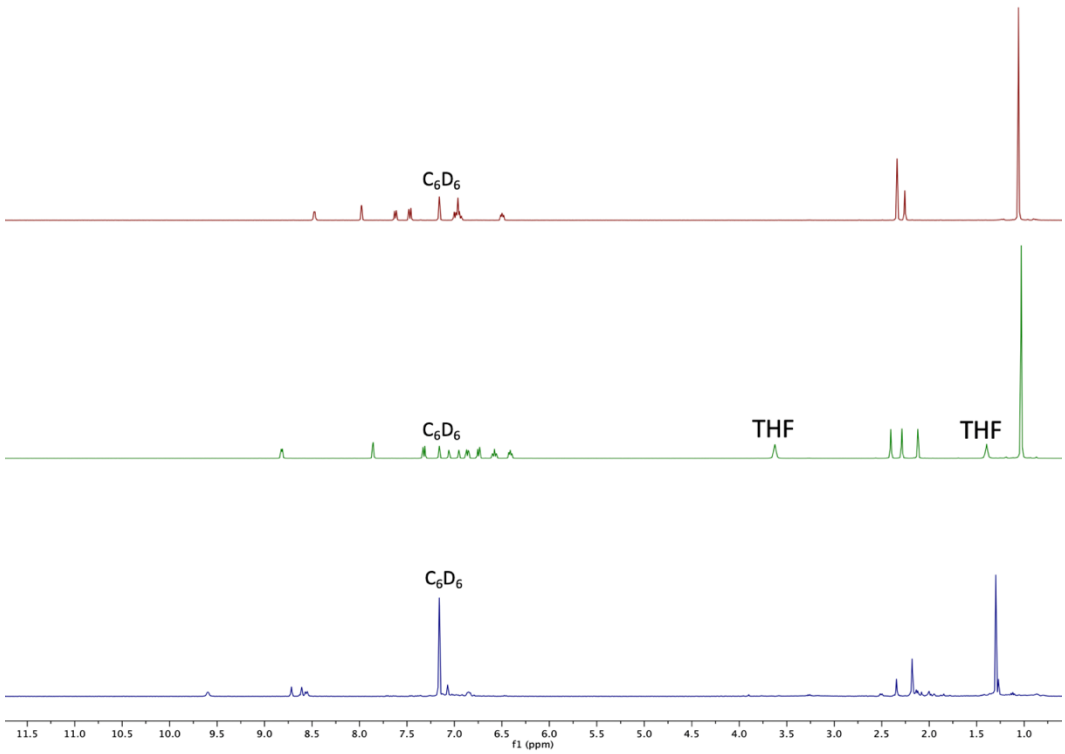

Figure 6. ^{1}H NMR spectra (400 MHz, C_6D_6) of **11a** (top), **11a-ZnCl$_2$** (middle), and **13a-ZnI$_2$** (bottom).

Single crystals were obtained from evaporation in a concentrated C_6H_6 solution into a pool of hexamethyldisiloxane (HMDSO). The solid state structure (Figure 7) of **13a-ZnI$_2$** confirms the formation of a Zn complex bearing a B, N-containing polyaromatic hydrocarbon ligand;[22] metal complexation and formation of a fully conjugated polyaromatic hydrocarbon had eluded synthesis according to the work of Wagner and co-workers.[12,13,23] The mesityl group sits possesses a ~90º dihedral angle with respect to the π system. To establish a tetrahedral geometry around Zn, the metal center lies outside of the plane of the π system. Moreover, this is necessary to accommodate the nitrogen atoms pointing above the plane.

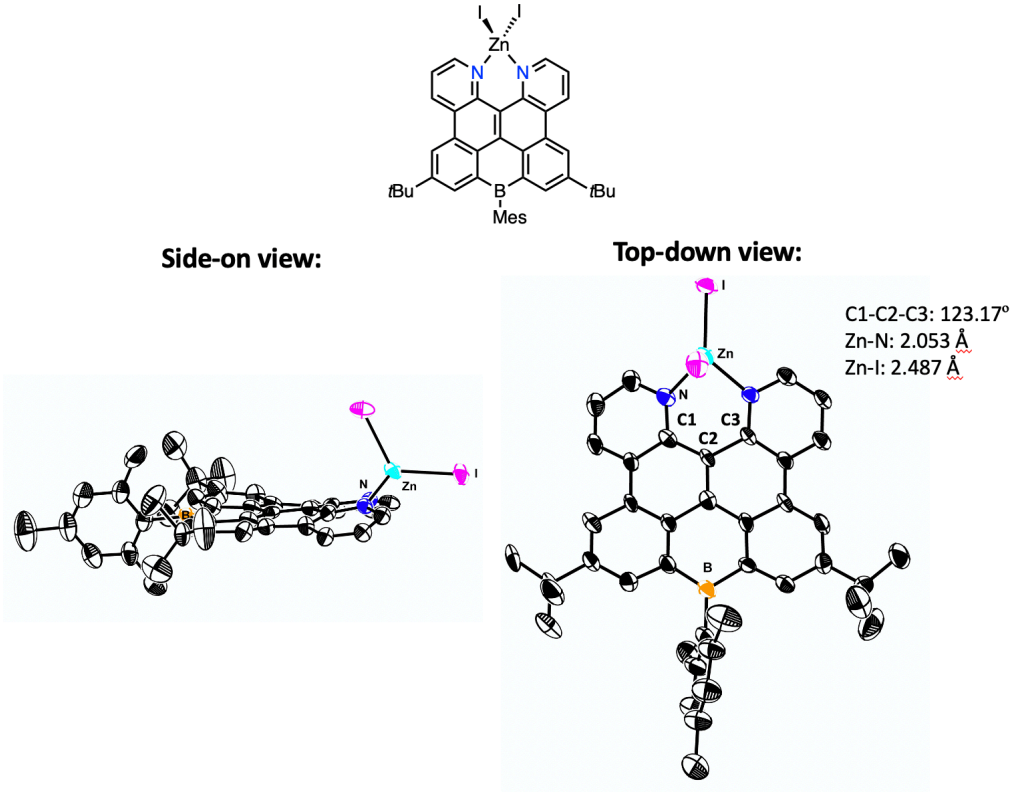

Figure 7. Solid state structure of **13a-ZnI$_2$** as determined by single-crystal XRD. Thermal ellipsoids displayed at 50% probability. Hydrogen atoms were omitted for clarity.

Scheme 8. Proposed synthesis of **Znbpy** and **ZnAcac**

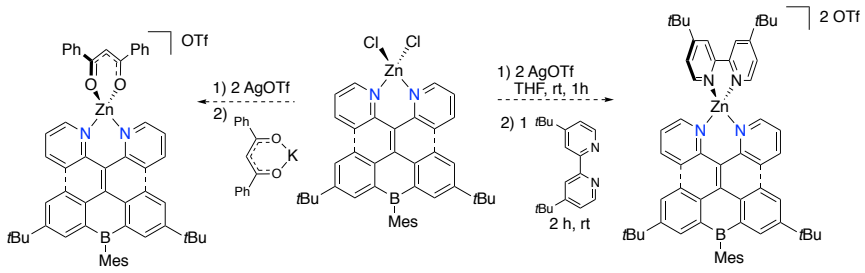

Halide abstraction was performed followed by addition of a solubilizing bidentate ligand (4,4'-di-*tert*-butyl-2,2'-bipyridine or dibenzoylmethyl potassium) to make a cationic species, proposed to have relatively positive reduction potentials ammenable for oxygen reduction (Scheme 8). Attempts to incorporate the bipyridine lead to promising NMR spectra, but crystallization attempts have been thus far unsuccessful.

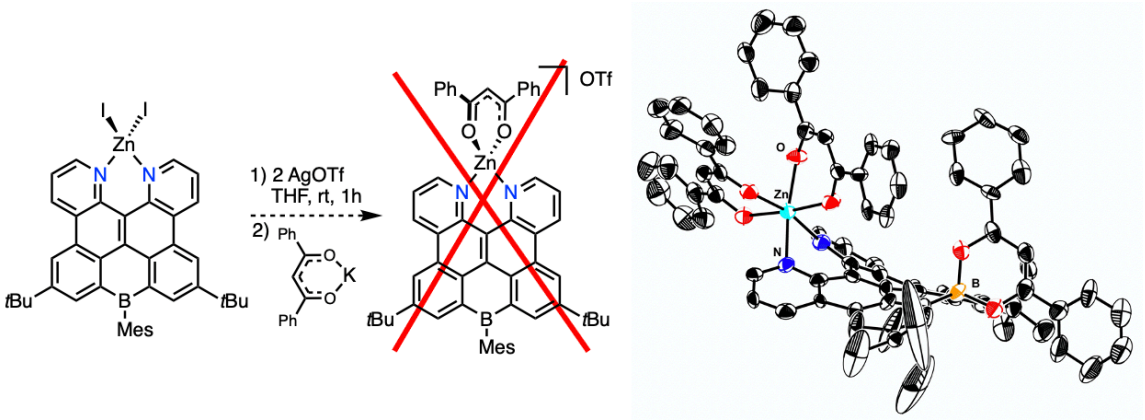

Figure 8. Attempted incorporation of **acac** and resulting solid state structure. Thermal ellipsoids drawn at 50% probability. Hydrogen atoms omitted for clarity.

Attempting to incorporate diphenylacetylacetonate (**acac**) resulted in formation a complex where two **acac** motifs were bound to Zn, forming a pseudooctahedral complex around the metal (Figure 8). Moreover, the mesityl group appeared to be substituted for an additional equivalent of **acac**. To circumvent this phenomenon, an analogous ligand bearing

2,4,6-triisopropylphenyl moiety at boron was sought after. Numerous isolation attempts of an analytically pure sample have been attempted.

ii) Attempts to isolate metal complexes of ***HPC-N$_{12}$(Ar^{tBu})$_6$*** *and* ***HPC-N$_{12}$(Ar^{OMe})$_6$***

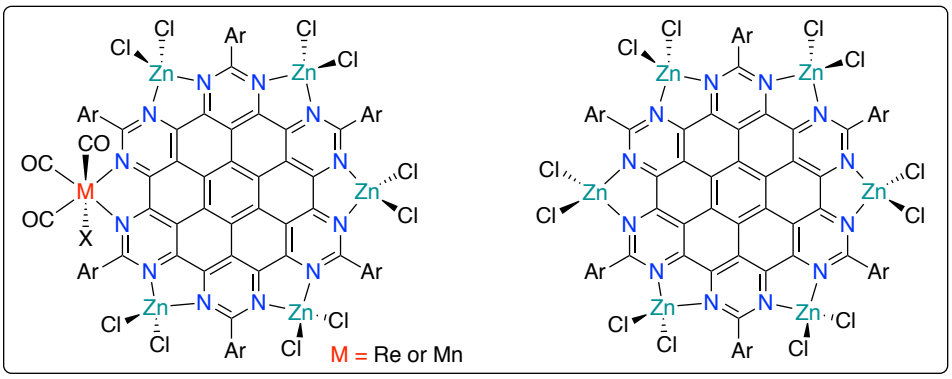

Figure 9. Proposed multi-metallic complexes from hexabenzocoronene compounds with twelve nitrogen dopants.

With the synthesis of **HPC-N$_{12}$(Ar^{tBu})$_6$** established (see Chapter VII), metal complexes were sought after that would be amenable to electrocatalytic CO_2R or oxygen reduction studies. Owing to the negative reduction potentials observed in the CV of **HPC-N$_{12}$(Ar^{tBu})$_6$**, complexation with zinc chloride was attempted to make these potentials more positive to facilitate ORR electrocatalysis.[24,25,26] Refluxing a THF solution of excess $ZnCl_2$ and **HPC-N$_{12}$(Ar^{tBu})$_6$** (Scheme 9) resulted in the formation of an orange precipitate with a rather complicated ^{1}H NMR spectrum that illustrated the presence of multiple species. The mother liquor contained no aromatic resonances. Unfortunately, crystallization of these crude mixtures proved to be quite challenging, and no definitive characterization of any components of this mixture was obtained.

Scheme 9. Proposed synthesis of **$LN_{12}(ZnCl_2)_6$**.

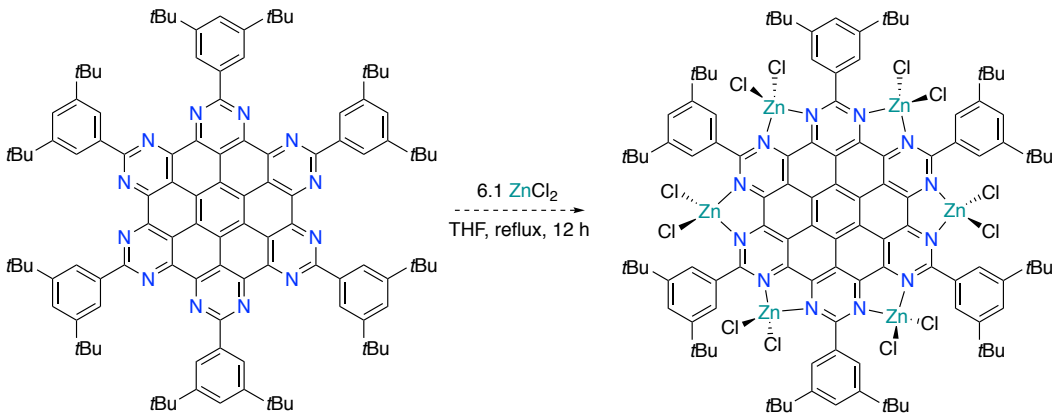

Reactions with one equivalent of $Mn(CO)_5Br$ in refluxing diethyl ether or toluene in the dark resulted in apparent unreacted starting material by ^1H NMR. Resonances corresponding to protons on **HPC-$N_{12}(Ar^{tBu})_6$** did not observably shift upfield or downfield, and no further characterization via single crystal XRD or mass spectrometry could be obtained. Infrared (IR) spectroscopy revealed intractable mixtures. Significant π-stacking may have played a role in inhibiting $Mn(CO)_5Br$ coordination. The HBC ligand developed by Li and co-workers likely circumvented any π-stacking with the development of long-chain aliphatic substituents. The steric bulk on **HPC-$N_{12}(Ar^{OMe})_6$** was envisioned to circumvent issues in metalating **HPC-$N_{12}(Ar^{tBu})_6$**.

Refluxing one equivalent of $Mn(CO)_5Br$ with **HPC-$N_{12}(Ar^{OMe})_6$** in the dark in diethyl ether lead to intractable mixtures by ^1H NMR spectroscopy. IR spectroscopy revealed three new ν(CO) stretches at 2044, 1988, and 1963 cm^{-1} distinct from the starting materials, and they are all blue-shifted compared to the analogous $Mn(bpy)(CO)_3Br$ complexes. Crystallization of these mixtures have not been fruitful thus far.

EXPERIMENTAL

General considerations. Unless otherwise specified, all operations involving air- or water-sensitive reagents were carried out in an MBraun drybox under a nitrogen atmosphere or using standard Schlenk and vacuum line techniques. Glassware was oven-dried at 140 ºC for 2 h prior to use on the Schlenk line or in the MBraun drybox. Tetrahydrofuran (THF), diethyl ether, toluene, pentane, and hexanes for air- and moisture-sensitive reactions were dried by the method of Grubbs.[27] Dry *N,N*-dimethylformamide (DMF) was purchased from Millipore Sigma and cannula transferred to freshly-activated 3 Å molecular sieves and stored in a Teflon-sealed Schlenk tube under N_2 atmosphere for 12 hours prior to use. Hexamethyldisiloxane were each vacuum transferred from sodium benzophenone ketyl. Deuterated solvents were purchased from Cambridge Isotope Laboratories and C_6D_6 vacuum transferred from sodium benzophenone ketyl before use. CD_2Cl_2 was vacuum transferred from CaH_2 before use. $CDCl_3$ was used as received. All solvents, once dried and degassed, were stored under a nitrogen atmosphere over 3 Å molecular sieves. 2-bromomesitylene, 2,4,6-triisopropylbromobenzene, dichlorodimethylsilane, and trimethylsilyl chloride were each distilled from CaH_2. Sodium hydride dispersion in oil was washed multiple times with hexanes and dried in vacuo before used. Benzyl potassium[28] and The synthesis for **7-9** and **9a-11a** were all carried out according literature-reported preparations.[12,13] All other reagents were used as received. ^{1}H, and ^{13}C{^{1}H} spectra were recorded on Varian Mercury 300 MHz or Varian 400 MHz spectrometers at ambient temperatures, unless otherwise denoted. ^{1}H and ^{13}C{^{1}H} NMR spectra are reported referenced internally to residual solvent peaks reported relative to tetramethylsilane. Gas chromatography-mass spectrometry (GC-MS) were performed on an Agilent 6890A instrument using a HP-5MS column (30 m length, 0.25 mm diameter, 0.50 μm film) and an Agilent 5973N mass-selective EI detector. Photolyses were conducted using an Oriel Instruments arc lamp housing and an Osram 75 W Xe arc lamp set to a current of 5.4 A.

Crystallographic Information: X-ray diffraction data was collected at 100 K (175 K for **LN_{12}**) on a Bruker PHOTON100 CMOS based diffractometer (microfocus sealed X-ray tube, Mo Kα (λ) = 0.71073 Å or Cu Kα (λ) = 1.54178 Å). All manipulations, including data collection, integration, and scaling, were carried out using the Bruker APEXII software. Absorption corrections were applied using SADABS. Structures were solved by direct methods using XS (incorporated into SHELXTL) and refined by using ShelXL least squares on Olex2-1.2.7 to convergence. All non-hydrogen atoms were refined using anisotropic displacement parameters. Hydrogen atoms were placed in idealized positions and were refined using a riding model. Most crystals included solvent-accessible voids that contained disordered solvent. In most cases the solvent could be modeled satisfactorily.

Synthesis

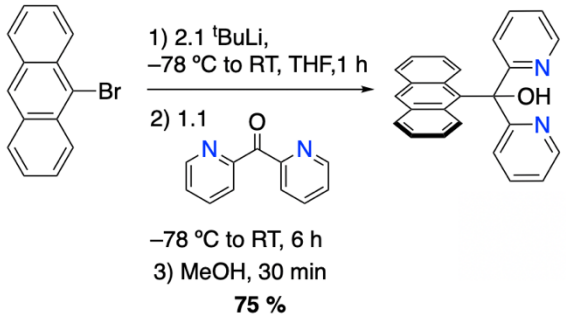

Anthracen-9-yldi(pyridin-2-yl)methanol (5). Modified from a previously-reported procedure:[29] In an N_2-purged glovebox, a 500-mL Schlenk flask fitted with a screw-in Teflon stopper was charged with 9-bromoanthracene (15.69 g, 61 mmol) and 200 mL THF. A separate 100-mL Schlenk flask was charged with di-(2-pyridyl)ketone (12.4 g, 67 mmol) and 50 mL of THF. The flask was sealed, brought out of the box, cooled to –78ºC, and a pentane solution of *tert*-butyllithium (68 mL, 1.9 M) was added dropwise via cannula forming a yellow-green solution. The flask was slowly warmed to room temperature and stirred for 1 h. The flask was cooled back down to –78ºC, and the di-(2-pyridyl)ketone solution in THF was added dropwise via cannula. The resulting light-blue solution was stirred at room temperature for 6 h. Methanol (50 mL) was added to form a yellow solution, and the volatiles were removed under reduced pressure. The crude solid was taken up in DCM (200 mL) and washed with deionized H_2O (3 x 50 mL). The organic layer was washed with brine, dried over $MgSO_4$, and filtered. The volatiles were removed from the filtrate under a reduced pressure. The crude red-yellow solid was re-dissolved in a minimum amount of DCM, and pentane (100 mL) was added to form a light-yellow precipitate, which was then filtered and washed with pentane (3 x 50 mL) and dried in vacuo (13 g, 75%). ^{1}H NMR (400 MHz, C_6D_6) δ = 8.21 (s, 1H, Ar*H*), 8.16 (ddd, 2H, Ar*H*), 7.96 (dq, 2H, Ar*H*), 7.76 (dquint, 2H, Ar*H*), 7.67 (br s, 1H, -O*H*), 7.62 (dt, 2H, Ar*H*), 7.07 (td, 2H, Ar*H*), 6.84-6.92 (m, 4H, Ar*H*), 6.45 (qd, 2H, Ar*H*).

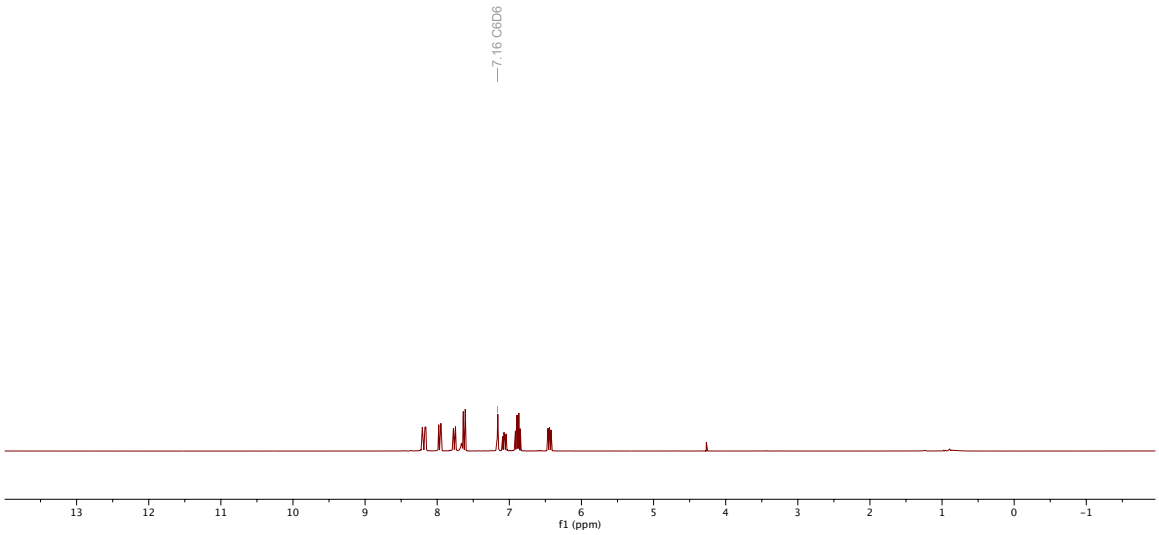

Figure 10. ^{1}H NMR (400 MHz, C_6D_6) of **5**.

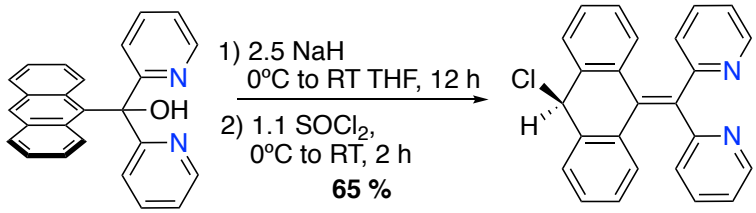

Synthesis of 6a. Modified from a previously-reported procedure:[30] A 100-mL Schlenk flask fitted with a screw-in Teflon stopper was charged with anthracen-9-yldi(pyridin-2-yl)methanol **(5)** (1.5 g, 4.1 mmol) and THF. The flask was cooled to 0ºC, and sodium hydride (0.248 g, 10.3 mmol) was added as a solid under positive pressure of N_2. The resulting yellow suspension was allowed to stir at room temperature for 8 h. The flask was cooled again to 0ºC and charged with thionyl chloride (0.33 mL, 4.5 mL). The resulting red suspension was stirred at room temperature for 4 h, and all the volatiles were removed under a reduced pressure until a tan solid remained. The flask was sealed and brought into an N_2-purged glove box. THF was added to the flask and filtered over a glass frit. DCM was added to extract any remaining material. Volatiles were removed from the filtrate in vacuo, and the solid was triturated with diethyl ether (3 x 50 mL) and dried for an additional 12 h under vacuum. The resulting tan solid was used without further purification (1.02 g, 65%) ^{1}H NMR (400 MHz, C_6D_6) δ = 8.46 (dq, 2H, Ar*H*) 7.59 (dt, 2H, Ar*H*), 7.28 (dd, 2H, Ar*H*), 7.1 (app d, 2H, Ar*H*), 6.79-6.86 (m, 4H, Ar*H*), 6.68 (td, 2H, Ar*H*), 6.47 (qd, 2H, Ar*H*) 5.90 (br s, 1H, C*H*ClCC).

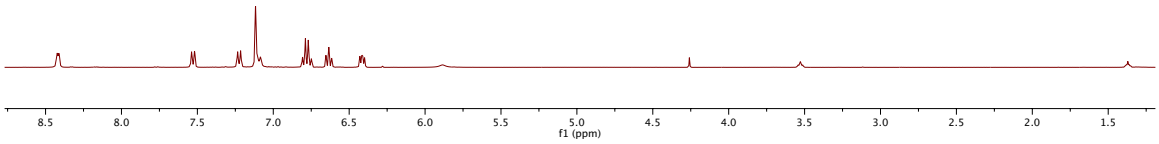

Figure 11. ^{1}H NMR (400 MHz, C_6D_6) of **6a**.

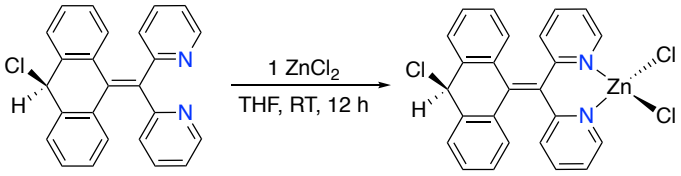

Synthesis of 6a-ZnCl$_2$. In an N_2-purged glovebox, compound **6a** (100 mg, 0.263 mmol) was suspended in THF in a 20-mL scintillation vial and charged with zinc chloride (35.8 mg, 0.263 mmol) with the aid of some THF. The pink suspension was stirred at room temperature for 8 h and subsequently filtered over a bed of celite. The filtrate was pumped down to dryness. Colorless, X-ray quality crystals were grown from slow evaporation of pentane into a saturated dichloromethane solution of the crude solid (30 mg, 22%) ^{1}H NMR (400 MHz, C_6D_6) δ = 8.63 (d, 2H, Ar*H*), 7.19 (d, 2H, Ar*H*), 6.98 (q, 4H, Ar*H*), 6.79 (t, 2H, Ar*H*), 6.61 (t, 2H, Ar*H*), 6.38 (t, 2H, Ar*H*), 6.21 (app t, 2H, Ar*H*), 5.68 (s, 1H, C*H*ClCC).

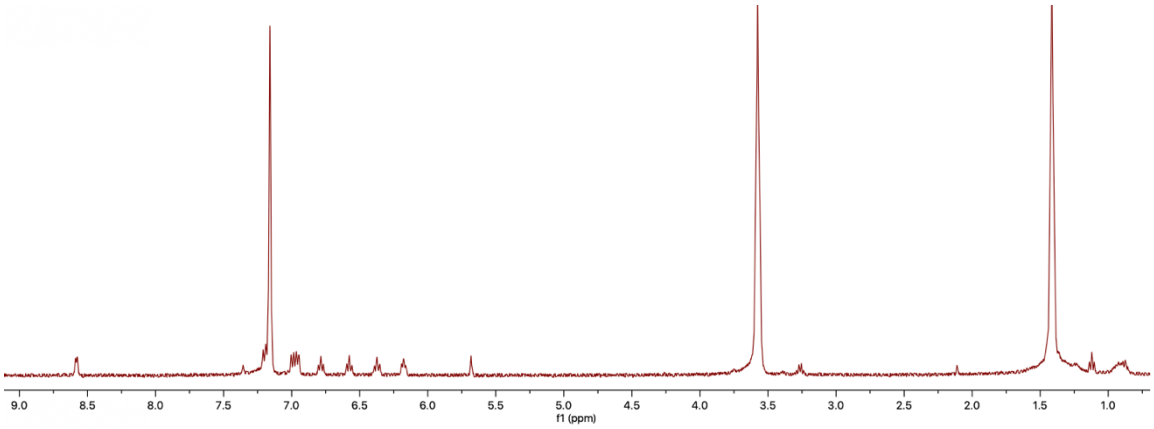

Figure 12. ^{1}H NMR (400 MHz, C_6D_6) of **6a-ZnCl$_2$.**

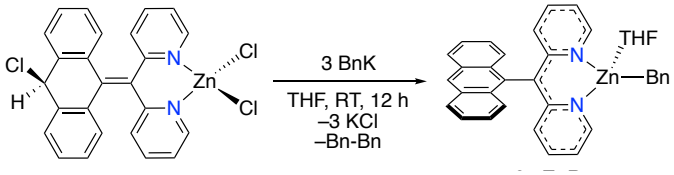

Synthesis of 6a-ZnBn. A 20-mL scintillation vial was charged with **6a-ZnCl$_2$** (50 mg, 0.1 mmol) and dissolved in THF. Benzyl potassium (41.7 mg, 0.32 mmol) was dissolved in THF and added dropwise to the vial at room temperature, resulting in a deep-red solution that was stirred for 6 h, resulting in a cloudy red suspension. Volatiles were removed under a reduced pressure until dryness, and the crude red solid was extracted with benzene (3 x 5 mL) and placed under vacuum until dryness. Red X-ray quality crystals were grown from pentane diffusion into a saturated dichloromethane solution in a –35 ºC freezer. (47 mg, 82%) ^{1}H NMR (400 MHz, C_6D_6) δ = 8.40 (s, 1H, Ar*H*), 8.27 (d, 2H, Ar*H*), 7.98 (d, 2H, Ar*H*), 7.52 (app d, 2H, Ar*H*), 7.30 (t, 2H, Ar*H*), 7.21 (m, 2H, Ar*H*), 7.09 (m, 4H, Ar*H*), 6.17 (m, 4H, Ar*H*), 5.81 (s, 2H, Ar*H*), 5.77 (br s, 4H), 3.42 (br s, 4H, THF), 2.75 (s, 2H, PhC*H*$_2$-Zn), 1.30 (br s, 4H, THF).

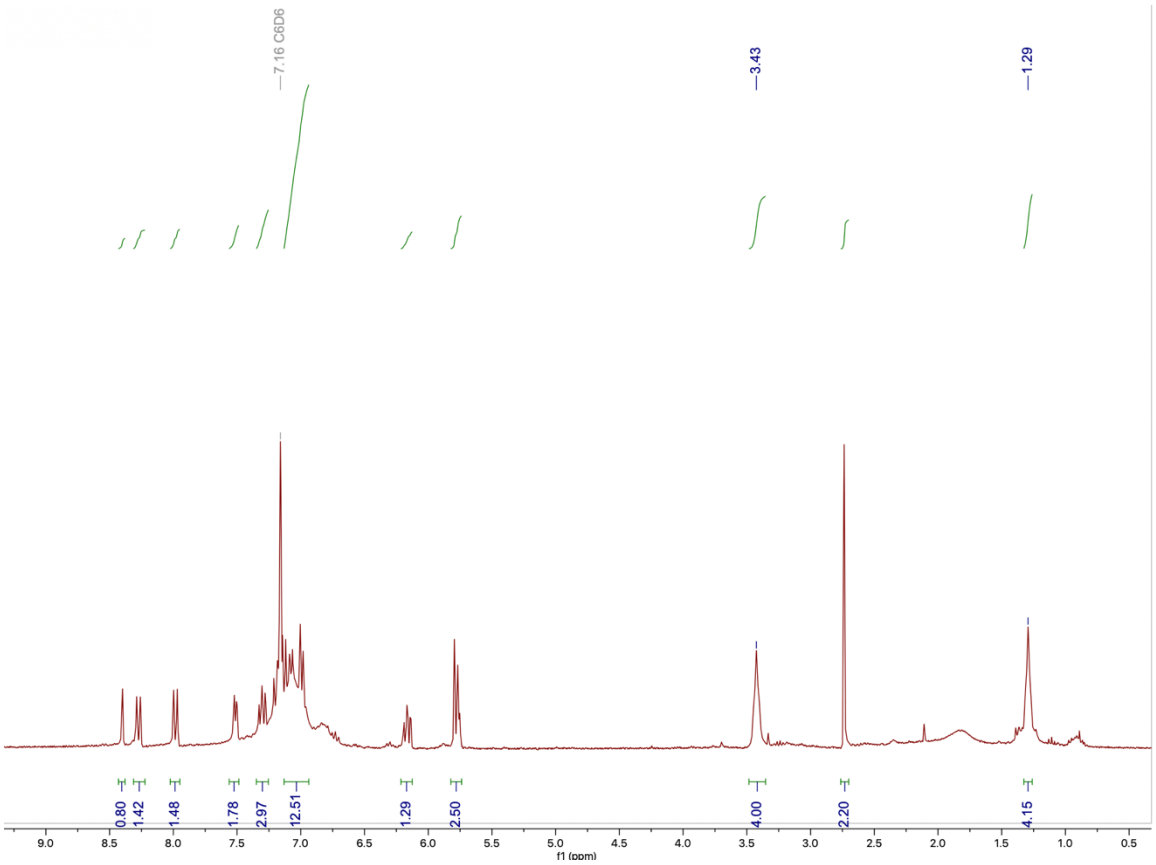

Figure 13. ^{1}H NMR (400 MHz, C_6D_6) of **6a-ZnBn.**

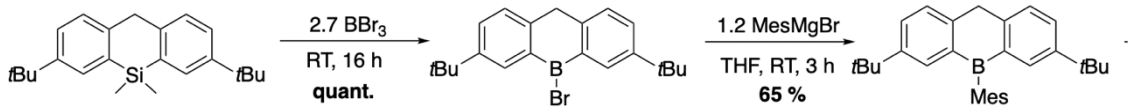

3,7-di-tert-butyl-5-mesityl-5,10-dihydrodibenzo[b,e]borinine (9a). In an inert-atmosphere glovebox, a 250-mL Schlenk tube with a screw-in Teflon stopper was charged with 3,7-di-*tert*-butyl-5,5-dimethyl-5,10-dihydrodibenzo[*b*,*e*]siline (**9**) (5.00 g, 15 mmol). The flask was sealed, brought outside of the glove box, and placed in a water bath. Under positive N_2, boron tribromide (3.8 mL, 40 mmol) was added dropwise, forming a red solution, which was stirred at room temperature for 16 h. Excess boron tribromide was removed in vacuo on the Schlenk line (note: close the system from mercury bubbler when flask is under vacuum) until dryness. The crude red solid was triturated with dry toluene (3 x 25 mL). The solid was allowed to dry under vacuum for an additional 12 h. The flask was sealed and brought into an N_2-purged glove box to check the ^{1}H NMR in benzene-d_6, which revealed consumption of the Me_2Si- speak. In a separate Schlenk flask was added activated magnesium turnings (4.38 g, 180 mmol) and 2-bromomesitylene (3.6 g, 18 mmol) as a solution in THF. The solution turned black, and the flask became slightly warm. The mixture was heated to 70 ºC for 0.5 h and stirred at room temperature for 1.5 h. The original flask containing **9-BBr** was cooled to 0ºC with an ice water bath. The mesityl magnesium bromide (18 mmol) was added dropwise over a period of 15 minutes, forming a dark yellow solution which was stirred at room temperature for 3 h. The crude mixture was quenched with methanol, and volatiles were removed on a rotary evaporator. The crude material was taken up in hexanes and added to a 200-mL sintered glass funnel containing silica gel, which was washed with hexanes (500 mL) and finally ethyl acetate (300 mL) to yield a yellow solution. The ethyl acetate fraction was concentrated in vacuo to yield a yellow-red oil which solidified when placed under high vacuum. This material was stirred in diethyl ether and calcium hydride and filtered in an N_2-purged glove box over a bed of alumina to yield the yellow solid **9a**. (4 g, 65%) ^{1}H NMR (400 MHz, C_6D_6) δ = 8.10 (app d, 2H, Ar*H*), 7.53 (dd, 2H, Ar*H*), 7.35

(d, 2H, Ar*H*), 6.99 (s, 2H, Ar*H*). 4.33 (s, 2H, ArCH_2Ar), 2.29 (s, 3H Ar-CH_3), 2.18 (s, 6H Ar-CH_3), 1.19 (s, 18H, C(CH_3)$_3$).

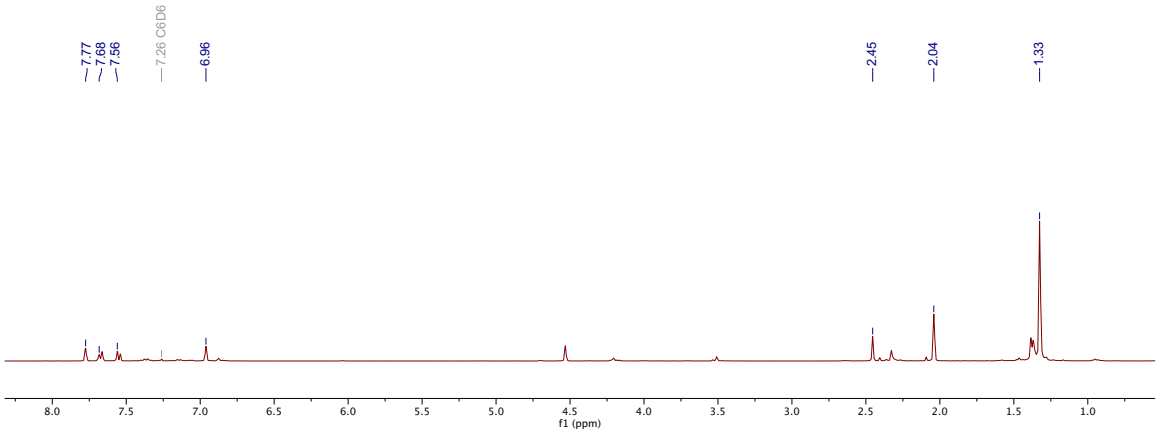

Figure 14. ^{1}H NMR (400 MHz, $CDCl_3$) of **9a**.

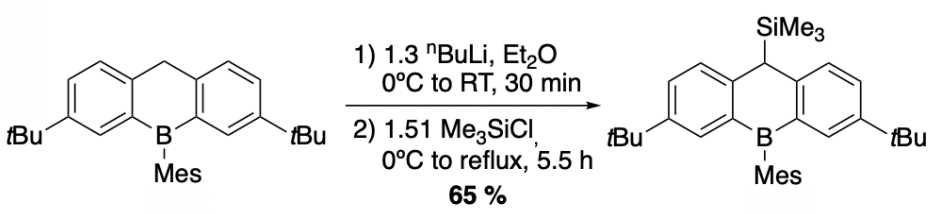

(3,7-di-tert-butyl-5-mesityl-5,10-dihydrodibenzo[b,e]borinin-10-yl)trimethylsilane (10a). In an inert-atmosphere glovebox, a 200-mL Schlenk tube fitted with a screw-in Teflon stopper was charged with 3,7-di-tert-butyl-5-mesityl-5,10-dihydrodibenzo[b,e]borinine (**9a**) (3.42 g, 8.4 mmol) and diethyl ether (75 mL). The flask was sealed and cooled to 0ºC while hooked up to the Schlenk line under positive N_2 flow. *N*-butyllithium (4.4 mL, 2.5 M in hexanes) was added dropwise via syringe. The reaction mixture was stirred at room temperature for 30 minutes. The flask was cooled to 0ºC again under positive N_2 flow, and trimethylsilyl chloride (1.6 mL, 13 mmol) was added dropwise via syringe, forming a red solution, which was refluxed for 5.5 h and gradually turned yellow. The flask was allowed to cool to room temperature, and the reaction mixture was quenched with saturated $NaHCO_{3(aq)}$. The organic layer was separated and washed with water (3 x 50 mL), brine (2 x 30 mL) and dried over magnesium sulfate and filtered. Volatiles were removed from the filtrate on the rotary evaporator to yield a yellow oil which solidified when placed under high vacuum. The crude material was taken up in hexanes and added to a 200-mL sintered glass funnel containing silica gel, which was washed with hexanes (500 mL) and finally ethyl acetate (300 mL) to yield a yellow solution. The ethyl acetate fraction was concentrated in vacuo to yield a yellow oil which solidified when placed under high vacuum. This material was stirred in diethyl ether and calcium hydride and filtered in an N_2-purged glove box over a bed of alumina to yield the yellow solid **10a**. (2 g, 50%) ^{1}H NMR (400 MHz, $CDCl_3$) δ = 7.68 (app d, 2H, Ar*H*), 7.52 (app dd, 2H, Ar*H*), 7.34 (d, 2H, Ar*H*), 6.68 (d, 2H, Ar*H*), 4.39 (s, 2H, ArCH_2Ar), 2.39 (s, 3H Ar-CH_3), 2.11 (s, 3H Ar-CH_3), 1.81 (s, 3H Ar-CH_3), 1.24 (s, 18H, C(CH_3)$_3$), –0.15 (s, 9H, -Si(CH_3)$_3$).

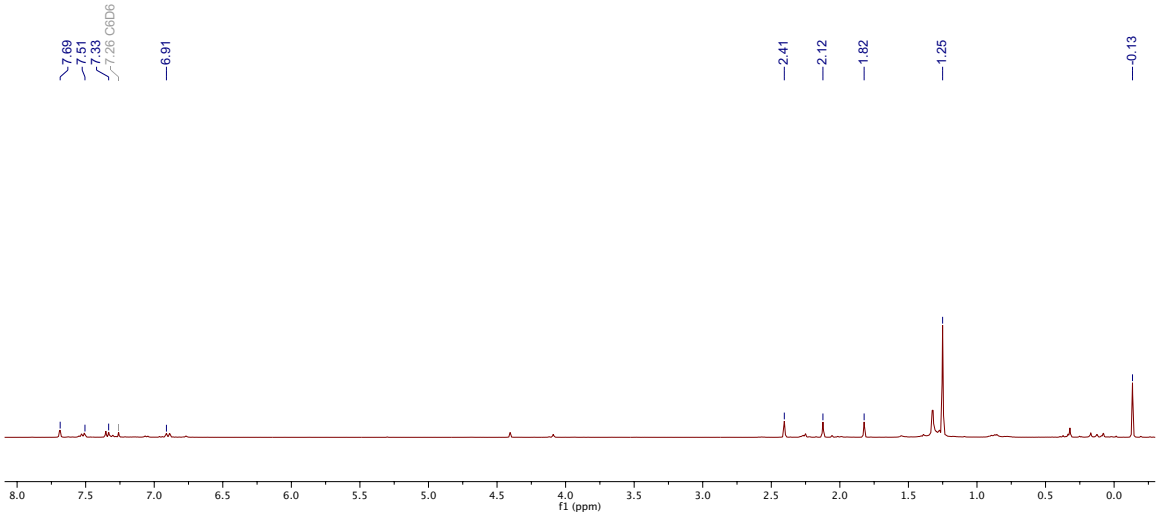

Figure 15. ^{1}H NMR (400 MHz, $CDCl_3$) of **10a**.

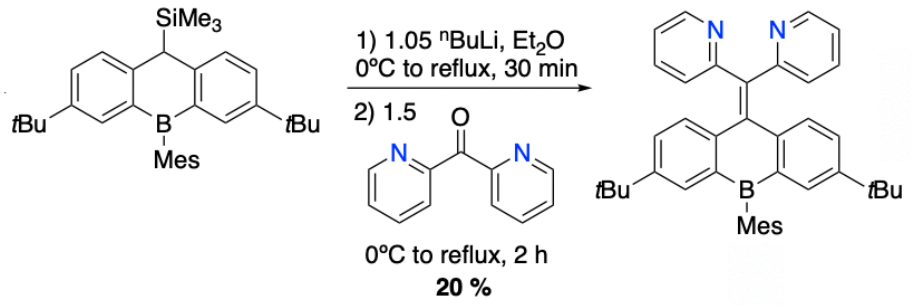

Synthesis of 11a. In an inert-atmosphere glovebox, a 100-mL Schlenk tube fitted with a screw-in Teflon stopper was charged with (3,7-di-tert-butyl-5-mesityl-5,10-dihydrodibenzo[b,e]borinin-10-yl)trimethylsilane (**10a**) (1.00 g, 2.2 mmol) and diethyl ether (40 mL). The flask was sealed and cooled to 0ºC while hooked up to the Schlenk line under positive N_2 flow. *N*-butyllithium (0.9 mL, 2.5 M in hexanes) was added dropwise via syringe. The reaction mixture was refluxed for 1 h. The flask was cooled to 0ºC again under positive N_2 flow, and di-2-pyridyl ketone (607 mg, 3.3 mmol) in 8 mL THF was added dropwise via syringe, forming a blue solution, which was refluxed for 2 h. The flask was allowed to cool to room temperature, and the reaction mixture was quenched with saturated $NaHCO_{3(aq)}$. The organic layer was separated and washed with water (3 x 50 mL), brine (2 x 30 mL) and dried over magnesium sulfate and filtered. Volatiles were removed from the filtrate on the rotary evaporator. The crude oil was dissolved in a mixture of 40% ethyl acetate/hexanes and loaded onto a 200-mL sintered glass funnel containing silica gel. The silica gel was washed with 40% ethyl acetate/hexanes until a tan fraction eluted, which was isolated and concentrated on a rotary evaporator under reduced pressure to yield a tan solid. The crude solid was dissolved in 20 mL of hexanes and sonicated for 30 minutes to yield a white precipitate, which was filtered through a sintered glass funnel and washed with 3 mL hexanes. The white solid was dried at 60ºC for 12 h in vacuo and stored in an inert-atmosphere glovebox (0.250 g, 20%). ^{1}H NMR (400 MHz, C_6D_6) δ = 8.48, (br d, 2H, Ar*H*), 7.98 (app d, 2H, Ar*H*), 7.63 (d, 2H, Ar*H*), 7.48 (d, 2H, Ar*H*), 6.96 (m, 6H, Ar*H*), 6.50 (app t, 2H, Ar*H*), 2.34 (s, 6H, Ar-CH_3), 2.26 (s, 3H, Ar-CH_3), 1.06 (s, 18H, C(CH_3)$_3$).

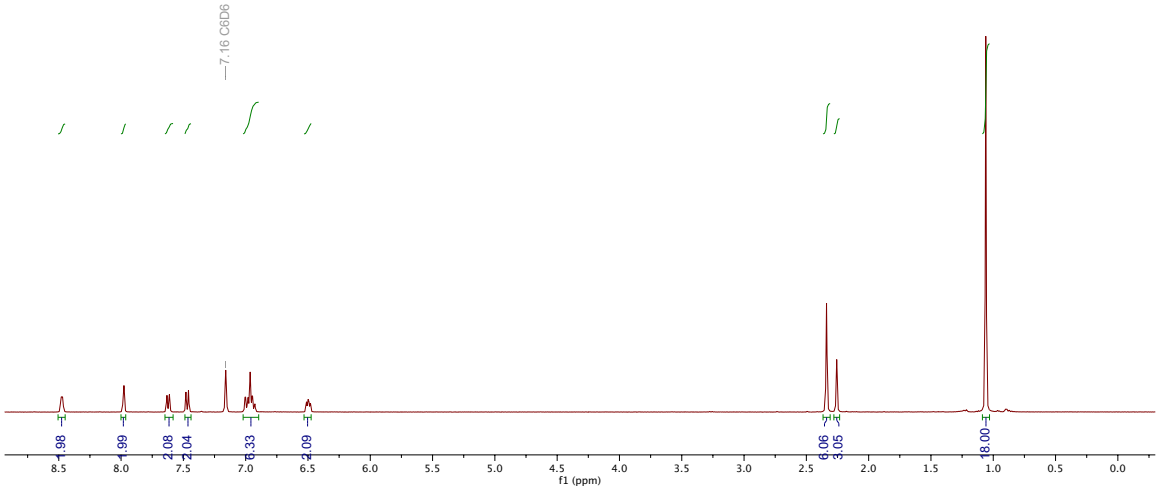

Figure 16. ^{1}H NMR (400 MHz, C_6D_6) of **11a**.

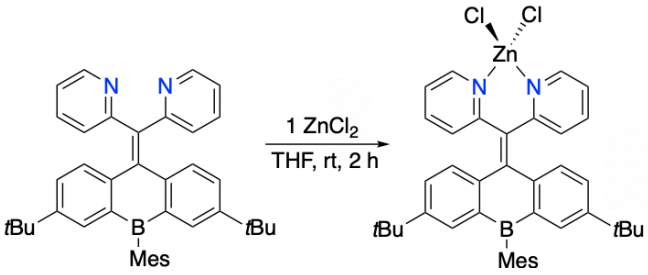

Synthesis of 11a-ZnCl₂. 11a (20 mg, 0.035 mmol) was dissolved in THF in a 20-mL scintillation vial. $ZnCl_2$ (4.8 mg, 0.035 mmol) was added to the vial as a solution in 3 mL THF. The mixture was stirred at room temperature for 2 h and became colorless. The volatiles removed in vacuo, and the remaining white solid was extracted with benzene to afford **11a-ZnCl₂**. (23 mg, 94%). ^{1}H NMR (400 MHz, C_6D_6) δ = 8.82, (br d, 2H, Ar*H*), 7.86 (br s, 2H, Ar*H*), 7.31 (d, 2H, Ar*H*), 7.06 (s, 1H, Mes-*H*), 6.95 (s, 1H, Mes-*H*), 6.86 (br d, 2H, Ar*H*), 6.76 (br d, 2H, Ar*H*), 6.58 (br t, 2H, Ar*H*), 6.41 (br t, 2H, Ar*H*), 2.40 (s, 3H, Ar-CH_3), 2.29 (s, 3H, Ar-CH_3), 2.12 (s, 3H, Ar-CH_3), 1.03 (s, 18H, C(CH_3)$_3$).

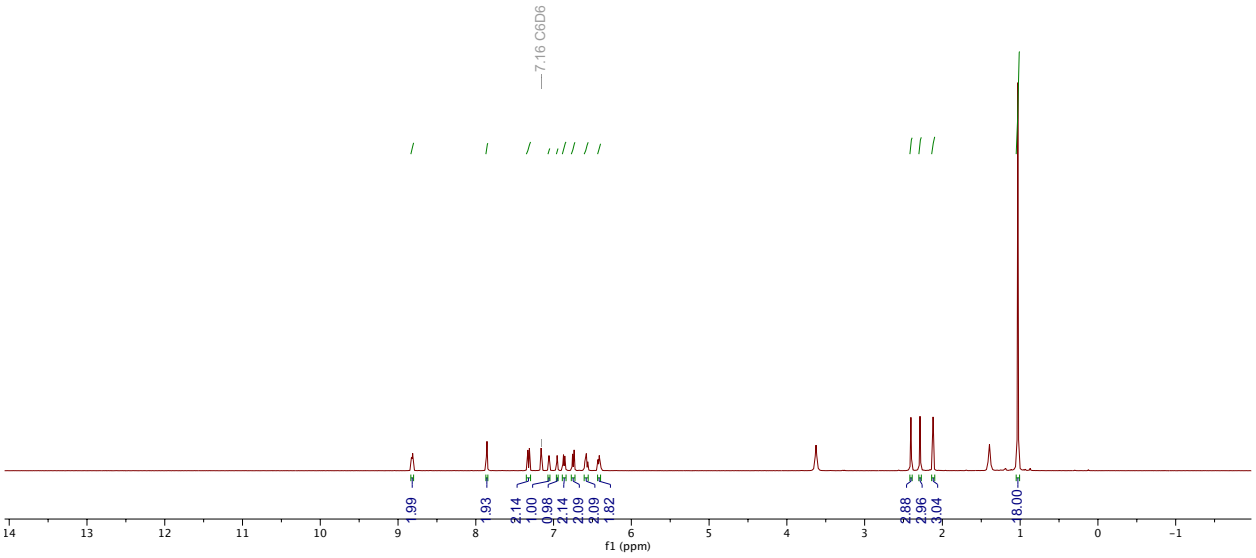

Figure 17. ^{1}H NMR (400 MHz, C_6D_6) of **11a-ZnCl₂.**

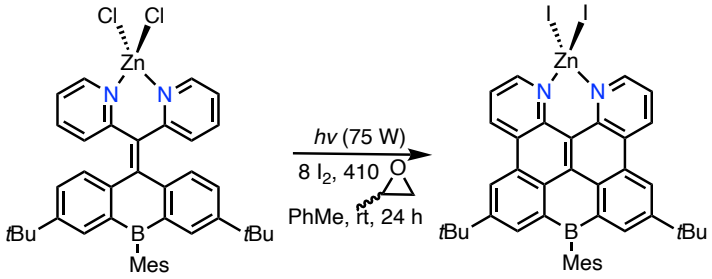

Synthesis of 13a-ZnI$_2$. In an N_2-purged glovebox, (12 mg, 0.017 mmol) **11a-ZnCl$_2$** was dissolved in toluene (50 mL) and transferred to a quartz Schlenk tube fitted with a screw-in Teflon stopper. The flask was charged with (±) propylene oxide (0.5 mL, 0.0072 mmol), sealed, and brought outside of the glove box. Iodine (30 mg, 0.136 mmol) was added under positive N_2 counterflow. The flask was sealed, and photolyzed with UV light for 24 h. Volatiles were removed carefully on a Schlenk line until all unreacted iodine was removed. The flask was sealed and brought into an N_2-purged glovebox. The crude material was extracted with benzene and concentrated in vacuo to yield a yellow solid. The crude material was recrystallized from slow evaporation of a saturated benzene solution into hexamethyldisiloxane. ^{1}H NMR (400 MHz, C_6D_6) δ = 9.60, (br s, 2H, Ar*H*), 8.72 (s, 2H, Ar*H*), 8.61 (s, 2H, Ar*H*), 8.55 (d, 2H, Ar*H*), 7.07 (s, 2H, Ar*H*), 6.85 (m, 2H, Ar*H*), 2.34 (s, 3H, Ar-CH_3), 2.18 (s, 6H, Ar-CH_3), 1.30 (s, 18H, C(CH_3)$_3$).

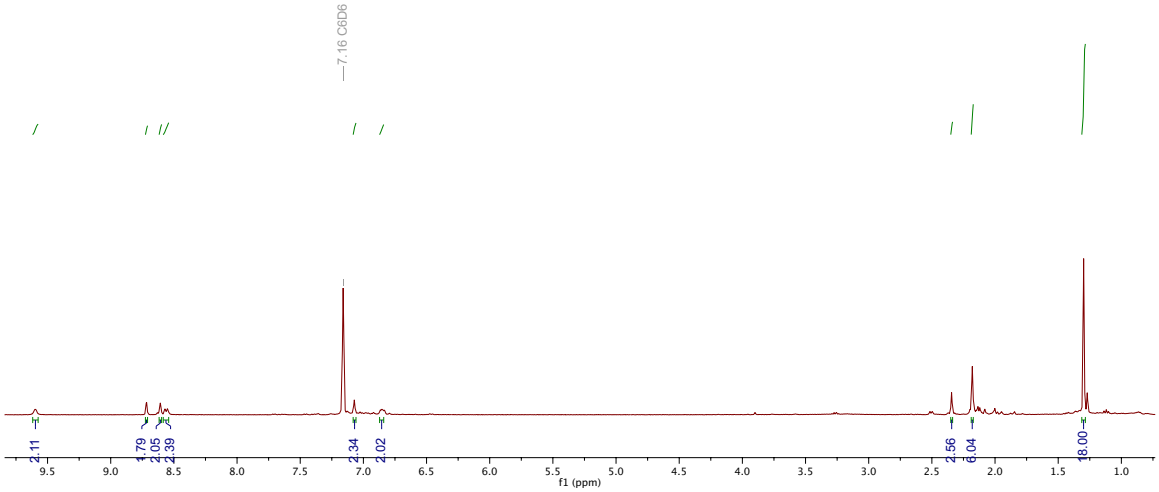

Figure 18. ^{1}H NMR (400 MHz, C_6D_6) of **13a-ZnI_2.**

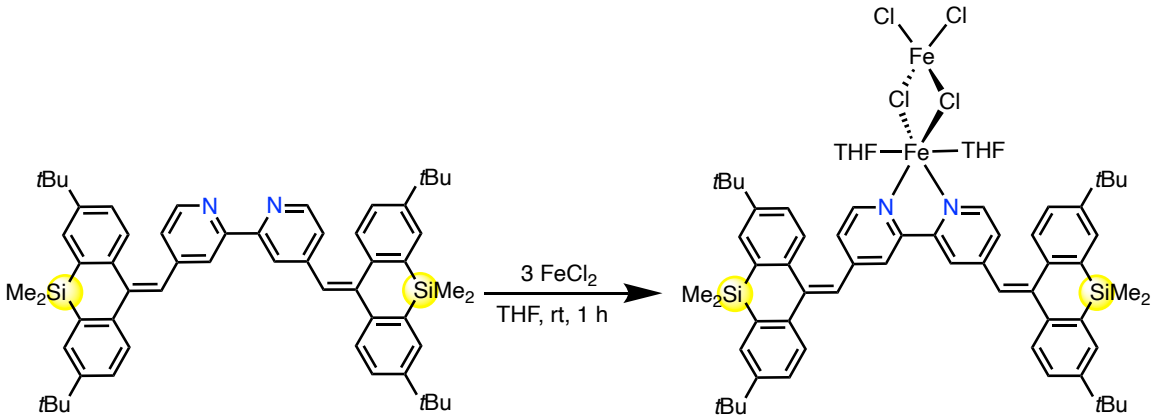

bpy$^{\mathbf{SiMe2}}$ (10 mg, 0.10 mmol) was dissolved in THF in a 20-mL scintillation vial and added to a solution of $FeCl_2$ (3.8 mg, 0.030 mmol). The mixture was stirred at room temperature for 1.5 h and pumped down to dryness. Extraction with benzene was carried out (3 x 3 mL) to removed excess $FeCl_2$. X-ray quality crystals of the benzene-insoluble material were grown from pentane vapor diffusion into a concentration THF solution. (13 mg, 94%). ^{1}H NMR (400 MHz, THF, paramagnetic) δ = 85.1 (br, s), 72.5 (br s), 50.5 (br s), 22.1 (br, s)

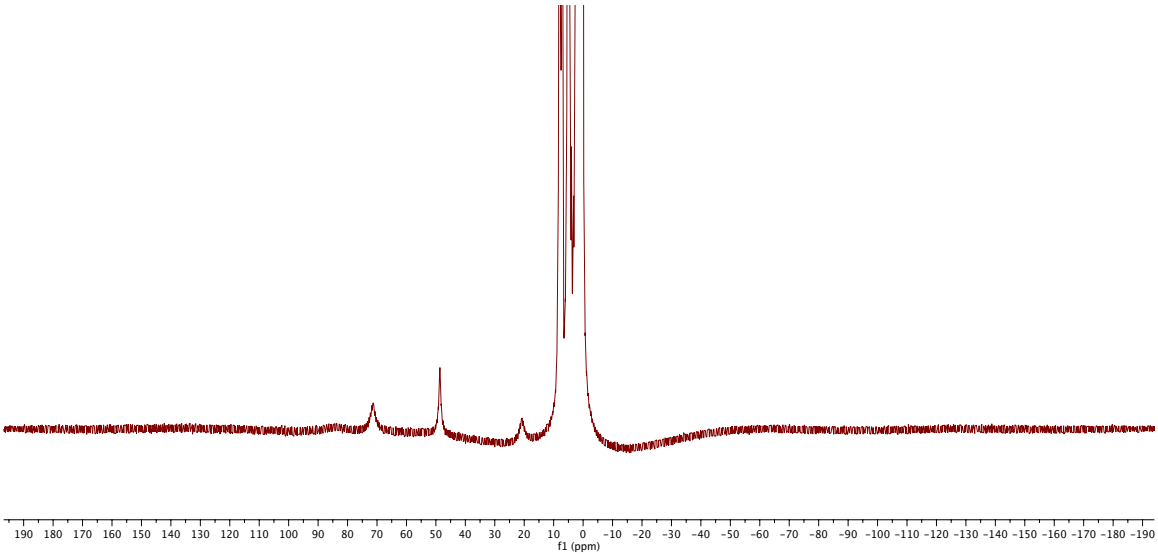

Figure 19. ^{1}H NMR spectrum (400 MHz, THF, paramagnetic) of **bpy**$^{\mathbf{SiMe2}}$**Fe$_2$Cl$_4$**.

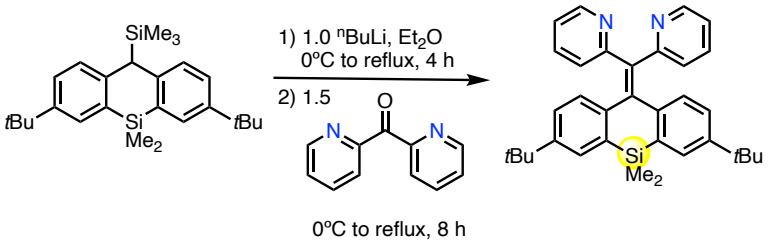

Synthesis of 11b. In an inert-atmosphere glovebox, a 100-mL Schlenk tube fitted with a screw-in Teflon stopper was charged with 3,7-di-*tert*-butyl-5,5-dimethyl-10-(trimethylsilyl)-5,10-dihydrodibenzo[*b*,*e*]siline (**10b**) (1.00 g, 2.4 mmol) and THF (40 mL). The flask was sealed and cooled to 0ºC while hooked up to the Schlenk line under positive N_2 flow. *N*-butyllithium (1 mL, 2.5 M in hexanes) was added dropwise via syringe. The reaction mixture was refluxed for 1 h. The flask was cooled to 0ºC again under positive N_2 flow, and di-2-pyridyl ketone (674 mg, 3.4 mmol) in 8 mL THF was added dropwise via syringe, forming a blue solution, which was refluxed for 2 h. The flask was allowed to cool to room temperature, and the reaction mixture was quenched with saturated $NaHCO_{3(aq)}$. The organic layer was separated and washed with water (3 x 50 mL), brine (2 x 30 mL) and dried over magnesium sulfate and filtered. Volatiles were removed from the filtrate on the rotary evaporator. The crude oil was dissolved in a mixture of 40% ethyl acetate/hexanes and loaded onto a 200-mL sintered glass funnel containing silica gel. The silica gel was washed with 40% ethyl acetate/hexanes until a tan fraction eluted, which was isolated and concentrated on a rotary evaporator under reduced pressure to yield a tan solid. The crude solid was dissolved in 20 mL of hexanes and sonicated for 30 minutes to yield a white precipitate, which was filtered through a sintered glass funnel and washed with 3 mL hexanes. The white solid was dried at 60ºC for 12 h in vacuo and stored in an inert-atmosphere glovebox (0.250 g, 20%). ^{1}H NMR (400 MHz, $CDCl_3$) δ = 8.68, (d, 2H, Ar*H*), 7.56 (s, 2H, Ar*H*), 7.34 (t, 2H, Ar*H*), 7.06 (d, 2H, Ar*H*), 7.01 (s, 2H, Ar*H*), 6.99 (app d, 4H, Ar*H*), 1.25 (s, 18H, $C(CH_3)_3$), 0.72 (d, 6H, $-Si(CH_3)_2$).

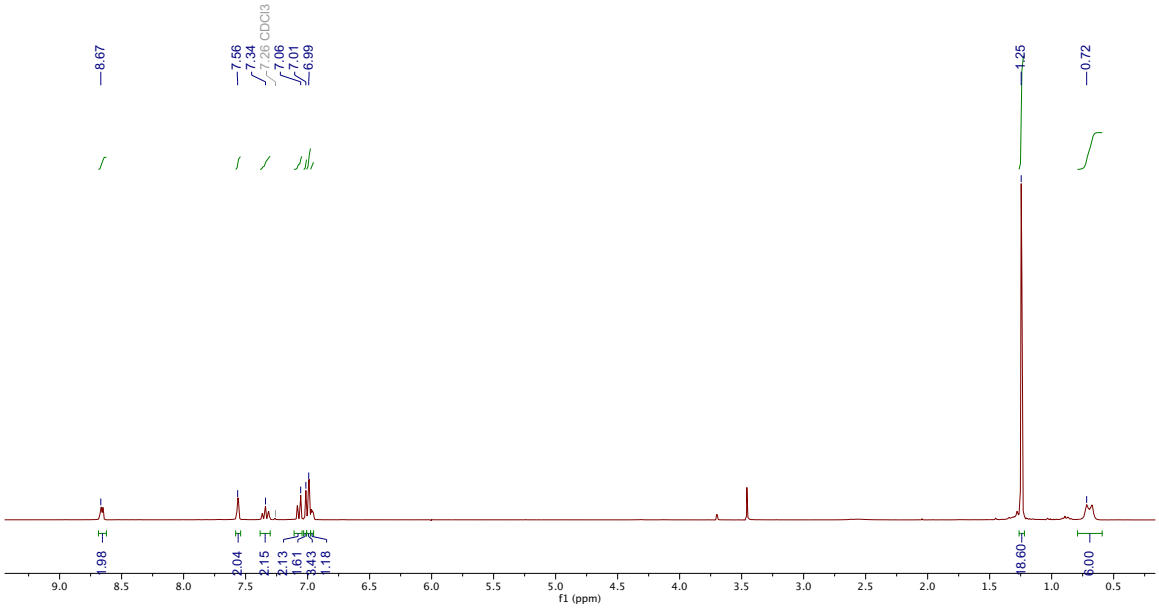

Figure 20. ^{1}H NMR (400 MHz, $CDCl_3$) of **11b.**

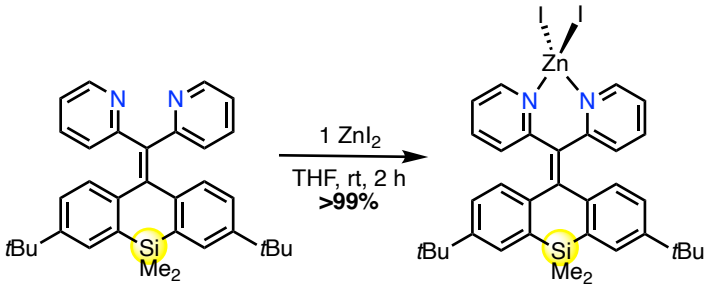

Synthesis of 11b-ZnI$_2$. 11a (20 mg, 0.04 mmol) was dissolved in THF in a 20-mL scintillation vial. $ZnCl_2$ (12.8 mg, 0.04 mmol) was added to the vial as a solution in 3 mL THF. The mixture was stirred at room temperature for 2 h and became colorless. The volatiles removed in vacuo, and the remaining white solid was extracted with benzene to afford **11b-ZnI$_2$**. (23 mg, 94%).

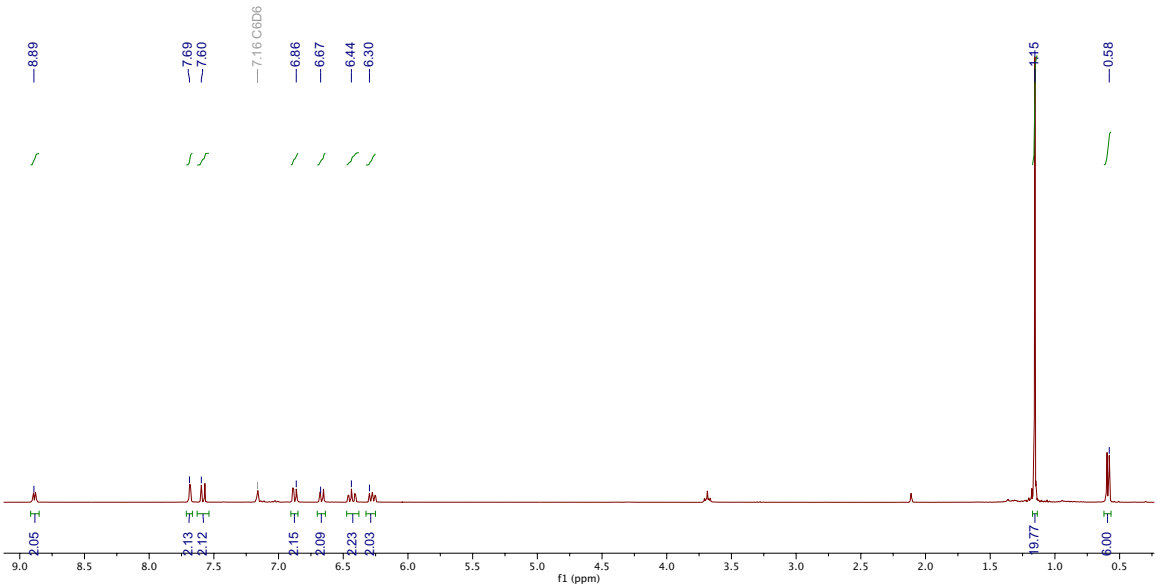

Figure 21. ^{1}H NMR (400 MHz, C_6D_6) of **11b-ZnI$_2$**.

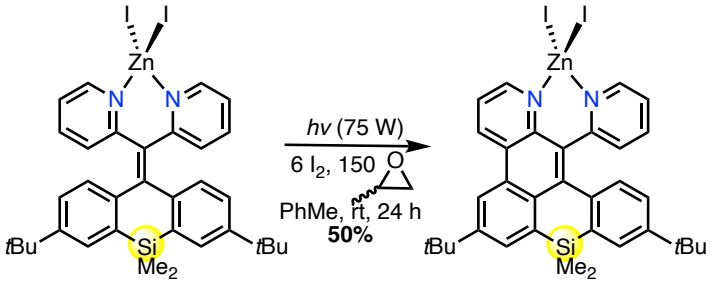

Synthesis of 13b-ZnI$_2$. In an N_2-purged glovebox, (11.2 mg, 0.014 mmol) **11b-ZnI$_2$** was dissolved in toluene (50 mL) and transferred to a quartz Schlenk tube fitted with a screw-in Teflon stopper. The flask was charged with (±) propylene oxide (0.15 mL, 0.0020 mmol), sealed, and brought outside of the glove box. Iodine (21 mg, 0.082 mmol) was added under positive N_2 counterflow. The flask was sealed, and photolyzed with UV light for 24 h. Volatiles were removed carefully on a Schlenk line until all unreacted iodine was removed. The flask was sealed and brought into an N_2-purged glovebox. The crude material was extracted with benzene and concentrated in vacuo to yield a yellow solid. The crude material was recrystallized from slow evaporation of a saturated benzene solution into hexamethyldisiloxane. X-ray quality crystals were generated for the desired **13b-ZnI$_2$** in addition to unreacted starting material, **11b-ZnI$_2$**. (50% conversion) ^{1}H NMR (400 MHz, C_6D_6) δ = 9.60, (br s, 2H, Ar*H*), 8.72 (s, 2H, Ar*H*), 8.61 (s, 2H, Ar*H*), 8.55 (d, 2H, Ar*H*), 7.07 (s, 2H, Ar*H*), 6.85 (m, 2H, Ar*H*), 2.34 (s, 3H, Ar-CH_3), 2.18 (s, 6H, Ar-CH_3), 1.30 (s, 18H, C(CH_3)$_3$).

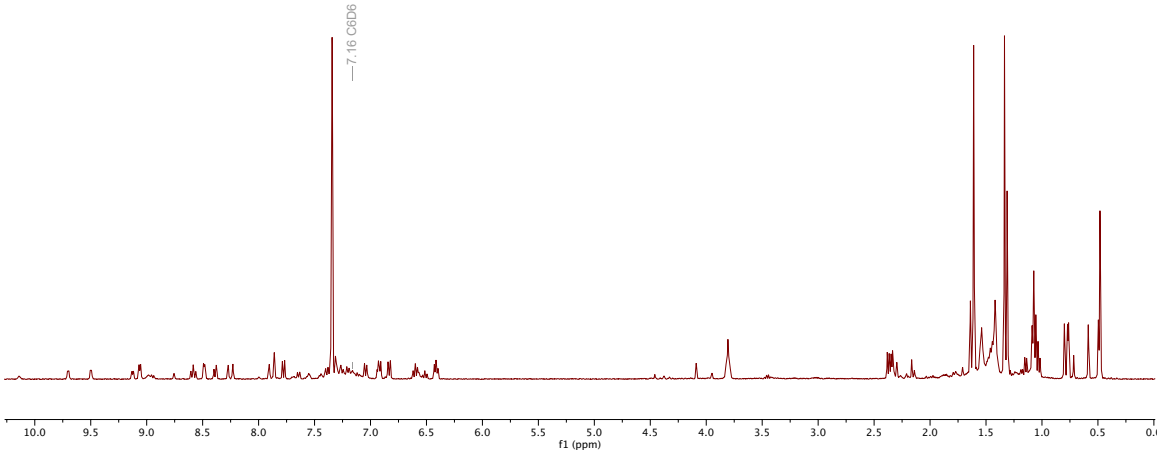

Figure 22. ^{1}H NMR (400 MHz, C_6D_6) of **13b-ZnI$_2$** and **11b-ZnI$_2$**.

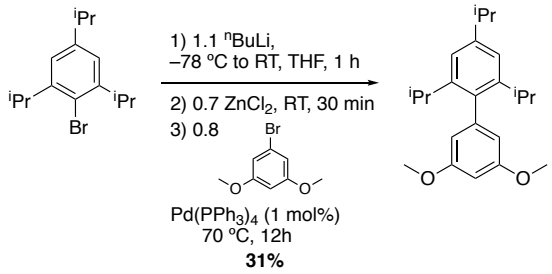

2,4,6-triisopropyl-3',5'-dimethoxy-1,1'-biphenyl (ArO^{Me}-H). In an N_2-purged glove box, a Schlenk flask fitted with a screw-in Teflon stopper was charged with a solution of 2,4,6-triisopropylbromobenzene (17 g, 60 mmol) in THF (100 mL). The flask was sealed and brought outside of the box and cooled to –78 °C with a dry ice/acetone bath. A hexanes solution of *n*-butyllithium (31 mL, 2.5 M, 78 mmol) was added dropwise via cannula. The reaction was allowed to warm to room temperature and stirred for 1 h forming a yellow solution. The reaction was then brought into an N_2-purged glovebox and $ZnCl_2$ (6.52 g, 48 mmol) was added slowly to the reaction resulting in the loss of the yellow coloration and formation of a white precipitate. The mixture was allowed to stir at room temperature for 30 min. 3,5-dimethoxybromobenzene (10.33 g, 48 mmol) and $Pd(PPh_3)_4$ (0.691 g, 0.60 mmol) were added, the flask sealed, and brought outside of the box. The vessel was fitted with an oven-dried reflux condenser and warmed to 70 °C for 12 h. After cooling to room temperature, water (50 mL) was added to quench the reaction, and the mixture concentrated in vacuo to about 100 mL. The resulting suspension was taken up in CH_2Cl_2 (200 mL) and washed with 5 x 100 mL of water. The organic layer was washed with brine (2 x 100 mL), dried over $MgSO_4$, and filtered. Volatiles from the filtrate were removed on a rotary evaporator. The crude material was purified via silica gel column chromatography with 5% Et_2O/Hexanes as eluent to yield a white solid, which was dried in vacuo for 12 h on the Schlenk line and stored long-term in an N_2-purged glovebox (5 g, 31%). ^{1}H NMR (400 MHz, $CDCl_3$) δ = 7.05 (s, 2H, Ar*H*), 6.46 (s, 1H, Ar*H*), 6.36 (br d, 2H, Ar*H*), 3.79 (s, 6H, -OCH_3), 2.94 (sept, 1H, *para*-C*H*(CH_3)$_2$), 2.69 (sept, 2H, *ortho*-C*H*(CH_3)$_2$), 1.30 (d, 6H, *para*-CH(CH_3)$_2$), 1.10 (d, 12H, *ortho*-CH(CH_3)$_2$. ^{13}C{^{1}H} NMR (101 MHz, $CDCl_3$) δ =

160.43 (aryl-*C*), 148.01 (aryl-*C*), 146.48 (aryl-*C*), 143.10 (aryl-*C*), 137.07 (aryl-*C*), 120.07 (aryl-*C*), 108.09 (aryl-*C*), 98.73 (aryl-*C*), 55.45 (-O*C*H$_3$), 34.40 (*para*-*C*H(CH$_3$)$_2$), 30.36 (*para*-CH(*C*H$_3$)$_2$), 24.58 (*ortho*-CH(*C*H$_3$)$_2$), 24.23 (*para*-*C*H(CH$_3$)$_2$). HRMS (FAB+) m/z Calcd. for [M + H$^+$] $C_{23}H_{33}O_2$ 341.2481, found 341.2485.

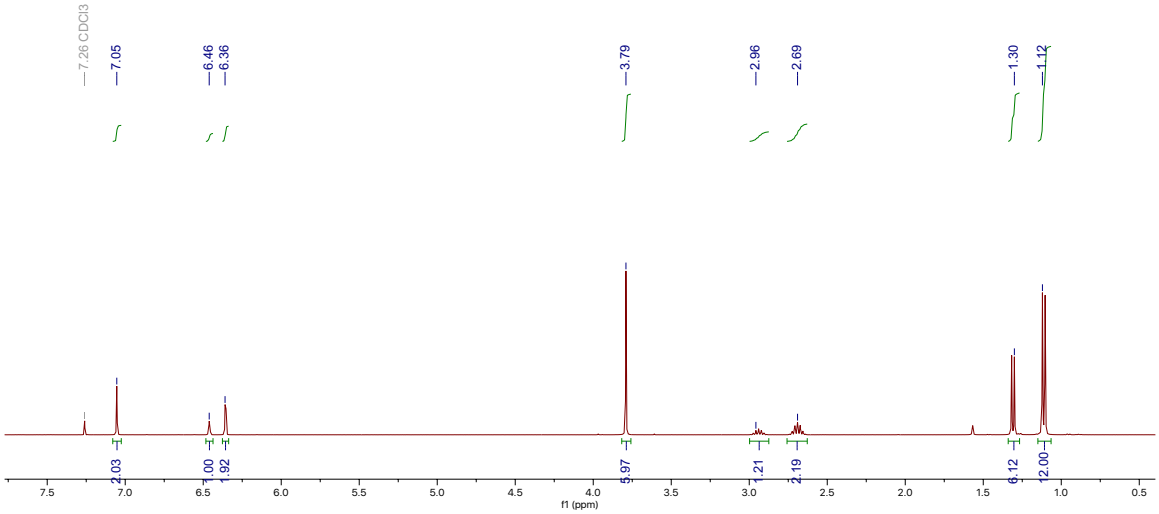

Figure 23. ^{1}H NMR spectrum (400 MHz, $CDCl_3$) of 2,4,6-triisopropyl-3',5'-dimethoxy-1,1'-biphenyl **(ArO^{Me}-H)**.

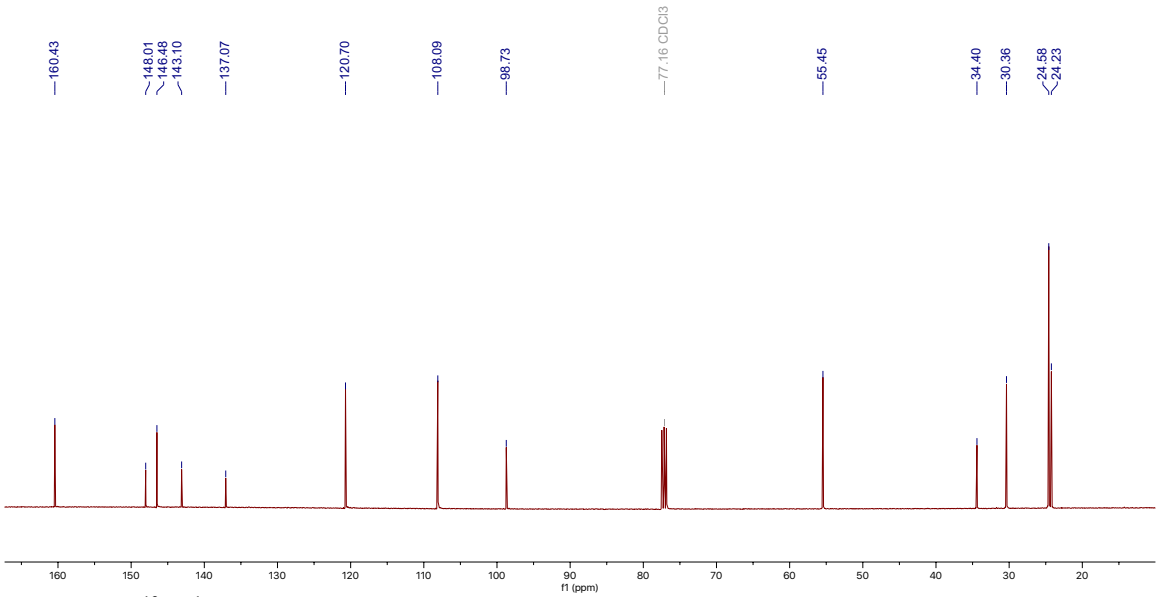

Figure 24. $^{13}C\{^1H\}$ NMR spectrum (101 MHz, $CDCl_3$) of 2,4,6-triisopropyl-3',5'-dimethoxy-1,1'-biphenyl **(ArO^{Me}-H)**.

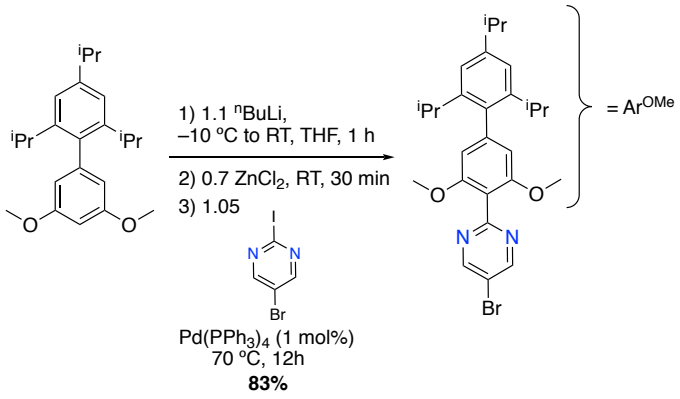

5-bromo-2-(2',4',6'-triisopropyl-3,5-dimethoxy-[1,1'-biphenyl]-4-yl)pyrimidine (1b). In an N_2-purged glove box, a Schlenk flask fitted with a screw-in Teflon stopper was charged with a solution of 2,4,6-triisopropyl-3',5'-dimethoxy-1,1'-biphenyl **(ArO^{Me}-H)** (5 g, 15 mmol) in THF (40 mL). The flask was sealed and brought outside of the box and cooled to –10 °C with an ice/acetone bath. A hexanes solution of *n*-butyllithium (7 mL, 2.5 M, 17 mmol) was added dropwise via syringe. The reaction was allowed to warm to room temperature and stirred for 1 h forming a yellow solution. The reaction was then brought into an N_2-purged glovebox and $ZnCl_2$ (1.38 g, 10.2 mmol) was added slowly to the reaction resulting in the loss of the yellow coloration. The mixture was allowed to stir at room temperature for 30 min. 2-iodo-5-bromopyrimidine (4.31 g, 15 mmol) and $Pd(PPh_3)_4$ (0.503 g, 0.44 mmol) were added, the flask sealed, and brought outside of the box. The vessel was fitted with an oven-dried reflux condenser and warmed to 70 °C for 12 h. After cooling to room temperature, water (50 mL) was added to quench the reaction, and the mixture concentrated in vacuo to about 100 mL. The resulting suspension was taken up in CH_2Cl_2 (200 mL) and washed with 5 x 100 mL of water. The organic layer was washed with brine (2 x 100 mL), dried over $MgSO_4$, and filtered. Volatiles from the filtrate were removed on a rotary evaporator. The crude material was purified via Kugelrohr distillation at 70ºC on the Schlenk line under dynamic vacuum. A minimal amount of a white, oily solid was transferred, and a red/yellow solid remained in the flask, which is the desired product **1b** (6.37 g, 83%). ^{1}H NMR (400 MHz, $CDCl_3$) δ= 8.95 (s, 2H, Ar*H*), 7.08 (s, 2H, Ar*H*), 6.49 (s, 2H, Ar*H*), 3.70 (s, 6H, -OCH_3), 2.95 (sept, 1H, *para*-C*H*(CH_3)$_2$), 2.77 (sept, 2H, *ortho*-C*H*(CH_3)$_2$),

1.30 (d, 6H, *para*-CH(CH_3)$_2$), 1.13 (d, 12H, *ortho*-CH(CH_3)$_2$. ^{13}C{^{1}H} NMR (101 MHz, $CDCl_3$) δ=158.12 (aryl-*C*), 157.62 (aryl-*C*), 148.39 (aryl-*C*), 146.58 (aryl-*C*), 144.10 (aryl-*C*), 136.96 (aryl-*C*), 120.88 (aryl-*C*), 118.77 (aryl-*C*), 108.08 (aryl-*C*), 105.94 (aryl-*C*), 56.18 (-O*C*H$_3$), 34.44 (*para*-*C*H(CH$_3$)$_2$), 30.34 (*para*-*C*H(CH$_3$)$_2$), 24.63 (*ortho*-CH(*C*H$_3$)$_2$), 24.23 (*para*-CH(*C*H$_3$)$_2$). HRMS (FAB+) m/z Calcd. for [M + H$^+$] $C_{27}H_{34}N_2O_2Br$ 497.1804, found 497.1812

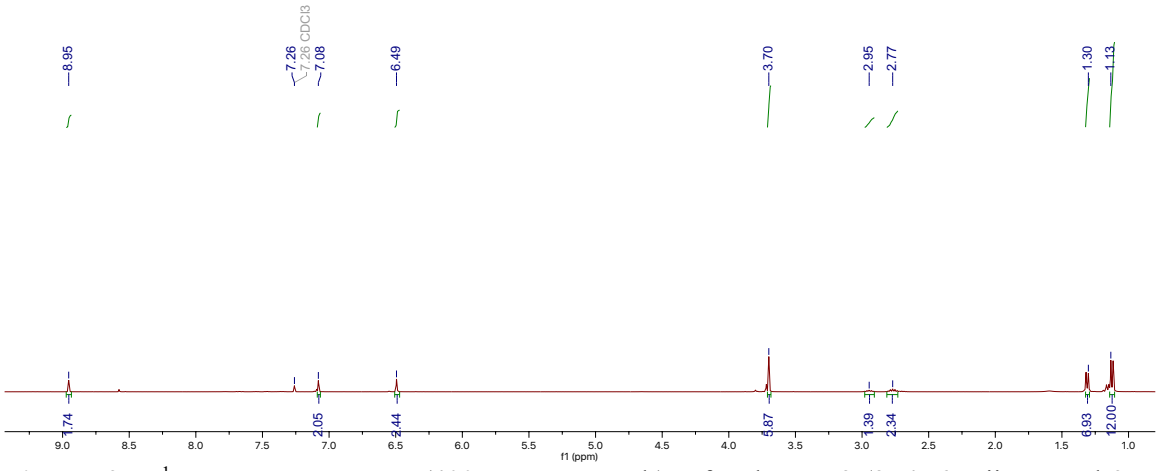

Figure 25. ^{1}H NMR spectrum (400 MHz, $CDCl_3$) of 5-bromo-2-(2',4',6'-triisopropyl-3,5-dimethoxy-[1,1'-biphenyl]-4-yl)pyrimidine **(1b)**.

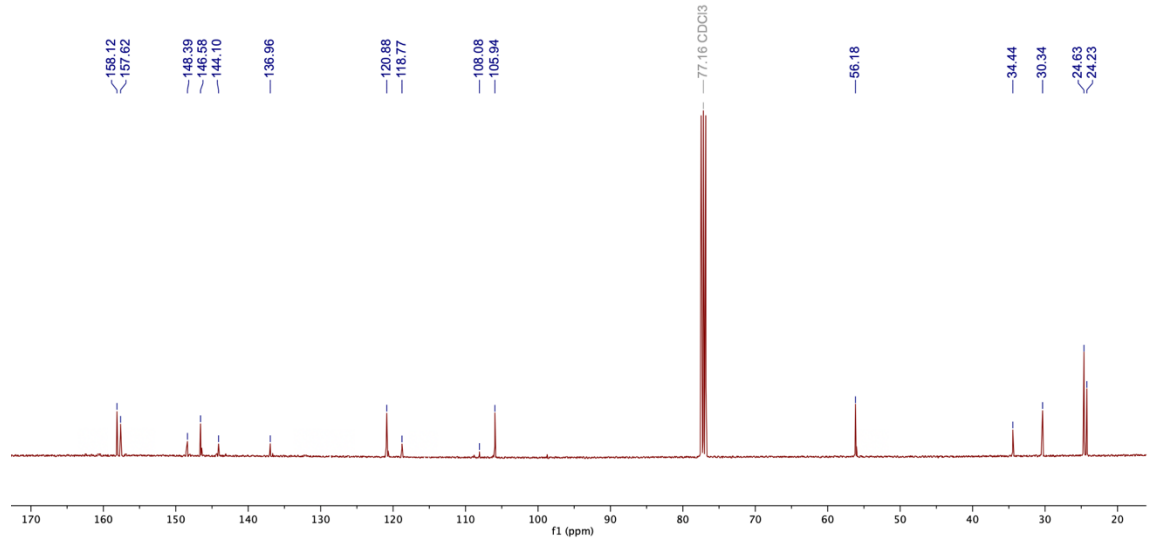

Figure 26. ^{13}C{^{1}H} NMR spectrum (101 MHz, $CDCl_3$) 5-bromo-2-(2',4',6'-triisopropyl-3,5-dimethoxy-[1,1'-biphenyl]-4-yl)pyrimidine **(1b)**.

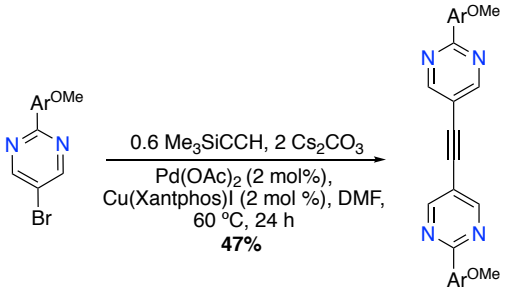

1,2-bis(2-(2',4',6'-triisopropyl-3,5-dimethoxy-[1,1'-biphenyl]-4-yl)pyrimidin-5-yl)ethyne (2b). Adapted from a previously-reported procedure:[22] A 500-mL, oven-dried Schlenk flask was allowed to cool under vacuum on the Schlenk line. Under a positive pressure of N_2, the Schlenk flask was charged with 5-bromo-2-(2',4',6'-triisopropyl-3,5-dimethoxy-[1,1'-biphenyl]-4-yl)pyrimidine (**1b**) (6.37 g, 13 mmol), cesium carbonate (10.43 g, 32 mmol), and palladium (II) acetate (58 mg , 0.26 mmol). DMF (120 mL) was added to the Schlenk flask via cannula. To this mixture was added trimethylsilylacetylene (1.09 mmol, 7.7 mmol) under positive N_2. The reaction mixture was degassed via one cycle of freeze-pump-thaw. Bis(diphenylphosphino)-9,9-dimethylxanthene]copper(I) (200 mg, 0.26 mmol) was added under positive N_2. The reaction mixture was subject to two more cycles of freeze-pump-thaw, and the mixture was heated to 60 ºC for 12 h. Volatiles were removed under a reduced pressure, and the crude solid was charged with CH_2Cl_2 (300 mL) and filtered to remove excess cesium carbonate. The filtrate was concentrated under a reduced pressure and purified via column chromatography with 1% MeOH/CH_2Cl_2 as the eluent. The light brown solid was dried under vacuum for 8 h at room temperature prior to the next step (2.6 g, 47%). ^{1}H NMR (400 MHz, $CDCl_3$) δ = 9.09 (s, 2H, Ar*H*), 7.09 (s, 2H, Ar*H*), 6.52 (s, 2H, Ar*H*), 3.73 (s, 6H, -OCH_3), 2.96 (sept, 1H, *para*-C*H*(CH_3)$_2$), 2.79 (sept, 2H, *ortho*-C*H*(CH_3)$_2$), 1.33 (d, 6H, *para*-CH(CH_3)$_2$), 1.13 (d, 12H, *ortho*-CH(CH_3)$_2$. ^{13}C{^{1}H} NMR (101 MHz, $CDCl_3$) δ = 163.25 (aryl-*C*), 159.20 (aryl-*C*), 157.66 (aryl-*C*), 148.39 (aryl-*C*), 146.58 (aryl-*C*), 144.22 (aryl-*C*), 136.96 (aryl-*C*), 120.88 (aryl-*C*), 116.30 (aryl-*C*), 115.58 (aryl-*C*), 105.95 (aryl-*C*), 89.56 (alkyne-*CC*), 56.21 (-O*C*H_3), 34.44 (*para*-

*C*H(CH$_3$)$_2$), 30.35 (*ortho*-*C*H(CH$_3$)$_2$), 24.63 (*ortho*-CH(*C*H$_3$)$_2$), 24.23 (*para*-CH(*C*H$_3$)$_2$). HRMS (FAB+) m/z Calcd. for [M + H$^+$] $C_{56}H_{67}N_4O_4$ 859.5162, found 859.5173

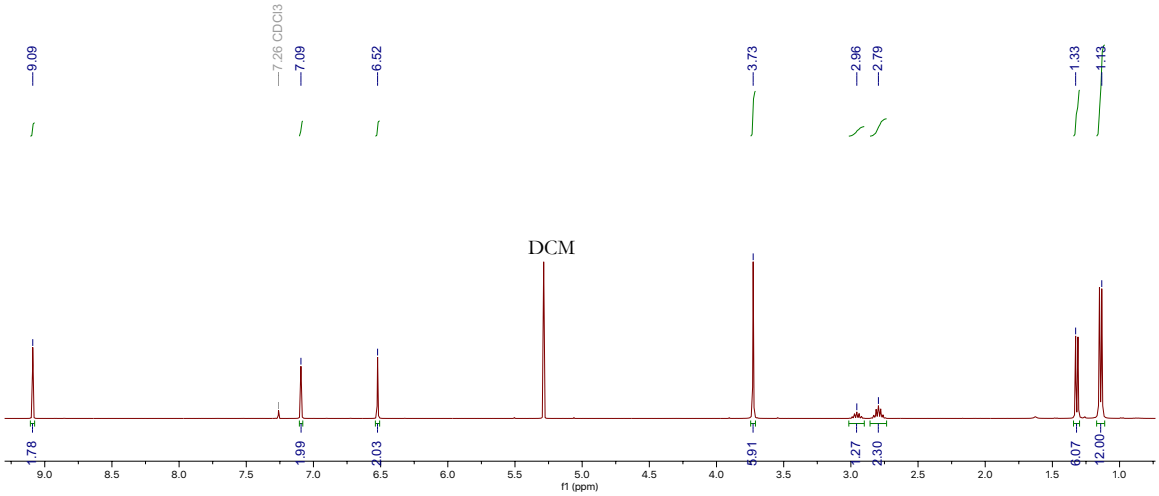

Figure 27. ^{1}H NMR spectrum (400 MHz, $CDCl_3$) 1,2-bis(2-(2',4',6'-triisopropyl-3,5-dimethoxy-[1,1'-biphenyl]-4-yl)pyrimidin-5-yl)ethyne **(2b).**

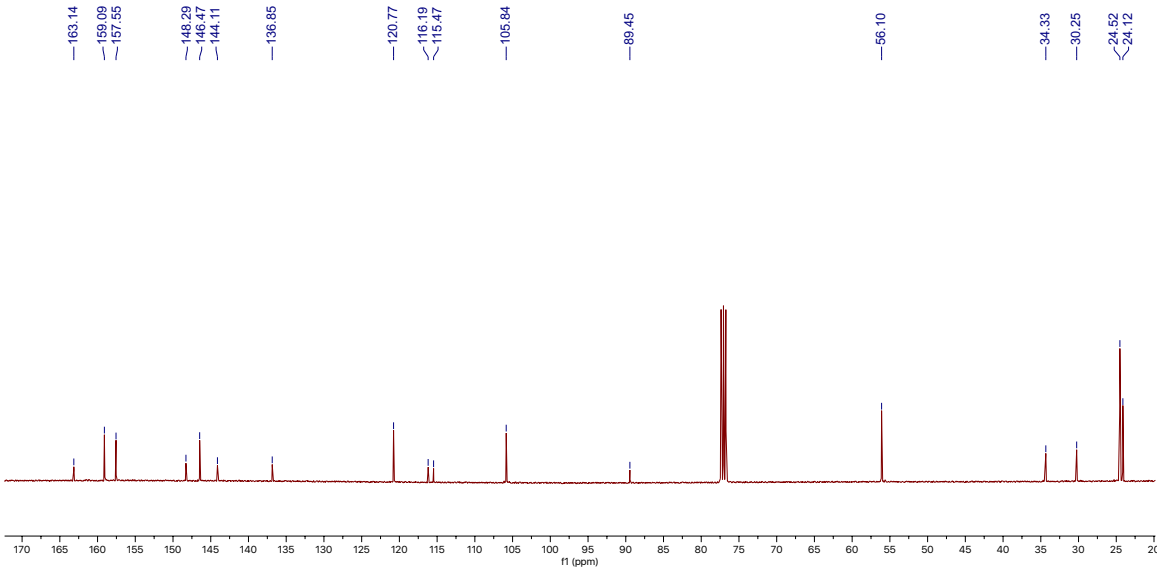

Figure 28. $^{13}C\{^1H\}$ NMR spectrum (101 MHz, $CDCl_3$) 1,2-bis(2-(2',4',6'-triisopropyl-3,5-dimethoxy-[1,1'-biphenyl]-4-yl)pyrimidin-5-yl)ethyne **(2b).**

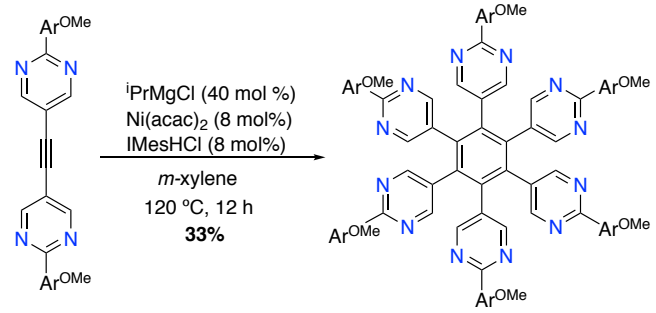

1,2,3,4,5,6-hexakis(2-(2',4',6'-triisopropyl-3,5-dimethoxy-[1,1'-biphenyl]-4-yl)pyrimidin-5-yl)benzene (3b). Adapted from a previously-reported procedure:[23] An oven-dried Schlenk tube fitted with a screw-in Teflon stopper was charged with 1,2-bis(2-(3,5-di-*tert*-butylphenyl)pyrimidin-5-yl)ethyne (**2b**) (600 mg, 0.7 mmol), IMesHCl (54 mg, 0.06 mmol), and bis(acetylacetonato)nickel (II) (41 mg, 0.06 mmol). The flask was then charged with 8 mL of *m*-xylene via syringe. The solution was subject to three cycles of freeze-pump-thaw and left under nitrogen. Isopropylmagnesium chloride (0.20 mL, 1.39 M in THF) was added via syringe, and the solution was warmed to 120 ºC for 36 h. Volatiles were removed under a reduced pressure. The crude solid was dissolved in 20 mL of a 20% EtOAc/Hexanes solution and filtered over a sintered glass funnel containing a bed of silica gel. The filtrate was concentrated on the rotary evaporator until a white solid crashed out and was subsequently filtered. This process was repeated two more times for the filtrate to yield additional white solid, which is the desired compound **3b** (300 mg, 50%). ^{1}H NMR (400 MHz, $CDCl_3$) δ = 8.65 (s, 2H, Ar*H*), 7.04 (s, 2H, Ar*H*), 6.38 (s, 2H, Ar*H*), 3.52 (s, 6H, -OCH_3), 2.92 (sept, 1H, *para*-C*H*(CH_3)$_2$), 2.68 (sept, 2H, *ortho*-C*H*(CH_3)$_2$), 1.29 (d, 6H, *para*-CH(CH_3)$_2$), 1.05 (d, 12H, *ortho*-CH(CH_3)$_2$. ^{13}C{^{1}H} NMR (101 MHz, $CDCl_3$) δ = 163.21 (aryl-*C*), 157.72 (aryl-*C*), 148.29 (aryl-*C*), 146.39 (aryl-*C*), 143.89 (aryl-*C*), 138.04 (aryl-*C*), 136.61 (aryl-*C*), 129.13 (aryl-*C*), 122.59 (aryl-*C*), 120.79 (aryl-*C*), 115.51 (aryl-*C*), 105.65 (aryl-*C*), 55.81 (-OCH_3), 34.37 (*para*-*C*H(CH_3)$_2$), 30.33 (*ortho*-*C*H(CH_3)$_2$), 24.50 (*ortho*-CH(*C*H_3)$_2$), 24.17 (*para*-CH(*C*H_3)$_2$). Anal. calcd. (%) for $C_{167}H_{196}N_{12}O_{12}$: C, 78.29; H, 7.74; N, 6.52. Found: C, 78.04; H, 7.52; N, 6.41.

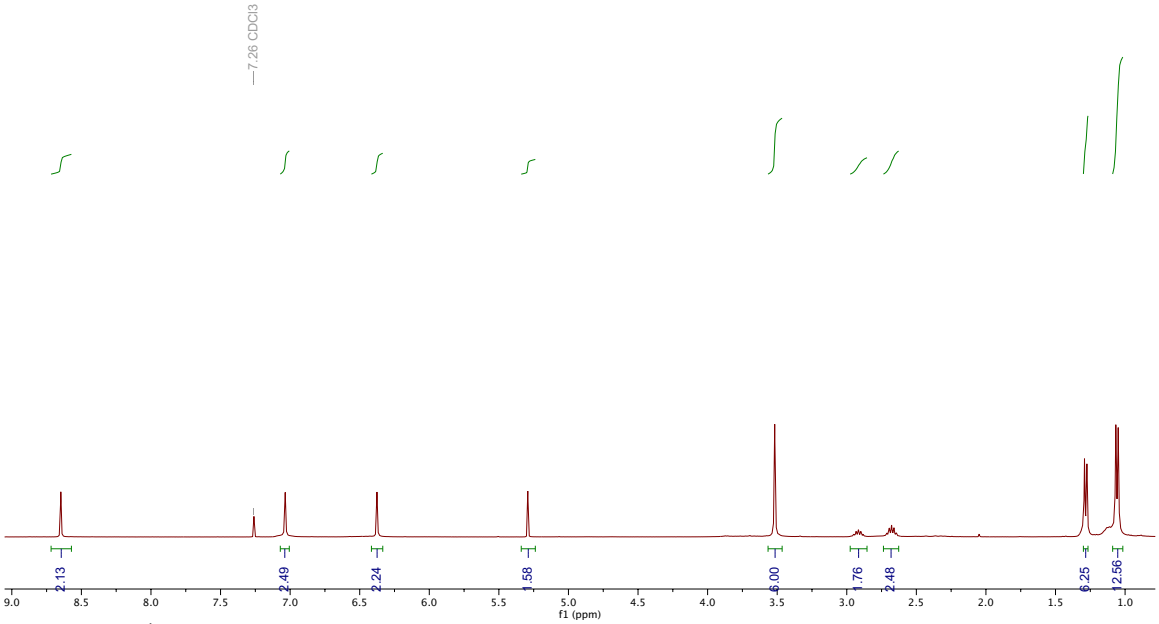

Figure 29. ^{1}H NMR spectrum (400 MHz, $CDCl_3$) 1,2,3,4,5,6-hexakis(2-(2',4',6'-triisopropyl-3,5-dimethoxy-[1,1'-biphenyl]-4-yl)pyrimidin-5-yl)benzene **(3b).**

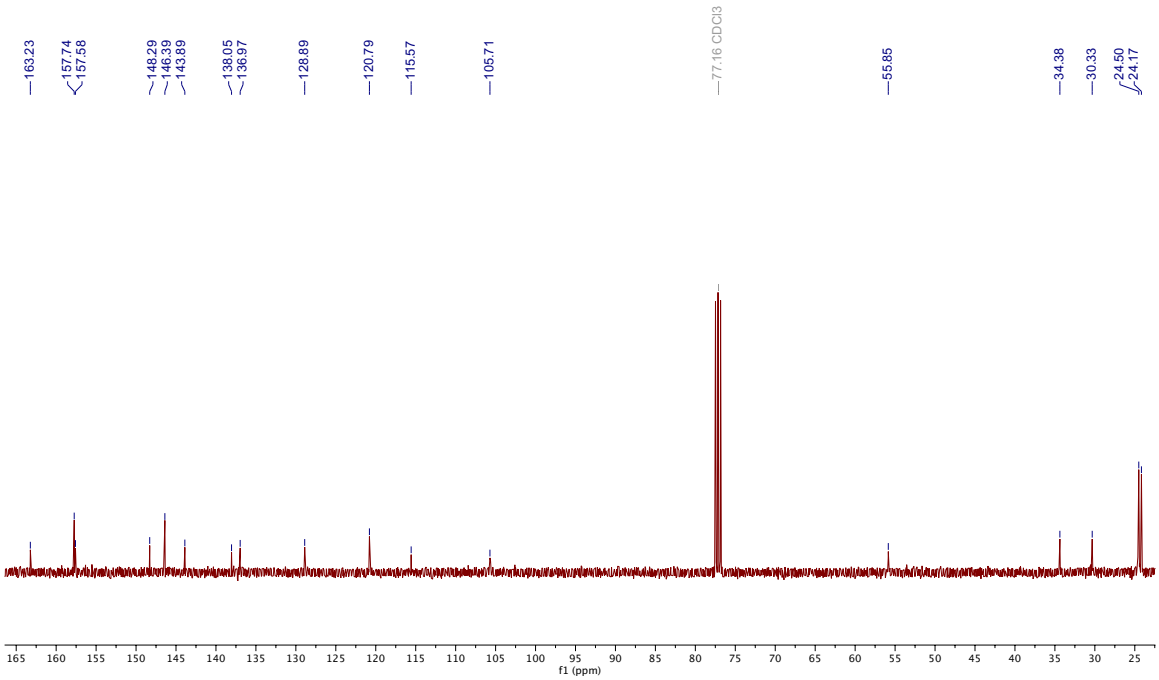

Figure 30. $^{13}C\{^{1}H\}$ NMR spectrum (101 MHz, $CDCl_3$) 1,2,3,4,5,6-hexakis(2-(2',4',6'-triisopropyl-3,5-dimethoxy-[1,1'-biphenyl]-4-yl)pyrimidin-5-yl)benzene **(3b).**

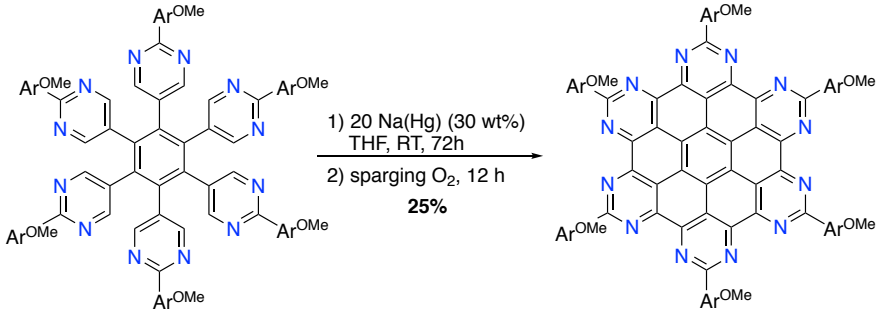

Synthesis of HBC-N$_{12}$(Ar^{OMe})$_6$. In an N_2-purged glovebox, a 20-mL scintillation vial is charged with 1,2,3,4,5,6-hexakis(2-(2',4',6'-triisopropyl-3,5-dimethoxy-[1,1'-biphenyl]-4-yl)pyrimidin-5-yl)benzene (**3b**) (100 mg, 0.039 mmol), 5 mL THF and a magnetic pre-reduced stir bar. In a separate vial, sodium (18 mg, 0.8 mmol) and mercury (40 mg, 30 wt%) are weighed out and carefully mixed with agitation. The solid alloy is added directly to the vial containing the stirring suspension of **3b** and stirred at room temperature for 72 h. The solution becomes a homogeneous deep red color after 20 min. The scintillation vial is brought outside of the box and quenched with isopropanol over 1 h. This solution is then sparged with dioxygen for 12 h, concentrated under a reduced pressure, and extracted with chloroform and filtered. *Caution: Hg is toxic and should be handled and disposed of in an exclusive container*. The crude solid is charged with ethyl acetate and is filtered over a bed of silica gel on a sintered glass funnel. The frit is continuously washed with ethyl acetate until the filtrate is colorless. Dichloromethane is added until the filtrate runs colorless. This fraction is concentrated under reduced pressure on a rotary evaporator to yield a yellow solid, which is the desired compound **HBC-N$_{12}$(Ar^{OMe})$_6$** and is dried at 70ºC for 12 h and stored in an N_2-purged glovebox. (20 mg, 25%) ^{1}H NMR (400 MHz, $CDCl_3$) δ = 7.15 (s, 2H, Ar*H*), 6.65 (s, 2H, Ar*H*), 3.83 (s, 6H, -OCH_3), 3.02 (br m, 3H, *ortho* and *para* C*H*(CH$_3$)$_2$), 1.25 (s, 18H, *ortho* and *para* CH(CH_3)$_2$). ^{13}C{^{1}H} NMR (101 MHz, $CDCl_3$) δ = 161.42 (aryl-*C*), 160.40 (aryl-*C*), 148.45 (aryl-*C*), 146.46 (aryl-*C*), 146.24 (aryl-*C*), 137.04 (aryl-*C*), 120.86 (aryl-*C*), 120.69 (aryl-*C*), 112.91 (aryl-*C*), 108.07 (aryl-*C*), 105.52 (aryl-*C*), 98.72 (aryl-*C*), 55.45 (-O*C*H$_3$), 34.38 (*para*-*C*H(CH$_3$)$_2$), 30.34 (*ortho*-*C*H(CH$_3$)$_2$), 24.57 (*ortho*-

$CH(CH_3)_2$), 24.21 (*para*-$CH(CH_3)_2$). Anal. calcd. (%) for $C_{167}H_{184}N_{12}O_{12}$: C, 78.66; H, 7.31; N, 6.55. Found: C, 78.65; H, 7.32; N, 6.50.

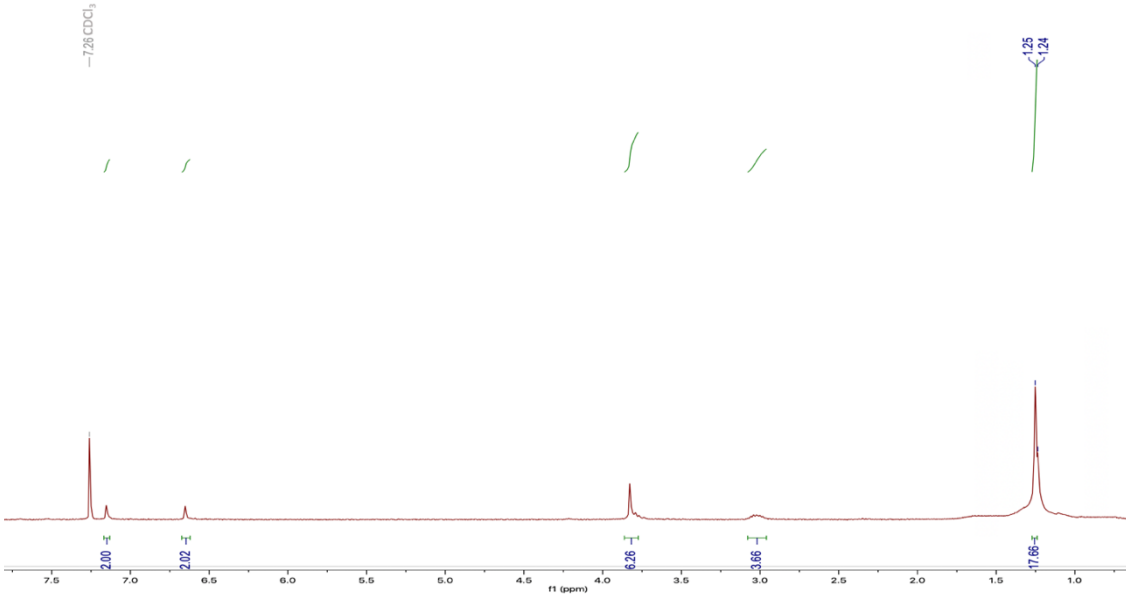

Figure 31. ^{1}H NMR spectrum (400 MHz, $CDCl_3$) of **HBC-N_{12}(Ar^{OMe})$_6$.**

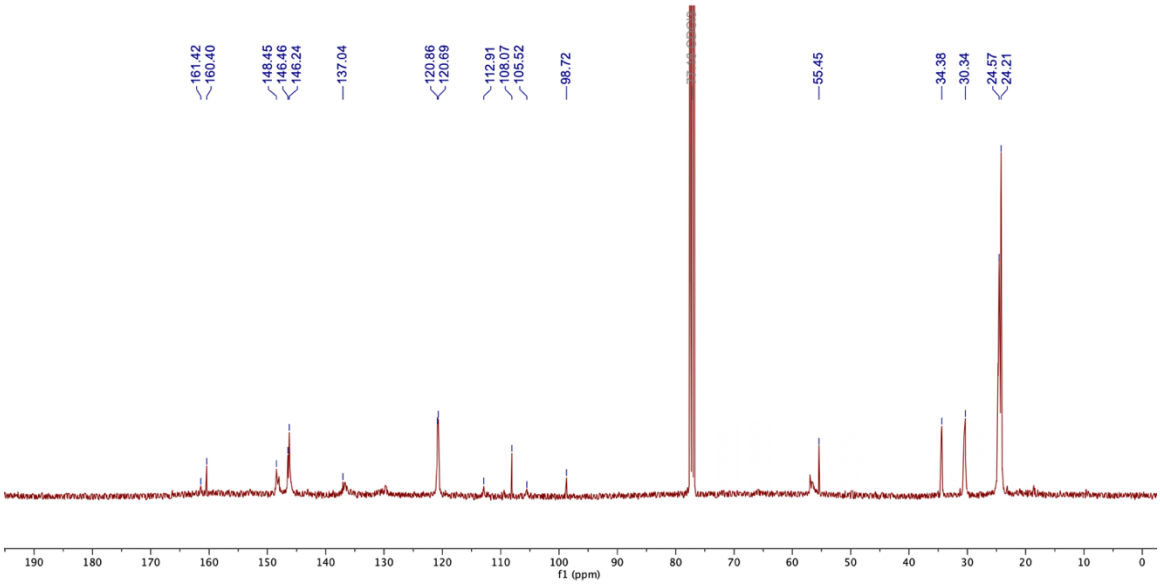

Figure 32. $^{13}C\{^{1}H\}$ NMR spectrum (101 MHz, $CDCl_3$) of **HBC-N_{12}(Ar^{OMe})$_6$.**

SUPPLEMENTARY DATA/FIGURES

Additional crystal structures

*****Unless otherwise stated, thermal ellipsoids are drawn at 50% probability for all structures displayed below. Hydrogen atoms and solvent molecules are omitted for clarity.*

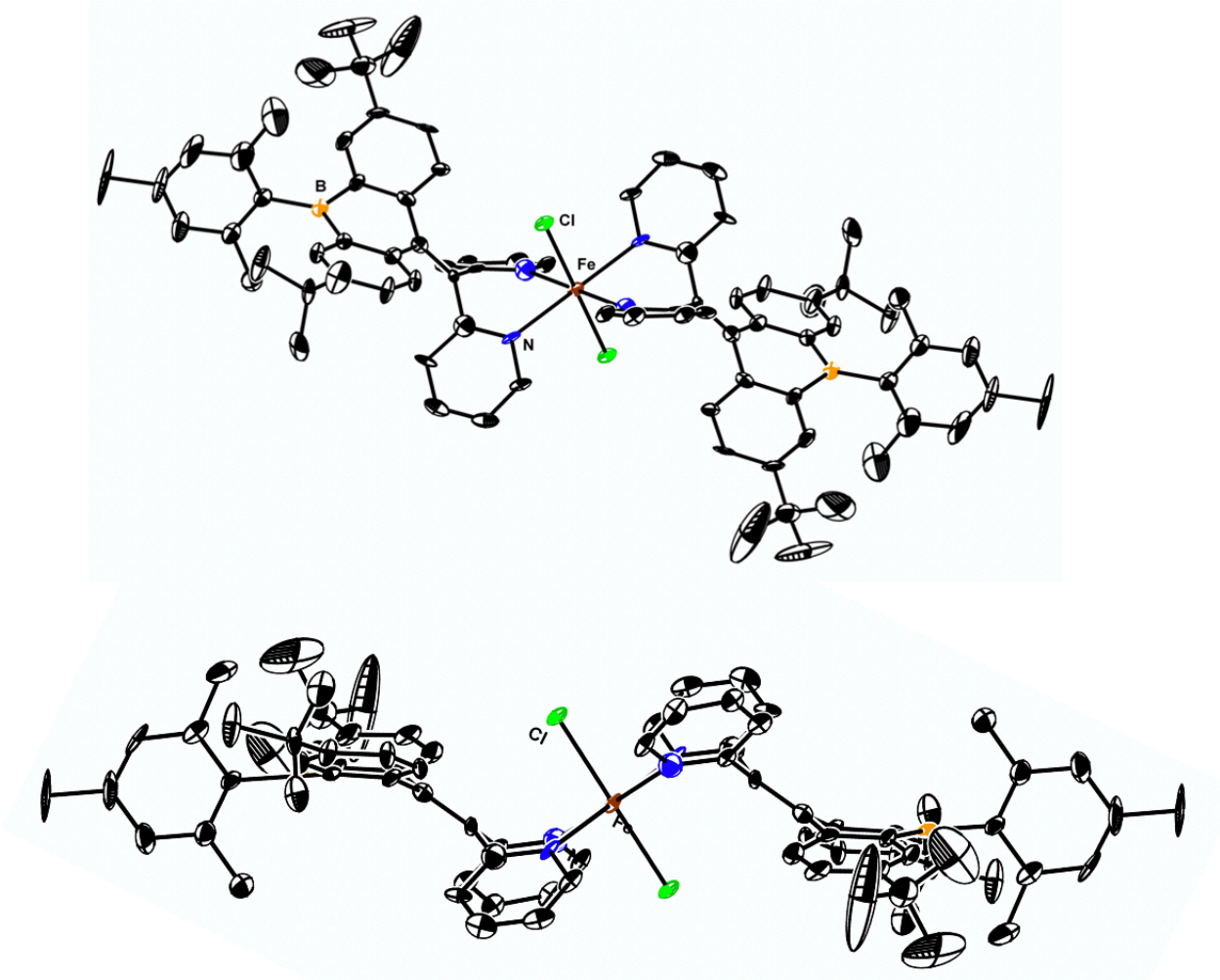

Figure 33. Solid state structure from single crystal XRD of **(11a)$_2$FeCl$_2$.**

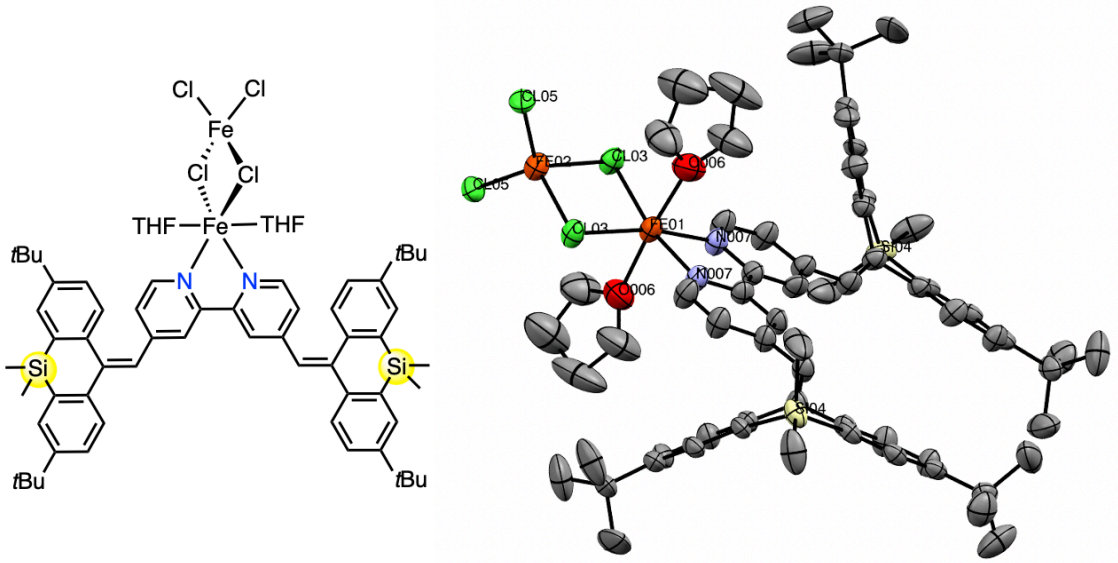

Figure 34. Solid state structure from single crystal XRD of **(bpy^{SiMe2})Fe$_2$Cl$_4$(THF)$_2$.**

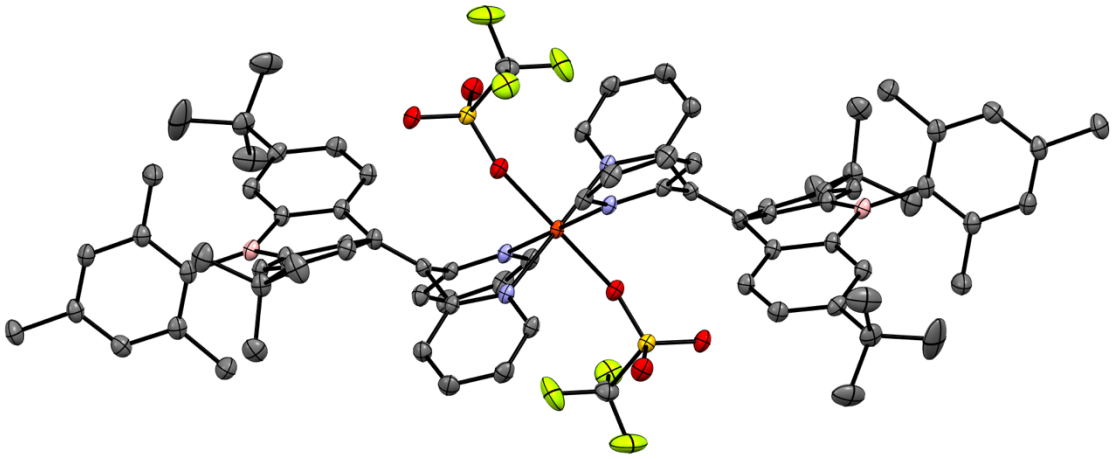

Figure 35. Solid state structure from single crystal XRD of **(11a)$_2$Fe(OTf)$_2$.** Orange: Fe; red: O; lime green: F; yellow: S; pink: boron; gray: C; blue: N.

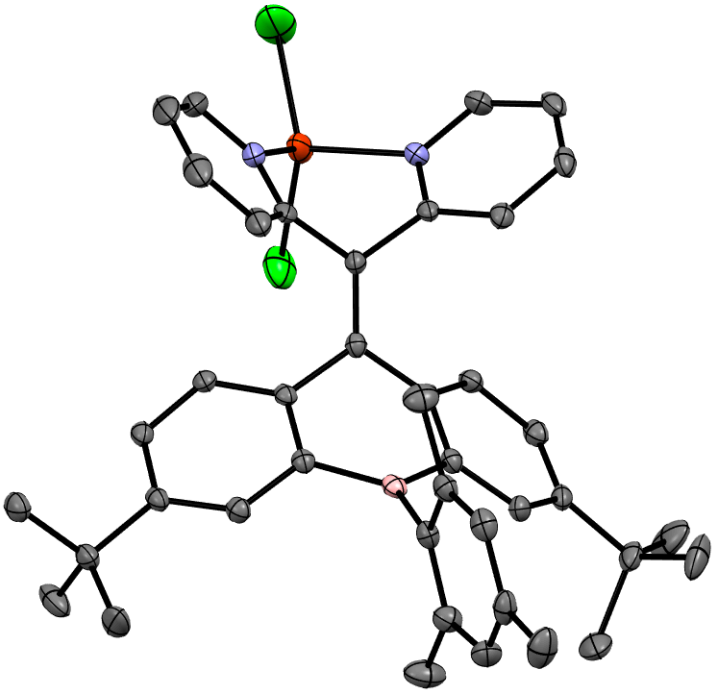

Figure 36. Solid state structure from single crystal XRD of (**11a**)$FeCl_2$. Orange: Fe; green: Cl.

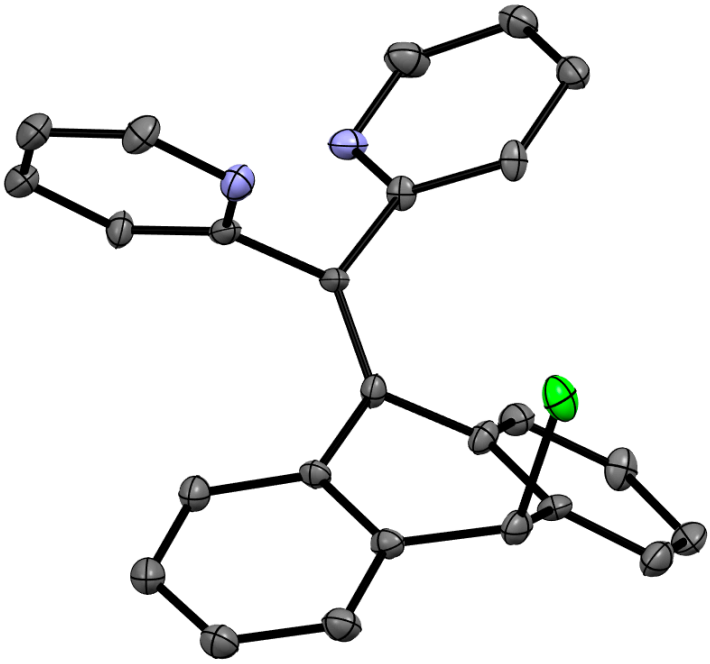

Figure 37. Solid state structure from single crystal XRD of **6a**.

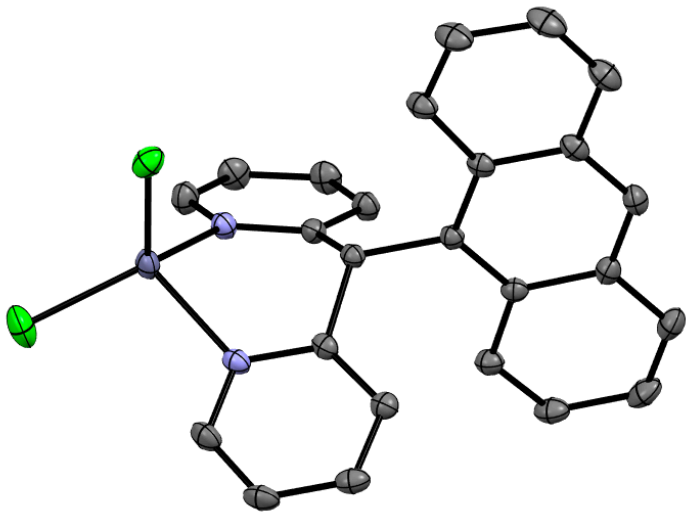

Figure 38. Solid state structure from single crystal XRD of **$Cl_2Zn(py)_2CH(9\text{-anthracenyl})$.**

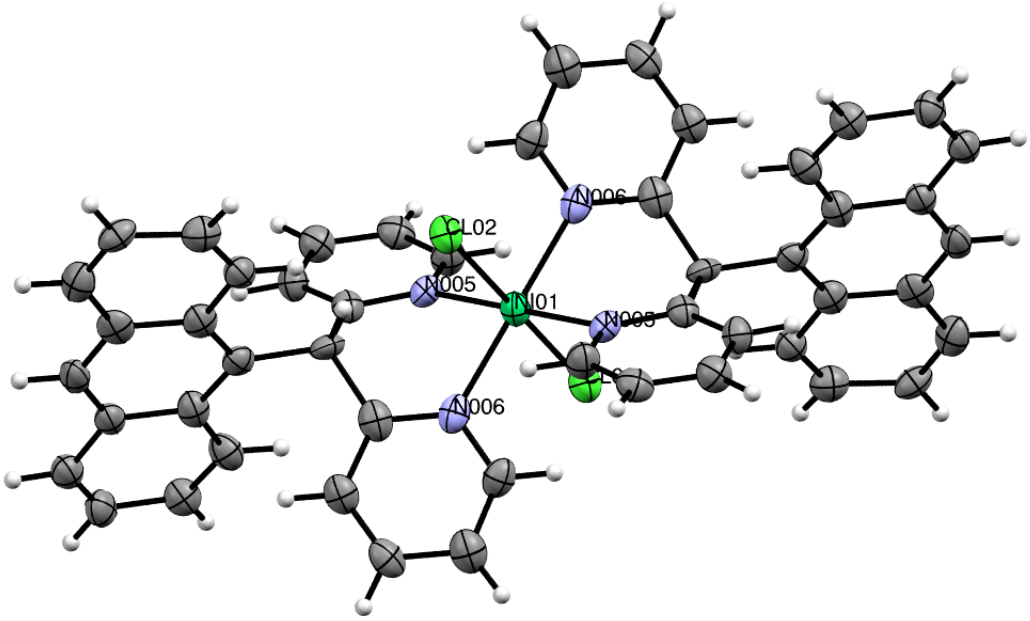

Figure 39. Solid state structure from single crystal XRD of **[Ni]**. Hydrogen atoms displayed.

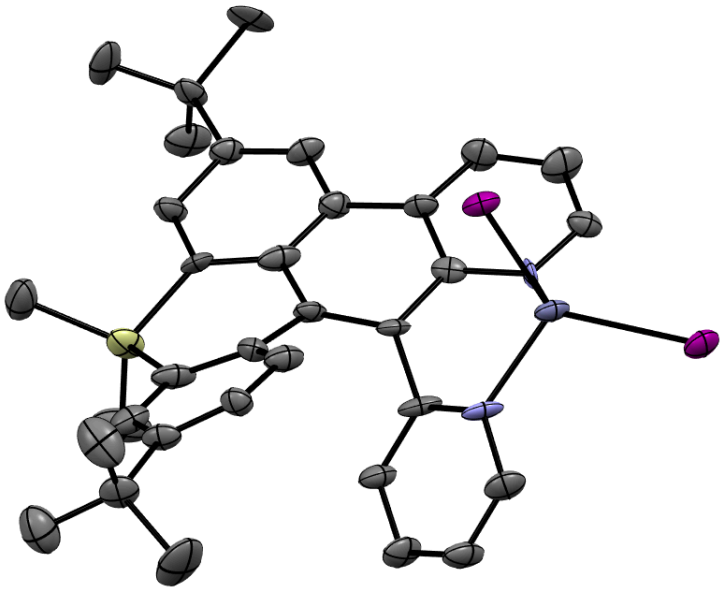

Figure 40. Solid state structure from single crystal XRD of **13b-ZnI$_2$**.

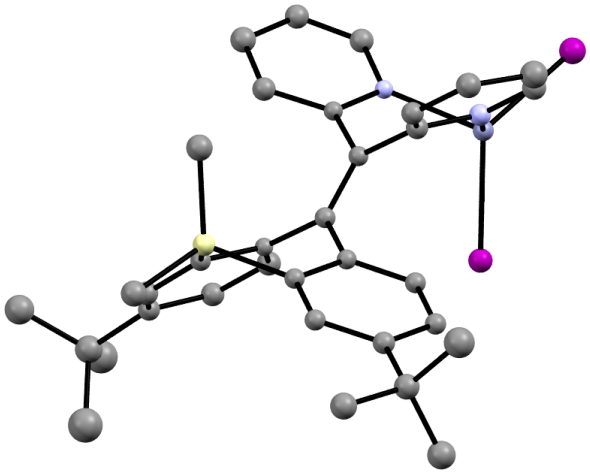

Figure 41. Solid state structure from single crystal XRD of **11b-ZnI$_2$**. Structure could not be anisotropically refined.

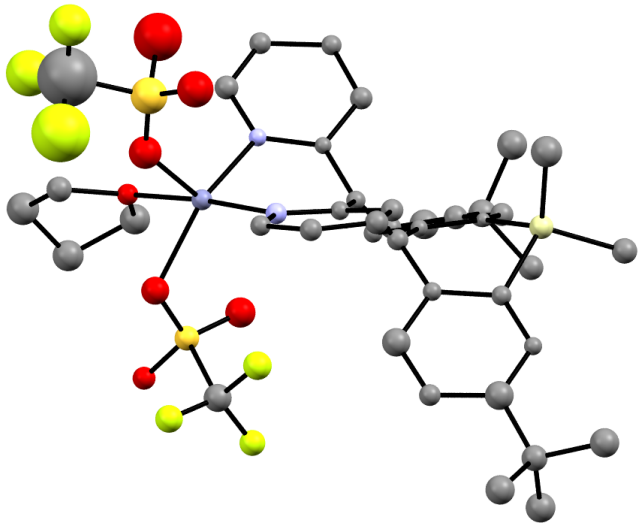

Figure 42. Solid state structure from single crystal XRD of **11b-Zn(OTf)$_2$**. Structure could not be anisotropically refined.

REFERENCES

(1) Draper, S. M.; Gregg, D. J.; Madathil, R. Heterosuperbenzenes: A New Family of Nitrogen-Functionalized, Graphitic Molecules. *J. Am. Chem. Soc.* **2002**, *124* (14), 3486–3487.

(2) Draper, S. M.; Gregg, D. J.; Schofield, E. R.; Browne, W. R.; Duati, M.; Vos, J. G.; Passaniti, P. Complexed Nitrogen Heterosuperbenzene: The Coordinating Properties of a Remarkable Ligand. *J. Am. Chem. Soc.* **2004**, *126* (28), 8694–8701.

(3) Lytle, F. E.; Hercules, D. M. Luminescence of Tris(2,2'-Bipyridine)Ruthenium(II) Dichloride. *J. Am. Chem. Soc.* **1969**, *91* (2), 253–257.

(4) Qiao, X.; Li, Q.; Schaugaard, R. N.; Noffke, B. W.; Liu, Y.; Li, D.; Liu, L.; Raghavachari, K.; Li, L. Well-Defined Nanographene–Rhenium Complex as an Efficient Electrocatalyst and Photocatalyst for Selective CO2 Reduction. *J. Am. Chem. Soc.* **2017**, *139* (11), 3934–3937.

(5) Li, Q.; Noffke, B. W.; Wang, Y.; Menezes, B.; Peters, D. G.; Raghavachari, K.; Li, L. Electrocatalytic Oxygen Activation by Carbanion Intermediates of Nitrogen-Doped Graphitic Carbon. *J. Am. Chem. Soc.* **2014**, *136* (9), 3358–3361.

(6) Koenig, J. D. B.; Dubrawski, Z. S.; Rao, K. R.; Willkomm, J.; Gelfand, B. S.; Risko, C.; Piers, W. E.; Welch, G. C. Lowering Electrocatalytic CO2 Reduction Overpotential Using N-Annulated Perylene Diimide Rhenium Bipyridine Dyads with Variable Tether Length. *J. Am. Chem. Soc.* **2021**, *143* (40), 16849–16864.

(7) Schaugaard, R. N.; Raghavachari, K.; Li, L. Redox "Innocence" of Re(I) in Electrochemical CO2 Reduction Catalyzed by Nanographene–Re Complexes. *Inorg. Chem.* **2018**, *57* (17), 10548–10556.

(8) Wang, M.; Torbensen, K.; Salvatore, D.; Ren, S.; Joulié, D.; Dumoulin, F.; Mendoza, D.; Lassalle-Kaiser, B.; Işci, U.; Berlinguette, C. P.; et al. CO2 Electrochemical Catalytic Reduction with a Highly Active Cobalt Phthalocyanine. *Nat. Commun.* **2019**, *10* (1), 3602.

(9) Kumar, B.; Asadi, M.; Pisasale, D.; Sinha-Ray, S.; Rosen, B. A.; Haasch, R.; Abiade, J.; Yarin, A. L.; Salehi-Khojin, A. Renewable and Metal-Free Carbon Nanofibre Catalysts for Carbon Dioxide Reduction. *Nat. Commun.* **2013**, *4* (1), 2819.

(10) Zhang, L.; Fischer, J. M. T. A.; Jia, Y.; Yan, X.; Xu, W.; Wang, X.; Chen, J.; Yang, D.; Liu, H.; Zhuang, L.; et al. Coordination of Atomic Co–Pt Coupling Species at Carbon Defects as Active Sites for Oxygen Reduction Reaction. *J. Am. Chem. Soc.* **2018**, *140* (34), 10757–10763.

(11) Yuan, K.; Lützenkirchen-Hecht, D.; Li, L.; Shuai, L.; Li, Y.; Cao, R.; Qiu, M.; Zhuang, X.; Leung, M. K. H.; Chen, Y.; et al. Boosting Oxygen Reduction of Single Iron Active Sites via Geometric and Electronic Engineering: Nitrogen and Phosphorus Dual Coordination. *J. Am. Chem. Soc.* **2020**, *142* (5), 2404–2412.

(12) Hertz, V. M.; Massoth, J. G.; Bolte, M.; Lerner, H.-W.; Wagner, M. En Route to Stimuli-Responsive Boron-, Nitrogen-, and Sulfur-Doped Polycyclic Aromatic Hydrocarbons. *Chem. – A Eur. J.* **2016**, *22* (37), 13181–13188.

(13) Hertz, V. M.; Bolte, M.; Lerner, H.-W.; Wagner, M. Boron-Containing Polycyclic Aromatic Hydrocarbons: Facile Synthesis of Stable, Redox-Active Luminophores. *Angew. Chemie Int. Ed.* **2015**, *54* (30), 8800–8804.

(14) Mallory, F. B.; Butler, K. E.; Evans, A. C.; Brondyke, E. J.; Mallory, C. W.; Yang, C.; Ellenstein, A. Phenacenes: A Family of Graphite Ribbons. 2. Syntheses of Some [7]Phenacenes and an [11]Phenacene by Stilbene-like Photocyclizations. *J. Am. Chem. Soc.* **1997**, *119* (9), 2119–2124.

(15) Derivatives of compound 5 in which the 10 positions of the anthracene bears either a trimethylsilyl or 3, 5-di-tert-butylaryl substituent would yield intractable mixtures upon reaction with thionyl chloride.

(16) Smid, W. I.; Schoevaars, A. M.; Kruizinga, W.; Veldman, N.; Smeets, W. J. J.; Spek, A. L.; Feringa, B. L. Synthesis and Dynamic Behaviour of New Metallo-Based Sterically Overcrowded Alkenes. *Chem. Commun.* **1996**, No. 19, 2265–2266.

(17) Volpi, G.; Garino, C.; Breuza, E.; Gobetto, R.; Nervi, C. Dipyridylketone as a Versatile Ligand Precursor for New Cationic Heteroleptic Cyclometalated Iridium Complexes. *Dalt. Trans.* **2012**, *41* (3), 1065–1073.

(18) Sandoval, J. J.; Palma, P.; Álvarez, E.; Rodríguez-Delgado, A.; Cámpora, J. Dibenzyl and Diallyl 2,6-Bisiminopyridinezinc(Ii) Complexes: Selective Alkyl Migration to the Pyridine Ring Leads to Remarkably Stable Dihydropyridinates. *Chem. Commun.* **2013**, *49* (60), 6791–6793.

(19) Guo, D.; Shibuya, R.; Akiba, C.; Saji, S.; Kondo, T.; Nakamura, J. Active Sites of Nitrogen-Doped Carbon Materials for Oxygen Reduction Reaction Clarified Using Model Catalysts. *Science (80-.).* **2016**, *351* (6271), 361 LP – 365.

(20) Lewiński, J.; Marciniak, W.; Lipkowski, J.; Justyniak, I. New Insights into the Reaction of Zinc Alkyls with Dioxygen. *J. Am. Chem. Soc.* **2003**, *125* (42), 12698–12699.

(21) Mukherjee, D.; Ellern, A.; Sadow, A. D. Remarkably Robust Monomeric Alkylperoxyzinc Compounds from Tris(Oxazolinyl)Boratozinc Alkyls and O2. *J. Am. Chem. Soc.* **2012**, *134* (31), 13018–13026.

(22) Iodide generated from the photolysis reaction appeared to replace chlorides bound to Zn. No Title.

(23) Kirschner, S.; Mewes, J.-M.; Bolte, M.; Lerner, H.-W.; Dreuw, A.; Wagner, M. How Boron Doping Shapes the Optoelectronic Properties of Canonical and Phenylene-Containing Oligoacenes: A Combined Experimental and Theoretical Investigation. *Chem. – A Eur. J.* **2017**, *23* (21), 5104–5116.

(24) Reath, A. H.; Ziller, J. W.; Tsay, C.; Ryan, A. J.; Yang, J. Y. Redox Potential and Electronic Structure Effects of Proximal Nonredox Active Cations in Cobalt Schiff Base Complexes. *Inorg. Chem.* **2017**, *56* (6), 3713–3718.

(25) Sampson, M. D.; Kubiak, C. P. Manganese Electrocatalysts with Bulky Bipyridine Ligands: Utilizing Lewis Acids To Promote Carbon Dioxide Reduction at Low Overpotentials. *J. Am. Chem. Soc.* **2016**, *138* (4), 1386–1393.

(26) Zhanaidarova, A.; Steger, H.; Reineke, M. H.; Kubiak, C. P. Chelated [Zn(Cyclam)]2+ Lewis Acid Improves the Reactivity of the Electrochemical Reduction of CO2 by Mn Catalysts with Bulky Bipyridine Ligands. *Dalt. Trans.* **2017**, *46* (37), 12413–12416.

(27) Pangborn, A. B.; Giardello, M. A.; Grubbs, R. H.; Rosen, R. K.; Timmers, F. J. Safe and Convenient Procedure for Solvent Purification. *Organometallics* **1996**, *15* (5), 1518–1520.

(28) Schlosser, M.; Hartmann, J. Transmetalation and Double Metal Exchange: A Convenient Route to Organolithium Compounds of the Benzyl and Allyl Type. *Angew. Chemie Int. Ed. English* **1973**, *12* (6), 508–509.

(29) Tsui, E. Y.; Day, M. W.; Agapie, T. Trinucleating Copper: Synthesis and Magnetostructural Characterization of Complexes Supported by a Hexapyridyl 1,3,5-Triarylbenzene Ligand. *Angew. Chemie Int. Ed.* **2011**, *50* (7), 1668–1672.

(30) Canty, A. J.; Minchin, N. J.; Engelhardt, L. M.; Skelton, B. W.; White, A. H. <P>Synthetic and Structural Studies of Binuclear Organopalladium(II) Complexes Including a Bis(Pyridin-2-Yl)Phenylmethyl Complex With Four- and Eight-Membered Palladocycle Rings, <I>trans</I>(N,N)-(Pd(μ-Py_2PhC-N,N',C')Cl)$_2$.&#189. *Aust. J. Chem.* **1988**, *41* (5), 651–665.

APPENDIX D

POTASSIUM-CONTAINING IONOMERS ENHANCE CO_2R PERFORMANCE ON Au ELECTRODES

ACKNOWLEDGEMENTS

I am grateful to Meaghan A. Bruening for carrying out the synthesis of the polymers. This material is based on work performed by the Liquid Sunlight Alliance, which is supported by the U.S. Department of Energy, Office of Science, Office of Basic Energy Sciences, Fuels from Sunlight Hub under Award DE-SC0021266. The Resnick Sustainability Institute at Caltech is acknowledged for support of the laboratory facilities in which this research was conducted.

INTRODUCTION

The results presented in Chapter III highlight elevated CO_2R performance to C_{2+} products consistent with elevated CO_2 mass transport; high FE_{C2+} was observed. It is of interest to investigate effects on CO_2R performance as coatings on other metallic electrodes to get a more complete picture on the films' effects on the microenvironment. Pyridinium-derived films that demonstrated HER suppression on polycrystalline Cu foil demonstrated a similar effect on Ag foil; no hydrogen was detected with nearly all current going towards generation of CO (95% FE).[1]

RESULTS AND DISCUSSION

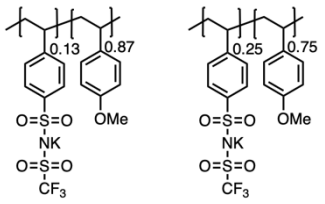

22 **21**

Coatings were drop casted onto Au/PTFE in a similar fashion to the experiments on Cu/PTFE. Several potentials were tested for each bare Au and Au coated with **21**. Improvement in FE_{CO} was observed relative to unmodified Au at nearly every potential tested, with the highest selectivity observed at –0.62 V vs. RHE in 1 M $KHCO_3$ (96%). $|j_{CO2R}|$ increased as well, improving by a factor of 3 at this potential (Figure 1). Insignificant suppression of $|j_{H2}|$ was observed, consistent with our results on Cu. Comparing between ionomers of different potassium content (**21** vs. **22**, Figure 2), $|j_{CO}|$ correlates with relative concentration of the K^+-containing comonomer. Along with observations from CO_2R on Cu, these results altogether highlight that elevated CO_2 mass transport is the most likely impact of the ionomer films on the microenvironment.

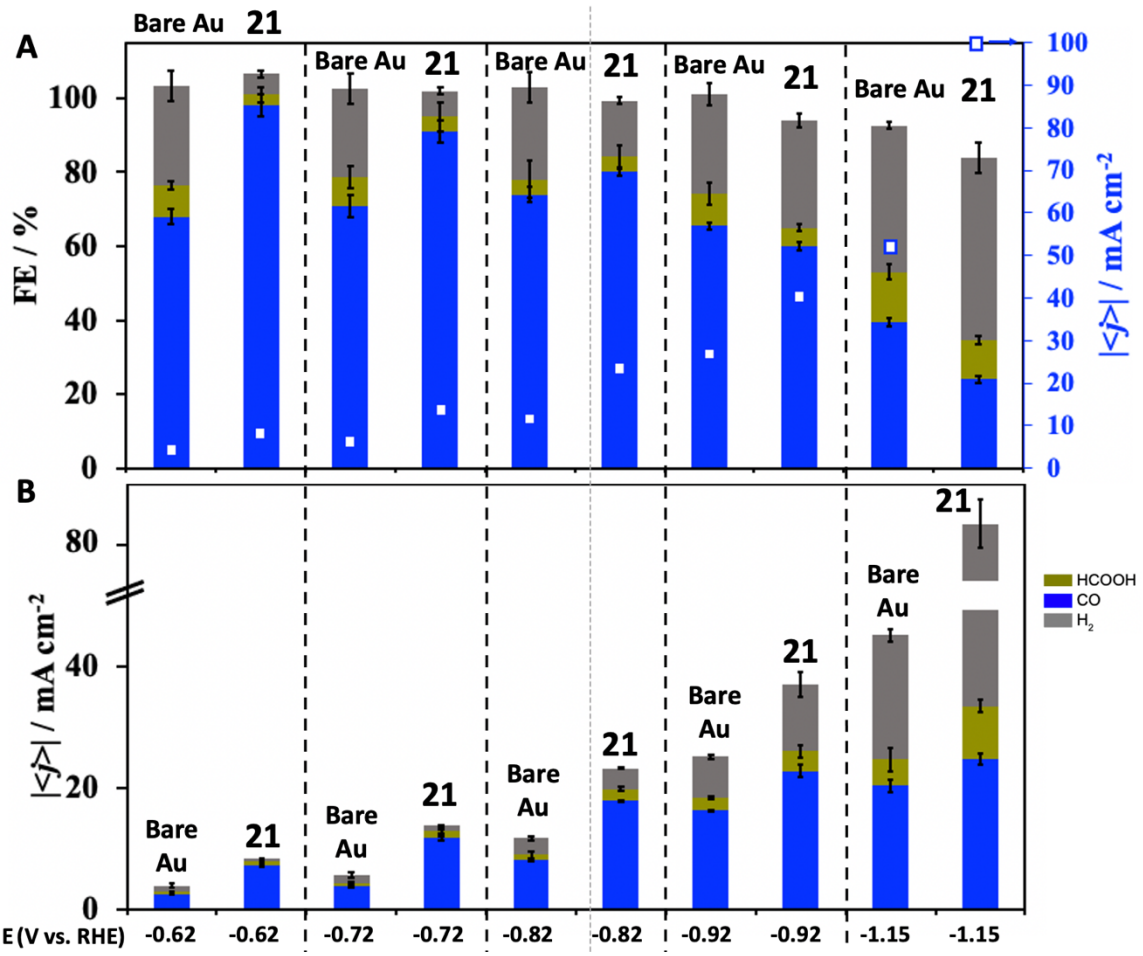

Figure 1. A. Faradaic efficiency (FE, columns) and current density (white squares) for CO_2R products on Au/PTFE in the presence of ionomer films casted from a solution of **21.** Electrolysis performed in 1 M $KHCO_{3(aq)}$ for 30 minutes. B. Partial current densities for trials shown in panel A.

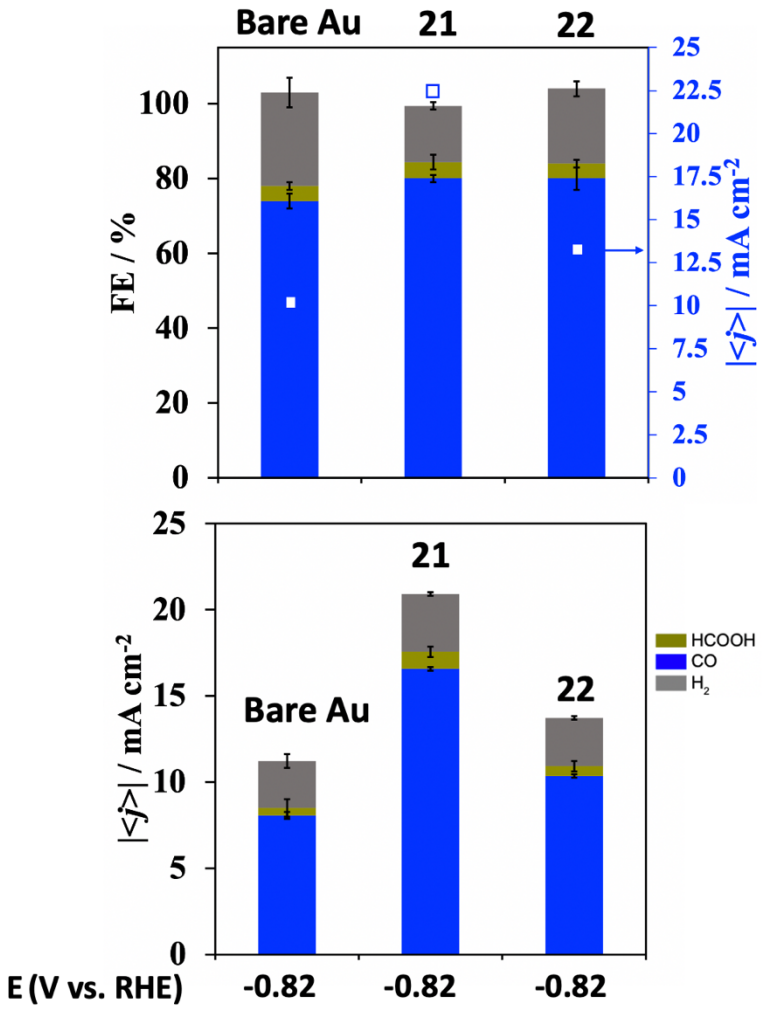

Figure 2. A. Faradaic efficiency (FE, columns) and current density (white squares) for CO_2R products on Au/PTFE in the presence of ionomer films casted from a solution of **21** and **22.** Electrolysis performed in 1 M $KHCO_{3(aq)}$ for 30 minutes. $E_{applied}$ = –0.82 V vs. RHE. B. Partial current densities for trials shown in panel A.

EXPERIMENTAL

Materials and Methods

General Considerations. All solvents and reagents were obtained from commercial sources (Aldrich, Merck, and Combi Blocks) and used as received, unless stated otherwise. 4-Methoxystyrene was dried with CaH_2 and filtered under inert atmosphere. **K-STFSI** was prepared based on a previously reported synthesis.[2] Acetonitrile was dried by passing over activated alumina by the method of Grubbs[3] and stored over 3 Å molecular sieves in a N_2-filled glovebox.

Potassium carbonate (99.995%), 4-methoxystyrene, solution (99%), isopropanol (HPLC grade), and ethanol (HPLC grade) were purchased from Sigma Aldrich. Polytetrafluoroethylene (PTFE) was purchased from McMaster-Carr. The leakless Ag/AgCl reference electrode was purchased from Innovative Instruments. Platinum mesh (99.99% Pt, 25 mm × 25 mm × 0.05 mm) was purchased from Alfa Aesar. CO_2 (research grade) was purchased from Airgas. Deuterium oxide (D 99.96%) and CD_3CN (99.9%) were purchased from Cambridge Isotope Laboratories. The ^{1}H and ^{19}F NMR solution-state NMR spectra were recorded on a Bruker 400 MHz with broadband auto-tune OneProbe. ^{13}C solution-state NMR spectra were recorded on a Bruker 400 MHz instrument with a prodigy broadband cryoprobe. Shifts were reported relative to the residual solvent peak.

Water was purified by a Nanopure Analytical Ultrapure Water System (Thermo Scientific) or a Milli-Q Advantage A10 Water Purification System (Millipore) with specific resistance of 18.2 MΩ·cm at 25 °C. A VWR sympHony™ pH meter (calibrated with a pH = 1.68 standard) was used to determine the pH of the electrolytes before experiments.

Electrochemistry

Electrolyte Preparation

Potassium bicarbonate electrolyte (1 M $KHCO_{3(aq)}$) was prepared by sparging an aqueous solution of potassium carbonate (0.5 M $K_2CO_{3(aq)}$) with CO_2 for at least 1 hour prior to electrolysis. This process converts K_2CO_3 into $KHCO_3$ and saturates the electrolyte solution with CO_2.

Electrode Preparation

The gas diffusion electrodes (GDEs) were prepared by sputtering 300 nm Au onto a 5 cm x 5 cm portion of polytetrafluoroethylene membrane (pore size of 450 nm, with polypropylene support on backside) using a pure Au target (99.99%) at a sputtering rate of 1 Å s^{-1}.

A 0.3 mg mL^{-1} stock solution of the ionomer was prepared in 50% v/v EtOH/^{i}PrOH and sonicated for 30 minutes to ensure complete dissolution. For a standard loading, 15 μL were drop casted (4.5 μg) onto a 2.5 cm^2 electrode, ensuring complete coverage of the Cu nanoparticles, and allowed to dry under ambient conditions for 1 hour.

Electrochemical Measurements in the GDE (Flow) Cell

CO_2R and COR measurements were conducted in a gas-tight liquid-electrolyte flow cell. Chronoamperometry experiments were carried out in a custom-made PEEK liquid-electrolyte cell similar to the one reported by Sargent and co-workers.[4] The liquid-electrolyte flow cell consists of three compartments: gas chamber, catholyte chamber, and anolyte chamber. The PTFE electrode was sandwiched between CO_2 gas chamber and catholyte chamber with an exposure area of 0.5 cm^{-2}. Catholyte and anolyte chambers were separated by a Selemion AMV anion-exchange membrane (AGC Engineering Co.). The reference electrode was calibrated against H^+/H_2 on Pt in a 0.5 M sulfuric acid solution (0 V vs. RHE) and saturated calomel electrode (SCE) (+0.241 V saturated vs. RHE). An Autolab PGSTAT204 in a potentiostatic mode was used as electrochemical workstation. The PTFE electrode, leakless Ag/AgCl electrode (Innovative Instruments), and Pt mesh (rinsed with

water and annealed with a butane torch) were employed as working, reference and counter electrodes, respectively. The applied potentials were converted to the reversible hydrogen electrode (RHE) scale with iR correction through the following equation:

$$E_{corrected}\,(\text{vs. RHE}) = E\,(\text{vs. Ag/AgCl}) + (0.059 \times \text{pH}) + 0.210 + iR. \quad (1)$$

$E_{applied}$ in this report is the applied potential without iR compensation. In order to convert from potential vs. Ag/AgCl, we use the following relationship:

$$E_{applied}\,(\text{vs. RHE}) = E\,(\text{vs. Ag/AgCl}) + (0.059 \times \text{pH}) + 0.210 \quad (2)$$

where i is the current at each applied potential and R is the equivalent series resistance measured via potentioelectrochemical impedance spectroscopy (PEIS) in the frequency range of 10^5 – 0.1 Hz with an amplitude of 10 mV. The appropriate gas-saturated electrolyte was used as both catholyte and anolyte and was circulated through the flow cell using peristaltic pumps with a silicone Shore A50 tubing. The electrolyte was bubbled with the desired gas during the entire electrolysis process. The electrolyte flow rate was kept at 10 mL min^{-1}. The flow rate of the gas flowing into the gas chamber was kept at 30 sccm by a digital mass flow controller.

Ohmic resistance values were determined with procedures described elsewhere[5,6] and employed in our prior work[4,7,8] PEIS measurements were carried out prior to and after each electrolysis experiment to determine the Ohmic resistance of the flow cell and ensure it is unchanged during the experiment.[9,10] The impedance measurements were carried out at frequencies ranging from 200 kHz to 100 MHz. A Nyquist plot was obtained, and in the low-frequency region (containing a Warburg element) a line was plotted to determine the value of the intersection with the x-axis, representing the

Ohmic resistance.[5] An average of 3 measurements was taken to calculate the value of R. Typically, small resistances were measured, ranging from 4 to 7 Ω. The potentiostat was set to compensate for 85 % of the Ohmic drop, with the remaining 15 % being compensated for after the measurements.[5,6]

All chronoamperometric experiments were performed for 30 min at 25 °C. Before each electrolysis experiment, the ionomer was drop casted onto a 2.5 cm^2 Cu/PTFE electrode. The entire Ohmic drop was compensated before and after the measurement. The effluent gas stream coming from the cell (30 mL min^{-1}) was flowed into the sample loops of a gas chromatograph (GC-FID/TCD, SRI 8610C, in Multi Gas 5 configuration) equipped with HayeSep D and Molsieve 5A columns. Methane, ethylene, ethane, and carbon monoxide were detected by a methanizer-flame ionization detector (FID) and the hydrogen was detected by a thermal conductivity detector (TCD). Every 15 minutes, 2 mL of gas was sampled to determine the concentration of gaseous products. After electrolysis, the liquid products in the catholytes were quantified by both HPLC (Thermo Scientific Ultimate 3000) and ^{1}H NMR spectroscopy (Bruker 400 MHz Spectrometer).

For ^{1}H NMR analysis, 630 µL of the electrolyte sample were combined with 30 µL of internal standard solution (10 mM DMSO and 50 mM phenol) and 70 µL of D_2O. Water suppression was achieved with a presaturation sequence.[7,10]

The Faradaic efficiencies for gaseous products was calculated from the following equations:

$$F_m = \frac{pF_v}{RT} \tag{3}$$

$$FE_{prod} = \frac{n_{prod} F x_{prod} F_m}{i}. \quad (4)$$

F_m is the molar flow, defined by the pressure p, the volume flow F_v, the gas constant R, and temperature T. FE_{prod} is the Faradaic efficiency of a gaseous product $prod$, defined by the electron transfer coefficient of the product n_{prod}, Faraday's constant F, the fraction of the product x_{prod}, the molar flow F_m, and the current i.

Error bars shown in all figures and tables represent standard deviations from at least three replicate measurements.

REFERENCES

(1) Thevenon, A.; Rosas-Hernández, A.; Fontani Herreros, A. M.; Agapie, T.; Peters, J. C. Dramatic HER Suppression on Ag Electrodes via Molecular Films for Highly Selective CO2 to CO Reduction. *ACS Catal.* **2021**, *11* (8), 4530–4537.

(2) Luo, G.; Yuan, B.; Guan, T.; Cheng, F.; Zhang, W.; Chen, J. Synthesis of Single Lithium-Ion Conducting Polymer Electrolyte Membrane for Solid-State Lithium Metal Batteries. *ACS Appl. Energy Mater.* **2019**, *2* (5), 3028–3034.

(3) Pangborn, A. B.; Giardello, M. A.; Grubbs, R. H.; Rosen, R. K.; Timmers, F. J. Safe and Convenient Procedure for Solvent Purification. *Organometallics* **1996**, *15* (5), 1518–1520.

(4) Li, F.; Thevenon, A.; Rosas-Hernández, A.; Wang, Z.; Li, Y.; Gabardo, C. M.; Ozden, A.; Dinh, C. T.; Li, J.; Wang, Y.; et al. Molecular Tuning of CO2-to-Ethylene Conversion. *Nature* **2020**, *577* (7791), 509–513.

(5) Lazanas, A. C.; Prodromidis, M. I. Electrochemical Impedance Spectroscopy─A Tutorial. *ACS Meas. Sci. Au* **2023**, *3* (3), 162–193.

(6) Zheng, W. IR Compensation for Electrocatalysis Studies: Considerations and Recommendations. *ACS Energy Lett.* **2023**, *8* (4), 1952–1958.

(7) Han, Z.; Kortlever, R.; Chen, H.-Y.; Peters, J. C.; Agapie, T. CO2 Reduction Selective for C≥2 Products on Polycrystalline Copper with N-Substituted Pyridinium Additives. *ACS Cent. Sci.* **2017**, *3* (8), 853–859.

(8) Nie, W.; Heim, G. P.; Watkins, N. B.; Agapie, T.; Peters, J. Organic Additive-Derived Films on Cu Electrodes Promote Electrochemical CO2 Reduction to C2+ Products Under Strongly Acidic Conditions. *Angew. Chemie Int. Ed.* **2023**, *n/a* (n/a).

(9) Heenan, A. R.; Hamonnet, J.; Marshall, A. T. Why Careful IR Compensation and Reporting of Electrode Potentials Are Critical for the CO2 Reduction Reaction. *ACS Energy Lett.* **2022**, *7* (7), 2357–2361.

(10) Ma, M.; Zheng, Z.; Yan, W.; Hu, C.; Seger, B. Rigorous Evaluation of Liquid Products in High-Rate CO2/CO Electrolysis. *ACS Energy Lett.* **2022**, *7* (8), 2595–2601.

APPENDIX E

INVESTIGATING CO_2 ADSORPTION TO POTASSIUM-CONTAINING IONOMERS VIA SOLID STATE NMR SPECTROSCOPY

ACKNOWLEDGEMENTS

I am grateful to Dr. Sonjong Hwang and Matthew Salazar training me on solid state NMR spectroscopy. This material is based on work performed by the Liquid Sunlight Alliance, which is supported by the U.S. Department of Energy, Office of Science, Office of Basic Energy Sciences, Fuels from Sunlight Hub under Award DE-SC0021266. The Caltech Solid State NMR Facility is thanked for instrumentation and experimental support.

INTRODUCTION

The 2 Phase Thermodynamics calculations (see Chapter III) suggest that the polymers create more favorable, solvation-type interactions between K^+ and CO_2, leading to minimized Helmholtz free energy. Enhanced CO_2 adsorption in polymers has been modeled to be inversely proportional to mass transport,[1] but some experiments have demonstrated that both solubility and diffusion coefficient can be elevated in some polymers.[2] In an attempt to validate the model and enhance our understanding of polymer-CO_2 interactions, we turned to ^{13}C solid state NMR spectroscopy, where adsorption of CO_2 in metal-organic frameworks (MOFs) and coordination polymers has been previously investigated.[3–7]

RESULTS AND DISCUSSION

Each polymer (44 mg) was dissolved in acetonitrile and mixed with 30 mg of glycine hydrochloride ethyl ester, the latter compound serving as a standard to facilitate CO_2 quantification. This solution mixture was pumped down to dryness before loading the solid powder into an NMR rotor and packed tightly, all to ensure reproducibility. The rotor was loaded into a glassware apparatus charged with 1.3×10^{-6} mol of isotopically-enriched $^{13}CO_{2(g)}$, sealed, then submitted for ^{13}C solid state NMR with a magic angle spin (MAS) rate of 8 kHz.

Figure 1 shows resulting spectra for each ionomer ranging from no K^+ to 37 mol%. In each case, a peak unrelated to polymer or glycine hydrochloride ethyl ester appears between 160 and 170 ppm, which is consistent with chemisorbed CO_2. Previous literature has proposed the formation of a bond between amines in MOFs and CO_2 leading to formation of a carbamate.[4] Physisorbed CO_2 resulting from noncovalent interactions with the material were suggested to appear ~120 ppm.[7] $^{13}CO_2$ physisorbed is not evident in the spectra in

Figure 1; such a conformation cannot be ruled out since polymer peaks were evident in this region. Moreover, the greatest amount of $^{13}CO_2$ adsorbed relative to the internal standard was found with **10**, likely due to formation of a carbonate species between the methoxy substituent and CO_2.

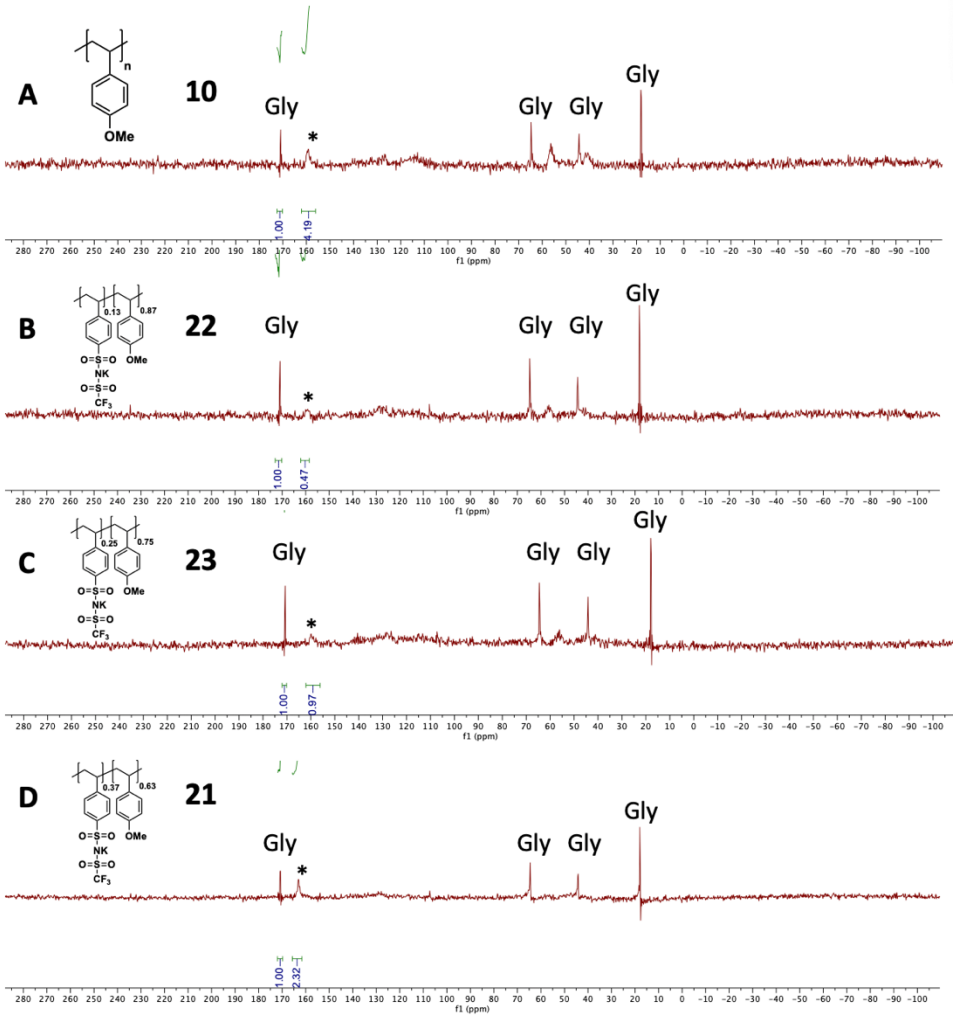

Figure 1. A-D. ^{13}C solid state NMR spectra methoxystyrene series of polymers (**10**, **21**-**23**). Peaks labeled "Gly" represent glycine hydrochloride ethyl ester peaks. Starred peak in each spectrum represents chemisorbed $^{13}CO_2$. Magic angle spinning (MAS) at 8 kHz.

As such, CO_2 adsorption cannot be attributed to the K^+ in the charged comonomer, which was previously hypothesized to lead to enhanced CO_2 interactions. While these results

do not necessarily validate the simulations discussed in Chapter III, the difficulty in simulating electrochemical microenvironment conditions to obtain CO_2 adsorption measurements is recognized; solid state NMR might not be the most judicious pursuit of such measurements. Limiting current measurements with ultramicroelectrodes to measure CO_2 diffusion coefficient could provide experimental verification of the 2-Phase Thermodynamics computations.[8]

EXPERIMENTAL

Solid state NMR spectroscopy

Solid state ^{13}C NMR spectra were recorded on a Bruker DSX500 (500 MHz for ^{1}H signal; 126 MHz for ^{13}C) spectrometer and a Bruker 4 mm MAS probe. The MAS rate was set to 8 kHz. 100 scans were recorded for each spectrum, and the delay time between each transient was set to 60 s. The chemical shifts were reported with respect to external references of tetramethylsilane.

To ensure reproducibility from well-mixed samples, unless otherwise specified, 44 mg of polymer and 30 mg of glycine hydrochloride ethyl ester were dissolved in acetonitrile, and the volatiles were removed on a rotary evaporator. The dry powder mixture was packed tightly into the probe.

The unsealed rotor was placed in a glassware apparatus to allow for gas addition. The apparatus was pumped down to ~1 mtorr using a high vacuum line.[9] $^{13}CO_2$ (Millipore Sigma, 99.0% ^{13}C, <3% ^{18}O) was used without further purification and measured to 7.0 mmHg in a manometer. The glassware apparatus containing the rotor was exposed to $^{13}CO_2$ for 5 minutes before sealing and removing from the line. The sealed rotor was kept in the sealed glassware until immediately before adding to the NMR spectrometer.

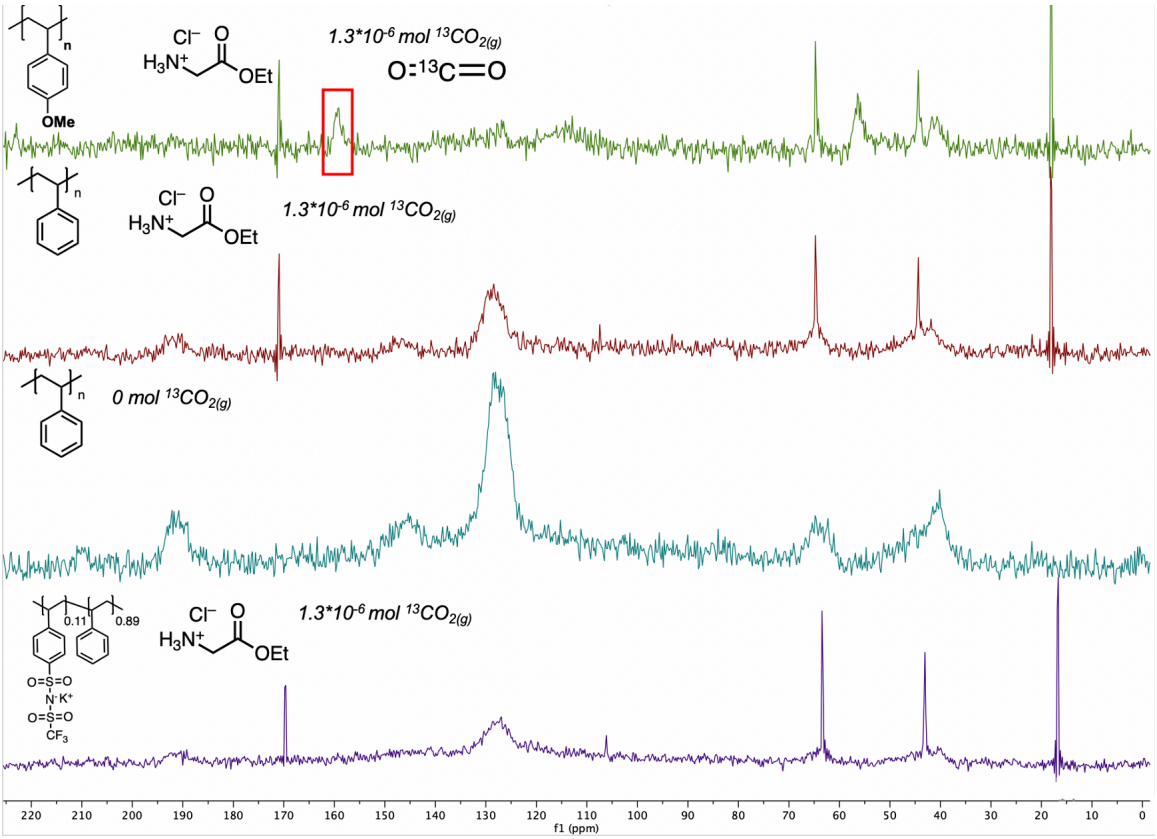

Figure 2. ^{13}C solid state NMR spectra of various polymers. Unless otherwise specified, 44 mg of polymer were mixed with 30 mg of glycine standard. The peak highlighted in the red box is $^{13}CO_2$.

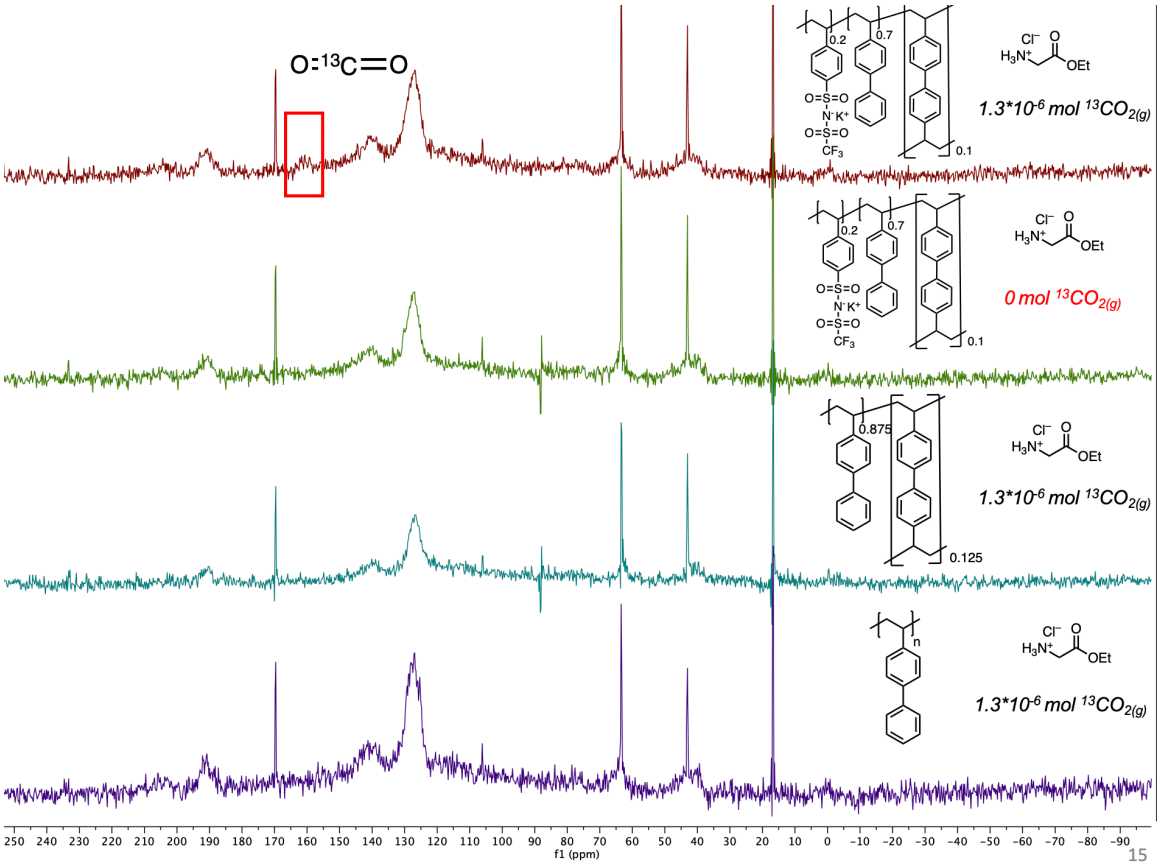

Figure 3. ^{13}C solid state NMR spectra of various polymers. Unless otherwise specified, 44 mg of polymer were mixed with 30 mg of glycine standard. The peak highlighted in the red box is $^{13}CO_2$.

REFERENCES

(1) Kim, C.; Bui, J. C.; Luo, X.; Cooper, J. K.; Kusoglu, A.; Weber, A. Z.; Bell, A. T. Tailored Catalyst Microenvironments for CO2 Electroreduction to Multicarbon Products on Copper Using Bilayer Ionomer Coatings. *Nat. Energy* **2021**, *6* (11), 1026–1034.

(2) Sato, Y.; Takikawa, T.; Sorakubo, A.; Takishima, S.; Masuoka, H.; Imaizumi, M. Solubility and Diffusion Coefficient of Carbon Dioxide in Biodegradable Polymers. *Ind. Eng. Chem. Res.* **2000**, *39* (12), 4813–4819.

(3) Ebner, A. D.; Gray, M. L.; Chisholm, N. G.; Black, Q. T.; Mumford, D. D.; Nicholson, M. A.; Ritter, J. A. Suitability of a Solid Amine Sorbent for CO2 Capture by Pressure Swing Adsorption. *Ind. Eng. Chem. Res.* **2011**, *50* (9), 5634–5641.

(4) Pinto, M. L.; Mafra, L.; Guil, J. M.; Pires, J.; Rocha, J. Adsorption and Activation of CO2 by Amine-Modified Nanoporous Materials Studied by Solid-State NMR and 13CO2 Adsorption. *Chem. Mater.* **2011**, *23* (6), 1387–1395.

(5) Ilkaeva, M.; Vieira, R.; Pereira, J. M. P.; Sardo, M.; Marin-Montesinos, I.; Mafra, L. Assessing CO2 Capture in Porous Sorbents via Solid-State NMR-Assisted Adsorption Techniques. *J. Am. Chem. Soc.* **2023**, *145* (16), 8764–8769.

(6) Witherspoon, V. J.; Xu, J.; Reimer, J. A. Solid-State NMR Investigations of Carbon Dioxide Gas in Metal–Organic Frameworks: Insights into Molecular Motion and Adsorptive Behavior. *Chem. Rev.* **2018**, *118* (20), 10033–10048.

(7) Vieira, R.; Marin-Montesinos, I.; Pereira, J.; Fonseca, R.; Ilkaeva, M.; Sardo, M.; Mafra, L. “Hidden” CO2 in Amine-Modified Porous Silicas Enables Full Quantitative NMR Identification of Physi- and Chemisorbed CO2 Species. *J. Phys. Chem. C* **2021**, *125* (27), 14797–14806.

(8) Petrovick, J. G.; Radke, C. J.; Weber, A. Z. Gas Mass-Transport Coefficients in Ionomer Membranes Using a Microelectrode. *ACS Meas. Sci. Au* **2022**, *2* (3), 208–218.

(9) Burger, B. J.; Bercaw, J. E. Vacuum Line Techniques for Handling Air-Sensitive Organometallic Compounds. In *Experimental Organometallic Chemistry*; ACS Symposium Series; American Chemical Society, 1987; Vol. 357, pp 4–79.

ABOUT THE AUTHOR

Gavin Paul Heim was born and raised in Irvine, California. He completed his undergraduate education in 2018 at the University of California, San Diego, receiving a B.S. in Biochemistry and Chemistry. He was an undergraduate researcher in the lab of Professor Cliff Kubiak studying electron transfer in mixed-valent ruthenium clusters. He defended his PhD dissertation March 2024 at the California Institute of Technology under the advisement of Professor Theo Agapie. His work focused on developing and understanding electrocatalysts for converting small molecule precursors to value-added chemicals. In his free time, Gavin enjoys running, lifting weights, cycling, reading, watching soccer, and spending time with his family. He is looking forward to advancing his career starting a position as Module Development Engineer at Intel in Hillsboro, OR.